UNIVERSITÀ DEGLI STUDI DI PALERMO

Dottorato in Energia e Tecnologie dell'informazione

Dipartimento di Energia, Ingegneria dell'Informazione e Modelli Matematici

Mathematical methods and modeling of energy technologies to support the renewable energy sources integration and the buildings energy flexibility

IL DOTTORE

Airò Farulla Girolama

Il COORDINATORE

Prof. Maurizio Cellura

TUTOR

Prof. Maurizio Cellura

COTUTOR

Ing. Marco Ferraro

Index

Sommario

I dibattiti dell'attuale scenario politico, ambientale ed ecologico sono incentrati sul tema dello "Sviluppo Sostenibile". Nell'ottica di una società in continua evoluzione tale tema sintetizza un problema di grande complessità ovvero rendere compatibili le esigenze dell'economia ed il rispetto dell'ambiente. Per soddisfare l'esigenza di rispondere alle necessità del presente senza compromettere l'uso delle risorse energetiche alle generazioni future, la comunità scientifica è impegnata nel promuovere l'utilizzo di fonti energetiche rinnovabili e lo sviluppo dei relativi processi non solo a livello industriale ma anche residenziale.

Il settore residenziale è responsabile di circa il 40% dell'energia consumata e di quasi il 40% della CO2 emessa a livello globale. La domanda di energia in tale settore negli ultimi 40 anni è cresciuta di quasi il 2% l'anno, si è passati da 1819 Mtep nel 2000 a 2790 Mtep nel 2010. Si prevede un consumo intorno a 4500 Mtep nel 2050. É noto che i principali consumi negli edifici residenziali, e non solo, sono dovuti principalmente a riscaldamento, raffrescamento, produzione di acqua calda sanitaria, illuminazione, elettricità utilizzata per il funzionamento dei dispositivi elettronici e della ventilazione meccanica. In tale settore l'uso delle fonti fossili rimane dominante mentre è marginale quello delle fonti rinnovabili.

In futuro il sistema energetico dovrà basarsi prevalentemente su energia rinnovabile puntando all'ambizioso traguardo della generazione "CO2 free". In accordo a quanto discusso al tavolo della Conferenza delle Nazioni Unite sui cambiamenti climatici di Parigi tenutasi nel dicembre 2015, per limitare l'aumento della temperatura media globale al di sotto di 1,5 ° C al di sopra del livello preindustriale, l'emissione netta di CO2 dovrebbe essere prossima allo zero entro il

2050. Considerando che nel 2050 almeno il 70% del patrimonio edilizio esistente sarà ancora utilizzato e che è previsto almeno un aumento del 25% della superficie costruita è necessario prevedere efficienti tecnologie non solo a supporto della diffusione di nuovi edifici ma anche a rafforzamento delle prestazioni energetiche di quelli esistenti. La necessità di trasformazione del settore edilizio nasce non solo dalla richiesta di soluzioni abitative maggiormente confortevoli ma soprattutto dall'obiettivo di ridurre gli impatti energetico-ambientali. Gli edifici ad energia quasi zero (nZEB) e netta zero (NZEB), caratterizzati da una richiesta energetica minima, sono tra i principali protagonisti dello sviluppo sostenibile. Un edifico nZEB, realizzato in accordo ai principi della progettazione sostenibile e bioclimatica, ha un fabbisogno energetico molto basso, o quasi nullo, poiché la parta significativa della sua richiesta energetica è ricoperta da energia rinnovabile prodotta in situ. La precisa definizione di nZEB è consultabile nella Direttiva Europa 31/2010/UE recepita dal Dlgs192 del 2005.

Costruzione di nZEB e soluzioni di retrofitting in edifici esistenti stanno giocando un ruolo cruciale sia per raggiungere alti livelli di autosufficienza che per incrementare le prestazioni energetiche degli edifici.

Utilizzo di materiali avanzati, aggiunta di strati di isolante, miglioramento dell'involucro edilizio sono esempi di misure adottate con lo scopo di migliorare le prestazioni energetiche degli edifici. Isolamento termico esterno e pareti ventilate sono le soluzioni di retrofit maggiormente adottate. La parete ventilata elimina l'irraggiamento diretto consentendo un risparmio energetico fino al 20%,

Le pareti ventilate, in particolare si possono considerare come una soluzione intermedia tra le facciate continue e i sistemi a cappotto. L'aspetto peculiare della parete ventilata è l'intercapedine delimitata tra la parete stessa e il rivestimento esterno dell'edifico. In essa, infatti, l'aria che entra dal basso verso l'alto crea un efficace moto convettivo che favorisce la traspirabilità dell'edificio. Lo sfruttamento di tale ventilazione e l'adozione di un adeguato sistema isolante permette di ridurre la dispersione di calore durante la stagione invernale ed evitarne l'accumulo durante quella estiva. In estate i moti convettivi premettono all'aria surriscaldata che si forma

di essere espulsa dalla sommità dell'edifico diminuendo gli apporti termici. In inverno, la ventilazione favorisce l'eliminazione del vapore d'acqueo riducendo il fenomeno della condensa e la dispersione di calore verso l'esterno associato ad eventuali penetrazioni di acqua all'interno dell'edifico.

Tra le opzioni maggiormente investigate vi sono le pareti ventilate integrate con pannelli fotovoltaici che ad oggi rappresentano la tecnologia maggiormente sviluppata sul mercato. L'utilizzo del fotovoltaico come materiale da costruzione rappresenta una delle più grandi innovazioni tecnologiche nel settore edilizio. Il materiale fotovoltaico si può anche utilizzare in sostituzione di materiali da costruzione convenzionali in parti dell'involucro edilizio come il tetto e i lucernari.

Nelle pareti ventilate con fotovoltaico integrato, l'effetto camino che si instaura nella cavità fra il pannello e la parete dell'edificio consente non solo di migliorare le prestazioni termofisiche dell'edificio ma anche di incrementare l'efficienza del fotovoltaico. È noto, infatti, che in condizioni di funzionamento reale il rendimento fotovoltaico diminuisce all'aumentare della temperatura delle celle. Alte temperature della cella determinano una riduzione della potenza prodotta dal pannello a parità di radiazione solare.

All'interno di questa area di ricerca a supporto dell'efficientamento e della produzione di energia da fotovoltaico, alla Maker Faire di Roma, il principale evento europeo sull'innovazione, il CNR-ITAE (Istituto tecnologie avanzate per l'energia "Nicola Giordano") ha presentato un prototipo ibrido di facciata attiva denominato E-Brick. Si tratta di un componente edilizio da installare in pareti verticali esterne allo scopo di realizzare facciate continue per la riqualificazione energetica degli edifici. Nello specifico l'E-Brick è costituito da un modulo fotovoltaico (70 cm ×70 cm) in silicio policristallino da 64W inserito in un sandwich a doppio vetro, una batteria al titanato di litio da 23 Ah integrata nell'intercapedine ed un pannello isolante in lana di roccia per l'isolamento dell'edificio.

Raffrescamento della parete, isolamento termico dell'edificio, produzione, accumulo e distribuzione dell'energia elettrica costituiscono il cuore di E-Brick.

In tale lavoro di tesi è stato analizzato il modulo E-Brick per valutarne le

prestazioni termiche. Si è analizzato in dettaglio un prototipo sito presso il CNR-ITAE (Messina) la cui peculiarità è l'utilizzo di componenti elettronici all'interno della cavità. Nello specifico sulla parete isolante due boxes, uno contenete l'inverter l'atro la batteria a ioni-litio, contribuiscono alla dissipazione del calore all'interno della cavità. Il pannello, in questo modo, si riscalda sia per effetto della radiazione termica diretta sia per effetto dell'energia elettrica dissipata per effetto Joule dal pannello stesso. Obiettivo di questo specifico design innovativo è stata la valutazione dell'incidenza dei componenti integrati (PV e componenti elettronici) sulla distribuzione di temperatura all'interno del canale e sulle prestazioni energetiche globali della parete ventilata. Valutare le temperature superficiali raggiunte dal pannello è fondamentale per stabilire non solo la sua efficienza ma anche per stabilire la compatibilità con i materiali con cui è costruito l'involucro edilizio con il quale il pannello è accoppiato.

Allo scopo di verificare se le condizioni termiche imposte possano favorire un regime di moto convettivo efficiente per la corretta funzionalità della parete ventilata sono state condotte una serie di simulazioni termo fluidodinamiche. È stato utilizzato il software agli elementi finiti Comsol 5.6 il cui Workbench integra i simulatori di diverse problematiche fisiche, i tools per la generazione delle griglie di calcolo e i tools di ottimizzazione ed esplorazione di design. I dati di producibilità del pannello da utilizzare come input del modello fluidodinamico sviluppato sono stati ricavati sperimentalmente collegando i pannelli ai terminali del circuito a bassa impedenza di un carico elettronico in corrente continua.

L'ibrido proposto ha dei benefici sia dal punto di vista del pannello che dell'edificio. Dal punto di vista del pannello ne migliora la producibilità sfruttando l'effetto di raffrescamento indotto dalla cavità, dal punto di vista dell'edifico, poiché viene eliminato l'irraggiamento diretto, si ha un risparmio energetico.

Un edificio, integrato di E-brick soddisfa sia l'esigenza di un minor fabbisogno energetico sia una piena ed efficace integrazione delle rinnovabili. Risparmio energetico e integrazione delle rinnovabili sono i due aspetti principali della flessibilità energetica. La transizione verso una società sostenibile e un'economia

climaticamente neutra entro il 2050 richiede un ampio dispiegamento nell'uso di fonti energetiche rinnovabili che, a causa dell'aleatorietà e non programmabilità della maggior parte di esse, può compromettere seriamente la stabilità delle reti energetiche. In questo contesto, gli edifici sono sempre più visti come una potenziale fonte di flessibilità energetica per la rete elettrica.

Se in futuro l'obiettivo è una eco-design di successo, per qualsiasi tipo di edificio, e ancor più nel caso degli nZEB, si deve tenere conto anche della flessibilità energetica dei suoi sistemi energetici, dell'interazione con l'infrastruttura a cui l'edificio sarà collegato e della fornitura di servizi a questa infrastruttura.

Fra le varie definizioni disponibili in letteratura è qui riportata quella approvata nel contesto dell'Annex 67: capacità di un edificio di gestire la propria domanda e generazione in base alle condizioni climatiche locali, alle esigenze degli utenti e ai requisiti della rete.

La quantificazione della flessibilità energetica è un processo complesso che fa fronte alle esigenze sia degli utenti che dei gestori di rete. Questa complessità ha fatto sì che, ad oggi, manca sia una definizione univoca di flessibilità energetica di un edificio che un metodo per quantificarla.

Ad oggi, il modo migliore per incrementare la flessibilità degli edifici, consentendo al contempo una maggiore integrazione delle rinnovabili, è l'utilizzo di tecnologie basate sull'accumulo termico sensibile, latente o termochimico.

I sistemi termochimici accoppiati alla conversione power-to-heat stanno ricevendo una crescente attenzione grazie alle loro migliori prestazioni rispetto alle tecnologie di accumulo di calore sensibile e latente, in particolare, in termini di dinamica del tempo di accumulo e densità energetica. Ad oggi una seri di limiti li rende poco redditivi dal punto di vista commerciale ma l'elevata efficienza nel bilanciare l'eccesso di generazione rinnovabile è l'aspetto chiave che potrebbe portare questa applicazione verso un crescente sviluppo nel prossimo futuro.

Il lavoro di tesi, sommariamente descritto, è stato articolato come segue:

- Capitolo1: il focus è l'importanza rivestita dal settore edilizio nel contesto della "clean energy transition". Sono brevemente riportate e descritte le principali

direttive emanate a livello europeo per raggiungere il target di edifico ad energia quasi zero (nZEB): EPBD (Energy Performance of Building Directive), EED (Energy Efficiency Directive), RED (Renewable Energy Directive). Vengono descritte le principali strategie di efficienza energetica discusse dagli esperti nel contesto del SET-Plan europeo.

- Capitolo 2: il focus è un'analisi approfondita dello stato dell'arte sulla flessibilità energetica degli edifici con lo scopo di evidenziare le sue potenzialità e criticità nel processo di decarbonizzazione ed integrazione delle energie rinnovabili. Nello specifico più di 300 articoli sono stati selezionati, studiati, analizzati criticamente e classificati con particolare focus sugli obiettivi di ricerca evidenziati nel contesto dell'Annex 67. Sono stati riportati e descritti i principali indicatori di flessibilità ad oggi presenti in letteratura. Gli indicatori, classificati in indicatori di rete e indicatori energetici, sono stati selezionati da studi teorici, sperimentali e numerici sviluppati nel contesto delle principali strategie di flessibilità del "demand side management". L'analisi degli indicatori di flessibilità ha permesso di definire le attuali lacune esistenti in questo campo e sottolineare gli aspetti da affrontare in futuro.
- Capitolo 3: il focus è un'analisi approfondita dello stato dell'arte degli studi teorici, sperimentali e numerici disponibili in letteratura sui sistemi di accumulo di energia termica termochimica e sul loro utilizzo nelle applicazioni "power-to-heat" per l'integrazione di fonti di energia rinnovabili. Viene sottolineato come la risoluzione di sfide specifiche, ad esempio la durata e la stabilità del materiale di stoccaggio e l'alto costo dei sistemi di riscaldamento/termochimici potrebbe aumentare il livello di prontezza tecnologica di questo concetto emergente di integrazione dei sistemi energetici.
- Capitolo 4: vengono descritti i test sperimentali condotti pannelli fotovoltaici per valutarne la producibilità. Nello specifico sono riportati i dati raccolti durante i seguenti test: caratterizzazione in modalità potenziostatica, caratterizzazione con inseguimento del punto di massima potenza, caratterizzazione con simulatore

solare a temperatura controllata. I dati raccolti mostrano l'effetto della variazione solare, angolo di inclinazione dei pannelli e ombreggiamento sulla producibilità. Nella seconda parte del capitolo sono descritti i test condotti sul prototipo E-brick allo scopo di valutare la riposta termica dello stesso.

- Capitolo 5: viene descritto il modello termofluidodinamico dell'E-Brick. La modellizzazione del caso studio è stata articolata come segue:

  1 modello numerico del pannello fotovoltaico in modalità "free standing" al fine di studiarne la risposta termica per differenti condizioni esterne di temperatura e irraggiamento;

  2 modello numerico della parete ventilata per valutare gli effetti sul comportamento termo-elettrico del pannello tramite un analisi di sensitività al variare delle condizioni al contorno

  3 modello numerico della parete ventilata integrata con componenti elettronici per valutare gli effetti sul comportamento termo-elettrico del pannello.

Abstract

The debates of the current political, environmental and ecological scenario are centred on the theme of "Sustainable Development". From the perspective of a constantly evolving society, this issue summarizes a problem of great complexity, namely making the needs of the economy and respect for the environment compatible. To meet the need to respond to the needs of the present without compromising the use of energy resources for future generations, the scientific community is committed to promoting the use of renewable energy sources and the development of related processes not only at an industrial level but also residential.

The residential sector is responsible for about 40% of the energy consumed and almost 40% of the CO2 emitted globally. The demand for energy in this sector in the last 40 years has grown by almost 2% per year, it has gone from 1819 Mtoe in 2000 to 2790 Mtoe in 2010. Consumption is expected to be around 4500 Mtoe in 2050. It is known that the main consumptions in residential buildings, and not only, are mainly due to heating, cooling, production of domestic hot water, lighting, electricity used for the operation of electronic devices and mechanical ventilation. In this sector, the use of fossil sources remains dominant while that of renewable sources is marginal.

In the future, the energy system will have to be mainly based on renewable energy, aiming at the ambitious goal of “CO2 free” generation. In accordance with what was discussed at the table of the United Nations Conference on Climate Change in Paris held in December 2015, to limit the increase in the global average temperature to below 1.5 ° C above the pre-industrial level, the emission net CO2 should be close to zero by 2050. Considering that in 2050 at least 70% of the existing building stock

will still be used and that at least a 25% increase in the built area is expected, it is necessary to provide efficient technologies not only to support the diffusion of new buildings but also to strengthen the energy performance of existing ones. The need for transformation in the construction sector arises not only from the demand for more comfortable housing solutions but above all from the goal of reducing energy-environmental impacts. Nearly zero energy (nZEB) and net zero (NZEB) buildings, characterized by minimal energy demand, are among the main protagonists of sustainable development. An nZEB building, built in accordance with the principles of sustainable and bioclimatic design, has a very low or almost zero energy requirement, since the significant part of its energy demand is covered by renewable energy produced in situ. The precise definition of nZEB can be consulted in the Europe Directive 31/2010 / EU implemented by Legislative Decree 192 of 2005.

Construction of nZEB and retrofitting solutions in existing buildings are playing a crucial role both in achieving high levels of self-sufficiency and in increasing the energy performance of buildings.

The use of advanced materials, adding layers of insulation, improving the building envelope are examples of measures taken with the aim of improving the energy performance of buildings. External thermal insulation and ventilated walls are the most adopted retrofit solutions. The ventilated wall eliminates direct radiation allowing energy savings of up to 20%.

Ventilated walls, in particular, can be considered as an intermediate solution between curtain walls and external insulation systems. The peculiar aspect of the ventilated wall is the gap defined between the wall itself and the external cladding of the building. In it, in fact, the air that enters from the bottom upwards creates an effective convective motion that favours the breathability of the building. The exploitation of this ventilation and the adoption of an adequate insulating system allows to reduce the dispersion of heat during the winter season and avoid its accumulation during the summer. In summer, convective motions press the overheated air that forms to be expelled from the top of the building, reducing the heat input. In winter, ventilation favours the elimination of water vapor by reducing

the phenomenon of condensation and the dispersion of heat to the outside associated with any penetration of water inside the building.

Among the most investigated options are the ventilated walls integrated with photovoltaic panels which today represent the most developed technology on the market. The use of photovoltaics as a building material represents one of the greatest technological innovations in the construction sector. The photovoltaic material can also be used to replace conventional building materials in parts of the building envelope such as the roof and skylights.

In ventilated walls with integrated photovoltaics, the chimney effect that is established in the cavity between the panel and the building wall allows not only to improve the thermophysical performance of the building but also to increase the efficiency of the photovoltaic. It is known, in fact, that in real operating conditions the photovoltaic yield decreases as the temperature of the cells increases. High cell temperatures cause a reduction in the power produced by the panel with the same solar radiation. Within this research area to support the efficiency and production of photovoltaic energy, at the Maker Faire in Rome, the main European event on innovation, the CNR-ITAE (Institute of advanced technologies for energy "Nicola Giordano" Presented a hybrid prototype of an active facade called E-Brick. It is a building component to be installed in external vertical walls in order to create curtain walls for the energy requalification of buildings. Specifically, the E-Brick consists of a photovoltaic module (70 cm × 70 cm) in 64W polycrystalline silicon inserted in a double glass sandwich, a 23 Ah lithium titanate battery integrated in the cavity and an insulating panel in rock wool for building insulation.

Wall cooling, thermal insulation of the building, production, storage and distribution of electricity are the heart of E-Brick.

In this thesis work the E-Brick module was analysed to evaluate its thermal performance. A prototype site at the CNR-ITAE (Messina) was analysed in detail, the peculiarity of which is the use of electronic components inside the cavity. Specifically, on the insulating wall two boxes, one containing the inverter and the other the lithium-ion battery, contribute to the dissipation of heat inside the cavity. In

this way, the panel heats up both due to the effect of direct thermal radiation and the effect of the electrical energy dissipated by the Joule effect from the panel itself. The objective of this specific innovative design was the evaluation of the incidence of integrated components (PV and electronic components) on the temperature distribution inside the duct and on the overall energy performance of the ventilated wall. Evaluating the surface temperatures reached by the panel is essential to establish not only its efficiency but also to establish compatibility with the materials with which the building envelope with which the panel is coupled is constructed.

In order to verify whether the thermal conditions imposed can favour an efficient convective motion regime for the correct functionality of the ventilated wall, a series of thermo-fluid dynamics simulations have been carried out. Finite element software COMSOL 5.6 was used, whose Workbench integrates simulators of various physical problems, tools for generating calculation grids and tools for design optimization and exploration. The manufacturability data of the panel to be used as input of the developed fluid dynamics model were obtained experimentally by connecting the panels to the terminals of the low impedance circuit of a direct current electronic load.

The proposed hybrid has benefits from both the panel and the building point of view. From the point of view of the panel it improves its producibility by exploiting the cooling effect induced by the cavity, from the point of view of the building, since direct radiation is eliminated, there is an energy saving.

A building, integrated with E-brick, satisfies both the need for a lower energy requirement and a full and effective integration of renewables. Energy saving and integration of renewables are the two main aspects of energy flexibility. The transition to a sustainable society and a climate-neutral economy by 2050 requires a wide deployment in the use of renewable energy sources which, due to the uncertainty and non-programmability of most of them, can seriously compromise the stability of energy networks. In this context, buildings are increasingly seen as a potential source of energy flexibility for the electricity grid.

If in the future the goal is a successful eco-design, for any type of building, and even more so in the case of nZEB, we must also take into account the energy

flexibility of its energy systems, the interaction with the infrastructure to which the building will be connected and service provision to this infrastructure.

Among the various definitions available in the literature, here is the one approved in the context of Annex 67: ability of a building to manage its own demand and generation based on local climatic conditions, user needs and network requirements.

The quantification of energy flexibility is a complex process that addresses the needs of both users and grid operators. This complexity has meant that, to date, there is a lack of both a univocal definition of a building's energy flexibility and a method to quantify it.

To date, the best way to increase the flexibility of buildings, while allowing greater integration of renewables, is the use of technologies based on sensitive, latent or thermochemical thermal storage.

Thermochemical systems coupled to power-to-heat conversion are receiving increasing attention due to their better performance than sensible and latent heat storage technologies, in particular, in terms of accumulation time dynamics and energy density. To date, a series of limits make them not very profitable from a commercial point of view but the high efficiency in balancing the excess of renewable generation is the key aspect that could lead this application towards a growing development in the near future.

The thesis work, briefly described, was structured as follows:

- Chapter 1: the focus is on the importance of the construction sector in the context of the "clean energy transition". The main directives issued at European level to reach the target of almost zero energy building (nZEB) are briefly reported and described: EPBD (Energy Performance of Building Directive), EED (Energy Efficiency Directive), RED (Renewable Energy Directive). The main energy efficiency strategies discussed by the experts in the context of the European SET-Plan are described.
- Chapter 2: the focus is an in-depth analysis of the state of the art on the energy flexibility of buildings with the aim of highlighting its potential and critical issues in the process of decarbonization and integration of renewable energy.

Specifically, more than 300 articles have been selected, studied, critically analyzed and classified with particular focus on the research objectives highlighted in the context of Annex 67. The main flexibility indicators currently in the literature have been reported and described. The indicators, classified into network indicators and energy indicators, were selected from theoretical, experimental and numerical studies developed in the context of the main flexibility strategies of "demand side management". The analysis of the flexibility indicators made it possible to define the current gaps in this field and highlight the aspects to be addressed in the future.

- Chapter 3: the focus is an in-depth analysis of the state of the art of theoretical, experimental and numerical studies available in the literature on thermochemical thermal energy storage systems and their use in "power-to-heat" applications for integration of renewable energy sources. It is emphasized that the resolution of specific challenges, such as the durability and stability of the storage material and the high cost of heating / thermochemical systems could increase the level of technological readiness of this emerging concept of energy systems integration.
- Chapter 4: the experimental tests conducted on photovoltaic panels are described to evaluate their producibility. Specifically, the data collected during the following tests are reported: characterization in potentiostatic mode, characterization with tracking of the maximum power point, characterization with a solar simulator at a controlled temperature. The data collected show the effect of solar variation, the inclination angle of the panels and shading on the producibility. The second part of the chapter describes the tests conducted on the E-brick prototype in order to evaluate its thermal response.
- Chapter 5: the thermo-fluid dynamic model of the E-Brick is described. The modeling of the case study was structured as follows:

    1 numerical model of the photovoltaic panel in "free standing" mode in order to study its thermal response for different external conditions of temperature and radiation.

2 numerical model of the ventilated wall to evaluate the effects on the thermo-electrical behavior of the panel through a sensitivity analysis when the surrounding conditions vary

3 numerical model of the ventilated wall integrated with electronic components to evaluate the effects on the thermo-electrical behavior of the panel.

Chapter 1

NZEB concept and its improvement

1. Introduction

The integration of renewable energy sources (RES) while replacing the conventional based on fossil fuels energy sources is the main goal of several specific legislative tools, i.e., the European Commission [1,2].

In future, world energy system must be predominantly based on renewable power aiming the ambitious target of the "CO_2-free power generation". According to the Paris UN Climate Change Conference held inDecember2015 [3], to limit the global mean temperature rise under 1.5 °C above the preindustrial level the CO_2 net emission to be close to zero by 2050. The global atmospheric CO_2 concentration (GACC) is the central theme of several climate policies whose aim is to stop its growth trend. Charles David Keeling started GACC measurements in1958 at Mauna Loa Observatory (Hawaii). As shown in Figure 1, GACC level over the years it is rapidly growing, it has been predicted that its level continues to increase the consequent global warming would seriously disrupt the climate [4]. In 1895, the chemist Arrhenius calculated that doubling the CO_2 concentration in atmosphere its average temperature will increase by about 5-6 °C [5]. It is for this reason that the G8 leaders expressed their goodwill with all countries the goal of reaching at least 50% reduction

of global emission by 2050.

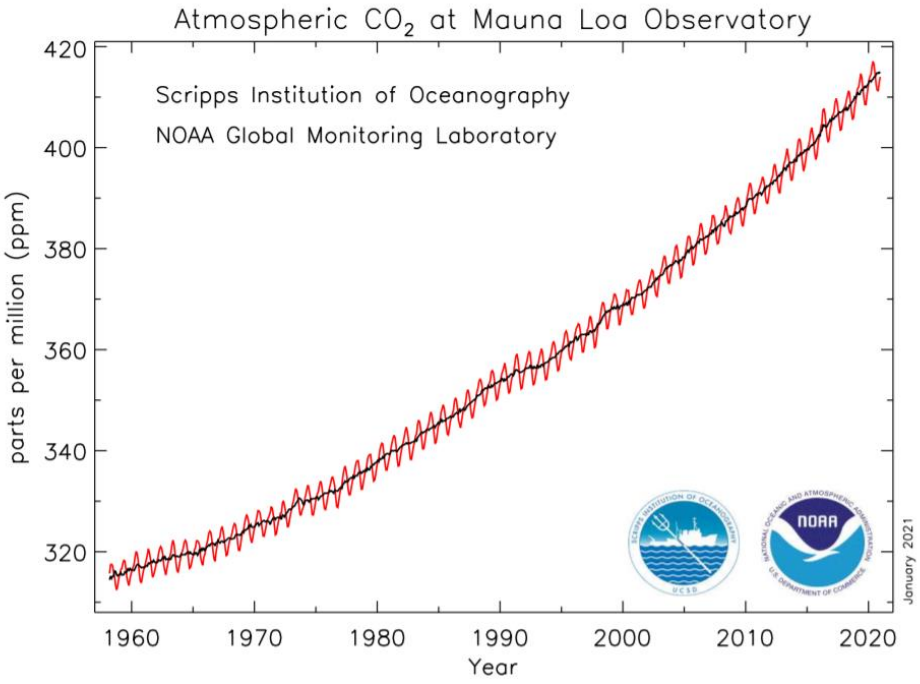

Figure 1: Annual trend of mean CO2 concentration in dry air [6].

The only way to reduce GACC is to adopt pathways for shifting away from fossil fuels. Replacing fossil fuels with renewable energy sources, energy efficiency improvement, CO_2 capture and storage, CO_2 recycling are the main pathways investigated to reach this goal.

In many developed countries, active policies are contributing to address the current market barriers and promote the investments to facilitate RES penetration [7]. For instance, Italy set a target of 30% RES as an average for electrical energy, thermal energy and transport systems [8], Denmark a target of 100% by 2050 [9]. Increasing the EU's climate ambition for 2030 and 2050 is among the goals of the European Green. China emits around one-quarter of the world's greenhouse gases, the largest share in the world so the ccountry has made massive investments in renewables, depositing 0.9% of its gross domestic product (GDP) into the sector in 2015 [10].

It is the third-highest amount worldwide after Chile and South Africa, which each invested 1.4% of GDP. The growing renewable penetration is leading to important challenges in planning and controlling the energy production, transmission and distribution [11–13]. In particular, the traditional distribution systems are transforming from uni-directional centralized systems to bi-directional decentralized systems [14]. The renewable production is usually not adjusted in order to match electricity demands [15,16]. The renewable production is not dispatchable so the increasing penetration of RES maybe lead to a loss of generation control and predictability affecting the stability of the energy system[17]. To facilitate the RES integration in the existing infrastructures the flexibility of the power system must be increased aiming to achieve , the instant balance of temporal and spatial mismatches between generation and loads [18–21]. Import and export of energy over the system boundaries, energy storage, power-to-X technologies, as well as different demand response mechanisms, are example of flexibility sources [22].

The future power system will be characterized by a transition from a system dispatching energy following electrical demand to a Smart Grid (SG) handling a portfolio of controllable demand to match uncontrollable supply [23,24]. Building sector is expected to have an important role in future Smart Grids/Energy networks [25]. Smart grids where both demand and local production in the distribution networks are controlled to stabilize the energy networks are a more intelligent way of consuming electricity in order to avoid congestion problems [26]. The Smart Grid context is creating the opportunity for consumers to behave prosumers offering services to utility grids [27–29].

Looking at the consume of energy, several reports indicate for the building sector an account for about 35-40 % of primary energy and 36% of CO_2 emissions [30,31] and the biggest contributors of final power consumption followed by industry and transport [32]. Heating, ventilation and air conditioning (HVAC) systems are responsible for almost half of the buildings' energy consumption [33,34]. This sector shows a high potential for energy saving opportunities [35–37].

The main challenge in this sector is to achieve zero energy buildings producing,

at least, as much as energy as they consume [38,39]. Reducing energy needs, energy consumption and increasing of the renewable energies are crucial steps imposed by the reference standard of nearly zero energy buildings (nZEBs) or Net zero energy buildings (NZEBs) [40–43]. The energy performance of a building shall be determined on the basis of the calculated or actual annual energy that is consumed in order to meet the different needs associated with its typical use and shall reflect the heating energy needs and cooling energy needs (energy needed to avoid overheating) to maintain the envisaged temperature conditions of the building, and domestic hot water needs. The ambitious concept of nZEB imposed by the European Union (EU) has several challenges as buildings no longer only consume (consumers), but also generate energy (prosumers) [44,45]. The transition from passive consumers to active prosumers buildings end-users will play a more active role in the management of electric power supply and demand [46]. Consequently, the grid must be restructured to account both the energy demand and the local energy generation [47]. Smart grids with real time control capabilities as well as bidirectional communications with prosumers are needed to facilitate the fast development of sustainable energy productions and utilizations [48].

1.1. Building energy demand

In order to be able to develop and implement successful energy strategies in the buildings it is necessary to know their energy demand. Buildings represent about 40% of EU final consumption and 60% of electricity consumption [49]. In 2016, the residential energy consumption amounted to 25 % of the EU's final energy consumption, representing the second largest consuming sector after transport (33.2%) [50]. As shown in Figure 2 around two thirds of the energy consumption of buildings is for residential buildings. In some countries such as Luxembourg or Malta, non-residential buildings (i.e. services) are dominant and represent more than half of the total consumption of buildings. Non-residential buildings, comprising a more complex and heterogeneous sector compared to the residential sector, account

for 25% of the total stock in Europe. In the residential sector energy is mainly used for heating space and domestic heat water (DHW). Energy consumption depends on the external weather conditions, HVAC systems used and on the building characteristics. Really, energy consumption is also affected by other possible determinants, i.e., economic conditions, population status, climatic conditions, household characteristics, energy prices.

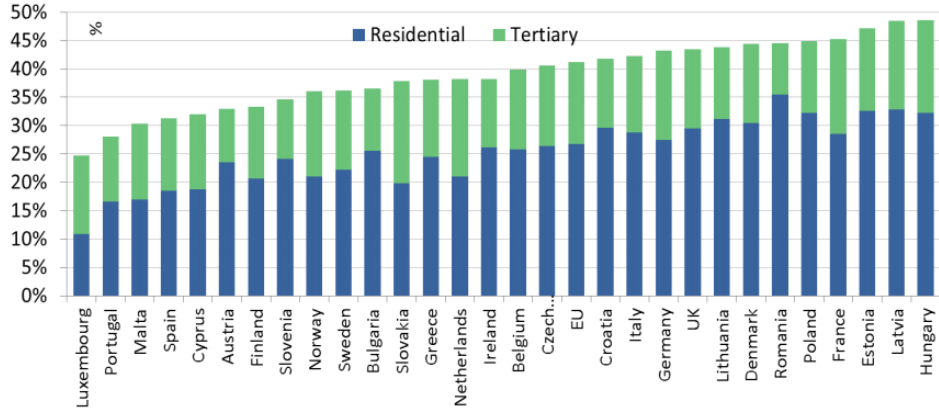

Figure 2: Building energy consumption [51].

In Figure 3 it is reported the final residential energy consumption trend at European level as function of the weather conditions measured in Heating Degree Days (HDD). The energy consumption trend follows a fluctuating dynamic. In particular it can be observed that after a peak in 2010 (322 MTOE) the energy consumption reached its minimum value (267 MTOE) in 2014. These data are the maximum and the minimum values monitored for the 29-years period from 1990 to 2018. During this time framework the final residential energy consumption has dropped by 4.5%, from 291.3 MTOE to 278.1 MTOE while it dropped by 1.6% compared to 2017. Figure 3 shows that there is a strong correlation between weather conditions and final energy consumption in residential sector. Weather and climate are environmental conditions that affect energy consumption in fact, for instance, hot summer seasons or severity of winter can lead to occasional consumption peaks.

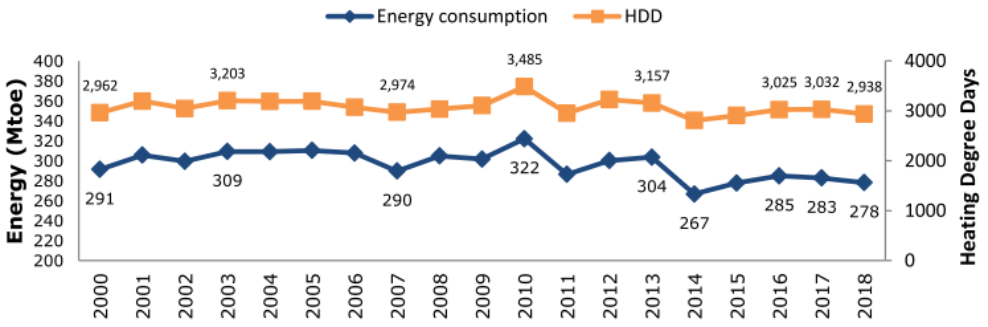

Figure 3: Final residential energy consumption and HDD in the EU-28, 2000-2018 [52].

In 2009 the society crisis concern and the economic repercussion may explain the negative correlation between both variables (final energy consumption and HDD) On the contrary the final consumptions increased in 2013 despite a reduction of HDD, probably because of new positive outlook for the European economy.

In particular economic development is positively correlated with total final energy consumption. Economic growth is usually accompanied by a more efficient usage of energy, due to the adoption of more energy efficient equipment resulting in lower energy consumption levels. In the household sector a development in this sense can translate into more efficient appliances and systems and better insulated buildings.

In Figure 4 it is reported the yearly growth rate percentage. It can be observed that from 2003 to 2006 the consumption remained quasi-constant while the highest change of -0.8% was reached between 2005 and 2006. Since 2007 onwards, the final residential energy consumption has registered an almost continuous fluctuation.

It can be noted that when consumption decreases, the growth rate is higher compared to when the energy consumption grows. Natural gas and electricity are the main energy sources for the residential sector as shown Figure 5 referred to the final residential energy consumption in the EU-28 in 2018.

In 2018, natural gas has accounted for 36.2% of the consumption, followed by electrical energy (24.6%) and renewable energies and biofuels (17.6%). Compared to the year 2000, there are several changes in the ranking and the share of energy

sources. In particular, the share of renewable energies has increased from 10.3% to 17.6%. Renewable energies are the third contributor to the energy mix in residential sector in 2018 while it was the fourth one in 2000. Electricity also increased its share from 21.2% to 24.6%. On the other hand, oil and petroleum products reduced their share from 19.8% in 2000 to 10.8% in 2017. Natural gas reduced its share but it maintains the first ranking position also in 2018. From 2017 to 2018, there are no changes in the ranking of energy sources and slight changes in their shares.

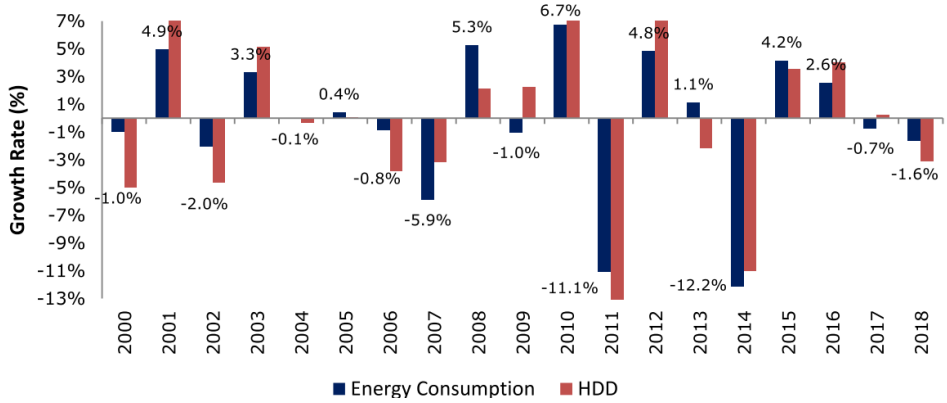

Figure 4: Final residential energy consumption and HDD annual growth rates [52].

More of the 45% of the existing building stock were constructed before the 1970s when energy building regulation was very limited. In contrast to new buildings that can be constructed with high performance levels, most of Europe's exiting building stock is energetically inefficient. In the existing buildings lies the largest energy saving potential, for instance, through renovation or retrofitting energy demand could be largely reduced as far as it is economically and technically feasible. Improvement of the energy performance and renovation of the existing building stock are expected to have a key role in the reduction of the building energy demand. The term renovation can be used for a wide variety of improvements. Installation of renewable energy sources technologies and replacement of building element to reduce energy consumption are example of renovate and, in the meanwhile innovative solutions.

Achieving energy savings and high energy performance in the building sector is a complex process requiring a long vision strategy.

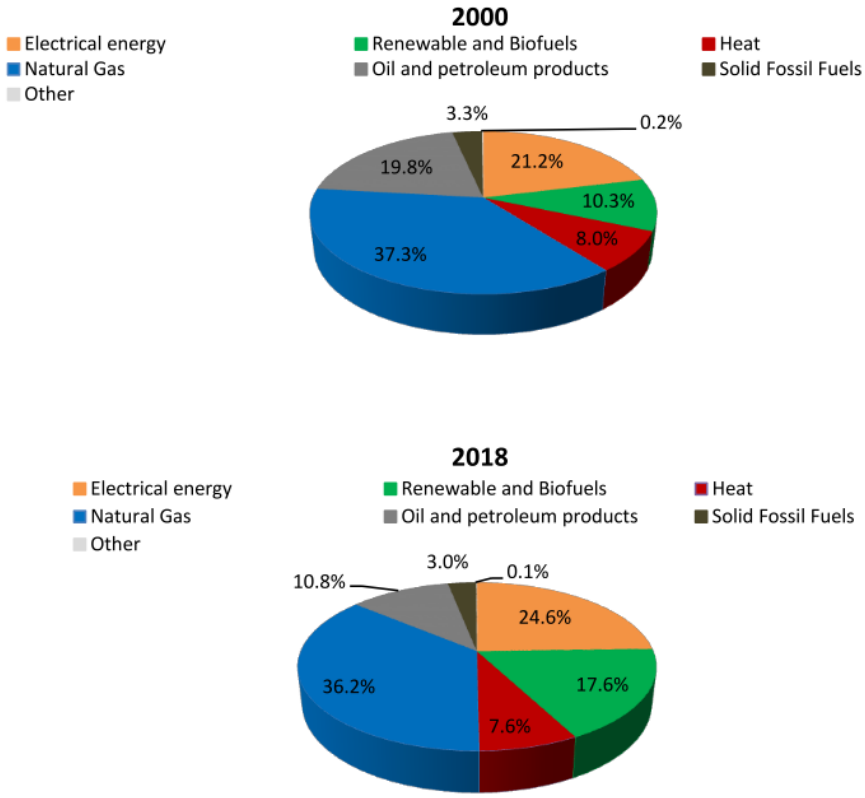

Figure 5: Specific final residential energy consumption in the EU-28, 2000 and 2018 [52].

1.2. Building CO_2 emissions

Buildings account for about a third of greenhouse gas emissions, of which about two-thirds are attributed to residential buildings. With the adoption of nZEB throughout the EU from 2020 onwards, these values will be reduced in a sustainable way. As shown in Figure 6 Greenhouse gas (GHG) emissions from the building sector have more than doubled since 1970 to reach 9.18 $GtCO_2eq$ in 2010. Most of GHG emissions (6.02 Gt) are indirect CO_2 emissions owing to electricity use in buildings.

In contrast to direct emissions showing a dynamic growth the direct emissions have roughly stagnated.

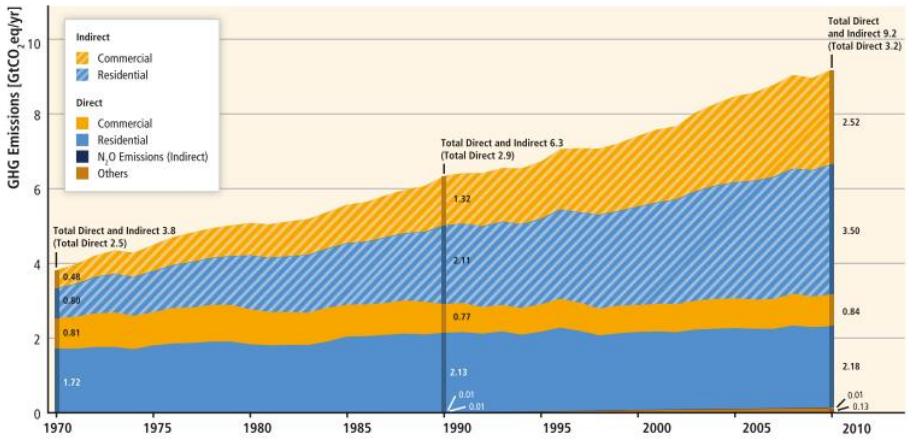

Figure 6: GHG emissions in the building sector [53].

According to the current energy usage and emission intensity it is estimated that carbon emission share of the building sector will be up to 50% by 2050 [54]. High energy performances buildings are crucial to support the reducing GHG emissions. The primary energy use of a building reflects the depletion of fossil fuels and is almost proportional to CO_2 emissions so a reduced energy consumption should lead to a proportional reduction of CO_2 emissions.

Promoting sustainable energy systems technologies, CO_2 reduction strategies have become crucial aspects of the energy planning, energy supply and policymaking at world level. Solar energy technologies are among the most investigated alternatives to help to mitigate carbon emissions by replacing more carbon intensive sources for heat and power. Higher is the amount of conventional heat displaced higher is the amount of mitigated emissions.

On March 2011, the European Commission adopted the "Roadmap for moving to competitive low carbon economy" establishing a long-term goal of reducing CO_2 emissions for the building sector by 88-91% by 2050 compared to 1990 levels [55]. EU policymakers recognise the importance of energy efficient buildings to mitigate

climate change, according to future challenges without any reduction regulation CO_2 emissions could be triple by 2050.

2. EU Regulatory Directives on buildings

Directives setting minimum requirements, obligations and measures for all Member States are the main EU instrument reducing energy consumption of buildings. They play a key role since the Member States are encouraged to adopt innovative solutions to harness energy savings opportunities in the building sector [56]. They are essential both in the addressing the reduction of the environmental impacts and in by targeting different aspects of energy savings and in the influencing the consumers behaviour.

Update directives, such as the Energy Performance of Building Directive (Directive 2018/844/EU), can be considered concrete deliveries of the "Clean energy for all Europeans package" (CEP), the latest update in the European energy policy framework. Aiming to facilitate a clean energy transition and the implementation of the Energy Union strategy goals, CEP is the most ambitious set of energy proposals ever presented by the European Commission [57].

Energy efficiency, renewable energy sources implementation, clean and safe mobility, circular economy, infrastructures and interconnections, bio economy, carbon capture and storage (CCS), carbon capture and utilization (CCU) are strategical area inside the CEP. Its final version released on 22 May 2019 marked the final step in the European Union's overhaul of its existing energy policy in order to facilitate the clean energy transition.

To act on the energy performance of buildings, renewable energy, energy efficiency, governance and electricity market set of eight legislative acts, four Directives and four Regulations:

- Energy Performance of Building Directive EPBD (Directive (EU)2018/844);
- Renewable Energy Directive RED (Directive (EU) 2018/2001)
- Energy Efficiency Directive EED (Directive (EU) 2018/2002);

- Governance of the Energy Union (Regulation (EU) 2018/1999);
- Electricity Regulation ER (Regulation (EU) 2019/943);
- Electricity Directive ED (Directive (EU) 2019/944);
- Risk Preparedness (Regulation (EU) 2019/941);
- Union Agency for the Cooperation of Energy Regulators ACER (Regulation (EU) 2019/942).

The Clean Energy Package sets the following targets for the EU for 2030:

- 40% cut in greenhouse gas emissions compared to 1990 levels;
- a binding renewable energy target of at least 32% ,
- an energy efficiency target of at least 32.5% with a possible upward revision in 2023.

2.1 Energy Performance of Building Directive (EPBD)

To improve the energy performance of buildings in the 2002 the European Commission (EC) released the first legislative instrument "Energy Performance of Building Directive (EPBD)" that became the core reference for future studies in the matter of energy performance buildings. The schematic structure of EPBD is shown in in Figure 7.

The Directive was focused on the following aspects:

- implementation of a methodology to calculate the energy performance of buildings taking into account of all factors affecting energy use;
- regulations to set minimum energy requirements for new buildings and for large (>1000m²) existing buildings when they were refurbished;
- energy performance certificates available whenever buildings were constructed, sold or rented out;
- regulations in matter of inspections of boilers and air-conditioning systems.

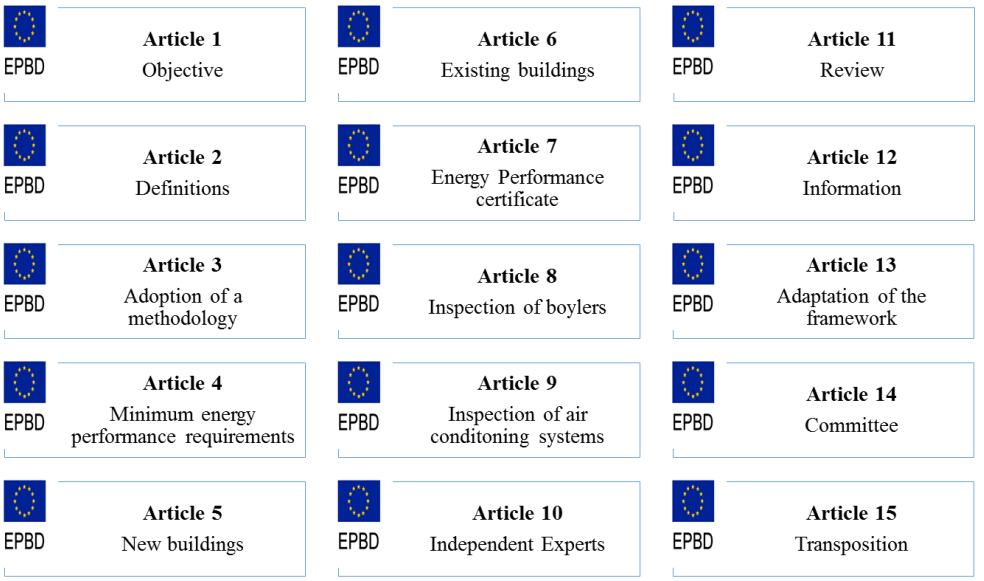

Figure 7: Schematic structure of EPBD [58].

According to the above cited aspects, EU Member States were required to implement a number of measures such as the introduction of Energy Performance Certificates.

The first Directive demonstrates the EU's ambitious efforts to align with the challenges of climate change and energy emanating from the EU's building stocks by making new and existing buildings more energy efficient. In Italy, the Directive 2010/31/EU is implemented in the Italian Ministerial Decree (MD) 26/06/2015 "Application of the energy performance calculation methods and establishment of prescriptions and minimum requirements of buildings"[59]. The MD sets both the methodology calculation of the energy performance of buildings and the minimum energy performance requirements. Moreover, it introduces new prescriptions, both for new buildings and for the energy refurbishment and renovation of existing ones. Requirements of nZEBs that will be applied to new buildings from 1st January 2019 for the public buildings from 1st January 2021 for all the other buildings are widely specified.

In the last decades, the first version was updated in 2010 and 2018, to take into account both new technologies and new materials having better energy performances [60–62]. In particular, the 2010 recast is considered the EU's main legislation covering the reduction of energy consumption. It promotes the developments of new building designs based on the use of renewable energy sources aiming the reduction of the energy consumption and in the meanwhile the reduction of CO_2 emissions. Cost effective improvement of the overall energy performance can be considered the main topic of the recast directive. [63].

In contrast to first one, the recast 20210 focuses on enhanced quality assurance improvements to ensure reliability and robustness of energy efficiency [64].

In the recast EPBD it was introduced the nZEB concept and a target of 2018/2020 for their integration. In particular, article 10 states that all new and existing buildings should be nZEB by 31 December 2020 while new buildings occupied and owned by public authorities after 31 December 2018 [60].

An nZEB is defined as a building that has a very high energy performance whose energy needs should be covered by energy from renewable sources.

Despite the Directive sets out a general framework within nations, regions and groups, different definitions of NZEB can be found. It is left to the Member States in their national plans to provide a rigorous NZEB definition within the context of their own national efforts. The directives do not settle minimum performance requirements that make on which to rely in order to consider a building as an NZEB. Member States are required to fix these requirements following a common methodology.

Member States must specify in detail the condition of NZEB, reflecting national and regional conditions and including a numerical indicator of primary energy consumption. While the NZEB goal is common for all Member States, the approaches and calculation methods to practically reach it are left as a prerogative of each Country, acknowledging the variety of climatic, cultural and economic conditions throughout Europe.

In the matter of NZEBs the recast EPBD focuses the following aspects:

- use of common methodologies for the calculation of buildings energy consumption;
- adoption of new performance requirements on buildings;
- new guidelines about energy performance certificates;
- new regulations about inspections of heating and air conditioner systems;

Articles 6 and 7 state that Member States must give information on policies, financial or other measures adopted for the promotion of NZEBs, including details on the use of RES in new buildings and existing buildings undergoing major renovation. It is also discussed in matter of measures to improve the energy performance of buildings including all relevant elements and technical systems, such as passive elements aiming to reduce the energy needs for heating or cooling, the energy use for lighting and for ventilation and hence improve thermal and visual comfort.

To promote the smart technologies in the building sector and to streamline the existing rules, in 2016 the European Commission proposed an update to EPBD that was approved in 2018 and published on the Official Journal of the EU (Directive 2018/844/EU). Moreover, a new buildings database – the EU Building Stock Observatory – to track the energy performance of buildings across Europe was published. Member States are requested to promote the implementation of intelligent energy consumption metering systems both in new and existing renovated buildings. The recast directive supports the ambitious commitments of the Energy and Climate Policy Framework for 2030: a sustainable decarbonized energy system by ensuring a 40% GHG emissions reduction, increase renewable energy uptake by 27% and improve energy efficiency by 30% [65].

Since the building sector has a large potential towards a carbon-neutral and competitive economy, this directive sent a strong political signal to EU's commitment. It is discussed in matter of renovation strategies to support the renovation of national building stocks in order to transform the exiting building stock

into highly energy efficient and decarbonized buildings. Moreover, it was settled out a common framework to evaluate buildings' energy performance including the indicators and the calculations to be used. A lack in the EBDP is that it does not take into account the environmental impacts generated by building construction, maintenance and disposal [63]. It is promoted the role of Information and Communications Technologies and smart technology in buildings to help deliver the EU 30 energy and climate goals. The recast EPBD is in line with international obligations and commitments to accelerate the decarbonisation of the building stock.

Summarising, under the last recast EPBD:

- Energy performance certificates are to be included in all advertisements for the sale or rental of buildings;
- inspection schemes for heating and air conditioning systems must be established
- all new buildings must be nearly zero energy buildings by 31 December 2020 (public buildings by 31 December 2018);
- • EU countries must set minimum energy performance requirements for new buildings,
- EU countries must set minimum energy performance requirements for the renovation of buildings and for the replacement or retrofit of building elements (heating and cooling systems, roofs, walls, etc.);
- EU countries have to draw up lists of national financial measures to improve the energy efficiency of buildings.

2.2 Energy Efficiency Directive (EED)

With the aim to establish a common framework for the promotion of energy efficiency it was introduced the "Energy Efficiency Directive EED" (Directive 2012/27/EU) [66]. The European Commission stated 'Energy efficiency is the most

cost-effective way to reduce emissions, improve energy security and competitiveness, make energy consumption more affordable for consumers as well as create employment, including in export

industries' [66]. With its 30 articles it establishes a common framework of measures to promote energy efficiency within the European Union in order to ensure the EU 2020 20% headline target on energy efficiency is achieved, and to pave the way for further energy efficiency improvements beyond that date.

In the meanwhile, it offers a direct response to increased dependence on energy imports, climate change mitigation actions, and energy security within the EU Member States[67].

Reducing energy consumption by 20% means a saving of 368 (MTOE) of primary energy. The directive is an element to progress towards the Energy Union [68]. All EU countries are required to use energy more efficiently at all stages of the energy chain, including energy generation, transmission, distribution and end-use consumption [69].

It is offered a great responsibility for utility companies to be major players in reducing the customers' energy use of buildings and other sectors. Each Member State must set an indicative national energy efficiency target, based on either primary or final energy consumption, primary or final energy savings, or energy intensity.

EDD has relevant articles linked to buildings. For instance, article 4 states that Member States shall establish a long-term strategy for mobilising investment in the renovation of the national stock of residential and commercial buildings, both public and private. EDD is considered a key policy instrument to convert national building stocks from energy consumers to energy producers [56].

The obligation to the building stock renovation, important driver in reducing GHG emissions, complements the Directive 2010/31/EU.

Renovating the EU building stock is a widely investigated research field so it will improve the energy efficiency while driving the clean energy transition.

The main topics of the directive can be summarized as following:

- 32.5% energy efficiency target by 2030;

- policy measures to achieve energy savings equivalent to annual reduction of 1.5%;
- energy efficient renovations to at least 3% per year of building owned and occupied by central governments;
- national long-term renovation strategies for the EU building stock;
- energy performance certificates for the sale and rental of buildings;
- rules on energy metering and billing, strengthening consumer rights, in particular for people living in multi-apartment buildings;
- national rules on the allocation of the cost of heating, cooling and hot water services in multi-apartment and multi-purpose buildings where these services are shared;
- obligation schemes for energy companies to achieve energy savings equivalent to a reduction of 1.5% of annual sales to final consumers.

Among the above cited topics, the energy performance certificates (EPCs) are crucial in promoting energy efficiency owing to the useful information provided to the public. As part of the CEP in 2018 it was promulgated the new amending EED in good agreement to update the policy climate framework and beyond. A headline energy target of at least 32.5% for 2030 is the key element of the recast directive. Reaching this target means that EU energy consumption should be lower than 1273 MTOE of primary energy use and/or no more than 956 MTOE of final energy. B

The recast directive will help to reach the goals of the European Green Deal by means the EU is increasing its climate ambition to become the first climate-neutral continent by 2050. By 2024 it was required a general review of the Energy Efficiency Directive in order to meet 2030 greenhouse gas emission targets (reduction of at least net 55%).

2.3 Renewable Energy Directive (RED)

In accordance with Article 194 of the Treaty on the Functioning of the European Union (TFEU), promoting renewable forms of energy is one of the goals of the Union energy policy. The increased use of energy from renewable sources constitutes an important part of the package of measures needed to reduce greenhouse gas emissions and comply with the Union's commitment under the 2015 Paris Agreement on Climate Change following the 21st Conference of the Parties to the United Nations Framework Convention on Climate Change (the 'Paris Agreement'), and with the Union 2030 energy and climate framework, including the Union's binding target to cut emissions by at least 40 % below 1990 levels by 2030.

In the building sector renewable energy and energy efficiency are the two most important pillars to reduce GHGs [70].To this aim, in November 2016, the European Commission published as part of the CEP package a recast of the Renewable Energy Directive (Directive 2018/2001/EU).[71].

The recast Directive, amending the Directive 2001/77/EC and the Directive 2009/28/EC, entered into force in December 2018. Aim of the recast Directive is to promote the use of the energy renewable sources to limit GHG emissions. Like EED also the RED set a package of measures that create the conditions for significant and long-term improvements in the energy performance of the European building stock.

National energy targets were established for all Member States based on their overall renewable production. To promote green buildings and high energy efficiency all Member States are required the adoption of policies and targets able to enhance the uptake of RES mainly for cooling and heating of new and existing buildings.

Member States have also the obligation to adopt a requirement for the minimum level of RES [72].

RED can be considered the strongest action to provide a consistent growth of renewable production towards a significant GHG emission reduction, energy supply and technology innovation [73]. RED plays a crucial key for the introduction of nZEBs characterised by the combination of renewable energy sources with high

efficiency technologies.

Directive 2009/28/EC specified national renewable energy targets for 2020 for each country going from a low of 10% in Malta to a high of 49% in Sweden. In the last recast Directive, with a view to showing global leadership on renewables, the EU has set an ambitious, binding target of 32% for renewable energy sources in the EU's energy mix by 2030 [74].

EU Member States must adopt the provisions of the recast Directive and transpose them into national legislation by 30 June, 2021 [74]. Among several technical details will need to be determined in the near- to medium-term by the Commission are cited:

- the Commission will review the overall 32% RES target by 2023 and could propose to increase them;
- the Commission must set a GHG reduction threshold for recycled carbon fuels by January 2021, and by December 2021 must specify the methodology for GHG accounting for these fuels and for renewable fuels of non-biological origin;
- in 2026, the Commission must propose a regulatory framework for the promotion of renewable energy for the post-2030 period.

2.4 Net Zero Energy Building challenge

Net-zero energy buildings (NZEBs) are emerging as a key concept and a promising solution to minimizing the environmental impact of buildings and to reach the building energy renovation considered one of the pillars upon which the 2050 European low carbon goals are based [75].

The NZEB concept has become a key topic of research to reduce the fossil energy consumption and greenhouse gas emissions in the building sector. Owing to the rapid development of urbanization and the improvement of living standards of residents, the energy consumption and carbon emissions of the building sector is expected to increase in the near future so in many countries long-term plans were adopted to develop and implement nZEB concept.

According to the article 2 of EPBD, in Europe all new buildings to be nearly ZEB

by 2020. In the US, the Executive Order 13514 requires all new buildings should be net ZEB by 2030, the Energy Independence and Security Act of 2007 requires that all new commercial buildings should be NZEB by 2030 [76]. Buildings should be designed to use energy efficiently to offset their growing energy demand. The transition towards NZEB concept requires an high effort to realize the potential for energy savings in the building stock [77].

In the following section it is reported a brief review of definitions and a description of the main technologies and measures improved to reach the NZEB target.

3. NZEB definitions and classification

Different definitions have been launched especially after the NZEB definition given in the EPBD recast, depending on the boundaries and metrics [78].

In Table 1 are reviewed some of the definitions can be consulted in literature. Many other terminologies can be found within the ZEB concept: autonomous house, net-zero energy house, self-sufficient buildings, net zero carbon house, carbon-neutral, carbon-positive, hybrid building, net-zero source energy, net-zero energy costs, net-zero energy emissions [79]. Often the definition net zero energy building is approached to that one of zero-carbon building defined as a building that over a year does not use energy that entails carbon dioxide emission.

As stated in the work of Laustsen et al. [87] a net zero energy building does not automatically mean that it is zero carbon and vice versa.

Table 1: Some NZEB definitions.

Building that has a very high energy performance. The nearly zero or very low amount of energy required should be covered to a very significant extent by energy from renewable sources, including on-site or nearby production.	EPDB(**2010/31/EU)** [80] (2010)
Residential or commercial building with greatly reduced energy needs through efficiency gains such that the balance of energy needs can be supplied with renewable energies	Torcellini et al. [81] (2010)
Building which produces as much energy as its users can consume within a given time period, .i.e. monthly, annually	Hernandez et al. [82] (2010)
Building that generates and uses energy through a combination of energy efficiency and RE collected within the building footprint.	Pless et al. [81] (2010)
Building itself can generate electricity, which can be further connected to the public grid or use the public grid to power, making primary energy production and consumption balanced, with the development of solar photovoltaic technology	Voss et al. [83] (2011)
Building with a national cost optimal energy use greater than zero primary energy	Voss et al. [84] (2012)
Building with greatly reduced energy needs and/or carbon emissions, achieved through efficiency gains, such as the balance of energy needs supplied by renewable energy	Panagiotidou et al. [85] (2013)
Energy-efficient building where, on a source energy basis, the actual annual delivered energy is less than or equal to the on-site renewable exported energy.	National Renewable Energy Laboratory)[86] (2015)

In Torcellini et al. [81] four well-documented definitions to improve the understanding of what net-zero means can be found:

- **Net Zero Site Ener**gy: a site NZEB produces at least as much renewable energy (RE) as it uses in a year, when accounted for at the site;
- **Net Zero Source Energy**: a source NZEB produces or purchases at least as much RE as it uses in a year, when accounted for at the source. (Source energy refers to the primary energy used to generate and deliver the energy to the site),
- **Net Zero Energy Costs**: in a cost NZEB, the amount of money the utility pays the building owner for the RE the building exports to the grid is at least equal to the amount the owner pays the utility for the energy services and energy used over the year;
- **Net Zero Energy Emissions**: A net-zero emissions building produces or purchases enough emissions-free RE to offset emissions from all energy used in the building annually.

These concepts can be applied to a wide range of constructions including residential and commercial buildings. For buildings based on RE sources the same authors proposed a classification (NZEB:A to NZEB:D) showing the many possible RE supply options. The classification, shown in Figure 8, depends on the site constraints and locally RE options. According to above classification, owners and designers are encouraged to use RE sources and technologies located on the building as possible cost-effective energy efficiency strategies.

A further classification of NZEBs is that one proposed by Lund et al. [87] based on energy demand and installed renewable topology:

- **PVZEB**: building with a relatively small electricity demand and a photovoltaic installation;
- **WIND ZEB**: building with a relatively small electricity demand and a small on-site wind turbine;

- **PV-Solar Thermal-Heat Pump ZEB**: building with a relatively small heat and electricity demand and a photovoltaic installation combined with a solar thermal collector, a heat pump and heat storage;
- **Wind-Solar Thermal-Heat Pump ZEB**: building with a relatively small heat and electricity demand and a wind turbine combined with a solar thermal collector, a heat pump and heat storage.

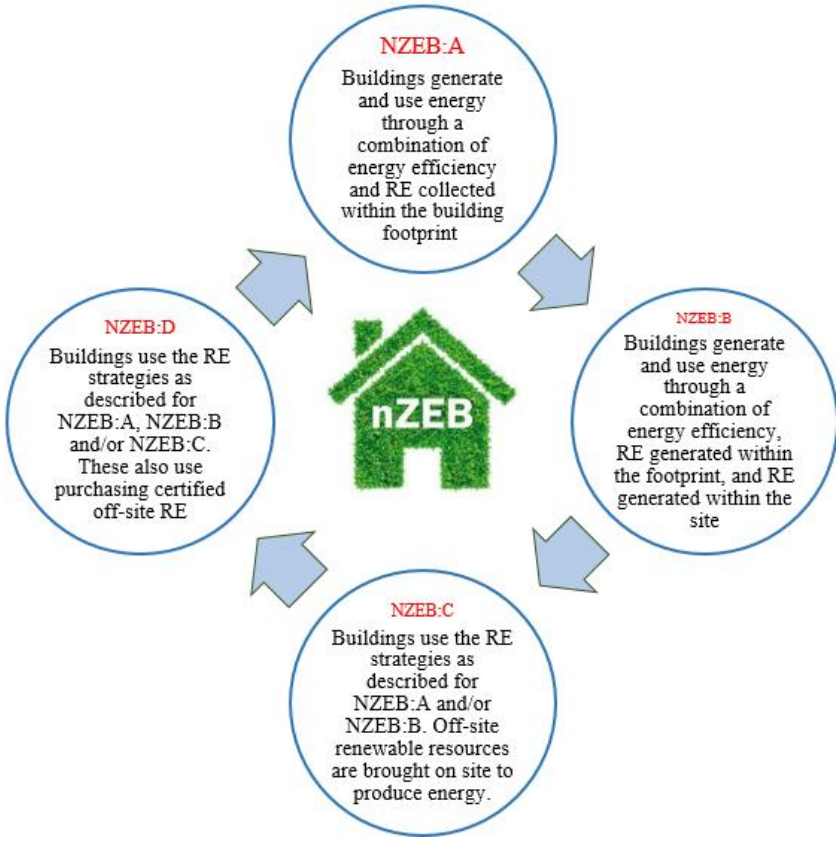

Figure 8: Classification of NZEBs based on RES and their location [81].

Based on the definitions reported, a NZEB not only it is a building that produces as much as or more energy than it uses annually but it exports excess renewable energy generation to offset the energy used.

3.1 NZEB energy balance

The core of the NZEB concept is the exchange of energy from and to the grid. The recast EPBD 2010 considers the primary energy uses the main metric to account the balance for an NZEB. As stated in the work of Hernandez et al. [82] it has the advantage to allow a differentiation between electricity and fossil fuel use including, in the meanwhile, an indication of the efficiency of delivering heating, hot water, lighting. A schematic representation of energetic fluxes in the concept of NZEB is shown in Figure 9. The dashed lines represent energy transfer within the site boundary while the solid lines energy transfer entering and/or leaving the site boundary used for zero energy accounting.

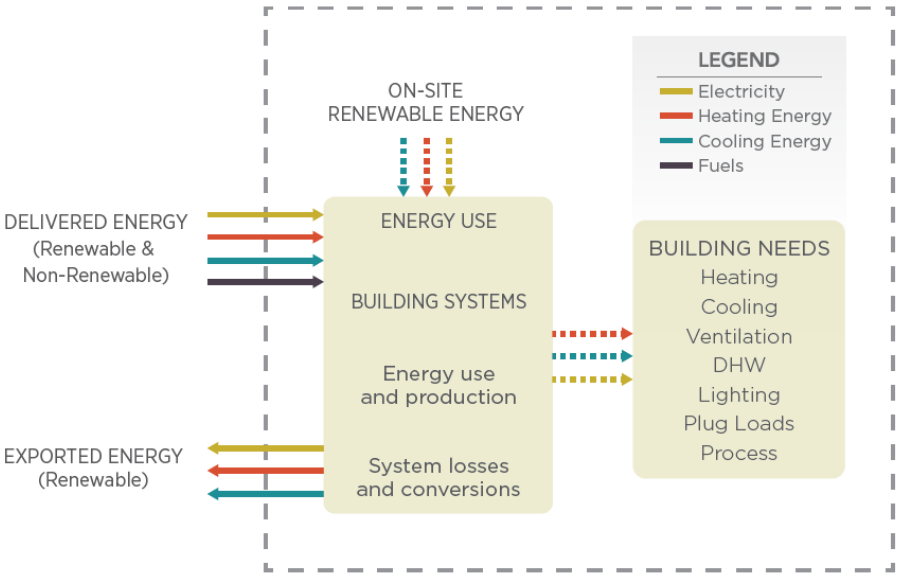

Figure 9: Energy exchanges in the nZEB concept [86].

The site boundary is the point where the energy inflows and outflows of the system are carried out in order to identify the energy from renewable sources on-site or offsite. The site boundary can be around the building footprint if the on-site renewable energy is located within the building footprint. In contrast, if on-site

renewable energy is on-site but not within the building footprint it is around the building site. It forms from delivered energy on-site renewable energy production, building energy and exported energy.

Delivered energy includes grid electricity, district heat and cooling, renewable and non-renewable fuels. It is energy from the grids to buildings (imported) specified for each energy carrier.

A NZEB balances its energy use so that the exported energy to the grid is equal to or greater than the delivered energy to the building on an annual basis. The load (building's energy demand) may not coincide with delivered energy owing to self-consumption of on-site renewable energy production.

On-site Renewable Energy includes both any renewable energy generated and used within the site boundary and the excess renewable energy exported outside the site boundary. The concept of site boundary is complex since, as explained in the work of Sartori et al. [84], it accounts both physical boundary and the balance boundary. The first encompass a single building or a group of buildings and specifies which renewable sources are considered as on-site and off-site, while the second one which energy uses (e.g., cooling, heating, appliances) are included in the balance.

In literature are widely used two kinds of balance: import/export balance and load/generation balance [84]. The first one is particular useful in the design phase of a building while the second one in operational monitoring.

Following the approach suggested in the work of Sartori et al. [84] the import/export balance is given as:

$$\sum_i e_i \times w_{e,i} - \sum_i d_i \times w_{d,i} = E - D \geq 0 \qquad (1.1)$$

where

- e is the exported energy;
- d is the delivered energy ;
- i is the specific energy carrier (kWh/y or kWh/ m2y);
- w is the weighting factor (energy conversion factor);

- E is the weighted exported energy;
- D is the delivered exported energy.

According to this balance, the net energy balance of an NZEB can be reached following two approaches: reducing the amount of delivered energy (axis x) or increasing the energy production (axis y).

The load/generation balance is given as follows:

$$\sum_i g_i \times w_{e,i} - \sum_i l_i \times w_{d,i} = G - L \geq 0 \qquad (1.2)$$

where

- g is the building's energy generation;
- l the building's energy demand;
- G is the weighted generation;
- L is the weighted load.

A schematic representation of both of balances is shown in Figure 10. The load/generation balance gives the points for weighted demand and supply most far away from the origin; while with import/export balance the points a closer to the origin due to the self-consumption. The balances above reported are referred to on-grid (or grid-connected, or grid-integrated) NZEBs. Examples of off-grid or stand-alone buildings are also provided in literature [88,89].

The period considered for the energy balance plays an important role since owing the intrinsic variability of the RES it could affect the achievability of the fixed goal. For example, based on an annual energy balance a building could meet net zero energy requirements while its energy consumption on monthly balance may exceed energy production. To take into account the full meteorological cycle and the complete operating energy range of the building the annual balance is the most used balancing period [84].

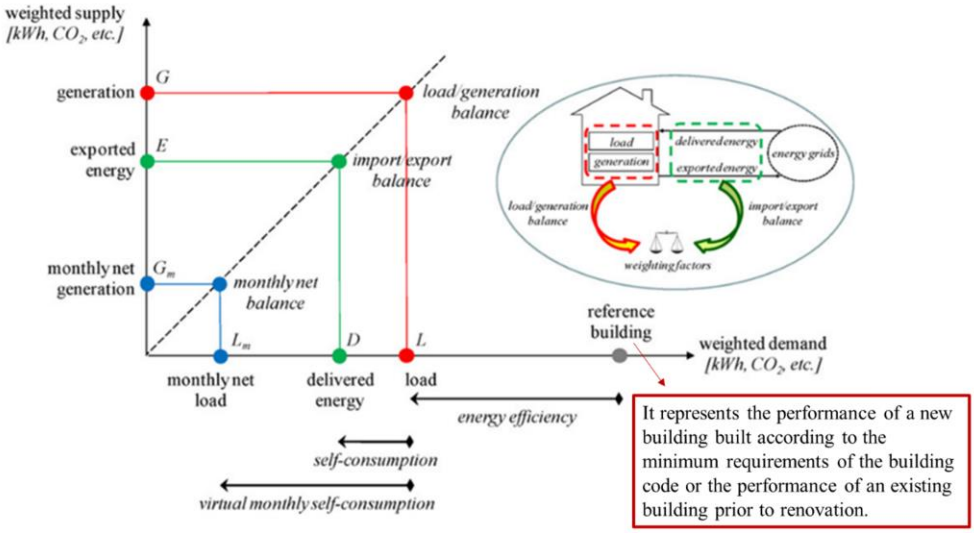

Figure 10: Energy Balance of NZEB [84].

An example of monthly net balance is shown in Figure 10: for each energy carrier, generation and load occur- ring in the same month are assumed to balance each other off; only the monthly residuals are summed up to form the annual totals. On monthly base the load/generation balance can be expressed as follows:

$$\begin{cases} \sum_i g_{m,i} \times w_{e,i} - \sum_i l_{m,i} \times w_{d,i} = G_m - L_m \geq 0 \\ g_{m,i} = \sum_m max\,[0, g_i(m) - l_i(m)] \\ l_{m,i} = \sum_m max\,[0, l_i(m) - g_i(m)] \end{cases} \quad (1.3)$$

where the subscript m stands for month.

As shown in Figure 10 the monthly balance gives the points closer to the origin in comparison to import/export balance and load/generation balance due to virtual monthly self-consumption. The import/export balance is expected to be always in

between the two other ones since there usually is some amount of self-consumption that hardly will be more than the virtual monthly self-consumption.

The NZEB energy balance may be achieved in several ways such a combination of solar technologies, heat pumps, combined heat and power, and energy efficiency measures to reduce energy consumption for lighting and appliances [75].

3.2 NZEB future evolution: positive energy building (PEB)

A possible future evolution of the NZEB concept is the Positive Energy Building that can be defined as a sort of NZEB, but so efficient as to produce more energy than they consume, leaving users with extra energy to employ in other ways, such as powering mobile devices, electric tools or even the electric car [90].

Some characteristics of the PEB model that allow a distinction with the NZEB model are resumed in Figure 11. While the NZEB design model has now become part of the regulatory system of European countries, thanks to Directive 2010/31/EU, the PEB model is not yet known uniformly at European level. Pilot projects of PEBs have indeed proven successful, leading to developments in some countries such as France or Germany where these innovative building practices have been integrated into the legislation.

By producing more energy than necessary to their needs, PEBs could contribute to the energy support of other buildings connected to them, creating a system of units connected together at the neighbourhood level.

In literature it is widely used the term producers (PRO-ducers + con-SUMERS) referring to buildings that not only use the energy produced on site from renewable energy sources for self-consumption, but which also share the excess of energy produced with their neighbours through the connection to a smart grid. Buildings acting as energy providers create a scenario that opens up completely new ways of securing the energy supply.

Buildings equipped with smart technologies in order to stimulate production by pro- active energy customers and active In the EPB on-site produced renewable

energy should at a minimum supply all energy consumed for heating, cooling, ventilation, dehumidification, and domestic hot water and integrated lighting systems. The PEB concept is changing the traditional distribution systems that are transforming from uni-directional centralized systems to bi-directional decentralized systems [14]. A bi-directional flow of energy and in- formation is therefore triggered between the public network and users [91].

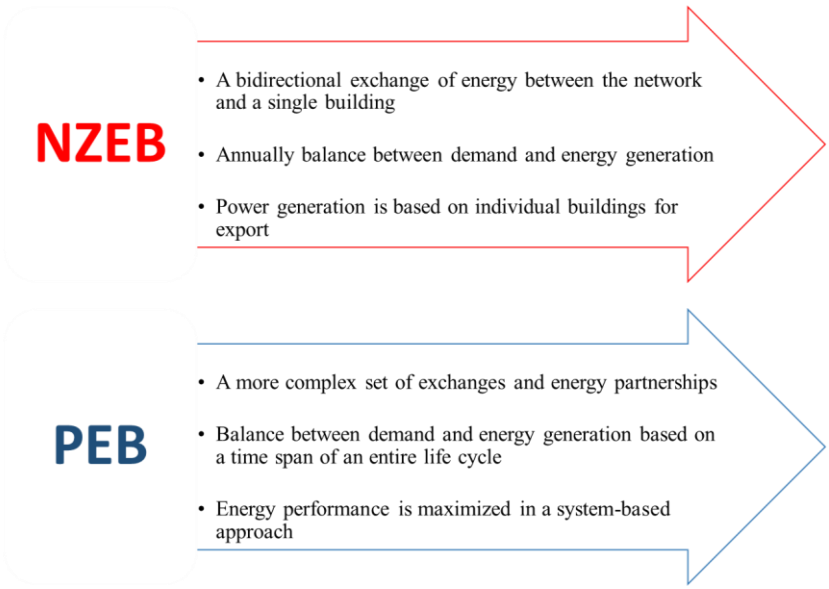

Figure 11: NZEB and PEB concepts distinction [92].

On future energy systems NZEBs will play the dual role of being producers and consumers of heat and electricity providing for the needs of their occupants by coordinating on-site generation with energy imports from the utility grid [93]. Their relationship with the electricity grid is far more complex than that one of conventional connected buildings so NZEBs also export energy [43]. In particular, when the on-site generation exceeds the building's load, energy is exported to the utility represented, for instance, by electric grid, district hot water system or other central energy distribution system [81]. If a large share of the buildings would be NZEB, the impact on the electricity grid could be substantial so the electricity grid being used as

a virtual electricity storage, with power supplied to the grid by the distributed generation (DG) systems and consumed when needed [94]. This combination is up until now the most effective way to reach the NZEB target [95].

4. Energy efficiency strategies towards the NZEB target

The introduction of the NZEB/PEB target in the building design has the aim to encourage a decrease in the amount of energy required, thus abandoning fossil fuel dependency and reducing CO2 emissions.

The NZEB target is based on three fundamental pillars:

- increasing the building's energy efficiency as much as possible;
- reducing the energy demand improving the building's energy performance;
- encouraging use of renewable energy sources to cover the residual energy demand.

Building's energy efficiency can be enhanced adopting the following criteria[90]:

- building position and orientation allow to control the solar radiation contributions on the transparent and opaque envelope and the wind exposition;
- building thermal mass allow to reduce the temperature gradients due to the outdoor climatic conditions;
- insulation material allows to shield the interior of the building from the exterior environment minimizing thermal transfer (heat losses or gains) through the envelope;
- thermal regulation allows to maintain the design indoor conditions and, in the meanwhile, to guarantee the internal comfort and a reduced energy consumption;
- natural ventilation allows to provide a cooling effect to decrease the indoor temperature;
- daylighting incorporated into the building trough top and side lighting allows to reduce annual energy consumption.

Energy efficiency may be further improved by low heating system temperatures, warm-water and ventilation systems, avoiding hot water circulation, including heat recovery systems in ventilation and wastewater systems, hydraulic balancing of all systems, using demand-controlled heating and ventilation systems.

Energy efficiency measures can be adopted both for residential and commercial buildings even if with some differences. Example of measures adopted for residential buildings are: increasing solution, installing double-glazed windows, draught-proofing, metering solutions with demand response capabilities [96]. Example of measures adopted for commercial buildings are optimization of ventilation and air-conditioning, heating systems and lighting.

Among energy efficiency measures (EEMS), the use of RE is encouraged both to cover energy requirements and to reduce CO2 emissions. Renewable energy-based technologies (Rets) can be divided into supply-side RE generation technologies and demand-side RE technologies.

The supply side options can be further divided into on-site and off-site options [81]. The on-site options use RE source available in the building footprint to generate on site energy directly connected to the building's electricity or hot water system. These options are applied only to a single building and since RE generated is directly connected into building's energy distribution infrastructure transmissions and distribution losses are minimized. This category includes, as an example, PV technologies mounted on the building roof of façade, passive solar thermal systems, building mounted wind turbine. Grid-connected PV systems installed on buildings have been the fastest growing market in the PV industry.

On-site options also address RE generated on the building site but not within its footprint. On-site RE is ideally connected to the building's electricity system. Example within this category are PV systems mounted to shading structures, wind turbines mounted in a neighbouring field, on-site solar-thermal absorption chillers, ground-mounted solar thermal systems.

Off-site supply options use RE sources available off-site to generate energy on-site and connected to the building's electricity or hot water distribution system. These

options are used in buildings such as hospitals or laboratories where RE generation capacity is not sufficient. RE off-site is importing on site to generate energy on site. It is for this reason that these buildings are also referred as NZEB. Off-site is usually provided by biomass, wood pellets, ethanol or any purchases of renewable energy produced outside the building's site.

The two categories above descripted show how energy source availability is the first criterion in selecting renewable technologies to implement in a building.

Among renewable energy sources available for buildings, solar and PV systems are widely used since they are easy to install (especially on building rooftops), solar energy has a high capacity compared with other energy sources, the life span of PV modules is very long. Moreover, life cycle assessment of PV products from various source show lifetime CO_2 emission per kWh is almost 5 to 40 times less than traditional electricity.

PV systems are a mature technology owing to incentive programs for governments having the aim to increase PV production and decreasing cost of PV systems. PV modules, available as flat or flexible surfaces, made with cells or laminates, can be integrated into every part of the building envelope.

In grid-connected PV system the electric grid acts as a virtual storage system since the excess of PV production is sent into it during the day. At night electricity from the grid can be used to meet the building demand.

To increase the energy efficiency of buildings there is not a 'best' technology. The choice of measures depends on climate conditions, micro-climate and available environmental energy, but also on saving potentials and cost-efficiency.

4.1 Energy Efficient Buildings: The European SET Plan

The Strategic Energy Technology Plan (SET Plan), adopted by the European Union in 2008, is the principal decision-making support for European energy policy in order to establish an energy technology policy [97]. It consists of the SET Plan Steering Group, the European Technology and Innovation Platforms (ETIPs), the

European Energy Research Alliance (EERA), and the SET Plan Information System (SETIS).

The Set Plan is the key stepping-stone to boost the transition towards a climate neutral energy system through the development of low-carbon technologies in a fast and cost-competitive way to reach the following goals:

- accelerating knowledge development, technology transfer and up-take;
- maintaining EU industrial leadership on low-carbon energy technologies;
- fostering science for transforming energy technologies to achieve the 2020 Climate goals;
- contributing to the worldwide transition to a low carbon economy by 2050.

To reach the above cited goals two crucial timelines has been fixed:

- **For 2020**, the SET-Plan provides a framework to accelerate the development of low carbon technologies in order to the EU reach its 20-20-20 goals of a 20% reduction of CO2 emissions, a 20% share of energy from low-carbon energy sources and 20% reduction in the use of primary energy by improving energy efficiency by 2020;
- **For 2050**, the SET-Plan is targeted at limiting climate change to a global temperature rise of no more than 2°C, in particular by matching the vision to reduce EU greenhouse gas emissions by 80-95%.

Ten actions were identified for research and innovation [97]. In particular, Action 5, focused on Energy efficiency in buildings (EEB), states "Develop new materials and technologies for, and the market uptake of, energy efficiency solutions for buildings". To coordinate the work relating to this issue especially regarding the multiplicity of obstacles to be overcome in new buildings and in the existing building stock it was created the temporary working group 5 (TWG5).

The membership of TWG 5 is composed of Member States and non-EU countries, industrial stakeholders, non-governmental organizations and research institutes. The

SET Plan TWG 5 was divided in two subgroups to address these aspects :

- New materials and technologies for energy efficiency solutions (5.1);
- Cross cutting heating and cooling technologies for buildings (5.2).

A detail of the Energy Efficiency targets fixed within subgroup 5.1 is shown in Figure 12. Nowadays, materials and technologies for building construction must be in agreement with high quality requirements: energy performance, technical and handling aspects, environmental and sustainability aspects.

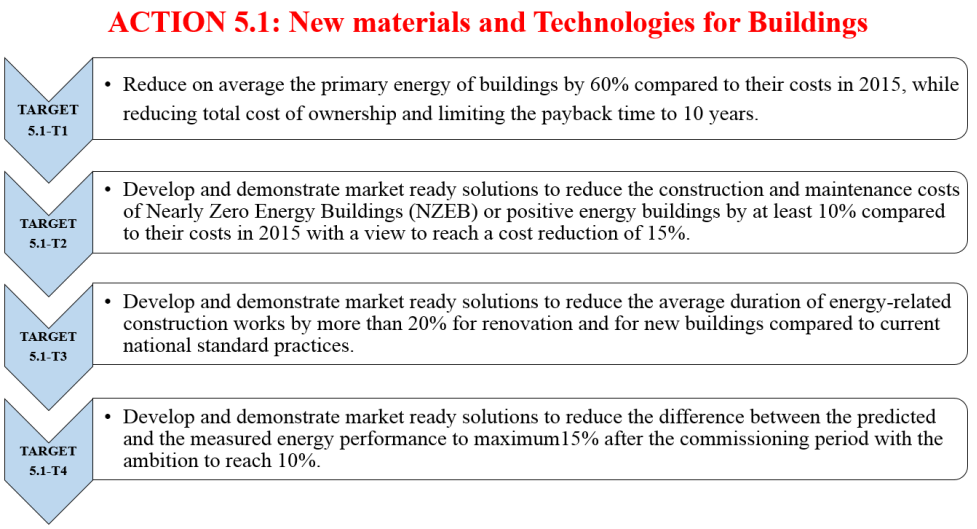

Figure 12: Energy efficiency targets in manner of new material and technologies.

The construction sector is developing a new approach that takes into consideration the whole cycle of both energy and carbon. The embodied energy, i.e., the energy used to produce a given material will be a crucial topic related to materials and energy worth. The use of the life cycle assessments (LCA) method in the building sector has the advantage to put materials and technologies into a larger context considering the energy used in each life cycle phase from raw material to end of life. The construction sector is under permanent check concerning its waste management. According to the principle of the “circular economy”, regulation need to guarantee high rate of

reusability/recyclability of the raw materials.

The circular economy approach has a strong positive impact on the life cycle energy consumption contributing in a positive way towards the energy transition. Among solutions explored it is encouraged the use of biomaterials since they are highly recyclable and, most of them are also biodegradable.

Materials like mineral foams, phase change materials or silicate aerogels for specific needs are widely investigated solutions that can be further developed. Traditional materials like bricks and concrete have the potential to evolve into recyclable/reusable materials. Among the most innovative technological solutions there is the use of PV as construction material.

The building integrated photovoltaic (BIPV) is usually used as a façade or roof element. PV as an active energy-producing unit renders an aesthetic value to the whole construction. Besides harvesting energy, well-integrated BIPV modules contribute to the comfort of the building so they serve, as an example, as weather protection, heat insulation, shading modulation, noise protection, thermal isolation and electromagnetic shielding.

BIPVs are the most energy retrofit solutions investigated. The peculiar aspect of the ventilated façades is the chimney effect that is established in the cavity between the PV panel and the wall of the building. It allows not only to improve the thermophysical performance of the building but also to increase the efficiency of the photovoltaic. It is known that in real operating conditions the photovoltaic yield decreases as the temperature of the cells increases. Ventilated façades offer a great opportunity to host in a modular way active, passive and storage technologies giving a great contribute to decarbonize the building sector. BIPV can produce energy where it is needed and without covering extra surface or green field sites.

A detail of the energy efficiency targets fixed within subgroup 5.2 is shown in Figure 13. Nowadays, heating and cooling of buildings is strongly based on use of fossil fuels, for this reason, heating and cooling technologies show a high potential for reduction of the energy demand at building level. Heating and cooling more efficient and sustainable is a priority of the Energy Union Strategy [98]. For

renewable heating and cooling of buildings, R&I is investigating the "Cross-cutting technologies". With this term the "Renewable Heating & Cooling European Technology Platform" indicates energy technologies or infrastructures which can be used either to enhance the thermal energy output of RES or to allow the exploitation of RES which would be difficult to use in building-specific applications.

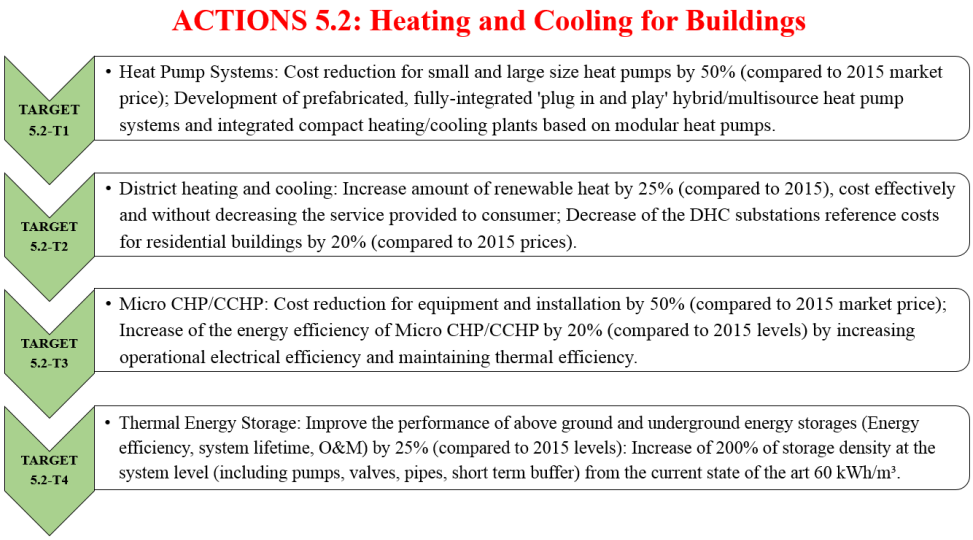

Figure 13: Energy Efficiency targets in manner of heating and cooling technologies.

Heat pumps (HPs); district heating and cooling (DHC), micro combined heat and power (CHP)/ combined cooling heat and power (CCHP), thermal energy storage (TES) are the most widely investigated heating and cooling technologies.

HPs are considered as one of the most important technology to reduce CO_2 emissions in the residential building sector, especially when the electricity-generation system is to decarbonize by means of large-scale introduction of renewable electric power generation sources. They are a versatile energy technology able to provide both heating and cooling in a great variety of building applications and contexts combining high energy conversion with the capability of utilising different energy sources at useful temperature levels. An advantage is that they can be combined with smart technologies and storage providing flexibility for the electricity system.

A study conducted by the European Heat Pump Association estimated that a large-scale introduction of HPs could be reduced CO_2 emissions by 34% to 46% in the building sector. Development of HPs to replace exiting boilers; development of smart HPs to deliver extra service to the grid; development of absorption HPs (thermally driven systems) to increase the utilisation of renewable and recovered heat are examples of active research activities. Aim is the development of the next generation of cost-efficient heat pumps for new and existing buildings.

District heating and cooling (DHC) are playing a key role to increase the amount of renewable in a cost-efficient manner. In particular DHC networks can integrate most of the renewable energy sources, waste heat as well as renewable electricity. They can avoid domestic heating or cooling by solid fuel's combustion. If coupled to storage systems offer flexibility to the energy system.

DH networks usually operate with high supply temperatures in order to reduce the investment costs. The required transport capacity is reached with small pipe diameters and using cost effective customer installations. The integration of renewables and waste heat sources in the building sector requires an adaptation of the temperatures in the DH networks. It is crucial to minimize the return temperature in order to reduce the mass flow rate and the network distribution losses improving the generation efficiency. Return temperature affect the heating system elements of the buildings, i.e., the radiators.

DC is investigated as an efficient community technology able to integrate a variety of cold sources. DC networks usually operates at 6-7 °C but an increase of this range would integrate new sources and technologies while decreasing loads. To follow this aim it is necessary to redesign DC distribution and control systems to make suitable to operate at higher temperatures by limiting necessary flows. DC grids operating at 12 °C could be used for natural cooling. Example of advantages of higher temperature DC are: cutting of the electricity peaks demand, increasing in the efficiency of cooling and in the share of natural cooling.

Micro CHP/CCHP technologies have gained interest in recent years owing to their potential of providing efficient, clean and cost-effective energy requirements. They are considered a highly important power generation and H/C source, a promising technology for secure and sustainable micro-scale polygeneration. Integrated with RES, micro-CHP/CCHP technologies allow for CO_2 neutral power generation. In this sector the challenge is the development of a new generation of micro technologies to smooth the integration of RES and storage characterised by high technology flexibility and energy efficiency.

Short term and long-term thermal energy storage technologies are investigated to increase both the efficiency of heating and cooling systems and the share of RES. These systems enable the storage of available renewable or grid electricity for short or intermediate periods in power to heat configurations or of solar thermal energy for seasonal thermal storage, using a minimal amount of space in the building. Hot water stores, for example, are a common solution used in combination with RE technology. Several technologies in sensible, latent and thermochemical form are available as competitive solutions for energy storage, each of them characterized by different and specific advantages when coupled with RES. To provide enhanced solutions for the market, research is investigating for more compact solutions. This aim can be reached by increasing their storage density at the system level. Improving materials for the system the performance of TES systems can be increased.

The work of the TWG 5 was followed by the Implementation working Group (IWG) that outlined the following 8 key R&I activities to achieve the ambitious targets for the building sector:

1) New materials for buildings ;

2) Prefabricated active modules for façades and roofs or enabling technologies for active building skins;

3) Digital planning and operational optimization;

4) Living labs - Energy technologies and solutions for decarbonized European quarters and cities;

5) Cost-efficient, intelligent, flexible heat pumps (also thermally driven) and heat pumps for high temperatures;

6) Multi-source district heating integrating renewable and recovered heat sources, higher temperature district cooling and optimization of building heating system to minimize the temperature levels in district heating networks;

7) Cost reduction and increase in efficiency of micro CHP/CCHP;

8) Compact thermal energy storage materials, components and systems.

A list of ongoing European projects on these topics is reported in Table 2 [97].

Table 2: European Projects regarding the energy efficiency building.

Name Project	Description	Deadline
BIM2SIM (Germany)	Development of methods and tools focussing on creating executable simulation models out of data models such as building information model (BIM)	04/2021
SIMQUALITY (Germany)	Integration of building energy simulation programs into the planning process	07/2021
ADOSAN-LXB (Germany)	Development and demonstration of a gas driven adsorption heat pump system for retrofit of the building stock	07/2021
Biofassade (Germany)	Development of a facade insulation system using biopolymers and cellulose acetate hollow fibres with very high insulation properties.	09/2021
HYBUILD (Spain)	Development, realization and validation of hybrid electric/thermal storage solutions for Mediterranean and Continental climates	09/2021

Name Project	Description	Deadline
PV-HoWoSan (Frankfurt, Germany)	Development of a cost-efficient structural - physical functional and secure concept for restoration of multi-story apartment buildings with PV façades.	10/2021
SCORES (Nederland)	Demonstration of a Heat and Electric storage unit, with application of heat pumps & electric heaters for conversion from power to heat	10/2021
MPC GEOTABS (Berlin)	Project on combining geotabs with heat pump technology	12/2021
Smart Thermal Subgrid (Germany)	Implementation of innovative sub grids to promote the integration of local renewable energies	12/2021
SWS-HEATING (Greece)	Development and validation of a compact seasonal storage for heating demand of single-family houses, based on innovative composite sorbent materials.	05/2022
OOM4ABDO (Germany)	Object-oriented monitoring as a basis for more efficient operation, as well as cost-effective optimization of existing buildings through the utilization of machine learning-techniques, the application of virtual laboratories and the augmented, "transparent" operation of buildings and districts	11/2022
Innovation lab act 4 energy (Austria)	Innovation laboratory project to solve the problems of renewable energies integration with a focus on photovoltaic power paired with local consumption, linked to the high fluctuation of renewable energies.	12/2022
H2020 TEMPO (EU-project, coordinator Berlin)	Development and implementation of solution package for low temperature DH networks	12/2022

5. Conclusion

Around of the 40% of the final energy consumption in Europe is due to the building sector that, for this reason, shows the highest potential to reduce emissions and to save energy. 40% is more than any other sector of the European economy. Energy savings potential arises both from new buildings with a high energy performance and from the refurbishment (i.e., envelope, heating and cooling systems, management and control systems) of existing ones owing due to their larger number and the high energy demand. Energy efficient buildings is the main requisite to reach the ambitious goal of a sustainable future. Nowadays, it is estimated that around 75 % of the existing buildings are inefficient and that around 80% of their energy efficiency potential is untapped.

Energy efficiency in buildings plays a strategic role in a large number of EU energy policies, in particular by limiting EU's energy demand and therefore improving its energy security of supply.

In the last decades, the EU has imposed directives which set minimum requirements, obligations and measures for all Member States. The "Energy Performance of Building Directive (EPBD)", in particular, imposes specific energy efficiency standards to reduce the energy demand of the building sector. As part of the Energy Union Strategy of 25 February 2015, the European Commission is currently reviewing its directive.

EPBD sets out a framework for long-term strategies both to support the renovation of existing buildings into highly energy-efficient and decarbonized buildings by 2050 and to facilitate the introduction of nearly zero energy buildings (nZEBs) or Net zero energy buildings (NZEBs).

An NZEB is defined as a building with very high energy performance where the nearly zero or very low amount of energy required should be extensively covered by renewable sources produced on-site or nearby. A large variety of concepts and examples exist for NZEBs within Europe.

The existing NZEBs definitions among the EU Member States have common

approaches but there is a need to aggregate and improve the existing concepts in order to harmonize them to the nZEB requirements as indicated by the EPBD. Each country designs national plans for increasing the number of NZEBs reflecting national, regional or local conditions. It is crucial to translate the concept of NZEBs into practical and applicable measures. Reducing energy needs, energy consumption and increasing of the renewable energies are the crucial pillars imposed by the reference standard of NZEB.

R&I activities to accelerate greater energy efficiency in buildings regard the development both new materials and technologies and cross cutting heating and cooling technologies.

Despite materials can reduce energy consumption of existing building by more than half the rate of renovation is still < 1.2% due to a series of obstacles such as social and technical barriers. Often building owners obstacle options for improving their home's energy efficiency, among the reasons, there is the high cost of renovation.

For instance, the cost for renovating an apartment building block to NZEB is around 360 €/m2 while that one of a single family house is around 540 €/m2 [99]. Despite a series of barriers, new materials and technologies that better respond to the market's needs are a great opportunity to implement the EU policies and favour the transition of the existing building stock towards the NZEB target.

R&I in the field of material, should lead to the development of new sustainable, resilient and more performant materials with improved thermal properties, less embodied energy and more multi-functionality (insulation, heat/ cooling supply, electricity generation, energy storage).

According to policies towards Zero-Energy Buildings, the use of PV as a building material is highly increasing. Building Integrated Photovoltaic (BIPV) materials are essential parts of the development strategies of both the PV sector and the building sector.

Renovation of the existing building stock is equally crucial to reduce heating and cooling energy demand in buildings. Heating and cooling is responsible for 51% of

the EU's final energy consumption.

The vast majority of the energy needs is covered through the combustion of fossil fuels such as oil, gas and coal with a damaging environmental impact arising primarily from the associated greenhouse gas emissions.

Owing to the massive use of fossil fuels heating and cooling technologies show a high potential for reduction of the energy demand at building level. Development of efficient renewable heating and cooling technologies

is a basic pillar in the strategy supported by EU to meet its renewable and CO_2 reduction targets.

District heating and cooling, thermal storage and renewable energy hybrid systems and heat pumps are the most widely investigated options to increase the RES integration. By 2030 renewable heating and cooling technologies could supply over half of the heat used in Europe. Despite several advantages arising from the theoretical and technical potential of renewable energy sources, the market for these innovative technologies is not simple since it could need the replacement of existing infrastructures based on fossil fuels.

In this chapter it was given a brief overview on the state of art of the building sector with a particular focus on the most innovative challenges set to reach the climate targets discussed at international level. It was highlighted how, today there is a great opportunity to define the right directions for the building sector and to exploit the requirements set to reach the NZEB target towards a sustainable future.

Nomenclature

BIPV	Building integrated photovoltaic
CCHP	Combined cooling heat and power
CCS	Carbon capture and storage
CCU	Carbon capture and utilization
CEP	Clean energy package
CHP	Combined heat and power
d	Delivered energy
D	Delivered exported energy
DHC	District heating and cooling
DHW	Domestic heat water
e	Exported energy
E	Weighted exported energy
EC	European Commission
ED	Electricity Directive
EEB	Energy efficiency in buildings
EED	Energy Efficiency Directive
EPBD	Energy Performance of Building Directive
EPCs	Energy performance certificates
ETIPs	European Technology and Innovation Platforms
EU	European Union
g	Building's energy generation
G	Weighted generation
GACC	Global atmospheric CO2 concentration
GDP	Gross domestic product
GHG	Greenhouse gas
HDD	Heating degree days
HPs	Heat Pumps
HVACs	Heating, ventilation and air conditioning systems
i	Specific energy carrier (kWh/y or kWh/ m2 y)
l	Building's energy demand
IWG	Implementation working Group
L	Weighted load
LCA	Life cycle assessments
MD	Ministerial Decree

Nomenclature

MTOE	Million tons of oil equivalent
nZEB	Nearly zero energy buildings
NZEB	Net zero energy buildings
PEB	Positive energy building
RED	Renewable Energy Directive
RE	Renewable energy
RES	Renewable energy sources
SET Plan	Strategic energy technology plan
SETIS	SET Plan Information System
SG	Smart grid
TES	Thermal energy storage
TFEU	Treaty on the Functioning of the European Union
TWG	Temporary working group
w	Weighting factor

Chapter 2

Energy Flexibility Buildings to support the renewable energy sources integration: a state of art of positive energy districts and sector coupling

1. Introduction

With the aim to achieve the goals of several climate policies, the increasing world electricity demand is envisioned to be entirely supplied by renewable energy sources (RES) [100]. Deployment of RES and reduction of the total demand are critical aspects towards the decarbonization of the electricity system [101,102].

The trend of penetration of RES is increasingly rapidly worldwide and it is expected will continue to grow in the future playing an important role in the clean energy transition [103].

The growing renewable penetration is leading to important challenges in planning and controlling the energy production, transmission and distribution since it is usually not adjusted in order to match electricity demands [15,16]. The increasing penetration of RES maybe lead to a loss of generation control and predictability owing to the no dispatchability of the renewable production [17]. For this reason the flexibility of the power system must be increased to allow an easier RES integration in the existing

infrastructures. Flexibility is a crucial condition to have an instant balance of temporal and spatial mismatches between loads and generation [18–21]. In literatures several examples of flexibility sources are reported, i.e., energy storage, different demand response mechanisms, as well as, power-to-X technologies [22].

The transition from a system dispatching energy following electrical demand to a Smart Grid (SG) will characterize the future power system [23,24].

In future Smart Grids/Energy networks building sector is expected to play an important role [25] since the Smart Grid context is creating the opportunity for consumers to behave prosumers offering services to utility grids [27–29].

Prosumers can provide flexible services by managing their distributed energy resources (DERs) [104]. As an example, a smart building as a prosumer can manage its resources trading energy and flexibility with other smart buildings [105]. Grid developers consider buildings a key element to improve the operational flexibility of the power systems [106]. The flexibility of the energy system can be significantly increased shifting in time a large part of the building energy demand [107,108]. In particular, decoupling thermal-electric loads is among challenges restricting renewable consumption to improve the operational flexibility of the demand in the energy system [109].

The building sector is responsible of a high portion of consume of energy, several reports indicate an account for about 35-40 % of primary energy and 36% of CO2 emissions [30,31] and the biggest contributors of final power consumption followed by industry and transport [32].

The main challenge in this sector is to achieve the reference standard of nearly zero energy buildings (nZEBs) or Net zero energy buildings (NZEBs imposed by the European Union (EU)) [40–43]. NZEBs can be defined as buildings producing, at least, as much as energy as they consume [38,39].

In the ambitious concept of nZEB, the future energy systems should be dominated by buildings acting both as consumers and prosumers [44,45]. In the management of electric power supply and demand the transition from passive consumers toward active prosumers buildings will play a crucial role [46]. Owing this transition, the

current configuration of the electricity grid will change since the grid must be restructured to account both the energy demand and the local energy generation [47]. To facilitate the fast development of sustainable energy productions and utilizations smart grids with real time control capabilities as well as bidirectional communications with prosumers are needed [48].

1.1. Energy Flexible Building (EFB)

It is common in literature the concept for which buildings as a source of power systems flexibility can provide grid services accelerating the transition toward a low carbon energy system [110].

Buildings can supply flexibility services in different ways such as shifting of plug loads [111,112], utilization of thermal mass [113,114], adjustability of HVAC systems [115–117] and charging of electric vehicles [118–121]. How to provide such Energy Flexibility Buildings (EFB) was the main topic of the research project International Energy Agency- Energy Buildings and Communities (IEA EBC) Annex 67 [122].

It was started to increase knowledge on critical aspects and possible solutions about the Energy Flexibility (EF) provided by buildings. Expert focused both to individual buildings and to clusters since surrounding energy networks are influenced by the individual buildings, but it is their total energy demand which is detected within the same distribution network [122].

Starting from the literature exiting, the experts participating of the Annex 67 defined the EF of a building as "the ability to manage its demand and generation according to local climate conditions, user needs and grid requirements". Moreover, it was stated that "Energy Flexibility of buildings will thus allow for demand side management/load control and thereby demand response based on the requirements of the surrounding energy networks"[122]. Other definitions of the flexibility of buildings reviewed in literature are listed in Table 3.

Most of the literature antecedent to Annex 67 have concentrated more on flexibility in power systems than on flexibility in thermal systems or buildings since the theme originated in the context of electrical engineering and the SG [123].

Flexible buildings are crucial both for building owners and for grid operators, in particular, for the first ones the benefit in the utilizing buildings' flexibility is in terms of cost savings, for the second ones is in terms of recognition of how much of their request/need for demand response can be activated [124,125].

In the context of Smart Flexible Buildings, in literature are widely used the so-called key performance indicators (KPIs) to account several aspects connected to the ability of a building to response to an external signal.

In this chapter KPIs and their acronyms, types and applications in the context of the demand side management flexibility strategies including theoretical, experimental and numerical studies, are reported and descripted.

Table 3: Some definitions of Flexible Building.

References	**The flexibility of building is "…"**
Bertsch et al. [126]	The capability to balance rapid changes in renewables generation and forecast errors within a power system.
Capuder et al. [127]	The capability to respond to price signals in real time.
De Coninck et al. [128]	The ability to deviate from its reference electric load profile during a certain time span data.
Finck et al. [129]	The ability to adapt the energy consumption to fluctuations in supply.
Fischer et al. [130]	The ability to modify energy generation or consumption in response to external signals.
Hurtado et al. [131]	The ability to adjust dynamically the electrical power consumption patterns in response to external signals, either voluntary or mandatory.
Junker et al. [132]	The ability to respond to an external penalty signal
Le Dreau et al. [133]	The ability to shift the energy use from high to low price periods.
Lopes et al. [134]	The deviation of electricity consumption under different scenarios of electricity costs and thermal comfort provision.

Masy et al. [135]	The ability to shift the (heat pump) electric loads from peak to off-peak hours
Reynders et al. [136]	The ability to shift the electricity use without jeopardizing thermal comfort
Salom et al. [93]	The ability to contribute in a positive way in the context of a system with high share of renewables.
Salom et al. [137]	The ability to respond to signals from smart grids, price signals or to some residents 'action, and consequently adjust load, generation and storage control strategies aiming to serve the grid, the building needs, or adjust to favorable market prices for energy exports or imports.
Nuytten et al.[138]	The ability to shift the consumption of a certain amount of electrical power in time.
Vigna et al. [139]	The capacity of a building to react to one or more forcing factors in order to minimize CO2 emissions and maximize the use of renewable energy sources
Stinner et al. [140]	The power and the energy that can be delivered by his energy systems (such as a CHP coupled to storage devices)

1.2. Building Flexibility: characterization and quantification

There are different definitions of flexibility, as a consequence, different methods focus on quantifying building flexibility are used in literature [141]. According to Lund et al. [15] time, energy and costs (Figure 14) can be considered as the three main properties: All quantification methods and their corresponding performance indicators in literature have typically revolved around these three metrics [142].

Usually two approaches are used to quantify the flexibility [143]. The first approach is focused on the technical aspects of the flexibility such as energy can be shifted over time or power and discharge time of storage technologies [144,145].

In the second approach, flexibility is quantified by financial indicators to account the costs avoided due to shifting consumption to periods with low energy prices under different scenarios of market costs and thermal conditions [146].

Both approaches required detailed modelling of the energy systems, including technical constraints and boundary conditions [147,148]. Moreover the potential energy flexibility can be found either deductively by building simulation tools or inductively by statistical time series analysis [149,150].

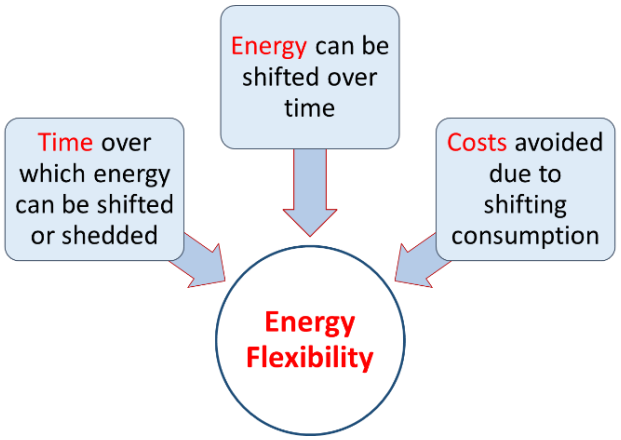

Figure 14: Energy Flexibility properties.

Flexibility modelling is affected by several factors such as physical characteristics (thermal mass, insulation, and architectural layout), technologies (ventilation, heating, and storage equipment), control systems [151–155].

The approach to quantify the flexibility as amount of time is particularly used with strategies focused on minimizing costs and maximizing the energy consumption [138]. For instance, D'Hulst et al. [110] implemented a method to quantify the flexibility as power increase or decrease during an interval of time, Six et al. [156] as number of hours the respective consumption can be delayed or anticipated, Oldewurtel et al. [157] as the amount of power can be increased or decreased during a specific interval of time compared to a baseline power consumption.

Reynders et al. [136] classified the several definitions of flexibility and the corresponding methods of quantification in five categories:

- methods focused on the improving the performance of the energy grid;

- methods based on the compensating power imbalances in the grid;
- methods based on energy price as external signal;
- methods based on the secondary effects of activating energy flexibility, i.e., the impact on thermal comfort;
- methods based on the level of individual technologies.

Investigating the energy flexibility on the basis of the potential flexibility going from individual energy systems components (HVAC, CHP, HPs…) is among the most investigated approach reported in literature [140]. As an example, Nuytten et al. [138] reported a study on the use of a residential heat pump combined both with TES and with a CHP quantifying the flexibility as number of hours the respective energy consumption can be delayed or anticipated. The same approach was applied by Arteconi et al. [158] in a study on the flexibility potential of TES system coupled with a heat pump in a residential house in UK. Hedegaard et al. [159] showed how heat pumps coupled with passive thermal storage not only increase the potential flexibility but also are an important cost-effective solution to integrate renewable energy (wind in their study). Miezis et al. [160] demonstrated that HPs with use of MPC can contribute both to limit the peak power demands and to maximize the self-consumption of the on-site produced electricity.

A schematic representation of the concept of flexible building is shown in Figure 15. In a flexible building, able to respond to external penalty or control signals by a controller, the relationship between the external input and the resulting energy demand could be expressed by a flexibility function or flexibility indicators [161,162]. The reaction of a building to external signals is defined ramping rate [163]. The power can be delivered in response to a given request dependent on the purpose is defined power capacity and it expresses the value of utilizing the flexibility [164]. If there is a decrease in the power demand the demand response action is referred as up regulation otherwise down regulation [165]. The capacity to modulate the energy in-feed into the power systems, based on control signals, was defined as operational

flexibility by Ulbig et al. [166,167]. In particular, if the aim of the external penalty or signal is to minimize the total energy consumption the building is referred as “energy efficient”, if the aim is to minimize the total energy price is referred as “cost efficient”, if the aim is to minimize the total carbon emission related to the power consumption it is referred as “emission efficient” [168].

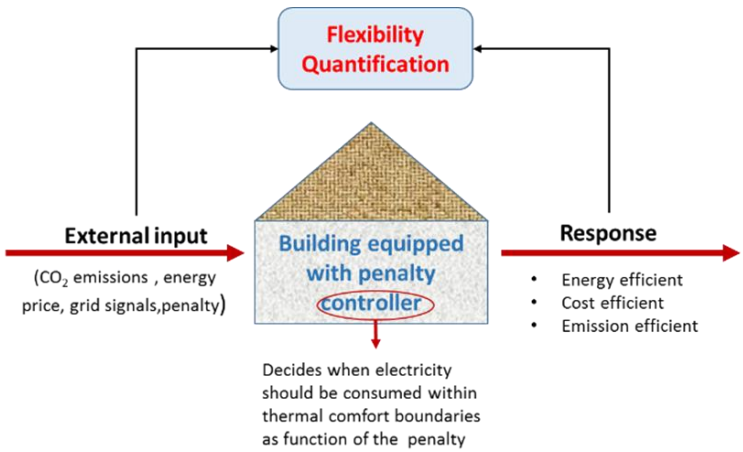

Figure 15: Mechanism of flexibility in building.

Control strategies to deploy demand side flexibility are crucial instruments to activate the energy flexibility of the building in order to improve grid interaction, lower energy costs, perform load shifting or reduce energy needs [169–174].

2. Demand Side Management instrument to support the EFB

Demand side management (DSM) can be defined as the ability of balancing the supply of electricity on the network with the electrical load by adjusting or controlling the load consumption [175]. Its main objective is to encourage the consumer both to use less energy during peak hours and to move the time of energy use to off-peak times such as night to flatten the demand curve [176,177]. As a consequence, the energy system is improved at the side of the end-user in terms of consumption and

cost effectiveness [178]. As shown in Figure 16 load shifting, peak shaving, reduction of energy use or valley filling are examples of different ways to made flexible the demand building profile [179,180].

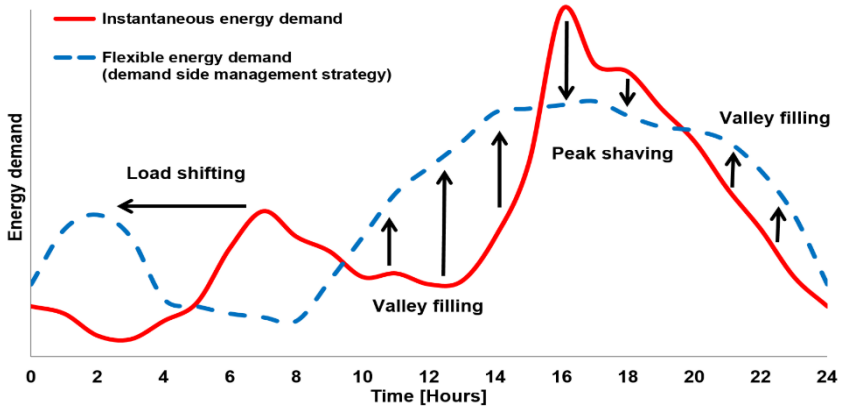

Figure 16: Examples of demand side management flexibility strategies [181].

According to its definition, DSM reduces the total electricity cost of each consumer alleviating the aggregate peak to ratio subjected to real time pricing policy [182,183]. It is crucial in the smart grid context, especially, to increase the integration of RES without jeopardizing the security and stability of the electric system [184,185]. By flexible programs allowing customers a greater role in shifting their own demand for electricity during peak periods, DSM adds significant economic value to all actors involved in the modern energy network [186,187]. With respect to power system flexibility, useful strategies may be those ones fall under the category of demand response (DRe) [188].

DRe can be defined as “intentional electricity consumption pattern modifications by end-users customers by altering the timing, level of instantaneous demand or total electricity“[189]. It allows to manage local power consumption in response to supply conditions such as peak demand or high market prices [190,191]. The potential for using a building for DRe purposes to react to changes in energy demand supply and

demand is defined as energy or demand flexibility [192,193].

DSM strategies will be a crucial instrument to foster their role and to evaluate their impact into the future energy regime [194,195]. DSM programs evaluate buildings as a source of demand side flexibility (DSF) in terms of specific parameters such as power demand, energy consumption, limits of operational flexibilities, systems' response times, indoor comfort [196–198].

Dispatchable and non-dispatchable DR programs are available to both commercial and residential consumers [199,200]. In dispatchable or incentive-based programs, the consumers can allow the system operators to control some of their electric appliances directly during the peak or emergency periods [201]. The participants who are enrolled in these programs or are offered some incentives in exchange to the reduction of their loads or might be penalized if they are not responding [202].

In non-dispatchable or price-based programs consider dynamic pricing rates in which the main objective is to flatten the demand curve by offering higher price during peak periods and lower ones during off-peak periods [203]. The participants voluntarily schedule their consumptions profile according to electricity tariffs. Time of use (TOU), critical peak pricing (CPP), and real time pricing (RTP) are typical non dispatchable programs [204,205]. In recent works on demand flexibility the carbon intensity, emission of CO_2 per unit of energy consumption, is considered as an alternative external control signal [206–209].

According to DSM context, a flexible energy building is able to get high benefits, both economic and environmental, operating at low tariff periods, associated to low CO2 emissions rates and low electricity demand in electricity grid [210]. DSM control strategies play a crucial role as shown in [211].

2.1 DSM flexibility control strategies

Demand side control strategies are implemented with the aim both of increasing demand shifting potential of buildings energy demand and offering solutions to use RES more efficiently [212–215]. The control strategies act upon certain control

inputs parameters such as building envelope characteristics, climate properties, indoor temperature, occupancy and behavioural patterns, characteristics of the end-use equipment and their flexibility, load or generation profiles [216–218].

In the building sector among the control strategies, rule-based control (RBC) and model-predictive control (MPC) to deploy demand side flexibility are widely investigated [219–224].

RBC is an heuristic methods having the form "if (condition is verified), then (action is triggered)"[146]. It is so called since it usually relies on the monitoring of a specific "trigger" parameter on which a threshold value has been fixed. Time, power, energy price, residual load, PV power, voltage deviation, CO_2 levels are example of trigger parameter monitored [225]. Since trigger parameters are fixed RBC is not a dynamic method so it does not adapt to real conditions [226].

MPC is a well-established method able to exploit both the predictions of future disturbances (e.g., internal gains, weather, etc.) and given requirements (e.g., comfort ranges) in order to anticipate the energy needs of the building and optimize its thermal behaviour [227,228]. Compared to RBC control, designed to improve only one control objective, MPC is more complex and able to compute an optimum schedule compromising different control objectives [229–231].Usually it is used to control and optimize residential appliances [232], the building interaction with a smart grid or micro-grid [233] or an on-site renewable energy generation system [234].

The common feature of all MPC strategies is that they make use of models of the processes to estimate a future control signal by minimizing an objective over a receding horizon as shown in [235]. Since they can deal with time-varying operating conditions have a great potential for deploying demand side flexibility contributing to peak shaving and load shifting of the electricity consumption [236].

The most common MPC is the economic model predictive control (EMPC) whose aim is to reduce monetary costs optimizing an objective function [237,238]. This kind of control is widely applied to account the potential flexibility offered by energy systems and storage systems [239–241].

The control strategies play a key role both in quantifying the potential flexibility of buildings and in defining the key performance indicators (KPIs) measuring different aspects of energy flexibility [242]. The most common strategies are listed and discussed briefly in the next sections.

Load shifting with fixed scheduling

It is a strategy in which a controller try to avoid or force the operation of the energy systems during fixed hours to avoid peak power demand or high electricity rates [243]. The predefined hours can be identified based on the already available information of a national electricity grid or the availability of static time-of-use tariff [244]. As an example. Lee et al. [245] by set-point modulation reduced the use of the HP during the grid peaks achieving a reduction in the energy consumption of 80% for cooling and 64% for heating. The usage of thermal energy storage (TES) systems is a strategy widely investigated for shifting load [246–249]. In particular, the surplus of electricity is stored as thermal energy during off-peak times and then used during peak-hours in order to flatten the customer's load profile [250–253].

In the study of Klein at al. [254] fixed schedule was used to load shifting local PV surplus generation with the aim to maximize on-site renewable energy. Shifting the electrical loads towards off-peak electricity leads to a cost reduction as shown in the study of Koh et al. [255].

Peak shaving

It is the reduction of the demand peak in order to support the grid operation [256]. As trigger parameter monitored the power exchange of the building with the grid can be used defining thresholds both for the export and in the import powers. Thresholds values must be chosen without influencing the outcome of the controller [257]. This strategy is widely used in buildings equipped with heat pumps. As an example, in the study of Sartori et al. [258] when the building is consuming more than the import threshold (fixed at 2500V), the heat pump is switched off. Conversely, if the building injects more power in the grid than the export thresholds (fixed at 5000 V), the heat pump is started. Peak shaving is also used in order to increase the self-consumption

from PV systems [259,260]. Pimm et al. [261] showed the potential of electricity storage for peak shaving on distribution networks with a particular focus on residential sector. Peak shaving strategy has the disadvantage that the highest peaks could not be eliminated since are caused by non-controllable loads such as domestic appliances [262].

Strategies of reducing of energy costs

These are all control strategies rely on the variations of energy price in time with the objective of reducing the energy costs for the end-users with profitable for both the grid side and the consumer side [263–265]. A controller on the basis of high and low price thresholds must be able to decide when electricity should be consumed as a function of present and future electricity tariff evolution [210]. Economy (E7) and Electricity spot price contract are examples of electricity tariffs considered for DSM strategies to reduce energy cost. A detailed description of electricity tariffs is out of this work, specific literature is reported in [266–269]. Le Drau et al. [133] analysed energy cost savings by using the storage potential of the building thermal mass to load reduction during peak price periods based on the availability of electricity the spot market price observed in Nordic market.

D'Ettorre et al. [270] performed a study on the flexibility offered by a water storage tank for building applications. A price-based program was implemented and a MPC was solved in order to meet the load at minimum cost. To assess the flexibility cost the hybrid system without thermal storage was chosen as reference scenario. Their results showed over on horizon of 24 hours it was obtained a reduction cost up to 35%. Moreover, the authors showed that reducing the storage size the maximum achievable cost savings decreased according to several studies in literature.

Strategies of improving the consumption of RES

These are all control strategies whose objective consists in improving on-site generation and self-consumption [271,272]. Among the advantages, there is the minimization of the energy exports caused by the excess of on-site generation [273].

In the study of Schibuola et al. [173] a heat pump is forced to switch on when the PV panels are generating electricity, enabling to reduce the electricity exported by up to 12% and the electricity imported by up to 22%, thus improving the self-consumption. Several studies were performed with the aim to align HP to improve on-site generated PV [274,275]. In the work of De Coninck et al. [276] an HP is coupled to a sensible storage tank for domestic heat water (DHW) production. PV surplus is used to charge the storage when the voltage increases over the threshold (fixed to 2500 V) as consequence of the excess of PV production. The set-point for the DHW tank is raised in order to utilize more electricity and avoid the PV inverter shutdown. Voltage at the distribution feeder, PV production, residual load at the local or global scale are typical trigger parameters monitored to improve RES consumption [277,278]. Storage set-point control with PV is an application widely investigated to increase self-consumption and lower peak grid injection so storage offers the possibility to decouple demand and supply [279–281]. Bandera et al. [282] performed a study showing how self-consumption can be increased by harnessing thermal mass storage of the building. The main aspect of the study is that the self-consumption occurring without surplus to the grid avoid the inherently constraints of the power system. The management of RES is receiving a more attention so new technological solutions regarding a grid with more potential are a crucial challenge [283,284].

3. Building Indicators: an overview

Indicators are metrics used to quantify several aspects of building such as the impact that technologies, components or control strategies have on the available flexibility [122]. As regards flexibility indicators, in literature it is a common way to refer to them with the name of key performance indicators (KPIs) to highlight that if applied correctly improve the building performances in terms of energy flexibility and operational energy costs savings [285]. KPIs assessing building energy flexibility and the interact with the grid, are usually related to final energy use, primary energy use energy needs; cost of energy, CO_2 emissions, services offered to the grid [286].

As shown in Figure 17, in this work indicators were divided into two main groups: energy indicators and load matching and grid interaction (LMGI) indicators.

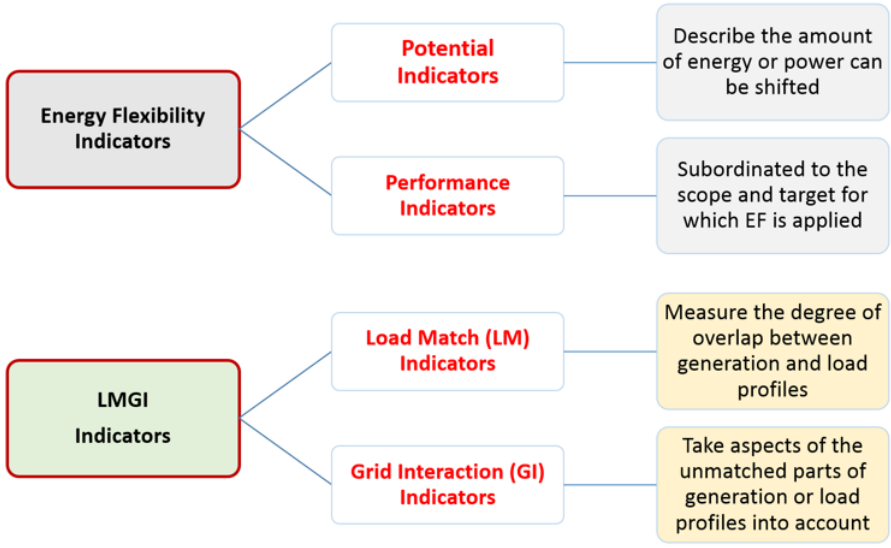

Figure 17: Performance building indicators: classification.

According to the classification adopted by Claub et al. [287], energy potential indicators provide detailed information about energy consumption in relation to the power grid and are useful to identify performance issues of the current energy system [288]. The potential indicators depend on the physical/ technological properties of the building while the performance ones are dependent on the specific application of the energy flexibility.

Indicators for load match and grid interaction are considered relevant with time and research progress on nZEB concept providing a better understanding of the interplay between generation and demand [289,290]. LMGIs are crucial to investigate the coupled performance among grid, RES and building and to assess the degree of success of grid control strategies, or storage, sizing or investment decisions [291]. Building Flexibility represents a key issue to be addressed not only to single level but

also at cluster level as an effective ng low carbon strategy [292].

A cluster can be defined as a group of buildings located in the same area and, on the other hand, a portfolio of buildings geographically far but owned by a single person or set of occupants [293]. The cluster concept is transforming the energy system by shifting on-site energy generation from a single Net Zero building to a system of "Net Zero clusters"able to share distributed power generation and storage devices with the maximum efficiency [294].

3.1 Potential Indicators

Le Dreau et al. [133] defined the **Flexibility Factor (FF)** as the ability to shift the energy use from periods with high energy prices to periods with low energy prices:

$$FF = \frac{\int_{lpt} q_h dt - \int_{hpt} q_h dt}{\int_{lpt} q_h dt + \int_{hpt} q_h dt} \tag{2.1}$$

where

- q_h is the heating demand;
- subscript h stands for heating;
- subscripts lpt and hpt stand for low price time and high price time respectively.

$$-1 \leq \text{FF} \leq 1 \tag{2.2}$$

FF gives an indication of when energy is consumed. In particular, if no demand load occurs during low price time ($\int_{lpt}^{2} l(t)dt$=0) the value factor is -1, if no demand load occurs during high price time ($\int_{hpt}^{2} l(t)dt$=0) the value factor is 1, if demand load is similar during both price time ($\int_{lpt}^{2} l(t)dt = \int_{hpt}^{0} l(t)dt$) the value is 0.

The authors quantified the energy can be shifted in terms of heat stored by thermal mass. FF can also be classified as thermal indicator. Activation of thermal mass was realized by a thermostat whose set point corresponds to a neutral thermal sensation.

In case of low price of energy, heat conservation is realized by decreasing the temperature set point (downward modulation) while in case of high price of energy heat is released by increasing the temperature set point (upward modulation).

The utilization of FF is limited to the kind of grid which corresponds the energy price. Level of insulation, changes in climate conditions and energy systems are the main parameters affecting the value of FF.

Finck et al. [295] performed a study on the demand flexibility showing that thermal storage devices coupled to heat generator increase FF. Here the flexibility factor, as indicator of flexibility in the dimension of operational costs, is referred to high and low-price periods determined based on the standard deviation of the daily electricity price. The authors quantified the energy can be shifted in terms of power to heat conversion founding that the highest value of this factor (0.86) was reached with sensible storage in comparison to latent (0.67) and thermochemical (0.15) thermal energy storage.

Similar to FF it is the **Shift Flexible Factor FFS** defined by Taddeo et al. [296]. It is defined as the ability to measure the capability to shift the energy consumption towards sunlight hours in order to maximize the use of on-site photovoltaic (PV) generation.

$$FF_s = \frac{\int_{DT} l(t)dt - \int_{NT} l(t)dt}{\int_{DT} l(t)dt + \int_{NT} l(t)dt} \tag{2.3}$$

where

- $l(t)$ is the building electrical load;
- subscripts DT and NT stand for daytime and nighttime respectively.

The authors quantified the flexibility of a semi-virtual simulated building equipped with a PV and battery in terms of heat and electrical storage during the day/night hour's strategy. Heat is stored by thermal mass whose activation is realized by a thermostat: during late daylight upward modulation is applied in order to

increase the consumption to pre-heat the building (storage). Electrical energy is stored during sunlight hours if the PV production is higher than the building electrical demand. RES production is settled as forcing factor to measure the building reaction.

RES production settled as forcing factor to measure flexibility building is a strategy applied also in the study of Vigna et al. [297] on flexibility assessment of a cluster. Energy flexibility is quantified as the measure of the cluster reaction to PV production. Flexibility is provided by storage in the thermal mass activated by a thermostat whose set point is settled according to the PV production. To quantify the flexibility in terms of reduction of the heating energy demand not covered by RES was introduced the **Flexibility Index FI**

$$FI = \frac{\int \left(q_{match}^{REF} - q_{match}^{SMART} \right) dt}{q_{consumed}^{REF}} \tag{2.4}$$

where

- q is the residual demand that is the energy demand non covered by RES and thus satisfied with non-renewable energy sources;
- REF is referred to the reference scenario (cluster managed by a control system not awaring of the forcing factor);
- $SMART$ is referred to flexibility scenario (control sharpened according to the forcing factor);
- $q_{consumed}^{REF}$ is the reference heating demand.

Shifting flexible loads from peak to off-peak hours, minimizing the procurement costs, is a way to reduce the cost of electricity supply.

Masy et al. [193] defined the **Procurements Cost avoided Flexibility Factor** $\boldsymbol{FF_{PC}}$ to quantify the building flexibility in terms of procurement costs avoided (cost savings):

$$FF_{PC} = \frac{PC_{max} - PC}{PC_{max} - PC_{min}} \tag{2.5}$$

where

- PC is the total procurement cost of the electricity consumed (€/year);
- the subscript max and min refers to procurement costs evaluated using the maximum and minimum values of the electricity tariff available in the spot market.

$$0 \leq FF_{PC} \leq 1 \tag{2.6}$$

The minimum value 0 is reached when the electricity required is used at the time with the highest price ($PC_{max} = PC$) while the maximum value 1 at the time with the lowest price ($PC_{min} = PC$). Since the electricity cost is not constant, the value of the value of $FF_{PC}$is not unique.

To account the flexibility in economic terms the authors defined the **Volume Shifted Flexibility Factor FF_{VS}**:

$$FF_{VS} = \frac{FF_{PC} - FF_{PC,ref}}{FF_{PC,ref}} \tag{2.7}$$

If this metric has a value >1 it means that in comparison with the flat tariff, there is an overconsumption and higher cost of electricity supply. This indicator is similar to the annual cost saving ratio (ACSR) defined by Wang et al. [298].

Analysing the operational cost savings is a common approach to quantify indirectly the impact of energy flexibility [299–301].

Energy price is not the only penalty signal used to shift the load from peak hours to off peak hours, CO_2 emission defined as the ratio between the total amount of CO2 emitted divided by the total electricity generated in each hour is among indicators used to DSM control [302]. It means that buildings, as a source of demand side flexibility, can be evaluated not only in terms of specific energetic parameters but also in terms of environmental impacts [303].

3.2 Performance indicators for energy storage systems (ESS)

In the research field focusing on the flexibility potential offered by buildings, energy storage systems (ESS) play a key role for power grid support [304]. Several studies show that overcoming the mismatch of generation and load profiles is the main characteristic of all ESS leading to an increase of the overall efficiency and better reliability , moreover, building owners may save cost since storage charging occurs during off-peak hours [305].

In the building sector ESS play a key role since without them the high targets for RES penetration may not be achieved [306]. Renewable power is converted and stored to meet the demand so that the utilization of RES can be maximized [307]. The use of efficient storage measures are promising options to deploy low-carbon technologies in the electricity networks without the need of reinforcing existing infrastructures [308,309].In the context of the flexibility their main purposes are to decrease the peak power demand, the non-renewable energy consumption and the running costs [310].

Among energy storage solutions, the implementation of thermal energy storage systems (TESs) is among the most developed DSM options to provide flexibility in the energy system shifting the electricity demand and minimizing the stress on the grid [311–313]. In the building sector a such typical sensible storage is the domestic hot water tank is the most used storage system to provide short-term flexibility [314–316]. It occurs when the charge and discharge of the storage takes place within an interval of several hours or days [317].

Valsomatzis et al. [18] in a study on individual flexibility building measures showed that electricity-only solutions could not provide sufficient system flexibility. In contrast, additional energy flexibility can be obtained by integrating electrical and thermal systems as a whole by offering cost-effective flexibility [318,319]. In literature it is widely investigated the use of power-to-heat (PtH) systems combined to TES devices [320,321]. The connection between electrical and thermal systems increases the flexibility of the electricity demand and energy system due to the inertia

of thermal systems [322]. PtH is considered the most relevant flexibility option of the DSM especially to ensure the integration of the RES [323,324].In particular, when there is an excess of generation, electricity is converted into heat contributing to peak shaving, load shifting and energy balance [325,326].

The flexibility of a building quantified at level of its energy storage systems has been defined in the pioneering work of Makarov et al. [327]: the intrinsic building flexibility to adapt its demand can be quantified on the level of individual technologies.This approach was applied , in the context of the thermal storage technologies, by Stinner et al. [328].

The authors discussed as flexibility options in the building sector the introduction of different heat generators coupled to TES systems. Flexibility quantification is based on the comparison of power profiles over the time periods of forced and delayed flexibility. According to Nuytten et al. [138], the forced flexibility (τ_{forced}) is the time during which an heat generator can operate at maximum power until the storage is completely charged. The delayed flexibility ($\tau_{delayed}$) is the time during which the heat generator can be in switch-off mode until the storage is completely discharged. τ_{forced} and $\tau_{delayed}$, are affected by the storage losses and size [329]. In particular, τ_{forced} increases proportionally with the storage size. Moreover, the type of generator affects them. As an example for the same thermal power, HPs have lower temporal flexibility than a CHP [330].

Stinner et al. [328] defined the **power flexibility ($\boldsymbol{\pi}$)** indicator as the difference among the **maximum power ($\boldsymbol{\pi_{forced}}$)** or the **minimum power ($\boldsymbol{\pi_{delayed}}$)** with a reference case (buildings supplied without storage).

$$\begin{cases} \pi_{forced}(t, \xi - t) = \pi_{max}(\xi) - \pi_{ref}(\xi) \\ \xi | t \leq \xi \leq t + \tau_{forced}(t) \end{cases} \tag{2.8}$$

$$\begin{cases} \pi_{delayed}(t, \xi - t) = \pi_{ref}(\xi) - \pi_{min}(\xi) \\ \xi | t \leq \xi \leq t + \tau_{delayed}(t) \end{cases} \tag{2.9}$$

where t is the starting time of power flexibility. (π) is the amount of power that can be increased or decreased during a specific amount of time compared to a baseline power consumption. Power curves are calculated for the electrical power side so they are useful for a comparison with the flexibility demand of the electrical grid. Power flexibility can be used to determine flexibility towards power grid stabilization [295].

The integration of the power curve over forced or delayed operation period was defined **energy flexibility $\boldsymbol{\varepsilon}$** [328]:

$$\varepsilon_{forced} = \int_0^{\tau_{forced}(t)} \pi_{forced}(t, \xi)\, d\xi \tag{2.10}$$

$$\varepsilon_{delayed} = \int_0^{\tau_{delayed}(t)} \pi_{delayed}(t, \xi)\, d\xi \tag{2.11}$$

Buildings can supply flexibility using their mass as sensible heat storage tolerating large changes in heat supply as shown in the study of Kensby et al. [331]. The use of structural mass as storage system is a promising cost-effective solution to gain flexibility and to improve the penetration of RES [332]. All buildings have thermal mass embedded in their construction useful to store sensible heat (or cold in case of air-conditioned buildings) [333]. Active demand response (ADR) using the thermal mass of buildings is considered a key technology towards the transition to a sustainable energy market [334]. Energy cost savings, increased uptake of RES production and greenhouse gas emission reductions are among advantages in the use of this form of storage [335]. The modulation of the thermal mass is affected by several factors, such as, level of insulation and type of emitter [336]. For this reason different buildings need different control strategies in order to find the best compromise among energy demand, flexibility and indoor thermal comfort [337].

Among the earliest Annex 67 studies presented on the potential flexibility of the structural mass there is the work of Reynders at al. [124]. The authors defined the following KPIs: available structure storage capacity (C_{ADR}), power shifting capability

(PSC).and storage efficiency (η_{ADR}). These indicators are not useful only for thermal mass but also for every kind of storage systems as proposed by Oldewurtel et al.[338].

The **available structure storage capacity C_{ADR}** is defined as the amount of heat can be added to the mass of a dwelling, in the time-frame of an active demand response (ADR) event without jeopardizing thermal comfort [124]:

$$C_{ADR} = \int_0^{l_{ADR}} (Q_{ADR} - Q_{ref})\, dt \tag{2.12}$$

where

- Q_{ADR} is the thermal power during the ADR event;
- Q_{ref} is the thermal power corresponding to the reference case (heating profile keeping the temperature equal to the minimum comfort temperature corresponding to a scenario whereby the heat demand is minimized at building level);
- l_{ADR} is the duration of the ADR event.

In Figure 18 it is reported a schematic representation of the descripted indicator.

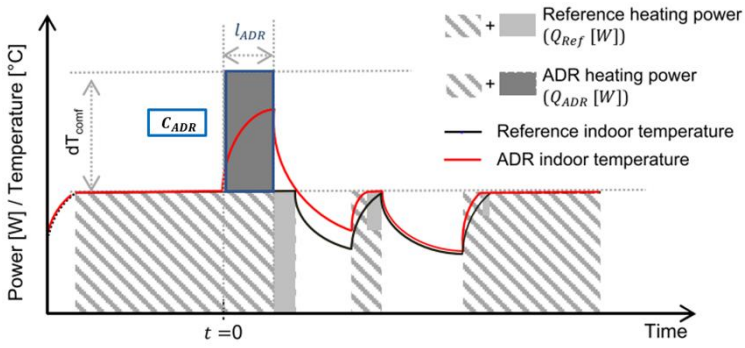

Figure 18: Graphic representation of the available storage capacity indicator C_{ADR}. The dark grey area delimited by the blue line is the energy that can be shifted (heat stored) during an ADR event of flexibility modulation- Adapted from [124].

C_{ADR} represents the surplus/deficit of heat that can be stored/released during an ADR event given the boundary conditions for thermal comfort, climate, and occupant behaviour in the building envelope. [339]. The ADR event implemented in the work of Reynders at al. [124] is the modulation of the energy use by changing the temperature set point. The temperature set point is increased (heat storage), as shown in, or decreased (heat discharged) respect to the reference indoor temperature .In the duration of the flexibility modulation it is analysed the response of building in terms of energy can be shifted.

In (2.12) the difference inside the integral is defined **heating power** or **thermal power shifting Q_δ**:

$$Q_\delta = Q_{ADR} - Q_{ref} \tag{2.13}$$

The amount of energy increasing during heat storage (upward storage capacity) is defined charged heat and it is given as follows [133]:

$$\Delta Q_{heat\ charged} = \int_0^\infty Q_\delta\ (>0) dt \tag{2.14}$$

The amount of energy decreasing during heat discharging (downward storage capacity) is defined discharged heat and it is given as follows [133]:

$$\Delta Q_{heat\ discharged} = \int_0^\infty Q_\delta\ (<0) dt \tag{2.15}$$

The power shifting capability is defined as the relation between the change in heating power and the duration (t_δ) that this shift can be maintained before the normal operation of the system is jeopardized taking into account the future boundary conditions[124]:

$$PSC = t_\delta(Q_\delta) \tag{2.16}$$

Whilst C_{ADR} and η_{ADR} can be interpreted as characteristic properties of the building, PSCallows to account the instantaneous energy [295].

For a building in which the storage is charged by an electrical grid connected generator such as an HP or electric heater, the power shifting capability must include not only the thermal (heating) power shifting $Q_{\delta,th}$ but also the electrical power shifting due to the electricity consumption of the heat generator $Q_{\delta,el}$ as shown in the work of Finck et al. [295]. The authors introducing the instantaneous power flexibility $Q_{ist} = f(Q_{\delta,th}, Q_{\delta,el})$ representing the potential flexibility towards the power grid in any case of charging, discharging or idle mode.

The storage efficiency or shifting efficiency η_{ADR} is defined as the fraction of heat that can be stored during ADR event in order to be used subsequently to reduce the heating power needed to maintain thermal comfort [124]:

$$\eta_{ADR} = 1 - \frac{\int_0^{\infty} Q_{\delta}\, dt}{\int_0^{t_{ADR}} Q_{\delta}\, dt} = 1 - \frac{\int_0^{\infty} Q_{\delta}\, dt}{C_{ADR}} \tag{2.17}$$

The numerator represents thermal storage losses that is the fraction of the heat stored during the ADR event that is not recovered after a long period [340]. With the activation of the storage capacity the transmission, ventilation and infiltration losses increase and only a part of the stored heat can be used effectively to maintain thermal comfort and reduce the heating power in the period following the ADR event [276]. Both C_{ADR} and η_{ADR} increases with a higher time of storage. η_{ADR} is affected by indoor temperature. In particular, it decreases if indoor temperature increases since thermal losses from storage are higher. Finck et al. [288] showed that η_{ADR}, ratio between discharging and charging energy, is almost similar for all form of TES (0.98 for water tank, 0.97 for PCM and 0.96 for TCM) and that the heat losses are low , <1% of storage efficiency. Owing to η_{ADR} refers only to thermal power it is not useful for aggregators or grid [341].

Starting from Reynders' indicators, Kathirgamanathan et al. [342] proposed the following modified indicators: available electrical energy flexibility (AEEF) Capacity E_{AEEF}. and available electrical energy flexibility efficiency η_{AEEf}.

These indicators, dealing with the building power consumption rather than thermal loads are more applicable for use from the grid-side.

$$E_{AEEF} = \int_{j}^{l_{ADR}} (P_j^{flex} - P_j^{ref})\, dt \tag{2.18}$$

where

- P_j^{flex} is the building electrical power consumption during the ADR event;
- P_j^{ref} is the building electrical power consumption in the reference case.

E_{AEEF} is positive in upward flexibility and negative in downward flexibility. Since E_{AEEF} considers the electrical energy is a more relevant indicator in the context of NZEBs as active players in the grid management. In the work of Zhang et al. [343] the same index was defined Flexible energy E_f.

The authors defined two **available electrical energy flexibility efficiency η_{AEEf}.** to be used for upward (power consumption increasing) and downward (power consumption decreasing) flexibility respectively:

$$\eta_{AEEF}{}^{(up-flex)} = \frac{\left|\int_0^{hor} (P_j^{flex} - P_j^{ref})^- \, dt\right|}{\int_0^{hor} (P_j^{flex} - P_j^{ref})^+ \, dt} \tag{2.19}$$

$$\eta_{AEEF}{}^{(down-flex)} = 1 - \frac{\int_0^{hor} (P_j^{flex} - P_j^{ref})^+ \, dt}{\left|\int_0^{hor} (P_j^{flex} - P_j^{ref})^- \, dt\right|} \tag{2.20}$$

where

- the subscript up and down stand for upward, and downward respectively;
- hor stands for horizon;
- the positive or negative superscript refers to positive or negative area of the $P_j^{flex} - P_j^{ref}$ curve (Figure 19).

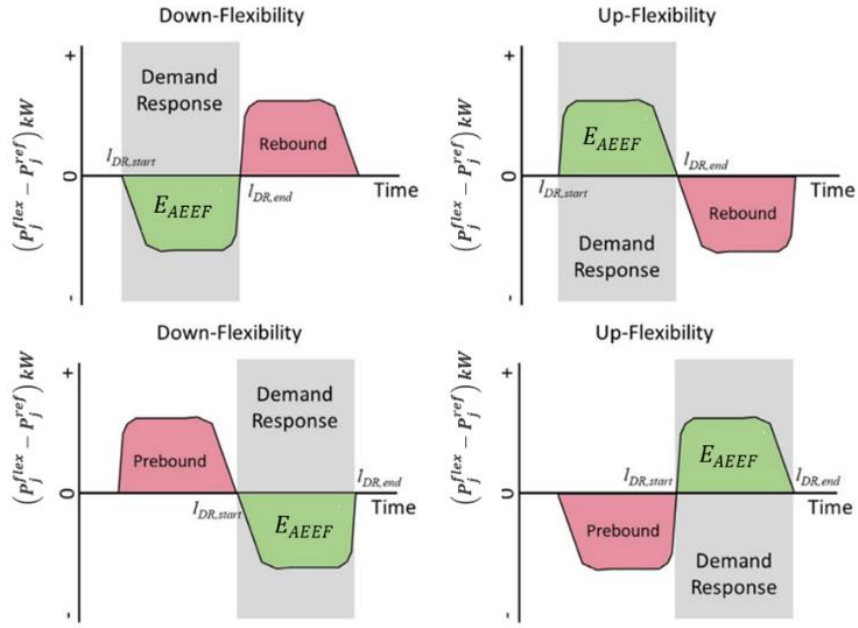

Figure 19: Graphic representation of the available electrical energy flexibility (AEEF) Capacity indicator. Rebound effect for downward and upward flexibility during a DR event is showed. Adapted from [142].

Demand response event to shift the power consumption can be associated to a prebound or rebound energy effect depending on whether if a change in consumption occurs before or after the event [344]. The rebound effect takes place when a proportion of the energy savings after a retrofit is consumed by additional energy use [345]. As an example, it can be due to increased internal temperature and comfort expectations or financial savings being spent on new appliances or energy consumption effect [346,347].

In a recent study Kathirgamanathan et al. [142] defined the **rebound energy** as follow:

$$E_{rb} = \int_{-\infty}^{t_{DR,start}} \left(P_{DR} - P_{Ref}\right) dt + \int_{t_{DR,end}}^{+\infty} \left(P_{DR} - P_{Ref}\right) dt \qquad (2.21)$$

Kathirgamanathan et al. [142] defined the **flexible energy efficiency η_f** indicator as a measure of how much energy can be shifted relative to a rebound effect:

$$\eta_f = \left|\frac{E_f}{E_{rb}}\right| \cdot 100\ \% \tag{2.22}$$

In Table 4 a summarize of the above descripted indicators is reported with the strengths and weaknesses for each of them**.**

Table 4. Energy flexibility indicators.

KPI	Definition	Strengths (S) / Weaknesses (W)
Flexibility Factor [133]	Ability to shift the energy use during time with high prices to low energy prices periods $FF = \frac{\int_{lpt} q_h dt - \int_{hpt} q_h dt}{\int_{lpt} q_h dt + \int_{hpt} q_h dt}$	**(S)** It explains how the energy demand is distributed in comparison to the energy peaks. **(W)** It doesn't give any further information on how much local load can be shifted.
Flexibility Index [297]	Ability of the building to minimize the heating energy usage during the absence of renewable energy sources production and maximize it during periods of available renewable production $FI = \frac{\int \left(q_{match}^{Ref} - q_{match}^{SMART}\right) dt}{q_{cons}^{REF}}$ $q_{match}^{REF} = \int\ max\left(0, q_{cons}^{Ref} - q_{prod}^{Ref}\right) dt$ $q_{match}^{SMART} = \int\ max\left(0, q_{cons}^{SMART} - q_{prod}^{SMART}\right) dt$	**(S)** It takes into account the self-consumption. **(W)** It doesn't give any further information on how much local load can be shifted.
Procurements Cost avoided Flexibility Factor [193]	Ability to shift the heat pump electric load from peak to off-peak hours in terms of electricity price $FF_{PC} = \frac{PC_{max} - PC}{PC_{max} - PC_{min}}$	**(S)** It takes into account the operational cost savings. **(S)** Although, the authors use this KPI to evaluate the ability to shift the heat pump electric load, it can be used to investigate the flexibility of any other electrical equipment.

KPI	Definition	Strengths (S) / Weaknesses (W)
Volume Shifted Flexibility Factor [193]	Ability to shift the heat pump electric load from peak to off-peak hours in terms of energy shifted compared to a reference profile $$FF_{VS} = \frac{FF_{PC} - FF_{PC,ref}}{FF_{PC,ref}}$$	**(S)** It can be used to investigate the flexibility of any other electrical equipment.
Available structure storage capacity [124]	Amount of heat can be added to the mass of a building, over time of an ADR event $$C_{ADR} = \int_0^{\tau_{ADR}} (q_{h,ADR} - q_{h,ref})\, dt$$	**(S)** It takes into account climate condition, occupant behavior and HVAC system. **(S)** It is not useful only for thermal mass but also for every kind of storage system.
Storage efficiency [124]	Fraction of heat that can be stored in the timeframe of an ADR event in order to be used subsequently aiming to reduce the heating power needed $$\eta_{ADR} = 1 - \frac{\int_0^{\infty} Q_\delta dt}{\int_0^{\tau_{ADR}} Q_\delta dt} = 1 - \frac{\int_0^{\infty} Q_\delta dt}{C_{ADR}}$$ $$Q_\delta = q_{h,ADR} - q_{h,ref}$$	
Available electrical energy flexibility efficiency [342]	It shows the storage efficiency based on whether upward or downward flexibility is provided $$\eta_{AEEF}{}^{(up-flex)} = \frac{\left\lvert \int_0^{\tau} \left(P_{el}^{flex} - P_{el}^{ref}\right)^{-} dt \right\rvert}{\int_0^{\tau} \left(P_{el}^{flex} - P_{el}^{ref}\right)^{+} dt}$$ $$\eta_{AEEF}{}^{(down-flex)} = 1 - \frac{\int_0^{\tau} (P_{el}^{flex} - P_{el}^{ref})^{+} dt}{\left\lvert \int_0^{\tau} (P_{el}^{flex} - P_{el}^{ref})^{-} dt \right\rvert}$$	**(S)** They capture the size of the deviation in consumption due to a demand response event.
Flexible energy efficiency [142]	It measures of how much energy was shifted taking into account the rebound effect $$\eta_f = \left\lvert \frac{E_f}{E_{rb}} \right\rvert \cdot 100\ \%$$	**(S)** It takes into account the rebounds effects. **(S)** Since any kind of rebound behavior is seen as less than ideal, it gives priority to the grid operator's point of view.

3.3 Load matching and grid interaction (LMGI) indicators

To support the transition to a renewable energy system with intermittent generation a change is to adjust the demand to the available generated power [348]. Time periods characterized by either peak injection or consumption would occur

simultaneously as the weather conditions dictate to a large extent both the electricity production (such as via PV) and consumption (such as via the heat pumps) [349,350]. This simultaneity can cause grid stability problems [351].

Considerations about the interplay between on-site generation and the building loads, often called load matching (LM), and the resulting import/export interaction with the surrounding energy grid, commonly named grid interaction (GI) are becoming increasingly important both at design and operation level [354,355].

The simplicity of their mathematical definition makes them a useful tool for a first performance evaluation. Among advantages, LM and GI indicators need not be limited to a single building so they could also be used to describe the performance of building clusters or larger communities [354]. The issues of load matching and grid interaction have become part of the discussions of the IEA activity Task 40/Annex 52 "Towards Net Zero Energy Solar Buildings" (IEA, 2008)[357,358].

In the context of load management strategies, by LMGI indicators the flexibility of a building design to respond to variable generation levels, loads and grid conditions may be gauged.

3.3.1 Load matching indicators

These indicators are useful to describe the degree of the utilization of on-site energy generation related to the local energy demand in NZEBs [357]. For a major understanding of the nomenclature used in this section it is reported the sketch showed in Figure 20. These indicators refer to how the local energy generation compares with the building load. In the research field aiming the developments of nZEBs, load matching indicators may guide the design team in comparing different design/project scenarios [137]. Moreover, they could be useful in sizing energy storage devices and HVAC components or in optimizing the control strategy for building integrated CHP systems [94].

In the following is reported the mathematical definition of quantitative indicators existing in literature.

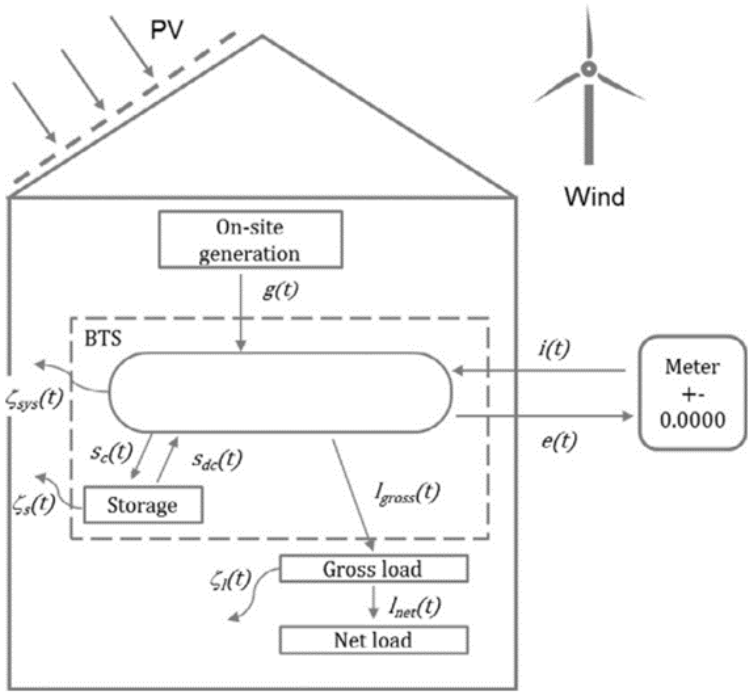

Figure 20: Graphic representation of the energy flows from/ to grid and NZEB. Nomenclature: g=generation, l=electric load, ζ= loss due to building technical systems (subscript sys) or storage (subscript S), S= storage (subscripts c and dc stand for charge and discharge respectively), i and e = imported and exported energy; net= net energy (e-i).Taken from [93].

The load cover factor or self-generation factor γ_{load} is defined as the percentage of the electrical demand covered by on-site electricity generation [93]:

$$\gamma_{load} = \frac{\int_{\tau_1}^{\tau_2} min[g(t) - S(t) - \zeta(t), l(t)]dt}{\int_{\tau_1}^{\tau_2} l(t)dt} \quad (2.23)$$

where

- $g(t)$ is the on-site electricity generation [kW];
- $S(t)$ is the storage [kW];
- $\zeta(t)$ are the power losses [kW];

- $l(t)$ is the electric power load [kW];
- τ is the evaluation period (the time resolution often is one hour or an annual period [287]).

It is an index widely used in literature [358–361]. In periods with no on-site generation the load cover factor value is zero while the highest values are reached when there is a coincidence between the profile shape of electricity load and self-generation [93]. γ_{load} is 1 when on-site produced energy is higher than that one needed. Higher is this index, better is the coincidence between the load and the onsite generation [289]. γ_{load} shows daily and seasonal variations by different self-generator such as PV and CHP [287]. In the case of PV installations, it shows a significant seasonal variation since self-generation depends by the solar azimuth and altitude throughout the year [361]. Usually during the summer months, the electricity load during the day is almost covered by the on-site generation and γ_{load} reaches the highest values. In contrast, in the other seasons γ_{load} decreases reaching its minimum value in winter.

Simulating a zero energy residential buildings equipped with a PV installation in combination with a heat pump, Salom et al. [93] estimated an annual γ_{load} between 0.18–0.21. The values are comparable to those ones evaluated by Baetens et al. [362]. For a residential zero-energy neighbourhood in which heat pumps and building integrated photovoltaic (BIPV) systems cover the electricity consumption on an annual basis, the authors estimated an annual γ_{load} equal 0.32 ± 0.04. In the case of CHP installations for on-site electricity generation the cover factor is influenced by the electricity load profile as well as the heat load profile and its control strategy. When the building does not require any space heating and CHP is in off- mode the load cover factor value is zero. Bart et al. [94] by single-buildings simulations showed that higher values are reached including daytime control, so a higher probability of power generation during increased demand, and the buffer effect leading to a lower demand at times with a lower probability of generation.

The supply cover factor or self-consumption factor γ_{supply} is defined as the percentage of the on-site generation that is used by the building [93]. It is the complementary index of the load cover factor:

$$\gamma_{supply} = \frac{\int_{\tau_1}^{\tau_2} min[g(t) - S(t) - \zeta(t), l(t)]dt}{\int_{\tau_1}^{\tau_2} g(t)dt} \quad (2.24)$$

γ_{supply} is among the commonly used load matching indicators [363–366]. A building becomes almost fully self-sufficient when γ_{supply} is 1, this condition can be reached introducing battery for electric storage [367].

Cover factor indicators are mostly suited to evaluate controls aimed at decreasing grid dependence [368]. They have the disadvantage not to give a direct information on net energy, consumption or supply, no information on peaks in power exchange and no information on connection capacity usage. An advantage in the calculation of the cover factors ($\gamma_{load}, \gamma_{supply}$) is the possibility to investigate the influence of different strategies and measures of load modulation [369]. γ_load is useful when supply to the grid is prohibited by regulations while γ_{supply} when electricity tariffs are high [94].

The loss of load probability $LOLP_b$ index is defined as the time share during which the local generation does not cover the building demand, and thus how often energy must be supplied by the grid. It indicates how often the on-site supply fails to cover the on-site load [370]:

$$LOLP_b = \frac{\int_{\tau_1}^{\tau_2} f(t)dt}{T} \quad (2.25)$$

where

- the subscript b stands for building;
- T is the evaluation time ($\tau_2 - \tau_1$);

- $f(t)$ is a function accounting the time that local demand exceeds the local generation.

$$f(t) = \begin{cases} 1 \; if \; ne(t) < 0 \\ 0 \; if \; ne(t) \geq 0 \end{cases} \tag{2.26}$$

$ne(t)$ is net exported electricity to the grid (kW):

$$ne(t) = e(t) - d(t) \tag{2.27}$$

where

- $e(t)$ is the exported energy;
- $d(t)$ is the delivered energy (i(t) in Figure 20).

The net grid $ne(t)$ affects voltage levels and reverse power flow so it is a critical parameter to be considered in order to quantify the frequency and magnitude of the net power interactions with the grid [371].

The $LOLP_b$ index is useful in order to evaluate different load control strategies in a building and when the aim is increasing the suitability of a distributed generation (DG) system for covering the local load profile decreasing the need to consume power from the grid [94]. It can be done by controlling demand with or without the inclusion of a storage system or adjusting the local generation, for instance, by changing the orientation of PV panels, increasing generation during morning and evening peaks in power demand. From this point of view, this factor has the advantage to evaluate the suitability of DG, control and storage to cover the load decreasing the need to consume energy from grid. In contrast, it has the disadvantage not to show indication on net energy, consumption or generation, no information on peaks in power exchange and on use of capacity connection [94]. So referring at the$LOLP_b$, a generation system could be over dimensioned leading to higher peaks in supply [372]. Tumminia et al. [373] demonstrated that $LOLP_b$ value is affected by on-site electricity generator size. The authors estimated a value varying between 0.03 (with a PV peak

power of 5.76 kW) and 0.84 (with a PV peak power of 0.24 kW).

Known $LOLP_b$, it can be estimated the **energy autonomy A** as "the fraction of the time when 100% of the load can be matched by on-site generation "[93]:

$$A = 1 - LOLP_b \tag{2.28}$$

Zhou et al. [374] defined the time duration during which the renewable generation is higher than the total electric load as "renewable electricity (REe) surplus period" and the time duration during which the renewable generation is smaller than the total electric load as "REe shortage period".

A metric able to show how well local generation matches local demand during a specific time interval is the **load match index *LMI*** defined in Voss.et al [289]:

$$LMI = \frac{1}{\tau}\int_0^{\tau} min\left[1, \frac{g(t)}{l(t)}\right] dt \tag{2.29}$$

This index describing the matching degree between on-site energy generation and the building load is used to give an indication of the relative amount of energy locally generated [375]. Although the concept to assess the on-site generation was specifically developed for single buildings, this index can be applied to building clusters connected to the same grid.

If the local generation occurs by PV this index is also called solar fraction describing the ratio of the PV yield to the load [289]. Since all generated power exceeding the load is considered as part of the grid electricity the maximum LMI value reached is of 100% [289]. The annually based load match index is per definition equal to 1. As an example Voss et al. [83] estimated that the annual average LMI for a photovoltaic system that meets the total annual electricity demand of a building is on the order of 60 to 80%. A value of LMI of one (100%) does not mean no grid dependence during a specific time interval but that the integration of generation at least equals that of demand as shown in the work of Bart et al. [94]. This factor

focuses only on the relationship between demand and supply so it cannot be used to describe the interaction between building and grid [376].

A common feature of the indicators above described it is that they do not need any additional information besides load and generation profile [137]. Generation and load are the main characteristics evaluated in the implementation of different control strategies to cover the load building [377].

In the work of Vladimir et al. [359] the load cover factor named as **self-consumption rate (SCR)** is defined as the share of PV generated energy (E_{pv}) consumed on site, the load cover supply named as **self-sufficiency rate (SSR)** as the share of the electricity demand (E_{load}) covered by PV generator.

The LOLP was defined as the percentage of time during which a household with a rooftop PV generator acts as a net consumer. Moreover, the authors defined the **generation-to-demand ratio $\boldsymbol{GTDR\ indicator}$** :

$$GTDR = \frac{SSR}{SCR} = \frac{E_{pv}}{E_{load}} \tag{2.30}$$

The authors showed that households with larger PV generators are characterized by higher GTDR but lower load matching capabilities. GTDR is useful to categorize different buildings according to their annually consumed and generated energy. The authors found that this index provides a reliable estimate to other indicators such as γ_{cover}, γ_{supply} and LOLP.

In the work of Luthander et al. [378] is given a graphical approach of this indicator. To visualize on-site renewable energy supply-load matching, the authors proposed the energy chart. This chart, shown in Figure 21, provides information regarding the matching in both size and time.

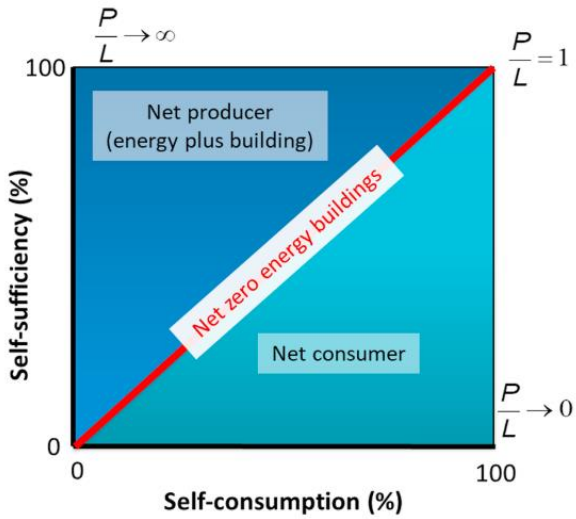

Figure 21: The principals of the Energy matching chart reported in Luthander et al. [378].($^{P}/_{L} = GTDR$) Perfect matching is achieved in the top right corner since both self-sufficiency and self-consumption is 100%. Poor matching in time is achieved in the lower left corner. Net zero energy buildings, which produce as much electricity as they consume are represented by the red diagonal (GTDR=1), net producer (GTDR>1) are above having a higher electricity production than load.

Similar to γ_{load} and γ_{supply} respectively are the on-site electrical mismatch indices defined in the work of Cao et al.[379]: **on-site energy fraction OEF** and **on-site energy matching OEM.**

OEF measures how much of the on-site production is used to cover the local demand:

$$OEF = \frac{\int_{t_1}^{t_2} Min[G(t), L(t)]dt}{\int_{t_1}^{t_2} L(t)\,dt}; 0 \leq \text{OEF} \leq 1 \tag{2.31}$$

OEM measures the degree of utilization of the local generation respect to the local energy demand. OEM indicates the proportion of the on-site generated energy used in the load rather than be exported:

$$OEM = \frac{\int_{t_1}^{t_2} Min[G(t), L(t)]dt}{\int_{t_1}^{t_2} G(t)\, dt}; 0 \leq \text{OEM} \leq 1 \quad (2.32)$$

A graphical representation of on-site indicators OEF and OEM is in Figure 22.

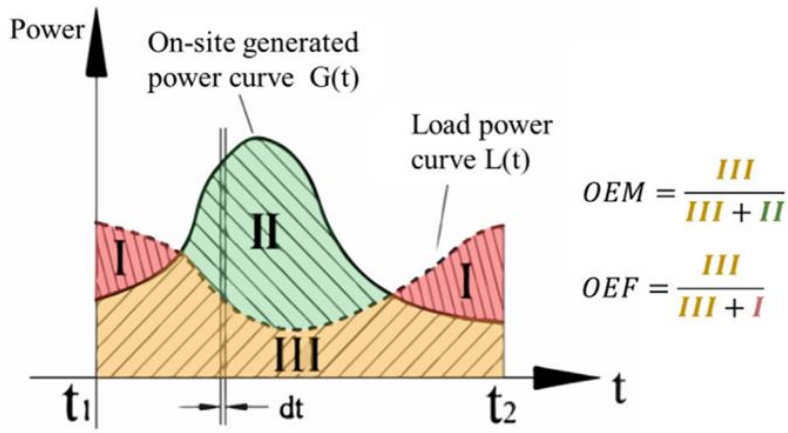

Figure 22: Graphical sketch of on-site energy indicators [371].

Starting from the definition of OEF and OEM, the authors derived six matching indices aiming to (1) assess the on-site matching including electrical, heating, and cooling energy forms; (2) assess the interaction and conversion between different on-site energy forms; (3) assess the influence of various energy storages (4) assess the export of generated on-site surplus energy to the grid. The six indices were defined: on-site electrical energy fraction (OEFe), on-site heating energy fraction (OEFh), and on-site cooling energy fraction (OEFc), on-site electrical energy matching (OEMe), on-site heating energy matching (OEMh), and on-site cooling energy matching (OEMc). A detailed formulation of their equation is reported in [374,379].

A disproportional size of the generation system to the demand of the building could lead to a high value of OEM and to a low value of OEF. For example, if a large share of on-site produced energy is used for the local demand; the OEM ilding the

OEF is low. In contrast, with a large-sized on-site energy generation system and low energy demand if a noticeable share of demand is covered by on-site generation low values of OEM and high values of OEF are reached respectively. The matching indices are useful to handle

The same concept expressed by GTDR and OEF is remarked by the on-site energy ratio OER indicator used in the work Ala-Juusela et al. [380], a study on energy positive neighbourhoods. These ones generate more power than their needs including the management of local energy sources and the connection to the power grid. They are able to maximize usage of renewable sources whilst contributing to the security and optimization of the wider power grid [92].

The on-site energy ratio OER is defined as "the ratio between energy supply from local renewable sources and energy demand":

$$OER = \frac{\int_{\tau_1}^{\tau_2} G(t)dt}{\int_{\tau_1}^{\tau_2} L(t)dt} \tag{2.33}$$

where

- $dt = 1\ year$;
- $L(t)$ is the load power of all energy types together (heating, cooling, electricity).

OER , rather than considering only the generation of more exported energy versus its importation to the grid or individual buildings, emphasis shifting to the maximization of energy performance in a system-based approach. If OER has a value of 1 it means that, considering a net annual balance, the energy demand is completely covered by RES supply. A value higher than 1 implies that the annual energy demand is lower than the annual energy supply from local renewable energy sources.

OER does not take into account the different energy types separately. It express the condition for which demand is covered by on-site production without accounting the energy mismatch for each energy type. OER indicates how well a neighborhood

is able to balance demand and supply in the short term. In their study the authors defined the annual mismatch ratio as the amount of energy imported into the neighborhood for each energy type in the year; maximum hourly surplus as the maximum hourly ratio of difference between on-site generation and load over the load for each energy type and maximum hourly deficit as the maximum value of how much bigger the hourly local demand is compared to the local renewable supply during that hour (per year), taking also into account the energy retrieved from local storage to cover the load.

Lund et al. [87] analyzed the mismatch arising from hourly differences in energy production and consumption at the aggregated building level. Levelling out the mismatch of individual buildings can be compared to the design of power supply systems. In particular, power plants are not designed to cover the maximum need of each consumer so all consumers do not peak in consumption at the same time. At the aggregated level investments in transmission lines and power stations are lower. The same concept can be applied to the mismatches created by changes in electricity demand and on-site power production at level of single building. Other buildings can compensate for each mismatch inside each building. It occurs, as an example, if a building is charging a battery whilst another building is discharging. In this way one would avoid inefficient investments in production unit where the mismatch should be compensated. To account the benefits in terms of cost savings, the authors defined a **mismatch compensation factor** $\boldsymbol{MCF}$ on the assumption that the mismatch of one ZEB can be identified at the aggregated level and compensated by increasing (if the net influence is negative) or decreasing (if the net influence is positive) the electricity production unit.

$$MCF = \frac{C_{cost,balance}}{C_{energy,balance}} \tag{2.34}$$

where

- $C_{cost,balance}$ is the capacity of the installation for which the cost of annual export and import of electricity is the same;

- $C_{energy,balance}$ is the capacity of renewable installation for which the cost of annual export and import of electricity is the same;

This indicator is useful to calculate how much to increase the production unit aiming to compensate for the influence of the mismatch on the electricity supply system outside the building. If the system that compensates for the mismatch is smaller than the system that gives a net zero energy balance generated electricity is, on average, worth more than demanded electricity so MCF value is >1. As an example, if MMC is 1.2 it means that the mismatch has a negative influence on the system and has to be compensated, i.e., by increasing the capacity of the PV installation by 20%. MCF is similar to market matching index reported in the work of Widen et al. [375].

In Table 5 a summarize of the above descripted indicators is reported with the strengths and weaknesses for each of them**.**

Table 5. Load match indicators.

KPI	Definition	Strengths (S) / Weaknesses (W)
Load cover factor [93,137]	Percentage of the electrical demand covered by on-site electricity generation $\gamma_{load} = \frac{\int_{\tau_1}^{\tau_2} min[g(t) - S(t) - \zeta(t), l(t)]dt}{\int_{\tau_1}^{\tau_2} l(t)dt}$	**(S)** They allow to analyze different control strategies and measures of load match. **(S)** They do not need any additional data besides load and generation profile. **(S)** They are widely used in literature, allowing to carry out also the comparison between different case studies. **(W)** They are a function of the time resolution used in the calculation. **(W)** They do not give a direct information on net energy, consumption or supply, peaks in power exchange or connection capacity usage.
Supply cover factor [93,137]	Percentage of the on-site generation that is used by the building $\gamma_{supply} = \frac{\int_{\tau_1}^{\tau_2} min[g(t) - S(t) - \zeta(t), l(t)]dt}{\int_{\tau_1}^{\tau_2} g(t)dt}$	
Loss of load probability [93,137]	Time share during which the building energy demand is not covered by the on-site energy generation	**(S)** They can be useful for the design and control of on-site energy generation systems.

KPI	Definition	Strengths (S) / Weaknesses (W)
	$LOLP_b = \frac{\int_{\tau_1}^{\tau_2} f(t)dt}{T}$ $f(t) = \begin{cases} 1 \; if \; ne(t) < 0 \\ 0 \; if \; ne(t) \geq 0 \end{cases}$ $ne(t) = e(t) - d(t)$	**(S)** It defines the fraction of time in which the building needs imported energy from the grid. **(S)** They are widely used in literature, allowing to carry out also the comparison between different case studies. (**W)** Omits the volume of grid imports. **(W)** The time resolution based on the net exported electricity to the grid is affected by the renewable energy sources stochasticity
Energy autonomy [93,137]	It reports the time share during which the entire local load can be covered by on-site generation $A_b = 1 - LOLP_b$	
Mismatch compensation factor [87]	Capacity of the local energy generation system for which the annual net exported energy is equal to zero divided by the capacity of the same system for which the economic value of annual import and export of electricity is the same $MCF = \frac{C_{cost,balance}}{C_{energy,balance}}$	**(S)** Even if it is used regard to economic balance, it could also refer to the CO_2 emission or the primary energy consumption of the system. **(S)** It can be used in the sizing of generation systems. **(W)** It is calculated using an annual time resolution. On the other hand, higher temporal resolution, such as hourly resolution, could provide more useful information.
On-site energy ratio [380]	Ratio between energy supply from local renewable sources and energy demand $OER = \frac{\int_{\tau_1}^{\tau_2} g(t)dt}{\int_{\tau_1}^{\tau_2} l(t)dt}$	**(S)** For its calculation it requires only the load and generation profiles. **(W)** In case of multiple renewable energy sources, it does not take into account the different energy types separately.

3.3.2 Grid Indicators

These indicators are used to measure how a building or a cluster of buildings utilize the grid connection [137]. In contrast to LMs that give an indication of the total amount of the exchanged energy with the grid, the GIs include also information about the quality of to the energy exchange between the building and the power grid [371]. Grid refers both to the physical utilization of the infrastructure and to the upstream energy system and market [381]. These indicators are particular useful in assessing and design the operation limits of the grid and in improving voltage

regulation in the case of high penetration rates of PV systems [382].

In Voss et al. [289] **the grid interaction index GII** is defined as "the variability of the exchanged energy between the building and the grid within a year normalized on the maximum absolute value":

$$GII = STD\left(\frac{ne(t)}{max|ne(t)|}\right) \tag{2.35}$$

This index describes the fluctuation of the energy exchange of the building with the grid but not the amount of grid electricity needed. It describes the average grid stress and it is useful to express the variation of the energy exchange between the grid and a building [139].

The capacity factor CF_b is defined as "total energy exchange with the grid divided by the exchange that would have occurred at nominal connection capacity" [93]:

$$CF_b = \frac{\int_{\tau_1}^{\tau_2}|ne(t)|dt}{E_{des} \cdot T} \tag{2.36}$$

where

- E_{des} is the nominal design connection capacity between the building and the grid;
- the subscript des stands for design value.

This indicator was originally used to assess the value of a generator plant or park [383]. From its definition, it is clear that when demand exceeds generation, such as increasing the temperature set point of the energy systems, the indicator decreases. Advantages and weaknesses are reported in the study of Bart et al. [94]. In particular, this indicator has the advantage to account energy exchange, concurrence of load and generation and information on use of connection capacity.

The connection capacity credit or power reduction potential E_c is defined as" the percentage of grid connection capacity that could be saved compared to a reference case (building with no local energy supply)" [93]:

$$E_c = 1 - \frac{DR}{DR_{ref}} \tag{2.37}$$

where DR is given as follow[94]:

$$DR = \frac{max[|ne(t)|]}{E_{des}} \tag{2.38}$$

DR is useful to monitor the highest power peak when a specific limit should never be exceeded. Positive values of $E_c$indicate a saving potential; negative values a need to increase the grid connection capacity with respect to the reference case. Moreover, decreasing this indicator could be a way to decrease the grid impact. A limit in the use of this indicator is that when it decreases it does not show if peaks are exceeded so another indicator should be used to monitor peaks. The main difference between E_c and DR is that DR monitors the highest peak powers related to the grid connection capacity while E_c those ones related to a reference scenario. Both indexes, useful to monitor the highest peak in power exchange, do not give any information neither on net energy exchange, consumption or supply nor on match between load and generation [384].

The **no grid interaction probability $P_{E=0}$ or grid dependence index GDI**is defined as "the probability that the building is acting autonomously of the grid" [373]:

$$P_{E=0} = \frac{\int_{\tau_1}^{\tau_2} dt_{|ne(t)|<0}}{\tau_2 - \tau_1} \tag{2.39}$$

$|ne(t)| < 0$ implies that the entire load is covered or by the direct use of renewable or by the energy stored to be use on demand. Grid dependency describes the interaction between the building and the grid without any information about the magnitude of the exchanged power with the grid. A value closer to 0, it means such

a more grid-independent building.

Appliances that use thermal storage are an example of reschedulable loads. When G_{cl} is 0 it means the absence of control by the central controller and the necessity of a major generation for demand supply.

A common way to characterize the energy flexibility building is by the variation in penalties used to shift the load from peak hours to off peak hours [385,386].

Peak power generation index $\bar{G}$ is defined as "the peak value of the on-site generation normalized to the nominal grid connection capacity":

$$\bar{G} = \frac{\max[g(t)]}{E_{des}} \tag{2.40}$$

Peak power load index $\bar{L}$ is defined as "the peak value of load energy normalized to the design connection capacity".

$$\bar{L} = \frac{\max[l(t)]}{E_{des}} \tag{2.41}$$

Peak powers are used to evaluate the generation multiple factor GM defined as "a metric relating the size of the generation system with the design capacity load" [93]. It can be calculated in terms of the ratio between generation / load peak powers:

$$GM_{(g/l)} = \frac{\max[g(t)]}{\max[l(t)]} \tag{2.42}$$

or in terms of the ratio between exported (e)/delivered (d) peak powers as follows:

$$GM_{(e/d)} = \frac{|\overline{ne_{max}}|}{|\overline{ne_{min}}|} \tag{2.43}$$

where $|\overline{ne}|$is the net exported energy normalized to the design connection capacity

$$|\overline{ne}| = \frac{ne(t)}{E_{des}} \tag{2.44}$$

GM index provides a large quantity of information such as imported and exported

peak values, amount of time when the building is exporting or demanding energy to or from the grid, period during which the building is self-sufficient by mean the presence of a storage system. By minimizing the absolute peak power, either supplied to or consumed from the grid, is a crucial way to have a grid-friendly building with the minimum stress on the electricity grid [387]. In a report on load match prepared as part of the IEA Task 40/ Annex 52 were defined the following relative peak power indicators normalized by the design **capacity load L_{des}:relative-in peak power PP_f, relative delivered peak power PP_d** and **relative grid interaction amplitude $A_{r,grid}$** [388]:

$$PP_f = \frac{\max[E(i)]}{L_{des}} \tag{2.45}$$

$$PP_d = \frac{\min[E(i)]}{L_{des}} \tag{2.46}$$

$$A_{r,grid} = PP_f - PP_d \tag{2.47}$$

where $E(i)$ is the is the net exported electricity to the grid.

The one percent peak power OPP is defined as "the mean power of the one percent highest quarter hourly peaks" [94]:

$$OPP = \frac{E_{1\%,peak}}{T} \tag{2.48}$$

where $E_{1\%,peak}$ is the power in the 1%highest peaks in power exchange.

This indicator is useful to monitor peaks so it could be used to evaluate controls aimed at limiting them, thereby limiting grid losses and facilitating keeping the grid within operational limits [389].

The peaks above limit PAL is defined as "the percentage of time during that net exported energy exceeds a certain limit:

$$PAL = \frac{t_{|P_{exch}|>|P_{lim}|}}{\Delta t} \tag{2.49}$$

where P_{exch} is the net power exchange. In their study, the authors used the above descripted index to account the percentage of time with a net grid exchange above 5000 W both for injection and consumption. A threshold of 5000 W has been chosen since it is according to rules for grid connection of DG often change.

In the NZEB concept the grid is considered as a virtual energy storage medium, Salom et al. [93] defined the **Equivalent hours of storage N_{hS}**:

$$N_{hS} = \frac{\max [S(t)]}{\max [ne(t)]} \tag{2.50}$$

To assess the grid interaction of a building's electricity consumption and generation, Klein et al. [390] introduced two metrics: absolute and relative grid support coefficients GSC_s. They 'weight" the electricity consumption profile with a time-resolved reference quantity expressing the availability of electricity in the public grid. Stock electricity price, residual load, cumulative energy consumption are examples of the availability of electricity in the grid. These metrics are useful for the grid support of shift able electricity producers or consumers. They are useful to characterize the flexibility in the design and planning phase of a building [390].

The absolute Grid Support Coefficient $\boldsymbol{GSC_{abs}}$ weights a time-resolved electricity consumption profile with a time-resolved reference quantity Gs (e.g., the residual load). It is used to evaluate the grid impact of either the heat supply system or the building (energy system view):

$$GSC_{abs} = \frac{\sum_{i=1}^{n} W_{el}^{i} \cdot G_s^i}{W_{el} \cdot \overline{G_s}} \tag{2.51}$$

where

- W_{el}^{i} is the electricity consumption in time step i [kWh];
- G_s^i is the value of the grid signal in time step i ;
- n is the total number of time steps.

$$W_{el} = \sum_{i=1}^{n} W_{el}^{i} \tag{2.52}$$

$$\overline{G_s} = \frac{1}{n} \sum_{i=1}^{n} G_s^i \tag{2.53}$$

If the grid signal is the residual load a value of GSC_{abs} of 0.9 means that electricity is, on average, consumed when the residual load assumes 90% of its mean value in the evaluation period [381]. In their study the residual load is defined as the difference between the net electrical load and the net feed-in power of the RES.

If the stock electricity price is used as reference quantity a value of GSC_{abs} of 0.9 means that electricity is, on weighted average, consumed at 90 % of the mean price during the evaluation interval. Intraday trajectory of electricity consumption, seasonal heating and cooling demand, seasonal trends and fluctuation range of reference quantity, evaluation period, possible data gaps in consumption profile are the main parameters affecting this indicator.

GSC_{abs} indicates whether additional loads occur at times with a relative electricity demand above or below average. Moreover, it allows an evaluation of the grid impact of a building from the energy system perspective. This metric can be used to analyze the electricity consumption profiles of energy generators, such as heat pumps, since load shifting is typically restricted to a few hours.

The relative Grid Support Coefficient GSC_{rel} relates the achieved value of the absolute GSC_{abs} to the worst and best possible potential boundaries (PB) on a scale of -100 to 100. In particular the lower potential boundaries are referred to the least favorable grid conditions, the upper ones to the least favorable grid conditions.

$$GSC_{rel} = 200 * \frac{GSC_{abs}(lowerPB) - GSC_{abs}(achieved)}{GSC_{abs}(lowerPB) - GSC_{abs}(upperPB)} - 100 \tag{2.54}$$

The potential boundaries are determines, as an example, by re-scheduling the electricity consumption. GSC_{rel} reflects how well a variable load is scheduled based on a grid signal. The Grid Support Coefficients require a grid signal so they are not suitable for design analysis but they are useful for ex-post performance considerations. They are referred to mean conditions of the grid so there is a limitation in their use for extreme situations, e.g., when grid operation is jeopardized. They are not designed in order to evaluate the physical grid utilization.

Klein et al. [381] showed that their value is affected by the type of energy system. In particular their results showed that for the same amount of thermal storage size GCSs values achievable with CHPs are higher than those ones reached with HPs.

GSC_{rel} is useful to describe whether a consumer is scheduled grid-supportively or grid adversely. Consumption profiles providing a high level of grid support ($GSC_{rel} > 0$) are referred grid-supportive. When $GSC_{rel} < 0$ the consumption profiles are referred as grid-adverse.

In Table 6 a summarize of the above descripted indicators is reported:

Table 6: Grid Interaction indicators.

KPI	Definition	Strengths (S) / Weaknesses (W)
Grid interaction index [137]	Standard deviation of the net exported energy within a year $GII = STD\left(\frac{ne(t)}{max\|ne(t)\|}\right)$	**(S)** It describes the average grid stress and it can be used to analyze the variation of the electricity interchange between a building and the grid.
No grid interaction probability [137]	Probability that the building is acting autonomously of the grid $P_{E=0} = \frac{\int_{\tau_1}^{\tau_2} dt_{\|ne(t)\|<0}}{\tau_2 - \tau_1}$	**(S)** For its calculation it requires only the load and generation profiles. **(S)** It is widely used in literature, allowing to carry out also the comparison between different case studies. **(W)** It describes the interaction between the building and the grid without any information about the magnitude of the exchanged power.
Capacity factor [137]	Ratio between the energy exchanged between the building and the grid and	**(S)** It takes into account energy exchange, concurrence of load and generation and

KPI	Definition	Strengths (S) / Weaknesses (W)
	the energy exchanged that would have occurred at nominal connection capacity $CF_b = \frac{\int_{\tau_1}^{\tau_2} \lvert ne(t) \rvert dt}{E_{des} \cdot T}$	gives information on use of connection capacity. **(W)** It doesn't show indication on generation and consume, indication of peaks in power exchange. **(W)** It is not suited for standalone evaluation of connection capacity use.
Connection capacity credit [93,137]	Percentage of grid connection capacity that could be saved compared to a reference case (building with no local energy supply) $E_c = 1 - \frac{DR}{DR_{ref}}$ $DR = \frac{max[\lvert ne(t) \rvert]}{E_{des}}$	**(S)** Decreasing this indicator could be a way to decrease the grid impact. **(W)** It does not give any information neither on net energy exchange, consumption or supply nor on match between load and generation.
One percent peak power [94]	Mean power of the one percent highest quarter hourly peaks $OPP = \frac{E_{1\%,peak}}{T}$	**(S)** They are useful to monitor power peaks. **(S)** They could be used to evaluate controls, aimed at limiting peaks, thereby limiting grid losses and facilitating keeping the grid within operational limits. **(W)** They do not to give any information neither on net energy exchange, consumption or supply nor on match between load and generation.
Peaks above limit [94]	Percentage of time during that net exported energy exceeds a certain limit $PAL = \frac{t_{\lvert P_{exch} \rvert > \lvert P_{lim} \rvert}}{T}$	
Absolute Grid Support Coefficient [381]	A measure of how a consumer's electricity consumption profile matches the availability of electricity assessed using a grid bases reference quantity $GSC_{abs} = \frac{\sum_{i=1}^{n} W_{el}^i \cdot G_s^i}{W_{el} \cdot \overline{G_s}}$ $W_{el} = \sum_{i=1}^{n} W_{el}^i, \overline{G_s} = \frac{1}{n} \sum_{i=1}^{n} G_s^i$	**(S)** They are metrics to 'weight" the electricity consumption profile with a time-resolved reference q **(S)** These metrics are useful for the grid support of shiftable electricity producers or consumers. **(S)** The grid signals could also refer to the CO2 emission or the primary energy consumption. **(S)** They allow an evaluation of the grid impact of a building from the energy system perspective.
Relative Grid Support Coefficient [381]	$GSC_{rel} = 200 * \frac{GSC_{abs}(lowerPB) - GSC_{abs}(achieved)}{GSC_{abs}(lowerPB) - GSC_{abs}(upperPB)} - 100$	

KPI	Definition	Strengths (S) / Weaknesses (W)
		(W) They require a grid signal per kWh for time-steps t so they are not suitable for design analysis, but they are useful for ex-post performance considerations.
Equivalent hours of storage [93]	$N_{hS} = \frac{max\,[S(t)]}{max\,[ne(t)]}$	**(S)** It coincides to the storage capacity expressed in hours. **(S)** It can be useful to compare and choose between different designs alternatives.

4. Energy flexibility from grid service perspective

Building energy flexibility can be exploited to respond to the needs of energy networks [391].

At building level, the demand side management could enable different grid services, as reported in Figure 23. In Section 2 the analysis of KPIs shows how the building flexibility to provide these grid services is affected by several aspects, such as on-site energy generation systems, thermal storage systems, electric storage systems, thermal mass of the building, building envelope characteristics, control strategies, and energy management strategies.

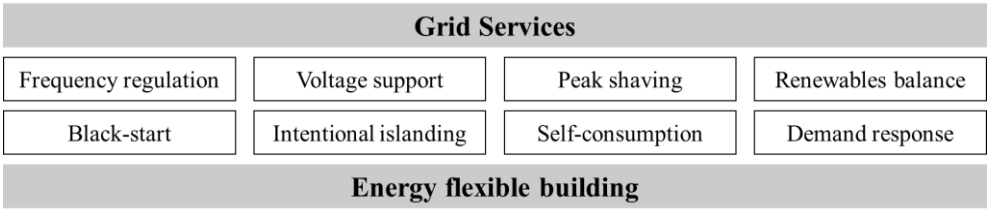

Figure 23: Energy flexible buildings to provide grid services.

A definition of the grid services reported in Figure 23 follows:

- *frequency regulation*: control of the active power supply in order to contribute in regulating the grid frequency;
- *voltage support*: control of the reactive power supply in order to contribute in regulating the grid voltage;
- *peak shaving*: modulation of the active power delivered/adsorbed to tone down high rate of power due to the renewables in the power network;
- *renewable balance*: compensation of renewable energy sources fluctuations;
- *black-start*: ability to re-start the power network or portions of power networks;
- *intentional islanding*: ability to operate in off-grid configuration;
- *self-consumption*: control of the active power and of the loads, to maximize the use of the local renewable energy source, minimizing the grid interaction;
- *demand response*: control of DSM and storage to perform load profiles, based on programs coming from signals of system operators.

Reductions in peak energy demand help avoid investments in infrastructure that would have been needed otherwise. Moreover, the large-scale use of distributed energy storage systems, would allow buildings to provide energy flexibility and at the same time which would increase the network resilience. This aspect could be crucial for town planning and urban design. The increasing share of renewable energy sources together with an extensive electrification of the energy demand are imposing new challenges to the management of energy systems due to the high stress of the electrical grid. Flexible buildings can contribute to reduce grid stress, creating a more resilient and reliable grid from with lowering costs for consumers. To flatten their demand curve, consumers are encouraged to use less energy during peak hours and to move the time of energy use to off-peak times such as night [176,177]. In this way, the energy system is improved at the side of the end-user in terms of consumption and cost effectiveness [178]. In this context, flexible buildings could benefit the operation of the electric grid and owners and occupants simultaneously, thus benefiting utilities and grid operators, customers, and society at-large [392]. From the

perspective of building owners, they can offer customer cost savings through more effective reduction in peak loads, taking advantage of utility time-of-use rates, and additional revenues from demand response program participation while also enhancing building performance and occupant comfort.

A grid service provided depends for example on the type of service offered and its timing, the location within the grid and the avoided cost compared to a less expensive alternative resource providing a comparable service.

For grid operators, in order to manage grid services, certain features, such as the duration of the service, the response time and the frequency of events [393], are of paramount importance. Therefore, for grid operators point of view, the flexibility KPIs should allow to take into account these aspects.

The KPIs should provide information on some key aspects of flexibility, such as:

- quantity and timing of demand flexibility provided to the grid;
- quality of demand flexibility provided (e.g., time required to achieve the desired change in demand);
- impacts on users and building non-energy services (e.g., occupants' comfort).

5. Discussion and final remarks

The design and the control of nZEBs is challenging in many ways, due to the high and complex performance required in terms of energy efficiency, economic feasibility and environmental sustainability and occupant satisfaction. However, the successful design of any type of building, and even more so of in the case nZEBs, should also take into account the energy flexibility of its energy systems, the interaction with the infrastructure to which the building will be connected and the provision of services to this infrastructure.

Benefits in terms of cost savings for building owners and benefits in terms of recognition of how much for demand response can be activated for grid operators are

among the advantages in the utilizing buildings' flexibility. The quantification of the energy flexibility is a complex process dealing with the requirements both of the costumers and of the grid operators. However, there is still a lack between the definition of building flexibility and its quantification. This dissimilarity among the two aspects gives rise to diversity of interpretation regarding the building flexibility concept.

In this context, the paper reviews and compares different building performance indicators, existing in literature, developed in the context of the demand side management strategies to quantify the main aspects of the building flexibility. In detail, after analysing a total of 28 indicators, they were divided into three categories as follows:

- indicators useful to describe the degree of the utilization of on-site energy generation related to the local energy demand in nZEBs. (Load matching indicators);
- indicators useful to describe the grid connection (Grid interaction indicators);
- indicators useful to provide information about energy can be shifted in relation to scope and target for which energy flexibility measurements are applied (Energy flexibility indicators).

The load matching indicators are useful to study and compare different types of energy systems based on the coincidence between the profile shape of electricity load and self-generation or to evaluate different load control strategies. Most of these indicators has the disadvantage not to show indication on net energy, consumption or generation, no information on peaks in power exchange and on use of capacity connection. A further disadvantage is the mathematical dependence from the time of resolution affected by the energy balance of the building. Due to the complexity to know in real time the changes in this balance, with the use of these indicators flexibility quantification could be underestimated / overestimated.

The grid interaction indicators are useful to express the variation over time of the

energy exchange between the grid and a building and to evaluate strategies control to limit peaks power in order to limit grid losses and facilitate keeping the grid within operational limits. A further advantage, these indicators allow to evaluate the grid impact from the energy system perspective including also information about the quality of the energy exchange between the building and the grid. Most of these indicators has the disadvantage not to give any information neither on net energy exchange, consumption or supply nor on match between load and generation.

The energy flexibility indicators are useful to evaluate how the energy demand is distributed as response to a demand response event or a grid external signal. They allow to investigate the energy flexibility on the basis of the potential flexibility going from individual energy systems components (HVAC, CHP, HPs or other appliances). They are widely used in the context of the storage technologies whose implementation is among the most developed DSM options to provide building flexibility. These indicators depend on several parameters, such as the physical/technological properties of the building, flexibility strategies control implemented and climate conditions. As a consequence, it is more difficult to compare different buildings based on their use. A comparison it is possible or among energy flexibility systems and dynamic strategies used in the same building or among similar buildings with the same climate conditions. The strong dependency from the climate conditions of the energy indicators is currently the strongest limitation in their utilization. The research allowed to analyse and compare the strengths and weaknesses of each investigated KPI. On the other hand, the KPIs review also led to highlight some of the current literature gaps. For example, one of the research gaps identified concerns the limited availability of real monitored data used to calculate these KPIs. Moreover, whilst the reviewed KPIs show the available energy flexibility of the building and its energy systems, they do not capture the cost of providing it. In this context, an economic KPI might be useful to allow a financial contract to be settled between users and network operators.

The study also pointed out that all the KPIs examined take into account energy

flexibility only on the side of the buildings. In particular, although DSM strategies are already widely used to reduce the buildings energy consumptions and increase their energy efficiency [301,394], in future they can be used to optimize the interaction between the buildings and the grid opening up new market opportunities. In this context there is also a need for metrics and indicators to assess demand flexibility performance for grid services.

From the point of view of grid operators the flexibility KPIs should be those related to the provision of services, which make it possible to take into account the duration of the service, the response time, the frequency of events and other requirements. For example, in a similar way to the battery energy storage systems state of charge and identifying for the energy flexible buildings the amount of energy that they can exchange with the grid, both by feeding energy and withdrawing it (a sort of dynamic state of charge of buildings). This indicator could lead to an improvement of the interactions between the buildings and the power grids.

Metrics beyond the simple quantity of any impact may become increasingly, due to the fact that the flexibility of building demand will become more commonly implemented and buildings will provide more ancillary services. For example, the grid owner may require as services a load reduction within a specified time frame or with a specified response time, the duration of the load change, or the level of reliability or persistence as the percentage of time available in one year. Therefore, new KPIs may include metrics that show the quality of demand flexibility provided by a building as a grid service.

In this context, the KPIs should provide information such as:

- *realization rate*: fraction of the expected reduction in load reduction or shift and energy generation that the building is able to provide in a given period of time;
- *compliance rate*: how constantly the building provides the expected network services;
- *technical feasibility* acceptable range of voltage and frequency support..

Nomenclature

A_b	Energy autonomy
C_{ADR}	Available structure storage capacity
$C_{cost,balance}$	Capacity of the local energy generation system for which the annual net exported energy is equal to zero
$C_{energy,balance}$	Capacity of renewable installation for which the cost of annual export and import of electricity is the same
CF_b	Capacity factor
DERs	distributed energy resources
DR	Sizing rate
DHW	Domestic heat water
DSF	Demand side flexibility
DSM	Demand side management
$d(t)$	Delivered energy
E	Shifted energy
$E_{1\%,peak}$	Power in the 1%highest peaks in energy exchange
E_c	Connection capacity credit
E_{des}	Nominal design connection capacity
$e(t)$	Exported energy
EF	Energy Flexibility
EFB	Energy Flexible Building
EU	European Union
FF	Flexibility Factor
FI	Flexibility Index
FF_{PC}	Procurements Cost avoided Flexibility Factor
FF_{VS}	Volume Shifted Flexibility Factor
GII	Grid interaction index
g(t)	On-site electricity generation
GDP	gross domestic product
GI	Grid interaction
$\overline{G_s}$	Peak power generation index

Nomenclature

G_s^i	Grid signal in time step i
GSC	Grid Support Coefficient
$l(t)$	Electric power load
LM	Load match
LMGIs	load matching and grid interaction indicators
$LOLP_b$	Loss of load probability
KPIs	Key Performance Indicators
MCF	Mismatch compensation factor
MPC	model-predictive control
N_{hS}	Equivalent hours of storage
n	Number of time steps
$ne(t)$	Net exported electricity to the grid
(n)NZEB	(nearly) Net zero energy buildings
OER	On-site energy ratio
OPP	One percent peak power
P	Power
$P_{E=0}$	No grid interaction probability
PAL	Peaks above limit
PB	Potential boundaries
PC	Procurement cost of the electricity consumed per year
PV	Photovoltaic
q	Residual demand non covered by RES
q_h	Heating demand
RBC	rule-based control
RES	Renewable energy systems
$S(t)$	Stored energy
SG	Smart grid
STD	Standard deviation
TES	thermal energy storage
W_{el}	Electricity consumption
γ_{load}	Load cover factor

Nomenclature

γ_{supply}	Supply cover factor
η_{ADR}	Storage efficiency
η_{AEEF}	Available electrical energy flexibility efficiency
η_f	Flexible energy efficiency
$\zeta(t)$	Power losses

Subscripts

abs	Absolute
ADR	Active demand response
AEEF	Available electrical energy flexibility
b	Building
c	Connection
cons	Consumed
des	Design
el	Electrical
exch	Exchanged
f	Flexibility
h	Heating
hpt	High price time
hS	Hours
lim	Limit
lpt	Low price time
PC	Procurement cost
prod	Production
rb	rebound
rel	relative
ref	Reference
s	(grid) signal
VS	Volume shifted

Chapter 3

Thermochemical Energy Storage Systems for Power Grid Support

1. Introduction

Decarbonisation of the power sector, increase of energy efficiency and energy security are the major focus of several policies to achieve ambitious climate targets in the next years [395,396]. In the evolution of the energy systems, renewable energy sources (RES) play a major role towards the achievement of environmental sustainability [12,13,397]. Power systems in the future are expected to be characterized by an increasing penetration of renewable energy sources systems.

Due to their stochastic nature, however, renewable energies are not programmable so their energy generation is usually not adjusted in order to match electricity demands [158,398]. To guarantee the stability of the power grids, the instant balance of temporal and spatial mismatch between generation and loads can be achieved introducing flexible elements in the power networks [15,16,399–402].

Several definitions of flexibility can be found in the literature [136,139,403].As an example, according to Bertsch et al. [126] flexibility can be defined as the capability to balance rapid changes in power generation while or according to

Denholm et al. [17] as the variation and uncertainty in net load.

To achieve the ambitious goals of the “clean energy transition”, energy storage is a key factor, needed in power system design and operation as well as power-to-heat, allowing more flexibility linking the power networks and the heating/cooling demands.

Energy storage systems (ESS) play a key role for power grid support [304]. In the building sector, as an example, several studies show that overcoming the mismatch of generation and load profiles is the main characteristic of all ESS leading to an increase of the overall efficiency and better reliability , moreover, building owners may save cost since storage charging occurs during off-peak hours [305].

In the building sector ESS play a key role since without them the high targets for RES penetration may not be achieved [306]. Renewable power is converted and stored to meet the demand so that the utilization of RES can be maximized [307]. The use of efficient storage measures are promising options to deploy low-carbon technologies in the electricity networks without the need of reinforcing existing infrastructures [308,309].In the context of the flexibility their main purposes are to decrease the peak power demand, the non-renewable energy consumption and the running costs [310].

As seen in the previous chapter energy storage systems are widely investigated to ensure energy flexibility buildings. Among energy storage solutions, the implementation of thermal energy storage systems (TESs) is among the most developed DSM options to provide flexibility in the energy system shifting the electricity demand and minimizing the stress on the grid [311–313].

Thermal storage systems (TESs) coupled to power-to-heat (PtH) are receiving an increasing attention due to their better performance in comparison with sensible and latent heat storage technologies, in particular, in terms of storage time dynamics and energy density. PtH based on the conversion of electricity into heat and its reverse process Heat-to-Power (HtP), are well recognized processes among the most mature demand-side management (DSM) options [404–406].These techniques are

particularly promising to provide renewable energy integration, power grid flexibility [407,408] and power sector decarbonisation contributing to a better utilization of existing assets supporting the RES penetration into the electricity supply mix [409–414]. Thermal energy storage systems (TESs) can be effective in improving the mismatch between energy generation and use in terms of time, temperature, power or site leading to an increase of the overall efficiency and reliability [304,415–418]. Reduced investment and running costs, lower pollution and less greenhouse gases (GHG) emissions are some of the advantages connected to the use of these technologies [419,420] including: sensible, latent and thermochemical storage [421–425].

Nowadays, power-to-heat conversion with heat pumps (HP) coupled to TES is the most mature and favourable technology enabling flexibility in smart grid operations [179,324].. There are several examples of sensible and latent thermal storage in power-to-heat applications, while only a limited number of applications of thermochemical storage in the power-to-heat field are available. In this chapter it is given a comprehensive review on the state of art of thermochemical storage systems and their applications in power-to-heat technologies. Aim was to show how a series of advantages such as additional flexibility, load management, power quality, continuous power supply and a better use of variable renewable energy sources could be crucial elements to increase the commercial profitability of these storage systems. Moreover, specific challenges, i.e., life span and stability of storage material and high cost of power-to-heat/thermochemical systems must be taken in consideration to increase the technology readiness level of this emerging concept of energy systems integration.

Theoretical, experimental and numerical studies available in literature on this topic are presented with a focus on applications with renewable energy sources. Recent advancements and their potential perspectives were also discussed.

1.1. Power-to-Heat Technologies: Classification

Power-to-heat (PtH) is the classification including all devices that perform the conversion of electricity into heat. With the aim to ensure the integration of the renewables, PtH technologies (PtHs) are considered crucial sources of system flexibility [140]. When there is an excess of generation, electricity is converted into heat, in this way, additional power in the situations of increased load, is provided contributing, in the same time, to peak shaving, load shifting and energy conservation [253]. Turning surplus of electricity into heat, including thermal energy storage, offers a significant additional flexibility with a great potential in stabilizing the power grid [248,249]. The conversion into thermal energy can be performed through centralized and decentralized options. In the centralized option the electricity is converted into heat at a location far from the point of actual heat demand [426]. By district heating systems (DHS) heat is distributed through pipelines to its use. In contrast, in the decentralized approach the conversion is in a point right or very close the location of heat demand [427]. Heat is distributed without districting networks. A schematic example of the power-to-heat concept is shown in Figure 24.

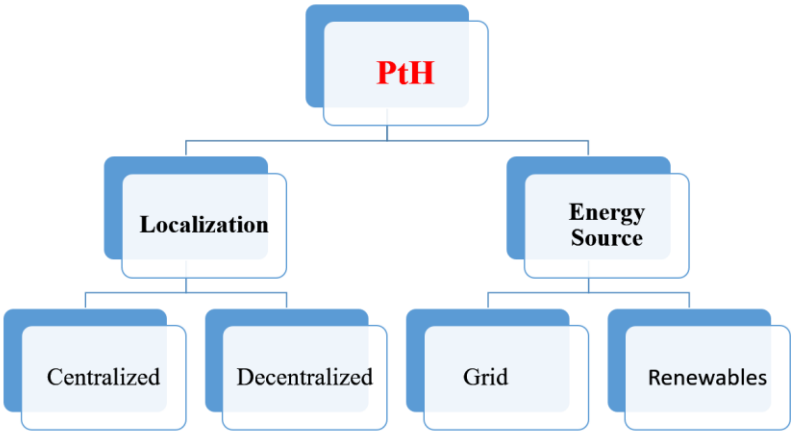

Figure 24: Schematic concept of power-to-heat technologies.

DHS are considered particularly promising due to several advantages in energy

production, distribution and consumption, especially for space heating applications [428,429]. In particular, the systems using RES have the advantage that can be placed on the energy supplier side in the actual distribution network or be installed on individual buildings [39,45,430]. District heating networks are one of the most effective solution towards a low-carbon feature [180,353,431–434]. Heat pumps (HPs) and resistive heaters are the main centralized technologies to draw electricity from the grid to generate heat to be connected to the thermal storage [430].

According to Lund et al. [427] in the decentralized approach the conversion occurs at a site very close to the location of heat demand without networks, grids and piping. The decentralized technologies have several advantages in energy production, distribution and consumption, in particular, providing a sustainable, economical and future-proof solution for heating large spaces [211,435]. A common classification of the decentralized options is among technologies combined with thermal energy, referred as thermal energy storage coupled heating, and technologies without energy storage, referred as direct heating [411]. Heat pumps, resistive boilers, smart electric thermal storage, fans, radiators are examples of the more widely used decentralized power-to-heat technologies [72–75]. Electric boilers are the cheapest alternative due to their low investment costs and can be switched on and off at low cost [159]. HPs enable flexibility in smart grid operations [77,78]. However, HPs usually function as a base load technology due to their higher efficiencies [440–442]. To further reduce energy use during operation, waste heat from industrial processes or renewable heat sources can be used as heat source with the advantage that they are not dependent from weather conditions and temperature fluctuations, like for example solar and ground sources. In this way heat generation is more stable and better suited as input for HPs [443,444].

1.2. Heat pumps coupled to PtH devices

Heat pumps used for power-to heat applications are electrically driven because

electricity is used to lift low exergetic heat to a higher temperature and consequently higher exergy level by running a vapour compression cycle [243]. Briefly, a basic vapor compression heat pump cycle comprises an evaporator, a condenser, a compressor, and an expansion device [177,178]. It is a most efficient heating and cooling system available in fact it generates more than one unit of heat for each unit of energy it consumes [179]. The performance of a heat pump can be quantified by means the coefficient of performance (COP) defined as the ratio between the thermal power output and the electrical power input [448]. COP strongly depends on the temperature levels both source (T_{source}) and sink (T_{sink}). In accordance to Carnot theory the ideal COP is expressed as follow [411]:

$$COP_{Carnot} = \frac{T_{sink}}{T_{sink} - T_{source}} \quad (3.1)$$

It is evident from equation (3.1) that a low source temperature as well as high sink temperature leading to a reduction of the COP cause an increase of the required power input. In heat pumps coupled with thermal storage devices (T_{sink}) is defined by the storage temperature lower set-points [438].

The capacity of the thermal storage is limited by the maximum condenser temperature of the heat pump. Thus, the maximal state of charge is reached when a predefined temperature in the storage is reached [325]. It is known that heat pumps (HPs) are systems that extract thermal energy from a low-temperature heat source to transfer it to a heat sink at higher temperature. Thermal energy is moved in the opposite direction of spontaneous heat transfer [449] Air, solar energy, waste heat , water or ground are typical examples of heat sources [444]. Energy extracted from these sources is converted into useful low-temperature heat that can be applied with high efficiency, e.g., for domestic heat water or space heating [450].

Among heat sources, heat from an open thermochemical system can be utilized into low temperature applications. This form of integration has the great advantage that the thermochemical systems are not dependent from local weather conditions and fluctuations of the temperature, like for example solar and ground sources, so heat

generation is more stable and better suited as input for a heat pump. Electricity renewable is an option to reduce the use of fossil fuel [451,452]. During periods of low demand and high renewable energy generation, the excess of electricity can be converted into heat and stored in TESs [453].

In contrast, the stored energy is released when demand is high and renewable power production is low [275,454,455]. In this way, HPs contribute to peak shaving, load shifting and energy conservation with benefits not only to the decarbonizing of the heating sector but also in the improving the capacity utilization of renewable power generation infrastructures [92]. In literature several examples of heat pumps coupled to TES systems, mainly sensible storage systems, are proposed [105–109]. These devices can both provide flexibility to the power system and increase the use of electricity from renewables plants [252,458,459].

2. Thermal Storage Systems

Coupling thermal energy storage to a PtH technology to provide flexibility to the power system is a promising option of the demand-side management strategies currently investigated [246,247]. In particular, turning surplus of variable renewable electricity (VRE) into heat to be stored as thermal energy offers a significant additional flexibility with a great potential in stabilizing the grid voltage [460]. In particular, during off-peak times, heating or cooling can be generated by thermal energy and then used during peak-hours flattening the customer's load profile [250]. In this way, customers can have a more efficient system and also be cost-efficient. They can take advantage of different electricity prices during peak and off-peak hours and for utilities that can spread the demand over the whole day [461,462].

Several studies examine the coupling of thermal storage with power-to-heat systems (PtHs) for several purposes, e.g., buffering, heating and cooling, transport of residual heat [463–465]. In general, small-scale PtH and TES applications can be applied in the residential and commercial sectors while large scale are mainly focus

on industrial applications such as district heating grids [38,128].Storage devices have great advantages not only in terms of flexibility of the entire power system [466,467] but also in terms of economic profitability with higher efficiency and cost effectiveness of the power grid as shown in the studies of Christidis et al. [468] and Jamshid et al. [469]. In a recent study Meroueh and Chen [470] provided a detailed analysis on the potential from TESs to provide a cost-effective solution for grid level integration in the near term for renewable-based plants. Several studies show the potential of heat pumps and thermal energy storages in terms of load shifting, energy consumption and increasing self-sufficiency [117–120].

2.1 Classification of Thermal Storage Systems

Storage technologies can be classified with respect to underlining heat storage principle into: sensible, latent and thermochemical [308,435].

Sensible thermal energy storage (STES) is based on storing thermal energy by cooling or heating of a liquid/solid storage medium. Sensible heat determines a temperature linear change (increase or decrease) in the thermal storage material, without changing its chemical composition or phase. Sensible heat Qs depends on the temperature change and the specific heat capacity of the storage material. The amount of energy stored (J) is given as followed (Figure 25):

$$Q_s = mc_p\Delta T \tag{3.2}$$

where:

- m is the mass of the storage medium (kg);
- c_p is the heat capacity of the storage medium (J/(kg K));
- ΔT is the temperature difference (°C).

It is important for sensible heat storage systems to use a heat storage material having high specific heat, good thermal conductivity, long-term stability under

thermal cycling, compatibility with its containment, recyclability, a low CO2 footprint and low cost [474]. Sensible heat storage is most widely used in building applications [415]. A list of material used for STES is reported in Table 7.

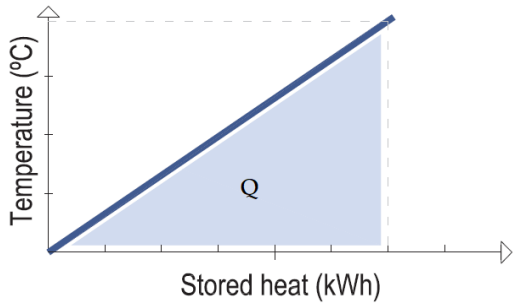

Figure 25: Sensible heat storage [475].

Table 7: List of Some Materials for sensible heat storage [123–125].

Materials	Density (Kg/m^3)	Specific Heat (J/(kg K))	Temperature Range (°C)
Sand	1555	800	20
Rock	2560[1]	879	20
Brick	1600	840	20
Concrete	2240	880	20
Granite	2640	820	20
Aluminium	2707	896	20
Cast Iron	7900	837	20
Water	1000	4190	0-100
Sand-rock minerals	1700	1300	200-300
Reinforced concrete	2200	850	200-400
Cast iron	7200	560	200-400
NaCl	2160	850	200-500
Cast steel	7800	600	200-700
Silica fire bricks	1820	1000	200-700

The performances of the thermal energy storage systems are strongly dependent on the nature of the storage material chosen in the system. High heat storage capacity and good heat transfer are important characteristics to improve the performance of the heat storage system. In the choice of the storage materials, material parameters such as the cost, environmental impact, and safety conditions should be also taken into account.

Despite many materials being widely investigated, research is always under development to increase material performance with respect to storage density and heat transfer properties [479].

Latent thermal energy storage (LTES) is based on storing heat into a storage medium undergoing a phase transition [480]. Thermal storage materials store their latent heat during phase change from solid to liquid. The latent heat is stored without a temperature change.

The amount of energy stored (J) is as followed (Figure 26):

$$Q_l = m\Delta h \tag{3.3}$$

where

2 Δh is the melting or phase change enthalpy (J/kg).

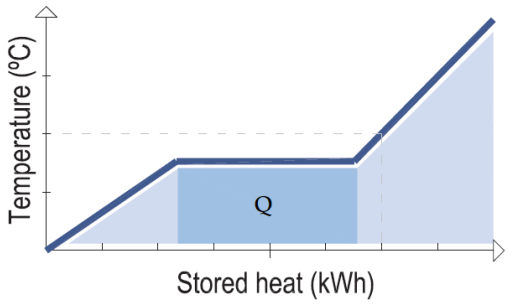

Figure 26: Latent heat storage [475].

Micro-encapsulated paraffin based phase change materials PCMs or water-based ice-storage are among methods most suitable can be used [481]. With respect to

material nature PCM are divided in organic, inorganic and eutectics (Figure 27).

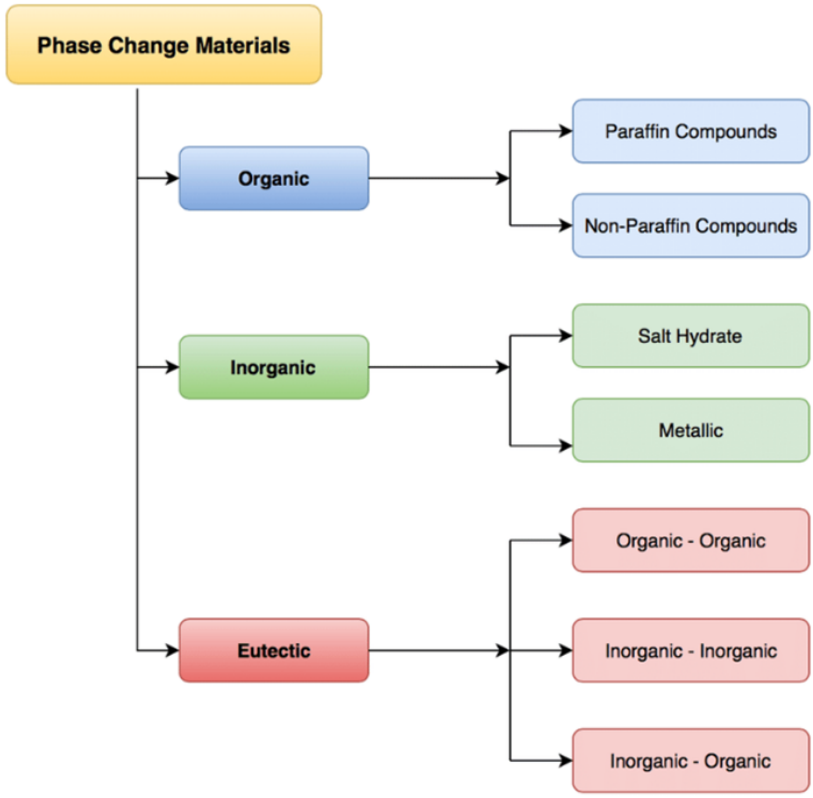

Figure 27: PCM materials classification [482].

Organic PCMs have the main advantage that they can melt and solidify without phase segregation [129–132]. Inorganic PCMs do not super-cool appreciably and their melting enthalpies do not degrade with cycling [133]. Eutectic materials are a combination of two or more low melting materials with similar melting and freezing points [488,489]. Among advantages, Eutectic materials have high thermal conductivities and densities and , usually, melt and freeze without segregation [490]. A more complex description of PCMs and their thermo-physical, kinetic and chemical properties is outside from this work.

Thermochemical or sorption thermal energy storage (TCTES) recovers the reaction enthalpy involved in a reversible chemical/adsorption reaction [313]. According to Scapino et al. [420] the chemical reaction takes place between a sorbent, which is typically a liquid or solid, and a sorbate, which is, e.g., a vapour.

During the charging process, a heat source is used to induce an endothermic reaction, the sorbent and sorbate are separated (Figure 28). The chemical/physical energy of the two components can then be stored separately. During the discharging process, an exothermic reaction occurs and heat stored is recovered.

The generic reversible chemical reaction used to store energy can be written as follow [474]:

Charging (Endothermic):

$$AB + heat \leftrightarrows A + B \tag{3.4}$$

Discharging (Exothermic):

$$A + B \leftrightarrows AB + heat \tag{3.5}$$

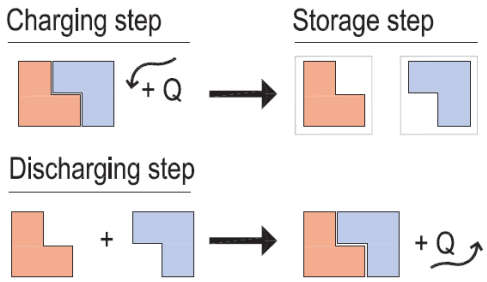

Figure 28: Thermochemical heat storage [475].

Supplying heat from any source the compound AB (storage material) can be split reversibly in A e B components. In accordance to Arrhenius law it's crucial for chemical reaction the reversibility in the temperature range of the energy source

[491]. It is known that a chemical reaction is governed by Clausius-Clapeyron equation[492] :

$$ln(P) = \frac{\Delta H}{RT} - \frac{\Delta S}{R} \quad (3.6)$$

Where P is the reaction equilibrium pressure, T is the temperature heat is supplied to the compound AB, R is the reaction equilibrium constant and ΔH e ΔS are the standard reaction enthalpy and entropy at 101325 Pa and 298.15 K. A detail on thermochemical materials and processes is given in section 3 of this chapter.

During the charging step (desorption) heat produced from a Power-to-heat (PtH) technology as external thermal energy must be used to dissociate a chemical reactant into reaction products so that heat can be recovered during the discharging step (sorption). is among the best strategies [15].

2.2 Characteristics of Thermal Storage Systems

The following features can be used to characterize an energy storage system [127]:

- ***Storage period*** defines how long the energy is stored (i.e., hours, days, weeks);
- ***Power*** defines how fast the energy stored in the system can be charged and discharged. In particular, power capacity (W) is the maximum amount of power that can be delivered by the storage system during discharging while Power density (W/l) is the ratio between the power capacity and the capacity of the energy storage system;
- ***Energy storage capacity or energy capacity*** is defined as the amount of energy absorbed in the storage system during the charging under nominal conditions. The quantity of stored energy in the system after it is charged depends on the storage process, storage medium and size of the system;
- ***Energy density or volumetric heat capacity*** is defined as the ratio between the stored energy and the volume of the energy storage system;

- ***Charge and discharge time*** defines how much time is needed to charge or discharge the system. The maximum number of charge-discharge cycles in the specified conditions is defined as the cycling capacity or number of cycles;
- ***Self-discharge*** is the amount of energy initially stored and dissipated over a specified non-use time;
- ***Efficiency*** is the ratio of the energy provided to the user to the energy needed to charge the storage system. It accounts for the energy losses during the storage period and the charge/discharge cycle;
- ***Response time*** is defined as the speed with which the energy is absorbed or released [h];
- ***Cycle life*** refers to how many times the storage system releases the energy after each recharge;
- ***Costs*** are indicators to define the overall cost normalized on the total amount of capacity (€/kWh) or power (€/kW). They are capital costs, and operation and maintenance costs of the storage equipment during its lifetime;
- ***Cost per output*** (useful) energy is the ratio of the cost per unit energy divided by the storage efficiency;
- ***Cost per cycle*** is defined as the cost per unit energy divided by the cycle life.

Typical values of the above-cited parameters for thermal energy storage technologies are reported in Table 8.

With respect to the storage period, TES methods are referred as short-term when heat input and output occur within an interval of several hours or days and, instead, as long-term if the time frame is within an interval of few months or even a whole season [317]. In contrast to STES and LTES, TCTES are particularly suitable for long term storage [493]. The reason is that during the storage phase there are no significant energy losses (no self-discharge) [408]. STES and LTES require insulation systems during storage so to avoid thermal losses, heat cannot be stored for a long time [406].

Table 8: Parameters of thermal energy storage systems (TESs).

TES System	Capacity (kWh/t)	Power (MW)	Efficiency (%)	Storage Period	Cost (€/kWh)
Sensible	10–50	0.001–10.0	50–90	days/months	0.1–10
Latent	50–100	0.001–1.0	75–90	hours/months	10–50
Thermochemical	120–250	0.01–1.0	75–100	hours/days	8–100

Despite its seasonal storage potential, TCTES for hot/cold demand is still in early development with few prototype set-ups [494].

Storage energy density is a crucial factor to select a thermal energy storage system for a particular application [495]. Because of its potentially higher energy storage density ,5 to 10 times higher than latent heat storage system and sensible heat storage system respectively [474], TCTES is receiving an increasing attention in several domains [494]. High energy density makes thermochemical thermal energy storage systems (TCTESs) such more compact energy systems so their use, reducing the volume of the system, could be very effective in the situations whereas space constraints are significant [496]. A further simplified economic comparison shows that STES is less expensive than LTES and TCTES. High capital costs are disadvantages that make TCTESs not widely available in the market [493].

3. Thermochemical Heat Storage: Description of Materials and Processes

A schematic classification of thermochemical heat storage principles is shown in Figure 29. With respect to type of reaction, thermochemical processes are divided into reversible chemical reactions and sorption processes [497]. The fixation or capture of a gas or a vapour by a sorbent is referred as sorption (adsorption and absorption) [498]. In contrast, chemical reactions (solid–gas, solid–liquid) are characterized by a change in the molecular configuration of the compound involved.

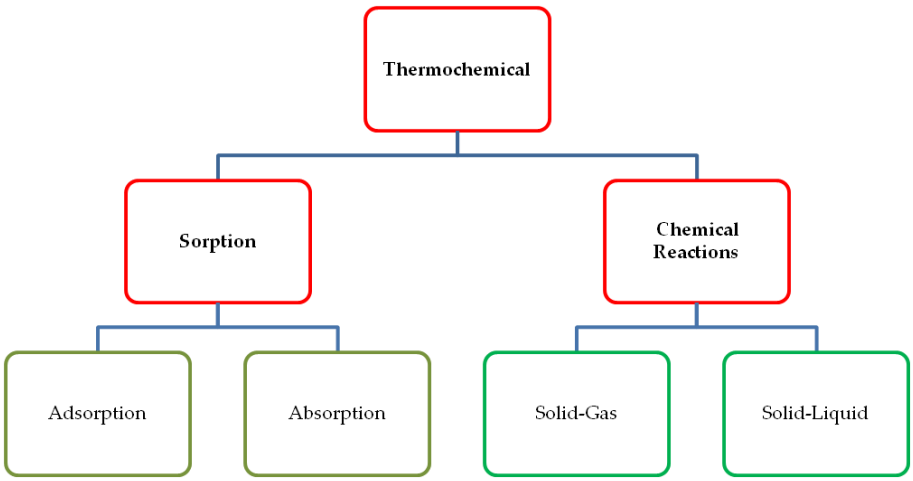

Figure 29: Thermochemical Heat Storage principles classification.

Some authors, e.g. Yu et al. [499], use the definition sorption storage to indicate both reversible chemical reactions and sorption processes. The thermochemical process consists of desorption, storage and sorption [500]. Desorption is the charging process during which heat, supplied to the storage material, is stored in the form of chemical potential by breaking the binders between the sorbent and the sorbate [501]. Storage is the phase in which the sorbent and the sorbate are separated [501]. Sorption is the discharging process aimed at recovering heat by contacting the sorbent and the sorbate [502]. Solar energy [503–505] or micro combined heat and power (CHP) [506–508] are examples of heat sources that can be used for desorbing the storage material.

3.1 Thermochemical processes and materials

According to Y. Ding [509], sorption is the phenomenon of fixation or capture of a gas or a vapor by a substance in a condensed state. As shown in Figure 29, sorption

processes are classified into absorption and adsorption. According to Nic et al. [510] absorption is defined as ‘‘the process of one material (absorbate) being retained by another (absorbent)”. According to Yu et al. [499], adsorption is defined as “a phenomenon occurring at the interface between two phases, in which cohesive forces act between the molecules of all substances irrespective of their state of aggregation”. An important difference is that absorption occurs at the sorbent molecular level by altering its composition and morphological structure, adsorption occurs at the surface of the adsorbent [152]. As shown in Figure 29, solid/gas and liquid/gas systems are example of working pairs used for sorption processes.

These processes are used to store both low-grade heat (<100°C) and medium-grade heat (100–400 °C) [512–514]. High kinetics at low temperatures make the sorption processes particularly attractive for low-temperature applications such as space heating, domestic hot water preparation or other low-grade and medium-grade heat uses [156–162]. Usually sorption materials are liquid, solid and composite sorbents [163]. Example of working pairs are:

- LiBr solution/H_2O [523,524];
- LiCl solution/H_2O [525–527];
- LiCl/activated alumina [528];
- LiCl/expanded graphite [529];
- $LiCl_2$ solution/H_2O [530];
- $CaCl_2$ solution/H_2O [531–533];
- Binary sales [534–542];
- Zeolite 13X [295,543–549], Zeolite 4A [550–556], Zeolite 5A [557,558];
- Aluminophosphates (ALPOs) [559] and Silico-aluminophosphates (SAPOs) [560–562];
- Composite materials made up by the combination of a salt hydrate and an additive with a porous structure and high thermal conductivity (expanded graphite [563,564], metal foam [565], carbon fiber [566] and activated carbon [566]).

(ALPOs) and (SAPOs) are among promising examples of sorption materials, in particular, for low temperature heat storage [567,568]. Among zeolites, Zeolite 13X is one of the most common thermochemical material in current research due to its hydrothermal and mechanical stability and corrosion behaviour [557]. Example of composite materials are $CaCl_2$-Silica gel/H_2O [569], $CaCl_2$-$FeKIL_2$/H_2O [570,571], LiBr-Silica gel/H_2O [572], $MgSO_4$-Zeolite/H_2O [573,574], $MgSO_4$-$MgCl_2$-/H_2O [575,576].

Chemical reactions are used to store medium (1000–400 °C) and high (>400 °C) grade heat [577–579]. Example of chemical reactions are:

- dehydration of metal hydroxides [580–585];
- dehydration of metal hydrides [586–591];
- dehydration of salt hydrates [478,519,592–596];
- deammoniation of ammonium chlorides [540,597–599];
- decarboxylation of metal carbonates [494,600–605];
- methane steam reforming [606–608];
- catalytic dissociation [609–611];
- metal oxide redox [612–615].

The interest towards dehydration of metal hydroxides is not recent, e.g., the hydration of MgO has been extensively studied as early as 1960 [616,617], the dehydration of $Ca(OH)_2$ has found wide attention as early as 1988. In particular, under support of the National Energy Administration, the American Pacific Northwest National Laboratory started the research on $Ca(OH)_2$/CaO as energy storage system [618]. In this context, Liu et al. [618] developed an experimental set up to investigate thermal cycling stability of the $Ca(OH)_2$/CaO system laying the foundation of applying this system to practical.

A similar experimental set up was developed by Schaube et al. [619]. $Ca(OH)_2$/CaO is among more used systems in chemical processes [618–622]. This system has numerous advantages, e.g., efficient reaction kinetics [623] and high

reaction enthalpy (104.4 KJ/mol) [624]. It is a very suitable material in thermal storage systems [625], in particular for high-temperatures (400–600 °C) applications [626]. In the context of power-to-heat applications the usage of $Ca(OH)_2/CaO$ thermochemical systems coupled to heat pumps is arousing great investigation with a particular focus on heat and mass transfer process [627–629].

Also the interest towards metal hydrides is not recent, these thermochemical storage systems were explored since the mid-1970s [630]. Several applications and different metal hydrides systems were explored for thermochemical heat storage [631–635]. Among metal hydrides, Mg-based systems are promising as thermochemical storage materials owing to high reaction enthalpy as shown in the studies of Gigantino et al. [591] and Shkatulov et al. [466]. Mg-based metal systems show cyclic stability over a temperature range from 250 °C to 550 °C in which high thermal energy densities of up to 2257 kJ/kg are reached [503].

The abundance of metal hydrides, low cost, high reaction enthalpy, high storage density are among characteristics attracting extensive investigations [587]. These systems, are suitable for both low and high temperature applications [636]. As an example, Sheppard et al. [637] investigated the potential of metal hydrides for low temperature applications while Ronnebro et al. [588] investigated their use for high temperatures applications, in particular based on experimental and modelling results they designed and fabricated a prototype to store both hydrogen and heat with solar technologies. In accordance to other studies, they showed that metal hydrides show both good reversibility and cycling stability combined with high enthalpies. A study about the future perspectives of thermochemical storage based on use of metal hydrides for solar technologies have been developed by Kandavel et al. [638].

High energy density and desorption temperatures make salt hydrates fitting with the use of power-to-heat technologies, waste heat sources, solar thermal collectors, particularly investigated and proposed for seasonal heat storage of solar energy in the built environment [518,639,640]. N'Tsoukope et al. [641] investigated 125 salt hydrates for low temperatures heat storage and found that $SrBr_2 \cdot 6H_2O$ and

$MgCl_2 \cdot 6H_2O$ are among the most promising choices for thermochemical storage applications. To investigate the potential energy storage density and the storage efficiency of salt hydrates, a micro-combined heat and power system was developed for the storage of heat generated. They found that for applications requiring lower discharging temperatures like 35 °C, the expectable efficiency and net energy storage density was low. Their results are in accordance to [642–645]. Salt hydrates are considered the most suitable materials for residential applications owing to their high energy density (400-870 kWh·m−3) and low turning temperature [646].

Metal carbonates have several advantages, e.g., high energy density, nontoxicity, low costs and widespread availability. All these properties make them suitable for thermochemical storage applications [647–649]. Among suitable alternatives, the combined use of $CaO/CaCO_3$ (density 0.49 kWh/kg), proposed by Barker in 1973 [650], is largely investigated. In a recent study Fernandez et al. [602] used the working pair $CaO/CaCO_3$ to develop a system referred as Photovoltaic-Calcium looping (PV-CaL) as large scale storage system. They showed that the high turning temperatures of the exothermic carbonation reaction allows using high-efficiency power cycles. $CaCO_3$ is one of the most abundant materials in nature. Its use avoiding the risk of resource scarcity may not compromise the economic and technical viability of a thermochemical storage system [602].

Note that among the various thermochemical storage materials described in this section, only few of them have been used so far in power-to-heat applications.

3.2 Thermochemical heat storage systems

Thermochemical heat storage systems with respect to system configuration can be divided in open and closed systems [299,300]. Open systems work at atmospheric pressure in contact with the environment while closed ones work with pure vapour, circulating in hermetically closed loops, at vacuum pressure [653]. A schematic sketch of a closed and open system is shown in Figure 30.

A closed system is usually based on a sorption reactor (heat exchanger), a condenser and an evaporator. During the charge process (desorption), heat must be supplied to the storage material at high temperature in the sorption reactor. Desorbed water vapour, released from the sorbent, is condensed at low temperature. The liquid is stored in the reservoir while the heat of condensation can be used either as a low-temperature source or rejected to the environment. After the accomplishment of the charging mode, the storage materials and components will cool down to ambient temperature so during storage no further energy losses occurs. When heat is needed, the valve between the evaporator and sorption reactor is turned on and discharging mode occurs. During the discharging process (adsorption), heat is supplied to the liquid stored in the evaporator at low temperature; the resulting steam is adsorbed in the absorber releasing heat. Adsorption is a completely reversible process so heat supplied for desorption is equal to the heat gained back during adsorption. Liu et al. [525] developed a seasonal storage system and evaluated that the storage capacity increases with the evaporator temperature and decreases with desorption temperature.

An open system is less complex in its design as it can be seen in Figure 30 b. It can be directly connected to the ambient air where the moisture for sorption process is obtained; there are no evaporator or condenser. During the charging mode hot air flows into the sorption reactor releasing water vapour into the air itself. Output is saturated warm air. When heat is needed, cold wet air from the environment is blown into the sorption reactor. Open systems are usually equipped with fans to ensure the ambient air flow into the sorption reactor [501]. The key component of the above-described systems is the thermochemical reactor. The reactor can be integrated [654] or separated [655]. In an integrated reactor, the material is stored in the tank where it reacts, while the chamber where the reaction takes place is separated from the thermochemical material storage tank. In a separate reactor the dissociation between the thermal power and the installation storage capacity increases the storage density of the process since there is no need for vapour diffusers and heat exchangers are integrated into the reactor. Moreover, this kind of reactor can also work in steady-

state conditions, providing a constant thermal power output [656].

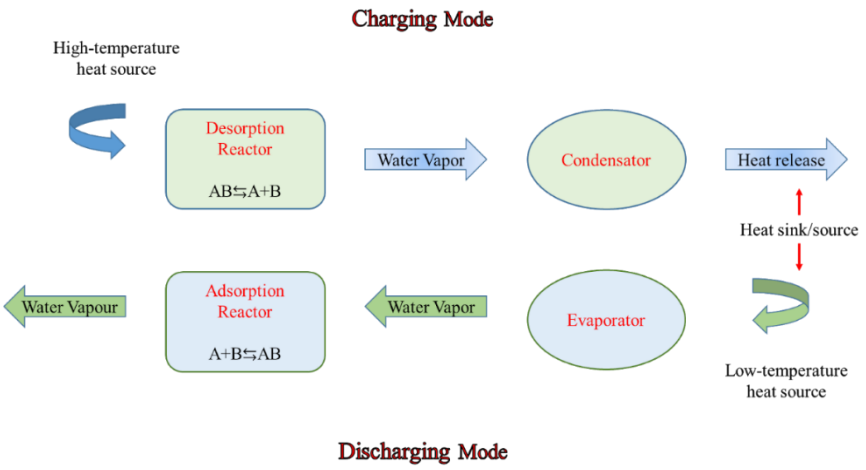

(a)

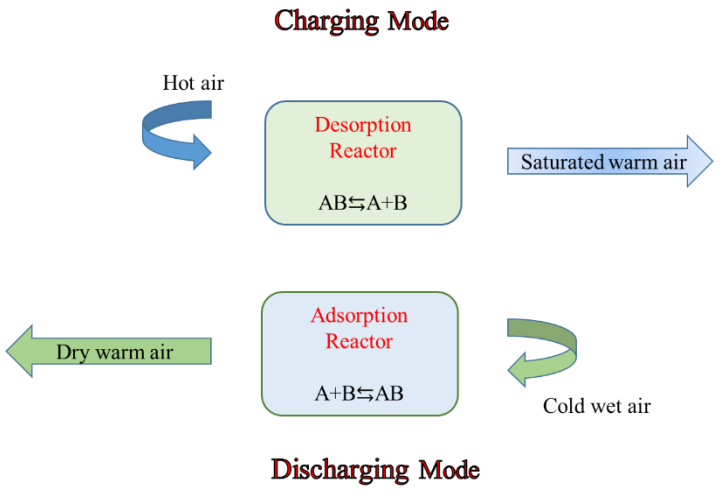

(b)

Figure 30: Schematic sketch of (**a**) closed and (**b**) open thermochemical system.

Energy and exergy methods to assess the performances of closed and open systems have been carried by Abedin and Rosen [657]. The authors compared open

and closed systems based on use of zeolites 13X. 50% and 9% are the values obtained for energy and exergy efficiency, respectively, in closed systems, 69% and 23% in open ones. Since the exergy efficiencies of both systems are lower than the energy efficiencies it means that there is a margin for loss reduction and efficiency for TCTESs [317]. From a numerical comparison between the two designs, Michel et al. [653] concluded that heat transfer is the main limitation in closed systems while it is mass transfer (vapour transfer to the adsorbent during discharging) in open ones.

Many prototypes of both type of systems have been developed. One of the first open prototypes, in operation since 1996, is the zeolite 13X storage system built in a school in Munich by ZAE Bayern [658]. The system, shown in Figure 31, was designed for peak shaving of the heating load in order to be operated jointly with district heating in winter to supply it during the off-peak in summer.

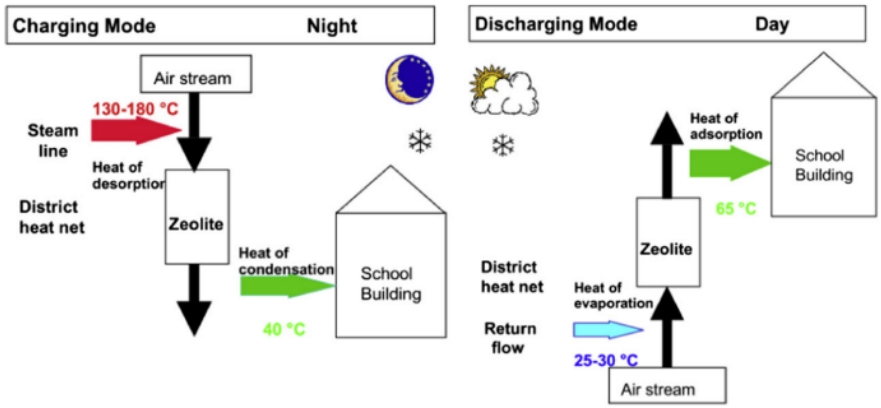

Figure 31: ZAE Bayern open system in Munich.

The charging temperature is about 130 °C while the storage capacity is 1300–1400 kWh. Heat released during the discharging mode is used to produce water vapour. A more recent prototype of ZAE Bayern was developed in 2015 [502]. It is an open system based on zeolite 13X for transportable sorption heat storage purposes. Waste heat from an incineration plant at 130 °C is used as thermal source during discharging mode. The charging temperature was 60 °C and the storage capacity 0.6 MJ/kg.

Among closed prototypes, one of the first was developed within the HYDES (High Energy Density Sorption Heat Storage) project [659]. The prototype in function from 1998 to 2001 was a solar thermal energy storage system for space heating purposes based on silica gel/H2O. Solar thermal collectors were used as low temperature heat source for the evaporator. The charging temperature was about 82 °C, the sorption one 32 °C, a power output of about 2.87 kW and 1.7 kW were measured during discharging and charging phase.

A prototype of closed system is currently being developed at GEPASUD laboratory (French Polynesia) [542]. It is a conventional mechanical vapour compression (MVC) driven by grid and PV electricity integrated with a thermochemical reactor based on the use of $BaCl_2/NH_3$ as working fluids pair. The prototype has the aim to demonstrate that a thermochemical reactor coupled with a PV-driven mechanical compressor is an effective innovative solution offering energy storage capabilities for cooling purposes. The prototype uses ammonia not only as thermochemical material but also as refrigerant liquid. Among thermochemical storage materials, ammonia is expected to be established in the market for small and medium refrigeration [660].

The existing prototypes show a mature development of the TCTESs in heat-to-heat and heat-to-power applications. Collectors and concentrating solar plants (CSP) are mainly used as a heat source for the evaporator of the thermochemical devices. In particular, coupling storage into CSP systems enables dispatchable generation, whereby utilities produce power to match demand overcoming intermittency challenges faced by renewable energy production. Another field of wide application of TCTESs is the recovery of industrial waste heat [661–664]. Kuwata et al. [665] investigated the potential of the ammonium chloride $SrCl_2$ in applications based on utilization of industrial waste heat.

Thermochemical energy storage could be a key technology able to bridge the gap between the wasted heat as the source and provided to customers at the time and place they need it [633,634]. A more detailed review on this field was developed in [666].

As an example, a list of some prototypes is given in Table 9 and in Table 10 for an open and closed thermochemical systems respectively.

Table 9: Example of prototypes of open systems for thermochemical storage.

Project Name/Institution	**Description**	**Storage System**
MONOSORP [667] (2006)	• Storage system for space heating • Charging temperature T_c = 20 °C • Discharging temperature T_d = 180 °C	Zeolite 4A
Institute for Solar Technology SPF [608] (2006)	° Storage system for space heating. ° T_c = 20 °C ° T_d = 180 °C	Zeolite 13X
ECN [1] [594] (2010)	• Lab scale packed bed reactor for seasonal storage of solar heat • Discharge time about 25 h • Storage energy density measured 0.14 MJ/kg	$MgCl_2 \cdot 6H_2O$
CWS [2] [668] (2011)	° System integrated with a water tank (STES) for heating purposes ° T_c = 35 °C ° T_d = 180 °C	LiCl with Zeolite 13X
ECN [579] (2013)	• Lab scale packed bed reactor for heating (Heat Power 150 W) • T_c = 10 °C • T_d = 50 °	$MgCl_2$ H_2O
Energy hub-ECN [546,547] (2013–2014)	° Lab scale two packed bed modules for heating purposes ° T_c = 70 °C ° T_d = 185 °C ° Heat Power 400 W	Zeolite 13X

Project Name/Institution	Description	Storage System
ASIC [3] [544] (2014)	• Storage system for space heating and domestic hot water • T_c = 25 °C • T_d = 180 (230)	Zeolite 4A (Zeolite 13X)
STAID [4] [548] (2015)	◦ Storage system integrated in a domestic ventilation system for space heating during peak hours ◦ T_c = 57 °C ◦ T_d = 120–180 °C ◦ Storage energy density 0.41 GJ/m^3	Zeolite 13X
ESSI [5] [669] (2016)	• Packed bed reactor for house heating • T_c = 25 °C • T_d = 80 °C • Thermal power measured during sorption mode 0.3–0.8 kW • Thermal power measured during desorption mode 0.4–1.6 kW	$SrBr_2 \cdot 6H_2O$
STAID [549] (2016)	◦ Storage system for space heating ◦ T_c = 20 °C, ◦ T_d = 120–180 °C	Zeolite 13X
NSFC [6] [528] (2017-2018)	• Lab-scale prototype experimentally investigated to store low-temperature heat for space heating • T_c = 20 °C • T_d = 30 °C • Thermal power (56.7–136) W	Activated alumina/LiCl

[1]Energy Research Center of the Netherlands. [2] Chemische WarmeSpeicherung. [3] Austrian Solar Innovation Center. [4] Stockage Inter Saisonnier de l'Energie Thermique dans les Batiments. [5] European. Support to Social Innovation. [6] Natural National Science Foundation of China.

Table 10: Example of prototypes of closed systems for thermochemical storage.

Project Name/Institution	Description	Storage System
SWEAT [1] /ECN [596] (2004)	• Solid sorption storage for cooling purposes. • T_c = 15–25 °C, • T_d = 77–86 °C • Thermal power measured in discharging mode 0.5–0.7 kW • Thermal power measured in charging mode 1.2 kW.	Na_2S/H_2O
MCES [2] [609] (2004)	○ Solid sorption storage for cooling and heating purposes. ○ T_c = 65 °C ○ T_d = 80–95°C ○ Storage energy density 8 MJ/kg.	$Na_2S{\cdot}9H_2O$ and graphite used as additive
MODESTORE [670,671](2006)	• Storage system for heating purposes • T_c = 25 °C • T_d = 88 °C • Thermal power measured during discharging mode 0.5 kW • Thermal power measured during charging mode 1 kW.	Silica gel
SOLAR-STORE [644] (2006)	○ Solid sorption storage for heating and cooling purposes. ○ T_c = 35 °C, ○ T_d = 80 °C ○ Heating density power 47–49 kWh/m^3 ○ Cooling density power 27–36 kWh/m^3	$SrBr_2$ with expanded natural graphite

Project Name/Institution	Description	Storage System
SOLAR-STORE [645] (2008)	• T_c = 35 °C • T_d = 80 °C • Heating power 60 kW • Cooling power 40 kW	$SrBr_2$
Fraunhofher [672] (2012)	° Solid sorption storage for waste heat industrial recovery ° T_c = 30 °C ° T_d = 9–200 °C ° Heat storage capacity 0.54–0.79 MJ/kg	Zeolite/$CaCl_2$
E-hub/Project [557] (2014)	° Lab-scale prototype for space heating ° T_c = 20–30 °C ° T_d = 80–120 °C ° Storage energy density 0.045 GJ/m^3	Zeolite 5A
COMTES [3] [673] (2015)	• Solid sorption system for space heating and domestic heat water. • T_d = 75 °C • Storage energy density 0.4 GJ/m^3	Zeolite 13XBF
COMTES [532] (2015)	° Liquid sorption system for diurnal storage ° T_d > 50 °C ° Power output approximately 1 kW	$NaOH/H_20$
SJTU [4] [529] (2016)	• Solid sorption system for space heating and domestic heat water. • T_c = 40 °C • T_d = 85°C • Storage energy density 0.873 kWh/kg.	LiCl with expanded graphite
HSR-SPF [5] [533] (2018)	° Liquid seasonal thermal storage system ° T_c = 22 °C, ° T_d = 50°C	$NaOH/H_20$

Project Name/Institution	Description	Storage System
Heat STRESS [539] (2019)	• Solid sorption system for seasonal thermal storage for domestic application • T_c = 40°C • T_d = 70°C	$CaCl_2/NH_3$
University of Newcastle [612] (2019)	° Hybrid energy storage system to store energy from wind, solar and/or off-peak electricity simultaneously. ° Reaction take places a T > 800 °C	Co_3O_4/CoO
RESTRUCTURE [614] (2019)	• Pilot prototype integrated with Concentrated Solar Power (CSP) for power production • Reaction take places in the temperature range (800–1000) °C	Co_3O_4/CoO

[1] Salt Water Energy Accumulation and Transformation. [2] Modular Chemical Energy Storage. [3] Combined Development of Compact Thermal Energy Storage Technologies. [4] Institute of Refrigeration and Cryogenics (China) [5] Institute fur Solartechnik.

3.3 Thermochemical Storage in Power-to-Heat Applications

PtH technologies show a mature development with latent and sensible storage while only a limited number of applications with thermochemical storage is available in literature [341–348]. Existing applications focus on different aspects, hence a net comparison was not possible. Based on the usage of the heat stored, in this work the applications were divided into power-to-heat and power-to-heat-to-power as shown in Figure 32. In the first case, heat stored is used in the form of thermal energy for heating and cooling purposes. In the second case, heat, released during the discharging phase, is used to generate electricity when it is needed.

The following studies are examples of power-to-heat- applications.

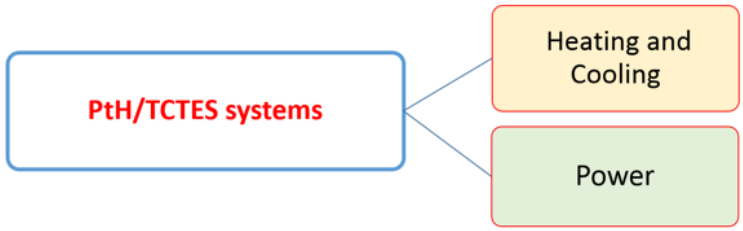

Figure 32: Thermochemical storage and power-to-heat uses.

Cammarata et al. [681] developed a hybrid thermochemical storage device to store the excess of power generation. The system was developed for household applications for low to medium temperature range (50-100 °C). The scheme of this case study is shown in Figure 33.

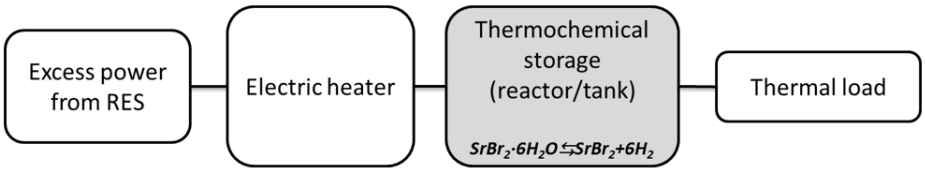

Figure 33: PtH/TCTES system developed by Cammarata et al. [681].

The system is based on the reversible hydration/dehydration of $SrBr_2 \cdot 6H_2O$ and graphite as additive material. The power converted into heat by a heat pump driven by solar and wind energy is carried out to the tank storage where the endothermic dehydration reaction takes place at temperature < 100 °C. From the reaction $SrBr_2$ (sorbent) and H_2O (sorbate) are formed ($SrBr_2 \cdot 6H_2O \leftrightarrows SrBr_2 + 6H_2O$), the sorbate is condensed for use in the discharging process in the case of closed system or released in the environment in the case of open system. Heat stored is use both heating demand and supply of electricity during the discharging phase. Their results showed that an energy storage density of 500 kJ/kg can be achieved at a temperature of 80 °C, a value of 600 kJ/kg by increasing the temperature to 150 °C. This study shows for the first

time how the composite formulation of $SbBr_2$ affects the energy density, heat and mass transfer and reaction kinetics.

Ferrucci et al. [542] developed a hybrid system for household applications. This integrates a thermochemical system with an air conditioning system driven by grid and photovoltaic electricity. The cooling system is a conventional Mechanical Vapor Compression (MVC) while the storage device is a packed-bed reactor with eight compartments based on the use of $BaCl_2/NH_3$ as working pair. The scheme of this case study is shown in Figure 34.

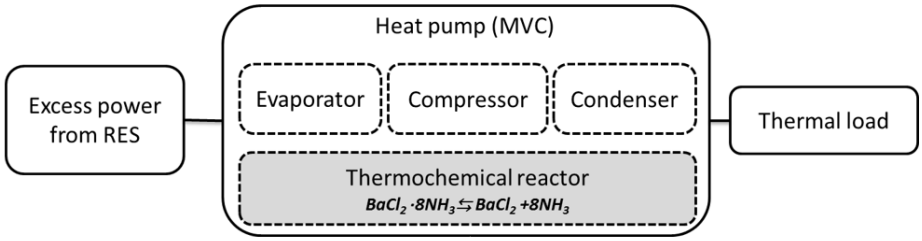

Figure 34: PtH/TCTES system developed by Ferrucci et al. [542] and by Fitò et al. [682].

When there is a surplus of electricity generation and no cooling needs, the extra power is used to run the compressor in order to store energy for later use. By means of a smart controller, during the storage process, the evaporator is disconnected from the circuit and the reactor is connected to the compressor. The desorption heat is provided by a low grade waste heat source at 50 °C or by an electric heater in direct contact with the thermochemical reactor. $BaCl_2$ reacts with ammonia (NH_3) to form $BaCl_2 \cdot 8NH_3$ with an energy density estimated in an approximate value of 200 kJ per kg of reactor. The coefficient of performance, exergy efficiency and cooling capacity were used as indicators to compare a traditional MVC cycle without thermochemical storage and the hybrid system proposed. As example, the authors showed that the COP of the hybrid system, for a given source temperature, is higher than the one of a

conventional one. The hybrid system was compared with alternative energy storage processes. In particular Pb and Li-ion batteries (electrochemical storage), ice and chilled water thermal storage was chosen as alternative devices to thermochemical reactor. Their results showed that the hybrid system proposed has a cooling capacity (60 Wh/L) six times larger than chilled water system but comparable to that one of ice storage systems. MVC systems with electrochemical batteries have the highest cooling capacity, 190 Wh/L for MVC and Pb battery and 420 Wh/L for MVC and Li battery respectively, but much shorter life span than MVC with thermochemical storage. The COP of the hybrid system (4.8) is comparable to Pb batteries (4.2), Li-ion batteries (4.2) and chiller (4.2) systems.

The hybrid system is an example of compressor-driven method for energy storage and deferred cooling. This application for space cooling is not yet widely explored in literature.

Fitò et al. [682] analyzed an ammonia-based refrigeration system consisting in the hybridization of compression refrigeration with thermochemical storage. The proposed hybrid system has the typical architecture of a MVC cycle (evaporator, compressor, condenser, reservoir and throttling valve), a grid-connected photovoltaic installation and a thermochemical storage reactor. The scheme of this case study is shown in Figure 34. The MVC cycle and thermochemical storage system have the same condenser, evaporator and refrigerant fluid (NH_3). The storage device is a packed-bed reactor based on the use of $BaCl_2/NH_3$ as working pair. Both the PV installation and the grid are used to meet the electricity requirements for cold production. When there is a surplus of power generation from RES and no cooling demand, the power in excess is used to store energy in the form of heat driving the desorption phase of the reactor. Thermochemical process enables the storage of energy in the form of chemical potential for a deferred cold production without running the compressor. The heat of desorption is provided by waste heat or solar collectors at about 50 °C. The authors demonstrated an overall thermochemical cycle

has a COP (1-1.4) higher than a conventional MVC operating without thermochemical storage.

Finck et al. [295] developed a hybrid compression thermochemical refrigeration system (HCTSR) to show the potential power flexibility of thermal storage and power-to-heat. Power flexibility is in this specific case defined as the thermal response of TES tanks and related electricity consumption of the heat pump during charging, discharging and store mode. The scheme of this case study is shown in Figure 35.

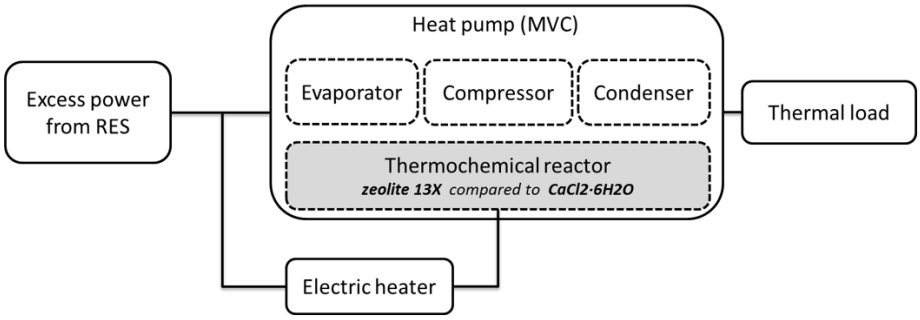

Figure 35: PtH/TCTES system developed by Finck et al. [295].

HCTRS, consists of an MVC cycle and a thermochemical reactor. The heat pump and an electric heater serve as power-to-heat conversion while the storage tank as the source of flexibility. The thermochemical storage device is a packed bed reactor based on zeolite 13X and water as working pair. During desorption, the electric heater serves as a dehydration source. During adsorption, the heat stored is used for space heating or domestic hot water. The system with thermochemical storage was compared with the one obtained coupling the same MVC to a sensible and latent storage tank. Water and $CaCl_2 \cdot 6H_2O$ were used as sensible and latent material respectively. Results show that assuming the same dimensions for the storage tank (a cylindrical vessel of 0.5 m3) and a volume flow of heat transfer medium of 1 m3/h, the thermochemical system has an energy capacity (0.05 GJ) lower than the other

storage systems (0.15 GJ). The available storage capacity (COC) and storage efficiency (η_{OC}) were used to compare the energy flexibility of the three different thermal storage systems. COC is defined as the amount of energy that is shifted during the optimal control to minimize the electricity consumption costs for operating the heat pump and the electric heater. η_{OC} indicates the effective use of the heat stored to compensate power-to-heat devices during optimal control. Results show that the thermochemical storage has the lower values for both COC (5.6 kWh) and η_{OC} (0.96).

The following studies are examples of power-to-heat-to-power applications in which the heat stored is converted into electricity by a power plant when it is needed.

Wu et al. [612] proposed a hybrid energy system to store excess energy from renewable sources. The system consists of a compressed air energy storage (CAES) integrated with a thermochemical reactor based on the use of the metal oxide redox pair Co_3O_4/CoO as sorption working material. In contrast to a conventional Compressed Air Energy Storage (CAES) [683] in which compressed air is superheated by means the combustion of fossil fuel, in the proposed hybrid system this function is replaced by the sorption reactor. The scheme of this case study is shown in Figure 36.

The proposed system consists of five compressors powered by electricity to compress air and an electric heater as heat source for the charging phase of the thermochemical storage process. The thermal charging phase takes place, in parallel with the CAES compression phase, with the reduction of Co_3O_4 into CO and CO_2 ($2Co_3O_4 \leftrightarrows 6CoO+O_2$) carried out at 870 °C and 0.1 bar. The discharging phase takes place and the energy stored in the compressed air and metal oxide CoO (heat released by the exothermic reaction is transferred to air) is converted back into electricity throw air turbines. A value of 3.9 kWh/m^3 was evaluated for the energy storage density, defined in this case as the total power output per unit volume of the stored air (the same as the volume of the storage cavern). Moreover, it was estimated that

65% of the energy storage density relies on thermochemical part of the system while the remaining 35% is achieved via the CAES. The authors demonstrated that, in terms of storage energy density, the hybrid system has a value comparable to a conventional CAES (3–6 kWh/m^3) operating at the same conditions. Based on a thermodynamic analysis it was estimated an efficiency of 56.4%. In comparison to conventional CAES plants, authors showed that this value is higher than the efficiency of the commercialized Huntfort (42%) and McIntosh (54%) CAES plants.

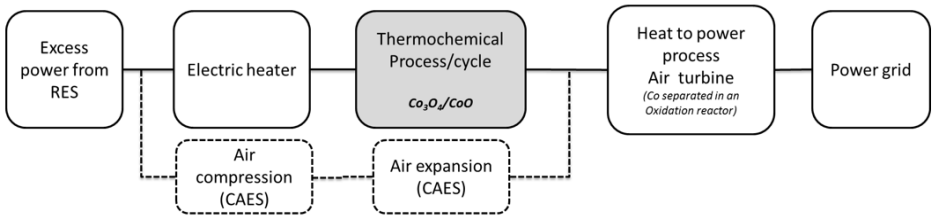

Figure 36: PtH/TCTES system developed by Wu et al. [612].

Fernandez et al. [602] developed a power-to-heat-to-power system based on the calcination/carbonation of calcium carbonate as sorption process and a closed CO_2 Brayton regenerative cycle. The scheme of this case study is shown in Figure 37. During the charging phase, the electric power is converted into thermal power by Joule effect to heat up the calciner (Fluidized bed thermochemical reactor). In the reactor the calcination endothermic reaction takes place under atmospheric pressure at 950 °C, CaO and CO_2 are formed ($CaCO_3 \leftrightarrows CaO+CO_2$). During the discharging phase, that takes place at 75 bar and 25 °C, power is generated in a CO_2 turbine connected to an asynchronous generator that converts mechanical power into electricity. CaO and CO_2 are carried out in the carbonator reactor where the exothermic carbonation reaction occurs. The presence of a calciner and a carbonator is indicative that in the system charging and discharging cycles are well differentiated and independent. The system is connected to the grid to export electrical power generated during the discharging phase. The proposed system was simulated under

different charging and discharging operations modes to assess its potential as large-scale electric energy storage system estimating a maximum reachable efficiency of 39%.

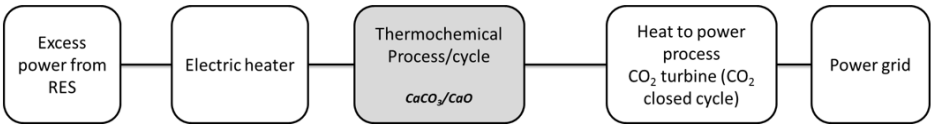

Figure 37: PtH/TCTES system developed by Fernandez et al. [602].

Wu et al. [684] developed a phase change redox (PCR) system to convert electricity surplus into heat and to store it using a CuO/Cu_2O cycle. The scheme of this case study is shown in Figure 38. When there is a surplus of electricity from grid or solar/wind plants heat provided by Joule heating is used for the charging phase of the sorption process. During this phase, CuO_2 is reduced into CuO and O_2 ($2CuO_2 \leftrightarrows 2CuO+O_2$). The molten CuO/CuO_2 requires a high temperature of about 1200 °C during the charging phase. When electricity demand in the grid occurs the discharging phase starts. During this phase, the exothermic reaction takes place and the stored molten CuO/CuO_2 is oxidized and cooled into an oxidation reactor using air. Heated air is used into a Brayton cycle coupled with a bottoming organic Rankine cycle (ORC).

Energy storage density and round-trip efficiency were the indicators used to assess the energy storage performances. Energy storage density is here defined as the heat stored per mass unit of the raw material CuO while the round-trip efficiency is the amount of electricity that can be recovered for a given energy input.

The PCR system coupled to the Brayton and Rankine power generation cycles is able to achieve a round trip efficiency of about 50%. Advantages of the proposed PCR system are high-energy storage density, high round trip efficiency, enhancement of CuO/Cu_2O reversibility, abundant and low-cost raw material and oxygen as a valuable by-product. The main disadvantages and potential limits can be summarized as systems complexity, high-temperature heat source, high operating temperature and

high equipment, operation and maintenance costs.

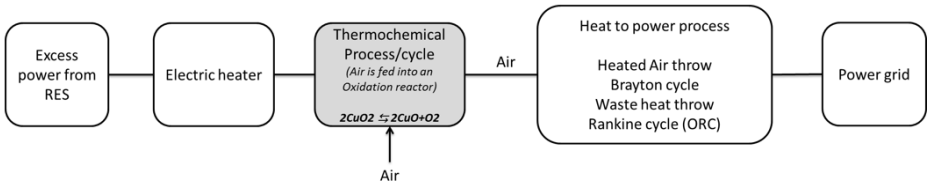

Figure 38: PtH/TCTES system developed by Wu et al. [684].

Rodriguez et al. [685] proposed an innovative hybrid absorption system based on the Thermochemical technology to store electrical energy at large scale. The system consists of two storage tanks to accumulate a liquid solution at two different levels of pressure, a compressor powered by the excess renewable energy, a thermochemical storage tank (using of $NH_3/LiNO_3$, where NH_3 is the solute while $LiNO_3$ is the sorbent) and an independent vapour expander/turbine (T) located between the high- and low-pressure tanks that drives an electrical generator. The scheme of this case study is shown in Figure 39. When there is an excess of renewable electricity generation, the charging phase takes place increasing the pressure difference between the two reservoirs. The authors highlighted that the amount of energy required to pressurize the gas in the proposed hybrid cycle is lower than pressurizing a gas with no phase change. During the discharging phase, the turbine transforms the stored energy into mechanical energy driving a generator and returning the electricity into the grid. Numerical simulations were carried out in order to evaluate the performance of the storage system. For a nominal renewable power of 18 kW and an energy output of 8 kW, 44.3% and 0.36 MWh were the values found for the efficiency and energy storage respectively. The viability of using of an absorption thermochemical energy stored system inherently combined with a gas compression cycle was demonstrated only theoretically.

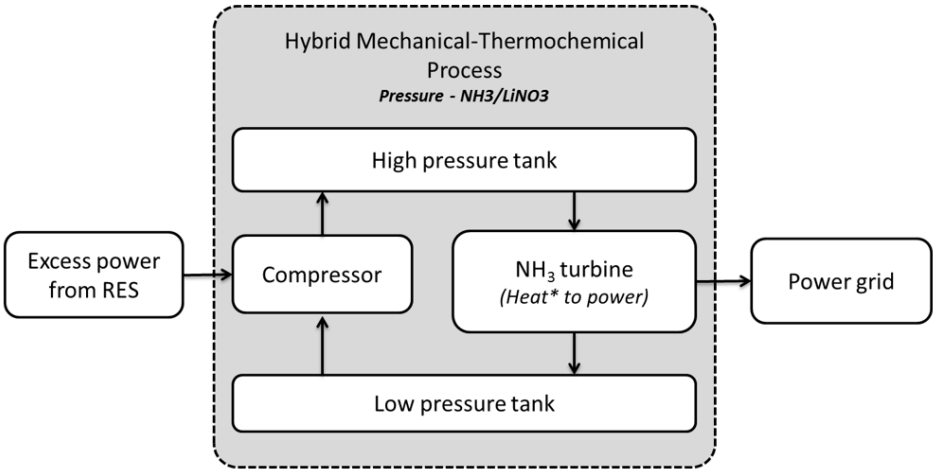

Figure 39: PtH/TCTES system developed by Rodriguez et al. [685]. *Heat is exchanged between the two tanks in order to compensate the ammonia expansion/compression cycle.

The features of the cases described in this section are summarized in Table 11

Discussion and Outlook

The articles reviewed show emerging power-to-heat/thermochemical applications as flexible coupling systems to address both integration of renewable energies and additional grid flexibility. High efficiency in balancing the excess of renewable generation is the key aspect that could led these applications towards an increasing development in the next future.

Investigating the demand flexibility of power-to-heat conversion with thermochemical systems was a common aim of all authors. All three dimensions of flexibility were investigated: size (energy), time (power) and costs. A number of indicators were proposed to quantify the energy flexibility in terms of available storage capacity and/or efficiency. The usage of a non-common quantification method to estimate the energy flexibility makes difficult a straightforward comparison among the reviewed studies. Despite this limit, important considerations can be argued as follows.

According to the thermodynamic and numerical analyses, the overall efficiency of the coupled system range from 39% to 56%. The highest value is obtained in power-to-heat/thermochemical applications coupled to power cycle [684], overcoming typical efficiencies of conventional power cycles. The reason lies in the use of raw thermochemical materials requiring higher operating temperatures, which increase the upper limit of the achievable thermodynamic efficiency according to Carnot principles. This suggests that more efforts should be paid to the design and test of thermochemical materials and related physical–chemical reactions, in order to boost further the process efficiency in view of the development of optimized systems.

The studies reported in [612] and [684] suggest that the high efficiency and flexibility of these innovative applications could be able to facilitate the integration in the power system not only of the photovoltaic but also of the wind power. A development in the wind energy integration could be crucial in energy systems characterized by a large share of wind power.

High storage density, low heat loss, long storage period, highly compact energy storage are the main advantages common to all the power-to-heat/thermochemical technologies. Despite this, a series of limits, such as the high costs of the materials and the complexity of the equipment, makes these applications still not mature for large scale/market adoption as shown by the few prototypes developed and tested so far. Costs abatement and process simplification in optimized systems require further efforts for the development of techno-economically competitive applications. Moreover, the deployment at large-scale of these potential low-carbon technologies will require significant investments and the revision of the present infrastructures.

Table 11: Thermochemical storage in PtH and PtH/HtP applications.

References	Description	Application	Storage Material	Performance indicators
Cammarata et al.[681]	Solar and wind electricity stored for household applications	Power to heat to heat	$SrBr_2/H_2O$	Energy density:500 kJ/kg
Ferrucci et al. [542]	Photovoltaic and grid electricity stored for household applications	Power to heat to heat	$BaCl_2/NH_3$	Energy density:200 kJ/kg COP=4.8
Fitò et al. [682]	Energy grid stored to cold production	Power to heat to heat	$BaCl_2/NH_3$	-
Finck et al.[295]	Energy grid stored to investigate the maximum flexibility towards the power grid	Power to heat to heat	Zeolite $13X/H_2O$	Capacity: 5.6kWh Efficiency: 0.96
Wu et al.[612]	Wind and off-peak electricity stored to power grid support	Power to heat to heat	Co_3O_4/CoO	Energy density:3.9 kWh/m^3 Efficiency: 56.4%
Fernandez et al. [602]	Photovoltaic electricity stored to heating and power grid support	Power to heat to heat	$CaCO_3/CaO$	Overall plant Efficiency: 39.21%
Rodriguez et al. [685]	Storage of mechanical and electrical (PV/grid) energy at large scales to cooling purposes	Power to heat to power	$NH_3/LiNO_3$	Capacity: 0.36 MWh Efficiency: 44.3%
Wu et al. [684]	Photovoltaic and grid electricity stored for grid support.	Power to heat to power	CuO/Cu_2O	Energy density:1600 kJ/kg Efficiency 50%:

4. Conclusions

In this work, to provide a comprehensive review on the state of art of thermochemical storage systems and their applications in power-to-heat technologies, theoretical, experimental and numerical studies and their recent advancements and potential perspectives were discussed.

This paper reviews the current literature that refers to the development and exploitation of thermochemical storage systems connected to power-to-heat technologies to power grid support. The operation principles both of thermochemical and of power-to-heat are presented, thermochemical materials and processes are compared. Power-to-heat conversion is likely the most mature and favourable technology enabling power flexibility. It is particularly suitable in energy systems with high shares of renewable generation. In order to increase the flexibility of the energy system, power-to-heat technologies coupled to thermal storage devices are among the most promising alternatives. Thermal storage is able to provide several benefits such as load management, power quality and continuous power supply. When there is an excess of generation, electricity is converted into heat and stored for subsequent use on demand. In this way, additional power in the situations of increased load is provided, thus contributing to peak shaving, load shifting and energy conservation. The conversion of power into heat is generally performed by electrical resistances or via heat pumps. Despite converting electric power into heat is not convenient from a thermodynamic perspective, power-to-heat applications are gaining an increasing attention due to the low prices of renewable electricity and the increasing surplus of produced electricity that cannot be used. Several advantages, e.g., high efficiency for balancing excess renewable generation and high potential on reduction of CO2 emissions and fossil fuels, could be the key elements for a larger development in the future trends of these technologies.

There are several examples of sensible and latent thermal storage in power-to-heat applications, while only a limited number of applications of thermochemical storage

in the power-to-heat field are available. High energy storage density, no heat loss during the storage, no self-discharge and long charge/discharge, broad availability and suitable temperature ranges are some important advantages of thermochemical storage systems.

However, the high complexity and costs of these technologies limit the real applications, while only few prototype-scale systems have been studied. To improve their implementation, comprehensive analyses and investigations are further required. In contrast, thermochemical storage is widely used into heat-to-power sector. Heat-to-power and power-to-heat sectors are among the most relevant options available to balance fluctuating renewable energy sources and hence power grid. This particular interaction between electricity and heat sectors will play an important role towards the cost-effective transition to a low carbon energy system with a high penetration of renewable generation.

Nomenclature

AB	Storage material
A,B	Reaction products
ALPOs	Aluminophosphates
CAES	Compressed air energy storage
Cp	Heat capacity (J/(kg K))
CHP	Combined heat and power
COP	Coefficient of Performance
CSP	Collectors and Concentrating Solar Plant
DHS	District heating systems
DSM	Demand-side management
Δh	Phase change enthalpy (°C)
ΔH	Standard reaction enthalpy (J/mol)
ΔS	Standard reaction entropy (J/(°C mol))
ΔT	Temperature difference (°C)
GHG	Greenhouse gases
HCTSR	Hybrid compression thermochemical refrigeration system
HPs	Heat pumps
HtP	Heat to power
LTES	Latent thermal energy storage
m	Mass (kg)
MVC	Mechanical vapor compression
ORC	Organic Rankine cycle
PCM	Phase change materials
PCR	Phase change redox
PtH	Power-to-heat
PV	Photovoltaic
PV-CaL	Photovoltaic Calcium looping
Q_l	Latent energy stored (J)
Q_s	Sensible energy stored (J)
RES	Renewable energy sources
SAPOs	Silico-aluminophosphates

Nomenclature

STES	Sensible heat storage
T	Turbine
T_c	Charging temperature (°C)
T_d	Discharging temperature (°C)
TCTES	Thermochemical thermal energy storage
TES	Thermal energy storage
TESs	Thermal energy storage systems
VRE	Variable renewable electricity

Chapter 4

Solar technologies to support the EFB
Case study: hybrid BIPV

1. Introduction

The increase of energy efficiency within the building sector is a major focus of several policy and research actions at international level [686]. Within this area of research, one of the most relevant steps towards improving energy performance of buildings is the construction of net-zero energy buildings or high-efficiency buildings in the massive use of renewable energies to achieve a higher level of self-sufficiency. Advancing energy efficiency in buildings involves not only the development of new buildings but also retrofitting solutions in the existing building stock.

Building retrofit offers the great opportunity to reduce energy consumption, increase the use of renewable energy sources and improve energy efficiency.

A number of measures can be taken to enhance building's performance such as employing advanced building materials, adding insulation layers and improving the envelope structure [687].External thermal insulation and ventilated façades are the most widely adopted retrofitting solutions [688–690]. External thermal insulation for the retrofit of existing building envelopes can be obtained in two ways [691]: External

Thermal Insulation Composite System (ETICS) and Ventilated Façades.

Ventilated Façades integrated with Photovoltaic (PV) cells have become a popular way of the Building Integrated Photovoltaic (BIPV) system to improve both the thermal-physical performances of the existing built environment [692,693] and PV conversion efficiency. BIPV applications are usually suggested as the core solution for achieving the NZEB target. Roof-mounted applications of BIPV are currently holding the dominant position in all BIPV markets with a share > 80% [694].

BIPV modules, apart from generating electricity, constitute an integral part of the building, replacing conventional building components such as tiles or ventilated façade elements [695].

PV panels shading the building reduce heat gain from solar radiation and the air cavity has a beneficial effect on the PV temperature, in fact, facilitating the buoyancy force resulted from the solar radiation, the ambient air is induced into the channel from the bottom and discharged at the top.

The chimney effect that is established in the cavity between the panel and the building wall allows not only to improve the thermophysical performance of the building but also to increase the efficiency of the photovoltaic system. In fact, it is known that high temperature of the PV module has negative influence on its efficiency since it causes a reduction in the power produced by the panel with the same solar radiation [696].

BIPVs allow significant direct contribution to building heating and if used with absorption or adsorption plant can provide also summer cooling. Their geometry affects not only the thermal performances but also the degree of available natural daylighting. The temperature distribution and the electrical performance are straightly correlated. Calculation of the thermal performance is a critical aspect since both the mixture of forced and natural convection and the effect of the external wind is difficult to model. Many studies in this area have been carried out both experimentally and numerically. In literature several papers explore different approaches to the problem of the thermal performance estimation.

CFD approach is utilized as the main method to achieve accurate and detailed results for modeling the temperature and airflow distributions. Several approaches simplify the real geometry of the ventilated façades considering the PV cells and the external wall of the building as two parallel plates with a surface heated from outside. Many aspects of ventilated façades have been studied theoretically and experimentally such as the effects of the air gap behind PV wall on the buoyancy and induced ventilation rate [697], effects of the PV panel orientation and wind direction on the overall performance of the BIPV [698]. In the following are reported some case studies.

Agathokleous et al. [699] carried out CFD simulations to investigate the thermal performance of a naturally ventilated BIPV system. It was shown how different design configurations affect temperature profiles and flow conditions. Correlations for heat transfer coefficients were found. In this work, moreover, energetic and exegetics analysis were performed. CFD simulations were carried out mainly to predict the temperature of PV panels and the energy production for one year.

Chi-Ming et al [700] integrated a PV system, a double-skin structure and a thermal flow mechanism to design BIPV curtain walls that can autogenously control an environment using buoyant force. Full-scale experiments and computational fluid dynamics (CFD) simulations were conducted to investigate the flow pattern characteristics for the channel airflow and the thermal performance of the ventilated BIPV under various heating conditions, wall thicknesses and types of openings. Results showed that channel flows for different channel widths under the same wall heating exhibited different flow patterns and therefore variations in thermal performance.

Gan et al.[701] performed CFD simulations to investigate the effects of the air gap on the thermal performance of BIPV in different mounting geometries. Results show that cavity cooling cannot be improved after a certain threshold for the air cavity size. It was found that there existed an optimum cavity width for maximizing the buoyancy-induced flow rate. Moreover, stepped multi-panels were recommended as

the best arrangement to achieve better cavity air circulations in comparison with a long single panel.

Getu et al. [702] presented a CFD study of a Building Integrated Photovoltaic Thermal (BIPV/T) system to predict the temperature profiles of the PV's back surface, the air inside the channel and the building envelope insulation. Obtained temperature profiles were used to establish relationships between the air flow velocity and the average/local convective heat transfer coefficients. A two-dimensional model was tested using both a k-w and k-ε turbulent model. Results showed that k-w model yielded the best agreement with the PV temperature obtained experimentally while the k-ε one with the air channel and insulation temperatures.

Kant et al. [703] performed CFD simulations to investigate heat and mass transfer of a BIPV system with nano-enhanced phase change material (PCM). PCM is integrated to the back of the BIPV system. Results showed that PCM reduced the operating temperature of the PV panel allowing an increase of its electrical conversion efficiency. The effect of several PCMs on heat transfer and melting of PCM has been investigated.

Lau et al. [704] performed a CFD numerical study to investigate the thermal behaviour and airflow characteristics of a BIPV façade. A three-dimensional model was implemented with the shear stress transport (SST) κ-omega turbulent interface. The effects of geometric configurations on the BIPV cell temperature in steady state are evaluated including the sizes of the bottom and top openings and the depth of the back air cavity (or so-called cavity depth). Results show that when the sizes of the inlet and outlet openings are the same, the effects on the decrease of cell temperature are limited, In contrast, enlarging the bottom (inlet) opening, the impact of ventilation in the cavity behind is more significant and the cell temperature decreases. It is also shown the effect of the cavity depth on BIPV cell temperature. Results show, moreover, how the wind velocity and the attack angle affect the cell temperature.

Mohammad et al. [705] developed a 3D CFD model CFD Simulations for evaluation of forced convective heat transfer coefficient on BIPV/T integrated on the

windward roof surface of a low-rise building. The investigation was mainly focused on the velocity field by comparison of the forced convective heat transfer using the Nusselt (Nu) number normalized by Reynolds (Re) number and studying various roof inclinations, wind angles. A similar study it can be found in [706].

Roeleveld et al. [707] performed CFD simulations to investigate the air flow conditions and thermal behaviour of a BIPV/T system. In particular, natural convection was investigated. Usually BIPV/T systems are integrated with fans allowing a forced convection within the air channel. In this work both of scenarios were analysed and compared in terms of removed heat and required energy.

Sandberg et al. [708] performed CFD simulations to derive temperature and velocity profiles in air gaps behind solar cells located on vertical facades. Both the geometry of the air gap and the location of the solar cell module are varied. Analytically expressions for the mass flow rate, velocity, temperature rise and location of neutral height (location where the pressure in the air gap is equal to the ambient pressure) were also obtained.

Zhang et al. [709] developed a 3D CFD microclimatic model to provide accurate predictions in complex arrangements of BIPVs under different climate conditions. The model was used to predict BIPV thermal performance including also the effects of relative PV position to the roof, solar radiation and wind speed.

The major limit of non-programmable renewable energy sources is the discontinuity in the production of electricity. Energy storage is paramount to allow renewable energies to be more competitive within the current market [710,711].

The increasing use of renewable energy systems might be easier and more effective under the adoption of energy storage systems to mitigate the mismatch between the power generation and the building's demand [457,712]. Batteries are the most used technology to store energy and their integration with a PV panel as a whole system is a flexible and already viable solution [713]. Battery Energy Storage (BES) allows the transition to a sustainable and secure energy system based on renewable

sources, with reduced greenhouse gas emissions. Batteries can store energy from on-peak renewable energy and release it when it is needed, offer grid support services like voltage control and frequency regulation [714]. The whole system PV- batteries lead to each PV module can be treated as a self-rechargeable unit.

However, in order to avoid the degradation of the efficiency of the entire system each battery must be at the proper working temperature to avoid damages and accelerated degradation [715]. Temperature, as a critical factor, not only impacts on the performance of batteries but also limits their applications.

Temperature variations can lead to the change of electrochemical reaction rate in a battery according to Arrhenius equation. Usually, a low temperature affects the property of electrolyte. With the decrease of temperature, the viscosity of the electrolyte increases while the ionic conductivity reduces. The effects at high temperatures are much more complex than those at low temperatures.

At high temperature thermal runaway often occurs triggering the exothermic reactions in the operating batteries [716]. Thermal runaway, which may lead to the explosion of the battery. Due to electrochemical reactions taking place during charge or discharge of batteries lead internal heat generation occurs. Thermal management of ion batteries is a crucial part of the design process to guarantee that temperatures remain within a narrow optimal range and to ensure good battery performance, safety and higher capacity. The battery systems, proposed over the years, can be classified into active and passive systems [717–719]. In the active thermal management, the cooling/heating rate is controlled actively by power-consuming equipment (fans, pumps, compressors) [720].In the passive systems, there is no power-consuming equipment, and they require no control system to vary the cooling/heating rate such as natural air convection, heat pipes and PCMs [719]. Many studies regarding thermal degradation and thermal management of ion batteries are available in literature. Some examples are reported in the following.

Ankur et al. [721] proposed the design of an optimized thermal management system for cooling system proposed for a kW scale Li-ion battery stack. An

immersion-based liquid cooling system has been designed to ensure the maximum heat dissipation. After using the immersion-based cooling technique the battery stack having a peak temperature of 49.76 ◦C at 2C discharging rate is reduced by 44.87% to 27.43 ◦C. It has been found that the liquid cooling is more efficient than air cooling. The peak temperature of the battery stack got reduced by 30.62% using air cooling and by 38.40% using the liquid cooling method.

Akbarzadeh et al. [722] proposed an innovative liquid cooling plate embedded with PCM for thermal management of Li-ion batteries to be used in electric vehicles. In their work several active and passive cooling strategies were analysed. CFD simulations were carried out to investigate the thermal behaviour of the system under real driving cycles. In comparison to a system without PCM, results showed a reduction in the energy consumption of the heat pump required for the circulation of the coolant up to 30%.

Chen et al. [723] performed experimental analysis on the thermal management of Li-ion batteries tested under different conditions including natural cooling, PCM cooling and extreme conditions. Results showed that PCM allowed the best thermal management during the charging and discharging processes. The highest temperature reached with PCM was about 12°C below than that one reached with natural convection.

Gao et al. [724] carried out molecular dynamics (MD) simulations to investigate the effect of temperature, salt concentration and degree of thermal degradation on electrolyte ionic diffusivity of Li-ion batteries. Ionic diffusivity affects both its power density and its usable energy density. The study was performed aiming both battery design optimization and better battery management.

Gumussu et al.[725] developed a CFD model to investigate the thermal behaviour of Li-ion batteries under natural convection. It is a predictive model developed to solve completely flow field around the battery as well as conduction inside it. Effects of different operational and environmental conditions on the thermal behaviour were widely investigated and discussed.

Huang et al. [726] investigated the thermal management of a Li-ion pack using as cooling strategy the use of a novel composite PCM (CPCM) based on paraffin as change material and expanded graphite as thermal conductivity enhancer. Temperature profiles of the battery were evaluated by discharging the battery module at different rates.

Jilte et al.[727] performed CFD simulations to investigate the cooling performance of a Li-ion pack based where heat is generated by 9 cells. Simulations were performed at constant current discharge of 6, 94 C (galvanostatic discharge) and results showed that at high battery discharging condition there was a significant increase in battery temperature.

Li et al. [728] developed a two-dimensional CFD model to perform detailed simulations of the thermal management of a battery pack containing 8 Li-ion cylindrical cells. Cooling was simulated within a wind tunnel where air flow velocity was fixed at 30 m/s. The model was developed to predict the maximum cell T in a battery module under different operational conditions. The effects of the geometry cavity on the maximum temperature reached was also simulated and discussed.

Liu et al. [729] investigated how thermal gradients can reduce the overall performance of a large-scale Li-ion battery pack. As temperature uniformly increases, the increased chemical kinetics and solid-state diffusion properties of the electrodes allows an increase in the accessible energy and power but, in the meanwhile, to an increase in the degradation rate.

1.1. E-Brick module

In October 2019 during Market Faire Rome, the most important European event regarding innovative technologies, CNR-ITAE presented the prototype of a hybrid active façade within the project “E-Brick” (Figure 40).

The prototype of 12 E-Bricks realized to carry out the experimental tests is shown in Figure 41.

Figure 40: E-Brick module shown at Market Faire Rome.

Figure 41: Modular E-Brick assembled for experimental tests.

E-Brick is an Italian project financed with the PON MISE Horizon2020 call funds. It is finalized to the development of building components for ventilated facades, photovoltaic and integrated electrical storage and made up of insulating materials. E-

Brick module is a building component to be installed in external vertical walls in order to create curtain walls for the energy requalification of buildings. In detail, the module comprises a polycrystalline silicon photovoltaic module (70 cm × 70 cm) inserted in a double-glazed sandwich, a 23 Ah lithium titanate battery integrated in the cavity and an insulating panel in rock wool for building insulation. Two casings contain the control electronics and the storage battery.

E-Brick produces electricity from solar sources, stores it thanks to an integrated battery and uses it when necessary, promoting self-consumption and limiting the use of the electricity grid. The system is plug and play both from a structural and plant engineering point of view. Its modular application on the wall facilitates the construction of ventilated walls, improving the thermal performance and comfort of buildings. The distributed control and monitoring system developed uniquely identifies the behaviour of the individual components, identifying possible malfunctions and facilitating maintenance. The main fields of application are residential and small industry.

2. Experimental tests

Experimental tests have been performed in CNR-ITAE in Messina (Italy) to evaluate the producibility of two distinct photovoltaic cell technologies that can be integrated into the hybrid module E-Brick (PV/insulation /electric equipment's) developed to cover the perimeter walls of a building.

Once connected the panels to the terminals of the low impedance circuit of an electronic direct current load, they were performed the following characterization tests:

- Potentiostatic tests;
- Maximum Power Point Tracking (MPPT) tests.

To evaluate the producibility of the tested PV modules, tests were carried out

under the following conditions:

- different solar radiation values;
- different shading values;
- different angles of incidence.

The selected modules allowed to produce electric energy also if vertically installed. In particular, the maximum recorded power values reached about 40% of the expected peak power value in case of optimal inclination. In MPPT conditions the recorded power delivered by the panel was proportional to the irradiation resisted on the panels' plane. Experimental tests were also performed to test the producibility of DSSC (Dye-Sensitized Solar Cell) technology. Tests carried out with DSSCs showed lower conversion efficiency values than Si-Poly technology modules. Experimental were carried out for different goals: characterization of PV panels to be used in the E-brick module, characterization of PV panels in hybrid configuration with Li-ion battery, monitoring of the hybrid BIPV.

2.1 Selected PV modules

Two modules, one in polycrystalline silicon with a metal frame and the other one in polycrystalline silicon with a double staggered glass, were selected to carry out the experimental tests. During the tests they were arranged vertically as shown in Figure 42. Table 12 reports the characteristics of the selected Si-Poly modules available in their datasheet. In the following are given the main definitions of the properties defined in Table 12.

Maximum power point (MPP): is the sweet spot of the solar panel power output where the product of the volts and amps results in the highest wattage.

Temperature coefficient of the maximum output power (X_P): is the power output reduction with increasing cell temperature.

Short-circuit current (I_{sc}):current through the solar cell when the voltage across

the solar cell is zero (i.e., when the solar cell is short circuited). It is due to the generation and collection of light-generated carriers. For an ideal PV cell with moderate resistive loss, ISC and the light-generated current are identical.

Maximum power current (Imp): current when the power output is the greatest. It is the actual amperage when the solar cell is connected to the MPPT solar equipment under standard test conditions.

Temperature coefficient of the short-circuit current (X_{sc}):is the reduction of the short-circuit current with increasing cell temperature.

Open circuit voltage (OCV) :maximum voltage available from a solar cell, and this occurs at zero current. The open-circuit voltage corresponds to the amount of forward bias on the solar cell due to the bias of the solar cell junction with the light generated current.

Temperature coefficient of the open circuit voltage (X_{ocv}): is the decrease of the short-circuit current with increasing cell temperature.

Maximum power voltage (Vmp): voltage when the power output is the greatest. It is the actual amperage when the solar cell is connected to the MPPT solar equipment under standard test conditions.

Nominal operating cell temperature (T_{NOCT}): temperature reached by open circuited cells in a module under the conditions of irradiance on cell surface 800 W/m^2, air Temperature 20°C, wind velocity1 m/s.

Figure 42: Installed PV panels to carry out producibility measurements in a vertical plane.

Table 12: Datasheet of the tested PV modules.

	PV Panel 1	PV Panel 2
Technology	Si-poly	Si-poly
Cells number	60	60
Dimensions (mm×mm)	1673×1003	1960×1020
Maximum power Pmax(W)	230	240
Temperature coefficient of Pmax (%/K)	-0.47	-0.47
Short circuit current I_{sc} (A)	8.28	8.21
Max. power current Imp (A)	7.61	7.69
Temperature coefficient of I_{sc} (mA/K)	2.39	2.47
Open circuit voltage OCV (V)	37.58	37.99
Max. power voltage (V)	30.61	31.12
Temperature coefficient of OCV (mV/K)	-161	-163
T_{NOCT} (°C)	44±2	44±2
Efficiency %	14	14

The DSSC panel used for the experimental tests is shown in Figure 43.

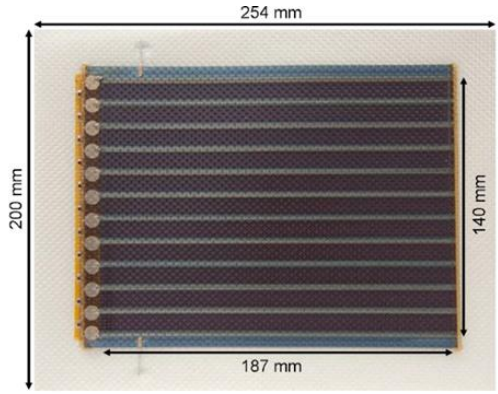

Figure 43: DSSC panel tested.

The internal dimensions are referred to the net area occupied by the photovoltaic

cells while the external ones include also the plastic support material for connection to the external process.

It is a panel of G24 Innovation (G24i), the world's first commercial manufacturer of DSSC technology for mass consumer use. In future their use in E-brick module is not excluded. These cells have several advantages: low-light performance, higher temperature performance; low energy manufacturing process, ecologically friendly solar. These solar cells panels are made up of photovoltaic cells, capable of producing electricity using a principle similar to that of chlorophyll photosynthesis [730].

2.2 Measurement Equipment

To carry out all characterization measurements, the panels were connected to the terminals of the low impedance circuit of the electronic direct current load Chroma 63640-80-80. This electronic load test equipment, showed in Figure 44, contains 5 modules each of them having a power of 400 W.

Figure 44: Chroma 63640-80-80 Load Module 80A/80V/400W used for tests.

To obtain the I-V characteristic of the PV panels the DC load was set in constant voltage mode. It means that the load behaves as a variable resistance and to maintain the value of voltage constant the current is regulated.

The current load behaviors like a variable resistance. Starting from the pairs of values V and I for each load condition was possible to construct I-V curves.

At each sweep the load checks the voltage at the output of the solar cell by

measuring the current whose waveform is simultaneously digitized and displayed through the graphic interface of the software used for the characterization test. The Maximum Power Point Tracking function was used for solar panel tests. In particular, once connected the solar panel to the 63600 loads, the loads tracked the maximum power point of the solar panels using a high-speed built-in algorithm. During the tests, the modules worked in synchronized parallel channels mode in order to subject the two panels to the same lighting conditions instant by instant.

Test were performed through quick sweeps in order to avoid the overheating of the PV cells. It is known that I-V characteristic is affected by cells temperature. In particular, as the cells temperature increases the short circuit current increases while the open circuit voltage decreases. During the tests, the air temperature in the vicinity of the panels and the temperature of the rear panel of each PV module were monitored.

In order to measure the solar irradiance (W/m^2) on the plane of the PV modules it was used the photovoltaic cell shown in Figure 45.

Figure 45: Digital Photovoltaic Pyranometer lite meter used for the experimental tests.

The solar radiation is captured by a monocrystalline silicon cell laminated on a performant glass. The photovoltaic cell was powered by two analogic outputs: 0-4 V (amplified output) and 0-80 mV (no-amplified output). The electricity generated is proportional to the solar radiation. The solarimeter used has an input range of 0-1000

W/m^2. The total solar radiation was measured by a pyranometer of a weather station placed at a short distance from the panels but raised to avoid the shading of obstacles on the plane of the test panels. The pyranometer is based on a thermopile sensor and on the Seebeck effect, the temperature difference between the center of the thermopile (hot junction) and the body of the pyranometer (cold junction), is converted into a potential difference measured by a multimeter connected to the pyranometer. By means of the calibration factor of the pyranometer it was possible to determine the total solar irradiation.

2.3 Potentiostatic characterization tests

Cyclical tests were carried out and at the end of each iterative test the maximum deliverable power was evaluated. As shown in Figure 46, step sweeps were conducted at regular time interval. In detail, tests were performed with step sweeps of 0.5 V every 2 seconds (2 Hz sampling).

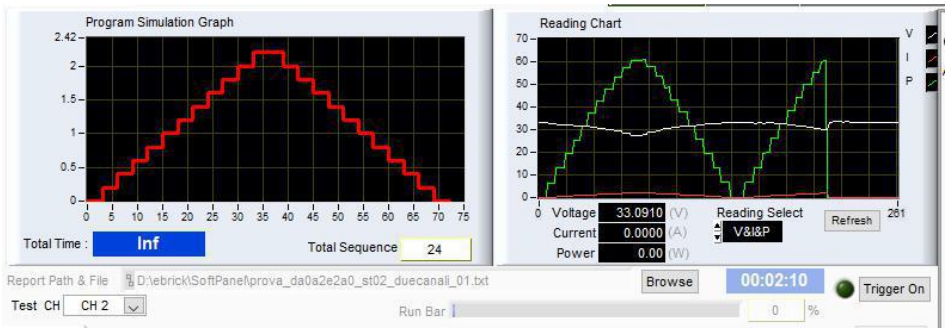

Figure 46: Graphic interface of the software used for the characterization tests.

The voltage was decreased from 34V until 0V. For both panels, the maximum voltage (34V) is less than their respective OCV, 37, 58 V for the first panel and 37, 99 V for the second one. The value of 34V, nevertheless, was found to be sufficient to measure current. Each panel generated current until the value of voltage of the electronic load was equal to the OCV of the panel itself.

The current was sampled in the last moments before the next step, in this way the signal was less affected by interference from capacitive current.

It was chosen the potentiostatic control mode since it avoids limiting the current in a no homogeneous way as the natural daylighting changes. Since tests were performed outdoor tests, performances were prevented to be affected by passing clouds. Another advantage is that potentiostatic tests make the control of the tests independent both from the photovoltaic efficiency and from the number of cells of every PV panel.

These experimental tests were conducted in the month of July since, for vertically arranged panels facing south, is the month with the lower electricity production. The reason is the different solar elevation over the course of the year.

Figure 47 shows a comparison between the solar elevation in the month of July (21st) and the solar elevation in the month of October (21st). It can be seen that in July the solar irradiation is perpendicular to the modules for a short time respect the month of October.

Data:	21/07/2017 | GMT1	
coordinate:	38.1543274, 15.516665	
località:	Via Cariddi, 98126 Messina ME, Italia	
ora	Elevazione	Azimut
04:51:32	-0.833°	62.9°
5:00:00	0.65°	64.21°
6:00:00	11.63°	73.05°
7:00:00	23.12°	81.54°
8:00:00	34.87°	90.39°
9:00:00	46.59°	100.68°
10:00:00	57.82°	114.61°
11:00:00	67.43°	137.37°
12:00:00	72.2°	176.62°
13:00:00	68.54°	217.98°
14:00:00	59.36°	242.74°
15:00:00	48.26°	257.53°
16:00:00	36.56°	268.16°
17:00:00	24.79°	277.13°
18:00:00	13.23°	285.62°
19:00:00	2.15°	294.36°
19:16:49	-0.833°	296.94°

Data:	21/10/2017 | GMT1	
coordinate:	38.1543274, 15.516665	
località:	Via Cariddi, 98126 Messina ME, Italia	
ora	Elevazione	Azimut
06:12:35	-0.833°	103.07°
7:00:00	8.07°	110.59°
8:00:00	18.68°	121.12°
9:00:00	28.05°	133.53°
10:00:00	35.47°	148.54°
11:00:00	40.01°	166.3°
12:00:00	40.83°	185.66°
13:00:00	37.74°	204.31°
14:00:00	31.39°	220.49°
15:00:00	22.71°	233.89°
16:00:00	12.54°	245.08°
17:00:00	1.45°	254.87°
17:11:59	-0.833°	256.72°

Figure 47: Comparison of solar path and solar elevation in 21st of July (left) and in 21st of October (right).

In the following are reported the results referred to three test days characterized by different irradiation and rainfall conditions.

First day of testing

It was carried out an antemeridian test (9:30-13:00 AM) and for each iterative cycle (2 seconds) the maximum power was evaluated. Figure 48 shows the maximum power distribution for the whole test.

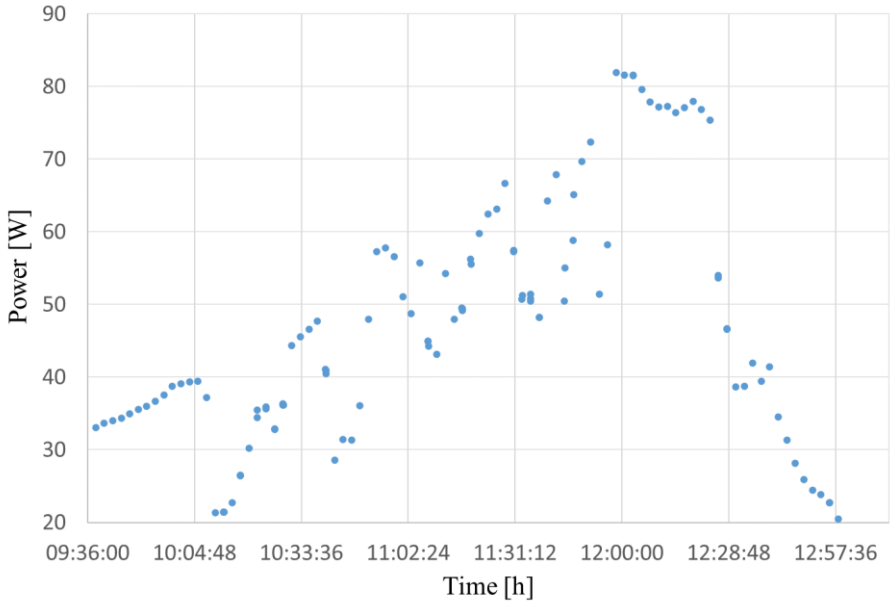

Figure 48: Power peaks measured in the first day of potentiostatic characterization testing.

The maximum peak power ~ 82 W was reached corresponding to an irradiance solar on the vertical plane (G_v) of 265 W/mq. It can be noticed an abrupt decrease in production due to a sudden precipitation. The peak powers were evaluated to a comparison with the results of the tests carried out in MPPT (Maximum power point tracking) control mode.

In correspondence of the maximum peak power, the characteristic I-V and P-V curves obtained for the whole potentiostatic test are shown in Figure 49. The trends are identical for both panels indicated with the subscripts 1 and 2. The maximum

power reached for the first panel was 82, 19 W while that one of the second panel was 80.92 W. As you can see the percentage difference is very low (~ 1.5%) so the two panels are almost identical from the point of view of the production.

Figure 50 shows the temperature profiles and solar irradiation measured on the plane of the tested panels for each iteration of the tests.

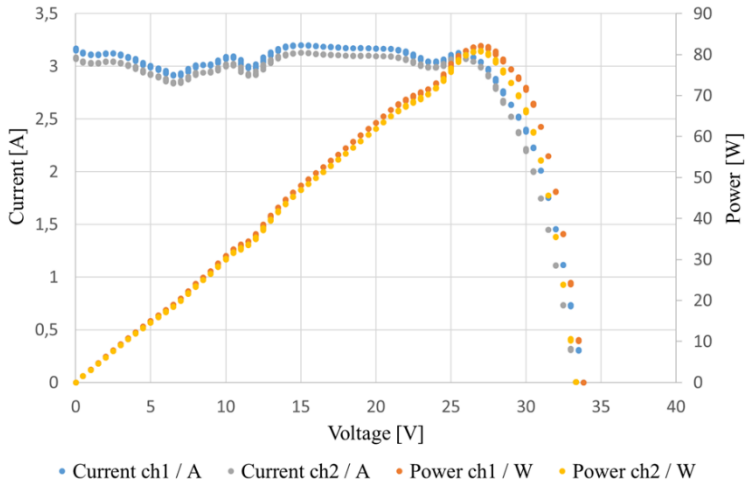

Figure 49: Characteristic curves corresponding to $G_v = 265\ {}^{W}/_{mq}$.

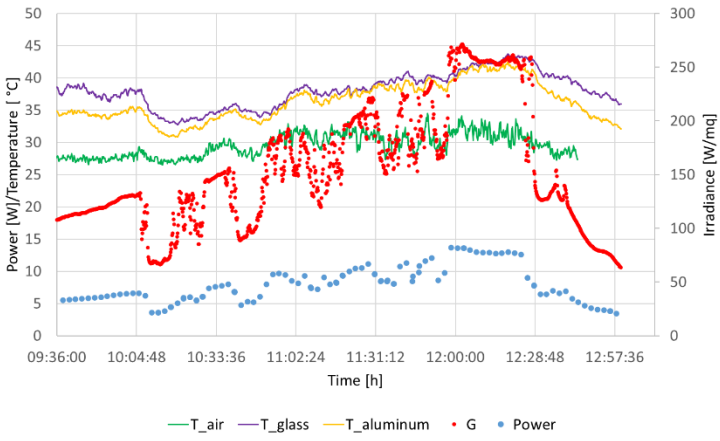

Figure 50: Temperature, power and irradiance measured in the first day of testing.

The data collected and related to the maximum power points were decimated on the basis of multiple samplings of each cycle.

Second day of testing

It was carried out an antemeridian test (10:00-14:00 AM) mainly to verify the performance of the panels registered in the first test day**.** In Figure 51 for both panels the power registered for each cycle it is reported while in Figure 52 the maximum peaks power distribution.

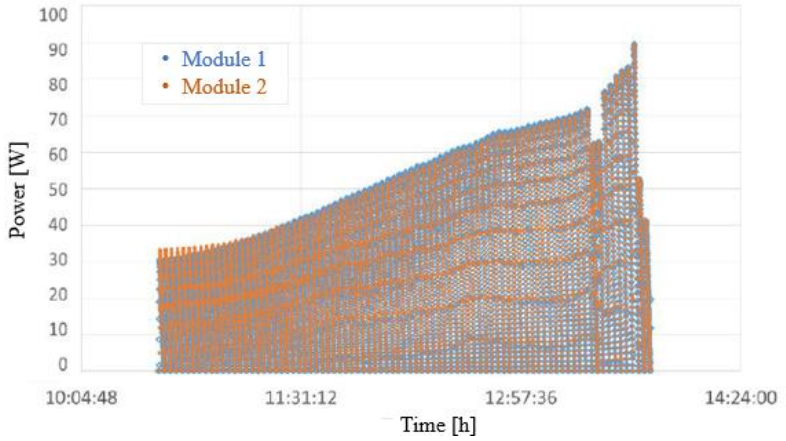

Figure 51: Power values measured during all cycles of the second day of testing.

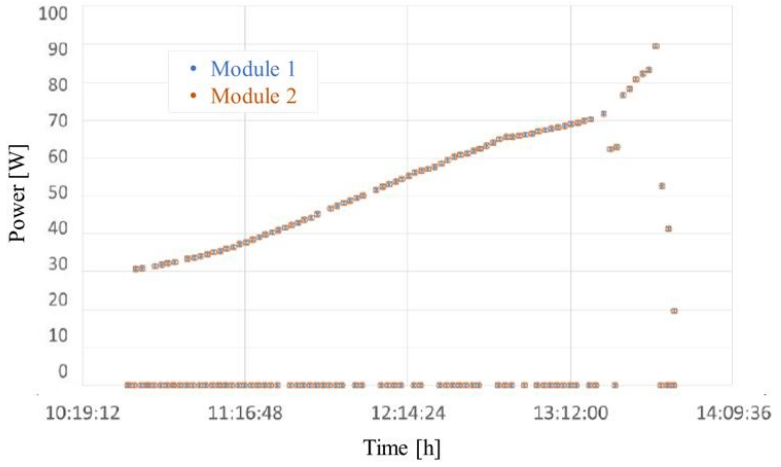

Figure 52: Power Peaks measured in the second day of testing.

The maximum peak power ~89 W was reached corresponding to an irradiance solar on the vertical plane (G_v) of 313 W/mq. The characteristic I-V and P-V curves corresponding to this value are shown in Figure 53. Temperature profiles and irradiance are shown in Figure 54. It can be noticed a negative peak both of irradiance and produced power. It was due to the overcast sky and to the presence of rain. Owing to these climate conditions tests were shorter than those ones of the first day.

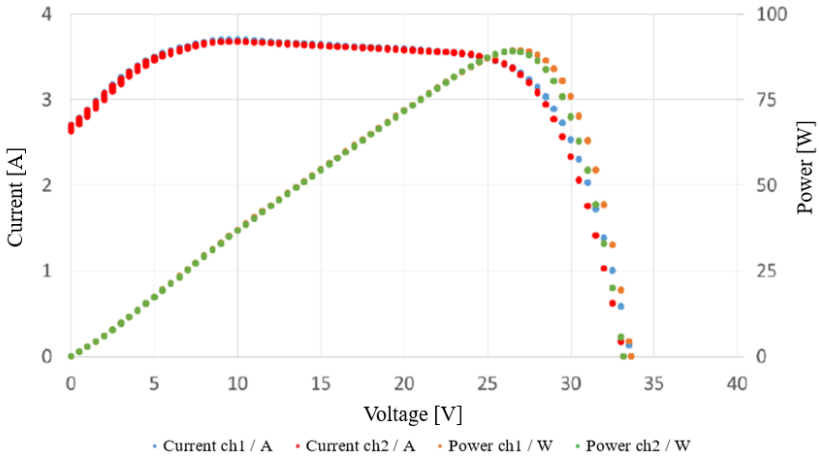

Figure 53: Characteristic curves corresponding to $G_v = 313\ {}^{W}/_{mq}$.

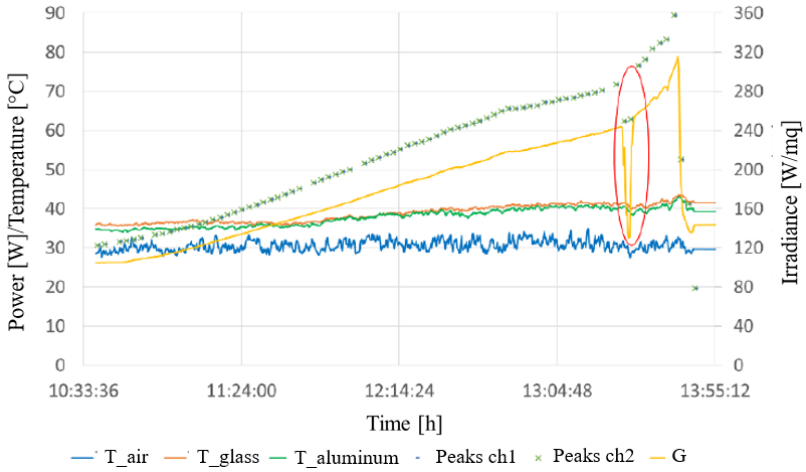

Figure 54: Temperature, power and irradiance measured in the second day of testing.

Third day of testing

Results of the third day of testing are shown from Figure 55 to Figure 57. The maximum peak power ~85 W was reached corresponding to an irradiance solar on the vertical plane (G_v) of 280 W/mq. In this day of testing the difference between the maximum and minimum irradiance was lower than that one of the first and second day of tests. The same trends can be observed in terms of PV production.

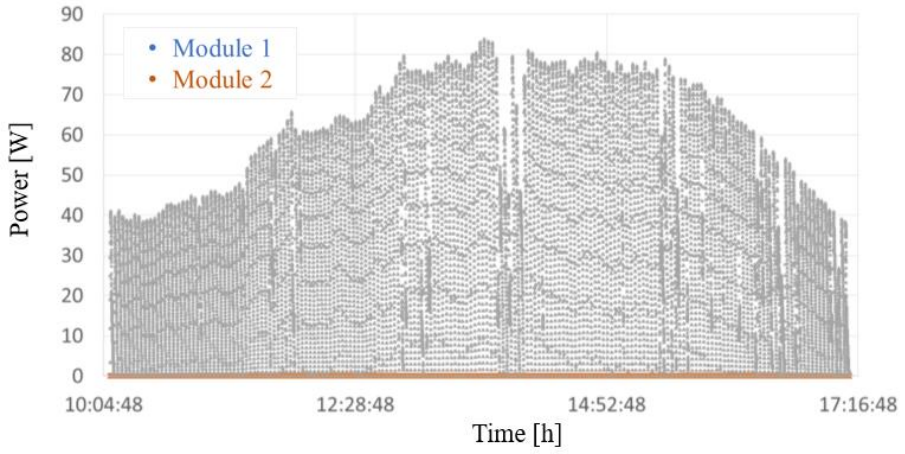

Figure 55: Power values measured during all cycles of the third day of testing.

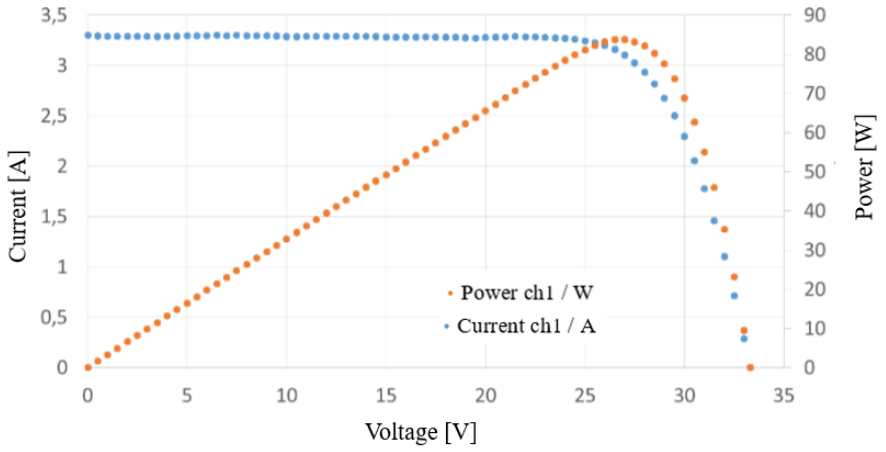

Figure 56: Characteristic curves of the first module corresponding to $G_v = 280\ {}^{W}/_{mq}$.

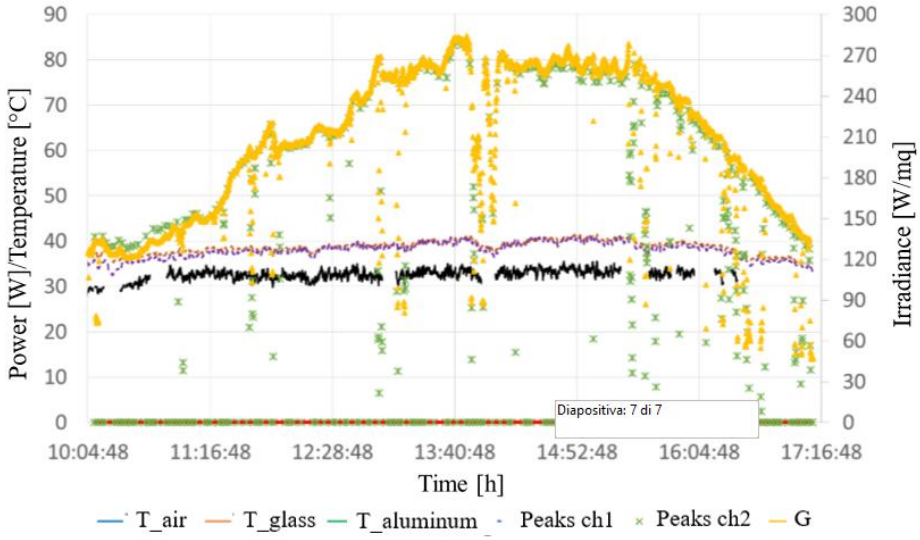

Figure 57: Temperature, power and irradiance measured in the third day of testing.

2.4 MPPT characterization tests

In the second phase of the experimental campaign panel were tested using the maximum power point tracking (MPPT) control. The dependency of the maximum power point (MPP) from the external conditions is strongly non-linear.

As already mentioned, dependency on the climate conditions of the V and I values is a particularly problematic feature of the PV cells. Open circuit voltage is inversely proportional to the temperature while the current intensity is directly proportional to the amount of incident light.

Once connected the PV panels to Chroma 63600-80-80 electronic load, the maximum power point was tracked using the high-speed built-in algorithm shown in Figure 58.

The algorithm executes continuous variations in the output voltage value of the photovoltaic panel. Comparing the power variation obtained with the voltage variation carried out by the algorithm establishes in which direction MPP can be found.

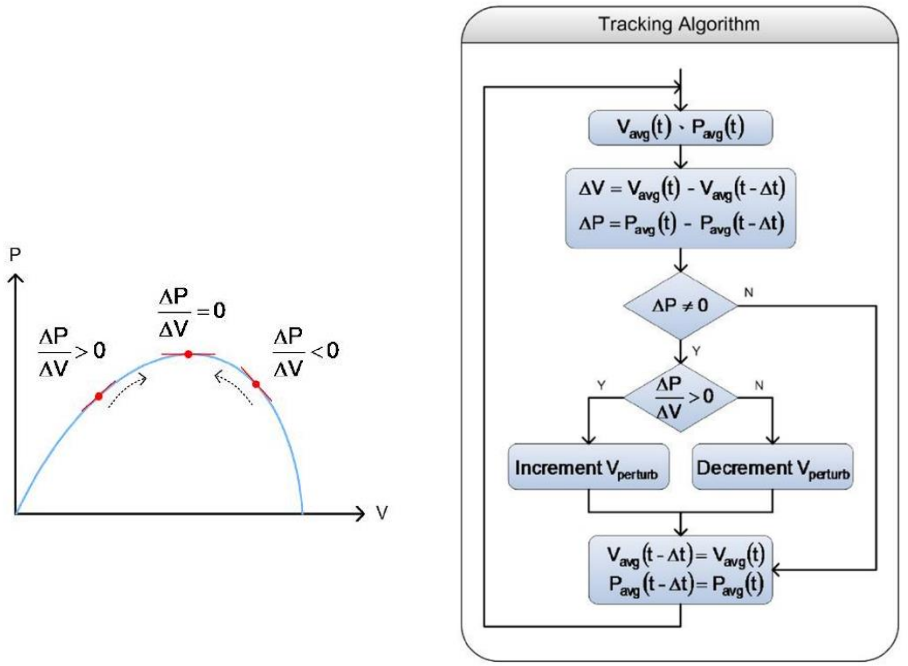

Figure 58: MPPT algorithm implemented in the Chroma 63640-80-80 Load Module used for the experimental tests.

Figure 59 shows, for example, the operating point (current and voltage) during a test with application of the MPPT algorithm in correspondence of a value of irradiance of 230 W/mq.

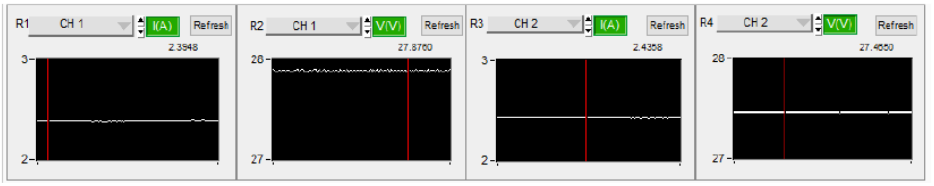

Figure 59: MPPT algorithm graphical interface.

In the following are reported the results referred to four test days characterized by different climate conditions The MMPT algorithm is strongly affected by weather conditions. Test were performed mainly to evaluate the daily PV production.

First day of MPPT testing

Figure 60 shows the trend of temperature profiles, irradiance and power produced in the first day of testing characterized by overcast sky and intermittent rain. The duration of the test was about 10 hours. In Table 13 shows the measures of solar radiation, air temperature and module temperature.

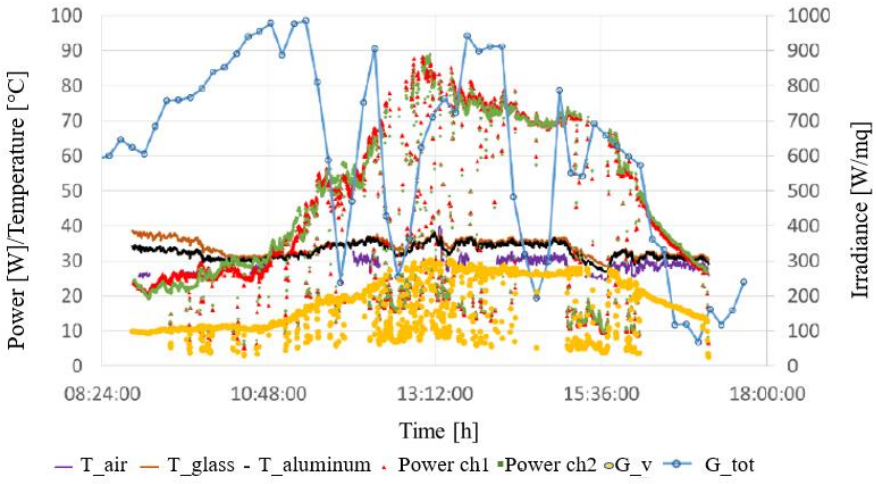

Figure 60: Temperature, power and irradiance measured in the first day of MPPT testing.

Table 13: Radiation and temperatures measured in the first day of MPPT testing.

Average value of global solar radiation (G_tot)	474 W/mq
Average value of vertical solar radiation (G_v)	163 W/mq
Average value of the generated power	41.5 W
Air temperature	Min: 24.5 °C
	Max: 40 °C
Backsheet temperature module 1	Min: 29.3 °C
	Max: 38.7 °C
Backsheet temperature module 2	Min: 27.7 °C
	Max: 38.1 °C

The peak power does not correspond to the maximum global solar radiation since the power production is affected by the inclination of the incident solar

radiation. In particular, in the morning when the global solar radiation is higher the produced power is significantly lower than that one recorded in the central part of the day (with the same global radiation). The characteristic I-V curve for the entire MPPT test is shown in Figure 61.

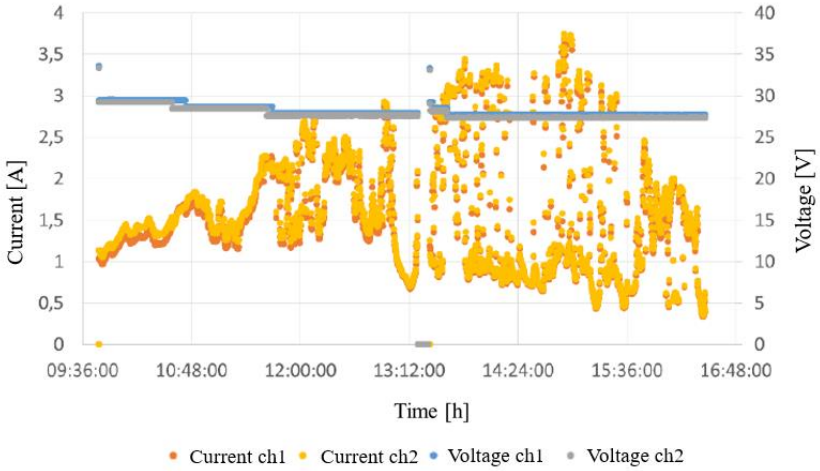

Figure 61: Characteristic I-V curves in the first day of MPPT testing.

Second day of MPPT testing

Figure 62 shows the results in the second day of testing characterized by overcast sky. Results are summarized in Table 14.

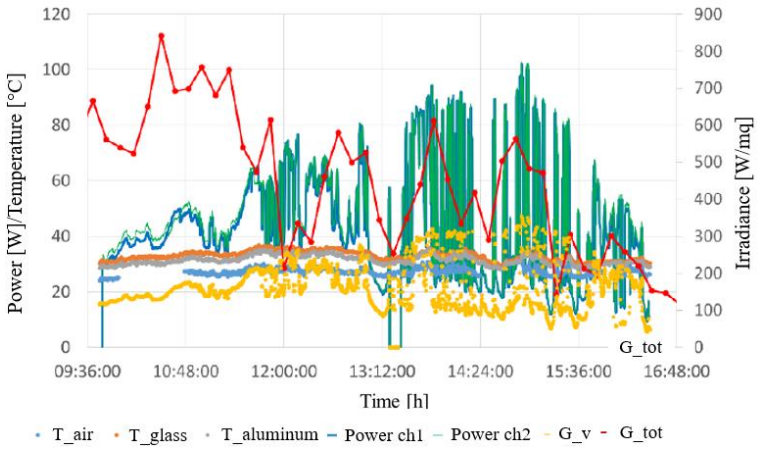

Figure 62: Temperature, power and irradiance measured in the second day of MPPT testing.

Table 14: Radiation and temperatures measured in the second day of MPPT testing.

Average value of global solar radiation (G_tot)	457 W/mq
Average value of vertical solar radiation (G_v)	160 W/mq
Average value of the generated power	42 W
Air temperature	Min: 24°C
	Max: 31 °C
Backsheet temperature module 1	Min: 29 °C
	Max: 36.9 °C
Backsheet temperature module 2	Min: 28 °C
	Max: 35.5 °C

Third day of MPPT testing

Figure 63 shows the trend of temperature profiles, irradiance and power produced in the third day of testing characterized by clear sky.

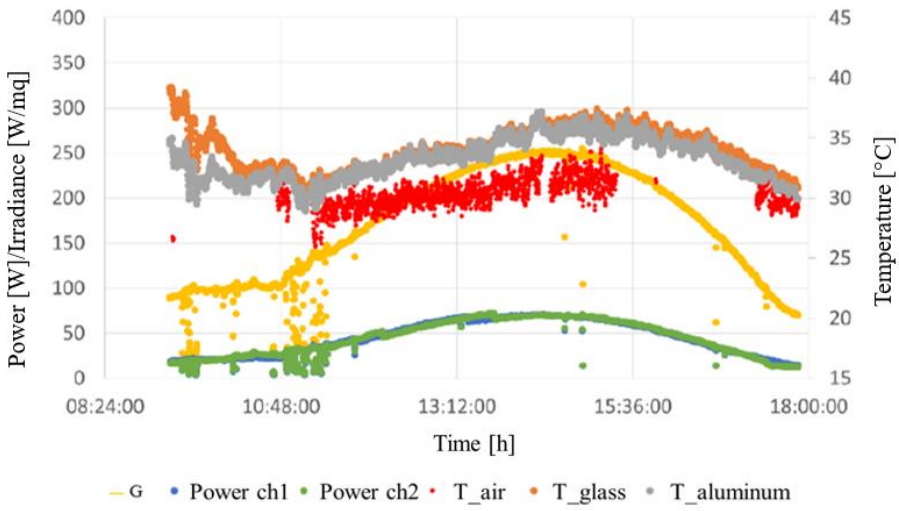

Figure 63: Temperature, power and irradiance measured in the third day of MPPT testing.

Compared to the previous two testing days it is possible to observe more uniform production values. Results are summarised in Table 15.

Table 15: Radiation and temperatures measured in the third day of MPPT testing.

Average value of global solar radiation (G_tot)	670 W/mq
Average value of vertical solar radiation (G_v)	171 W/mq
Average value of the generated power	44 W
Air temperature	Min: 25 °C
	Max: 34 °C
Backsheet temperature module 1	Min: 30.1 °C
	Max: 39.2 °C
Backsheet temperature module 2	Min: 28.9 °C
	Max: 37.2 °C

The characteristic I-V curve for the entire MPPT test is shown in Figure 64.

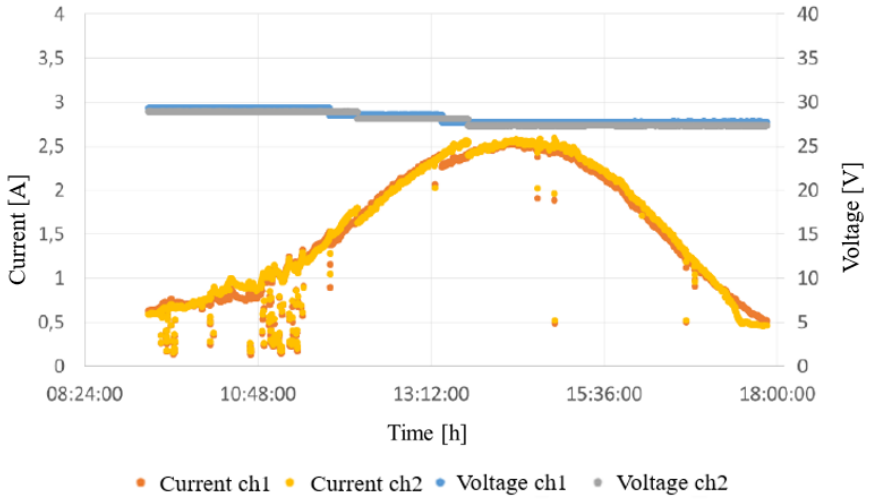

Figure 64: Characteristic I-V curves in the third day of MPPT testing.

Fourth day of MPPT testing

Figure 65 shows the trend of temperature profiles, irradiance and power produced in the fourth day of testing characterized by cloudy sky and no precipitation. The characteristic I-V curve for the entire MPPT test is shown in Figure 66.

Similarly to what it was observed in the previous three days of testing, the peak

power does not correspond to the maximum global solar radiation and in the morning the produced power is significantly lower than that one recorded in the central part of the day (with the same global radiation). Results are summarised in Table 16

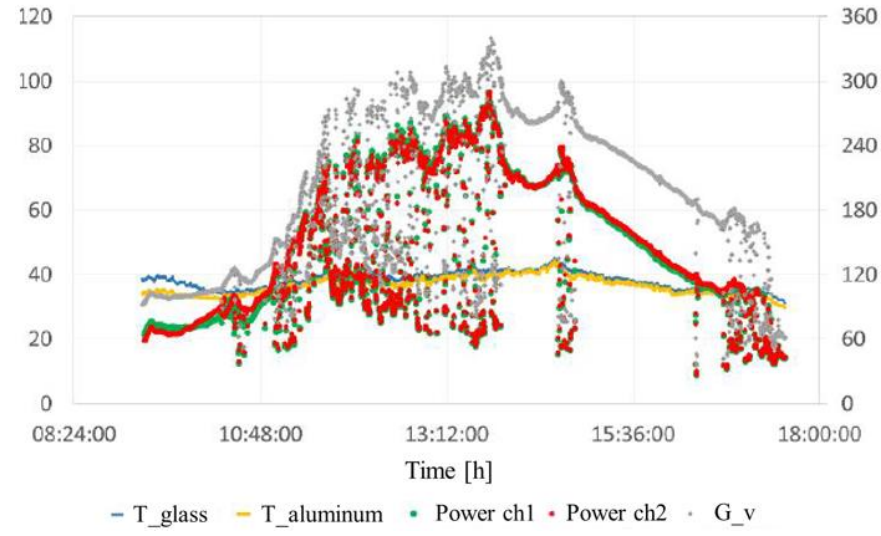

Figure 65: Temperature, power and irradiance measured in the fourth day of MPPT testing.

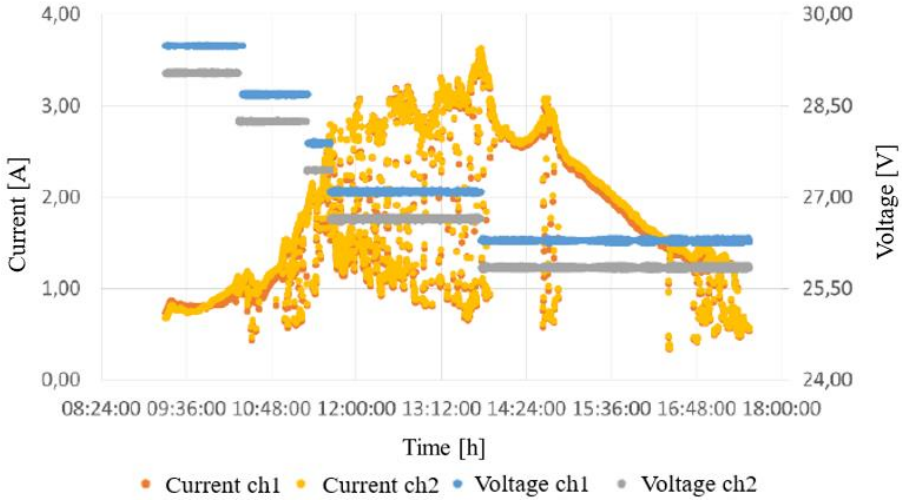

Figure 66: Characteristic I-V curves in the third day of MPPT testing.

Table 16: Radiation and temperatures measured in the fourth day of MPPT testing.

Average value of global solar radiation (G_tot)	607 W/mq
Average value of vertical solar radiation (G_v)	175 W/mq
Average value of the generated power	46 W
Air temperature	Min: 26.8 °C
	Max: 39.8 °C
Backsheet temperature module 1	Min: 31.3 °C
	Max: 45.2 °C
Backsheet temperature module 2	Min: 33.9 °C
	Max: 44.5 °C

2.5 Tests with solar simulator at controlled temperature

Aim of the tests was analyzing the performance of both modules under known, uniform and reproducible solar irradiation conditions. Test were performed at standard condition regarding the value of the solar radiation (G=1000 W/mq) and air mass (AM=1.5). To simulate the environmental condition, it was used a climatic chamber equipped with six temperature probes. 25 °C, 30 °C, 40 °C, 50 °C and 60 °C are the cell temperatures (Tc) chosen for the tests. Results of the first panel (Table 12) are reported from Figure 67 to Figure 71.

Results shown that a reduction of the maximum power delivered has as a consequence the reduction of the fill factor FF defined as follows:

$$FF = \frac{P_{max}}{I_{sc} \cdot OCV} \tag{4.1}$$

The maximum FF (73.15%) was reached for a value of the cell temperature of 25 °C while the minimum value (68, 37%) for a value of the cell temperature of 60 °C.

The reduction of the maximum available power is a consequence of the increase of the photocurrent and a decrease of the open-circuit voltage due to an increase of the cell temperature. The cell temperature is the main parameter affecting the conversion efficiency.

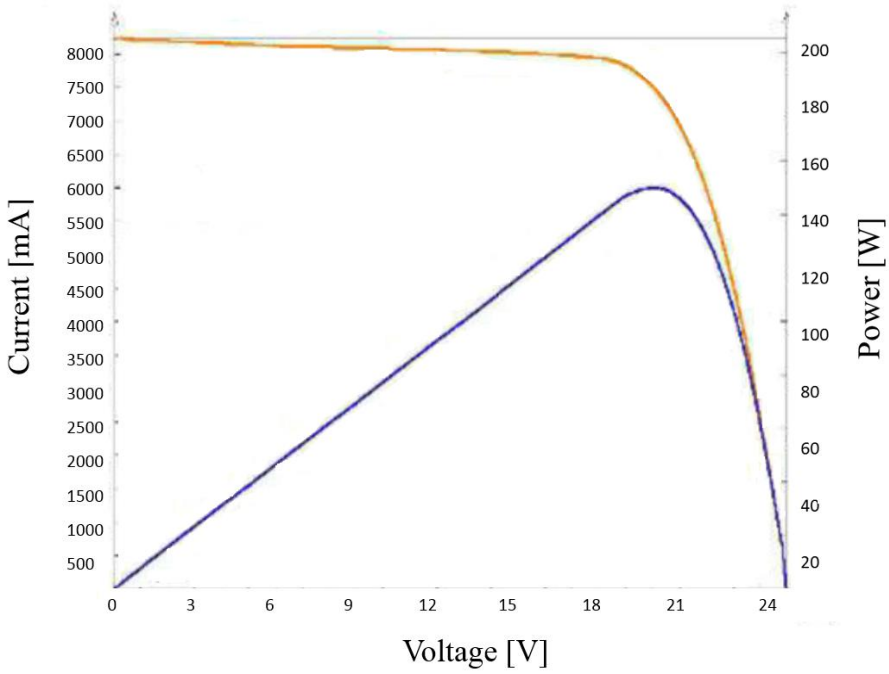

Open circuit voltage (V):24.960
Max. power voltage (V):19.863
Short circuit current (A):8.24
Max. power current (A):7.574
Max. power(W):152.033
Series resistance (Ω):0.268
Shunt resistance (Ω):57.622
Fill Factor (%):73.15
Cell efficiency (%):10.504
Module efficiency (%):9.081

Figure 67: Characteristic I/P-V curves at G=1000 W/mq and T_c=25°C.

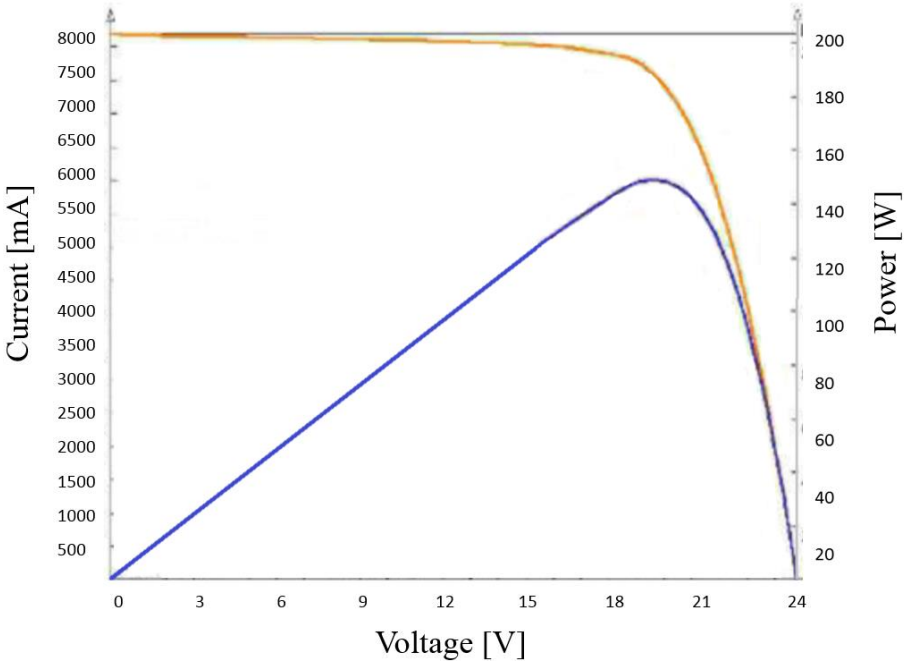

Open circuit voltage (V):24.799
Max. power voltage (V):19.629
Short circuit current (A):8.186
Max. power current (A):7.583
Max. power(W):148.844
Series resistance (Ω):0.375
Shunt resistance (Ω):115.359
Fill Factor (%):73.32
Cell efficiency (%):10.393
Module efficiency (%):8.984

Figure 68: Characteristic I/P-V curves at G=1000 W/mq and T_c =30°C.

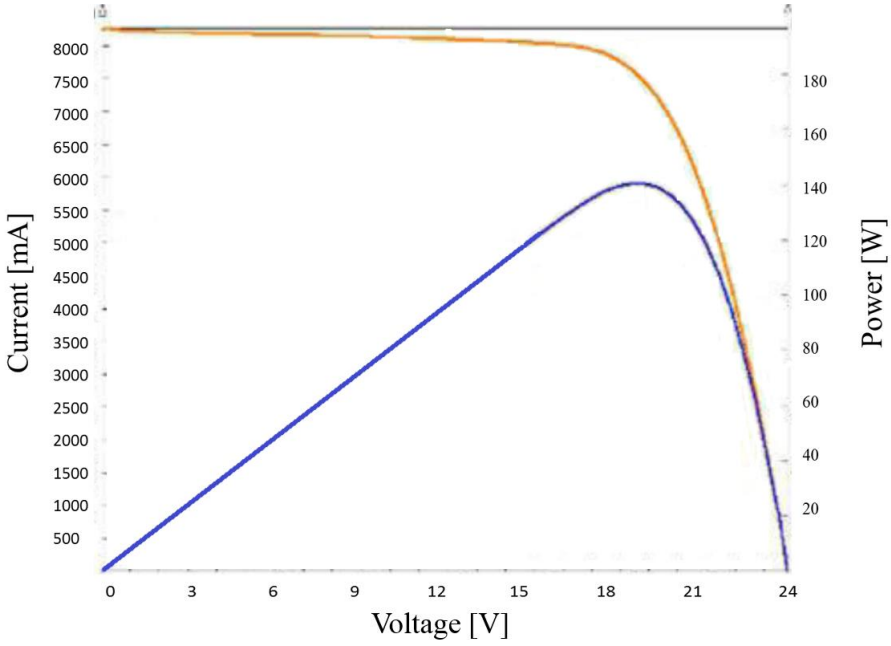

Open circuit voltage (V):23.395
Max. power voltage (V):18.603
Short circuit current (A):8.257
Max. power current (A):7.551
Max. power(W):140.469
Series resistance (Ω):0.338
Shunt resistance (Ω):53.373
Fill Factor (%):71.49
Cell efficiency (%):9.808
Module efficiency (%):8.479

Figure 69: Characteristic I/P-V curves at G=1000 W/mq and T_c =40°C.

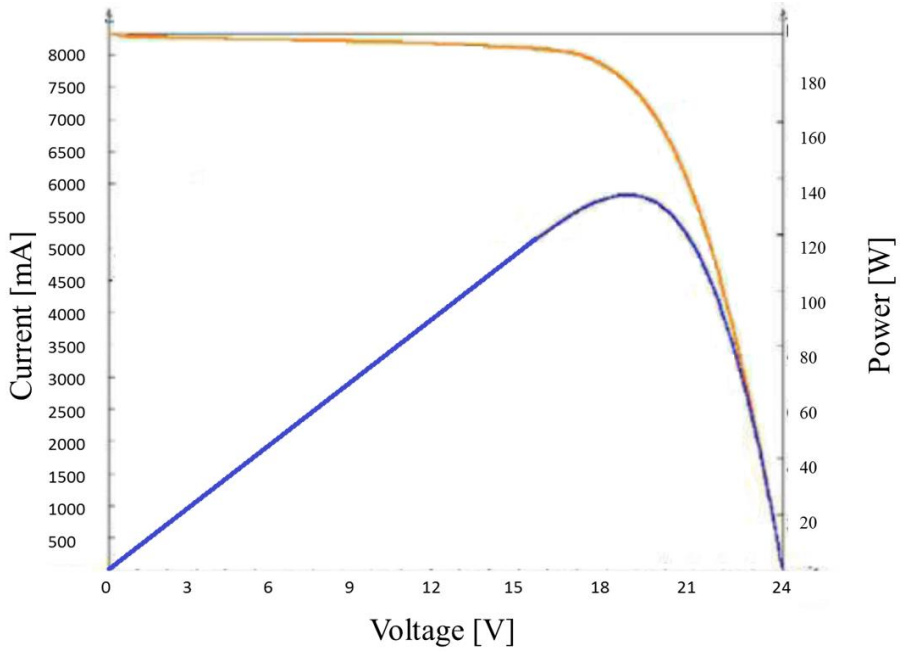

Open circuit voltage (V):23.010
Max. power voltage (V):17.756
Short circuit current (A):8.309
Max. power current (A):7.551
Max. power(W):134.084
Series resistance (Ω):0.381
Shunt resistance (Ω):55.721
Fill Factor (%):70.13
Cell efficiency (%):9.362
Module efficiency (%):8.094

Figure 70: Characteristic I/P-V curves at G=1000 W/mq and T_c =50°C.

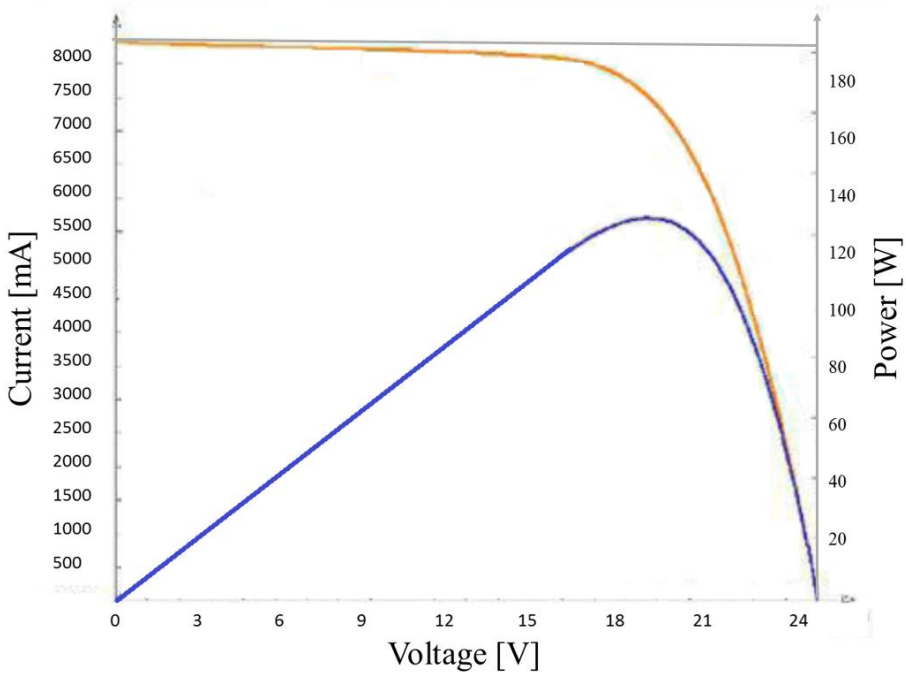

Open circuit voltage (V):22.007
Max. power voltage (V):16.740
Short circuit current (A):8.346
Max. power current (A):7.502
Max. power(W):125.575
Series resistance (Ω):0.364
Shunt resistance (Ω):48.868
Fill Factor (%):68.37
Cell efficiency (%):8.768
Module efficiency (%):7.580

Figure 71: Characteristic I/P-V curves at G=1000 W/mq and T_c =60°C.

As shown in Figure 72 there is a progressive reduction of the maximum power delivered as the cell temperature increases.

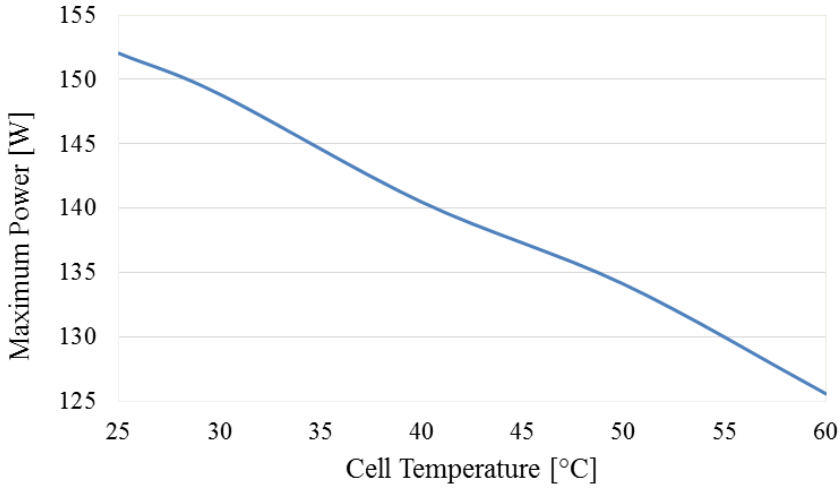

Figure 72: Power delivered as function of cell temperature.

2.6 Tests on DSSC technology cells

Tests were performed to study that photovoltaic production in terms of maximum power by varying the lighting conditions. In particular during the tests were changed the following parameters:

- angle of incidence of solar radiation (by tilting the DSSC module);
- shading on the module (by superimposing an opaque cover in increasing portions of the module).

During the tests to obtain a reference with respect to natural lighting, a calibrated photovoltaic cell equipped with an ambient thermometer was used to measure solar radiation and the temperature on the surface of the photovoltaic module. The temperature measured (in contact with the cell protection casing) during the entire set of tests varied in the range 28.5 ° C - 32.5 ° C. Tests were conducted varying the

voltage from OCV (8V) to 0V and measuring the current delivered to an electronic load operating in potentiostatic mode. The value of OCV was handily measured.

Tests without shading

Polarization curves for different angles of incidence of the solar radiation are shown in Figure 73-Figure 74.

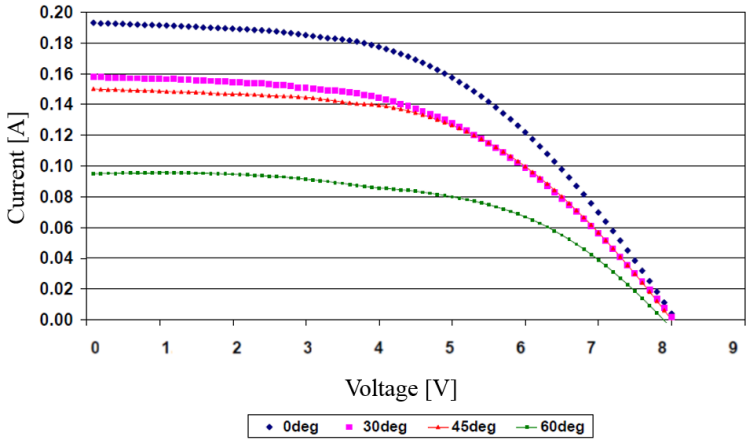

Figure 73: I-V curves at different inclinations (0% shading, G=1000W/mq).

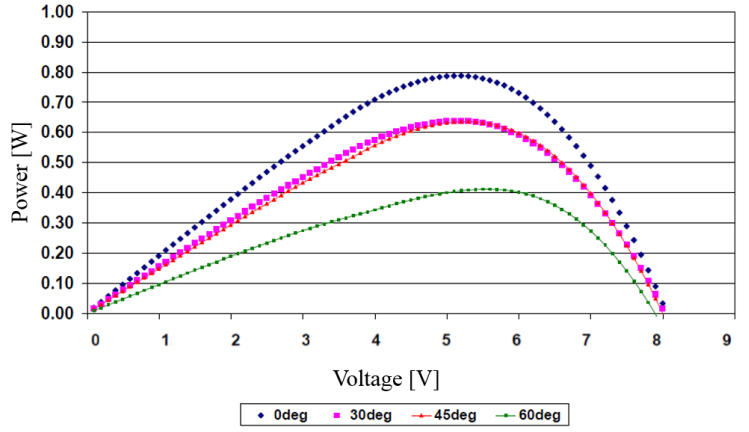

Figure 74: P-V curves at different inclinations (0% shading, G=1000W/mq).

According to normative UNI 8477 to take into account the effect of reflection

(albedo) due to light surfaces in the vicinity of the panel the measured values of power must be scaled applying the albedo factor. As an example, in Figure 75 are shown the P-V curves of Figure 74 obtained by applying an albedo factor of 0.6. This value is suggested to account the reflection of light surfaces of buildings. Figure 76-Figure 77 showh the I/I-V curves obtained (no corrected by albedo factor). Results are summarised in Table 17.

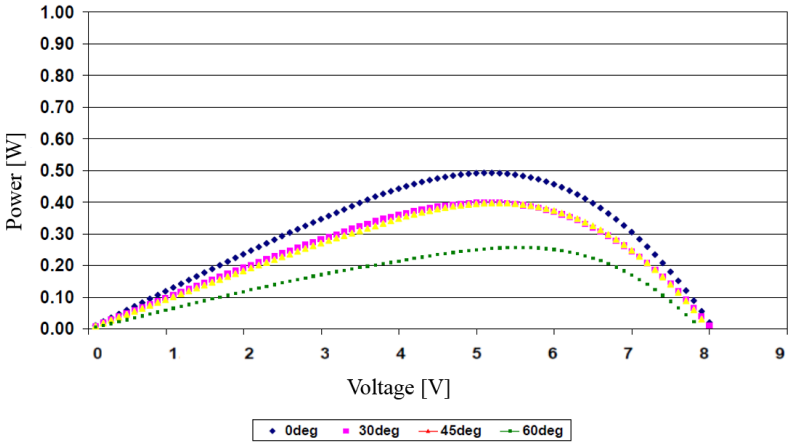

Figure 75: Correction of P-V curves for an albedo factor of 0.6.

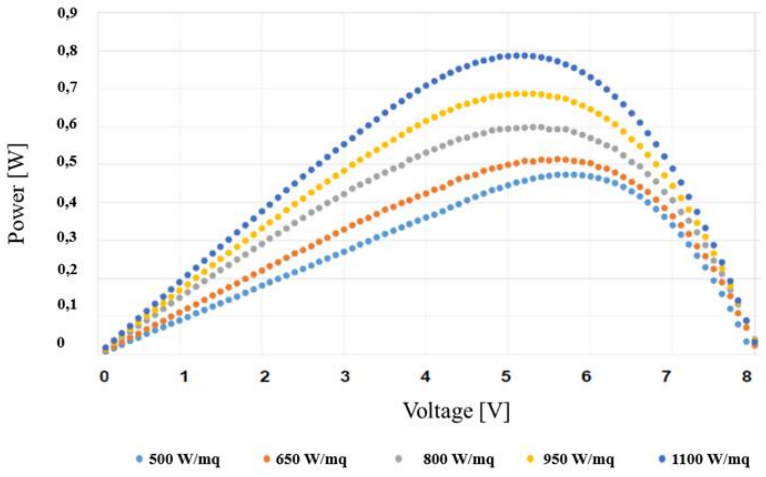

Figure 76: P-V curves at different solar radiation values (0% shading, 0 deg).

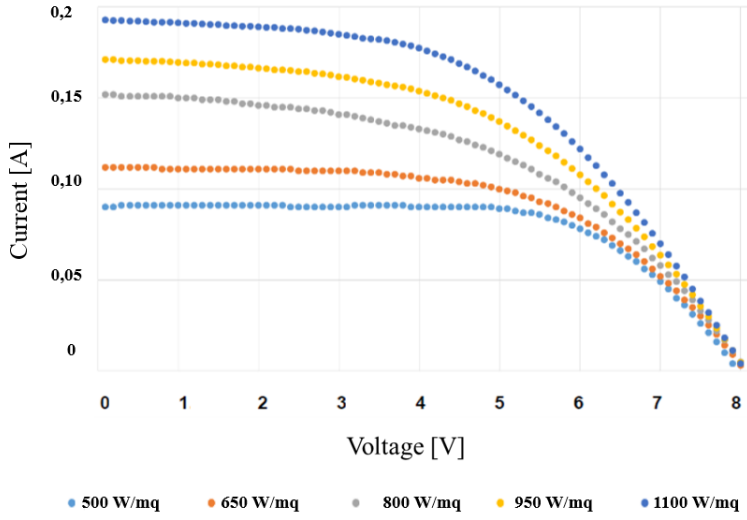

Figure 77: I-V curves at different solar radiation values (0% shading, 0 deg).

Table 17: Characteristic parameters for different irradiation conditions (0% shading, o deg).

Solar Radiation [W/mq]	500	650	800	950	1100
Open circuit voltage (V)	8	8	8	8	8
Max. power voltage (V)	5.798	5.598	5.297	5.197	5.097
Short circuit current (A)	0.091	0.112	0.152	0.171	0.193
Max. power current (A)	0.082	0.092	0.113	4.240	0.155
Max. power (W)	0.473	0.515	0.599	0.687	0.788

Polarization tests were for different values of the solar radiation were carried out in order to characterize the module in real conditions. Figure 78-Figure 79 show the characterization curves obtained for the module inclined at 45°.In the inclined module

a reduction in the delivered power of about 14% compared to the module arranged horizontally was evaluated.

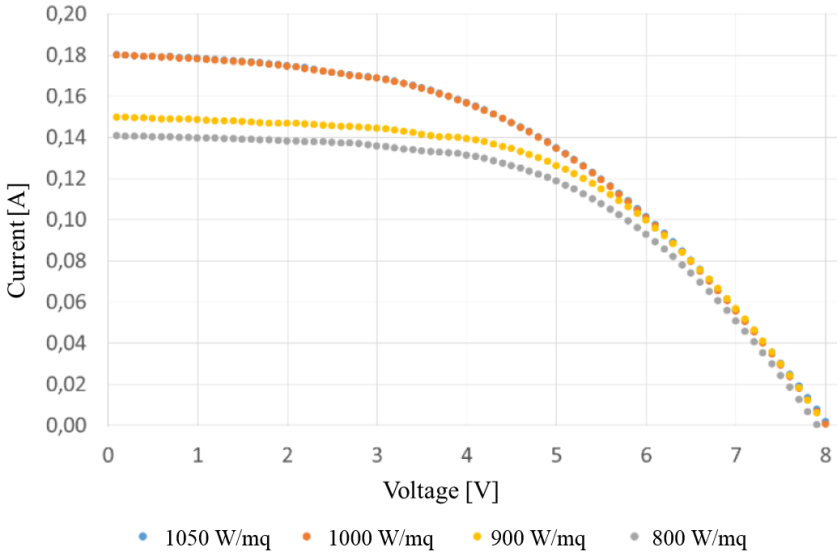

Figure 78: I-V curves at different solar radiation values (0% shading, 45 deg).

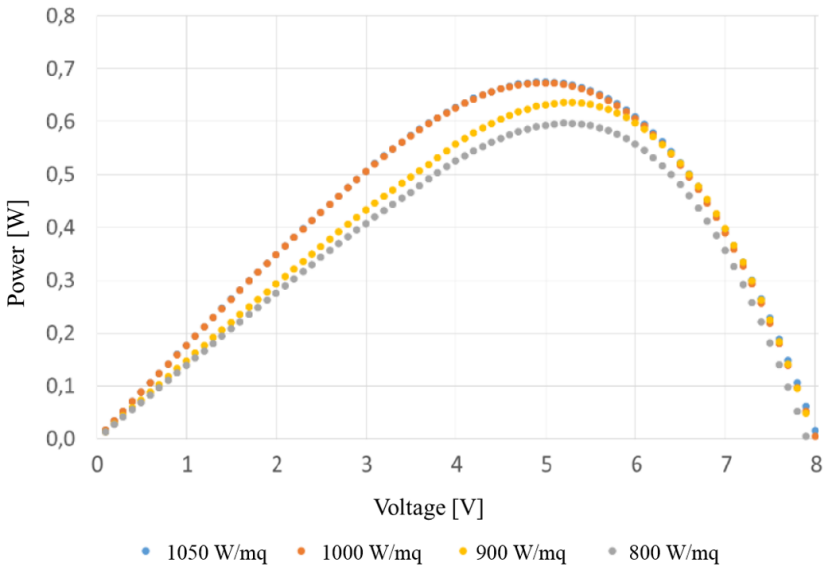

Figure 79: P-V curves at different solar radiation values (0% shading, 45 deg).

Tests with different shading values

To analyse the behaviour of the module for different shading values, tests were carried out after having superimposed on the module an opaque cover. Figure 80-Figure 81 show the I/P-V curves obtained (no corrected by albedo factor) for a 50% of shading in correspondence of two values of solar radiation (100W/mq and 500 W/mq) for the module horizontally disposed.

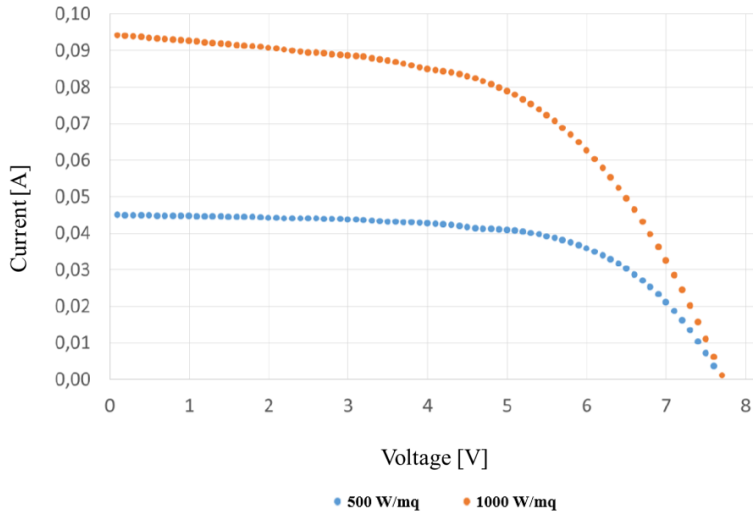

Figure 80: I-V curves at different solar radiation values (50% shading, 0 deg).

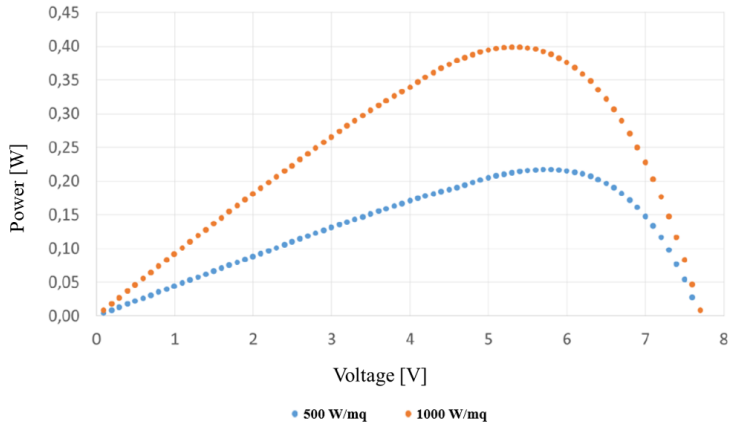

Figure 81: P-V curves at different solar radiation values (50% shading, 0 deg).

For the horizontal module, in Figure 82, the results of the tests carried out for different shading values at a solar irradiation value of 1000 W/mq are shown. Table 18 shows the results for three different angles of incidence: 0°, 30° e 45°.

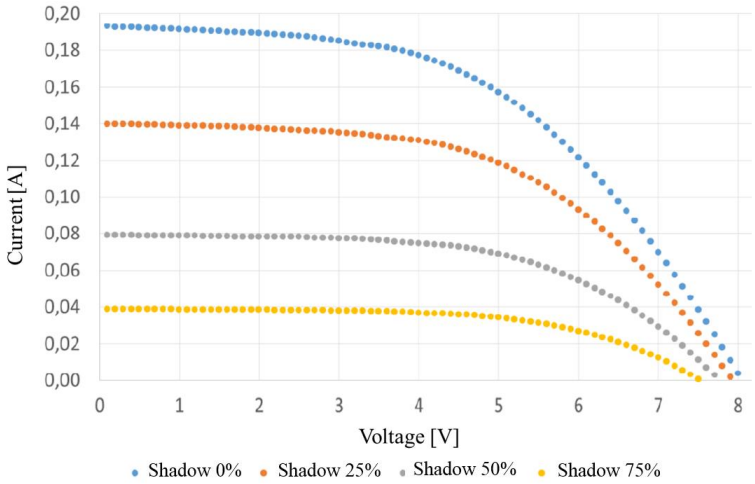

Figure 82: I-V curves at different shading values (1000W/mq, 0 deg).

Table 18: Characteristic parameters for different angles of incidence (50% shading, solar radiation 1000 W/mq).

Angle of incidence [deg]	0	45	60
Open circuit voltage (V)	7.2	7.7	7.7
Max. power voltage (V)	5.4	5.4	5.4
Short circuit current (A)	94	76	33
Max. power current (A)	74	62	27
Max. power (W)	399	336	146

It can be noticed that increasing the shading portion the OCV decreases. In particular a decrease of about 0.5 V between the fully exposed module and the 75% shaded configuration was measured. By tilting the panel, with the same radiation

value, the performance of the module in terms of delivered power is reduced.

In the module inclined by 45° from the horizontal the maximum power values are about the 75 % of the corresponding ones attended for horizontal arrangement. I/P-V curves for the module inclined by 45° are shown in Figure 83-Figure 84.

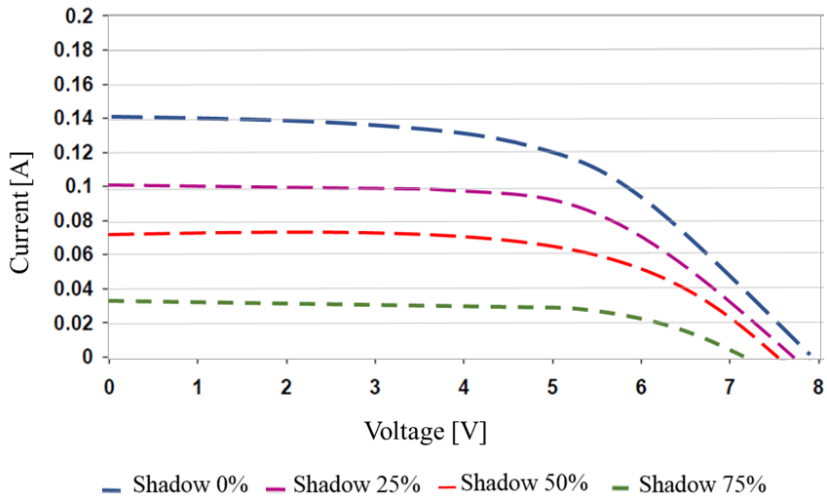

Figure 83: I-V curves at different shading values (1000 w/mq, 45deg).

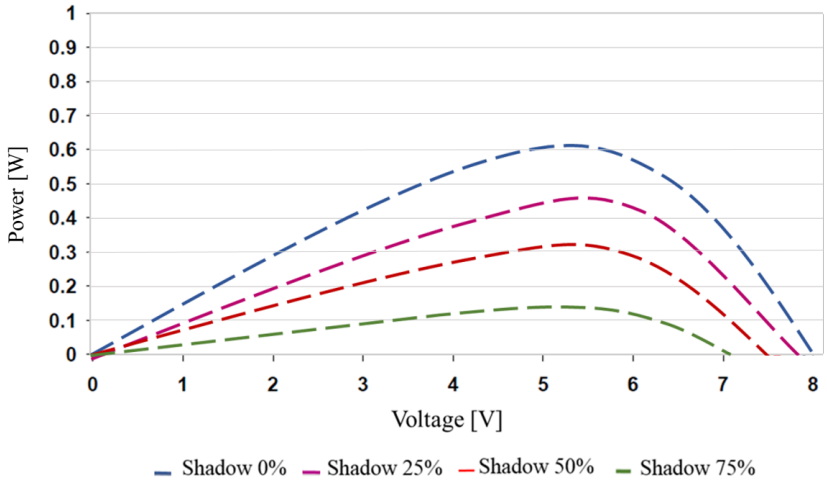

Figure 84: P-V curves at different shading values (1000 w/mq, 45deg).

In Table 19 shows the results of the module inclined by 60° from the horizontal while the corresponding I/P-V curves are shown in Figure 85-Figure 86.

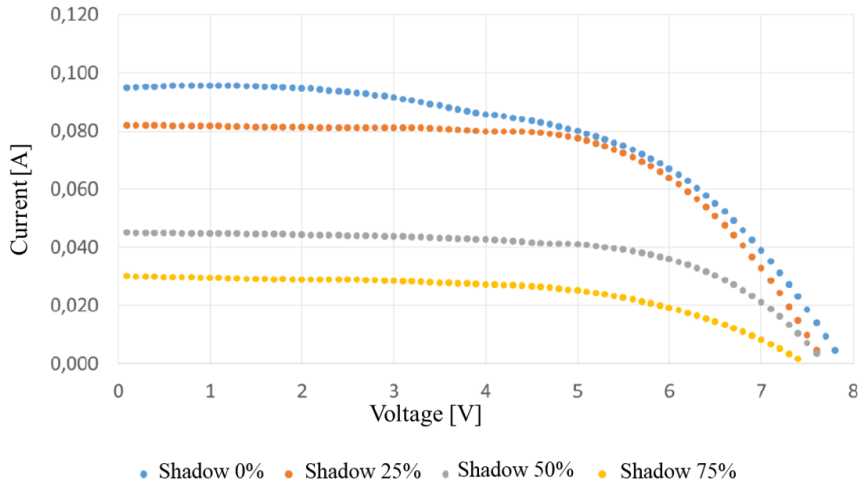

Figure 85: I-V curves at different shading values (1000 W/mq, 60 deg).

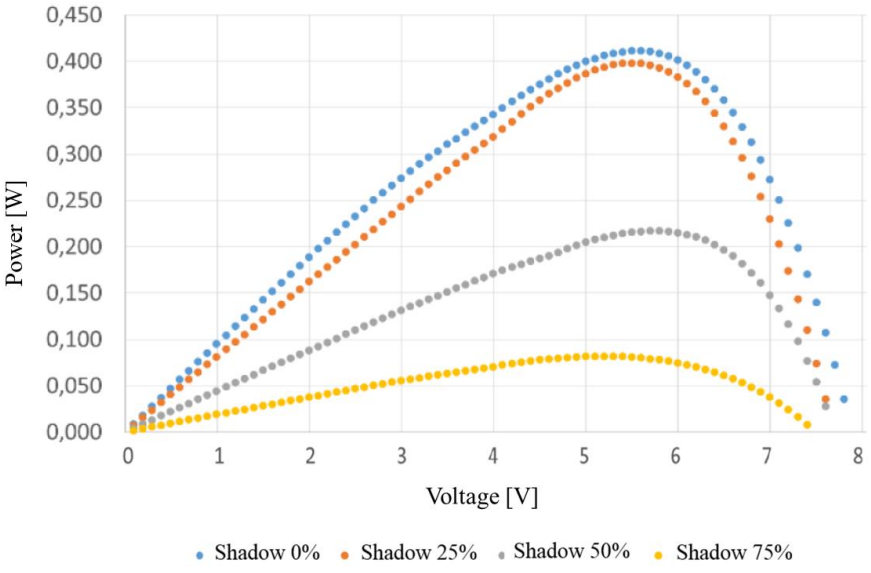

Figure 86: P-V curves at different shading values (1000 W/mq, 60 deg).

Table 19: Characteristic parameters measured at different shading conditions (1000 W/mq, angle of incidence 60 deg).

Shading [%]	0	25	50	75
Open circuit voltage (V)	7.9	7.7	7.6	7.5
Max. power voltage (V)	5.598	5.497	5.698	5.397
Short circuit current (A)	0.095	0.082	0.045	0.002
Max. power current (A)	0.082	0.092	0.038	0.015
Max. power (W)	0.412	0.398	0.217	0.082

Tests in hybrid configuration with lithium battery

For these texts it was used a Li-ion battery (OCV 4.1V and 700 mAh). Results are shown in Figure 87.

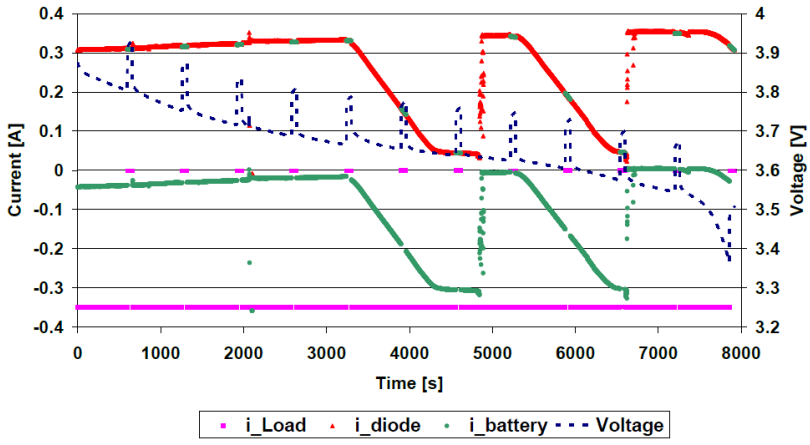

Figure 87: Hybrid system- constant load characterization test.

Due to the low power delivered by the single module, 3 modules were connected in parallel and coupled to the battery via a diode. Short endurance tests at constant current with load equal to half the nominal current of the battery (350mA) until the complete discharge of it.

2.7 Test results on battery

Tests have been carried out to identify a simplified battery model. As previously mentioned, the battery is simulated as heat source within the air cavity. It was assumed that energy loss in charge/discharge processes is attributed to heat generation.

The tested parallelepiped shape battery is composed by nano-scale spinel lithium titanium LTO ($Li_4Ti_5O_{12}$) in the anode and lithium nickel manganese cobalt oxide NCM (LiNi0.5Co0.2Mn0.3O2) with the following features: 2.7 V 23 Ah. Characterization of battery involved recording the charging and discharging behaviour and repeated charge/discharge cycles.

The battery has been tested by Electrochemical Impedance Spectroscopy with a Potentiostat Autolab PGSTAT302N (Figure 88) equipped with a Booster system to raise the current set points up to ±20A. The software suite Nova 2.1 has been used to realize test procedures and record data coming from the cell.

Figure 88: Potentiostat Autolab PGSTAT302N.

The small-signal impedance of the Li-ion batteries can be determined by applying a small sinusoidal current (galvanostatic mode) or voltage (potentiostatic mode) and measuring the amplitude and phase shift of the output voltage or current, respectively. In this work, the EIS measurements were performed in galvanostatic mode.

Charging/discharging tests at different current values were carried out to assess battery performance. Results for different C-rate curves at 25°C are shown in Figure 89.

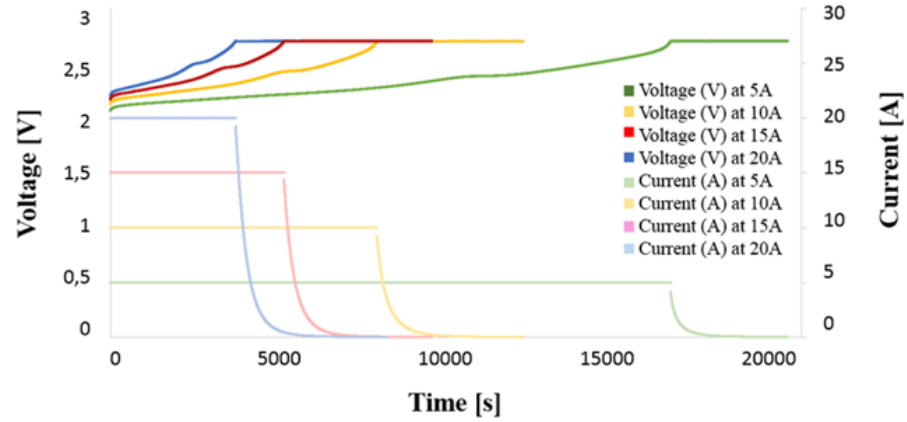

(a)

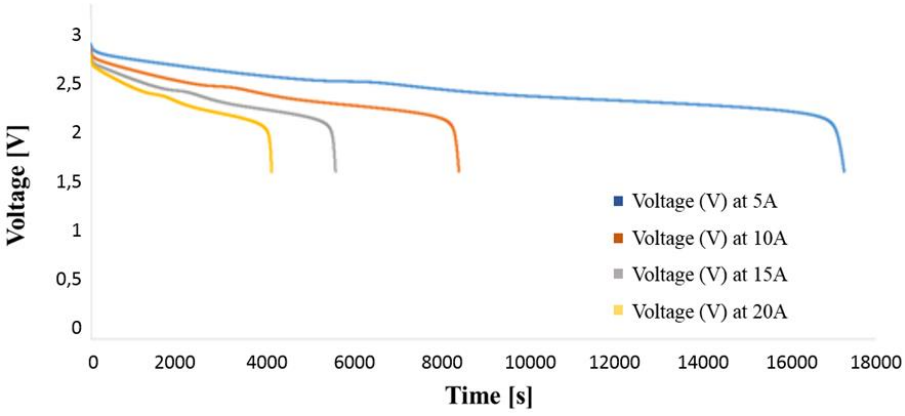

(b)

Figure 89: Charge (a) and discharge (b) curves at 25 °C for LTO cell.

Voltage increases steadily while charging the battery. During this step, lithium ions are extracted from the cathode and intercalate into the anode's layers. The battery's state of charge (SoC) 100% was reached by performing charge cycles with a galvanostatic phase until the upper voltage threshold is reached, followed by a potentiostatic phase at upper cut off voltage until the current goes under 0.01 A. This phase is needed due to typical voltage hysteresis of batteries, which increase/decrease operative voltage during charge/discharge phases, to fully charge the same. Discharge tests were performed starting from 100% SoC with constant current set-point (galvanostatic-mode) until reaching the lower cut off voltage (minimum allowable voltage defining the "empty" state of the battery). Charge and discharge rates are governed by C-rates. The capacity of a battery is commonly rated at 1C, meaning that a fully charged battery at 1Ah should provide 1A for one hour. C-rates estimated during the tests are listed in Table 20.

Table 20: Characteristic C-rates measured at different current conditions.

Current [A]	5	10	15	20
C-rate charge	0.18	0.3	0.36	0.72
C-rate discharge	0.2	0.45	0.6	0.9

It is known that charge/discharge rates affect the electrochemical process into a battery causing a reduction in its efficiency η_b. It can be defined as the ratio of the energy retrieved from the battery ($E_{discharged}$), to the energy provided to the battery ($E_{charged}$), when coming back to the same SoC state:

$$\eta_b = \frac{E_{discharged}}{E_{charged}} \tag{4.2}$$

$$E = \int_0^t V(t) i(t)\, dt \tag{4.3}$$

where

- $V(t)$ is the voltage (V);
- $i(t)$ is the current (A);
- t is the charge/discharge time (h).

In Table 21 shows the efficiencies at different charge/discharge currents.

Table 21: Battery efficiency at different charge/discharge rates at 25°C.

Current [A]	5	10	15	20
$\boldsymbol{\eta_b}$	0.9657	0.9281	0.8991	0.8740

In eq.(4.4) it is reported the polynomial formula interpolating the experimental data used to calculate the heat generated by the battery during its operation:

$$\eta_b = \begin{cases} 0.97 \;\; i \leq 5\ A \\ 0.001\, i^2 + 0.0092\, i + 1.0084, \qquad i > 5\ A \end{cases} \tag{4.4}$$

Handling lithium-ion batteries can present a variety of potential hazards. For this reason, during the tests to provide a controllable temperature range of -40 °C to +110 °C, the battery temperature has been controlled via the climatic chamber Angelantoni mod.600L and monitored by a Pt100 thermistor.

2.8 Test results on the E-brick prototype

As yet explained, in this work it is presented the study of the thermos-fluid dynamics performance of the prototype of E-brick active ventilated façade. To calibrate and validate the thermal model of the prototype, by comparing the monitored data to that of the model on the same time using recorded weather data as a model input, monitoring studies have been developed on the prototype. Figure 90 shows the monitored prototype, the installed sensors and their nomenclature. In detail, four thermocouples (chromel–alumel thermocouples type k), installed on both

sides of the PV module and on both sides of the insulation layer, were used. A weather station was installed near the prototype, recording global horizontal radiation, dry bulb temperature, wind velocity and direction.

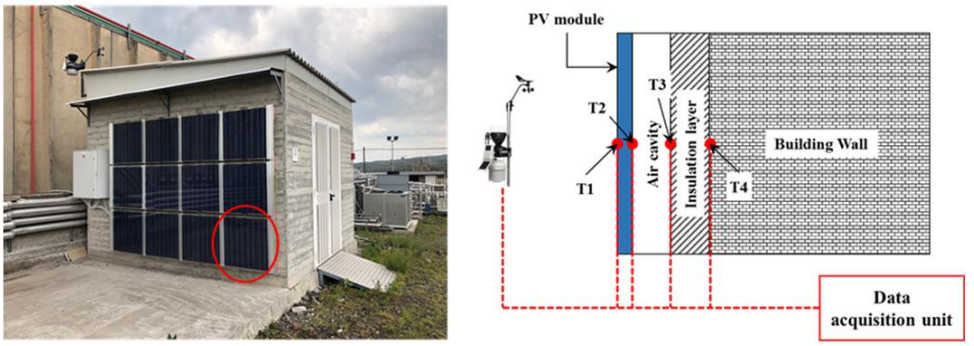

(a) (b)

Figure 90: (a) E-Brick prototype (b) Sensors position during the prototype monitoring.T1= external temperature of the PV panel, T2= temperature of the backsheet of the PV panel, T3= temperature of the inner insulation in contact with the air moving into the channel, T4= temperature of the external insulation.

The solar radiation on a vertical south oriented surface was calculated from the measured global horizontal radiation on horizontal surfaces using the mathematical model developed by Perez et al. [731].

Figure 91 shows the monitored weather data during the tests performed from April 17th to April 21st. Results shown that the outdoor air temperature varies between 9.6 °C and 23.6 °C, while T1 (the front sheet temperature of the PV module) varies between 9.4 °C and 41.8 °C.

Figure 92 , with a better detail, shows the outdoor air temperature, the global horizontal radiation and the solar radiation on a vertical south oriented surface for the April 19th

This monitored day was used for the validation of the thermal model as will be better explained in the next chapter.

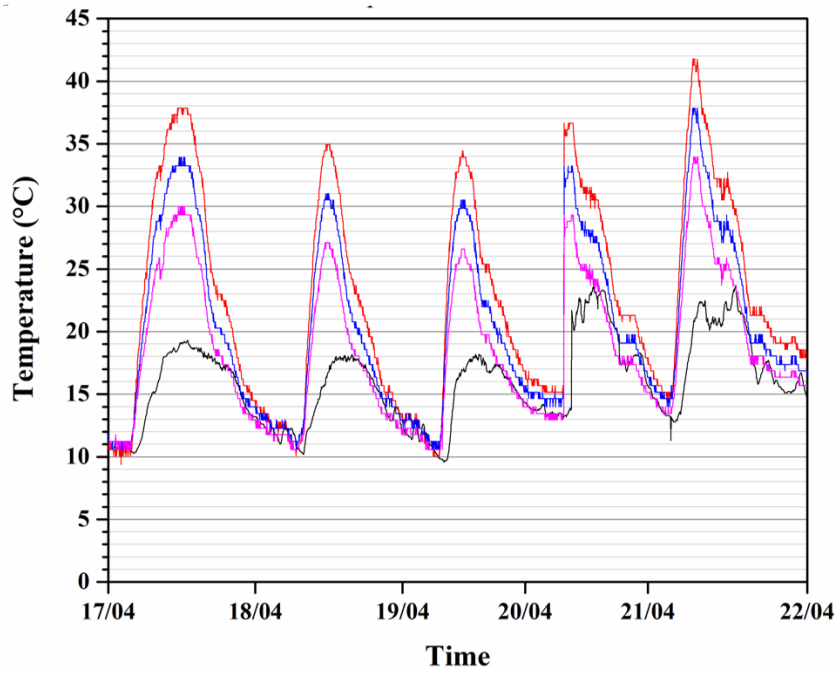

Figure 91: Monitored data from April 17th to April 21st (2019).

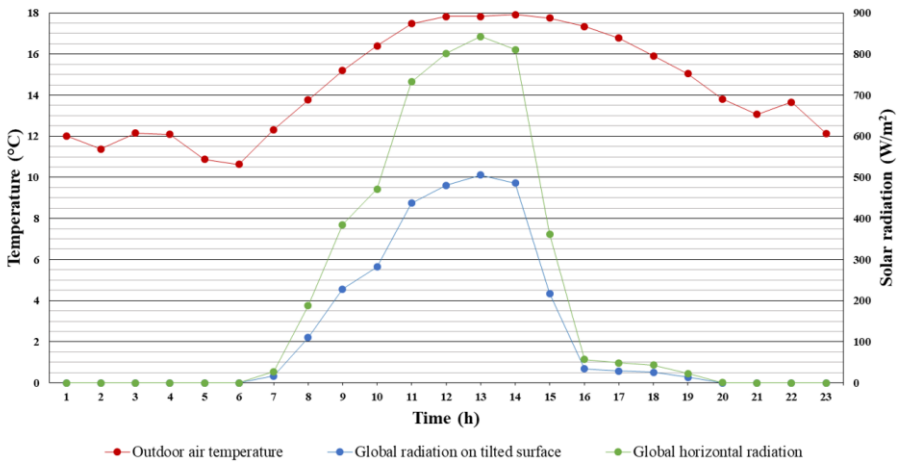

Figure 92: Monitored data April 19th (2019).

Figure 93 to Figure 98 show the solar radiation and the temperature profiles evaluated surface for the June 20th. Results of other experimental tests are not reported in this work. Air velocity values measured are listed in Table 22.

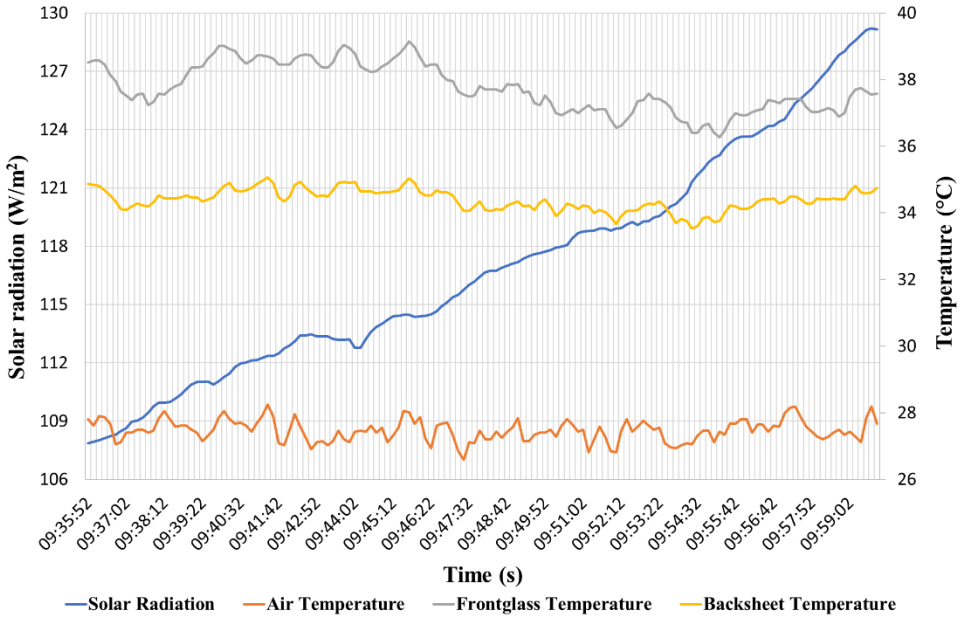

Figure 93: Monitored data June 20th (9:30- 10:00 AM).

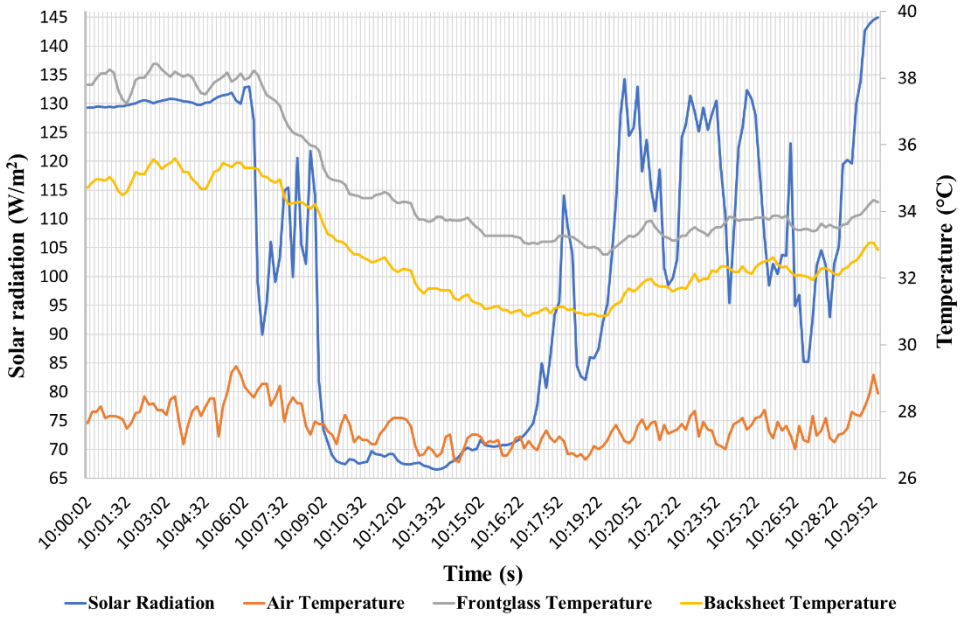

Figure 94: Monitored data June 20th (10:00- 10:30 AM).

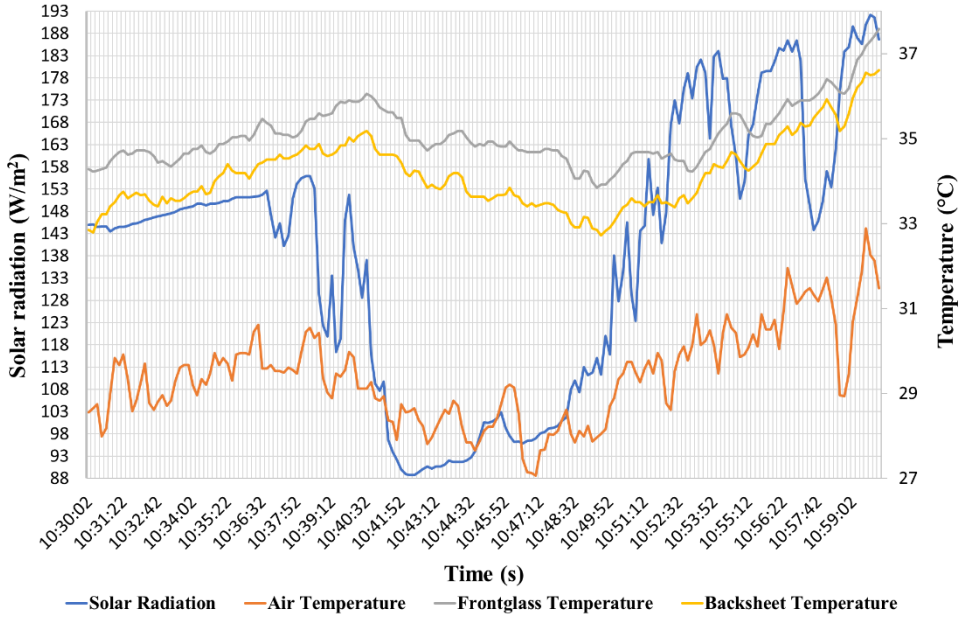

Figure 95: Monitored data June 20th (10:30- 11:00 AM).

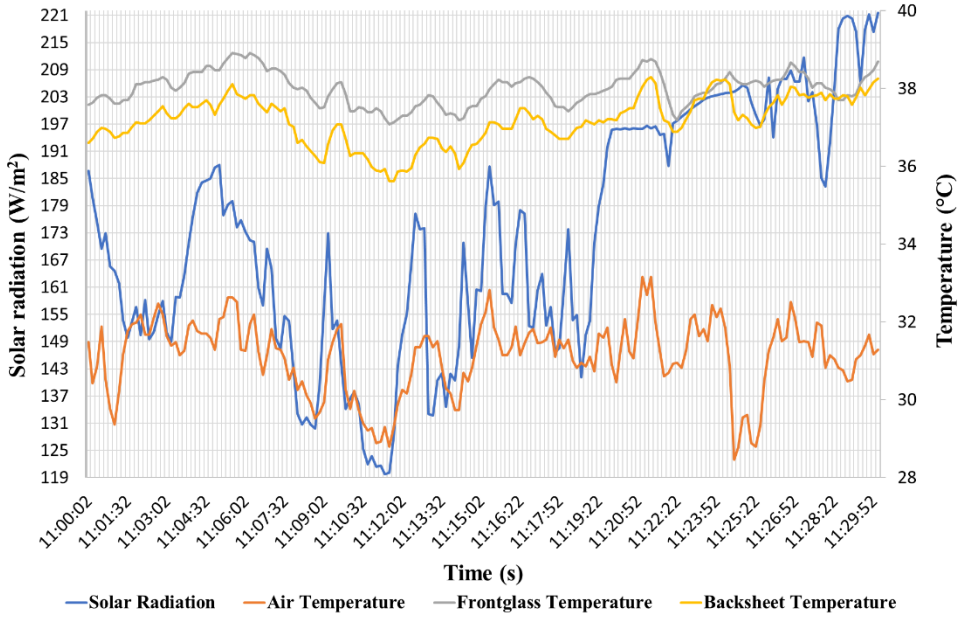

Figure 96: Monitored data June 20th (11:00- 11:30 AM).

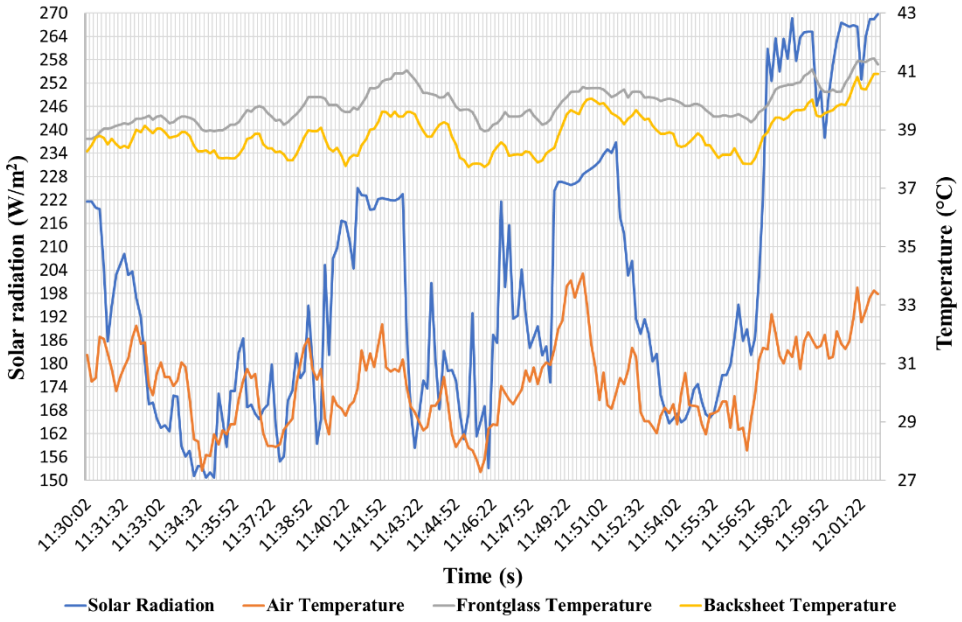

Figure 97: Monitored data June 20th (11:30- 12:00 AM).

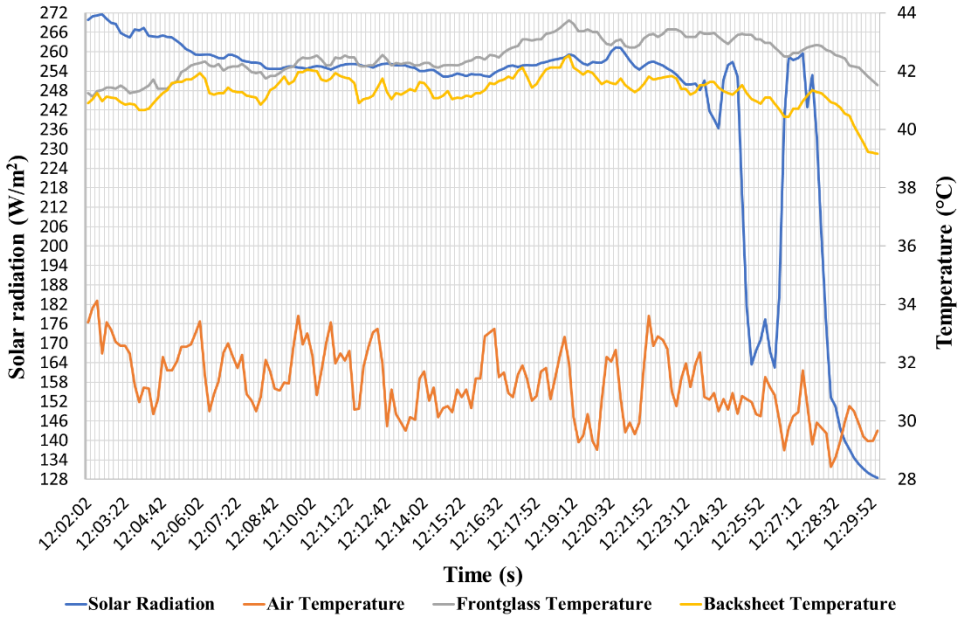

Figure 98: Monitored data June 20th (12:00- 12:30 PM).

Table 22: Measured air velocity data June 20th (9:00 AM- 12:30 PM).

Time	Wind velocity [m/s]	Wind direction [grad]
09:00	2,37	45,96
09:10	2,83	9,49
09:20	2,66	18,48
09:30	2,46	42,62
09:40	2,31	63,55
09:50	2,14	58,88
10:00	2,35	24,16
10:10	1,84	59,03
10:20	2,32	58,5
10:30	1,97	57,77
10:40	1,77	55,44
10:50	1,75	81,92
11:00	2,47	80,24
11:10	2,1	64,76
11:20	2,48	53,51
11:30	2,28	75,19
11:40	1,68	70,59
11:50	1,09	83,65
12:00	1,07	86,84
12:10	0,41	78,73
12:20	0,48	33,05
12:30	0,85	98,56

Nomenclature

AM	Air mass
DSSC	Dye sensitized solar cell
E_charged	Energy retrieved from the battery
E_discharged	Energy provided to the battery
FF	Fill factor
G_tot or G	Global solar radiation
G_v	Vertical solar radiation
Gv	Irradiance solar on the vertical plane
I(t)	Current
Imp	Maximum power current
I_sc	Short-circuit current
MPPT	Maximum power point tracking
OCV	Open circuit voltage
Pmax	Maximum power
SoC	State of charge
t	Charge/discharge time
T_air	Air temperature
T_aluminum	Aluminum temperature
Tc	Cell temperature
T_glass	Glass temperature
TNOCT	Nominal operating cell temperature
V(t)	Voltage
Vmp	Maximum power voltage
XOCV	Temperature coefficient of the open circuit voltage
X_P	Temperature coefficient of the maximum output power
η_b	Battery efficiency

Chapter 5

Numerical assessment of the hybrid active ventilated façade E-Brick

1. Introduction

Ventilated Façades integrating photovoltaic panels are a promising way to improve efficiency and the thermal-physical performances of buildings. Due the inherent intermittence of the non-programmable renewable energy sources, their increasing usage implies the use of energy storage systems to mitigate the mismatch between power generation and the buildings' load demand. In this work to investigate the thermo-fluid dynamic performances of a prototype integrating a photovoltaic cell and a battery as a module of an active ventilated façade, a numerical study in steady state conditions of flow through the air cavity of the module has been carried out and implemented in the fluid-dynamics Finite Element code COMSOL.

CFD simulations have been performed to investigate mainly the effects of the buoyancy-induced by thermal gradients within the air cavity of the ventilated façade and to investigate the effect of the air gap size on the PV performance.

The air gap reduces the overheating of the PV module and also building cooling load due to the presence of hot surfaces around the skin. CFD simulations were used

also to estimate the minimum air gap size to minimize the PV overheating. The air gap has the most important role on the thermal response and temperature distribution of the developed hybrid system. Many researchers found that a gap of 10-15 cm is adequate to maintain relatively low and effective PV temperature [732].

Thermal buoyancy is the principal mechanism for air flow in the air cavity. The geometry and dimensions of the air gap are the keys to predict the overall performance of the BIPV whose design is depends, e.g., on the amount of solar radiation falling on façade, variation of the ambient temperature and wind speed. The ventilated façade should both enhance the thermal stack effect, as well as have a better management of excess heat. In contrast to mechanical ventilation, in the duct there is not the advantage of the flexibility to adjust the air flow to remove the heated air or drive it into the building.

For the aim of this work, it was chosen the CFD modelling since it is a good option for complex temperature problems involving conduction, convection and radiation heat transfer mechanisms.

1.1. Hybrid Prototype

The E-Brick design includes a PV system as external façade and electronic components within the air cavity that contribute to the dissipation of heat inside the cavity itself. In detail, two casings, fixed on the insulation, contain a battery and an integrated control board comprising a MPPT (Maximum Power Point Tracker), a bidirectional battery charger (DC/DC) and a diode (Schottky). Figure 99 shows some pictures of the prototype installed and its constructive scheme. Both battery and control board act as heat source dissipating the generated heat through the casings. To ensure the electrical and electronic components operate within the nominal surrounding temperatures a proper cooling effect must be guaranteed. Installing the casings within an air cavity has the main advantage that heat dissipation is facilitated by natural convection leading to lower operation temperatures [476].

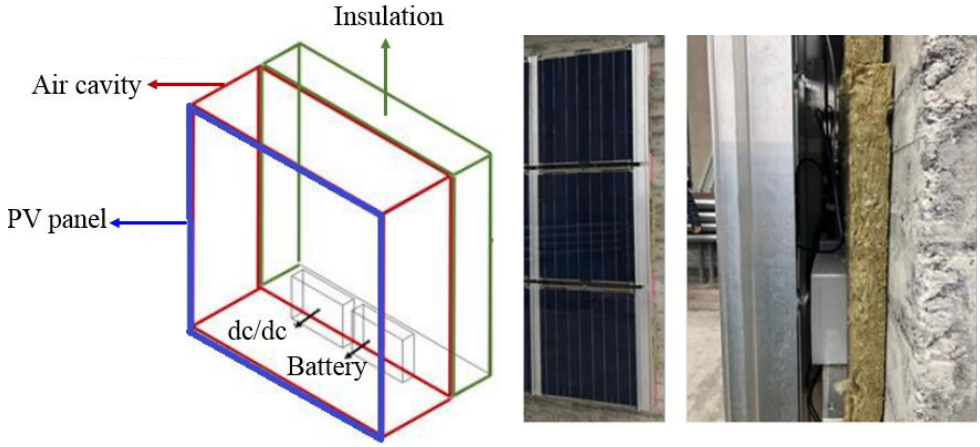

Figure 99: Schematic of the prototype.

The PV panel used in the performed module consists of a lower sheet of tempered prismatic glass (dimensions 680 x 680 mm x 3 mm), a layer of EVA 0.5 mm (vinyl acetate that undergoes temperature turns into inert adhesive), matrix of photovoltaic cells 0.2 mm, a layer of EVA0.5 mm and a sheet of tempered prismatic glass dimensions 680 x 680 mm x 3 mm. The air channel thickness is 20 cm [694]. On the other side of the air channel, typical construction materials made up the wall. The EVA and the PV cells are thin (compared with other computational domains) so the temperature difference across the EVA and PV cells is negligible. Therefore, the EVA sheets and PV cells are treated as a single domain for the heat transfer simulation. A similar approach was used by Nizetic et al. [733].The two casings containing a battery, an integrated MPPT and bidirectional battery charger (dc/dc). Have dimensions 18 cm × 14 cm × 4 cm The battery 116 mm × 106 mm × 22 mm has nominal capacity 23 Ah and nominal voltage 2.3 V. The diode (Schottky), consisting of metal-semiconductor junctions, has a slope resistance r 8.8 mΩ. The battery and the diode are available on the market and the data is reported in the manufacturers ’datasheets. The casings are closed to protect the battery and the electrodes of the diode from dust and moisture. As a result, generated heat by Joule effect is not well dissipated. Since both battery and diode dissipate heat is important

to assess whether the surface temperatures reached are compatible with the maximum temperatures that can be combined with the materials of which the casing is made.

The physical property [734] density ρ, thermal conductivity λ and specific heat c_p of each material utilized in the proposed prototype are listed in Table 23.

Table 23: Physical properties of prototype.

Material	**Component**	$\boldsymbol{\rho}$ $[\boldsymbol{kg/m^3}]$	$\boldsymbol{\lambda}$ $[\boldsymbol{W/m\,K}]$	$\boldsymbol{c_p}$ $[\boldsymbol{J/kg\,K}]$
EVA	PV module	935	0.29	2500
Glass	PV module	2500	1.04	750
Polycrystalline Silicon	PV module	2330	150	700
Polypropylene	Casings	1030	0.16	1400
Rockwood	Insulation	100	0.035	1030

Both geometrical dimensions and physical properties were used to develop a numerical heat transfer CFD model with temperature dependent air properties. A detail of the model with its assumptions and boundary conditions is given in the following. The numerical model developed to investigate the airflow and temperature distributions was implemented in the multi-physics Finite Element Code COMSOL.

The model has been calibrated and validated on experimental data carried out at CNR-ITAE. In particular, experimental data of solar radiation, air temperature and air velocity were used as boundary conditions in the numerical model.

As previously mentioned, the prototype consists of a PV panel mounted above a layer of insulation separated by an air channel. A battery and a dc/dc inverter are simulated as heat sources within the air cavity.

The calibrated model was used to perform a wide range of parametric analyses with different boundary conditions to explore the viability of the hybrid prototype.

The geometry of the prototype is very simple, but the physics involved make its solution complex enough.

1.2. Boundary conditions and assumptions

The following modeling hypothesis has been made:

- Steady state conditions (temperatures change no more than ± 1°h);
- The thickness of the PV panel (7 mm) is small relative to his width and height (680 mm × 680 mm) so it's reasonable to assume that conduction occurs exclusively in the direction orthogonal to the surface of the panel;
- The interstices between neighboring cells have a very small area so the thermal exchanges between photovoltaic cells and EVA can be neglected;
- Negligible Ohmic losses of PV cells so that the electrical photovoltaic conversion efficiency is linearly related to its operative cell temperature;
- Uniform heat fluxes;
- Negligible thermal contact resistance between two different layers;
- Isotropic materials with thermal and optical properties constant;
- Newtonian fluid and no slip conditions on the walls in contact with the fluid;
- The fluid was supposed to be a continuous system in order to its extensive properties are defined in an infinitesimal length scale and vary continuously from a point to another in the medium;
- The sky is treated as a blackbody;
- The multiple reflections and transmissions between the components (particularly between the photovoltaic cells and the front glass) and the radiation exchange of the PV cells to the glass are considered as negligible.

In Figure 100 a schematic representation of the boundary conditions assumed is

shown and in the following listed:

- Part of the vertical solar radiation GPV absorbed by the PV cells to generate electricity is dissipated in the form of heat. The volumetric heat generation was applied to the PV cells layer [735];
- Volumetric heat generation was applied to the heat sources within the air cavity. The sources were simulated as punctiform placed within the casings and the heat fluxes were supposed uniform;
- Since all energy fluxes are due to the incoming solar irradiance, direct insolation is assumed greater than diffuse radiation at peak heat gains;
- The external surface temperature was measured experimentally by a thermocouple and used as input (Dirichlet's condition);
- Both inlet and outlet section are at atmospheric pressure because air was provided to be free flow;
- The flow direction is assumed vertical since air is driven from the bottom to the top opening;
- The air flow is not affected from the sides of the air gap, lateral surfaces were set as adiabatic.

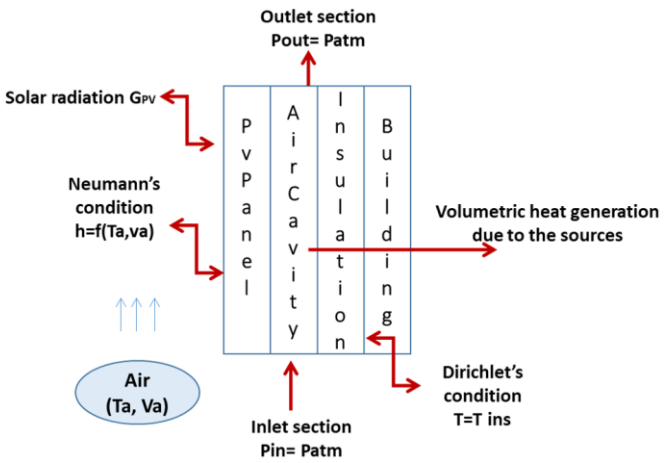

Figure 100: Schematic of the boundary conditions.

Part of the incident solar radiation on front glass is absorbed, the incoming flux per unit area (W/m^2) taking place in the thermal balance equations of the panel is was estimated as followed:

$$q_{fr} = \frac{\alpha_{glass} \cdot G_{PV}}{A_P} \tag{5.1}$$

where

- α_{glass} is the absorption coefficient of the glass cover (in accordance to [736] it was assumed 0.005 in this work);
- G_{PV} is the vertical solar radiation on the PV panel (W/m^2);
- A_P is the area of the panel (m^2).

The heat dissipation (W/m^3) in the PV panel was estimated as followed

$$q_{PV} = \frac{\tau_{glass} \cdot \alpha_{cell} \cdot G_{PV} \cdot (1 - \eta_{PV})}{s_{PV}} \tag{5.2}$$

where

- τ_{glass} is the transmittance of the glass (in accordance to [736] it was assumed 0.96 in this work). In practice, the absorptivity and the transmittance of the glass are not constant because they are dependent on sun position;
- α_{cell} is the absorptivity of the cell (in accordance to [736] it was assumed 0.93 in this work);
- η_{PV} is the efficiency of the PV panel;
- s_{PV} is the thickness of the PV layer (m).

q_{PV} has a negative effect on the PV efficiency mainly in ventilated façade with low wind cooling effects and limited ventilation behind the modules. Due to it the cooling method of the BIPV is crucial. In (5.2) it would be more correct to use an overall solar absorption coefficient for the whole PV panel. Every material has a

different absorptivity coefficient, so it is difficult to accurately predict the amount of absorbed heat. The amount of absorbed heat depends on the spectrum of irradiance and from which wavelengths are emitted from the sun. Eq. (5.2) is a good estimation of the PV cell heat output, its real value cannot be strictly defined so it depends on surrounding circumstances in which the PV panel operates, cell material and temperature, cell efficiency.

η_{PV} is strongly affected from cell temperature so it was not assumed constant. It was used the following expression proposed by Evans et al. [737] to correlate the module's efficiency to cell temperature (T_{cell}):

$$\eta_{PV} = \eta_{ref}\left[1 - X_p \cdot (T_{cell} - 25°) + \delta \cdot \ln\left(\frac{G}{G_{ref}}\right)\right] \quad (5.3)$$

where

- η_{ref} is the efficiency at standard test conditions available in the datasheet of the manufacturer;
- G_{ref} is 1000 W/m^2(standard rating conditions);
- X_P is the temperature coefficient of the maximum output power;
- δ is the solar irradiance coefficient (0.085 for single crystalline and 0.11 for poly-crystalline modules [698]).

Figure 101 illustrates the electrical connection between the different components, indicating the power flows and the heat generated by each component with an overview of relevant nomenclature.

The volumetric heat dissipation of DC-DC (q_d) and battery (q_b) were estimated using the following equations respectively:

$$q_d = P_{PV} \cdot (1 - \eta_d) + i^2 r \quad (5.4)$$

$$q_b = P_{PV} \cdot (1 - \eta_b) \cdot \eta_d \quad (5.5)$$

where

- η_d is the diode efficiency (assumed equal to 0.95);
- η_b is the battery efficiency;
- i is the current through the battery
- r is the electrical resistance of the diode (assumed equal to 0.08 mΩ).

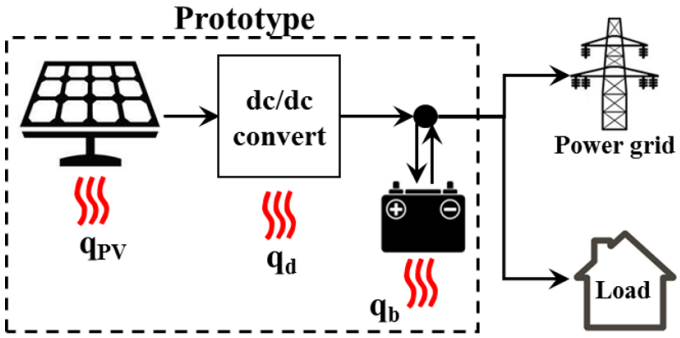

Figure 101: Schematic of electrical connection among PV panel, diode and battery.

1.3. Numerical Method implemented

The numerical model developed aiming the scope of this thesis was implemented in the COMSOL Multi-physics® Finite Element code.

The Finite Element method (FEM) is a general numerical technique for solving partial differential equations (PDEs) [738]. It is called in this way since the domain is subdivided into smaller parts called finite elements. The domain subdivision is achieved by a space discretization in the space by the construction of a mesh. The numerical domain for the solution has a finite number of points, the finite element method formulation of a boundary value problem finally results in a system of algebraic equations. The system of algebraic equations is then solved to compute the values of the dependent variable for each of the elements. The finite elements are connected at the nodal points located in the faces of the elements or within the volume of an element. The geometric positions and displacements of the element nodal points allow to completely describe the displacements and the geometry of each element.

By using the nodal values it is possible to interpolate the element geometry and the element displacements.

The Finite Volume Method (FVM) is an alternative technique for solving partial differential equations. The main difference can be expressed as follow: the FVM is a discretization based upon an integral form of the PDEs to be solved while the FEM is based upon a piecewise representation of the solution in terms of specified basis functions [739].

Similarly to the FEM the first step in the solution process is the discretization of the geometric domain which, in the FVM implementation, is discretized into finite volumes (non-overlapping elements). All the scalar unknowns are computed at the centre of each element, while the velocities are computed at the faces of the control volume. For Both methods, the time discretization is usually done with some type of time-stepping scheme for ordinary differential equations.

In contrast to FEM, in the FVM the terms of the conservation equation to be solved are turned into face fluxes and evaluated at the finite volume faces. The flux entering a given volume is identical to that leaving the adjacent volume as a consequence the FVM is strictly conservative. This advantage and the possibility to be formulated in the physical space on unstructured polygonal meshes makes FVM the preferred method in CFD. In contrast to FEM, FVM allows to implement more easily a variety of boundary conditions since the unknown variables are evaluated at the centroids of the volume elements rather than at their boundary faces. An advantage of FEM, in contrast to FVM, is the possibility to increase more easily the order of the elements, leading to accurate approximations of physics fields.

The complex mathematical formulation of both numerical methods is out of the aim of this thesis just as the discussion about the better method. The model described in the next section could be solved by both of methods.

CFD software FEM COMSOL was chosen since it is a Multiphysics and user friendly interface giving full insight and control over the modelling process. Its simulation environment facilitates all steps in the modelling process—definition of

the geometry, setting of the physics, meshing, solving, postprocessing of the results.

2. Mathematical model

The mathematical model for the prototype described in this work can be divided into two main parts: fluid model and heat transfer model.

2.1 Fluid model

Mass fluid enters and leaves the control volume exclusively through gross fluid motion according to a mechanism referred as advection [740].

Denoted with Φ a generic intensive property of the fluid it is possible to write a law of conservation within the control volume: the change of Φ over the time is equal to the sum of the net convective and/or diffusive flux through the walls of the control surface and its net generation in the control volume [741]. This law known as "***Reynolds transport theorem***" can be written as:

$$\frac{\partial}{\partial t}\int_{V_c} \emptyset \, dV_c = -\int_{S_c} \emptyset(\boldsymbol{u}\cdot\boldsymbol{n})dS_c - \int_{S_c} \boldsymbol{J}_\emptyset \cdot \boldsymbol{n}\, dS_c + \int_{V_c} S_\emptyset \, dV_c \qquad (5.6)$$

where

- V_c is the control volume [m3];
- S_c is the control surface [m2];
- $\boldsymbol{u}$ is the vector velocity (u,v,w) [m/s];
- $\boldsymbol{J}_\emptyset$ ·is the vector diffusive flux [[Φ]/(m2 s)];
- $S_\emptyset$ is the source of Φ [[Φ]/m3].

According to "Fick's law" $\boldsymbol{J}_\emptyset$ ·is given as follows:

$$\boldsymbol{J}_\emptyset = -\boldsymbol{\Gamma}\,\nabla\emptyset \qquad (5.7)$$

- $\boldsymbol{\Gamma}$ is the second order tensor (i.e., the thermal diffusivity tensor) [kg /(m s)];

- $\nabla\emptyset$ is the gradient operator [[Φ]/m].

$$\nabla\emptyset = \frac{\partial\emptyset}{\partial \mathrm{x}}\mathbf{i} + \frac{\partial\emptyset}{\partial \mathrm{y}}\mathbf{j} + \frac{\partial\emptyset}{\partial \mathrm{z}}\mathbf{k} \tag{5.8}$$

The last relation is analogous to that one existing between the Lagrangian and the Eulerian description of a fluid stream.

The surface integrals of eq. (5.6) can be written as volumetric integrals applying the "Gauss's divergence theorem":

$$\frac{\partial}{\partial t}\int_{V_c} \emptyset \, dV_c = -\int_{V_c} (\nabla \cdot \emptyset\boldsymbol{u}) dV_c - \int_{V_c} (\nabla \cdot \boldsymbol{J}_\emptyset) \, dV_c + \int_{V_c} S_\emptyset \, dV_c \tag{5.9}$$

where $\nabla\cdot$ is the divergence operator.

$$\nabla \cdot \emptyset\boldsymbol{u} = \frac{\partial\emptyset \mathrm{u}}{\partial \mathrm{x}} + \frac{\partial\emptyset \mathrm{v}}{\partial \mathrm{y}} + \frac{\partial\emptyset \mathrm{w}}{\partial \mathrm{z}} = \frac{\partial u_j}{\partial x_j} \tag{5.10}$$

In a similar way it can be expressed $(\nabla \cdot J_\emptyset)$ in a three-dimensional space rectangular coordinate system. Eq. (5.9) can be also expressed in differential form as:

$$\frac{\partial\emptyset}{\partial t} + \nabla \cdot (\emptyset\boldsymbol{u}) + \nabla \cdot J_\emptyset = S_\emptyset \tag{5.11}$$

Substituting the eq.(5.7) it is obtained the transport equation (convection-diffusion) of the scalar Φ:

$$\frac{\partial\emptyset}{\partial t} + \nabla \cdot (\emptyset\boldsymbol{u}) = \nabla\,(\boldsymbol{\Gamma}\,\nabla\emptyset) + S_\emptyset \tag{5.12}$$

The governance equations of the fluid dynamics implemented in COMSOL and briefly descripted in the following sections are: continuity, momentum and Navier-Stokes equations.

Continuity equations

Replacing $\emptyset$ with the fluid density ρ_f[kg/m^3] and supposing that there are no sources of mass, Eq. (5.11) can be written as follow:

$$\frac{\partial \rho_f}{\partial t} + \nabla \cdot \left(\rho_f \boldsymbol{u}\right) + \nabla \cdot J_{\rho_f} = 0 \tag{5.13}$$

For a fluid supposed isotropic ($\nabla \cdot J_{\rho_f} = 0$) and according to steady state conditions assumption the continuity equations can be written as:

$$\nabla \cdot \left(\rho_f \boldsymbol{u}\right) = 0 \tag{5.14}$$

or in differential form:

$$\frac{\partial (\rho_f u_j)}{\partial x_j} = \frac{\partial (\rho_f \mathrm{u})}{\partial \mathrm{x}} + \frac{\partial (\rho_f \mathrm{v})}{\partial \mathrm{y}} + \frac{\partial (\rho_f \mathrm{w})}{\partial \mathrm{z}} = 0 \tag{5.15}$$

It can be noticed that eq. (5.14), for an incompressible fluid, is valid both for transient and stationary conditions. Continuity equations are a general expression of the mass conservation requirement and must be satisfied a every point in the velocity boundary layer.

Momentum equations

Replacing $\emptyset$ with $\rho_f \mathbf{u}$ and based on the steady state conditions and incompressible flow assumptions, eq. (5.11) can be written as:

$$\nabla \cdot \left(\rho_f \, \mathbf{u} \cdot \boldsymbol{u}\right) = S_{\rho_f \mathrm{u}} \tag{5.16}$$

where $S_{\rho_f \mathrm{u}}$ is the forces per unit of volume [kg/(m^2 s^2)].

In the boundary layer two kinds of forces may act on the fluid: body forces, which are proportional to the volume, and surface forces, which are proportional to the area [742]. Gravitational, centrifugal, electrical are examples of body forces. The surface forces are mainly due to the fluid static pressure, as well as to viscous stresses. Based on this consideration:

$$S_{\rho_f \mathrm{u}} = f_i + \nabla \cdot T_{ij} \tag{5.17}$$

where

- f_i are the mass forces per unit of volume;

- T_{ij} is the total stress tensor.

where g is the gravity acceleration (m/s^2)

$$T_{ij} = \begin{pmatrix} t_{xx} & t_{xy} & t_{xz} \\ t_{yx} & t_{yy} & t_{yz} \\ t_{zx} & t_{zy} & t_{zz} \end{pmatrix} \tag{5.18}$$

where

- t_{ii} are the normal components of the total stress tensor producing a linear deformation;
- t_{ij} are the tangential components of the total stress tensor producing an angular deformation;;
- a double subscript notation is used for the stress components, the first one indicates the surface orientation by providing the direction of its outward normal while the second one indicates the direction of the force component.

For a fluid it is known that the hydrostatic pressure p is one-third of the trace of the stress tensor (compressive stress). As a consequence, T_{ij} can be written as follow:

$$T_{ij} = t_{ij} - \frac{1}{3}\, tr(T_{ij}) = t_{ij} - p\, \delta_{ij} \tag{5.19}$$

where $\delta_{ij}$is the Kronecker operator.

Substituting the eq.(5.19) in (5.17) and the obtained result in (5.16) the momentum equations can be written as:

$$\nabla \cdot \left(\rho_f\, \mathbf{u}\, \cdot \boldsymbol{u}\right) + \nabla \cdot \left(p\, \delta_{ij}\right) = f_i + \nabla \cdot t_{ij} \tag{5.20}$$

or in differential form as:

$$\frac{\partial \rho_f u_j u_i}{\partial x_j} + \frac{\partial p}{\partial x_i} = f_i + \frac{\partial t_{ij}}{\partial x_j} \tag{5.21}$$

The "convective term" $\nabla \cdot \left(\rho_f\, \boldsymbol{u}\, \cdot \boldsymbol{u}\right)$ for a fluid incompressible is given as:

$$\frac{\partial \rho_f u_j u_i}{\partial x_j} = \rho_f u_j \frac{\partial u_i}{\partial x_j} \tag{5.22}$$

In this work the studied fluid is air entering into a cavity in free convection. It means that the fluid motion is due to buoyancy forces within the fluid. Buoyancy is due to the combined presence of a body force proportional to density and a fluid density gradient. In the field of buoyancy-driven flow it can be assumed the so called *"Boussinesq approsimation"*. It assumes that variations in density have no effect on the flow field except that they are rise to buoyancy forces. Assuming that the gradient density is due to a temperature gradient and the body force is gravitational:

$$f_i = \rho_f \cdot g_i \cdot \beta \cdot (T_s - T_\infty) \tag{5.23}$$

where

- g_i is the acceleration due to gravity [m/s2];
- β is the volumetric thermal expansion coefficient [K-1].

$$\beta = -\frac{1}{\rho_f}\left(\frac{\delta \rho_f}{\delta T}\right)_p \tag{5.24}$$

Replacing the eq. (5.23) in (5.21) momentum equations for a fluid in free convection motion are obtained as :

$$\frac{\partial \rho_f u_j u_i}{\partial x_j} + \frac{\partial p}{\partial x_i} = \rho_f \cdot g_i \cdot \beta \cdot (T - T_\infty) + \frac{\partial t_{ij}}{\partial x_j} \tag{5.25}$$

Navier-Stokes equations

In the momentum equation the presence of t_{ij} poses an analytical closure problem. The fluid was supposed to be Newtonian. It means that the viscous stress is linearly correlated to the local strain (the stresses are proportional to the velocity gradients) [743] :

$$T_{ij} = 2\,\mu_f\, S_{ij} \tag{5.26}$$

where

- μ is the fluid dynamic viscosity [Pa s];
- S_{ij} is the strain rate tensor [1/s].

$$S_{ij} = \frac{1}{2}\left(\frac{\partial u_i}{\partial x_j} + \frac{\partial u_j}{\partial x_i}\right) \tag{5.27}$$

In the same way seen for T_{ij} in eq. (5.19) also for S_{ij} it can be written:

$$S_{ij} = s_{ij} - \frac{1}{3}\, tr(S_{ij}) \tag{5.28}$$

where

- s_{ii} are the normal components of the strain tensor;
- s_{ij} are the tangential components of the strain tensor.

According to continuity eq. (5.14)

$$\frac{1}{3}\, tr(S_{ij}) = \frac{1}{3}\left(\frac{\partial \mathrm{u}}{\partial \mathrm{x}} + \frac{\partial \mathrm{v}}{\partial \mathrm{y}} + \frac{\partial \mathrm{w}}{\partial \mathrm{z}}\right) = \nabla \cdot (\boldsymbol{u}) = 0 \tag{5.29}$$

Based on this consideration eq. (5.26) can be written as follow:

$$T_{ij} = 2\,\mu_f\, s_{ij} = \mu\left(\frac{\partial u_i}{\partial x_j} + \frac{\partial u_j}{\partial x_i}\right) \tag{5.30}$$

Substituting **constitutive equations** (5.30) in (5.21) Navier-Stokes equations in differential form (under steady state conditions) are obtained as follow:

$$\frac{\partial \rho_f u_j u_i}{\partial x_j} + \frac{\partial p}{\partial x_i} = \rho_f \cdot g_i \cdot \beta \cdot (T - T_\infty) + \frac{\partial}{\partial x_j}\left(\mu_f \left(\frac{\partial u_i}{\partial x_j} + \frac{\partial u_j}{\partial x_i}\right)\right) \tag{5.31}$$

or , if the density is constant, as :

$$\frac{\partial u_j u_i}{\partial x_j} + \frac{1}{\rho_f}\frac{\partial p}{\partial x_i} = \cdot\, g_i \cdot \beta \cdot (T - T_\infty) + \frac{\partial}{\partial x_j}\left(\nu_f \left(\frac{\partial u_i}{\partial x_j} + \frac{\partial u_j}{\partial x_i}\right)\right) \tag{5.32}$$

where ν is the fluid kinematic viscosity (N s/m^2).

2.2 Heat transfer model

Heat transfer is energy in transit owing to a temperature difference. It is common use the term conduction to refer to the heat transfer occurring across the medium, the term convection to refer the heat transfer occurring between a surface and a moving fluid when they are at different temperatures and the term radiation to refer to the heat emitted by a surface of finite temperature in the form of electromagnetic waves. As yet mentioned in this work, the basic model consists of two skins, building envelope and PV panels, separated by an air gap. Once PV panel is heated by the solar radiation a mass density gradient arises in the fluid. As a consequence, ambient air enters the duct from the bottom and becomes heated owing to the contact both with the hot PV back surface and with the electronic equipment containing boxes surfaces. Air moves from the bottom opening to the top based on the generated buoyancy and chimney effects. This natural motion ensures air circulation to the air without the use of external machines, i.e. fans, to drive it. The heat transfer between the air and the surfaces delimiting the cavity was treated as the case of heat transfer between vertical planes. This topic is widely descripted in many heat transfer books. The prototype proposed in this work was analysed with known empirical formulas, such as the correlation between the convection heat transfer h [W/m^2] and the Reynolds number.

The model was developed considering the following considerations:

- the PV panel is not isothermal so it is cooled at the bottom where the air enters the duct;
- PV panel is faced outside while the building envelope inside so the two skins will experience different thermal conditions;
- the system comprises several material so different heat transfer mechanism will take place.

Fluid domain: air in the cavity

Energy equations for the fluid domain, under steady state conditions, can be

obtained replacing $\emptyset$ with $\emptyset_{T,f} = \rho_f \, c_{p,f} \, T$ in Eq. (5.12):

$$\nabla \cdot \left(\rho_f \, c_{p,f} \, T_f \cdot \boldsymbol{u}\right) = \nabla \left(\boldsymbol{\Gamma}_{\emptyset_{T,f}} \, \nabla(\rho_f \, c_{p,f} \, T)\right) + S_{\emptyset_{T,f}} \tag{5.33}$$

where

- $c_{p,f}$ is specific heat of the fluid [J/(kg K)];
- T_f is the fluid temperature [K];
- $\boldsymbol{\Gamma}_{\emptyset_{T,f}}$ is the second order thermal diffusivity tensor [m2/s];
- $S_{\emptyset_{T,f}}$ is the volumetric heat generation source/sink in the fluid [W/m3];
- $(\boldsymbol{\Gamma}_{\emptyset_{T,f}} \, \nabla(\rho_f \, c_{p,f} \, T)$ is the conduction heat flux in the fluid [W/m2].

A general statement of the conduction rate is expressed by the Fourier's law:

$$(\boldsymbol{\Gamma}_{\emptyset_{T,f}} \, \nabla(\rho_f \, c_{p,f} \, T) = \alpha_f \, \nabla\left(\rho_f \, c_{p,f} \, T\right) = \lambda_f \nabla(\, T) \tag{5.34}$$

where

- α_f is the thermal diffusivity of the fluid [m2/s];
- λ_f is the thermal conductivity of the fluid [W/(m K)].

According to Fourier's law the energy eq. (5.33) can be written as:

$$\frac{\partial(\rho_f \, c_{p,f} \, T u_j)}{\partial x_j} = \frac{\partial}{\partial x_j}(\lambda_f \frac{\partial T}{\partial x_i}) + S_{\emptyset_{T,f}} \tag{5.35}$$

For the air moving inside the air cavity $S_{\emptyset_{T,f}}$ includes the volumetric heat dissipated by the diode (eq5.3) and by the battery (eq.5.4)

$$S_{\emptyset_{T,f}} = q_d + q_b \tag{5.36}$$

Solid domain: PV panels and building envelope

Photovoltaic cells gain energy directly from solar irradiance. One part of incident irradiation is converted into useful electrical energy by means of the photoelectric effect. The rest of the incident solar energy is mostly accumulated on the PV panel

by absorption as heat gain; a smaller portion is reradiated to the surroundings.

Since the ambient is almost always at a lower temperature than the PV cell, heat tends to dissipate into the surroundings. This dissipation is not a simple issue so it varies due to many parameters such as air flow (direction and magnitude), average air temperature and surrounding relative humidity, reflectivity of surfaces, etc. The effect of backside convective thermal profile and its impact on temperature distribution, i.e., on panel efficiency is still among investigated topics. A PV panel can be treated as a heat source in a pure thermodynamic aspect. The main heat dissipation occurs at the front and back side, at glass and back plate surfaces, respectively. The front surface temperatures are usually higher than the back surface temperature. This difference in temperature is mainly due to the PV panel composition and the solar radiation levels.

For the PV panel a basic heat equation can be written as follow:

$$Q_{heat} + \nabla\left(\lambda_i \nabla(T_i)\right) = Q_{r,fr} + Q_{r,bk} + Q_{c,fr} + Q_{c,bk} \tag{5.37}$$

where

- Q_{heat} is the heat due to the photoelectrical dissipation rejected to the surrounding [W];
- $Q_{r,fr}$ is the radiative heat dissipation from the surrounding and the front side of the PV panel [W];
- $Q_{r,bk}$ is the radiative heat dissipation from the surrounding and the backside of the PV panel [W];
- $Q_{c,fr}$ is the convection heat dissipation from the surrounding and the front side of the PV panel [W];
- $Q_{c,bk}$ is the convection heat dissipation from the surrounding and the backside of the PV panel [W];
- λ_i is the thermal conductivity of each material constituting the PV module.

$$Q_{heat} = q_{PV} \cdot s_{PV} \cdot A_p \tag{5.38}$$

The radiative terms are given as follows:

$$\begin{cases} Q_{r,fr} = \varepsilon_{fr} \cdot A_p \cdot \sigma \cdot (T_{fr}^4 - T_{sur}) \cdot F_{fr} \\ Q_{r,bk} = \varepsilon_{bk} \cdot A_p \cdot \sigma \cdot (T_{bk}^4 - T_{sur}) \cdot F_{bk} \end{cases} \quad (5.39)$$

where

- ε_{fr} is the front side emissivity coefficient (assumed 0.91[744]) ;
- ε_{bk} is the back side emissivity coefficient (assumed 0.85 [745]);
- F is the view factor;
- T_{sur} is the average temperature of the surrounding [°C];
- σ is the Boltzmann constant.

In this work, the average of the surrounding was assumed to be the ambient temperature. In literature, mainly for the front side it is also be assumed to be the sky temperature.

$$\begin{cases} F_{fr} = \dfrac{1 + \cos(\beta)}{2} \\ F_{bk} = \dfrac{1 + \cos(\pi - \beta)}{2} \end{cases} \quad (5.40)$$

where β is the tilted angle (90° for vertical plane).

The convective terms are given as follows:

$$\begin{cases} Q_{c,fr} = h_{fr} \cdot A_p \cdot (T_{fr} - T_{sur}) \\ Q_{c,bk} = h_b \cdot A_p \cdot (T_{bk} - T_{fsur}) \end{cases} \quad (5.41)$$

where

- h_{fr} is the front side convective heat transfer coefficient [W/(m2K)];
- h_{bk} is the back side convective heat transfer coefficient;
- T_{fr} is the average temperature of the front glass [°C];
- T_{bk} is the average temperature of the back glass [°C];

In most of the developed studies it was found that heat convection and thermal radiation are almost in the same order of magnitude. As an example, Nizetic et al. [746] found that around 57% of heat transfer was due to the convection and the rest due to the thermal radiation. According to it, in the developed model the thermal radiation was not neglected.

The convective heat transfer coefficient to surrounding air is not the same on the front and back side of the PV panel due to the presence of the duct. In contrast to the front side, in the backside the convective can be assumed natural. Outside and inside heat transfer coefficients are different due to the different temperature of the vertical surfaces delimiting the prototype.

The magnitude of the convection heat losses is proportional to the temperature difference between the surrounding air and the photovoltaic panel surface.

The estimation of the convective heat transfer coefficients is still now a challenge and many authors, based on experimental data, derived correlations to describe the thermal conditions of a BIPV system.

$$\begin{cases} h_{fr} = f(Re, Pr) \\ h_{bk} = f(Gr, Pr) \end{cases} \tag{5.42}$$

where

- Re is the Reynolds number;
- Pr is the Prandtl number;
- Gr is the Grashof number.

$$Re = \frac{\rho_f \cdot u \cdot D_{eq}}{\mu_f} \tag{5.43}$$

$$Pr = \frac{\mu_f \cdot c_{p,f}}{\lambda_f} \tag{5.44}$$

$$Gr = \frac{\rho_f^2 \cdot D_{eq}^3 \cdot g \cdot \beta_f \cdot (T_{bk} - T_f)}{\mu_f^2} \tag{5.45}$$

where

- D_{eq} is the equivalent diameter [m];
- B_f is the volumetric coefficient of thermal expansion [1/K].

The following equations given by Churchill and Chu for were used to estimate forced and natural convection coefficients over vertical plates [747]:

$$h_{natural} = \begin{cases} \dfrac{2 \cdot \lambda_f}{D_{eq}} \cdot \dfrac{0.3387 \cdot Pr^{1/3} \cdot Re^{1/2}}{\left(1 + \left(\dfrac{0.0468}{Pr}\right)^{2/3}\right)^{1/4}} & if\ Ra \leq 5 \cdot 10^5 \\ \dfrac{2 \cdot \lambda_f}{D_{eq}} \cdot Pr^{1/3} \cdot \left(0.037 \cdot Re^{4/5} - 871\right) & if\ Ra > 5 \cdot 10^5 \end{cases} \tag{5.46}$$

$$h_{forced} = \frac{\lambda_f}{D_{eq}} \cdot \left\{0.825 + \frac{0.387 \cdot Ra^{1/6}}{[1 + (0.492/Pr)^{9/16}]^{8/27}}\right\}^2 \tag{5.47}$$

where Ra is the Rayleigh number

$$Ra = Gr\ Pr \tag{5.48}$$

Equation 5.46, derived for vertical plates, can be adapted for inclined plates by multiplying for $cos\theta$, where θ is the angle of inclination from the vertical.

For the front glass natural convection conditions can be occurred. For the determination of the kind of convection it was applied the following criterion based on the ratio Gr/Re^2 [740]:

$$\begin{cases} \ll 1\ forced\ convection; \\ \gg 1\ natural\ convection; \\ (0.01, 100)\ combined\ convection \end{cases} \tag{5.49}$$

Surely, on days with little or no wind, the free convection is more significant. This

assumption is especially reasonable in cold climates where the temperature difference between the air and the panel surface may be relatively large. In situations of combined convection, the effective convection heat transfer coefficient (for the front surface of the PV panel) can be obtained as the combination of the free and forced convection as suggested in [747]:

$$h_{front} = \sqrt{h_{natural}^3 + h_{forced}^3} \tag{5.50}$$

Another expression widely used is that one proposed by Jones and Underwood [748]:

$$h_{front} = h_{forced} + h_{natural} \tag{5.51}$$

Heat transfer in the wall of the building is assumed pure conductive. Governing equation can be obtained from eq. 5.33 replacing the fluid properties with the solid properties and setting to zero the velocity:

$$\nabla \left(\lambda_{wall} \nabla (T_{wall}) \right) = 0 \tag{5.52}$$

Radiative heat transfer was assumed on the external wall (emissivity 0.75). BIPV strongly influences the heat transfer through the building envelope due to the change of the thermal resistance of the various building components.

Equations 5.15,5.31 and 5.33 with appropriate boundary conditions allow to describe in a completely exact way the behavior of a fluid both in laminar and turbulent conditions. In case a system exhibits a turbulent behavior, it is crucial the space-time resolution of the conditions that must be fulfilled so that the transfer of mechanical energy from the largest scales to those ones referred as “dissipative scales” is properly simulated. It is known that turbulence has an inherently complex and stochastic nature. In detail the behavior of a real fluid is extremely complex, for this reason, in this work is analyzed a fluid equivalent to the real one. This fluid with appropriate reformulated boundary conditions has a space-time behavior regular and predictable sufficiently. The equivalent fluid represents in a statical sense the real

one. Reynolds average Navier Stokes (RANS) k-ε is the turbulent modelling approached used in this work. RANS modelling is based on temporal filtering of the flow field through a linear operator acting as a filter function G(t,t') [749,750]. Applied to a generic quantity $\varphi(x,t)$, G(t,t') allows the Reynolds decomposition into a filtered component (average component) $< \varphi(x,t) >$ and a fluctuating component (residual or not resolved component) $\varphi'(x,t)$:

$$\varphi'(x,t) = \varphi(x,t) - < \varphi(x,t) > \tag{5.53}$$

Replacing $\varphi(x,t)$ with $u(x,t)$ the Navier equations can be expressed as follow:

$$\frac{\partial \rho_f \langle u_i \rangle \langle u_j \rangle}{\partial x_j} + \frac{\partial \langle p \rangle}{\partial x_i} = \frac{\partial}{\partial x_j}\left(\mu' \left(\frac{\partial \langle u_i \rangle}{\partial x_j} + \frac{\partial \langle u_j \rangle}{\partial x_i}\right)\right) - \frac{\partial \rho_f (\langle u_i u_j \rangle - \langle u_i \rangle \langle u_j \rangle)}{\partial x_i} \tag{5.54}$$

where $\langle u_i u_j \rangle - \langle u_i \rangle \langle u_j \rangle$ are the Leonard coefficients.

$$\mu' = \mu_f + \mu_t \tag{5.55}$$

where μ_t is the sub-grid or turbulent fluid dynamic viscosity [Pa s].

The presence of μ_t poses an analytical closure problem, several RANS models have been developed with the aim to express this term as function of resolved average quantities. The k-epsilon (k-ε) model is among the most used RANS model implemented in CFD codes. This model expresses μ_t as follow:

$$\mu_t = \rho_f \, C_\mu \frac{k^2}{\varepsilon} \tag{5.56}$$

where k is the turbulent kinetic energy, ε its dissipation and C_μ a constant (~0.1).

ε is obtained resolving the differential transport equations containing the term of generation, destruction, convection / diffusion and temporal variation.

The k-epsilon (k-ε) model is based on the implementation of the following two equations concerning k and ε respectively (turbulent Navier Stokes equations):

$$\begin{cases} \dfrac{\partial \rho_f \mathrm{k}}{\partial \mathrm{t}} + \dfrac{\partial \rho_f \langle \mathrm{u_i} \rangle \mathrm{k}}{\partial \mathrm{x}_i} = \dfrac{\partial}{\partial x_j}\left[\left(\mu_f + \dfrac{\mu_t}{\sigma_k}\right) \cdot \dfrac{\partial \mathrm{k}}{\partial \mathrm{x}_j}\right] + P - \rho_f\, \varepsilon \\ \dfrac{\partial \rho_f \varepsilon}{\partial \mathrm{t}} + \dfrac{\partial \rho_f \langle \mathrm{u_i} \rangle \varepsilon}{\partial \mathrm{x}_i} = \dfrac{\partial}{\partial x_j}\left[\left(\mu_f + \dfrac{\mu_t}{\sigma_\varepsilon}\right) \cdot \dfrac{\partial \varepsilon}{\partial \mathrm{x}_j}\right] + C_1 \cdot \dfrac{\varepsilon}{k} \cdot P - C_2 \cdot \dfrac{\varepsilon^2}{k} \cdot \rho_f \end{cases} \tag{5.57}$$

where σ_k is the turbulent Prandtl number for k, P is the production term of k, σ_ε is the turbulent Prandtl number for ε, $C_1$and C_2two corrective terms. Simulations were conducted assuming the following values: $\sigma_k = 1$, $\sigma_\varepsilon = 1.3$; $C_1 = 1.44$, $C_2 = 1.92$.

Manipulations similar to those described for the Navier-Stokes equations (5.31) can be repeated for the heat transport equation (5.33).

2.3 Electrical aspects

The thermal behavior of the prototype is strongly correlated to the electrical performance of the PV module. The development of an electrical model was out the aim of this work. Electrical values to be used as input of the model were or experimentally evaluated or calculated using existing correlation in order to avoid a further computational effort.

As shown in Figure 102 a solar cell can be represented by an equivalent circuit composed of a current source, an anti-parallel diode (D), a shunt/parallel resistance (R_p) and a series resistance (R_s).

This circuit has the aim to represent the electrical behavior of the PV panel arising from its structure. It is known that a photovoltaic panel is made up of two layers of doped semiconductor material, i.g. silicon, electrically connected to two metallic electrodes deposited on the outer surfaces. On the upper surface there are several metal elements, the fingers, whose position must maximize the absorbing face.

A PV cell can be sketched as a current source of intensity I_{ph} connected in parallel with a diode. In particular, when the PV panel is not illuminated, it behaves as a diode while, in contrast, the illumination generates in the semiconductor junction electron hole pairs yielding the photocurrent. I_{ph} and I_D are not constant, in fact, I_{ph}depends

on the solar irradiation while $I_D$on the cell temperature. R_p and R_s allow to account for dissipative effects causing parasite currents within the PV panel.

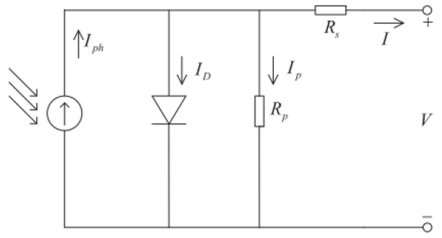

Figure 102: Equivalent circuit for a solar cell [751].

A photovoltaic generator is usually modeled by the relationship between current I and voltage V based on the Shockley diode [751]:

$$I = I_{ph} - I_D \cdot \left(e^{\frac{V+I \cdot R_s}{V_t}} - 1 \right) - \frac{V + I \cdot R_s}{R_p} \tag{5.58}$$

where

- I_{ph} is the photocurrent [A];
- I_D is the diode saturation current [A];
- V_t is the diode thermal voltage [V].

Eq. 5.50 is obtained handling the five equations obtained under the following conditions :

Short circuit point:

$$\begin{cases} I = I_{sc} \\ V = 0 \end{cases} \tag{5.59}$$

Open circuit point:

$$\begin{cases} I = 0 \\ V = V_{ocv} \end{cases} \tag{5.60}$$

Maximum power point:

$$\begin{cases} I = I_{MP} \\ V = V_{MP} \end{cases} \tag{5.61}$$

Derivative at the short circuit point:

$$\left(\frac{dI}{dV}\right)_{V=0, I=I_{sc}} = -\frac{1}{R_P} \tag{5.62}$$

Derivative at the open circuit point:

$$\left(\frac{dI}{dV}\right)_{V=V_{oc}, I=0} = -\frac{1}{R_s} \tag{5.63}$$

When a PV module is directly coupled to a load the PV module's operating point will be at the intersection of its *I–V* curve and the load line which is the *I–V* relationship of load. In general, the optimal intersection occurs at one particular operating point, called Maximum Power Point (MPP). The location of the MPP in the I–V plane changes dynamically depending on irradiance and temperature [752]. The analysis of the available current-voltage curves given by the manufactures don't allow to have a correct evaluation of the thermoelectrical behavior of a panel since these curves are obtained or at constant radiation or at constant temperature. The operation mode of the panel affects strongly the effectiveness of solar energy conversion into electrical energy. When the panel is connected to load , it makes the panel to work in a regime far away from the saturation condition. It is widely demonstrated that a quasi linear correlation between the power output and the solar radiation can be established: the power is maximum when the insulation is maximum.

In this work ,the panel was simulated as connected to an optimized and variable electrical load (maximum power tracking system).

Performing a parametric analysis, Lo Brano et al. [753] extrapolated the following logarithmic correlation between the maximum power voltage and the solar radiation:

$$V_{MPP} = 1.1686617 \cdot \ln\left(\frac{G}{G_{ref}}\right) + 23.5974267 \quad (5.64)$$

In order to optimize a BIPV power generation the adoption of a distributed MPPT approach, using a dc-dc converter per each panel, is suggested in literature overcoming major drawbacks due to the effect of module mismatching and of partial shading of the BIPV.

2.4 Simulation Strategy

Several simulations were carried out using the real weather data measured from the experimental procedure reported in the section 2.2. A complete three-dimensional CFD model was developed to investigate fluid flow and heat transfer of the prototype.

Simulations were computed by the Finite Element COMSOL Code and validated based on experimental data.

The computational analysis was carried out on three steps:

- The single PV panel, vertically arranged, was analyzed without the air cavity to study the effects of the heat transfer coefficients. Simulations were carried out for different weather conditions.
- The best heat transfer coefficients identified were used to investigate the thermal behavior of a ventilated façade. The effects of geometry dimensions on the thermal efficiency were investigated.
- The ventilated façade was evaluated simulating heat sources within it. A comparison among the three scenarios was reported and discussed.

3. Free PV Panel

The free convection of the PV panel to predict the temperature profile both backside and the frontside was simulated. As previously mentioned, the temperatures of both sides of the panel were measured during the experimental tests.

According to the several works in literature, an accurate prediction of temperature distribution in a photovoltaic panel depends mainly on two important parameters: the electrical output power and the convection heat transfer coefficient.

Free panel was investigated to try to find the best correlation for convective heat transfer coefficient with different operating conditions. To find an accurate and general expression is not simple due to the complexity of the three-dimensional wind flow and temperature distribution around the PV panel.

The analysis of the free panel was carried out not only to obtain the local heat transfer coefficient and temperature at each point but also to have a better understood of the convection transport at different environmental conditions.

3.1 Geometry and grid dependence

Figure 103 shows the geometry realized using COMSOL -CAD with a detail of the mesh used for the simulations. The characteristics of the shown panel are listed in Table 12. The geometry model consists of five solid domains: front cover, encapsulant, PV cells, encapsulant, back sheet. They are included in a metal frame in aluminum, the effects of which were not included since its surface, low in comparison to the pane area, has a negligible effect on the thermal response.

To carry out the CFD simulations a grid of about 50k elements was chosen after a grid dependence analysis. This sensitivity analysis was carried out since the accuracy of the simulations is linked to the mesh size. In particular, higher is the number of elements (mesh size decreasing) better is the accuracy toward the exact solution implemented. Increasing the number of elements will provide a more accurate solution but will also increase the computation resources required.

Un unstructured grid with tetrahedral cells was applied to PV layer, the mesh in the remaining domain was obtained by the function “Swept” in the axial direction (x). For each layer of the panel, it was chosen a number of swept elements of 10. The finest mesh was created at the vicinity of the PV module.

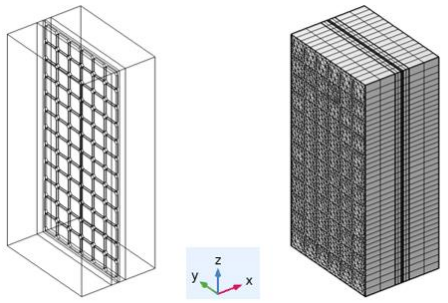

Figure 103: Geometry and mesh used for CFD simulations.

Grid dependency was carried out with the aim to minimize the discrepancy ε between approximated and exact solution. ε is given as follows:

$$\varepsilon\% = \frac{\left|x_i - x_{ref}\right|}{x_{ref}} \cdot 100 \tag{5.65}$$

where x_{ref} is the parameter value obtained with the finest grid.

The criterion used to select the grid for the final simulations was an average discrepancy below 1% in the predicted values of the average module temperature.

The grid dependency was performed by increasing the number of elements of the size mesh. In Table 24 are listed the inputs used for grid sensitivity analysis while results of the performed grids are listed in Table 25.

Results of Table 25 shown that thermal response is not strongly affected by the size of the grid. According to the discrepancy criterion, it was chosen the normal mesh to avoid a high computational effort so its $\varepsilon < 1\%$.

Table 24: CFD conditions for mesh dependency.

Solar Radiation [W/m^2]	1000
Air Temperature [°C]	20
Wind velocity [m/s]	1
Wind direction	90°(windward)
PV efficiency % [-]	0.14

Table 25: Grid dependency results.

Mesh	Number of elements	$T_{av}[°C]$	ε%
Coarse	140k	47.961	0.015
Normal	240k	47.959	0.010
Fine	520k	47.954	-

A model of infinite elements is the better choice but, at the same time, it is not convenient from the point of view of the computational effort. Limits imposed by finite computational resources and time suggest finding not the exact solution but the best approximation of the real solution.

3.2 Model validation

A first validation of the proposed thermal model was carried out using manufacturer data. In particular, the normal operating conditions temperature (NOCT) were simulated, the predicted average cell temperature was compared to the value provided in the module datasheet. Results reported in Table 26 show that the error between the NOCT reported in the datasheet and that one predicted by the model is less than 1%. Figure 104 shows the thermal distribution obtained in NOCT conditions (horizontally placed panel).

Table 26: Model validation in NOCT conditions.

Solar Radiation [W/m^2]	1000
Air Temperature [°C]	25
Wind velocity [m/s]	1
NOCT_datasheet [°C]	44
NOCT_model [°C]	44.29

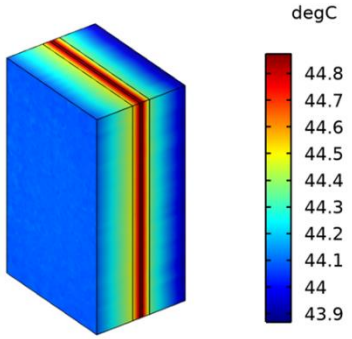

Figure 104: Temperature distribution in NOCT conditions.

As expected, the thermal distribution in not uniform for the entire module. A second validation was carried out by the comparison of the backsheet temperatures (T_{bk}) evaluated during the MPPT characterization tests (chapter 4 section 2.4) with those ones obtained with the model.

Results reported in Table 27 show that the average discrepancy between the compared values is less than 4%. The validated and calibrated model was used to develop the temperature profile of the PV module under different environmental conditions of solar radiation intensity, ambient temperature and wind velocity.

Table 27: Model validation in MMPT conditions.

	Test 1	**Test 2**	**Test 3**	**Test 4**
Solar Radiation [W/m^2]	163	160	171	185
Air temperature [°C]	24.5	24	25	26.8
Experimental_T_{bk} [°C]	29.3	29	30.1	31.3
Model_T_{bk} [°C]	30.12	29.61	30.96	31.25

Figure 105 shows a comparison between the numerical results and the experimental data during a test of about three hours.

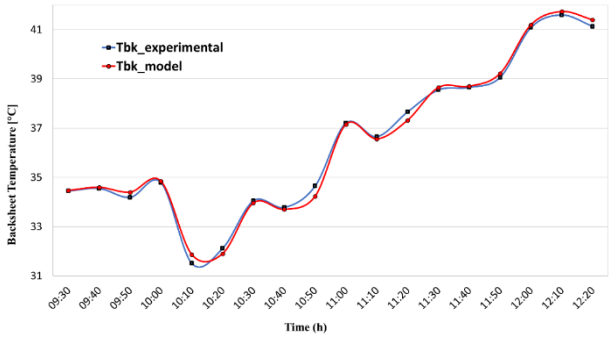

Figure 105: Comparison between experimental and numerical data.

Experimental data (averaged every ten minutes) are listed in Table 28.

Table 28: Experimental data simulated.

Time	G [W/m^2]	Wind velocity [m/s]	T_air [°C]
09:30	109.55	2.46	27.56
09:40	114.39	2.53	27.44
09:50	122.79	3.85	27.46
10:00	117.58	3.75	28.07
10:10	75.74	2.91	27.08
10:20	115.72	5.71	27.53
10:30	145.74	5.82	29.44
10:40	101.63	4.69	28.3
10:50	167.42	6.34	30.43
11:00	160.64	5.88	31.29
11:10	154.24	5.86	30.85
11:20	202.57	5.95	31.21
11:30	117.59	5.81	29.99
11:40	200.21	5.85	30.16
11:50	208.94	5.86	30.32
12:00	255.68	5.96	32.06
12:10	250.26	5.89	31.29
12:20	220.175	5.86	30.66

To validate the results produced from the numerical model the following statistical metrics were evaluated (Table 29):

Mean bias error (MBE):

$$MBE = \frac{\sum_{i=1}^{N}(y_i - x_i)}{N} \tag{5.66}$$

Root mean square error (RMSE):

$$RMSE = \left[\frac{\sum_{i=1}^{N}(y_i - x_i)^1}{N}\right]^{0.5} \tag{5.67}$$

Correlation coefficient (CC):

$$CC = \frac{\sum_{i=1}^{N}(y_i - y_{av}) \cdot (x_i - x_{av})}{\left\{\left[\sum_{i=1}^{N}(y_i - y_{av})^2\right] \cdot \left[\sum_{i=1}^{N}(x_i - x_{av})^2\right]\right\}^{0.5}} \tag{5.68}$$

MBE/AV:

$$MBE/AV = \frac{MBE}{x_{av}} \tag{5.69}$$

RMSE/AV:

$$RMSE/AV = \frac{RMSE}{x_{av}} \tag{5.70}$$

where

- y_i is the ith predicted value;
- x_i is the ith measured value;
- y_{av} is the predicted mean value;
- x_{av} is the measured mean value;

- N is the number of data analyzed.

Table 29: Model validation for the backsheet temperature.

$MBE\ (°C)$	0.01
$RMSE\ (°C)$	0.19
CC	1
$MBE/AV\ (\%)$	0.03
$RMSE/AV\ (\%)$	0.01

3.3 Effect of the heat transfer coefficients

In the following tables (Table 30-Table 34) is reported a comparison of the results obtained by using for the front side heat transfer coefficient some correlations available in literature instead of the complex correlation given by eq. (5.45).

The choice of the heat transfer coefficients is the most critical aspect of the thermal model. In literature there are several expressions of the heat transfer coefficients evaluated under different conditions. It is difficult to find the best correlation among the available ones. Most of the available coefficients have been derived based on experimental data so their empirical nature has the effect to produce different results.

Tables show how the accurate prediction of temperature distribution in a PV panel is strongly affected by the choice of the heat transfer coefficients, always correlated to wind velocity. In the following are listed the most used forms in literature:

- Linear equation form:

$$h = a + b\ v_w \tag{5.71}$$

- Power law equation form:

$$h = a + b\ {v_w}^n \tag{5.72}$$

- Boundary layer equation form:

$$\begin{cases} h = f(Nu) \\ Nu = a\ Re^m Pr^n + b \end{cases} \tag{5.73}$$

Table 30: Backsheet temperature for different heat transfer coefficients.[744].

Time	$T_{bk,model}$[°C]	$T_{bk,\text{Mc Adams}}$[°C]	$T_{bk,\text{Lunde}}$[°C]
09:30	34.90	31.79	32.46
09:40	35.04	31.80	32.50
09:50	34.98	31.34	32.06
10:00	35.32	31.86	32.53
10:10	32.17	29.86	30.32
10:20	33.08	30.53	31.11
10:30	35.06	33.15	33.86
10:40	34.36	31.24	31.78
10:50	35.32	34.47	35.25
11:00	37.97	35.34	36.12
11:10	37.35	34.75	35.50
11:20	37.72	36.24	37.19
11:30	34.89	33.01	33.59
11:40	40.05	35.17	36.15
11:50	40.73	35.53	36.55
12:00	43.11	38.33	39.51
12:10	44.43	37.48	38.66
12:20	42.37	36.14	37.21

Mc Adams et al.:

$$h = 3.8 \cdot v_w + 5.7$$

Lunde et al.

$$h = 2.9 \cdot v_w + 4.5$$

Table 31: Backsheet temperature for different heat transfer coefficients [744].

Time	$T_{bk,model}$ [°C]	$T_{bk,\text{Sharples}}$ [°C]	$T_{bk,\text{Watmuff}}$ [°C]
09:30	34.90	31.86	32.83
09:40	35.04	31.88	32.87
09:50	34.98	31.48	32.31
10:00	35.32	32.00	32.78
10:10	32.17	29.93	30.54
10:20	33.08	30.70	31.24
10:30	35.06	33.35	34.01
10:40	34.36	31.38	31.94
10:50	35.32	34.70	35.40
11:00	37.97	35.57	36.29
11:10	37.35	34.97	35.66
11:20	37.72	36.51	37.39
11:30	34.89	33.18	33.72
11:40	40.05	35.44	36.36
11:50	40.73	35.82	36.77
12:00	43.11	38.68	39.78
12:10	44.43	37.81	38.91
12:20	42.37	36.44	37.43

Sharples et al.:

$$h = 2.2 \cdot v_w + 8.3$$

Watmuff et al.:

$$h = 3.0 \cdot v_w + 2.8$$

Table 32: Backsheet temperature for different heat transfer coefficients [744].

Time	$T_{bk,model}$[°C]	$T_{bk,Cole}$[°C]	$T_{bk,Sparrow}$ [°C]
09:30	34.90	30.56	33.87
09:40	35.04	30.54	33.97
09:50	34.98	30.23	33.80
10:00	35.32	30.76	34.19
10:10	32.17	29.08	31.40
10:20	33.08	29.71	32.96
10:30	35.06	32.10	36.13
10:40	34.36	30.43	33.35
10:50	35.32	33.34	37.86
11:00	37.97	34.20	38.57
11:10	37.35	33.65	37.87
11:20	37.72	34.83	40.22
11:30	34.89	32.18	35.46
11:40	40.05	33.77	39.13
11:50	40.73	34.08	39.64
12:00	43.11	36.59	43.23
12:10	44.43	35.75	42.28
12:20	42.37	34.61	40.44

Cole et al.

$$h = 5.7 \cdot v_w + 11.4$$

Sparrow et al.

$$h = 4.96 \cdot {v_w}^{0.5} {D_{eq}}^{-0.5}$$

Table 33: Backsheet temperature for different heat transfer coefficients [744].

Time	$T_{bk,model}$[°C]	$T_{bk,Nolay}$[°C]	$T_{bk,Armstrong}$ [°C]
09:30	34.90	31.66	31.82
09:40	35.04	31.63	31.85
09:50	34.98	31.20	31.59
10:00	35.32	31.69	32.10
10:10	32.17	29.77	29.94
10:20	33.08	30.42	30.90
10:30	35.06	33.00	33.60
10:40	34.36	31.13	31.51
10:50	35.32	34.31	35.00
11:00	37.97	35.18	35.84
11:10	37.35	34.60	35.23
11:20	37.72	36.04	36.86
11:30	34.89	32.89	33.38
11:40	40.05	34.97	35.80
11:50	40.73	35.33	36.19
12:00	43.11	36.59	39.10
12:10	44.43	35.75	38.22
12:20	42.37	34.61	36.83

Nolay et al.

$$h = 4.1 \cdot v_w + 5.8$$

Armstrong et al.

$$h = 2.56 \cdot v_w + 8.55$$

Table 34: Backsheet temperature for different heat transfer coefficients [744].

Time	$T_{bk,model}$**[°C]**	$T_{bk,Skoplaki}$**[°C]**	$T_{bk,Charlesworth}$ **[°C]**
09:30	34.90	31.48	31.86
09:40	35.04	31.47	31.88
09:50	34.98	30.87	31.48
10:00	35.32	31.38	32.00
10:10	32.17	29.61	29.93
10:20	33.08	30.04	30.70
10:30	35.06	32.54	33.35
10:40	34.36	30.82	31.38
10:50	35.32	33.78	34.70
11:00	37.97	34.67	35.57
11:10	37.35	34.11	34.97
11:20	37.72	35.41	36.51
11:30	34.89	32.51	33.18
11:40	40.05	34.35	35.44
11:50	40.73	34.68	35.82
12:00	43.11	37.31	38.68
12:10	44.43	36.47	37.81
12:20	42.37	35.25	36.44

Skoplaki et al.

$$h = 5.7 \cdot v_w + 2.8$$

Charlesworth et al.

$$h = 3.3 \cdot v_w + 6.5$$

All simulations reported from Table 30 to Table 34 were performed supposing for the front surface “forced convection”. Really the exact prediction of the kind of flow is a complex operation due to the high variability of the wind velocity and its direction. As a consequence, on the front surface a condition of mist flow is not excluded. Table 35 shows a comparison of the thermal response of the panel under different heat transfer convection modes. The simulations were performed under the following conditions:

- Solar irradiation: 1000 W/m2;
- Wind velocity: 1 m/s;
- Air temperature: 25 °C;
- Sky temperature = Air Temperature.

Table 35: Backsheet temperature under different heat transfer convection conditions.

	T_{bk}[°C]
Test A	74.01
Test B	69.54
Test C	63.84

- Test A: forced convection on the front surface and natural convection on the backside;
- Test B: natural convection on both surfaces of the PV panel;
- Test C: mixed convection on the front surface and natural convection on the backside.

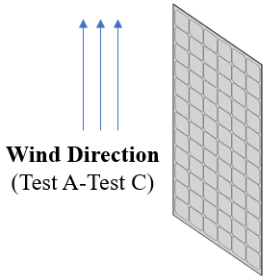

3.4 Effect of the wind

Effect of the wind on cooling was evaluated simulating the experimental conditions reported in Table 36. Figure 106-Figure 107 show the results.

Table 36: Experimental data simulated to study the effect of the wind.

Time	G [W/m^2]	Peak Power[W]
09:30	107.95	33.02
09:40	111.26	33.66
09:50	117.81	35.95
10:00	129.3	39.07
10:10	68.3	21.37
10:20	113.11	35.45
10:30	145.01	44.33
10:40	140.03	41.11
10:50	138.08	36.07
11:00	186.64	51.07
11:10	136.5	43.17
11:20	195.91	55.51
11:30	221.52	57.47
11:40	209.52	64.25
11:50	227.43	69.72
12:00	249.01	81.55
12:10	255.22	77.17
12:20	256.75	76.83
12:30	128.46	38.69

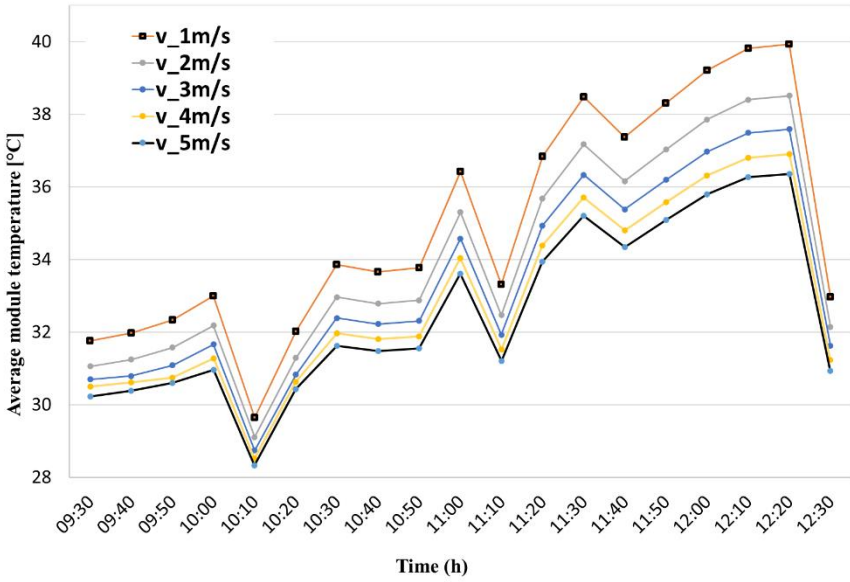

Figure 106: Average temperature of the PV module for different velocity and solar radiation values (Air temperature=25°C).

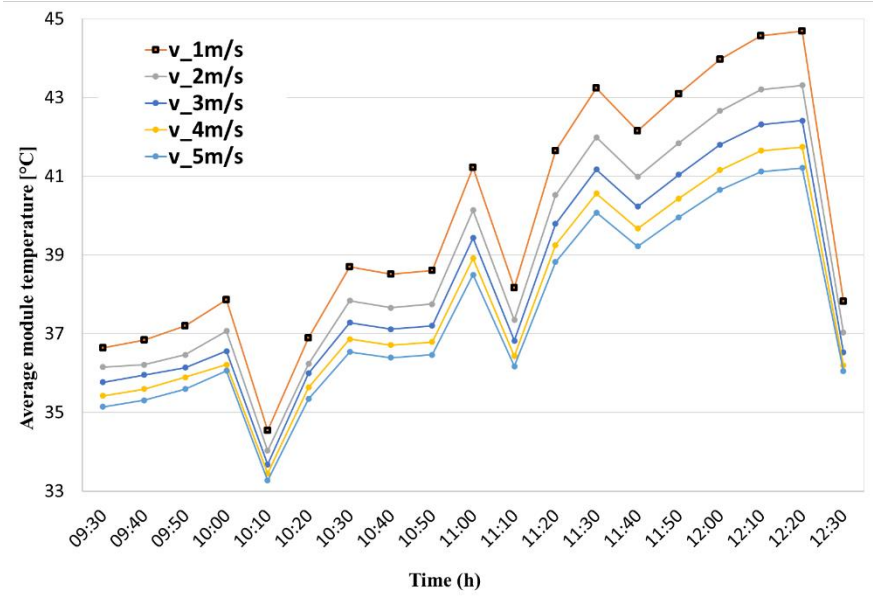

Figure 107: Average temperature of the PV module for different velocity and solar radiation values (Air temperature=30°C).

4. Ventilated Façade without heat sources

The thermal model developed in the previous section it was used to evaluate the thermal response of the ventilated façade shown in Figure 108. The characteristic of the PV panel used are listed in Table 37.

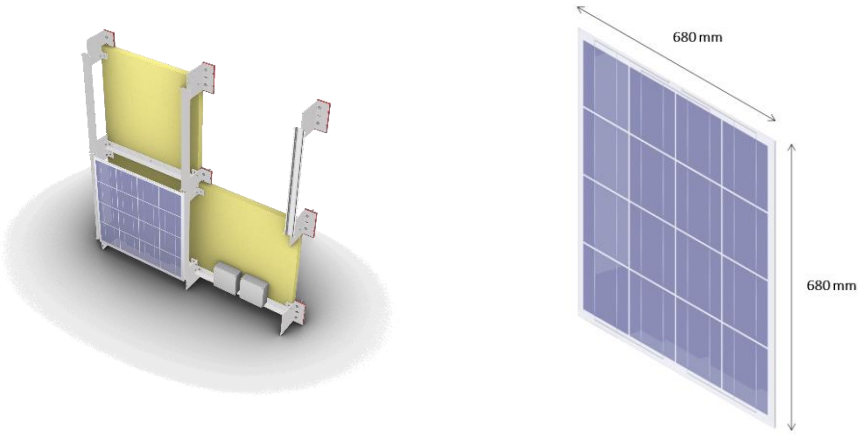

Figure 108: Ventilated façade structure.

Table 37: Datasheet of the PV modules installed in the ventilated façade.

	PV Panel 1
Technology	Si-poly
Cells number	16
Dimensions (mm×mm)	680×680
Maximum power Pmax(W)	64
Nominal current (A)	7.5
Temperature coefficient of I_{sc} (mA/K)	4.36
Nominal voltage (V)	8.5
Temperature coefficient of OCV (mV/K)	-122
Efficiency %	14.5

4.1 Geometry and grid dependence results

Figure 109 shows the geometry realized using COMSOL -CAD with a detail of the mesh used for the simulations.

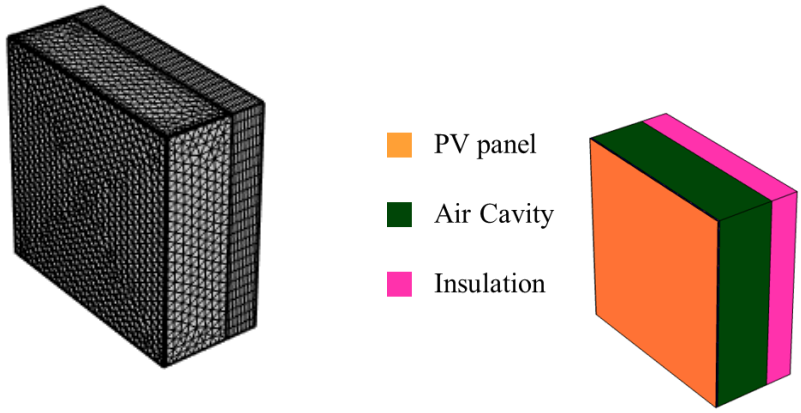

Figure 109: Geometry and mesh used for simulations of the ventilated façace.

Grid dependency was carried out using, as inputs, the data reported in Table 28.

To vary the number of elements in the air and insulation domain it was used the function “Swept” in the axial direction (x). For each layer of the panel, it was chosen a number of elements of 5 (Table 38).

Table 38: Grid dependency analysis results.

Mesh	Number of elements	$T_{bk}[°C]$	$\varepsilon\%$
MA	30K	64.84	3.10
MB	45K	65.36	2.32
MC	65k	66.05	1.28
MD	100k	66.91	0.00

Results of Table 38 show that thermal response of the PV panel is not strongly

affected by the size of the grid. According to the criterion to have a discrepancy $\varepsilon < 2\%$, it was chosen the MC mesh to avoid a high computational effort.

For the simulated four meshes is, furthermore, reported in Figure 110 the thermal profile of the backsheet that better shows the low dependency of the thermal response of the PV panel by the size of the mesh. Thermal profile, moreover, shows the better similarity of the chosen mesh with the finest one.

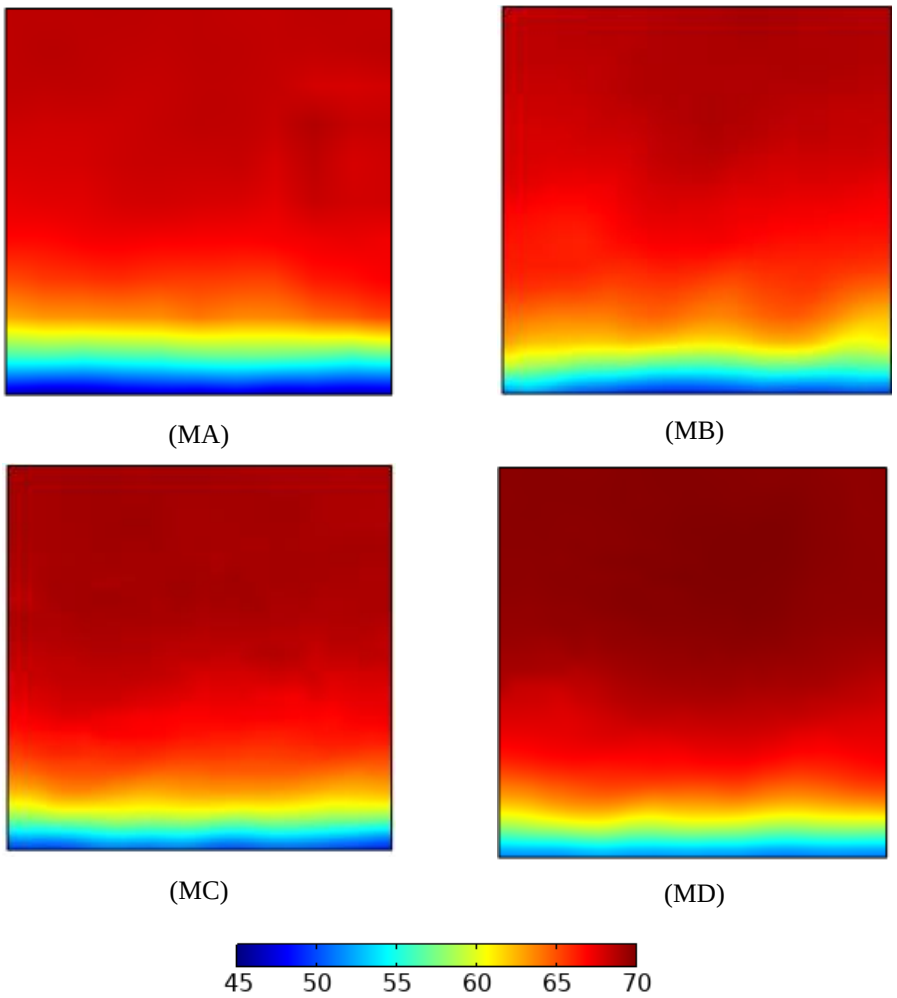

Figure 110: Thermal profile of the backsheet as function of the mesh size.

4.2 Effect of the air cavity on the PV cooling

Figure 111-Figure 112 show the cooling effect of the air cavity. Simulations were performed using the experimental data reported in Table 28.

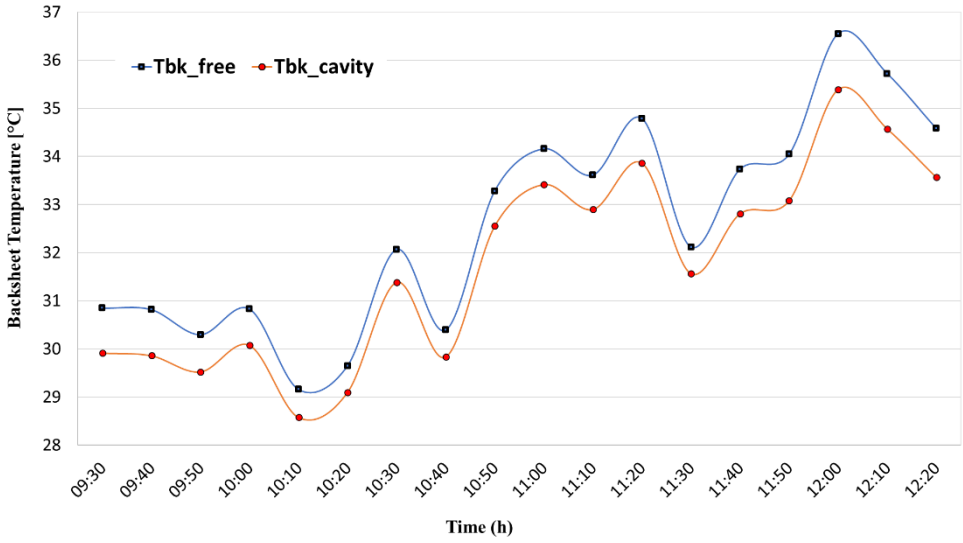

Figure 111: Effect of the air gap on the backsheet temperature.

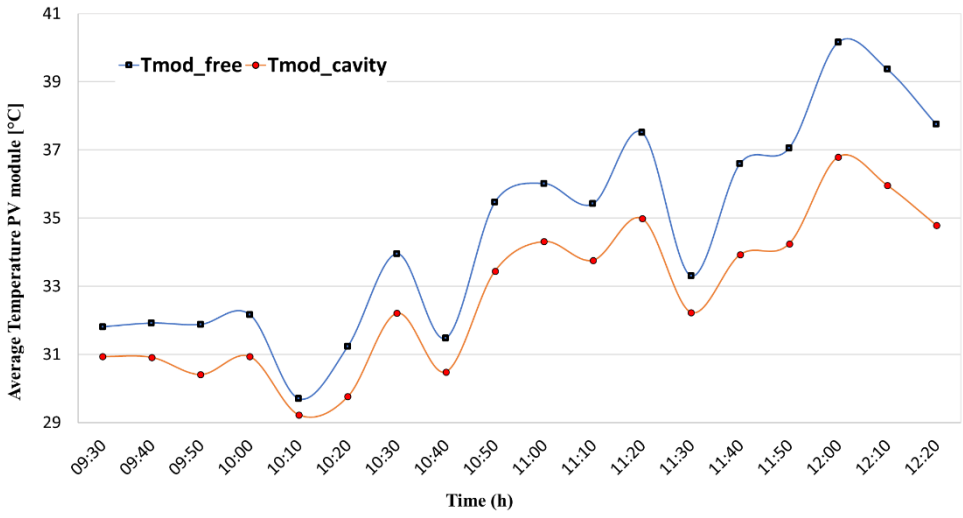

Figure 112: Effect of the air gap on the average temperature of the PV module.

As expected, the backsheet temperature is lower with the presence of the air gap due to the induced convection. The maximum reduction in the backsheet temperature evaluated was of 0.4% while in the entire module of 1.1%.

The temperature difference between the panel and the building envelope (insulation) generates buoyancy to push up the channel air and remove part of the heat by natural convection. A part of the heat energy will be transmitted into the indoor space by means of thermal conduction through the wall of the building. The outdoor air can flow into the air cavity generating force convection and removing the heat both the PV and the insulation. A mixed convection mechanism is generated within the air cavity. Figure 113 shows the effect of the air gap on PV efficiency. As expected, since the average temperature of the module decreases the efficiency increases. The maximum increase of 1.73% was evaluated for a value of G of 250.26 [W/m2], air velocity of 6 m/s and air temperature of 31 °C. The trend of the photovoltaic producibility, here not reported, is the same order of that one of the efficiencies. Producibility per unit area P_{PV} is given as:

$$P_{PV} = G_{PV} \cdot \alpha_{glass} \cdot \eta_{PV} \tag{5.74}$$

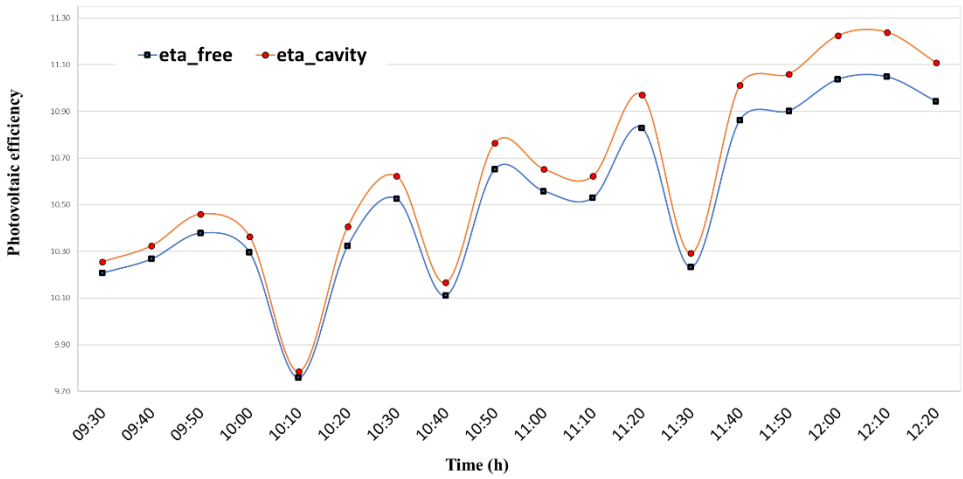

Figure 113: Effect of the air gap on the average temperature of the PV efficiency.

4.3 Parametric analysis on different conditions

The developed model was used to perform a wide range of parametric analyses on different climate and boundary conditions to explore its viability.

4.3.1 Effect of the wind module

Figure 114 shows the thermal performance of the module obtained under velocity wind of 1 m/s for different values of the solar radiation.

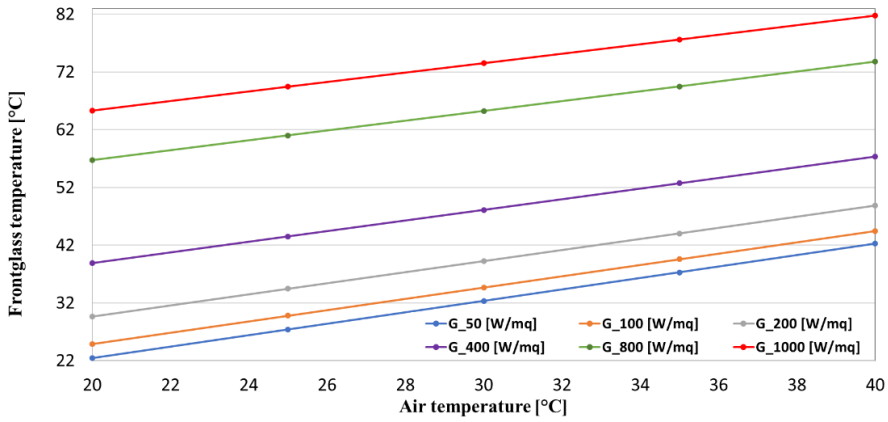

(a)

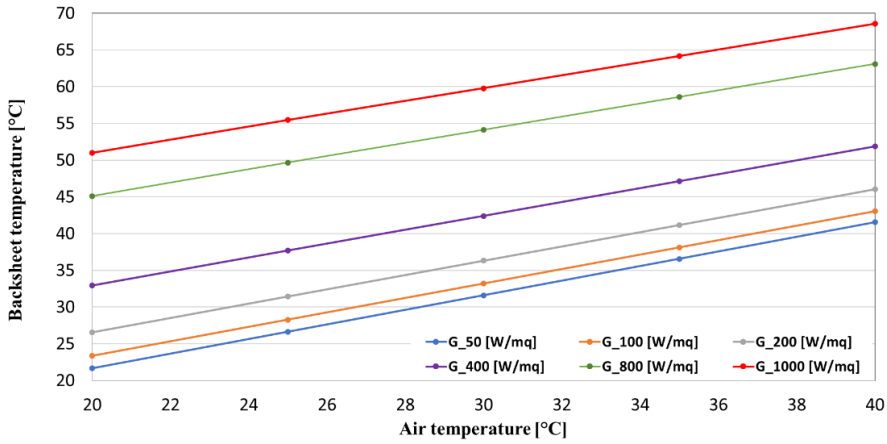

(b)

Figure 114: (a) Frontglass temperature (b) Backsheet temperature as function of the air temperature at wind velocity of 1 m/s (vertical) for different values of the solar radiation.

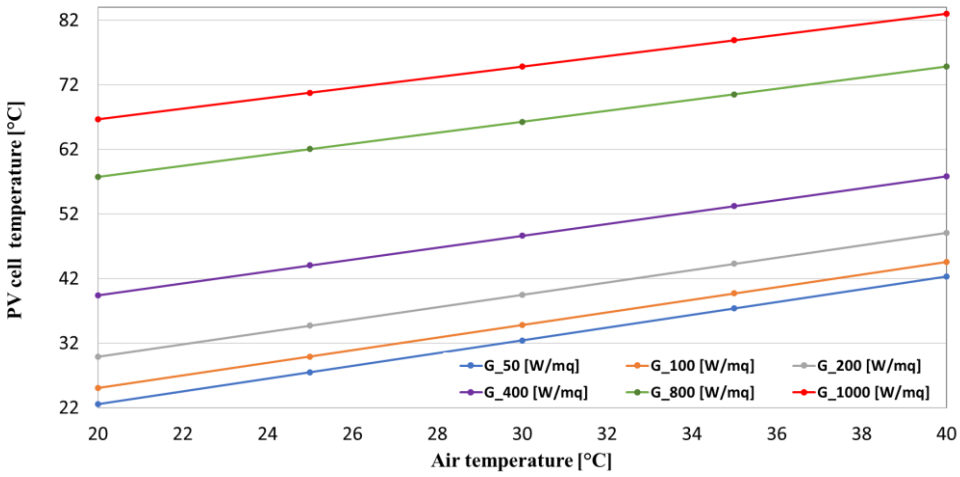

(c)

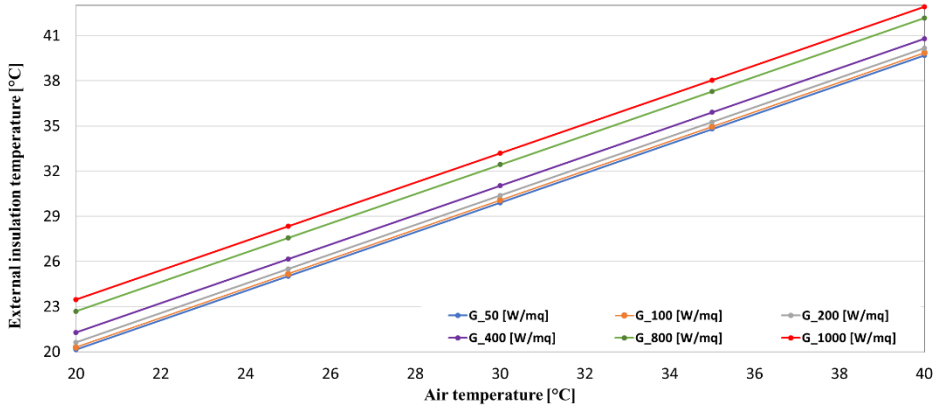

(d)

Figure 114: (c) PV cell temperature (d) External insulation temperature as function of the air temperature at wind velocity of 1 m/s (vertical) for different values of the solar radiation.

The results showed that the maximum values temperature reached by front glass, back glass, PV cell and external wall of the insulation respectively were 81.75 °C, 68.55 °C and 83.01 °C. The temperature of the internal wall of the insulation was fixed at 20 °C. Table 39 reports the convection heat transfer coefficients $h_{fr,Gvalue}$ of the backsheet evaluated, in

Table 40 the maximum photovoltaic producibility $P_{PV,Gvalue}$ and efficiency

$\eta_{PV,Gvalue}$.are listed.

Table 39: Backsheet convection heat transfer coefficients at wind velocity of 1 m/s (vertical) for different values of the solar radiation.

T_air [°C]	$\boldsymbol{h_{bk,50}}$	$\boldsymbol{h_{bk,100}}$	$\boldsymbol{h_{bk,200}}$
20	7.09	7.29	7.39
25	7.21	7.41	7.51
30	7.41	7.61	7.71
35	7.62	7.81	7.90
40	7.81	7.99	8.09
T_air [°C]	$\boldsymbol{h_{bk,400}}$	$\boldsymbol{h_{bk,800}}$	$\boldsymbol{h_{bk,1000}}$
20	7.44	7.46	7.47
25	7.56	7.59	7.59
30	7.76	7.78	7.79
35	7.95	7.97	7.98
40	8.13	8.15	8.16

Table 40: Maximum photovoltaic producibility and efficiency at wind velocity of 1 m/s (vertical) for different values of the solar radiation.

G [W/m^2]	$\boldsymbol{P_{PV}}$ [W/m^2]	$\boldsymbol{\eta_{PV}}$ [%]
50	4.19	9.52
100	9.20	10.45
200	19.79	11.24
400	41.47	11.78
800	83.22	11.82

1000	102.68	11.67

Air temperature affects the thermal distribution of the module as shown in Figure 115. As can be observed the front glass, consequently the entire PV panel, is cooler at the bottom side due to the fresh air entering the duct between the PV panel and the back insulation wall. The outlet air temperature depends on the temperature of the PV panel but also on the air velocity in the duct. The lower is the air velocity the hotter is expected its temperature.

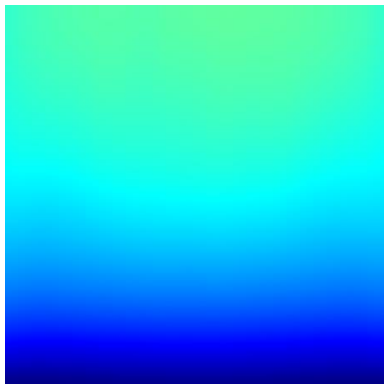

T_{air} =25°

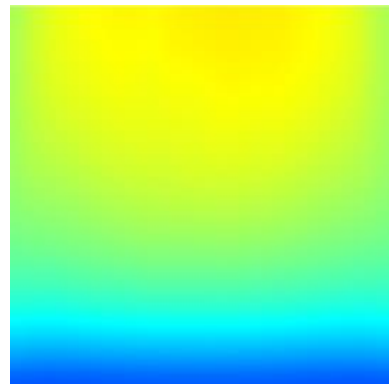

T_{air} =30°

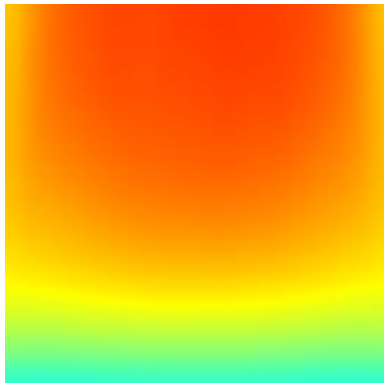

T_{air} =35°

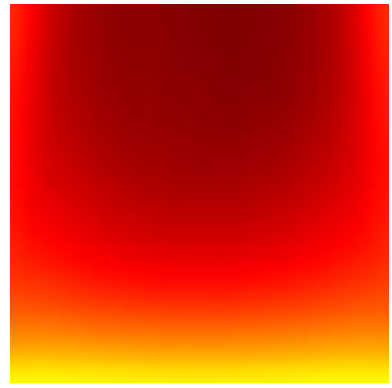

T_{air} =40°

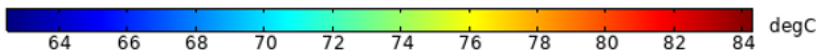

Figure 115: Thermal distribution of the front glass as function of the air temperature at wind velocity of 1 m/s and solar radiation of 1000 W/m^2.

The temperature distribution on the back glass is less uniform as shown in Figure 116Figure 120. In the same way observed for the front glass, the back glass is cooler at the bottom side due to the fresh air entering the duct between the PV panel and the back insulation wall.

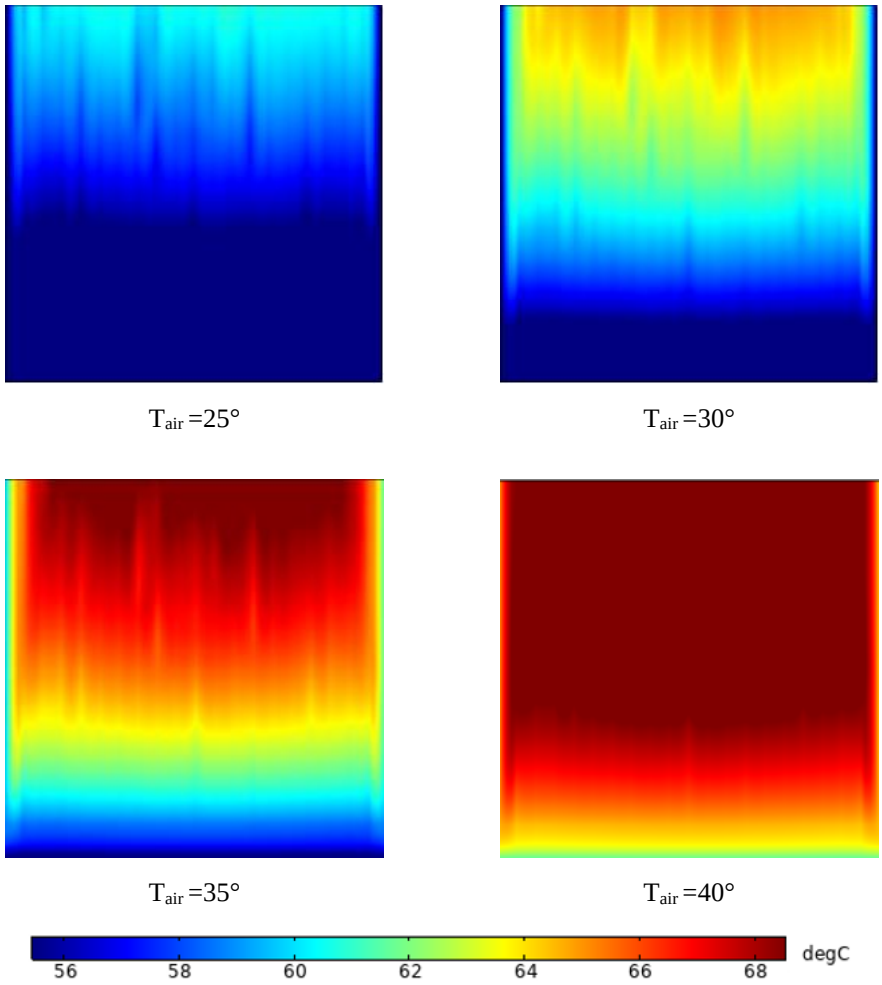

Figure 116: Thermal distribution of the back glass as function of the air temperature at wind velocity of 1 m/s and solar radiation of 1000 W/m^2.

Figure 117 shows the thermal distribution of the front glass as function of the solar radiation at wind velocity of 1 m/s and air temperature of 20°C.

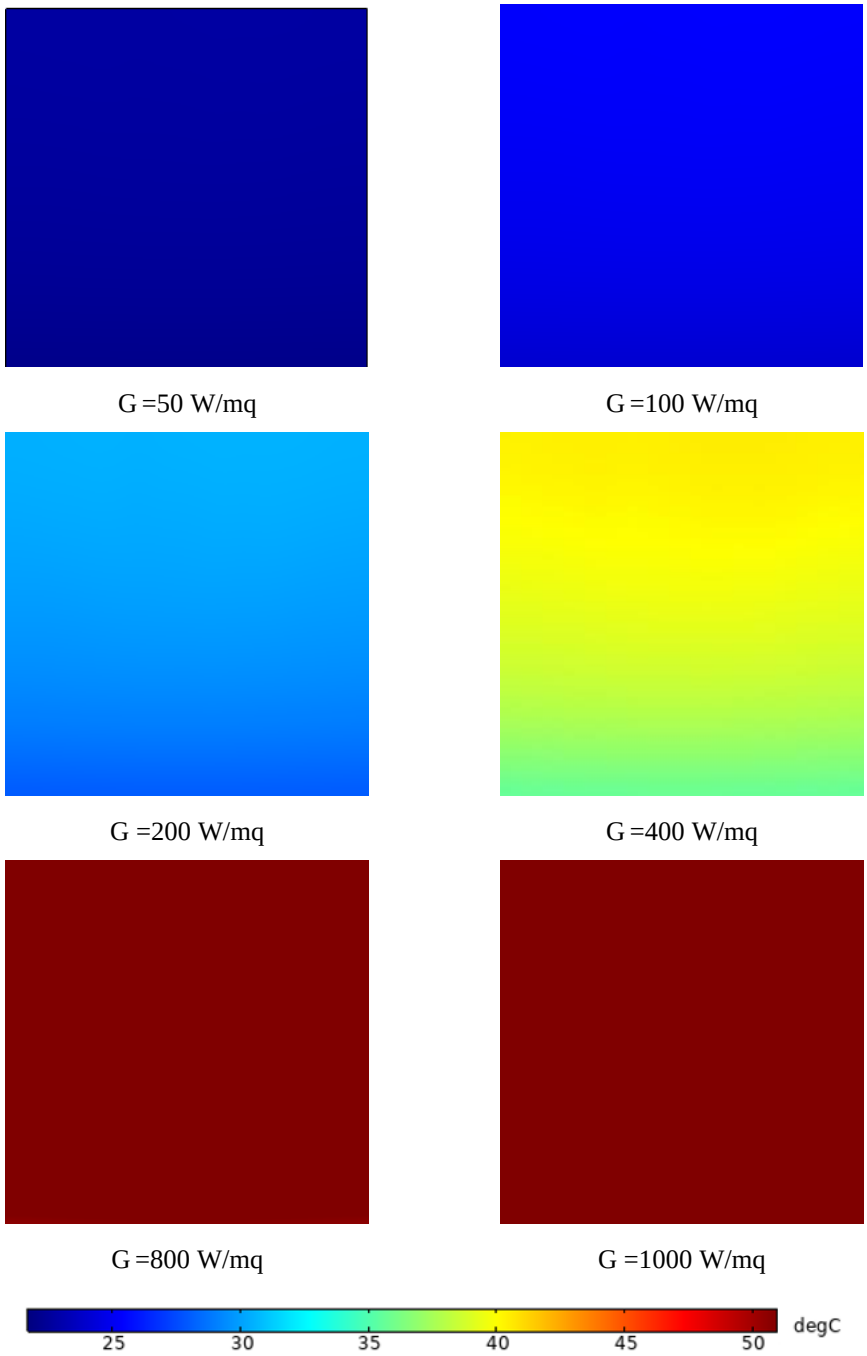

Figure 117: Thermal distribution of the front glass as function of the solar radiation at wind velocity of 1 m/s and air air temperature of 20°C.

Air temperature affects the air velocity distribution as shown in Figure 118. The velocity of the air in the middle of the air gap varies between 1 and 1.3 m/s. This range data gives results very close to those ones obtained simulating the model in "no-wind" condition. A variation of 0.3 m/s can be considered a reasonable variation without external disturbances (no-wind) created only by the buoyancy effects.

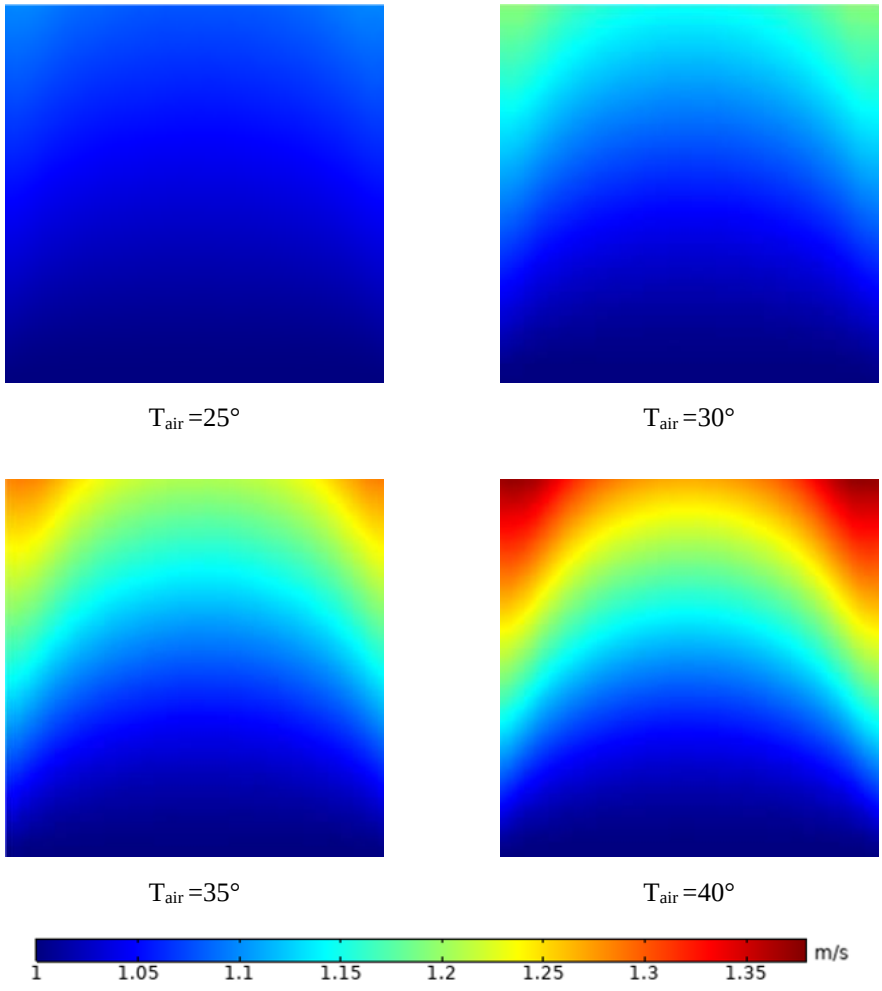

Figure 118: Air velocity distribution in the duct as function of the air temperature and solar radiation of 1000 W/m^2.

The thermal performance of the façade at v=2 m/s is shown in Figure 119. The results showed that the maximum values temperature reached by front glass, back glass, PV cell and external wall of the insulation respectively are 71.59 °C, 62.05 °C 72.75 ° and 41.43 °C. As expected, in comparison to the previous case (v=1 m/s), the cooling effect of the wind produces a reduction in front glass, back glass, PV cell and insulation temperature respectively of 12.43%, 17.27%, 12.36% and 3.47%.

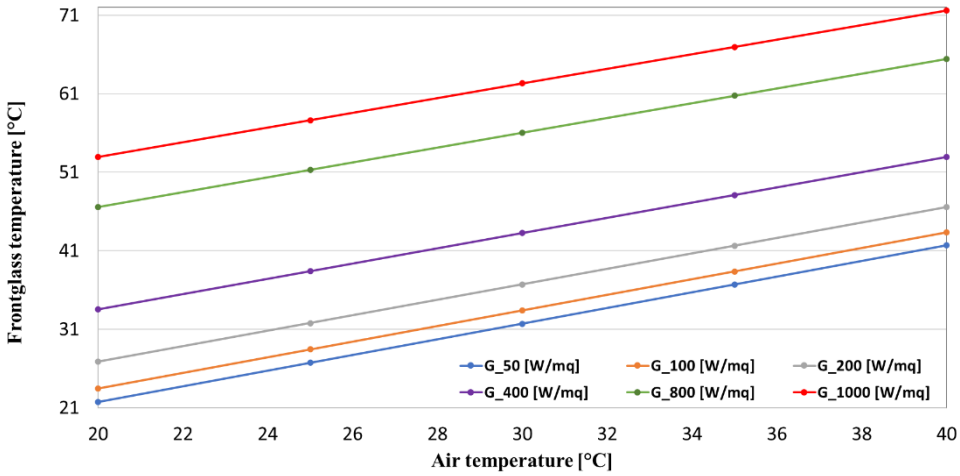

(a)

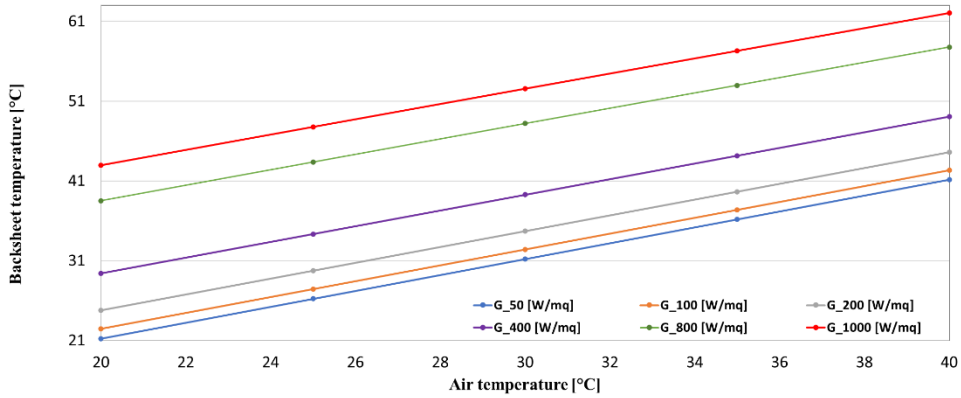

(b)

Figure 119: (a) Frontglass temperature (b) Backsheet temperature as function of the air temperature at wind velocity of 2 m/s (vertical) for different values of the solar radiation.

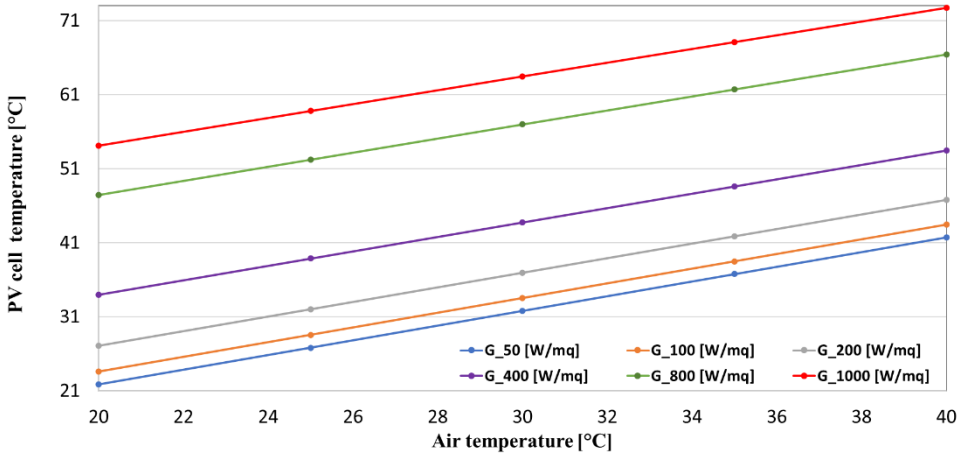

(c)

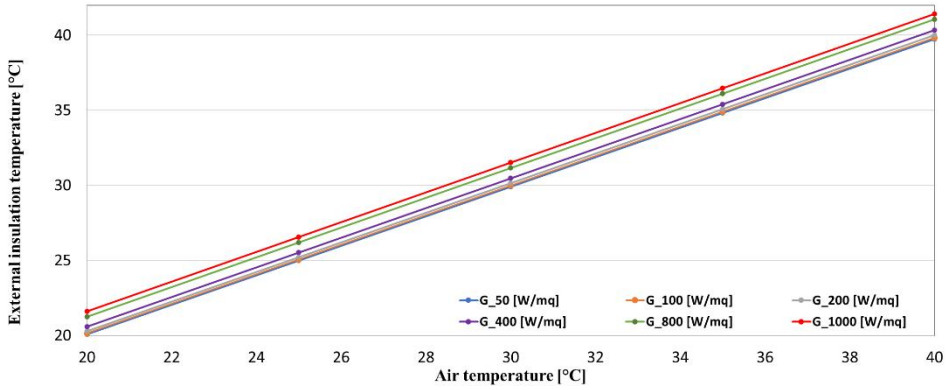

(d)

Figure 119: (c) PV cell temperature (d) External insulation temperature as function of the air temperature at wind velocity of 2 m/s (vertical) for different values of the solar radiation.

Table 41 reports the convection heat transfer coefficients $h_{bk,Gvalue}$ of the backsheet evaluated. As expected, in comparison to the previous case (v=1 m/s), the corresponding values are lower since the difference temperature between the backsheet of the panel and the air channel is lower.

In Table 42 the maximum photovoltaic producibility $P_{PV,Gvalue}$ and efficiency $\eta_{PV,Gvalue}$.are listed.

Table 41: Backsheet convection heat transfer coefficients at wind velocity of 2 m/s (vertical) for different values of the solar radiation.

T_air [°C]	$h_{bk,50}$	$h_{bk,100}$	$h_{bk,200}$
20	10.79	11.63	12.06
25	10.89	11.70	12.11
30	10.98	11.77	12.16
35	11.13	11.88	12.26
40	11.28	12.00	12.36
T_air [°C]	$h_{bk,400}$	$h_{bk,800}$	$h_{bk,1000}$
20	12.28	12.38	12.40
25	12.31	12.42	12.44
30	12.36	12.46	12.48
35	12.45	12.54	12.56
40	12.54	12.63	12.65

Table 42: Maximum photovoltaic producibility and efficiency at wind velocity of 2 m/s (vertical) for different values of the solar radiation.

G [W/m^2]	P_{PV} **[W/m^2]**	η_{PV} **[%]**
50	4.22	9.59
100	9.31	10.58
200	20.25	11.50

400	43.22	12.28
800	89.92	12.77
1000	112.93	12.83

The thermal performance of the façade at v=5 m/s is shown in Figure 120. The results showed that the maximum values temperature reached by front glass, back glass, PV cell and external wall of the insulation respectively are 59.82 °C, 53.94 °C 60.82 ° and 40.40 °C. As expected, in comparison to the previous case (v=2 m/s), the cooling effect of the wind produces a reduction in front glass, back glass, PV cell and insulation temperature respectively of 16.44%, 13.07%, 16.40%, 2.49%.

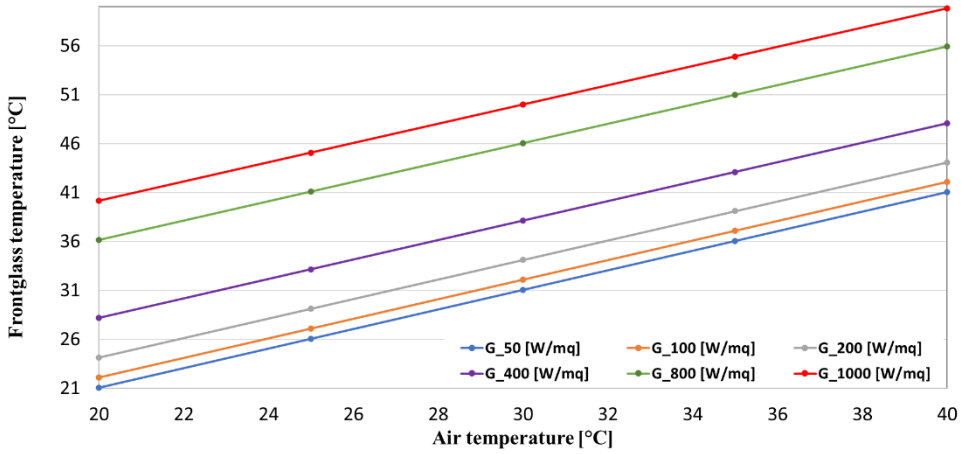

(a)

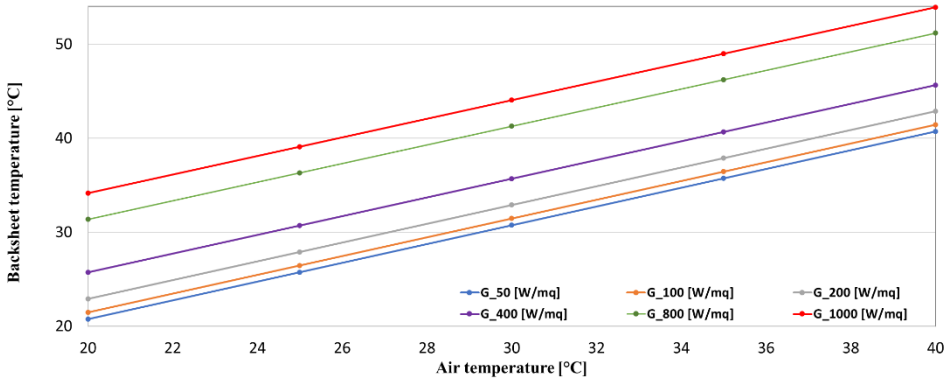

(b)

Figure 120: (a) Frontglass temperature (b) Backsheet temperature as function of the air temperature at wind velocity of 5 m/s (vertical) for different values of the solar radiation.

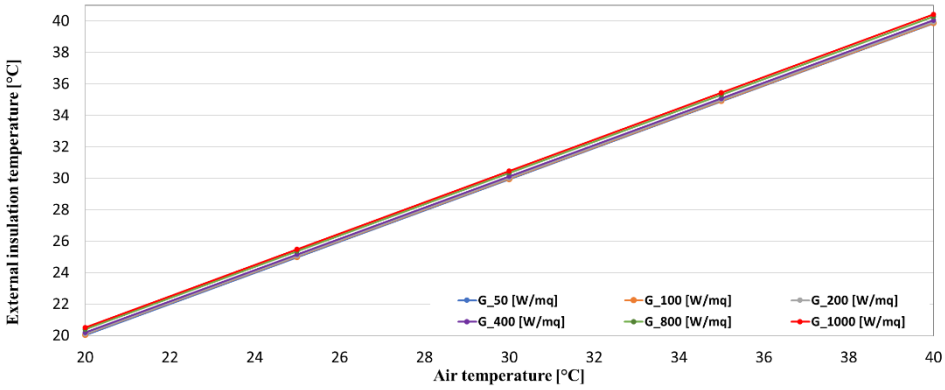

(c)

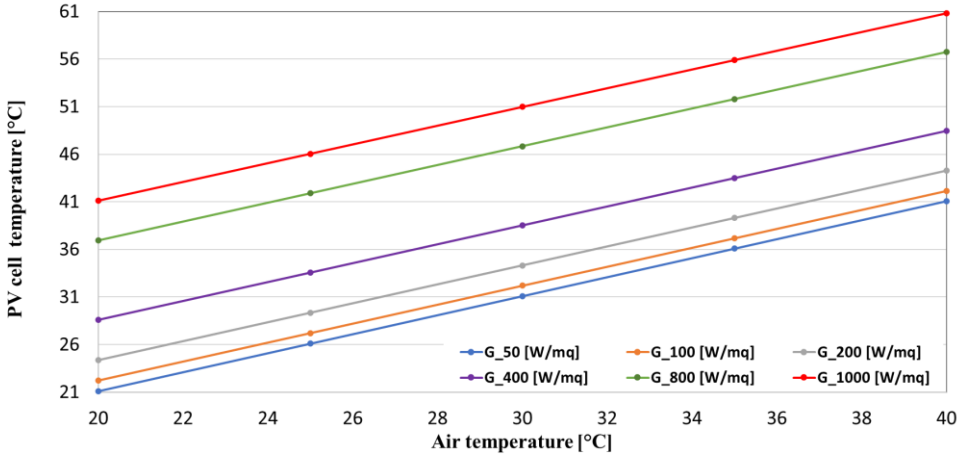

(d)

Figure 120: (c) PV cell temperature (d) External insulation temperature as function of the air temperature at wind velocity of 5 m/s (vertical) for different values of the solar radiation.

Table 43 reports the convection heat transfer coefficients $h_{fr,Gvalue}$ of the backsheet evaluated. In Table 44 the maximum photovoltaic producibility $P_{PV,Gvalue}$ and efficiency $\eta_{PV,Gvalue}$.are listed.

Results so far commented show that the wind speed affect the cell temperature,

and as a consequence the photovoltaic efficiency, significantly.

Table 43: Backsheet convection heat transfer coefficients at wind velocity of 5 m/s (vertical) for different values of the solar radiation.

T_air [°C]	$h_{bk,50}$	$h_{bk,100}$	$h_{bk,200}$
20	12.88	18.45	21.27
25	13.51	18.77	21.44
30	14.13	19.11	21.62
35	14.77	19.43	21.80
40	15.38	19.75	21.95
T_air [°C]	$h_{bk,400}$	$h_{bk,800}$	$h_{bk,1000}$
20	22.70	23.43	18.81
25	22.80	23.48	18.86
30	22.89	23.53	18.90
35	22.98	23.59	18.94
40	23.07	23.63	18.98

Table 44: Maximum photovoltaic producibility and efficiency at wind velocity of 5 m/s (vertical) for different values of the solar radiation.

G [W/m^2]	P_{PV} **[W/m^2]**	η_{PV} **[%]**
50	4.23	9.62
100	9.37	10.65
200	20.48	11.64
400	44.15	12.54
800	93.56	13.29

1000	118.57	13.47

The thermal performance of the façade at v=7 m/s is shown in Figure 121. The results showed that the maximum values temperature reached by front glass, back glass, PV cell and external wall of the insulation respectively are 56.48 °C, 51.55 °C, 57.42 °C and 40.23 °C. As expected, in comparison to the previous case (v=5 m/s), the cooling effect of the wind produces a reduction in front glass, back glass, PV cell and insulation temperature respectively of 5.58%, 4.43%, 5.59% and 0.42%.

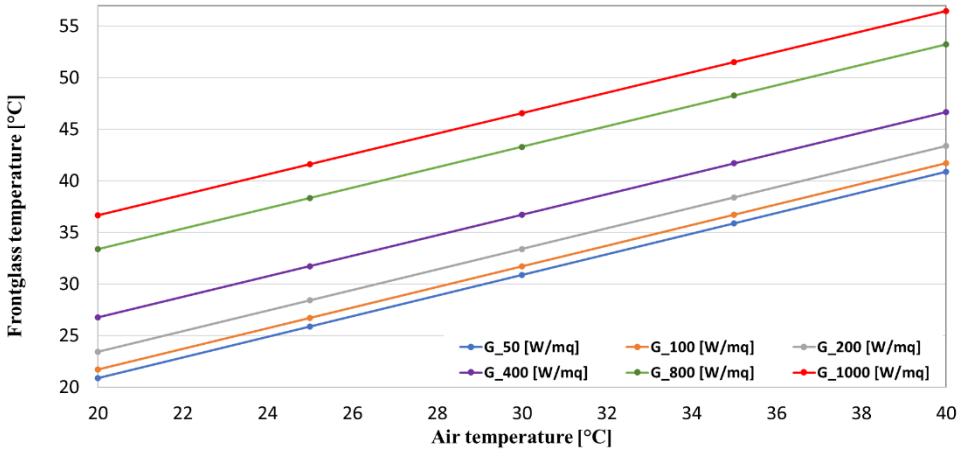

(a)

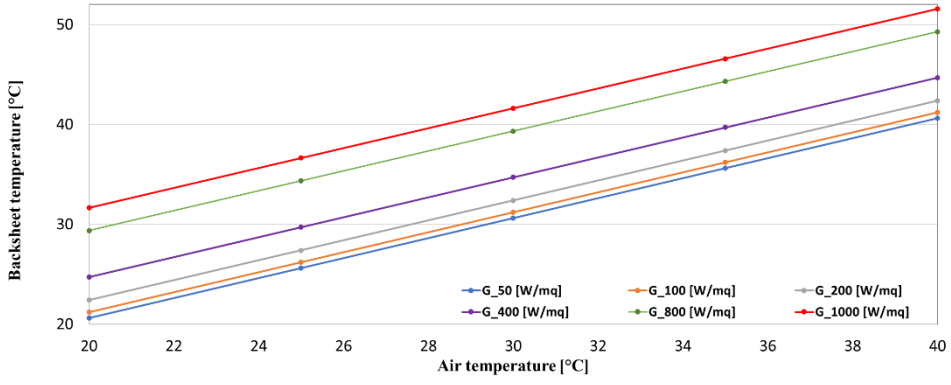

(b)

Figure 121: (a) Frontglass temperature (b) Backsheet temperature as function of the air temperature at wind velocity of 5 m/s (vertical) for different values of the solar radiation.

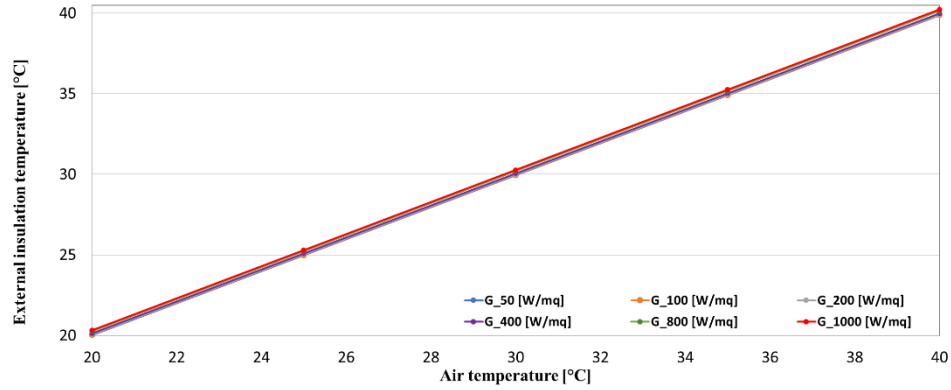

(c)

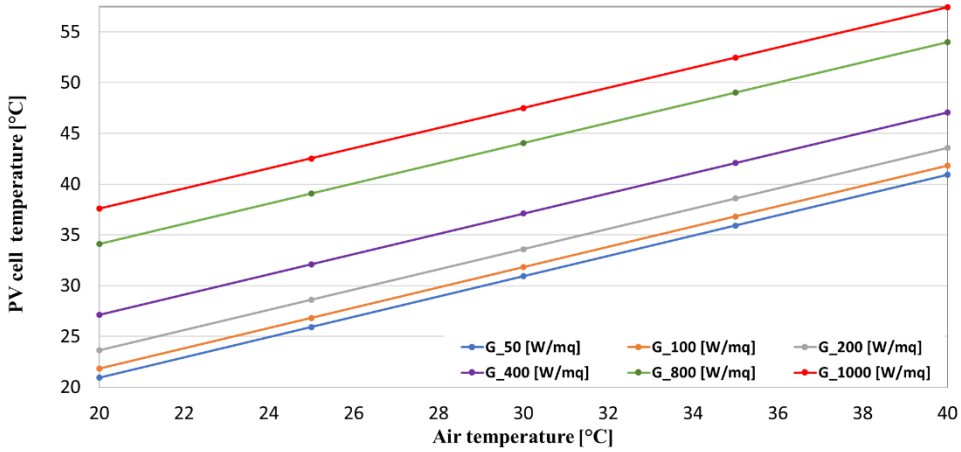

(d)

Figure 121: (c) PV cell temperature (d) External insulation temperature as function of the air temperature at wind velocity of 7 m/s (vertical) for different values of the solar radiation.

Table 45 reports the convection heat transfer coefficients $h_{fr,Gvalue}$ of the backsheet evaluated. In Table 46 the maximum photovoltaic producibility $P_{PV,Gvalue}$ and efficiency $\eta_{PV,Gvalue}$.are listed.

Table 45: Backsheet convection heat transfer coefficients at wind velocity of 7 m/s (vertical) for different values of the solar radiation.

T_air [°C]	$h_{bk,50}$	$h_{bk,100}$	$h_{bk,200}$
20	8.18	19.13	24.69
25	9.43	19.77	25.03
30	10.70	20.43	25.36
35	11.95	21.09	25.69
40	13.25	21.71	26.02
T_air [°C]	$h_{bk,400}$	$h_{bk,800}$	$h_{bk,1000}$
20	27.51	28.94	23.23
25	27.68	29.03	23.30
30	27.85	29.12	23.38
35	28.03	29.21	23.45
40	28.20	29.30	23.52

Table 46: Maximum photovoltaic producibility and efficiency at wind velocity of 7 m/s (vertical) for different values of the solar radiation.

G [W/m^2]	P_{PV} [W/m^2]	η_{PV} [%]
50	4.24	9.63
100	9.38	10.67
200	20.54	11.67
400	44.37	12.61

800	94.45	13.42
1000	119.95	13.63

4.3.2 Effect of the wind direction

Figure 122 shows the effect of the wind direction on the thermal behaviour of the developed ventilated façade.

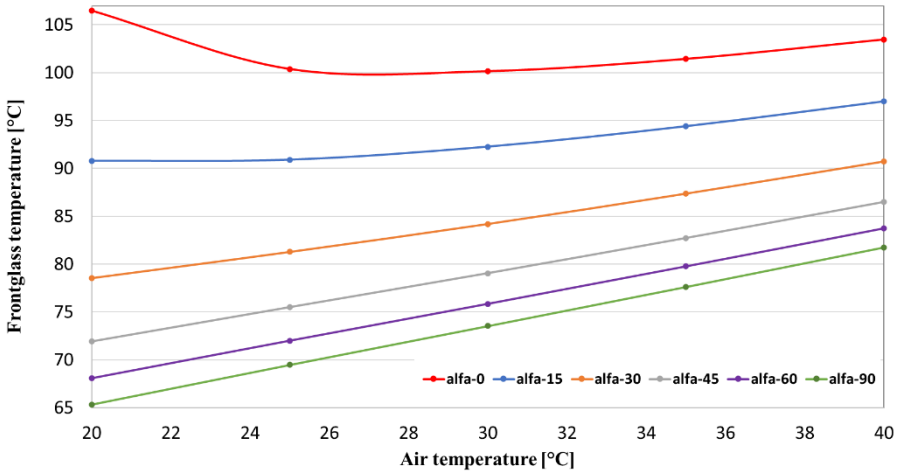

(a)

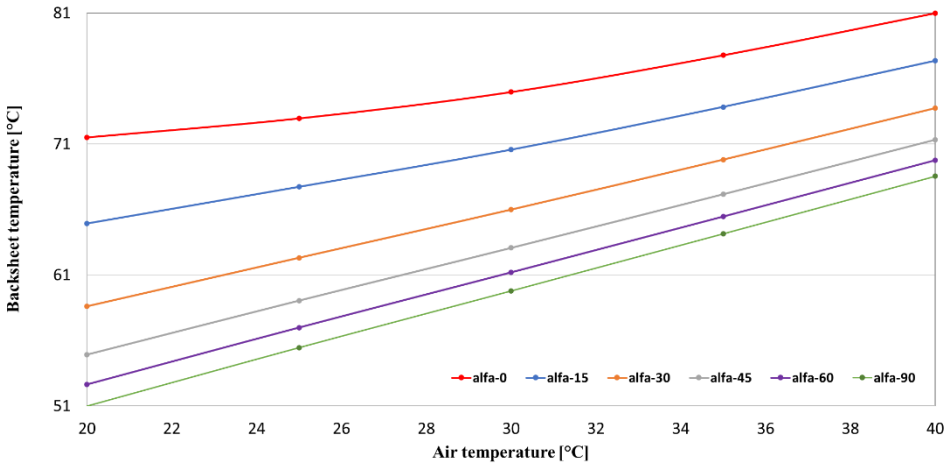

(b)

Figure 122: (a) Frontglass temperature (b) Backsheet temperature as function of the air temperature at wind velocity of 1 m/s (vertical) for different wind directions. Alfa is the angle between the wind direction and the normal to the surface panel.

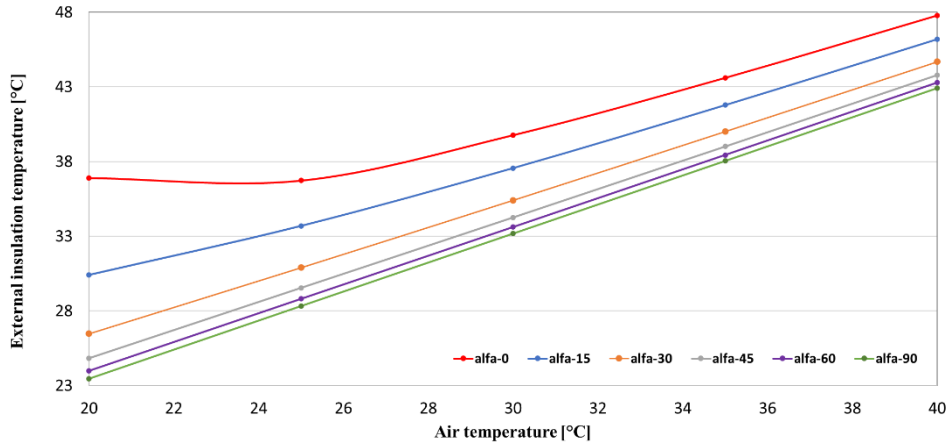

(c)

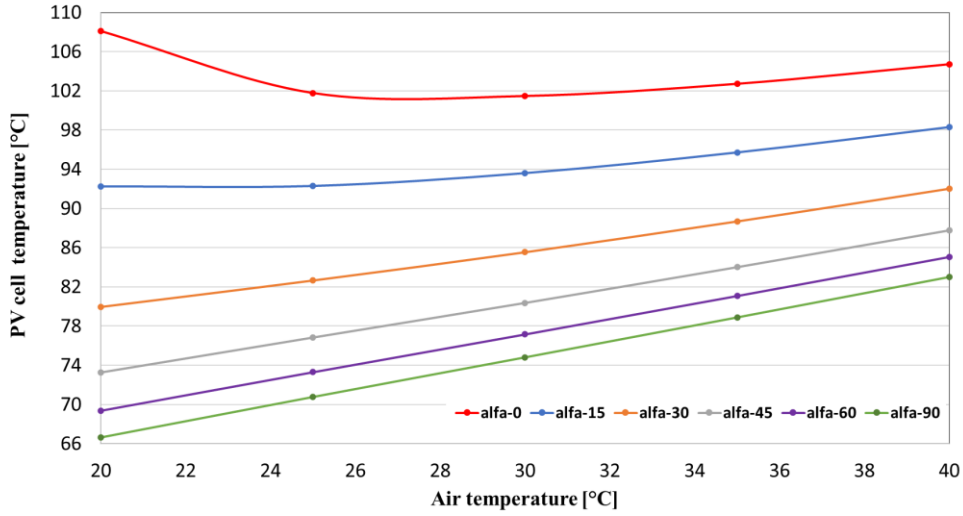

(d)

Figure 122: (c) PV cell temperature (d) External insulation temperature as function of the air temperature at wind velocity of 1 m/s (vertical) for different wind directions.

Table 47 reports the convection heat transfer coefficients $h_{fr,alfavalue}$ of the backsheet evaluated (alfa is the wind direction referred to the normal vector of the front glass). In Table 48 $P_{PV,alfavalue}$ and efficiency $\eta_{PV,alfavalue}$.are listed.

Table 47: Backsheet convection heat transfer coefficients at wind velocity of 1 m/s (vertical) for different values of the wind direction.

T_air [°C]	$\boldsymbol{h_{fr,alfa0}}$	$\boldsymbol{h_{fr,alfa15}}$	$\boldsymbol{h_{fr,alfa30}}$
20	0.69	2.52	4.43
25	1.96	3.05	4.78
30	2.81	3.63	5.14
35	3.37	4.10	5.46
40	3.79	4.49	5.75
T_air [°C]	$\boldsymbol{h_{fr,alfa45}}$	$\boldsymbol{h_{fr,alfa60}}$	$\boldsymbol{h_{fr,alfa90}}$
20	5.78	6.71	7.47
25	6.00	6.87	7.59
30	6.28	7.10	7.79
35	6.53	7.32	7.98
40	6.77	7.52	8.16

Table 48: Maximum photovoltaic producibility and efficiency at wind velocity of 1 m/s (vertical) for different values of the wind direction.

alfa[grad]	$\boldsymbol{P_{PV}}$ **[W/m^2]**	$\boldsymbol{\eta_{PV}}$ **[%]**

0	90.50	10.28
15	92.90	10.56
30	99.06	11.26
45	102.84	11.69
60	105.02	11.93
90	106.53	12.11

alfa-0

alfa-15

alfa-30

alfa-45

alfa-60 alfa-90

Figure 123: Thermal distribution of the front glass as function of the wind direction for solar radiation of 1000 W/mq and air air temperature of 25°C.

Evaluation of the effects of wind direction is useful to predict the PV performance more precisely. The dependency of the photovoltaic efficiency from the wind direction is not easy to predict so the wind may not be always at the same direction.

4.3.3 Effect of the air gap thickness

The effect of the air cavity depth on the thermal performance of the prototype were evaluated. The depths are in the range from 10 to 25 cm. Figure 124 shows the results of the simulation implemented for different air temperature values at wind velocity of 1 m/s and solar radiation of 1000 W/m^2.

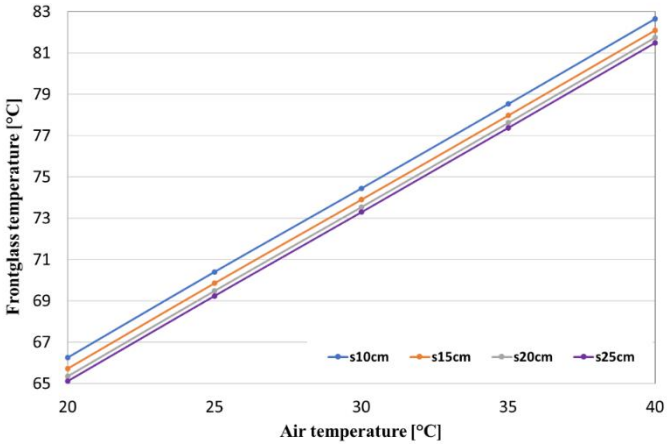

(a)

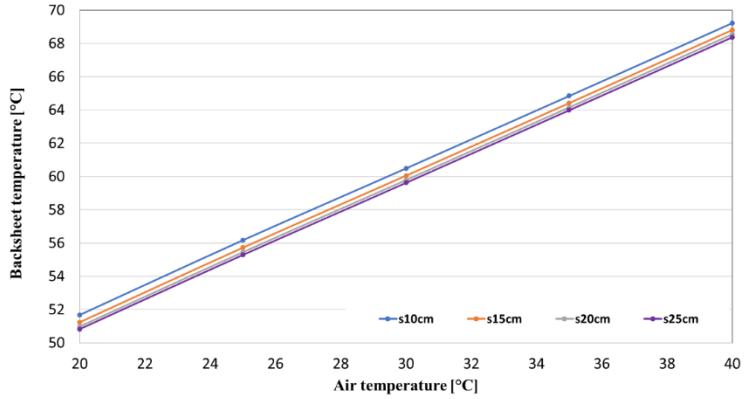

(b)

Figure 124: (a) Frontglass temperature (b) Backsheet temperature as function of the air gap thickness at wind velocity of 1 m/s ans solar radiation of 1000 W/m^2.

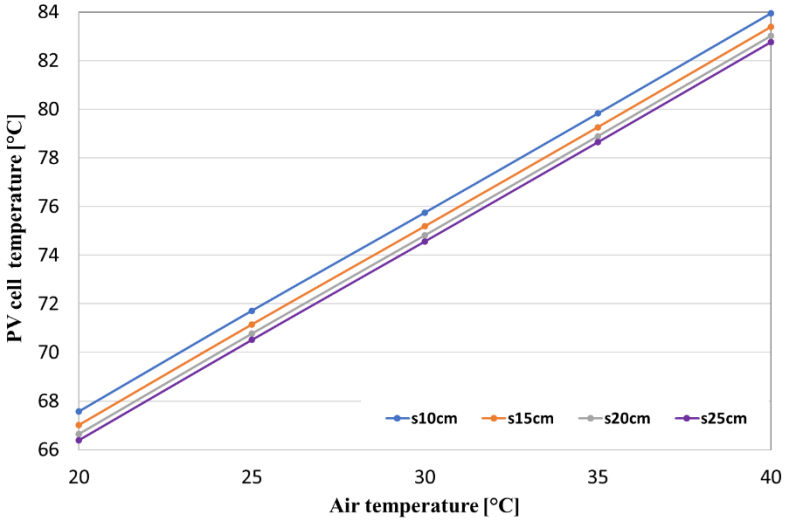

(c)

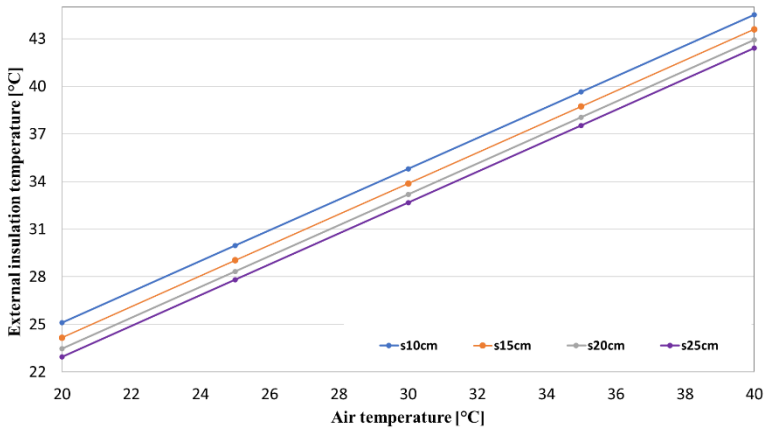

(d)

Figure 124: (c) PV cell temperature (d) External insulation temperature as as function of the air gap thickness at wind velocity of 1 m/s ans solar radiation of 1000 W/m^2.

The maximum and minimum cell average temperatures are 66.39 °C and 83.95°C, from 25 to 10 cm the temperature has an obvious drop. Table 49 reports the convection heat transfer coefficients $h_{fr,svalue}$ (s-value is the air gap thickness in cm). In Table 50 $P_{PV,svalue}$ and $\eta_{PV,svalue}$.are listed. When the cavity gap size is small, increasing its depth reduce the cell temperature with positive effect on photovoltaic efficiency.

Table 49: Backsheet convection heat transfer coefficients as function of the air gap thickness at wind velocity of 1 m/s ans solar radiation of 1000 W/m^2.

T_air [°C]	$h_{fr,s10}$	$h_{fr,s15}$
20	3.58	4.19
25	3.55	4.12
30	3.42	3.93
35	3.25	3.68
40	3.04	3.41

T_air [°C]	$h_{fr,s20}$	$h_{fr,s25}$
20	4.49	4.70
25	4.39	4.58
30	4.17	4.37
35	3.89	4.08
40	3.61	3.77

Table 50: Maximum photovoltaic producibility and efficiency as function of the air gap thickness at wind velocity of 1 m/s ans solar radiation of 1000 W/m^2.

s[cm]	P_{PV} [W/m^2]	η_{PV} [%]
10	106.37	12.09
15	106.47	12.10
20	106.53	12.11
25	106.58	12.11

5. Ventilated Façade with heat sources

In the following sections are reported the results of the E-Brick module.

5.1 Geometry and grid dependence results

Grid dependency was carried out using, as inputs, the data reported in Table 28.

To vary the number of elements in order to perform the grid analysis, in the air domain was changed the size of the elements by the size function already available in COMSOL. In particular, three meshes referred as coarse, normal and fine were simulated and compared. Results of grid analysis reported in Table 51 show that thermal response is not strongly affected by the size of the grid.

Table 51: Grid dependency analysis results for E-Brick module.

Mesh	Number of elements	$T_{bk}[°C]$	$\varepsilon\%$
Coarse	45K	49.28	0.42
Normal	90K	49.4	0.18
Fine	180k	49.49	-

According to criterion to have a discrepancy $\varepsilon < 1\%$, both coarse and normal could be used for simulations. Despite the computational effort is higher, it was chosen the normal mesh to have a better accuracy of the results.

5.2 Model validation

The validation of the model was performed by comparing monitored and simulated data for the 19th of April. In Figure 92 are shown the outdoor air temperature, the global horizontal radiation and the solar radiation on a vertical south oriented surface for the selected day. Data used as inputs are listed in Table 52.

Table 52: Measured data April 19th.

Time	G [W/mq]	T_air [°C]	T_ins [°C]
1:00	0.00	12.02	11.08
2:00	0.00	11.38	11.22
3:00	0.00	12.15	11.11
4:00	0.00	12.10	11.19
5:00	0.00	10.87	11.27
6:00	0.00	10.63	11.38
7:00	16.40	12.33	11.22
8:00	110.37	13.76	9.90
9:00	227.96	15.19	8.44
10:00	281.96	16.40	7.42

11:00	437.42	17.48	6.75
12:00	480.21	17.83	6.69
13:00	505.69	17.83	7.16
14:00	486.18	17.92	7.91
15:00	217.03	17.75	8.52
16:00	34.15	17.34	8.98
17:00	28.88	16.77	9.26
18:00	25.75	15.90	9.54
19:00	13.73	15.04	9.93
20:00	0.13	13.81	10.25
21:00	0.00	13.06	10.57
22:00	0.00	13.66	10.57
23:00	0.00	12.13	10.68

The following graph (Figure 125) reports the monitored temperatures (black lines) and the simulated average surface temperatures (red lines) for the 19th of April. During this day, there is a good agreement between simulated data and monitored ones (the difference is about -1.04 °C for T1 and +1.36 °C for T3).

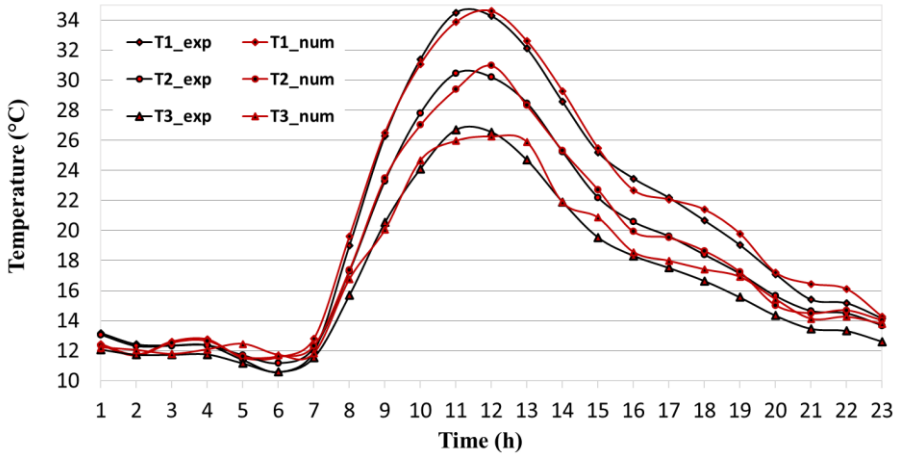

Figure 125: Experimental and numerical data of thermal profiles of PV panel and building insulation for the 19th of April. T1= temperature of the frontglass of the PV panel, T2= temperature of the backsheet of the PV panel, T3= temperature of the inner insulation in contact with the air moving into the channel.

Table 53 reports the results referred to the statistical techniques employed as a method to assess the accuracy of outputs.

Table 53: Model validation for the 19th of April.

Statistical metrics	T1	T2	T3
$\boldsymbol{MBE}$ ($°\boldsymbol{C}$)	0.25	0.05	0.56
$\boldsymbol{RMSE}$ ($°\boldsymbol{C}$)	0.61	0.47	0.81
$\boldsymbol{MBE/AV\ (\%)}$	0.03	0.03	0.05

The MBE of the simulated temperatures vary from -0.05 °C (T2) to 0.56 °C (T3) while the RMSE vary from 0.47 °C (T2) to 0.81 °C (T3).

The validated model allows to study the temperature gradients within the prototype's components and to check the temperatures in the worst conditions.

5.3 Effect of the air cavity on the PV cooling

It is known that an MPPT is an electronic DC to DC converter that optimizes the match between the solar array (PV panels), and the battery bank or utility grid. To do it thermal energy is dissipated. Aiming at properly integrates a photovoltaic panel and a Lithium based battery as a module of an active ventilated façade, the prototype design has been carried out in terms of thermo-fluid dynamics performance.

The experimental data reported in Table 28 together with the measured data of power peaks reported in Table 54 were used carry out the CFD simulations.

The simulations conducted varying both solar radiation and wind velocity made it more complex to find a dependence of the thermal profiles from the effects causing

heat generation in the prototype.

Table 54: Peak power measured during the experimental tests.

Time [h]	Power [W]	Time[h]	Power [W]
09:30	33.02	11:00	51.07
09:40	33.66	11:10	43.17
09:50	35.95	11:20	59.79
10:00	39.07	11:30	57.47
10:10	21.37	11:40	64.25
10:20	30.21	11:50	72.33
10:30	44.33	12:00	81.55
10:40	41.11	12:10	77.17
10:50	47.94	12:20	76.83

A comparison in terms of average temperature of the backsheet glass and insulation is shown in Figure 126- while a comparison in terms of PV efficiency is reported in Figure 127.

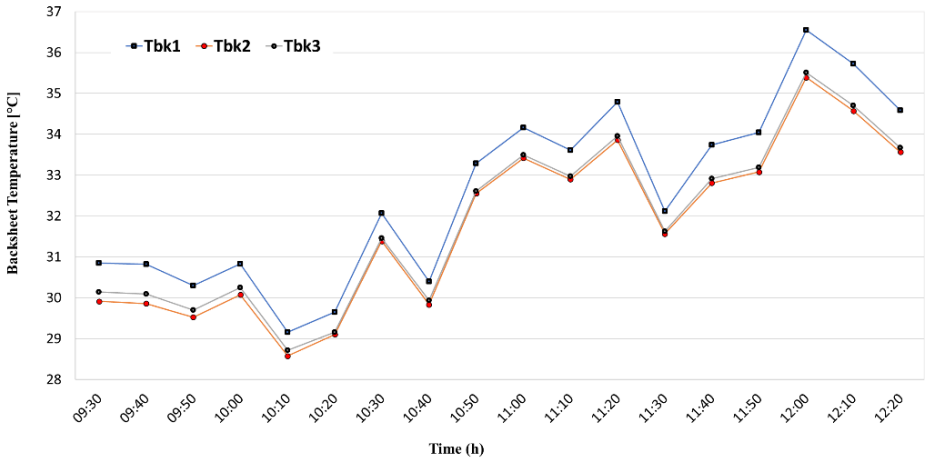

Figure 126: Backsheet temperature for free panel without ventilated façade (1), ventilated façade without heat sources (2) and ventilated façade with heat sources (3).

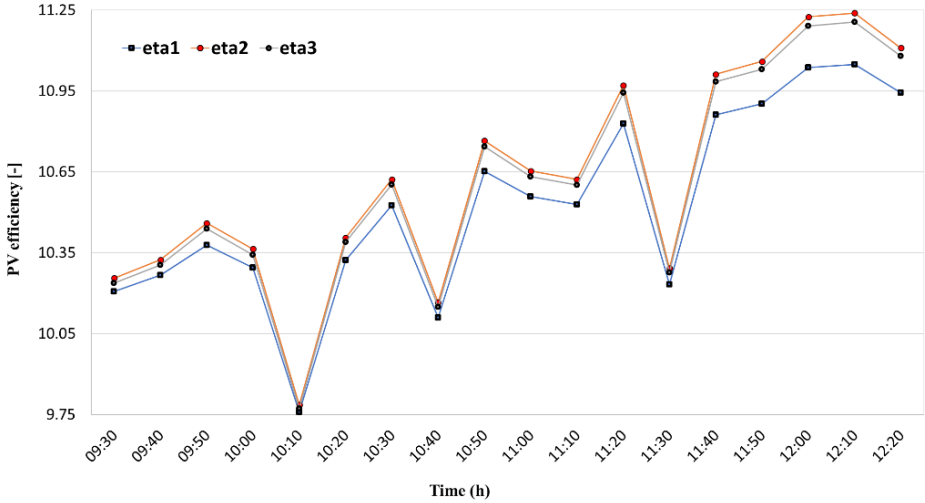

Figure 127: Photovoltaic efficiencies for free panel without ventilated façade (1), ventilated façade without heat sources (2) and ventilated façade with heat sources (3).

The results show that photovoltaic efficiency is not strongly affected by the presence of the heat sources. Efficiency values evaluated for the ventilated façade with and without heat sources differ less than 1%.

The presence of the heat sources leads to a reduction in the convective heat exchange causing an increase not only in the temperature of the backsheet but also in that one of the insulation layers as shown in Figure 128. Figure 129 shows the temperature distribution on the contact area casings -inner insulation.

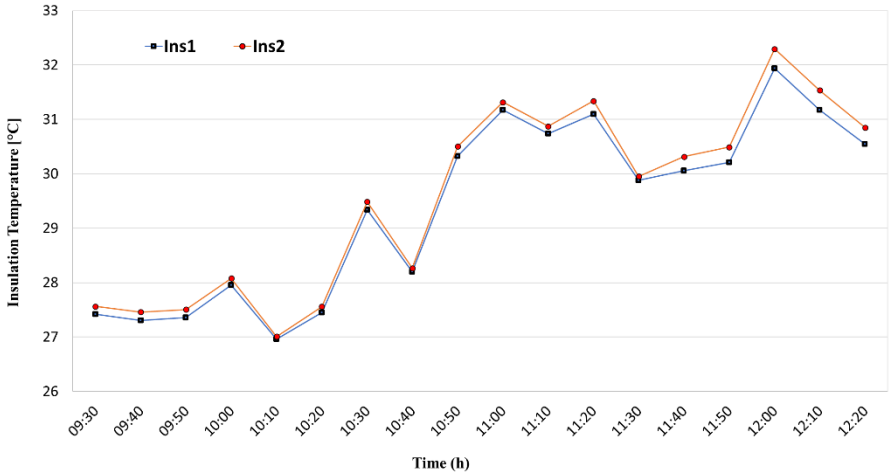

Figure 128: Insulation temperature without heat sources (1), and with heat sources (2).

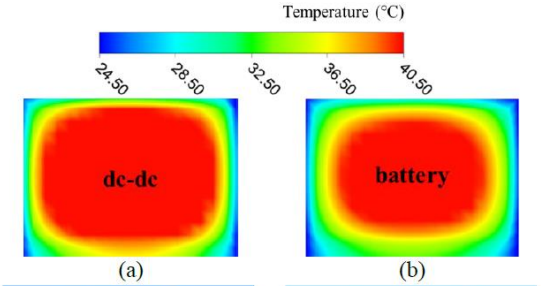

Tdcdc (°C)	
Min	Max
24,63	40,45

Tbattery (°C)	
Min	Max
24,53	40,15

Figure 129: Temperature distribution on the face of contact DC-DC/insulation and battery insulation. Minimum and maximum values evaluated for G= 500W/mq.

5.4 Sensitivity analysis on different conditions

A wide range of parametric analyses on different climate and boundary conditions was performed to explore the viability of the CFD model developed for E-brick.

5.4.1 Effect of the wind module

Figure 130 shows the thermal performance of the module obtained under velocity wind of 1 m/s for different values of the solar radiation.

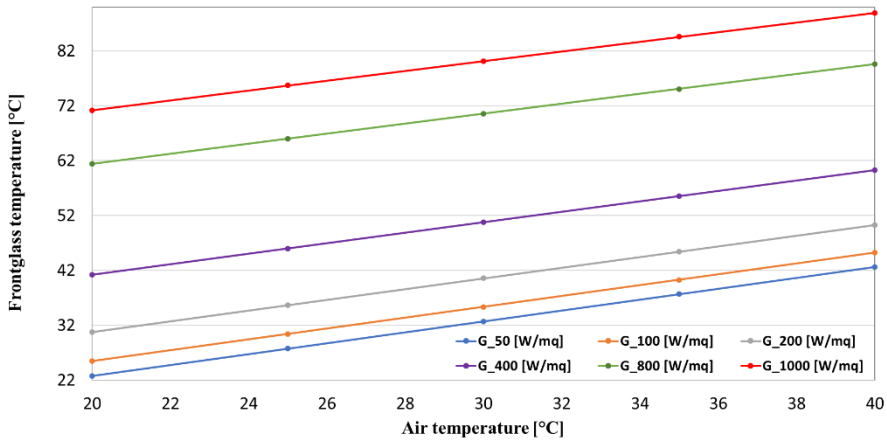

(a)

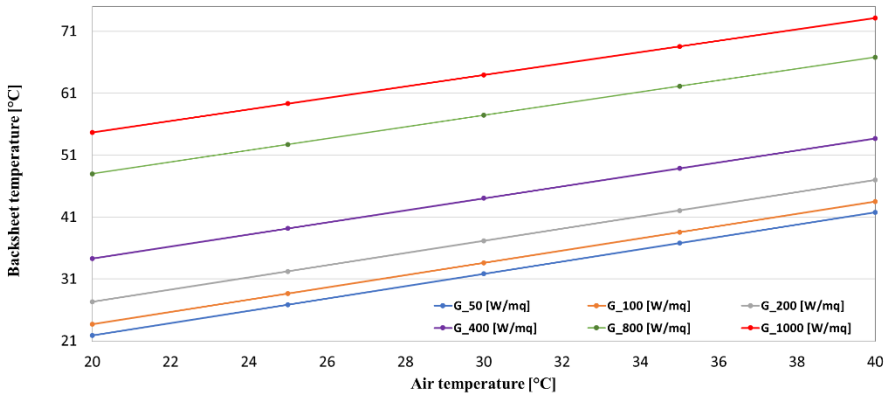

(b)

Figure 130: (a) Frontglass temperature (b) Backsheet temperature of the E-Brick module as function of the air temperature at wind velocity of 1 m/s for different values of G.

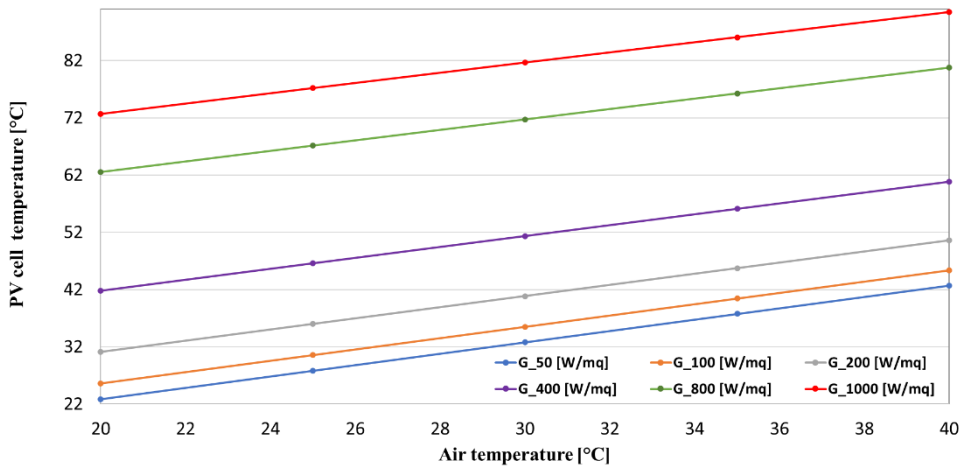

(c)

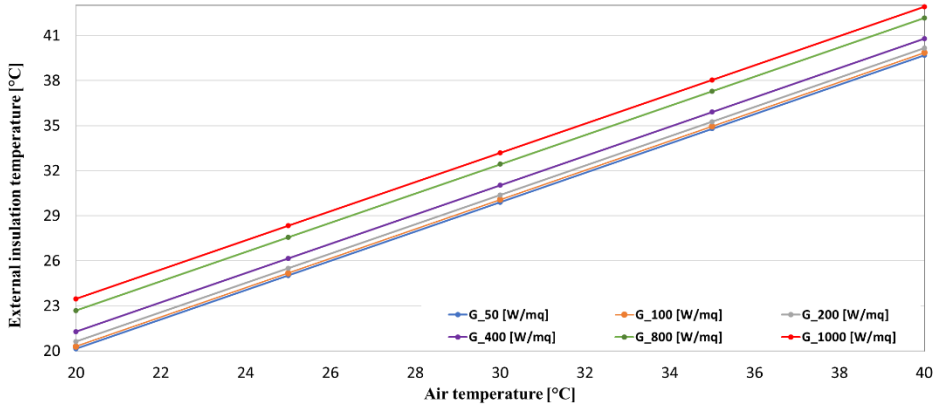

(d)

Figure 130: (c) PV cell temperature (d) External insulation temperature of the E-Brick module as function of the air temperature at wind velocity of 1 m/s for different values of G.

The results showed that the maximum values temperature reached by front glass, back glass, PV cell and external wall of the insulation respectively were 88.95 °C, 73.17 °C, 90.45 °C and 44.38 °C. The temperature of the internal wall of the insulation was fixed at 20 °C. Table 55 reports the convection heat transfer coefficients $h_{bk\_s,Gvalue}$ of the backsheet evaluated, in Table 56 the maximum photovoltaic producibility $P_{PV\_s,Gvalue}$ and efficiency $\eta_{PV\_s,Gvalue}$.are listed. The

subscript s stands for sources.

Table 55: Backsheet convection heat transfer coefficients at wind velocity of 1 m/s for different values of G in presence of heat sources within the air cavity.

T_air [°C]	$h_{bk\_s,50}$	$h_{bk\_s,100}$	$h_{bk\_s,200}$
20	8.06	7.84	7.73
25	8.20	7.92	7.79
30	8.41	8.05	7.87
35	8.66	8.20	7.97
40	8.84	8.32	8.06
T_air [°C]	$h_{bk\_s,400}$	$h_{bk\_s,800}$	$h_{bk\_s,1000}$
20	7.68	7.65	7.49
25	7.71	7.68	7.67
30	7.78	7.73	7.85
35	7.85	7.79	8.02
40	7.93	7.86	8.18

Table 56: Maximum photovoltaic producibility and efficiency at wind velocity of 1 m/s for different values of G in presence of heat sources within the air cavity.

G [W/m^2]	P_{PV_s} **[W/m^2]**	η_{PV_s} **[%]**
50	4.20	9.54
100	9.22	10.48
200	19.89	11.3
400	41.83	11.86
800	84.5	11.87
1000	104.54	11.88

The thermal performance of the E-Brick module at v=2 m/s is shown in Figure 131. The results showed that the maximum values temperature reached by front glass, back glass, PV cell and external wall of the insulation respectively are 75.78°C, 60.30 °C 77.11 ° and 43.48 °C. As expected, in comparison to the previous case (v=1 m/s), the cooling effect of the wind produces a reduction in front glass, back glass, PV cell and insulation temperature respectively of 14.8%, 10.94%, 14.75% and 2.03%.

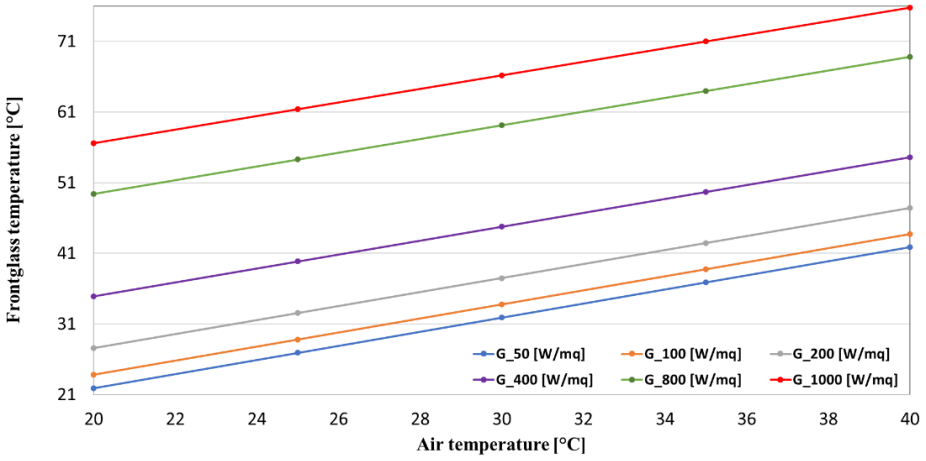

(a)

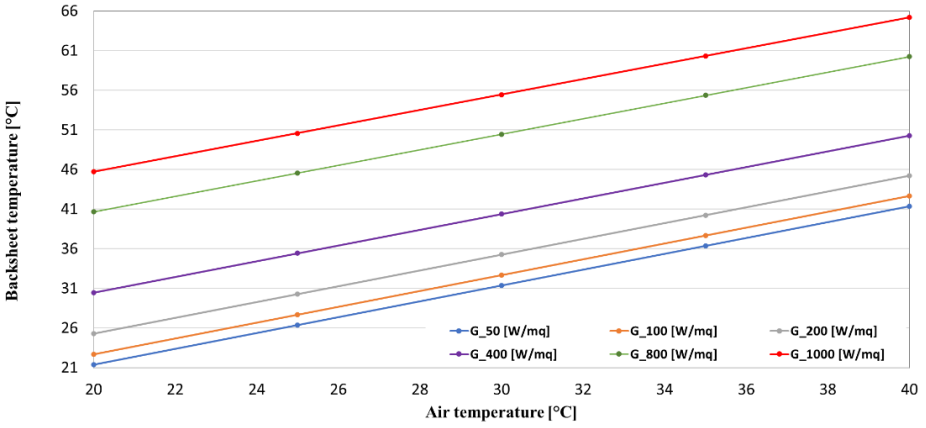

(b)

Figure 131: (a) Frontglass temperature (b) Backsheet temperature of the E-Brick module as function of the air temperature at wind velocity of 2 m/s for different values of G.

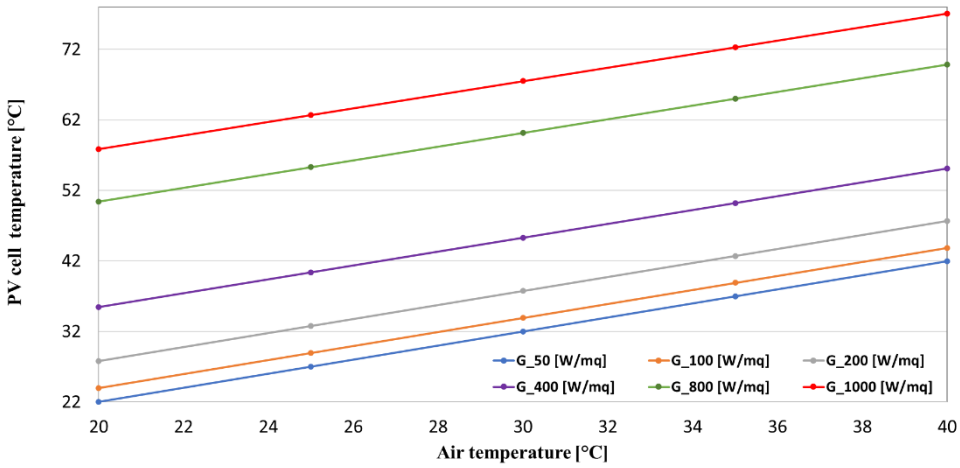

(c)

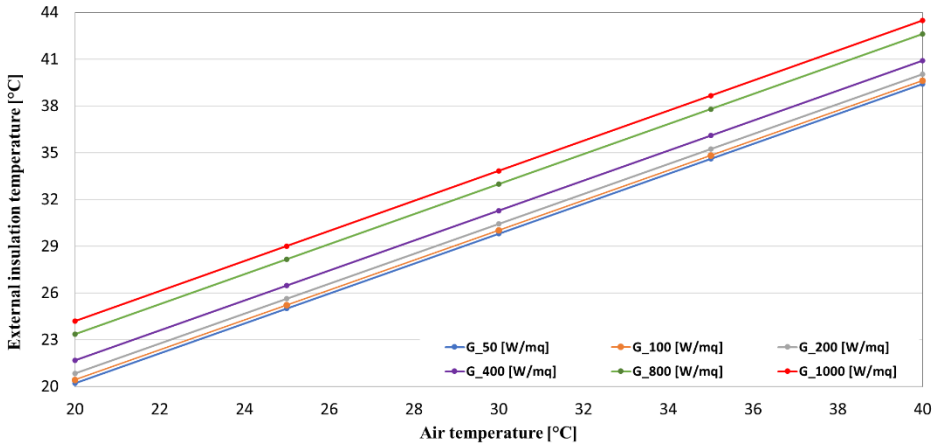

(d)

Figure 131: (c) PV cell temperature (d) External insulation temperature of the E-Brick module as function of the air temperature at wind velocity of 2 m/s for different values of G.

Table 57 reports the convection heat transfer coefficients $h_{bk\_s,Gvalue}$ of the backsheet evaluated. As expected, in comparison to the previous case (v=1 m/s), the corresponding values are lower since the difference temperature between the backsheet of the panel and the air channel is lower. In Table 58 the maximum

photovoltaic producibility $P_{PV\_s,Gvalue}$ and efficiency $\eta_{PV\_s,Gvalue}$ are listed.

Table 57: Backsheet convection heat transfer coefficients at wind velocity of 2 m/s for different values of G in presence of heat sources within the air cavity.

T_air [°C]	$h_{bk\_s,50}$	$h_{bk\_s,100}$	$h_{bk\_s,200}$
20	13.13	12.45	12.11
25	13.17	12.47	12.12
30	13.27	12.52	12.15
35	13.36	12.57	12.18
40	13.43	12.61	12.20
T_air [°C]	$h_{bk\_s,400}$	$h_{bk\_s,800}$	$h_{bk\_s,1000}$
20	11.93	11.84	11.82
25	11.94	11.85	11.83
30	11.96	11.86	11.84
35	11.97	11.87	11.85
40	11.99	11.88	11.86

Table 58: Maximum photovoltaic producibility and efficiency at wind velocity of 2 m/s for different values of G in presence of heat sources within the air cavity.

G [W/m^2]	P_{PV_s} **[W/m^2]**	η_{PV_s} **[%]**
50	4.22	9.59
100	9.31	10.58
200	20.22	11.49
400	43.12	12.25
800	89.49	12.71
1000	112.23	12.75

The thermal performance of the E-Brick module at v=5 m/s is shown in Figure 132. The results showed that the maximum values temperature reached by front glass, back glass, PV cell and external wall of the insulation respectively are 62.80°C, 55.08 °C,63.96 ° and 42.46 °C. As expected, in comparison to the previous case (v=1 m/s), the cooling effect of the wind produces a reduction in front glass, back glass, PV cell and insulation temperature respectively of 17.13%, 15.48%, 17.06% and 2.35%.

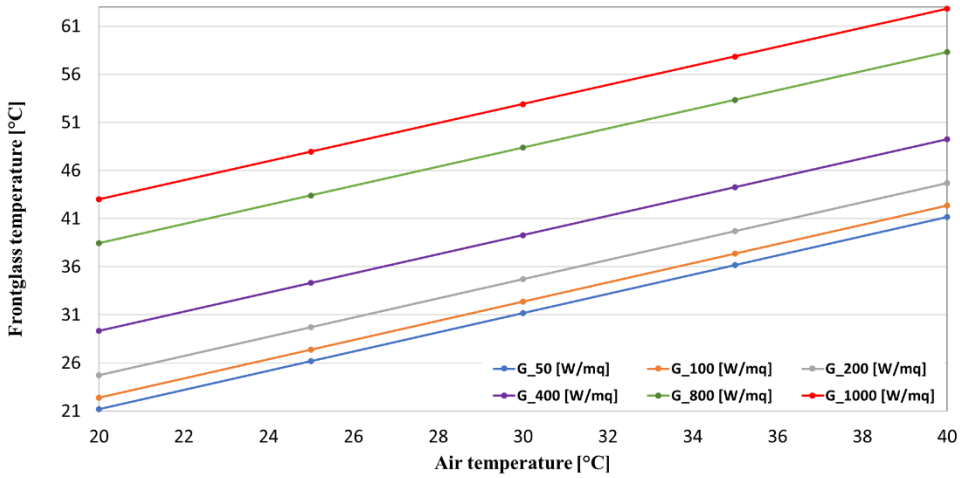

(a)

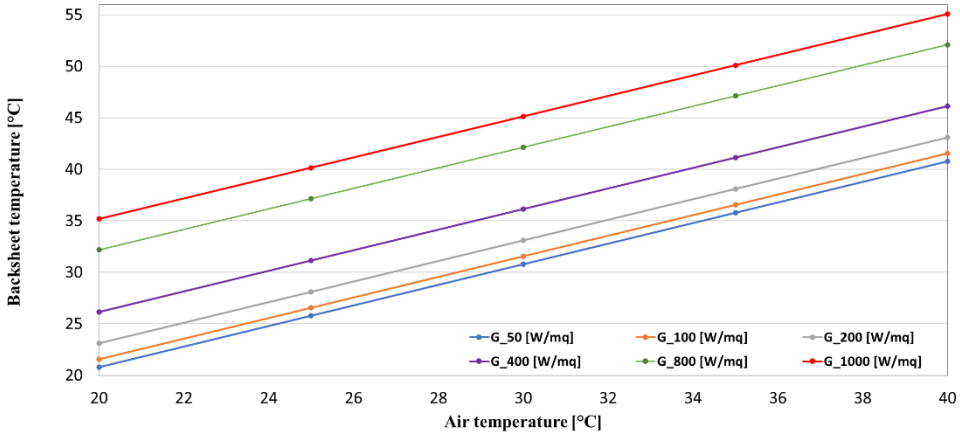

(b)

Figure 132: (a) Frontglass temperature (b) Backsheet temperature of the E-Brick module as function of the air temperature at wind velocity of 5 m/s for different values of G.

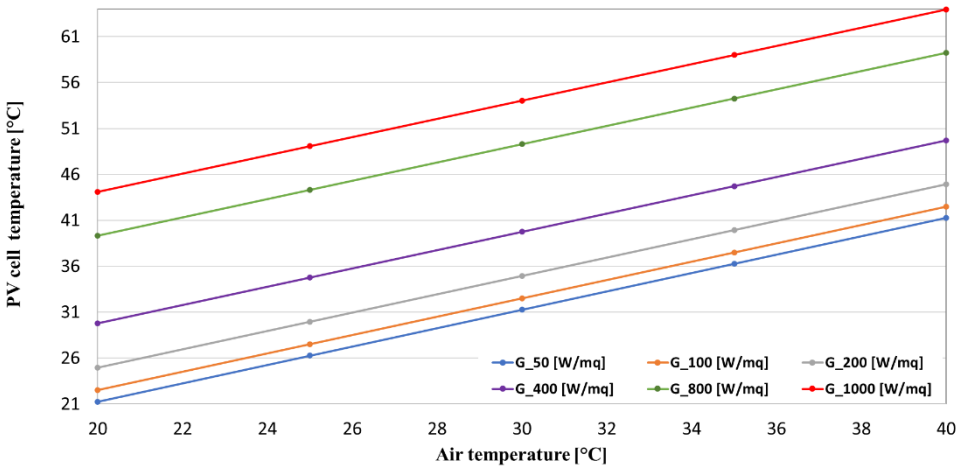

(c)

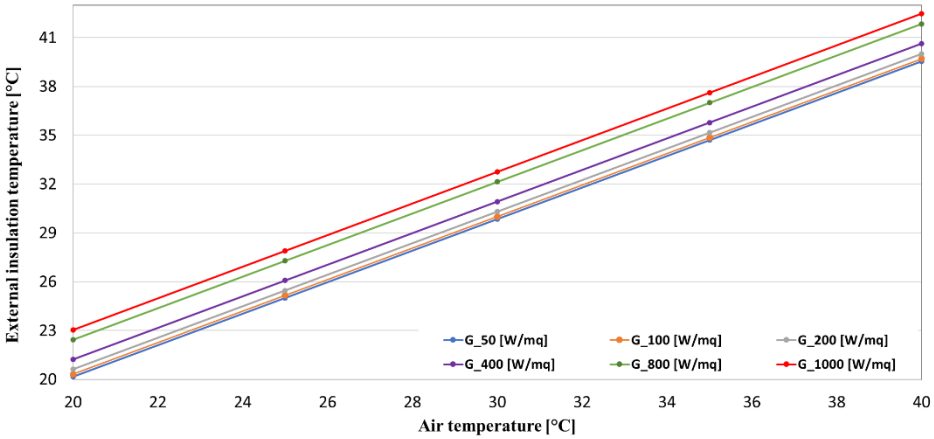

(d)

Figure 132: (c) PV cell temperature (d) External insulation temperature of the E-Brick module as function of the air temperature at wind velocity of 5 m/s for different values of G.

Table 59 reports the convection heat transfer coefficients $h_{bk\_s,Gvalue}$ of the backsheet evaluated. As expected, in comparison to the previous case (v=2 m/s), the corresponding values are lower since the difference temperature between the backsheet of the panel and the air channel is lower. In Table 60 the maximum

photovoltaic producibility $P_{PV\_s,Gvalue}$ and efficiency $\eta_{PV\_s,Gvalue}$ are listed.

Table 59: Backsheet convection heat transfer coefficients at wind velocity of 5 m/s for different values of G in presence of heat sources within the air cavity.

T_air [°C]	$h_{bk\_s,50}$	$h_{bk\_s,100}$	$h_{bk\_s,200}$
20	28.54	26.60	25.63
25	28.35	26.51	25.58
30	28.18	26.42	25.53
35	28.01	26.33	25.50
40	27.87	26.26	25.46
T_air [°C]	$h_{bk\_s,400}$	$h_{bk\_s,800}$	$h_{bk\_s,1000}$
20	25.13	24.88	24.83
25	25.10	24.87	24.82
30	25.08	24.85	24.81
35	25.06	24.85	24.80
40	25.04	24.84	24.79

Table 60: Maximum photovoltaic producibility and efficiency at wind velocity of 5 m/s for different values of G in presence of heat sources within the air cavity.

G [W/m²]	P_{PV_s} **[W/m²]**	η_{PV_s} **[%]**
50	4.23	9.62
100	9.36	10.65
200	20.46	11.63
400	44.09	12.52
800	93.30	13.25
1000	118.17	13.43

The thermal performance of the E-Brick module at v=7 m/s is shown in Figure 133. The results showed that the maximum values temperature reached by front glass, back glass, PV cell and external wall of the insulation respectively are 58.66°C, 51.97 °C 59.74 ° and 42.26 °C. As expected, in comparison to the previous case (v=5 m/s), the cooling effect of the wind produces a reduction in front glass, back glass, PV cell and insulation temperature respectively of 6.59%, 5.63%, 6.69% and 0.48%.

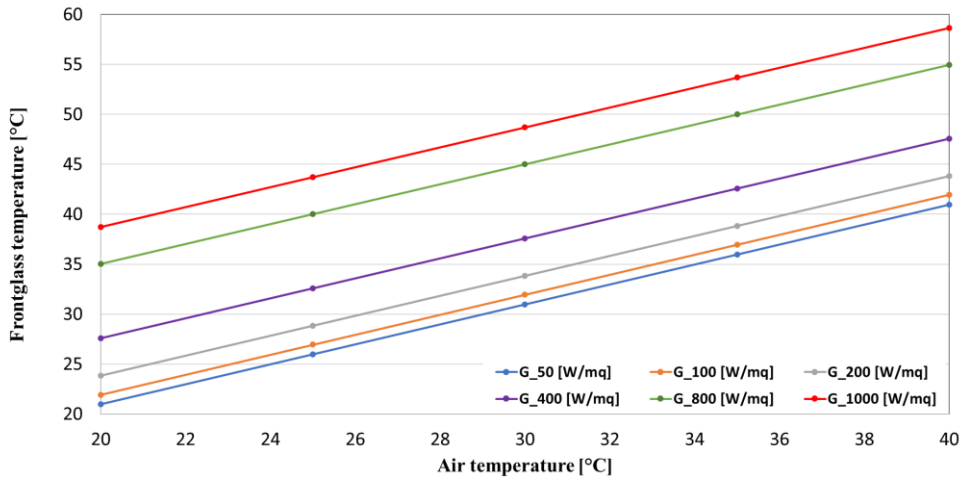

(a)

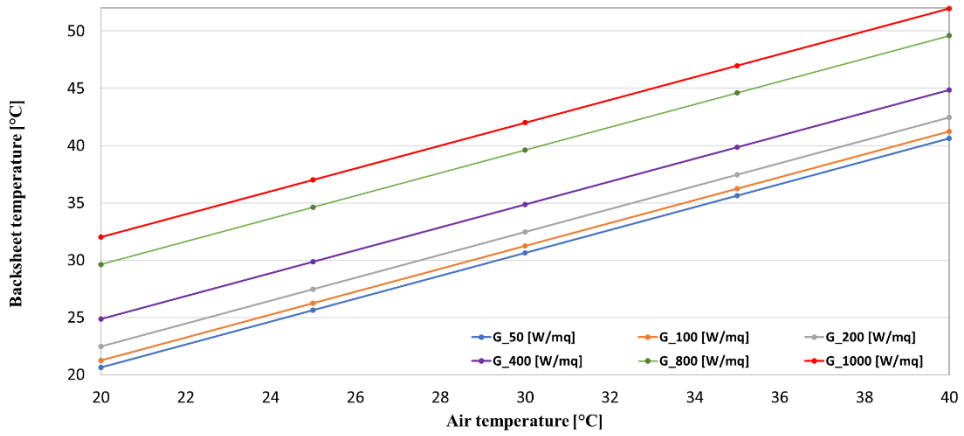

(b)

Figure 133: (a) Frontglass temperature (b) Backsheet temperature of the E-Brick module as function of the air temperature at wind velocity of 7 m/s for different values of G.

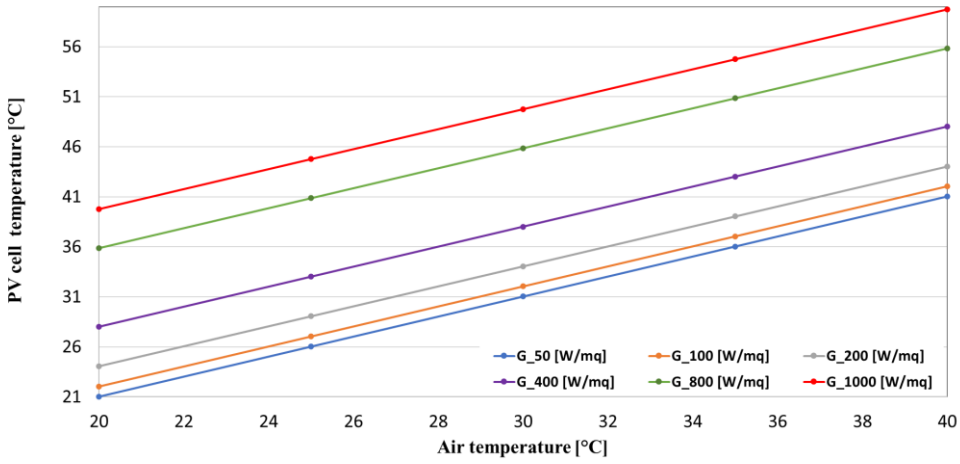

(c)

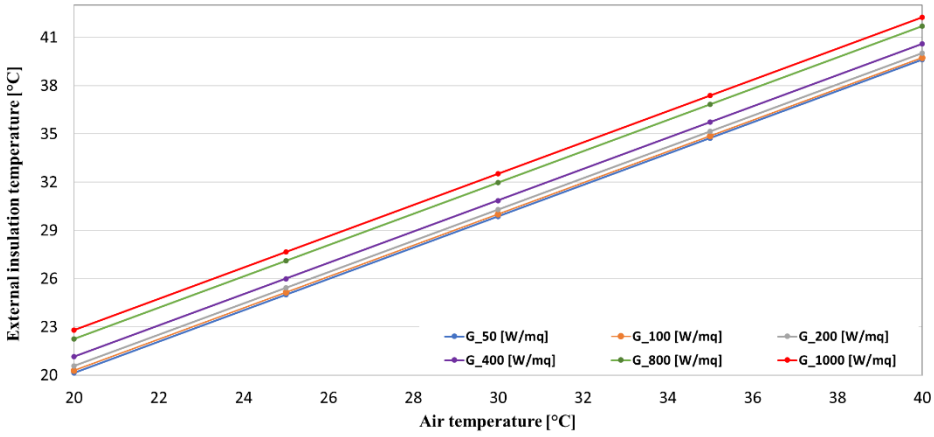

(d)

Figure 133: (c) PV cell temperature (d) External insulation temperature of the E-Brick module as function of the air temperature at wind velocity of 7 m/s for different values of G.

Table 61 reports the convection heat transfer coefficients $h_{bk\_s,Gvalue}$ of the backsheet evaluated. As expected, in comparison to the previous case (v=5 m/s), the corresponding values are lower since the difference temperature between the backsheet of the panel and the air channel is lower. In Table 62 the maximum

photovoltaic producibility $P_{PV\_s,Gvalue}$ and efficiency $\eta_{PV\_s,Gvalue}$ are listed.

Table 61: Backsheet convection heat transfer coefficients at wind velocity of 7 m/s for different values of G in presence of heat sources within the air cavity.

T_air [°C]	$h_{bk\_s,50}$	$h_{bk\_s,100}$	$h_{bk\_s,200}$
20	43.77	38.79	36.30
25	43.12	38.53	36.16
30	42.60	38.22	36.01
35	42.01	37.91	35.86
40	41.42	37.66	35.73
T_air [°C]	$h_{bk\_s,400}$	$h_{bk\_s,800}$	$h_{bk\_s,1000}$
20	35.04	34.41	34.27
25	34.97	34.36	34.24
30	34.89	34.33	34.22
35	34.82	34.29	34.19
40	34.75	34.26	34.16

Table 62: Maximum photovoltaic producibility and efficiency at wind velocity of 7 m/s for different values of G in presence of heat sources within the air cavity.

G [W/m^2]	P_{PV_s} **[W/m^2]**	η_{PV_s} **[%]**
50	4.24	9.63
100	9.38	10.66
200	20.51	11.66
400	44.25	12.57
800	93.96	13.35
1000	119.20	13.55

5.4.2 Effect of the wind direction

Figure 134 shows the effect of the wind direction on the thermal behaviour of the developed E-Brick module.

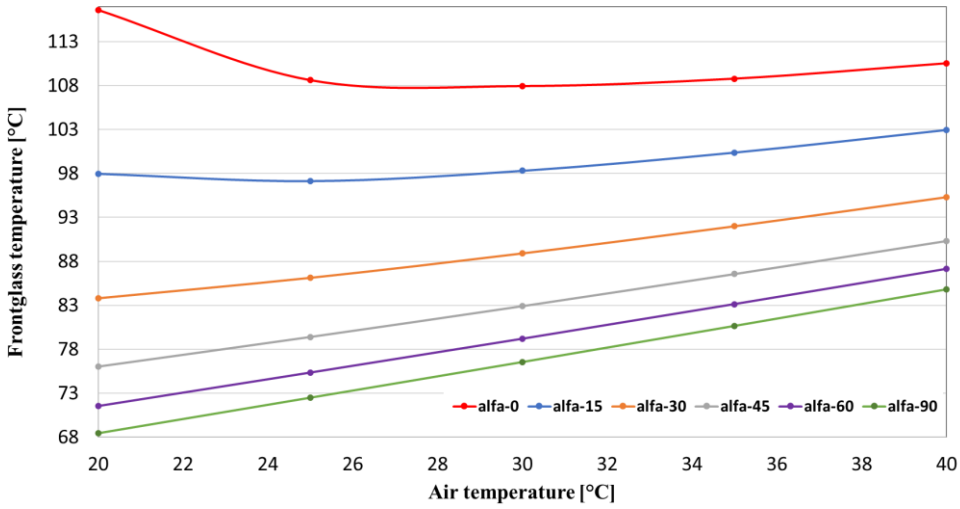

(a)

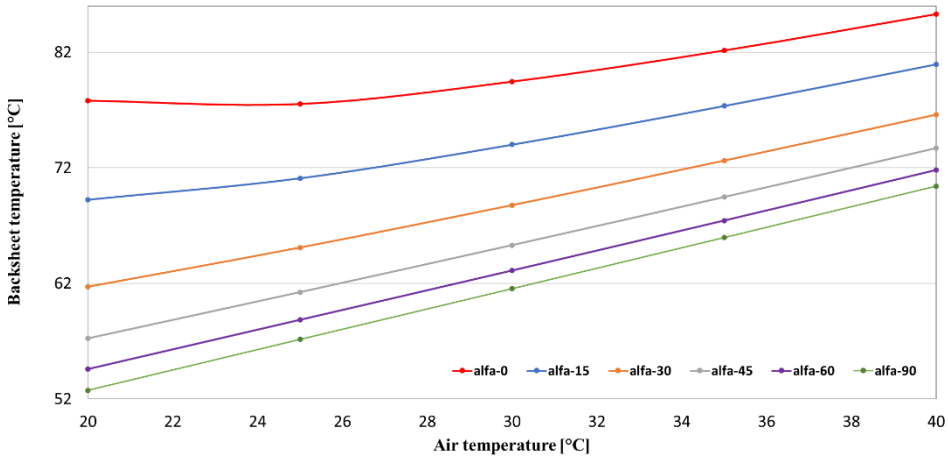

(b)

Figure 134: (a) Frontglass temperature (b) Backsheet temperature of the E-Brick module as function of the air temperature at wind velocity of 1 m/s for different wind directions.

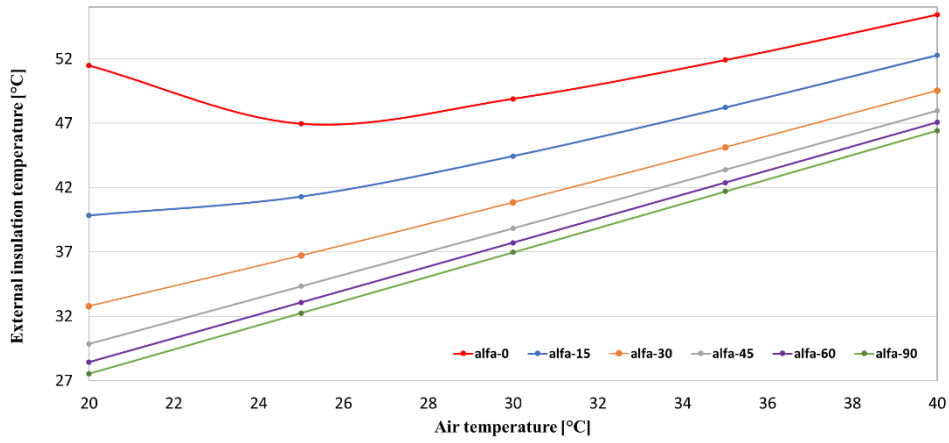

(c)

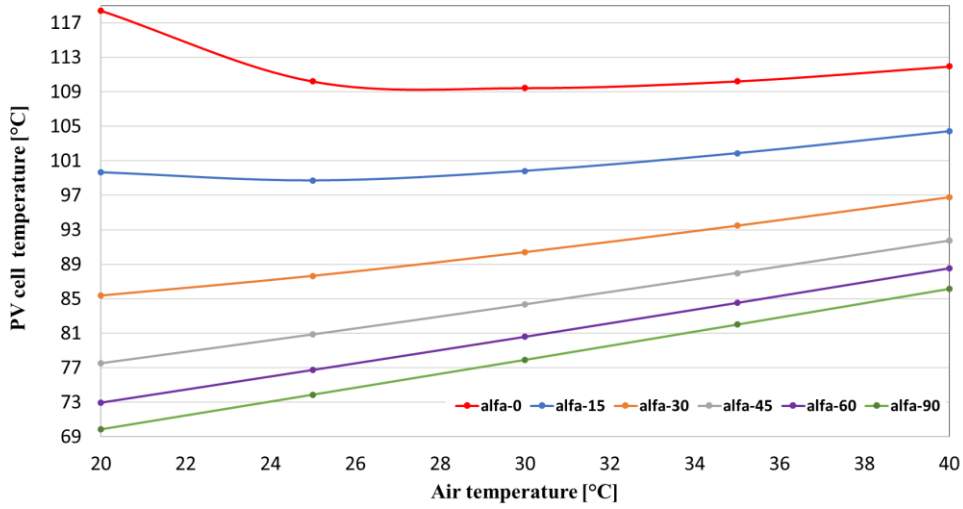

(d)

Figure 134: (c) PV cell temperature (d) External insulation temperature of the E-Brick module as function of the air temperature at wind velocity of 1 m/s for different wind directions.

The maximum and minimum cell average temperatures are 69.84 °C and 118.41°C, from alfa 0 to 90 deg the temperature has an obvious drop. Table 63 reports $h_{fr,alfavalue}$,in Table 64 $P_{PV,alfavalue}$ and $\eta_{PV,alfavalue}$.

Table 63: Backside heat transfer coefficients at wind velocity of 1 m/s for different values of the wind direction.

T_air [°C]	$h_{fr,alfa0}$	$h_{fr,alfa15}$	$h_{fr,alfa30}$
20	0.42	2.64	4.52
25	0.52	3.30	4.91
30	0.64	3.77	5.24
35	0.78	4.15	5.52
40	0.92	4.47	5.76
T_air [°C]	$h_{fr,alfa45}$	$h_{fr,alfa60}$	$h_{fr,alfa90}$
20	5.88	6.79	7.49
25	6.15	7.00	7.67
30	6.41	7.22	7.85
35	6.63	7.41	8.02
40	6.83	7.58	8.18

Table 64: Maximum photovoltaic producibility and efficiency at wind velocity of 1 m/s for different values of the wind direction.

alfa[grad]	P_{PV} [W/m^2]	η_{PV} [%]
0	85.15	9.68
15	88.56	10.06
30	96.73	10.99
45	101.24	11.51
60	103.80	11.80
90	105.52	12.10

5.5 Thermal behaviour of the battery

According to the data provided by the manufactures the maximum temperature admitted by the battery is ~ 60°C. Fixing the casing containing the battery to facilitate its cooling is crucial. The thermal behaviour of the battery was evaluated in terms both of the average surface temperatures reached and of the surface heat fluxes. The surface temperature is referred with T_bi while the heat flux with q_bi. The numeration of the faces of the battery is shown in Figure 135. Results for different operative conditions are reported from Table 65 to Table 88.

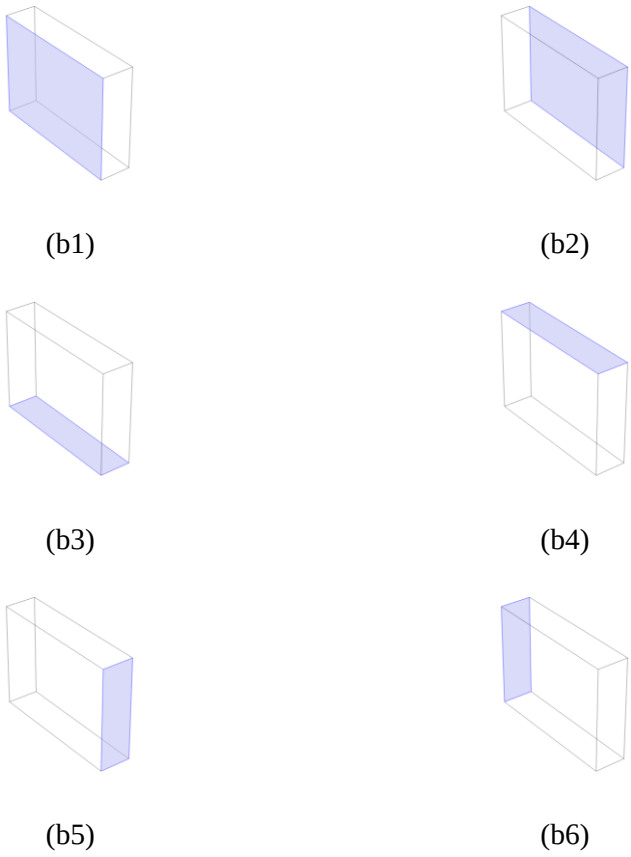

Figure 135: Schematic of the battery and numeration of the faces adopted.

Table 65: Surface heat fluxes and surface temperatures under the following conditions: solar radiation 50 W/mq and wind velocity 1m/s for battery casing.

T_air [°C]	q_b1 [kW/m^2]	T_b1 [°C]	q_b2 [kW/m^2]	T_b2 [°C]
20	-5.2406	20.12	0.0006	20.99
25	-4.9221	25.09	0.0016	25.04
30	-4.6047	30.06	0.0026	29.11
35	-4.2885	35.03	0.0035	33.19
40	-3.9730	40.00	0.0045	37.29

T_air [°C]	q_b3 [kW/m^2]	T_b3 [°C]	q_b4 [kW/m^2]	T_b4 [°C]
20	23.9470	20.07	-5.4869	20.23
25	22.5170	25.03	-5.2764	25.12
30	21.0860	29.99	-5.0433	30.01
35	19.6510	34.96	-4.7930	34.91
40	18.2210	39.92	-4.5240	39.80

T_air [°C]	q_b5 [kW/m^2]	T_b5 [°C]	q_b6 [kW/m^2]	T_b6 [°C]
20	-4.2452	20.10	-2.9573	20.07
25	-3.9345	25.05	-2.7825	25.04
30	-3.6331	30.01	-2.6075	30.00
35	-3.3404	34.97	-2.4321	34.97
40	-3.0555	39.93	-2.2568	39.94

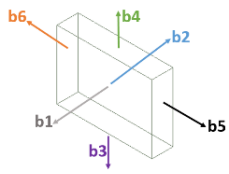

Table 66: Surface heat fluxes and surface temperatures under the following conditions: solar radiation 100 W/mq and wind velocity 1m/s.

T_air [°C]	q_b1 [kW/m^2]	T_b1 [°C]	q_b2 [kW/m^2]	T_b2 [°C]
20	-5.2381	20.26	0.0014	22.15
25	-4.9197	25.23	0.0023	26.18
30	-4.6023	30.20	0.0033	30.23
35	-4.2862	35.16	0.0043	34.29
40	-3.9707	40.13	0.0052	38.36

T_air [°C]	q_b3 [kW/m^2]	T_b3 [°C]	q_b4 [kW/m^2]	T_b4 [°C]
20	23.9480	20.15	-5.4819	20.49
25	22.5170	25.11	-5.2714	25.38
30	21.0870	30.07	-5.0384	30.27
35	19.6510	35.03	-4.7880	35.16
40	18.2210	40.00	-4.5191	40.05

T_air [°C]	q_b5 [kW/m^2]	T_b5 [°C]	q_b6 [kW/m^2]	T_b6 [°C]
20	-4.2433	20.21	-2.9554	20.15
25	-3.9327	25.16	-2.7806	25.11
30	-3.6313	30.12	-2.6057	30.08
35	-3.3386	35.07	-2.4303	35.05
40	-3.0538	40.03	-2.2551	40.01

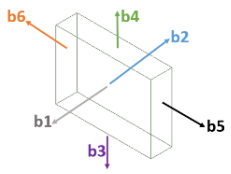

Table 67: Surface heat fluxes and surface temperatures under the following conditions: solar radiation 200 W/mq and wind velocity 1m/s.

T_air [°C]	q_b1 [kW/m^2]	T_b1 [°C]	q_b2 [kW/m^2]	T_b2 [°C]
20	-5.2327	20.57	0.0031	24.63
25	-4.9143	25.53	0.0040	28.61
30	-4.5971	30.49	0.0049	32.61
35	-4.2811	35.45	0.0058	36.61
40	-3.9657	40.41	0.0067	40.64

T_air [°C]	q_b3 [kW/m^2]	T_b3 [°C]	q_b4 [kW/m^2]	T_b4 [°C]
20	23.9490	20.32	-5.4712	21.05
25	22.5180	25.28	-5.2608	25.93
30	21.0880	30.24	-5.0278	30.81
35	19.6520	35.20	-4.7775	35.69
40	18.2220	40.16	-4.5087	40.57

T_air [°C]	q_b5 [kW/m^2]	T_b5 [°C]	q_b6 [kW/m^2]	T_b6 [°C]
20	-4.2393	20.45	-2.9514	20.32
25	-3.9287	25.40	-2.7767	25.28
30	-3.6274	30.35	-2.6018	30.25
35	-3.3348	35.30	-2.4265	35.21
40	-3.0501	40.25	-2.2513	40.17

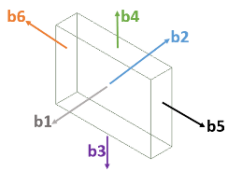

Table 68: Surface heat fluxes and surface temperatures under the following conditions: solar radiation 400 W/mq and wind velocity 1m/s.

T_air [°C]	q_b1 [kW/m^2]	T_b1 [°C]	q_b2 [kW/m^2]	T_b2 [°C]
20	-5.2212	21.23	0.0066	29.77
25	-4.9031	26.17	0.0074	33.66
30	-4.5860	31.12	0.0082	37.55
35	-4.2702	36.07	0.0090	41.47
40	-3.9551	41.01	0.0098	45.39

T_air [°C]	q_b3 [kW/m^2]	T_b3 [°C]	q_b4 [kW/m^2]	T_b4 [°C]
20	23.9510	20.69	-5.4488	22.22
25	22.5200	25.64	-5.2384	27.08
30	21.0900	30.60	-5.0055	31.95
35	19.6540	35.55	-4.7554	36.81
40	18.2240	40.50	-4.4867	41.68

T_air [°C]	q_b5 [kW/m^2]	T_b5 [°C]	q_b6 [kW/m^2]	T_b6 [°C]
20	-4.2306	20.96	-2.9429	20.69
25	-3.9203	25.89	-2.7683	25.64
30	-3.6192	30.83	-2.5935	30.60
35	-3.3268	35.77	-2.4183	35.56
40	-3.0422	40.72	-2.2433	40.52

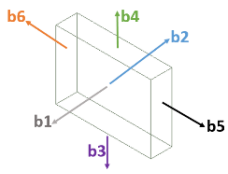

Table 69: Surface heat fluxes and surface temperatures under the following conditions: solar radiation 800 W/mq and wind velocity 1m/s.

T_air [°C]	q_b1 [kW/m^2]	T_b1 [°C]	q_b2 [kW/m^2]	T_b2 [°C]
20	-5.1977	22.56	0.0134	40.02
25	-4.8800	27.48	0.0140	43.73
30	-4.5633	32.40	0.0147	47.46
35	-4.2479	37.33	0.0153	51.20
40	-3.9331	42.25	0.0159	54.95

T_air [°C]	q_b3 [kW/m^2]	T_b3 [°C]	q_b4 [kW/m^2]	T_b4 [°C]
20	23.9550	21.45	-5.4022	24.66
25	22.5250	26.39	-5.1918	29.49
30	21.0940	31.33	-4.9590	34.32
35	19.6580	36.28	-4.7091	39.16
40	18.2280	41.22	-4.4408	43.99

T_air [°C]	q_b5 [kW/m^2]	T_b5 [°C]	q_b6 [kW/m^2]	T_b6 [°C]
20	-4.2128	22.01	-2.9252	21.44
25	-3.9028	26.93	-2.7508	26.39
30	-3.6021	31.85	-2.5763	31.34
35	-3.3101	36.77	-2.4013	36.29
40	-3.0259	41.69	-2.2265	41.24

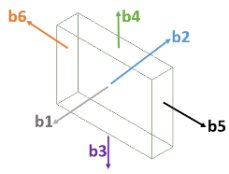

Table 70: Surface heat fluxes and surface temperatures under the following conditions: solar radiation 1000 W/mq and wind velocity 1m/s.

T_air [°C]	q_b1 [kW/m^2]	T_b1 [°C]	q_b2 [kW/m^2]	T_b2 [°C]
20	-5.1860	23.22	0.0167	45.00
25	-4.8684	28.13	0.0172	48.64
30	-4.5520	33.04	0.0178	52.28
35	-4.2367	37.96	0.0183	55.94
40	-3.9221	42.87	0.0189	59.62

T_air [°C]	q_b3 [kW/m^2]	T_b3 [°C]	q_b4 [kW/m^2]	T_b4 [°C]
20	23.9570	21.83	-5.3786	25.90
25	22.5270	26.77	-5.1682	30.72
30	21.0960	31.71	-4.9354	35.54
35	19.6600	36.64	-4.6856	40.35
40	18.2300	41.58	-4.4174	45.17

T_air [°C]	q_b5 [kW/m^2]	T_b5 [°C]	q_b6 [kW/m^2]	T_b6 [°C]
20	-4.2038	22.55	-2.9162	21.83
25	-3.8940	27.45	-2.7420	26.77
30	-3.5935	32.36	-2.5675	31.72
35	-3.3016	37.27	-2.3927	36.66
40	-3.0176	42.18	-2.2180	41.60

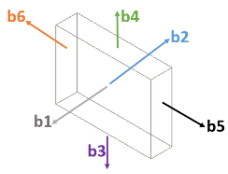

Table 71: Surface heat fluxes and surface temperatures under the following conditions: solar radiation 50 W/mq and wind velocity 2m/s.

T_air [°C]	q_b1 [kW/m^2]	T_b1 [°C]	q_b2 [kW/m^2]	T_b2 [°C]
20	-0.0057	20.24	0.0011	21.58
25	-0.0047	25.19	0.0021	25.48
30	-0.0053	30.14	0.0032	29.38
35	-0.0072	35.10	0.0042	33.31
40	-0.0099	40.05	0.0052	37.26

T_air [°C]	q_b3 [kW/m^2]	T_b3 [°C]	q_b4 [kW/m^2]	T_b4 [°C]
20	0.0583	20.54	-0.0308	20.18
25	0.0741	25.28	-0.1163	25.11
30	0.0890	30.06	-0.1762	30.04
35	0.1066	34.86	-0.2108	34.97
40	0.1257	39.65	-0.2238	39.88

T_air [°C]	q_b5 [kW/m^2]	T_b5 [°C]	q_b6 [kW/m^2]	T_b6 [°C]
20	-1.1192	20.34	0.8055	20.36
25	-0.8209	25.19	0.7001	25.19
30	-0.5783	30.03	0.6023	30.01
35	-0.4004	34.86	0.5131	34.84
40	-0.2810	39.70	0.4328	39.69

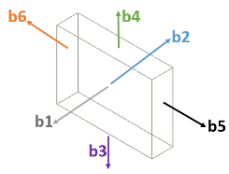

Table 72: Surface heat fluxes and surface temperatures under the following conditions: solar radiation 100 W/mq and wind velocity 2m/s.

T_air [°C]	q_b1 [kW/m^2]	T_b1 [°C]	q_b2 [kW/m^2]	T_b2 [°C]
20	-0.0029	20.48	0.0022	23.16
25	-0.0019	25.43	0.0032	27.05
30	-0.0025	30.38	0.0042	30.96
35	-0.0044	35.34	0.0053	34.88
40	-0.0071	40.30	0.0063	38.83

T_air [°C]	q_b3 [kW/m^2]	T_b3 [°C]	q_b4 [kW/m^2]	T_b4 [°C]
20	0.0600	21.05	-0.0289	20.35
25	0.0757	25.78	-0.1142	25.29
30	0.0906	30.56	-0.1741	30.23
35	0.1081	35.36	-0.2085	35.16
40	0.1272	40.17	-0.2215	40.09

T_air [°C]	q_b5 [kW/m^2]	T_b5 [°C]	q_b6 [kW/m^2]	T_b6 [°C]
20	-1.1166	20.68	0.8068	20.72
25	-0.8183	25.55	0.7014	25.55
30	-0.5759	30.39	0.6036	30.38
35	-0.3981	35.23	0.5144	35.20
40	-0.2788	40.08	0.4341	40.04

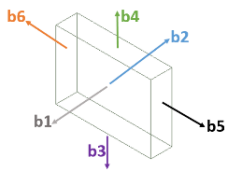

Table 73: Surface heat fluxes and surface temperatures under the following conditions: solar radiation 200 W/mq and wind velocity 2m/s.

T_air [°C]	q_b1 [kW/m^2]	T_b1 [°C]	q_b2 [kW/m^2]	T_b2 [°C]
20	0.0026	20.95	0.0043	26.29
25	0.0036	25.91	0.0053	30.18
30	0.0031	30.87	0.0064	34.08
35	0.0012	35.82	0.0074	38.00
40	-0.0015	40.78	0.0084	41.95

T_air [°C]	q_b3 [kW/m^2]	T_b3 [°C]	q_b4 [kW/m^2]	T_b4 [°C]
20	0.0632	22.05	-0.0247	20.71
25	0.0789	26.74	-0.1100	25.65
30	0.0937	31.54	-0.1697	30.61
35	0.1112	36.35	-0.2041	35.56
40	0.1302	41.18	-0.2169	40.51

T_air [°C]	q_b5 [kW/m^2]	T_b5 [°C]	q_b6 [kW/m^2]	T_b6 [°C]
20	-1.1113	21.36	0.8095	21.44
25	-0.8131	26.27	0.7041	26.27
30	-0.5711	31.12	0.6063	31.10
35	-0.3936	35.97	0.5170	35.92
40	-0.2745	40.82	0.4367	40.73

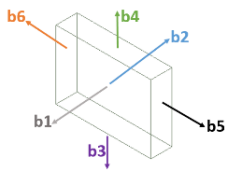

Table 74: Surface heat fluxes and surface temperatures under the following conditions: solar radiation 400 W/mq and wind velocity 2m/s.

T_air [°C]	q_b1 [kW/m^2]	T_b1 [°C]	q_b2 [kW/m^2]	T_b2 [°C]
20	0.0138	21.89	0.0086	32.50
25	0.0148	26.86	0.0096	36.39
30	0.0143	31.82	0.0106	40.29
35	0.0123	36.79	0.0116	44.20
40	0.0097	41.75	0.0127	48.13

T_air [°C]	q_b3 [kW/m^2]	T_b3 [°C]	q_b4 [kW/m^2]	T_b4 [°C]
20	0.0696	23.93	-0.0166	21.41
25	0.0853	28.60	-0.1016	26.38
30	0.1001	33.41	-0.1610	31.36
35	0.1174	38.26	-0.1951	36.35
40	0.1363	43.13	-0.2077	41.34

T_air [°C]	q_b5 [kW/m^2]	T_b5 [°C]	q_b6 [kW/m^2]	T_b6 [°C]
20	-1.1001	22.70	0.8148	22.86
25	-0.8027	27.68	0.7094	27.70
30	-0.5614	32.58	0.6116	32.54
35	-0.3845	37.45	0.5222	37.32
40	-0.2659	42.29	0.4421	42.08

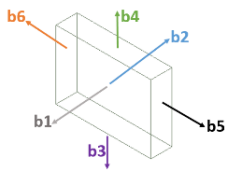

Table 75: Surface heat fluxes and surface temperatures under the following conditions: solar radiation 800 W/mq and wind velocity 2m/s.

T_air [°C]	q_b1 [kW/m^2]	T_b1 [°C]	q_b2 [kW/m^2]	T_b2 [°C]
20	0.0360	23.76	0.0169	44.72
25	0.0371	28.74	0.0179	48.62
30	0.0366	33.72	0.0189	52.52
35	0.0347	38.70	0.0200	56.41
40	0.0321	43.69	0.0210	60.34

T_air [°C]	q_b3 [kW/m^2]	T_b3 [°C]	q_b4 [kW/m^2]	T_b4 [°C]
20	0.0828	27.50	-0.0003	22.84
25	0.0984	32.13	-0.0847	27.85
30	0.1129	37.00	-0.1436	32.89
35	0.1301	41.93	-0.1771	37.96
40	0.1486	46.88	-0.1893	43.04

T_air [°C]	q_b5 [kW/m^2]	T_b5 [°C]	q_b6 [kW/m^2]	T_b6 [°C]
20	-1.0779	25.35	0.8256	25.67
25	-0.7819	30.46	0.7202	30.52
30	-0.5420	35.45	0.6222	35.37
35	-0.3664	40.40	0.5329	40.05
40	-0.2488	45.26	0.4531	44.72

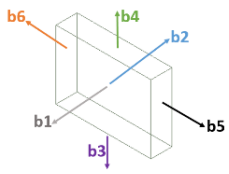

Table 76: Surface heat fluxes and surface temperatures under the following conditions: solar radiation 1000 W/mq and wind velocity 2m/s.

T_air [°C]	q_b1 [kW/m^2]	T_b1 [°C]	q_b2 [kW/m^2]	T_b2 [°C]
20	0.0472	24.69	0.0210	50.74
25	0.0483	29.68	0.0220	54.65
30	0.0478	34.67	0.0230	58.55
35	0.0459	39.65	0.0241	62.44
40	0.0433	44.65	0.0251	66.37

T_air [°C]	q_b3 [kW/m^2]	T_b3 [°C]	q_b4 [kW/m^2]	T_b4 [°C]
20	0.0894	29.22	0.0079	23.56
25	0.1049	33.85	-0.0762	28.60
30	0.1194	38.74	-0.1349	33.66
35	0.1364	43.71	-0.1681	38.77
40	0.1548	48.71	-0.1801	43.90

T_air [°C]	q_b5 [kW/m^2]	T_b5 [°C]	q_b6 [kW/m^2]	T_b6 [°C]
20	-1.0665	26.66	0.8310	27.06
25	-0.7714	31.83	0.7257	31.92
30	-0.5323	36.87	0.6275	36.75
35	-0.3573	41.87	0.5384	41.39
40	-0.2402	46.76	0.4586	46.02

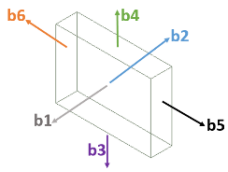

Table 77: Surface heat fluxes and surface temperatures under the following conditions: solar radiation 50 W/mq and wind velocity 5m/s.

T_air [°C]	q_b1 [kW/m^2]	T_b1 [°C]	q_b2 [kW/m^2]	T_b2 [°C]
20	-0.0196	20.11	0.0010	21.35
25	-0.0180	25.08	0.0020	25.36
30	-0.0167	30.06	0.0031	29.40
35	-0.0157	35.04	0.0041	33.45
40	-0.0149	40.02	0.0052	37.51

T_air [°C]	q_b3 [kW/m^2]	T_b3 [°C]	q_b4 [kW/m^2]	T_b4 [°C]
20	0.1036	20.33	-0.0814	20.08
25	0.1093	25.15	-0.1166	25.05
30	0.1139	30.00	-0.1454	30.02
35	0.1147	34.86	-0.1684	34.98
40	0.1126	39.73	-0.1857	39.95

T_air [°C]	q_b5 [kW/m^2]	T_b5 [°C]	q_b6 [kW/m^2]	T_b6 [°C]
20	-3.0367	20.16	2.1997	20.17
25	-2.7684	25.08	2.0446	25.09
30	-2.5094	30.00	1.8929	30.00
35	-2.2570	34.92	1.7442	34.90
40	-2.0148	39.84	1.5984	39.81

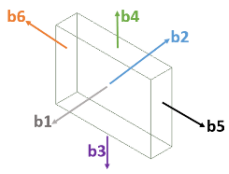

Table 78: Surface heat fluxes and surface temperatures under the following conditions: solar radiation 100 W/mq and wind velocity 5m/s.

T_air [°C]	q_b1 [kW/m^2]	T_b1 [°C]	q_b2 [kW/m^2]	T_b2 [°C]
20	-0.0168	20.21	0.0020	22.69
25	-0.0152	25.19	0.0030	26.70
30	-0.0140	30.17	0.0041	30.73
35	-0.0130	35.15	0.0051	34.77
40	-0.0121	40.13	0.0061	38.83

T_air [°C]	q_b3 [kW/m^2]	T_b3 [°C]	q_b4 [kW/m^2]	T_b4 [°C]
20	0.1054	20.66	-0.0793	20.16
25	0.1111	25.47	-0.1145	25.13
30	0.1158	30.30	-0.1434	30.10
35	0.1166	35.16	-0.1663	35.06
40	0.1144	40.02	-0.1835	40.03

T_air [°C]	q_b5 [kW/m^2]	T_b5 [°C]	q_b6 [kW/m^2]	T_b6 [°C]
20	-3.0338	20.32	2.2011	20.33
25	-2.7655	25.25	2.0460	25.26
30	-2.5064	30.17	1.8942	30.17
35	-2.2541	35.09	1.7456	35.08
40	-2.0119	40.01	1.5998	39.99

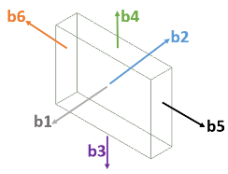

Table 79: Surface heat fluxes and surface temperatures under the following conditions: solar radiation 200 W/mq and wind velocity 5m/s.

T_air [°C]	q_b1 [kW/m^2]	T_b1 [°C]	q_b2 [kW/m^2]	T_b2 [°C]
20	-0.0113	20.42	0.0040	25.36
25	-0.0097	25.40	0.0050	29.37
30	-0.0084	30.38	0.0060	33.38
35	-0.0074	35.36	0.0070	37.41
40	-0.0066	40.34	0.0081	41.45

T_air [°C]	q_b3 [kW/m^2]	T_b3 [°C]	q_b4 [kW/m^2]	T_b4 [°C]
20	0.1091	21.29	-0.0751	20.32
25	0.1148	26.09	-0.1103	25.29
30	0.1194	30.91	-0.1391	30.26
35	0.1203	35.75	-0.1620	35.23
40	0.1181	40.60	-0.1793	40.19

T_air [°C]	q_b5 [kW/m^2]	T_b5 [°C]	q_b6 [kW/m^2]	T_b6 [°C]
20	-3.0279	20.64	2.2039	20.67
25	-2.7596	25.58	2.0487	25.60
30	-2.5005	30.51	1.8970	30.52
35	-2.2482	35.43	1.7482	35.43
40	-2.0061	40.35	1.6024	40.34

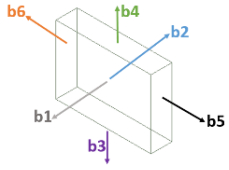

Table 80: Surface heat fluxes and surface temperatures under the following conditions: solar radiation 400 W/mq and wind velocity 5m/s.

T_air [°C]	q_b1 [kW/m^2]	T_b1 [°C]	q_b2 [kW/m^2]	T_b2 [°C]
20	-0.0003	20.83	0.0079	30.66
25	0.0014	25.81	0.0089	34.65
30	0.0026	30.80	0.0099	38.64
35	0.0036	35.78	0.0109	42.64
40	0.0045	40.76	0.0120	46.67

T_air [°C]	q_b3 [kW/m^2]	T_b3 [°C]	q_b4 [kW/m^2]	T_b4 [°C]
20	0.1166	22.50	-0.0668	20.63
25	0.1222	27.29	-0.1019	25.61
30	0.1268	32.08	-0.1307	30.58
35	0.1277	36.90	-0.1536	35.55
40	0.1255	41.75	-0.1708	40.52

T_air [°C]	q_b5 [kW/m^2]	T_b5 [°C]	q_b6 [kW/m^2]	T_b6 [°C]
20	-3.0160	21.28	2.2095	21.34
25	-2.7478	26.23	2.0543	26.28
30	-2.4887	31.18	1.9024	31.21
35	-2.2365	36.11	1.7537	36.13
40	-1.9944	41.03	1.6078	41.04

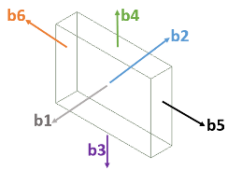

Table 81: Surface heat fluxes and surface temperatures under the following conditions: solar radiation 800 W/mq and wind velocity 5m/s.

T_air [°C]	q_b1 [kW/m^2]	T_b1 [°C]	q_b2 [kW/m^2]	T_b2 [°C]
20	0.0218	21.66	0.0157	41.10
25	0.0235	26.65	0.0167	45.05
30	0.0248	31.63	0.0176	49.00
35	0.0258	36.61	0.0186	52.97
40	0.0267	41.60	0.0196	56.96

T_air [°C]	q_b3 [kW/m^2]	T_b3 [°C]	q_b4 [kW/m^2]	T_b4 [°C]
20	0.1316	24.81	-0.0502	21.27
25	0.1370	29.57	-0.0852	26.24
30	0.1416	34.32	-0.1139	31.22
35	0.1424	39.12	-0.1366	36.19
40	0.1403	43.96	-0.1538	41.17

T_air [°C]	q_b5 [kW/m^2]	T_b5 [°C]	q_b6 [kW/m^2]	T_b6 [°C]
20	-2.9923	22.55	2.2208	22.67
25	-2.7241	27.54	2.0654	27.64
30	-2.4652	32.50	1.9134	32.59
35	-2.2130	37.46	1.7646	37.52
40	-1.9711	42.40	1.6187	42.45

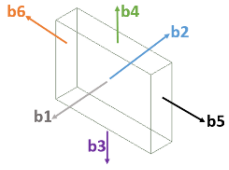

Table 82: Surface heat fluxes and surface temperatures under the following conditions: solar radiation 1000 W/mq and wind velocity 5m/s.

T_air [°C]	q_b1 [kW/m^2]	T_b1 [°C]	q_b2 [kW/m^2]	T_b2 [°C]
20	0.0329	22.07	0.0195	46.24
25	0.0346	27.06	0.0205	50.18
30	0.0359	32.05	0.0214	54.12
35	0.0369	37.03	0.0224	58.07
40	0.0379	42.02	0.0233	62.04

T_air [°C]	q_b3 [kW/m^2]	T_b3 [°C]	q_b4 [kW/m^2]	T_b4 [°C]
20	0.1391	25.92	-0.0418	21.59
25	0.1445	30.67	-0.0768	26.56
30	0.1491	35.41	-0.1055	31.54
35	0.1499	40.20	-0.1282	36.51
40	0.1477	45.03	-0.1452	41.49

T_air [°C]	q_b5 [kW/m^2]	T_b5 [°C]	q_b6 [kW/m^2]	T_b6 [°C]
20	-2.9805	23.19	2.2264	23.34
25	-2.7123	28.19	2.0709	28.32
30	-2.4534	33.17	1.9189	33.28
35	-2.2013	38.13	1.7700	38.22
40	-1.9595	43.08	1.6242	43.14

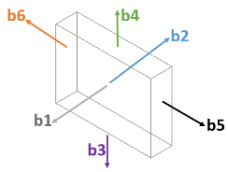

Table 83: Surface heat fluxes and surface temperatures under the following conditions: solar radiation 50 W/mq and wind velocity 7m/s.

T_air [°C]	q_b1 [kW/m^2]	T_b1 [°C]	q_b2 [kW/m^2]	T_b2 [°C]
20	-0.0288	20.08	0.0010	21.29
25	-0.0268	25.06	0.0020	25.35
30	-0.0250	30.05	0.0030	29.41
35	-0.0233	35.03	0.0041	33.50
40	-0.0218	40.02	0.0051	37.60

T_air [°C]	q_b3 [kW/m^2]	T_b3 [°C]	q_b4 [kW/m^2]	T_b4 [°C]
20	0.1451	20.27	-0.1157	20.06
25	0.1447	25.12	-0.1375	25.04
30	0.1433	29.98	-0.1560	30.01
35	0.1415	34.85	-0.1702	34.99
40	0.1381	39.74	-0.1804	39.97

T_air [°C]	q_b5 [kW/m^2]	T_b5 [°C]	q_b6 [kW/m^2]	T_b6 [°C]
20	-4.3078	20.12	3.1169	20.13
25	-3.9875	25.06	2.9131	25.06
30	-3.6762	30.00	2.7120	30.00
35	-3.3723	34.94	2.5132	34.93
40	-3.0747	39.88	2.3167	39.86

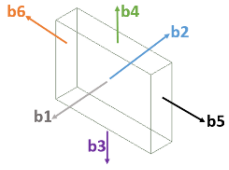

Table 84: Surface heat fluxes and surface temperatures under the following conditions: solar radiation 100 W/mq and wind velocity 7m/s.

T_air [°C]	q_b1 [kW/m^2]	T_b1 [°C]	q_b2 [kW/m^2]	T_b2 [°C]
20	-0.0260	20.16	0.0020	22.57
25	-0.0241	25.14	0.0030	26.62
30	-0.0222	30.13	0.0040	30.69
35	-0.0206	35.11	0.0050	34.76
40	-0.0191	40.09	0.0061	38.86

T_air [°C]	q_b3 [kW/m^2]	T_b3 [°C]	q_b4 [kW/m^2]	T_b4 [°C]
20	0.1470	20.54	-0.1136	20.12
25	0.1466	25.39	-0.1354	25.10
30	0.1452	30.24	-0.1539	30.07
35	0.1434	35.11	-0.1681	35.05
40	0.1400	39.99	-0.1783	40.03

T_air [°C]	q_b5 [kW/m^2]	T_b5 [°C]	q_b6 [kW/m^2]	T_b6 [°C]
20	-4.3048	20.24	3.1183	20.25
25	-3.9844	25.19	2.9145	25.19
30	-3.6732	30.13	2.7134	30.13
35	-3.3694	35.06	2.5146	35.06
40	-3.0717	40.00	2.3181	39.99

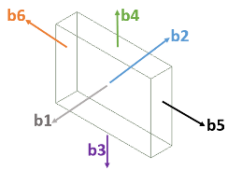

Table 85: Surface heat fluxes and surface temperatures under the following conditions: solar radiation 200 W/mq and wind velocity 7 m/s.

T_air [°C]	q_b1 [kW/m^2]	T_b1 [°C]	q_b2 [kW/m^2]	T_b2 [°C]
20	-0.0206	20.31	0.0039	25.13
25	-0.0186	25.29	0.0049	29.17
30	-0.0167	30.28	0.0059	33.22
35	-0.0151	35.26	0.0070	37.29
40	-0.0136	40.25	0.0080	41.36

T_air [°C]	q_b3 [kW/m^2]	T_b3 [°C]	q_b4 [kW/m^2]	T_b4 [°C]
20	0.1509	21.06	-0.1095	20.24
25	0.1504	25.91	-0.1312	25.21
30	0.1490	30.75	-0.1497	30.19
35	0.1472	35.61	-0.1639	35.17
40	0.1438	40.48	-0.1741	40.14

T_air [°C]	q_b5 [kW/m^2]	T_b5 [°C]	q_b6 [kW/m^2]	T_b6 [°C]
20	-4.2987	20.48	3.1212	20.50
25	-3.9784	25.43	2.9174	25.44
30	-3.6671	30.37	2.7162	30.38
35	-3.3633	35.31	2.5174	35.32
40	-3.0657	40.25	2.3209	40.25

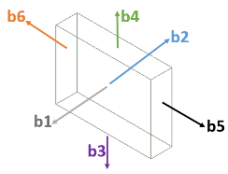

Table 86: Surface heat fluxes and surface temperatures under the following conditions: solar radiation 400 W/mq and wind velocity 7m/s.

T_air [°C]	q_b1 [kW/m^2]	T_b1 [°C]	q_b2 [kW/m^2]	T_b2 [°C]
20	-0.0096	20.61	0.0078	30.21
25	-0.0076	25.60	0.0088	34.23
30	-0.0057	30.59	0.0098	38.26
35	-0.0040	35.57	0.0108	42.30
40	-0.0025	40.56	0.0118	46.35

T_air [°C]	q_b3 [kW/m^2]	T_b3 [°C]	q_b4 [kW/m^2]	T_b4 [°C]
20	0.1586	22.08	-0.1011	20.47
25	0.1580	26.93	-0.1229	25.45
30	0.1566	31.76	-0.1413	30.43
35	0.1548	36.60	-0.1554	35.40
40	0.1514	41.45	-0.1656	40.38

T_air [°C]	q_b5 [kW/m^2]	T_b5 [°C]	q_b6 [kW/m^2]	T_b6 [°C]
20	-4.2867	20.96	3.1269	21.00
25	-3.9664	25.92	2.9230	25.94
30	-3.6550	30.87	2.7218	30.89
35	-3.3512	35.82	2.5230	35.83
40	-3.0536	40.76	2.3264	40.77

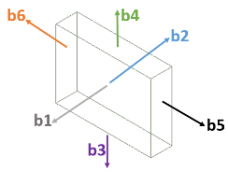

Table 87: Surface heat fluxes and surface temperatures under the following conditions: solar radiation 800 W/mq and wind velocity 7m/s.

T_air [°C]	q_b1 [kW/m^2]	T_b1 [°C]	q_b2 [kW/m^2]	T_b2 [°C]
20	0.0124	21.23	0.0155	40.22
25	0.0144	26.21	0.0164	44.20
30	0.0163	31.20	0.0174	48.19
35	0.0180	36.19	0.0183	52.18
40	0.0196	41.17	0.0193	56.19

T_air [°C]	q_b3 [kW/m^2]	T_b3 [°C]	q_b4 [kW/m^2]	T_b4 [°C]
20	0.1740	24.04	-0.0844	20.94
25	0.1732	28.89	-0.1061	25.92
30	0.1718	33.71	-0.1245	30.90
35	0.1699	38.52	-0.1385	35.88
40	0.1666	43.35	-0.1486	40.85

T_air [°C]	q_b5 [kW/m^2]	T_b5 [°C]	q_b6 [kW/m^2]	T_b6 [°C]
20	-4.2625	21.92	3.1383	21.99
25	-3.9422	26.89	2.9344	26.95
30	-3.6309	31.85	2.7331	31.90
35	-3.3271	36.81	2.5342	36.86
40	-3.0295	41.77	2.3376	41.80

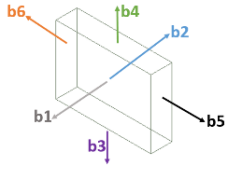

Table 88: Surface heat fluxes and surface temperatures under the following conditions: solar radiation 1000 W/mq and wind velocity 7m/s.

T_air [°C]	q_b1 [kW/m^2]	T_b1 [°C]	q_b2 [kW/m^2]	T_b2 [°C]
20	0.0234	21.53	0.0192	45.16
25	0.0255	26.52	0.0202	49.12
30	0.0274	31.51	0.0211	53.09
35	0.0291	36.49	0.0221	57.06
40	0.0307	41.48	0.0230	61.05

T_air [°C]	q_b3 [kW/m^2]	T_b3 [°C]	q_b4 [kW/m^2]	T_b4 [°C]
20	0.1817	25.00	-0.0760	21.17
25	0.1809	29.85	-0.0976	26.15
30	0.1794	34.65	-0.1160	31.13
35	0.1775	39.45	-0.1301	36.11
40	0.1741	44.27	-0.1401	41.09

T_air [°C]	q_b5 [kW/m^2]	T_b5 [°C]	q_b6 [kW/m^2]	T_b6 [°C]
20	-4.2505	22.39	3.1441	22.49
25	-3.9302	27.37	2.9401	27.45
30	-3.6188	32.34	2.7388	32.41
35	-3.3150	37.31	2.5398	37.37
40	-3.0174	42.27	2.3432	42.32

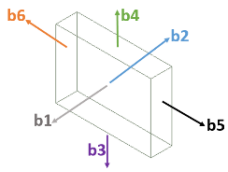

5.6 Thermal behaviour of the DC-DC

According to the data provided by the manufactures the maximum temperature admitted by the battery is ~ 150°C. The thermal behaviour of the DC-DC was evaluated in terms both of the average surface temperatures reached and of the surface heat fluxes. The surface temperature is referred with T_di while the heat flux with q_di. The numeration of the faces of the DC-DC is shown in Figure 136. Results for different operative conditions are reported from Table 89 to Table 112.

Results shown that the surfaces temperatures of the casing are higher since due to the heat generated by the DC-Dc is higher than battery generation.

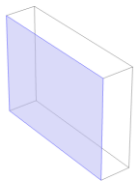

(d1)

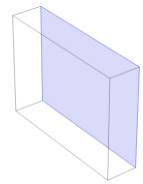

(d2)

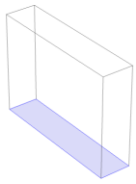

(d3)

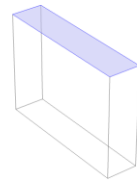

(d4)

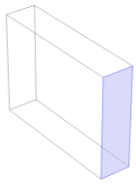

(d5)

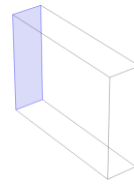

(d6)

Figure 136: Schematic of the DC-DC and numeration of the faces adopted.

Table 89: Surface heat fluxes and surface temperatures under the following conditions: solar radiation 50 W/mq and wind velocity 1m/s for DC-DC casing.

T_air [°C]	q_d1 [kW/m^2]	T_d1 [°C]	q_d2 [kW/m^2]	T_d2 [°C]
20	-5.2884	20.12	0.0007	21.03
25	-4.9685	25.09	0.0016	25.08
30	-4.6494	30.06	0.0026	29.16
35	-4.3307	35.03	0.0036	33.24
40	-4.0129	40.00	0.0046	37.34

T_air [°C]	q_d3 [kW/m^2]	T_d3 [°C]	q_d4 [kW/m^2]	T_d4 [°C]
20	23.7590	20.07	-5.5028	20.24
25	22.3400	25.03	-5.2611	25.13
30	20.9200	30.00	-5.0044	30.02
35	19.4960	34.96	-4.7364	34.92
40	18.0780	39.92	-4.4535	39.82

T_air [°C]	q_d5 [kW/m^2]	T_d5 [°C]	q_d6 [kW/m^2]	T_d6 [°C]
20	-2.5844	20.07	-3.7895	20.10
25	-2.4331	25.04	-3.5136	25.05
30	-2.2812	30.01	-3.2458	30.01
35	-2.1285	34.97	-2.9855	34.97
40	-1.9760	39.94	-2.7323	39.93

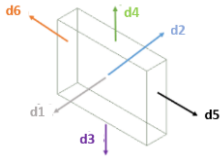

Table 90: Surface heat fluxes and surface temperatures under the following conditions: solar radiation 100 W/mq and wind velocity 1m/s for DC-DC casing.

T_air [°C]	q_d1 [kW/m^2]	T_d1 [°C]	q_d2 [kW/m^2]	T_d2 [°C]
20	-5.2857	20.27	0.0015	22.24
25	-4.9659	25.24	0.0024	26.27
30	-4.6469	30.20	0.0034	30.32
35	-4.3282	35.17	0.0043	34.38
40	-4.0105	40.14	0.0053	38.45

T_air [°C]	q_d3 [kW/m^2]	T_d3 [°C]	q_d4 [kW/m^2]	T_d4 [°C]
20	23.7590	20.16	-5.4977	20.51
25	22.3400	25.12	-5.2561	25.39
30	20.9210	30.08	-4.9994	30.28
35	19.4970	35.04	-4.7314	35.17
40	18.0780	40.00	-4.4486	40.07

T_air [°C]	q_d5 [kW/m^2]	T_d5 [°C]	q_d6 [kW/m^2]	T_d6 [°C]
20	-2.5825	20.16	-3.7876	20.21
25	-2.4311	25.12	-3.5117	25.17
30	-2.2793	30.09	-3.2439	30.12
35	-2.1266	35.05	-2.9837	35.08
40	-1.9741	40.02	-2.7306	40.03

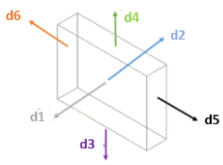

Table 91: Surface heat fluxes and surface temperatures under the following conditions: solar radiation 200 W/mq and wind velocity 1m/s for DC-DC casing.

T_air [°C]	q_d1 [kW/m^2]	T_d1 [°C]	q_d2 [kW/m^2]	T_d2 [°C]
20	-5.2800	20.59	0.0033	24.81
25	-4.9603	25.55	0.0041	28.79
30	-4.6414	30.51	0.0050	32.79
35	-4.3228	35.47	0.0059	36.80
40	-4.0052	40.43	0.0068	40.82

T_air [°C]	q_d3 [kW/m^2]	T_d3 [°C]	q_d4 [kW/m^2]	T_d4 [°C]
20	23.7600	20.34	-5.4868	21.08
25	22.3410	25.30	-5.2453	25.96
30	20.9220	30.26	-4.9887	30.83
35	19.4980	35.21	-4.7209	35.72
40	18.0790	40.17	-4.4382	40.60

T_air [°C]	q_d5 [kW/m^2]	T_d5 [°C]	q_d6 [kW/m^2]	T_d6 [°C]
20	-2.5782	20.33	-3.7834	20.46
25	-2.4270	25.30	-3.5076	25.41
30	-2.2752	30.26	-3.2399	30.36
35	-2.1226	35.22	-2.9798	35.31
40	-1.9701	40.19	-2.7268	40.26

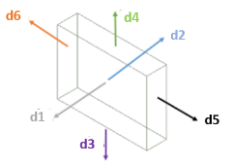

Table 92: Surface heat fluxes and surface temperatures under the following conditions: solar radiation 400 W/mq and wind velocity 1m/s for DC-DC casing.

T_air [°C]	q_d1 [kW/m^2]	T_d1 [°C]	q_d2 [kW/m^2]	T_d2 [°C]
20	-5.2680	21.25	0.0069	30.15
25	-4.9485	26.20	0.0077	34.03
30	-4.6298	31.15	0.0085	37.92
35	-4.3114	36.09	0.0093	41.83
40	-3.9940	41.04	0.0101	45.75

T_air [°C]	q_d3 [kW/m^2]	T_d3 [°C]	q_d4 [kW/m^2]	T_d4 [°C]
20	23.7630	20.72	-5.4640	22.28
25	22.3440	25.68	-5.2226	27.14
30	20.9240	30.63	-4.9662	32.00
35	19.5000	35.58	-4.6985	36.86
40	18.0810	40.53	-4.4160	41.73

T_air [°C]	q_d5 [kW/m^2]	T_d5 [°C]	q_d6 [kW/m^2]	T_d6 [°C]
20	-2.5692	20.71	-3.7746	20.97
25	-2.4181	25.67	-3.4990	25.91
30	-2.2665	30.63	-3.2315	30.85
35	-2.1140	35.59	-2.9716	35.79
40	-1.9617	40.55	-2.7187	40.73

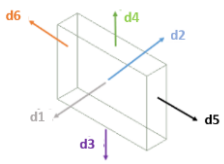

Table 93: Surface heat fluxes and surface temperatures under the following conditions: solar radiation 800 W/mq and wind velocity 1m/s for DC-DC casing.

T_air [°C]	q_d1 [kW/m^2]	T_d1 [°C]	q_d2 [kW/m^2]	T_d2 [°C]
20	-5.2434	22.61	0.0141	40.75
25	-4.9243	27.53	0.0147	44.44
30	-4.6059	32.45	0.0153	48.16
35	-4.2880	37.38	0.0160	51.89
40	-3.9710	42.30	0.0166	55.63

T_air [°C]	q_d3 [kW/m^2]	T_d3 [°C]	q_d4 [kW/m^2]	T_d4 [°C]
20	23.7680	21.52	-5.4165	24.78
25	22.3480	26.46	-5.1755	29.60
30	20.9290	31.40	-4.9195	34.43
35	19.5050	36.34	-4.6521	39.25
40	18.0850	41.28	-4.3701	44.08

T_air [°C]	q_d5 [kW/m^2]	T_d5 [°C]	q_d6 [kW/m^2]	T_d6 [°C]
20	-2.5506	21.50	-3.7564	22.04
25	-2.3997	26.45	-3.4811	26.96
30	-2.2483	31.40	-3.2140	31.88
35	-2.0961	36.35	-2.9544	36.81
40	-1.9440	41.29	-2.7019	41.73

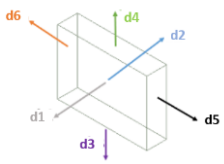

Table 94: Surface heat fluxes and surface temperatures under the following conditions: solar radiation 1000 W/mq and wind velocity 1m/s for DC-DC casing.

T_air [°C]	q_d1 [kW/m^2]	T_d1 [°C]	q_d2 [kW/m^2]	T_d2 [°C]
20	-5.2312	23.28	0.0175	45.88
25	-4.9123	28.19	0.0180	49.50
30	-4.5941	33.10	0.0186	53.13
35	-4.2763	38.02	0.0191	56.78
40	-3.9595	42.93	0.0197	60.44

T_air [°C]	q_d3 [kW/m^2]	T_d3 [°C]	q_d4 [kW/m^2]	T_d4 [°C]
20	23.7700	21.91	-5.3925	26.05
25	22.3510	26.85	-5.1516	30.86
30	20.9310	31.79	-4.8958	35.67
35	19.5070	36.73	-4.6286	40.48
40	18.0870	41.66	-4.3468	45.28

T_air [°C]	q_d5 [kW/m^2]	T_d5 [°C]	q_d6 [kW/m^2]	T_d6 [°C]
20	-2.5412	21.90	-3.7472	22.59
25	-2.3904	26.85	-3.4721	27.49
30	-2.2391	31.79	-3.2052	32.41
35	-2.0870	36.73	-2.9457	37.32
40	-1.9350	41.67	-2.6934	42.23

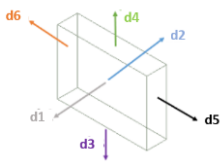

Table 95: Surface heat fluxes and surface temperatures under the following conditions: solar radiation 50 W/mq and wind velocity 2m/s for DC-DC casing.

T_air [°C]	q_d1 [kW/m^2]	T_d1 [°C]	q_d2 [kW/m^2]	T_d2 [°C]
20	-1.1273	20.18	0.0011	21.50
25	-1.0539	25.15	0.0021	25.50
30	-0.9818	30.12	0.0031	29.50
35	-0.9109	35.09	0.0042	33.52
40	-0.8413	40.06	0.0052	37.55

T_air [°C]	q_d3 [kW/m^2]	T_d3 [°C]	q_d4 [kW/m^2]	T_d4 [°C]
20	-0.7453	20.34	-1.5552	20.15
25	-0.6864	25.19	-1.5438	25.10
30	-0.6293	30.05	-1.5173	30.05
35	-0.5739	34.91	-1.4767	35.00
40	-0.5203	39.78	-1.4229	39.95

T_air [°C]	q_d5 [kW/m^2]	T_d5 [°C]	q_d6 [kW/m^2]	T_d6 [°C]
20	-1.2232	20.37	9.1206	20.10
25	-1.0742	25.21	8.5634	25.06
30	-0.9406	30.03	8.0079	30.02
35	-0.8207	34.86	7.4540	34.98
40	-0.7126	39.72	6.9023	39.94

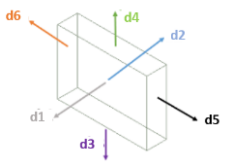

Table 96: Surface heat fluxes and surface temperatures under the following conditions: solar radiation 100 W/mq and wind velocity 2m/s for DC-DC casing.

T_air [°C]	q_d1 [kW/m^2]	T_d1 [°C]	q_d2 [kW/m^2]	T_d2 [°C]
20	-1.1244	20.36	0.0022	23.00
25	-1.0510	25.33	0.0032	26.99
30	-0.9789	30.30	0.0042	30.99
35	-0.9080	35.27	0.0053	35.00
40	-0.8383	40.24	0.0063	39.03

T_air [°C]	q_d3 [kW/m^2]	T_d3 [°C]	q_d4 [kW/m^2]	T_d4 [°C]
20	-0.7432	20.68	-1.5530	20.30
25	-0.6843	25.52	-1.5416	25.25
30	-0.6273	30.38	-1.5151	30.20
35	-0.5719	35.24	-1.4745	35.15
40	-0.5183	40.11	-1.4206	40.10

T_air [°C]	q_d5 [kW/m^2]	T_d5 [°C]	q_d6 [kW/m^2]	T_d6 [°C]
20	-1.2204	20.74	9.1217	20.20
25	-1.0716	25.59	8.5646	25.17
30	-0.9380	30.42	8.0091	30.13
35	-0.8181	35.24	7.4551	35.09
40	-0.7099	40.08	6.9035	40.05

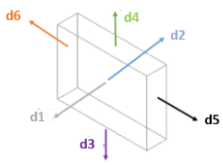

Table 97: Surface heat fluxes and surface temperatures under the following conditions: solar radiation 200 W/mq and wind velocity 2m/s for DC-DC casing.

T_air [°C]	q_d1 [kW/m^2]	T_d1 [°C]	q_d2 [kW/m^2]	T_d2 [°C]
20	-1.1185	20.72	0.0044	25.98
25	-1.0451	25.69	0.0054	29.97
30	-0.9729	30.66	0.0064	33.96
35	-0.9021	35.63	0.0074	37.96
40	-0.8324	40.60	0.0084	41.98

T_air [°C]	q_d3 [kW/m^2]	T_d3 [°C]	q_d4 [kW/m^2]	T_d4 [°C]
20	-0.7390	21.34	-1.5487	20.61
25	-0.6802	26.18	-1.5372	25.56
30	-0.6232	31.03	-1.5107	30.51
35	-0.5678	35.89	-1.4700	35.46
40	-0.5142	40.76	-1.4160	40.41

T_air [°C]	q_d5 [kW/m^2]	T_d5 [°C]	q_d6 [kW/m^2]	T_d6 [°C]
20	-1.2152	21.47	9.1241	20.41
25	-1.0663	26.36	8.5670	25.37
30	-0.9327	31.18	8.0115	30.33
35	-0.8127	35.99	7.4575	35.29
40	-0.7046	40.79	6.9057	40.25

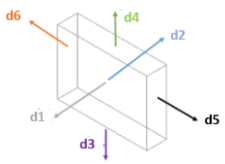

Table 98: Surface heat fluxes and surface temperatures under the following conditions: solar radiation 400 W/mq and wind velocity 2m/s for DC-DC casing.

T_air [°C]	q_d1 [kW/m^2]	T_d1 [°C]	q_d2 [kW/m^2]	T_d2 [°C]
20	-1.1067	21.44	0.0088	31.90
25	-1.0332	26.42	0.0098	35.88
30	-0.9611	31.39	0.0108	39.86
35	-0.8902	36.36	0.0117	43.84
40	-0.8206	41.32	0.0127	47.82

T_air [°C]	q_d3 [kW/m^2]	T_d3 [°C]	q_d4 [kW/m^2]	T_d4 [°C]
20	-0.7307	22.64	-1.5400	21.21
25	-0.6719	27.47	-1.5284	26.17
30	-0.6149	32.32	-1.5017	31.13
35	-0.5596	37.17	-1.4609	36.08
40	-0.5060	42.03	-1.4069	41.03

T_air [°C]	q_d5 [kW/m^2]	T_d5 [°C]	q_d6 [kW/m^2]	T_d6 [°C]
20	-1.2045	22.91	9.1289	20.82
25	-1.0557	27.87	8.5717	25.78
30	-0.9221	32.71	8.0162	30.74
35	-0.8020	37.47	7.4622	35.70
40	-0.6940	42.21	6.9105	40.67

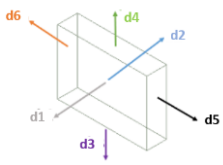

Table 99: Surface heat fluxes and surface temperatures under the following conditions: solar radiation 800 W/mq and wind velocity 2m/s for DC-DC casing.

T_air [°C]	q_d1 [kW/m^2]	T_d1 [°C]	q_d2 [kW/m^2]	T_d2 [°C]
20	-1.0830	22.89	0.0174	43.56
25	-1.0095	27.86	0.0183	47.54
30	-0.9374	32.83	0.0193	51.48
35	-0.8665	37.81	0.0202	55.41
40	-0.7968	42.78	0.0212	59.34

T_air [°C]	q_d3 [kW/m^2]	T_d3 [°C]	q_d4 [kW/m^2]	T_d4 [°C]
20	-0.7139	25.18	-1.5225	22.44
25	-0.6553	29.99	-1.5107	27.40
30	-0.5984	34.83	-1.4838	32.36
35	-0.5432	39.68	-1.4428	37.32
40	-0.4897	44.54	-1.3885	42.28

T_air [°C]	q_d5 [kW/m^2]	T_d5 [°C]	q_d6 [kW/m^2]	T_d6 [°C]
20	-1.1831	25.78	9.1383	21.64
25	-1.0345	30.82	8.5810	26.60
30	-0.9006	35.66	8.0254	31.57
35	-0.7807	40.34	7.4714	36.53
40	-0.6728	44.98	6.9196	41.49

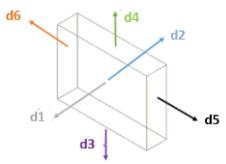

Table 100: Surface heat fluxes and surface temperatures under the following conditions: solar radiation 1000 W/mq and wind velocity 2 m/s for DC-DC casing.

T_air [°C]	q_d1 [kW/m^2]	T_d1 [°C]	q_d2 [kW/m^2]	T_d2 [°C]
20	-1.0711	23.61	0.0216	49.32
25	-0.9976	28.59	0.0225	53.28
30	-0.9255	33.56	0.0235	57.21
35	-0.8546	38.53	0.0244	61.11
40	-0.7849	43.50	0.0253	65.02

T_air [°C]	q_d3 [kW/m^2]	T_d3 [°C]	q_d4 [kW/m^2]	T_d4 [°C]
20	-0.7055	26.42	-1.5137	23.05
25	-0.6469	31.22	-1.5018	28.01
30	-0.5901	36.06	-1.4748	32.98
35	-0.5350	40.90	-1.4337	37.95
40	-0.4815	45.76	-1.3793	42.91

T_air [°C]	q_d5 [kW/m^2]	T_d5 [°C]	q_d6 [kW/m^2]	T_d6 [°C]
20	-1.1724	27.21	9.1429	22.05
25	-1.0239	32.27	8.5856	27.01
30	-0.8898	37.09	8.0300	31.98
35	-0.7701	41.74	7.4759	36.95
40	-0.6622	46.34	6.9241	41.91

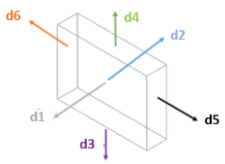

Table 101: Surface heat fluxes and surface temperatures under the following conditions: solar radiation 50 W/mq and wind velocity 5 m/s for DC-DC casing.

T_air [°C]	q_d1 [kW/m^2]	T_d1 [°C]	q_d2 [kW/m^2]	T_d2 [°C]
20	-2.9090	20.08	0.0010	21.32
25	-2.7328	25.07	0.0020	25.41
30	-2.5570	30.06	0.0031	29.52
35	-2.3815	35.04	0.0041	33.63
40	-2.2064	40.03	0.0051	37.76

T_air [°C]	q_d3 [kW/m^2]	T_d3 [°C]	q_d4 [kW/m^2]	T_d4 [°C]
20	-1.9926	20.18	-4.1053	20.07
25	-1.8666	25.10	-3.8961	25.05
30	-1.7420	30.02	-3.6820	30.02
35	-1.6184	34.94	-3.4629	35.00
40	-1.4959	39.87	-3.2392	39.98

T_air [°C]	q_d5 [kW/m^2]	T_d5 [°C]	q_d6 [kW/m^2]	T_d6 [°C]
20	-3.3435	20.17	23.9940	20.05
25	-3.1126	25.10	22.5550	25.03
30	-2.8859	30.01	21.1170	30.01
35	-2.6634	34.92	19.6790	34.99
40	-2.4449	39.83	18.2420	39.97

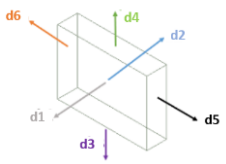

Table 102: Surface heat fluxes and surface temperatures under the following conditions: solar radiation 100 W/mq and wind velocity 5 m/s for DC-DC casing.

T_air [°C]	q_d1 [kW/m^2]	T_d1 [°C]	q_d2 [kW/m^2]	T_d2 [°C]
20	-2.9061	20.16	0.0021	22.64
25	-2.7299	25.15	0.0031	26.72
30	-2.5540	30.14	0.0041	30.82
35	-2.3786	35.12	0.0051	34.93
40	-2.2035	40.11	0.0061	39.05

T_air [°C]	q_d3 [kW/m^2]	T_d3 [°C]	q_d4 [kW/m^2]	T_d4 [°C]
20	-1.9903	20.36	-4.1031	20.15
25	-1.8644	25.28	-3.8939	25.12
30	-1.7397	30.20	-3.6797	30.10
35	-1.6162	35.12	-3.4607	35.07
40	-1.4937	40.04	-3.2370	40.05

T_air [°C]	q_d5 [kW/m^2]	T_d5 [°C]	q_d6 [kW/m^2]	T_d6 [°C]
20	-3.3406	20.35	23.9950	20.10
25	-3.1097	25.27	22.5560	25.08
30	-2.8830	30.19	21.1180	30.06
35	-2.6604	35.11	19.6800	35.04
40	-2.4420	40.01	18.2440	40.02

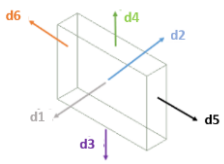

Table 103: Surface heat fluxes and surface temperatures under the following conditions: solar radiation 200 W/mq and wind velocity 5 m/s for DC-DC casing.

T_air [°C]	q_d1 [kW/m^2]	T_d1 [°C]	q_d2 [kW/m^2]	T_d2 [°C]
20	-2.9002	20.32	0.0041	25.26
25	-2.7240	25.31	0.0051	29.33
30	-2.5481	30.30	0.0061	33.42
35	-2.3727	35.28	0.0071	37.52
40	-2.1976	40.27	0.0082	41.63

T_air [°C]	q_d3 [kW/m^2]	T_d3 [°C]	q_d4 [kW/m^2]	T_d4 [°C]
20	-1.9859	20.72	-4.0986	20.29
25	-1.8600	25.64	-3.8894	25.27
30	-1.7353	30.56	-3.6753	30.24
35	-1.6117	35.48	-3.4562	35.22
40	-1.4893	40.40	-3.2325	40.20

T_air [°C]	q_d5 [kW/m^2]	T_d5 [°C]	q_d6 [kW/m^2]	T_d6 [°C]
20	-3.3348	20.69	23.9980	20.19
25	-3.1039	25.63	22.5590	25.17
30	-2.8772	30.55	21.1210	30.15
35	-2.6546	35.48	19.6830	35.14
40	-2.4361	40.39	18.2460	40.12

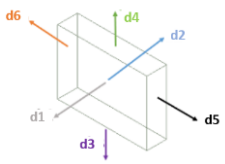

Table 104: Surface heat fluxes and surface temperatures under the following conditions: solar radiation 400 W/mq and wind velocity 5 m/s for DC-DC casing.

T_air [°C]	q_d1 [kW/m^2]	T_d1 [°C]	q_d2 [kW/m^2]	T_d2 [°C]
20	-2.8885	20.64	0.0082	30.46
25	-2.7122	25.63	0.0092	34.52
30	-2.5364	30.62	0.0102	38.59
35	-2.3609	35.61	0.0112	42.66
40	-2.1858	40.59	0.0122	46.75

T_air [°C]	q_d3 [kW/m^2]	T_d3 [°C]	q_d4 [kW/m^2]	T_d4 [°C]
20	-1.9770	21.44	-4.0897	20.58
25	-1.8511	26.36	-3.8805	25.56
30	-1.7265	31.28	-3.6663	30.54
35	-1.6029	36.20	-3.4473	35.51
40	-1.4804	41.12	-3.2235	40.49

T_air [°C]	q_d5 [kW/m^2]	T_d5 [°C]	q_d6 [kW/m^2]	T_d6 [°C]
20	-3.3232	21.38	24.0030	20.38
25	-3.0923	26.33	22.5640	25.36
30	-2.8655	31.28	21.1260	30.35
35	-2.6430	36.21	19.6880	35.33
40	-2.4245	41.13	18.2510	40.31

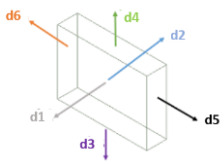

Table 105: Surface heat fluxes and surface temperatures under the following conditions: solar radiation 800 W/mq and wind velocity 5 m/s for DC-DC casing.

T_air [°C]	q_d1 [kW/m^2]	T_d1 [°C]	q_d2 [kW/m^2]	T_d2 [°C]
20	-2.8650	21.29	0.0164	40.74
25	-2.6887	26.28	0.0173	44.76
30	-2.5128	31.26	0.0182	48.78
35	-2.3373	36.25	0.0192	52.82
40	-2.1621	41.24	0.0201	56.87

T_air [°C]	q_d3 [kW/m^2]	T_d3 [°C]	q_d4 [kW/m^2]	T_d4 [°C]
20	-1.9592	22.87	-4.0720	21.17
25	-1.8333	27.79	-3.8627	26.15
30	-1.7087	32.70	-3.6484	31.12
35	-1.5852	37.62	-3.4293	36.10
40	-1.4627	42.54	-3.2055	41.08

T_air [°C]	q_d5 [kW/m^2]	T_d5 [°C]	q_d6 [kW/m^2]	T_d6 [°C]
20	-3.2998	22.76	24.0130	20.76
25	-3.0689	27.74	22.5740	25.75
30	-2.8422	32.71	21.1360	30.73
35	-2.6197	37.67	19.6980	35.71
40	-2.4012	42.61	18.2610	40.69

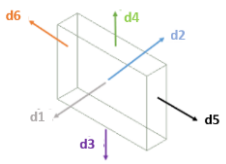

Table 106: Surface heat fluxes and surface temperatures under the following conditions: solar radiation 1000 W/mq and wind velocity 5 m/s for DC-DC casing.

T_air [°C]	q_d1 [kW/m^2]	T_d1 [°C]	q_d2 [kW/m^2]	T_d2 [°C]
20	-2.8532	21.61	0.0204	45.81
25	-2.6768	26.60	0.0213	49.81
30	-2.5009	31.59	0.0222	53.82
35	-2.3254	36.58	0.0231	57.83
40	-2.1503	41.57	0.0240	61.86

T_air [°C]	q_d3 [kW/m^2]	T_d3 [°C]	q_d4 [kW/m^2]	T_d4 [°C]
20	-1.9503	23.58	-4.0630	21.46
25	-1.8244	28.50	-3.8537	26.44
30	-1.6998	33.42	-3.6394	31.42
35	-1.5763	38.33	-3.4203	36.39
40	-1.4539	43.25	-3.1964	41.37

T_air [°C]	q_d5 [kW/m^2]	T_d5 [°C]	q_d6 [kW/m^2]	T_d6 [°C]
20	-3.2882	23.45	24.0180	20.96
25	-3.0573	28.45	22.5790	25.94
30	-2.8305	33.43	21.1410	30.92
35	-2.6080	38.40	19.7030	35.90
40	-2.3895	43.35	18.2660	40.89

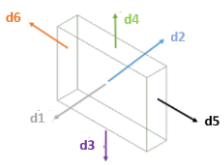

Table 107: Surface heat fluxes and surface temperatures under the following conditions: solar radiation 50 W/mq and wind velocity 7 m/s for DC-DC casing.

T_air [°C]	q_d1 [kW/m^2]	T_d1 [°C]	q_d2 [kW/m^2]	T_d2 [°C]
20	-4.0926	20.06	0.0010	21.28
25	-3.8464	25.05	0.0020	25.40
30	-3.6005	30.04	0.0030	29.53
35	-3.3548	35.03	0.0041	33.68
40	-3.1094	40.02	0.0051	37.83

T_air [°C]	q_d3 [kW/m^2]	T_d3 [°C]	q_d4 [kW/m^2]	T_d4 [°C]
20	-2.8102	20.14	-5.8006	20.06
25	-2.6373	25.08	-5.4801	25.04
30	-2.4653	30.02	-5.1563	30.02
35	-2.2940	34.95	-4.8291	35.00
40	-2.1236	39.89	-4.4985	39.98

T_air [°C]	q_d5 [kW/m^2]	T_d5 [°C]	q_d6 [kW/m^2]	T_d6 [°C]
20	-4.7401	20.13	33.8540	20.04
25	-4.4348	25.07	31.8270	25.02
30	-4.1324	30.01	29.8010	30.01
35	-3.8330	34.95	27.7760	34.99
40	-3.5365	39.88	25.7520	39.98

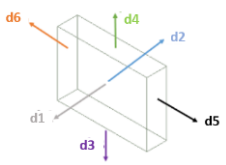

Table 108: Surface heat fluxes and surface temperatures under the following conditions: solar radiation 100 W/mq and wind velocity 7 m/s for DC-DC casing.

T_air [°C]	q_d1 [kW/m^2]	T_d1 [°C]	q_d2 [kW/m^2]	T_d2 [°C]
20	-4.0897	20.12	0.0020	22.55
25	-3.8435	25.11	0.0030	26.66
30	-3.5976	30.10	0.0040	30.79
35	-3.3519	35.09	0.0051	34.93
40	-3.1065	40.08	0.0061	39.08

T_air [°C]	q_d3 [kW/m^2]	T_d3 [°C]	q_d4 [kW/m^2]	T_d4 [°C]
20	-2.8079	20.28	-5.7984	20.11
25	-2.6351	25.22	-5.4778	25.09
30	-2.4631	30.16	-5.1541	30.07
35	-2.2918	35.09	-4.8268	35.06
40	-2.1213	40.03	-4.4962	40.04

T_air [°C]	q_d5 [kW/m^2]	T_d5 [°C]	q_d6 [kW/m^2]	T_d6 [°C]
20	-4.7372	20.26	33.8550	20.07
25	-4.4319	25.20	31.8280	25.06
30	-4.1294	30.14	29.8030	30.04
35	-3.8300	35.08	27.7780	35.03
40	-3.5335	40.02	25.7530	40.02

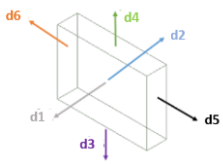

Table 109: Surface heat fluxes and surface temperatures under the following conditions: solar radiation 200 W/mq and wind velocity 7 m/s for DC-DC casing.

T_air [°C]	q_d1 [kW/m^2]	T_d1 [°C]	q_d2 [kW/m^2]	T_d2 [°C]
20	-4.0839	20.24	0.0041	25.08
25	-3.8377	25.23	0.0051	29.18
30	-3.5917	30.22	0.0061	33.30
35	-3.3460	35.21	0.0071	37.42
40	-3.1006	40.20	0.0081	41.56

T_air [°C]	q_d3 [kW/m^2]	T_d3 [°C]	q_d4 [kW/m^2]	T_d4 [°C]
20	-2.8034	20.56	-5.7939	20.22
25	-2.6306	25.50	-5.4734	25.20
30	-2.4586	30.44	-5.1496	30.18
35	-2.2873	35.37	-4.8223	35.17
40	-2.1168	40.31	-4.4917	40.15

T_air [°C]	q_d5 [kW/m^2]	T_d5 [°C]	q_d6 [kW/m^2]	T_d6 [°C]
20	-4.7312	20.52	33.8570	20.14
25	-4.4259	25.46	31.8310	25.13
30	-4.1235	30.41	29.8050	30.12
35	-3.8240	35.35	27.7800	35.10
40	-3.5275	40.29	25.7550	40.09

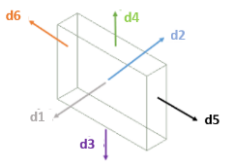

Table 110: Surface heat fluxes and surface temperatures under the following conditions: solar radiation 400 W/mq and wind velocity 7 m/s for DC-DC casing.

T_air [°C]	q_d1 [kW/m^2]	T_d1 [°C]	q_d2 [kW/m^2]	T_d2 [°C]
20	-4.0722	20.48	0.0081	30.11
25	-3.8259	25.47	0.0091	34.19
30	-3.5800	30.46	0.0101	38.28
35	-3.3343	35.45	0.0110	42.38
40	-3.0889	40.44	0.0120	46.50

T_air [°C]	q_d3 [kW/m^2]	T_d3 [°C]	q_d4 [kW/m^2]	T_d4 [°C]
20	-2.7945	21.12	-5.7850	20.44
25	-2.6216	26.06	-5.4644	25.42
30	-2.4496	31.00	-5.1406	30.40
35	-2.2783	35.93	-4.8133	35.39
40	-2.1079	40.87	-4.4827	40.37

T_air [°C]	q_d5 [kW/m^2]	T_d5 [°C]	q_d6 [kW/m^2]	T_d6 [°C]
20	-4.7193	21.03	33.8630	20.29
25	-4.4140	25.99	31.8360	25.27
30	-4.1116	30.94	29.8110	30.26
35	-3.8121	35.88	27.7850	35.25
40	-3.5156	40.83	25.7600	40.23

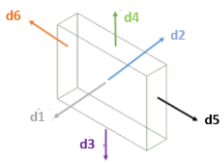

Table 111: Surface heat fluxes and surface temperatures under the following conditions: solar radiation 800 W/mq and wind velocity 7 m/s for DC-DC casing.

T_air [°C]	q_d1 [kW/m^2]	T_d1 [°C]	q_d2 [kW/m^2]	T_d2 [°C]
20	-4.0487	20.95	0.0161	40.04
25	-3.8024	25.94	0.0170	44.07
30	-3.5565	30.94	0.0180	48.12
35	-3.3107	35.93	0.0189	52.18
40	-3.0653	40.92	0.0199	56.25

T_air [°C]	q_d3 [kW/m^2]	T_d3 [°C]	q_d4 [kW/m^2]	T_d4 [°C]
20	-2.7765	22.24	-5.7671	20.88
25	-2.6036	27.18	-5.4465	25.86
30	-2.4316	32.11	-5.1226	30.84
35	-2.2604	37.05	-4.7953	35.83
40	-2.0899	41.99	-4.4647	40.81

T_air [°C]	q_d5 [kW/m^2]	T_d5 [°C]	q_d6 [kW/m^2]	T_d6 [°C]
20	-4.6955	22.07	33.8730	20.57
25	-4.3902	27.03	31.8470	25.56
30	-4.0877	32.00	29.8210	30.54
35	-3.7882	36.96	27.7960	35.53
40	-3.4917	41.91	25.7710	40.52

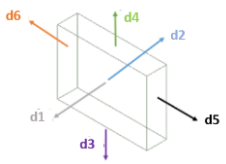

Table 112: Surface heat fluxes and surface temperatures under the following conditions: solar radiation 1000 W/mq and wind velocity 7 m/s for DC-DC casing.

T_air [°C]	q_d1 [kW/m^2]	T_d1 [°C]	q_d2 [kW/m^2]	T_d2 [°C]
20	-4.0370	21.19	0.0201	44.94
25	-3.7907	26.18	0.0210	48.95
30	-3.5447	31.17	0.0219	52.98
35	-3.2989	36.17	0.0228	57.01
40	-3.0535	41.16	0.0237	61.06

T_air [°C]	q_d3 [kW/m^2]	T_d3 [°C]	q_d4 [kW/m^2]	T_d4 [°C]
20	-2.7675	22.80	-5.7581	21.10
25	-2.5946	27.74	-5.4375	26.08
30	-2.4226	32.67	-5.1136	31.07
35	-2.2514	37.61	-4.7863	36.05
40	-2.0809	42.55	-4.4556	41.03

T_air [°C]	q_d5 [kW/m^2]	T_d5 [°C]	q_d6 [kW/m^2]	T_d6 [°C]
20	-4.6836	22.58	33.8780	20.71
25	-4.3782	27.56	31.8520	25.70
30	-4.0757	32.53	29.8260	30.69
35	-3.7762	37.49	27.8010	35.67
40	-3.4798	42.45	25.7760	40.66

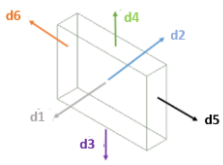

5.7 Results for the 9th of August

Once validated, the model was used to calculate the thermal behaviour of the prototype under different weather conditions. In this work it is only reported the study referred to the 9th of August. The simulations were carried out using climatic data, solar radiation and air temperature values for a typical summer day.

Comparing the data provided by the manufacturers the maximum temperature admitted by the diode (150 °C) is much higher than that of the battery (60 °C) so it's crucial to fix the casings to facilitate the cooling of the battery. The 9th of August is among the hottest summer days, so the results referred to this day are representative of the thermal behavior of the battery in bad climatic conditions.

It was used a typical meteorological year for the weather station nearest the prototype, from the "Building Technologies Office database of U.S. department of Energy's ". The maximum temperature occurs the 9th of August that, for this reason, was selected.

As shown in Figure 137, during this day the air temperature reaches the maximum value of 35°C and never drops below 25°C even during the night hours.

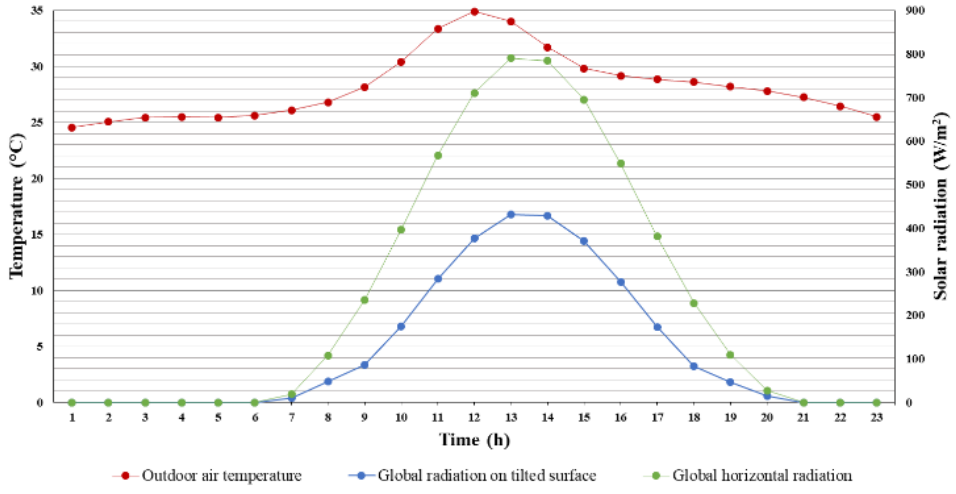

Figure 137: Outdoor weather data used for the simulation of the 9th of August.

The following Figure 138 shows the simulated temperature profiles

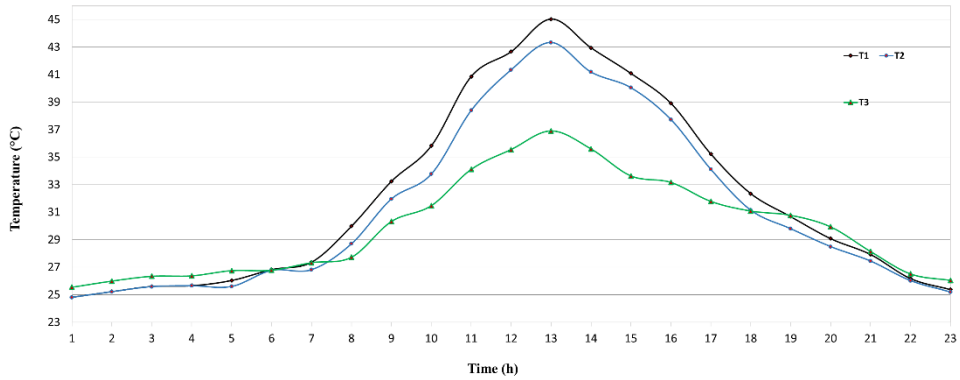

Figure 138: Thermal profile of the prototype in the 9th of August.

The six surfaces of the casing containing the battery have the thermal profiles reported in Figure 139.

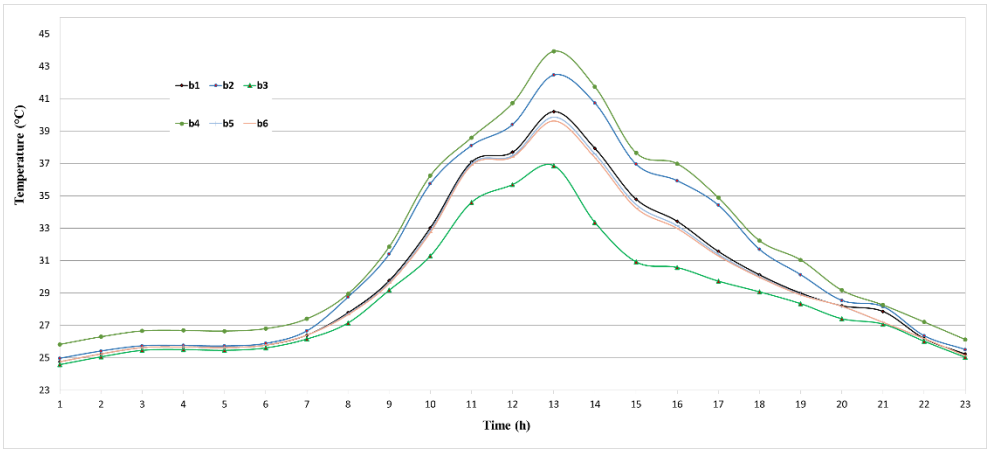

Figure 139: Thermal profile of the surface battery in the 9th of August.

The temperature distributions obtained are comparable to thermal profiles evaluated by Hammami et al. [715]. The authors proposed and analyzed an electric energy storage system fully integrated with a photovoltaic PV module, composed by a set of lithium-iron-phosphate ($LiFePO_4$) flat batteries as generation-storage PV unit. In contrast to the location proposed in the E-Brick module, the batteries were surface-

mounted on the back side of the PV module, distant from the PV backsheet, without exceeding the PV frame size.

As shown in Figure 140, during the simulated day the average temperature reached by the surfaces of the battery casing are below those the maximum battery operating temperature (~ 60°C).

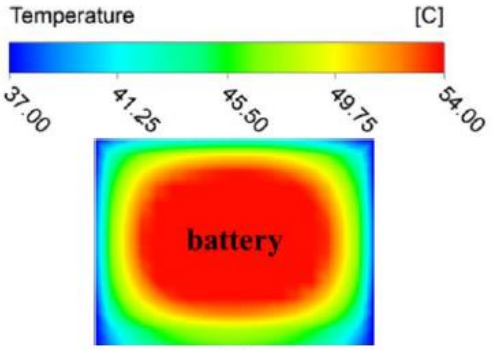

(a)

Tbattery (°C)	
Min	Max
37,83	52,38

Figure 140: Temperature distribution on the face of contact battery -insulation. Simulated case: G=500W/mq, Ta=35°C, v=0.5 m/s.

6. Results and Discussion

Simulations under different values of solar radiation were performed to evaluate to study its effect on heat generation, thus on cell temperature. In particular, results showed that, an overage, every 100 W/m2 increase in solar radiation caused an increase of about 5 °C in photovoltaic panel temperature. Also the wind velocity is a crucial factor on the natural ventilation cooling. The simulations were conducted varying both solar radiation and wind velocity so it was more complex to establish the dependence of the thermal profiles by the wind effects.

Six values of solar radiation (50, 100, 200, 400, 800 and 1000 w/mq) together with

four values wind velocity (1,2,5 and 7 m/s) were simulated to study the cooling effect of the module velocity on the proposed prototype. Air temperature was chosen in [20-40]° range. Thermal performance of the prototype was evaluated in terms of surface temperature of backsheet, frontglass and insulation.

Results showed that keeping the wind velocity and the air temperature constant the thermal performance of the prototype gets worse increasing the solar radiation.

As an example at 1m/s and air temperature 20°C, the backsheet temperature increases from 21.79°C at 50 W/mq to 52,74°C at 1000 W/mq, the frontglass temperature from 22.65°C to 68.48°C and insulation temperature from 20.32 °C to 27.54. At 2 m/s (air temperature 20°C) the backsheet temperature increases from 21.36°C at 50 W/mq to 45.69°C at 1000 W/mq, the frontglass temperature from 21.94°C to 56.59°C and the insulation temperature from 20.21°C to 24.18°C. At 5 m/s (air temperature 20°C) the backsheet temperature increases from 20.80°C at 50 W/mq to 35.18°C at 1000 W/mq, the frontglass temperature from 21.21°C to 42.99°C and the insulation temperature from 20.16°C to 23.05°C. At 7 m/s (air temperature 20°C) the backsheet temperature increases from 20.63°C at 50 W/mq to 32.01°C at 1000 W/mq, the frontglass temperature from 20.98°C to 38.74°C and the insulation temperature from 20.15°C to 22.81°C.

Keeping the wind velocity and the solar radiation constant the thermal performance of the prototype gets worse increasing the air temperature. As an example at 1m/s in correspondence of 1000 W/mq , the backsheet temperature increases from 52.74°C at 20 °C to 70.42°C at 40 °C, the frontglass temperature from 68.46°C to 84.81°C and the insulation temperature from 27.54°C to 32.25 °C. At 2 m/s (solar radiation 1000 W/mq) , the backsheet temperature increases from 45.69°C at 20 °C to 65.16°C at 40 °C, the frontglass temperature from 56.59°C to 75.78°C and the insulation temperature from 24.18°C to 43.48 °C. At 5 m/s (solar radiation 1000 W/mq) , the backsheet temperature increases from 35.18°C at 20 °C to 55.08°C at 40 °C, the frontglass temperature from 42.99°C to 62.8°C and the insulation temperature from 23.05°C to 42.40 °C. At 7 m/s (solar radiation 1000 W/mq) , the

backsheet temperature increases from 32.01°C at 20 °C to 51.97°C at 40 °C, the frontglass temperature from 38.74°C to 58.66°C and the insulation temperature from 22.81°C to 42.26 °C.

To investigate changes in the temperature field of the proposed prototype several simulation were performed varying the angle of attack f wind velocity. Six directions were simulated (α=0,30,45,60,90 deg).

Keeping the wind velocity and the solar radiation constant the thermal performance of the prototype gets worse decreasing the wind direction. As an example at 1m/s in correspondence of 1000 W/mq, the backsheet temperature increases from 52.74°C at 90 deg to 77.82°C at 0 deg, the frontglass temperature from 68.46°C to 116.57°C and the insulation temperature from 27.54°C to 51.48 °C.

Air was used as a coolant in this channel in order to reduce the temperature of the PV panel and increase its efficiency. Buoyancy-driven free convection was assumed to be the dominant event. Simulations were performed to obtain the heat transfer convection coefficient distribution on the backside of the panel since this aspect is lack in literature. Heat transfer coefficient, accounting for the heat transferred to the surrounding environment, is useful to establish the effectiveness of the cooling effect of the ventilated façade. Heat transfer coefficients h obtained by the simulation are in within the range of those ones available in literature.

Results showed that keeping the wind velocity and the air temperature constant the h value decreases with the solar radiation. As an example, at 1 m/s and air velocity 20°C h decreases from 8.06 [W/(mq K)] at 50 W/mq to 7.49 [W/(mq K)] at 50 W/mq, at 2 m/s decreases from 13.13 [W/(mq K)] to 11.82 [W/(mq K)], at 5 m/s decreases from 28.54 [W/(mq K)] to 24.83 [W/(mq K)] and at 7 m/s decreases from 43.77 [W/(mq K)] to 34.27 [W/(mq K)].

H value is affected from the wind direction, keeping the wind velocity and the solar radiation constant it decreases with lower incidence angle. As an example at 1 m/s, air velocity 20°C and solar radiation 1000 W/mq, h decreases from 7.49 [W/(mq K)] at alpha 90 deg to 0.42 [W/(mq K)] at alpha 0 deg.

Effect of the wind module and direction on photovoltaic efficiency weas also investigated. Results showed that the highest value of efficiency 13.55 was obtained corresponding to wind speed 7 m/s and solar radiation 1000 W/mq while the lowest value 9.54 corresponding to wind speed 1 m/s and solar radiation 50 W/mq.

The operating temperature is a crucial parameter affecting negatively the working performance of the battery within the ventilated façade. It is known that when a cell is heated above a certain threshold temperature, the rising overheating will accelerate the chemical reactions, rather than the desired galvanic reactions, causing thermal runaway. Simulations were performed to establish it the proposed prototype allows the battery work in a safe temperature range (20–60 C) [4]. The variation of the surfaces temperature of the battery follows the same trend of the photovoltaic panel and insulation. The highest temperature value (59.62 °C) is obtained at 1 m/s, air temperature 40°C and solar radiation 1000 W/mq. These condition is so far real working conditions.

7. Conclusions

The photovoltaic technology is a common way to convert solar energy into electricity. Green energy production is a crucial topic for environmental sustainability. Local power generation and energy saving are the primary strategy to achieve high-efficiency buildings and a higher level of self-sufficiency. PV panel have efficiency values (15-20%) that make theme not able to achieve a sufficient energy generation for buildings. Building integrated photovoltaic systems are a viable solution to extend the energy generation of PV systems. Among the crucial aspects in the study of a ventilated façade there is its cooling method. It is known that solar radiation incident on a PV panel is not adsorbed at all, partly is reflected by the external tempered glass layers and partly is absorbed by the solar cells. The portion of the absorbed energy not converted into electricity from the panel is converted into thermal energy with negative effect on the PV efficiency. Many studied have been

performed to evaluate the performance of the forced and natural convection and to highlight the strengths and weakness both of active and passive cooling methods proposed.

In the present study an innovative BIPV device integrating photovoltaic cells, a battery storing excess power and the needed electronics (MPPT and DC/DC converter) is described . It is a building component to be installed in external vertical walls in order to create curtain walls for the energy requalification of buildings. Specifically, the E-Brick consists of a photovoltaic module (70 cm × 70 cm) in 64W polycrystalline silicon inserted in a double glass sandwich, a 23 Ah lithium titanate battery integrated in the cavity and an insulating panel in rock wool for building insulation. In order to assess the thermal performance of the proposed BIPV module a 3D model was developed and validated with the experimental data . The numerical model was implemented in a COMSOL Multi-physics® Finite Element code.

Besides the validation, the thermal performance of the panel has been evaluated during the hottest summer day obtained from a typical meteorological year for the same location..

The conclusions are summarized as follows:

- The model was developed to predict the temperatures profiles inside the air cavity.
- Validation with experimental data set shows a good model temperature profiles prediction.
- Despite heat generation due to the electrical components (mainly DC/DC and battery), the dominant factor is the solar radiation affecting the thermal behavior of the entire prototype.
- To the specific weather conditions (Sicily, South of Italy), the maximum operating temperatures of all components are always below the nominal operating temperatures. In particular, the battery case surface temperatures are below the 60 °C also during the worst weather conditions (summertime

Nomenclature

A_P	Area of the photovoltaic panel
c_p	Specific heat
D_{eq}	Equivalent diameter
F	View Factor
g	Acceleration due to gravity
G_{PV}	Vertical solar radiation on the PV panel
I	Current
I_D	Diode saturation current
I_{ph}	Photocurrent
P_{PV}	Maximum photovoltaic producibility
Q_c	Convection heat dissipation
Q_r	Radiative heat dissipation
S_c	Control surface
T	Temperature
u	Vector velocity
V	Voltage
V_c	Control volume
V_t	Diode thermal voltage

Greek Letters

α	Thermal diffusivity
α_{cell}	Absorptivity of the cell
α_{glass}	Absorption coefficient of the glass cover
β	Volumetric thermal expansion coefficient
ε	Emissivity
η_b	Efficiency
λ	Thermal conductivity
μ	Fluid dynamic viscosityg
ρ	Density
σ	Boltzmann constan

Nomenclature

τ_{glass}	Transmittance of the glass
Φ	Generic intensive property

Subscripts

av	Average
b	Battery
bk	Backsheet
d	Diode
f	Fluid
fr	Frontglass
PV	Photovoltaic panel
Sur	Surrounding

Conclusions

To achieve ambitious targets of a sustainable society by 2050, various measures and pathways are being investigated by the research communities. All parts of society and economic sectors will play a role in this transition requiring a combination of economic, environmental and social challenges. In this context, the achievement of a carbon neutral energy system with a high spread of renewable energy systems requires for a paradigm shift in power systems.

Most of the current energy infrastructures have been designed to house large, centrally located, localized generation units that are managed to meet the instantaneous energy demand. However, to facilitate the RES integration in the existing infrastructures, the flexibility of the power system must be increased aiming to achieve the instant balance of temporal and spatial mismatches in a bi-directional decentralized system with a high penetration of smaller prosumers. Import and export of energy over the system boundaries, power-to-X technologies, energy storage technologies, as well as different demand response strategies are example of flexibility sources.

The carbon neutral climate transition is strongly affecting different sectors, including heating and cooling. In this context, the heating and cooling sector, at building level has a crucial role so this sector is responsible for about 40% of the energy consumed and almost 40% of the CO2 emitted globally.

It is estimated that in 2050 at least 70% of the existing building stock will still be used and that at least a 25% increase in the built area is expected.

For this reason, it is necessary to provide efficient technologies not only to support the diffusion of new buildings but also to strengthen the energy performance of

existing ones. In this context, the building sector is a key enabler of future energy systems as it will help to facilitate a larger share of renewables, distributed supply and demand-side energy flexibility.

Although the building design should be firstly based on the employment of passive design strategies to reduce energy requirements, implementation of energy efficient systems and adoption of RES to cover the building energy demand, the successful building design should also take into account the flexibility of its energy systems. Future buildings should play a crucial role in transforming the energy markets becoming interactive players in grid balancing.

Moreover, future buildings can provide grid services and flexibility, thereby they will be crucial players in the transition to a low carbon energy system. Buildings can provide significant benefits to the grid through a combination of actions that reduce or adjust electricity consumption to avoid or reduce electricity system costs.

Nearly zero energy (nZEB) and net zero (NZEB) buildings, characterized by minimal energy demand, are among the main protagonists of sustainable development. An NZEB building, built in accordance with the principles of sustainable and bioclimatic design, has a very low or almost zero energy requirement, since the significant part of its energy demand is covered by renewable energy produced in situ. Examples of measures can be taken with the aim of improving the energy performance of buildings are the use of advanced materials, adding layers of insulation, improving the building envelope. Nowadays the ventilated walls integrated with photovoltaic panels represent the most developed technology on the market. The use of photovoltaics as a building material represents one of the greatest technological innovations in the construction sector.

The main aspect of the BIPV (building integrated photovoltaics) concept is the chimney effect that is established in the cavity between the panel and the building wall. It allows not only to improve the thermophysical performance of the building but also to increase the efficiency of the photovoltaic. It is known that the photovoltaic efficiency decreases as the temperature of the cells increases. PV panel

have efficiency values (15-20%) that make theme not able to achieve a sufficient energy generation for buildings. BIPVs are a viable solution to extend the photovoltaic energy generation.

Within this research area to support the efficiency and production of photovoltaic energy the CNR-ITAE (Institute of advanced technologies for energy "Nicola Giordano") presented a hybrid prototype of an active facade called E-Brick. It is a building component to be installed in external vertical walls in order to create curtain walls for the energy requalification of buildings. Specifically, the E-Brick consists of a photovoltaic module (70 cm × 70 cm) in 64 W polycrystalline silicon inserted in a double glass sandwich, a 23 Ah lithium titanate battery integrated in the cavity and an insulating panel in rock wool for building insulation. Wall cooling, thermal insulation of the building, production, storage and distribution of electricity are the heart of E-Brick. The thermal performance of the E-brick is a crucial aspect affecting both the photovoltaic efficiency and the energy performance of the building.

In this work a numerical model of the E-Brick module has been developed to evaluate its thermal performance. In particular, an innovative BIPV device integrating photovoltaic cells, a battery storing excess power and the needed electronics (MPPT and DC/DC converter) is presented.

The numerical model developed has been implemented in the multi-physics Finite Element Code COMSOL. The model has been calibrated and validated on experimental data carried out at CNR-ITAE. In particular, experimental data of solar radiation, air temperature and air velocity were used as boundary conditions in the numerical model.

Experimental tests have been performed in CNR-ITAE in Messina (Italy) to evaluate the producibility of two distinct photovoltaic cell technologies that can be integrated into the hybrid module E-Brick (PV/insulation /electric equipment's) developed to cover the perimeter walls of a building. Experimental were carried out for different goals: characterization of PV panels to be used in the E-brick module,

characterization of PV panels in hybrid configuration with Li-ion battery, monitoring of the hybrid BIPV.

To evaluate the producibility of the tested PV modules, vertically placed, potentiostatic characterization tests, MPPT characterization tests and tests with solar simulator at controlled temperature tests were carried out under different solar radiation, shading and angles of incidence values. The selected modules allowed to produce electric energy also if vertically installed. In particular, the maximum recorded power values reached about 40% of the expected peak power value in case of optimal inclination. In MPPT conditions the recorded power delivered by the panel was proportional to the irradiation resisted on the panels' plane.

Experimental tests were also performed to test the producibility of DSSC (Dye-Sensitized Solar Cell) technology. Tests carried out with DSSCs showed lower conversion efficiency values than Si-Poly technology modules.

Tests on the battery have been carried out to identify a simplified thermal model so in the numerical model the battery is simulated as heat source within the air cavity.

Charging/discharging tests at different current values were carried out by Eelectrochemical Impedance Spectroscopy to assess battery performance.

In the last part of the experimental campaign, in order to calibrate and validate the thermal model of the prototype, by comparing the monitored data to that of the model on the same time using recorded weather data as a model input, monitoring studies have been developed on the prototype. In detail, four thermocouples (chromel–alumel thermocouples type k), installed on both sides of the PV module and on both sides of the insulation layer, were used. A weather station was installed near the prototype, recording global horizontal radiation, dry bulb temperature, wind velocity and direction. The solar radiation on a vertical south oriented surface was calculated from the measured global horizontal radiation on horizontal surfaces using the mathematical model developed by Perez et al. [731].

The computational analysis was carried out on three steps:

- The single PV panel, vertically arranged, was analyzed without the air cavity to study the effects of the heat transfer coefficients. Simulations were carried out for different weather conditions.
- The best heat transfer coefficients identified were used to investigate the thermal behavior of a ventilated façade. The effects of geometry dimensions on the thermal efficiency were investigated.
- The ventilated façade was evaluated simulating heat sources within it. A comparison among the three scenarios was reported and discussed.

The model developed to predict the temperatures profiles inside the air cavity shows a good agreement with experimental data. Results show that despite heat generation due to the electrical components (mainly DC/DC and battery), the dominant factor is the solar radiation affecting the thermal behaviour of the entire prototype. To the specific weather conditions (Sicily, South of Italy), the maximum operating temperatures of all components are always below the nominal operating temperatures. In particular, the battery case surface temperatures are below the 60 °C also during the worst weather conditions. This work of thesis wants to contribute to assess the viability of the prototype.

The developed model shows a high potential for follow-ups and future studies. For example, it could be applied for the evaluation of surplus energy of Positive Energy Buildings. In the context of the building flexibility, the proposed BIPV prototype could aim at containing energy consumption in order to design buildings with almost zero energy consumption. This work could provide a useful tool to quantify the building flexibility based on the level of individual technologies. Different building performance indicators, existing in literature, developed in the context of the demand side management strategies to quantify the main aspects of the building flexibility were reported and discussed in this work.

A theoretical study was conducted on the following indicators :

- indicators useful to describe the degree of the utilization of on-site energy generation related to the local energy demand in NZEBs. (Load matching indicators);
- indicators useful to describe the grid connection (Grid interaction indicators);
- indicators useful to provide information about energy can be shifted in relation to scope and target for which energy flexibility measurements are applied (Energy flexibility indicators).

A future step could be the integration of the obtained data and developed tools, especially the CFD modelling, with other data and/or models characterizing other features determining the flexibility performance of the building in order. This will allow to quantify some crucial indicators in the framework of sensitivity analyses and eventually optimization studies.

The study has been supported by the Ministry of Economic Development - Fund for sustainable growth (HORIZON 2020) - Project no. 181 “e-brick”.

Bibliography

1. Directive 2009/28/EC of the European Parliament and of the Council, Official J. Eur. Union L140/16 (2009) 1–47.
2. Commission regulation (EC) 185/2007, Official J Eur Union L63 (2007) 4–5.
3. Blanco, H.; Nijs, W.; Ruf, J.; Faaij, A. Potential for hydrogen and Power-to-Liquid in a low-carbon EU energy system using cost optimization. *Appl. Energy* **2018**, *232*, 617–639, doi:10.1016/j.apenergy.2018.09.216.
4. Ritter, S.K. Global warming and climate change. *Chem. Eng. News* **2009**, doi:10.1021/cen-v087n051.p011.
5. S. Arrhenius, London Edinburgh Dublin Philos. Mag. J. Sci. 41 (251) (1896) 237–276, https://doi.org/10.1080/ 14786449608620846.
6. https://www.esrl.noaa.gov/gmd/webdata/ccgg/trends/co2_data_mlo.pdf.
7. Mathiesen BV, L.H. Comparative analyses of seven technologies to facilitate the integration of fluctuating renewable energy sources. *IET Renew Power Gener* **2009**, *3*, 190–204.
8. PAE Italian Energy Efficiency Action Plan (EEAP), Summary (english) 2017.
9. New Danish energy agreement secured: 50 per cent of Denmark's energy needs to be met by renewable energy in 2030 - State of Green.
10. O'Meara, S. China's plan to cut coal and boost green growth. *Nature* **2020**, *584*, doi:10.1038/d41586-020-02464-5.
11. Cruz, M.R.M.; Fitiwi, D.Z.; Santos, S.F.; Shafie-khah, M.; Catalao, J.P.S. *Managing risk in electric distribution networks*; 2018;
12. Iovine, A.; Rigaut, T.; Damm, G.; De Santis, E.; Di Benedetto, M.D. Power management for a DC MicroGrid integrating renewables and storages. *Control Eng. Pract.* **2019**, *85*, 59–79, doi:10.1016/j.conengprac.2019.01.009.
13. Matamala, C.; Moreno, R.; Sauma, E. The value of network investment coordination to reduce environmental externalities when integrating renewables: Case on the Chilean transmission network. *Energy Policy* **2019**, *126*, 251–263, doi:10.1016/j.enpol.2018.10.065.
14. Kuang, Y.; Zhang, Y.; Zhou, B.; Li, C.; Cao, Y.; Li, L.; Zeng, L. A review of renewable energy utilization in islands. *Renew. Sustain. Energy Rev.* **2016**, *59*, 504–513, doi:10.1016/j.rser.2016.01.014.

15. Lund, P.D.; Lindgren, J.; Mikkola, J.; Salpakari, J. Review of energy system flexibility measures to enable high levels of variable renewable electricity. *Renew. Sustain. Energy Rev.* **2015**, *45*, 785–807, doi:10.1016/J.RSER.2015.01.057.
16. Salpakari, J.; Mikkola, J.; Lund, P.D. Improved flexibility with large-scale variable renewable power in cities through optimal demand side management and power-to-heat conversion. *Energy Convers. Manag.* **2016**, *126*, 649–661, doi:10.1016/J.ENCONMAN.2016.08.041.
17. Denholm, P.; Hand, M. Grid flexibility and storage required to achieve very high penetration of variable renewable electricity. *Energy Policy* **2011**, *39*, 1817–1830, doi:10.1016/j.enpol.2011.01.019.
18. Valsomatzis, E.; Hose, K.; Pedersen, T.B.; Šikšnys, L. Measuring and comparing energy flexibilities. *CEUR Workshop Proc.* **2015**, *1330*, 78–85.
19. Liu, W.; Song, M.S.; Kong, B.; Cui, Y. Flexible and Stretchable Energy Storage: Recent Advances and Future Perspectives. *Adv. Mater.* **2017**, *29*, doi:10.1002/adma.201603436.
20. Arnaudo, M.; Topel, M.; Laumert, B. Techno-economic analysis of demand side flexibility to enable the integration of distributed heat pumps within a Swedish neighborhood. *Energy* **2020**, *195*, doi:10.1016/j.energy.2020.117012.
21. Perera, A.T.D.; Nik, V.M.; Wickramasinghe, P.U.; Scartezzini, J.L. Redefining energy system flexibility for distributed energy system design. *Appl. Energy* **2019**, *253*, 113572, doi:10.1016/j.apenergy.2019.113572.
22. Dominković, D.F.; Dobravec, V.; Jiang, Y.; Nielsen, P.S.; Krajačić, G. Modelling smart energy systems in tropical regions. *Energy* **2018**, doi:10.1016/j.energy.2018.05.007.
23. Vardakas, J.S.; Zorba, N.; Verikoukis, C. V. A Survey on Demand Response Programs in Smart Grids: Pricing Methods and Optimization Algorithms. *IEEE Commun. Surv. Tutorials* **2015**, *17*, 152–178, doi:10.1109/COMST.2014.2341586.
24. Ma, R.; Chen, H.H.; Huang, Y.R.; Meng, W. Smart grid communication: Its challenges and opportunities. *IEEE Trans. Smart Grid* **2013**, doi:10.1109/TSG.2012.2225851.
25. Kolokotsa, D. The role of smart grids in the building sector. *Energy Build.* **2016**, *116*, 703–708, doi:10.1016/j.enbuild.2015.12.033.

26. Raghavan, S.S.; Khaligh, A. Impact of plug-in hybrid electric vehicle charging on a distribution network in a Smart Grid environment. In Proceedings of the 2012 IEEE PES Innovative Smart Grid Technologies, ISGT 2012; 2012.
27. Mohseni, A.; Mortazavi, S.S.; Ghasemi, A.; Nahavandi, A.; Talaei abdi, M. The application of household appliances' flexibility by set of sequential uninterruptible energy phases model in the day-ahead planning of a residential microgrid. *Energy* **2017**, doi:10.1016/j.energy.2017.07.149.
28. Ganji, M.; Shahidehpour, M. *Development of a residential microgrid using home energy management systems*; Elsevier Inc., 2018; ISBN 9780128031285.
29. Arcos-Aviles, D.; Pascual, J.; Guinjoan, F.; Marroyo, L.; Sanchis, P.; Marietta, M.P. Low complexity energy management strategy for grid profile smoothing of a residential grid-connected microgrid using generation and demand forecasting. *Appl. Energy* **2017**, *205*, 69–84, doi:10.1016/j.apenergy.2017.07.123.
30. European Commission National energy and climate plans (NECPs) | European Commission.
31. Chen, G.Q.; Wu, X.F. Energy overview for globalized world economy: Source, supply chain and sink. *Renew. Sustain. Energy Rev.* **2017**, *69*, 735–749, doi:10.1016/j.rser.2016.11.151.
32. Casado-Vara, R.; Martin-del Rey, A.; Affes, S.; Prieto, J.; Corchado, J.M. IoT network slicing on virtual layers of homogeneous data for improved algorithm operation in smart buildings. *Futur. Gener. Comput. Syst.* **2020**, *102*, 965–977, doi:10.1016/j.future.2019.09.042.
33. Shan, M.; Hwang, B. Green building rating systems: Global reviews of practices and research efforts. *Sustain. Cities Soc.* **2018**, *39*, 172–180, doi:10.1016/J.SCS.2018.02.034.
34. De Rosa, M.; Bianco, V.; Scarpa, F.; Tagliafico, L.A. Heating and cooling building energy demand evaluation; A simplified model and a modified degree days approach. *Appl. Energy* **2014**, *128*, 217–229, doi:10.1016/j.apenergy.2014.04.067.
35. Pérez-Lombard, L.; Ortiz, J.; Pout, C. A review on buildings energy consumption information. *Energy Build.* **2008**, *40*, 394–398, doi:10.1016/j.enbuild.2007.03.007.
36. Masoso, O.T.; Grobler, L.J. The dark side of occupants' behaviour on building energy use. *Energy Build.* **2010**, *42*, 173–177,

doi:10.1016/J.ENBUILD.2009.08.009.

37. Guerrero Delgado, Mc.C.; Sánchez Ramos, J.; Álvarez Domínguez, S.; Tenorio Ríos, J.A.; Cabeza, L.F. Building thermal storage technology: Compensating renewable energy fluctuations. *J. Energy Storage* **2020**, *27*, doi:10.1016/j.est.2019.101147.
38. Hachem-Vermette, C.; Guarino, F.; La Rocca, V.; Cellura, M. Towards achieving net-zero energy communities: Investigation of design strategies and seasonal solar collection and storage net-zero. *Sol. Energy* **2019**, doi:10.1016/j.solener.2018.07.024.
39. Cellura, M.; Ciulla, G.; Guarino, F.; Longo, S. redesign of a rural building in a heritage site in Italy: Towards the Net Zero energy target. *Buildings* **2017**, doi:10.3390/buildings7030068.
40. Toftum, J.; Baxter, V. Nearly-zero energy buildings. *Sci. Technol. Built Environ.* 2016.
41. D'Agostino, D.; Mazzarella, L. What is a Nearly zero energy building? Overview, implementation and comparison of definitions. *J. Build. Eng.* 2019.
42. Cellura, M.; Guarino, F.; Longo, S.; Mistretta, M. Different energy balances for the redesign of nearly net zero energy buildings: An Italian case study. *Renew. Sustain. Energy Rev.* **2015**, *45*, 100–112, doi:10.1016/j.rser.2015.01.048.
43. Marszal, A.J.; Heiselberg, P.; Bourrelle, J.S.; Musall, E.; Voss, K.; Sartori, I.; Napolitano, A. Zero Energy Building - A review of definitions and calculation methodologies. *Energy Build.* **2011**, *43*, 971–979, doi:10.1016/j.enbuild.2010.12.022.
44. Gonzalez-Longatt, F.; Sanchez, F.; Singh, S.N. *On the topology for a smart direct current microgrid for a cluster of zero-net energy buildings*; Elsevier Inc., 2019; ISBN 9780128177747.
45. Cellura, M.; Campanella, L.; Ciulla, G.; Guarino, F.; Lo Brano, V.; Cesarini, D.N.; Orioli, A. The redesign of an Italian building to reach net zero energy performances: A case study of the SHC Task 40 - ECBCS Annex 52. *ASHRAE Trans.* **2011**, *117*, 331–339.
46. Parag, Y.; Sovacool, B.K. Electricity market design for the prosumer era. *Nat. Energy* **2016**, doi:10.1038/nenergy.2016.32.

47. Hall, M.; Geissler, A. Different balancing methods for Net Zero Energy Buildings - Impact of time steps, grid interaction and weighting factors. In Proceedings of the Energy Procedia; 2017.
48. Golshannavaz, S.; Afsharnia, S.; Aminifar, F. Smart distribution grid: Optimal day-ahead scheduling with reconfigurable topology. *IEEE Trans. Smart Grid* **2014**, *5*, 2402–2411, doi:10.1109/TSG.2014.2335815.
49. Building-integrated, T. D2 . 3 - nZEB building concepts for the application of BIPV building elements. **2020**.
50. Tzeiranaki, S.T.; Bertoldi, P.; Diluiso, F.; Castellazzi, L.; Economidou, M.; Labanca, N.; Serrenho, T.R.; Zangheri, P. Analysis of the EU residential energy consumption: Trends and determinants. *Energies* **2019**, *12*, doi:10.3390/en12061065.
51. Bosseboeuf et al. Energy Efficiency Trends and Policies in the Household and Tertiary Sectors. **2015**, 97.
52. Tagliapietra, S. *Energy Consumption and Energy Efficiency*; 2020; ISBN 9789276210740.
53. Ürge-Vorsatz, D.; Lucon, O.; Zain Ahmed, A.; Akbari, H.; Bertoldi, P.; Cabeza, L.F.; Eyre, N.; Gadgil, A.; D Harvey, L.D.; Jiang, Y.; et al. Buildings. In: Mitigation. Working Group III contribution to the Fifth Assessment Report of the Intergovernmental Panel of Climate Change. **2014**, 671–738.
54. Rhodes, C.J. The 2015 Paris Climate Change Conference: Cop21. *Sci. Prog.* **2016**, *99*, 97–104, doi:10.3184/003685016X14528569315192.
55. Intergovernmental Panel on Climate Change *Climate Change 2014 Mitigation of Climate Change*; 2014;
56. D'Agostino, D.; Zangheri, P.; Castellazzi, L. Towards nearly zero energy buildings in Europe: A focus on retrofit in non-residential buildings. *Energies* **2017**, doi:10.3390/en10010117.
57. https://ec.europa.eu/energy/topics/energy-strategy/clean-energy-all-europeans_en.
58. Parliament, T.H.E.E.; Council, T.H.E.; The, O.F.; Union, E. Directive 2002/65/EC of the European Parliament and of the Council. *Fundam. Texts Eur. Priv. Law* **2020**, 65–71, doi:10.5040/9781782258674.0021.
59. Corrado, V.; Ballarini, I.; Dirutigliano, D.; Murano, G. Verification of the New

Ministerial Decree about Minimum Requirements for the Energy Performance of Buildings. In Proceedings of the Energy Procedia; 2016.

60. EPBD Energy performance of buildings directive 2010/31/EU (recast). *Off. J. Eur. Union* **2010**.
61. Europeu, P.; Europeia, C. da U. *EPBD*; 2015;
62. EU EPBD - Energy performance of buildings and Directive (EU) 2018/844. *Off. J. Eur. Union* **2018**.
63. Paleari, M.; Lavagna, M.; Campioli, A. The assessment of the relevance of building components and life phases for the environmental profile of nearly zero-energy buildings: life cycle assessment of a multifamily building in Italy. *Int. J. Life Cycle Assess.* **2016**, doi:10.1007/s11367-016-1133-6.
64. Burman, E.; Hong, S.M.; Paterson, G.; Kimpian, J.; Mumovic, D. A comparative study of benchmarking approaches for non-domestic buildings: Part 2 – Bottom-up approach. *Int. J. Sustain. Built Environ.* **2014**, doi:10.1016/j.ijsbe.2014.12.001.
65. European Commission 2030 climate & energy framework - Climate Action. *2030 Clim. Energy Framew.* 2018.
66. EED Directive 2012/27/EU of the European Parliament and of the Council of 25 October 2012 on energy efficiency. **2012**, 1–56.
67. https://ec.europa.eu/energy/topics/energy-efficiency/targets-directive-and-rules/energy-efficiency-directive_en.
68. European Parliament Directive 2018/2002/EU amending Directive 2012/27/EU on Energy Efficiency. *Off. J. Eur. Union* **2018**, *328*, 210–230.
69. Schiavo, G. Lo The new EU Directive on Energy Efficiency: A critical view. *Maastricht J. Eur. Comp. L.* **2013**, *20*, 321.
70. Prindle, B.; Eldridge, M. The Twin Pillars of Sustainable Energy: Synergies between Energy Efficiency and Renewable Energy Technology and Policy. *Am. Counc. an Energy Effic. Econ.* **2007**.
71. European Parliament Directive (EU) 2018/2001 of the European Parliament and of the Council on the promotion of the use of energy from renewable sources. *Off. J. Eur. Union* **2018**, *2018*, 82–209.
72. Sajn, N. Energy efficiency of buildings: A nearly zero-energy future? *Eur. Parliam. Res. Serv.* **2016**.

73. Oberthür, S. The European Union's Performance in the International Climate Change Regime. *J. Eur. Integr.* **2011**, doi:10.1080/07036337.2011.606690.
74. ICCT Final recast RED II: Renewable Energy Directive for 2021-2030 in the European Union. **2018**, 1–6.
75. Athienitis, A.; Cellura, M.; Chen, Y.; Delisle, V.; Bourdoukan, P.; Kapsis, K. Modeling and design of Net ZEBs as integrated energy systems. *Model. Des. Optim. Net-Zero Energy Build.* **2015**, 9–74, doi:10.1002/9783433604625.ch02.
76. Liu, Z.; Zhou, Q.; Tian, Z.; He, B. jie; Jin, G. A comprehensive analysis on definitions, development, and policies of nearly zero energy buildings in China. *Renew. Sustain. Energy Rev.* **2019**, *114*, 109314, doi:10.1016/j.rser.2019.109314.
77. Annunziata, E.; Frey, M.; Rizzi, F. Towards nearly zero-energy buildings: The state-of-art of national regulations in Europe. *Energy* **2013**, doi:10.1016/j.energy.2012.11.049.
78. Crawley, D.B.; Hand, J.W.; Kummert, M.; Griffith, B.T. Contrasting the Capabilities of Building Energy Simulation Software tools. Energy Performance Simulation Software tools. In Proceedings of the Ninth International IBPSA Conference; 2005.
79. Dr. Sam C. M. Hui 281901690_Zero_energy_and_zero_carbon_buildings_myths_and_facts @ www.researchgate.net. **2010**, 1–13.
80. Hermelink, A.; Schimschar, S.; Boermans, T.; Pagliano, L.; Zangheri, P.; Armani, R.; Voss, K.; Musall, E. Towards nearly zero- energy buildings: Definition of common principles under the EPBD. *Ecofys Eur. Union* **2013**.
81. Pless, S.; Torcellini, P. Net-Zero Energy Buildings : A Classification System Based on Renewable Energy Supply Options. *Contract* **2010**, 1–14, doi:10.2172/983417.
82. Hernandez, P.; Kenny, P. From net energy to zero energy buildings: Defining life cycle zero energy buildings (LC-ZEB). *Energy Build.* **2010**, doi:10.1016/j.enbuild.2009.12.001.
83. Voss, K.; Musall, E.; Lichtmeß, M. From low-energy to net zero-energy buildings: Status and perspectives. *J. Green Build.* **2011**, *6*, 46–57, doi:10.3992/jgb.6.1.46.
84. Sartori, I.; Napolitano, A.; Voss, K. Net zero energy buildings: A consistent definition framework. *Energy Build.* **2012**, *48*, 220–232,

doi:10.1016/j.enbuild.2012.01.032.

85. Panagiotidou, M.; Fuller, R.J. Progress in ZEBs-A review of definitions, policies and construction activity. *Energy Policy* **2013**, doi:10.1016/j.enpol.2013.06.099.
86. DOE US Department of Energy: A Common Definition for Zero Energy Buildings. **2015**, 22.
87. Lund, H.; Marszal, A.; Heiselberg, P. Zero energy buildings and mismatch compensation factors. *Energy Build.* **2011**, *43*, 1646–1654, doi:10.1016/j.enbuild.2011.03.006.
88. Attia, S. *Net Zero Energy Buildings (NZEB): Concepts, frameworks and roadmap for project analysis and implementation*; 2018; ISBN 9780128124628.
89. Good, C.; Kristjansdottír, T.; Houlihan Wiberg, A.; Georges, L.; Hestnes, A.G. Influence of PV technology and system design on the emission balance of a net zero emission building concept. *Sol. Energy* **2016**, doi:10.1016/j.solener.2016.01.038.
90. Magrini, A.; Lentini, G.; Cuman, S.; Bodrato, A.; Marenco, L. From nearly zero energy buildings (NZEB) to positive energy buildings (PEB): The next challenge - The most recent European trends with some notes on the energy analysis of a forerunner PEB example. *Dev. Built Environ.* **2020**, *3*, 100019, doi:10.1016/j.dibe.2020.100019.
91. Mahmud, K.; Khan, B.; Ravishankar, J.; Ahmadi, A.; Siano, P. An internet of energy framework with distributed energy resources, prosumers and small-scale virtual power plants: An overview. *Renew. Sustain. Energy Rev.* 2020.
92. Cole, R.J.; Fedoruk, L. Shifting from net-zero to net-positive energy buildings. *Build. Res. Inf.* **2015**, doi:10.1080/09613218.2014.950452.
93. Salom, J.; Marszal, A.J.; Widén, J.; Candanedo, J.; Lindberg, K.B. Analysis of load match and grid interaction indicators in net zero energy buildings with simulated and monitored data. *Appl. Energy* **2014**, *136*, 119–131, doi:10.1016/j.apenergy.2014.09.018.
94. Verbruggen, B.; Driesen, J. Grid impact indicators for active building simulations. *IEEE Trans. Sustain. Energy* **2015**, *6*, 43–50, doi:10.1109/TSTE.2014.2357475.
95. Noris, F.; Musall, E.; Salom, J.; Berggren, B.; Jensen, S.Ø.; Lindberg, K.; Sartori, I. Implications of weighting factors on technology preference in net zero energy buildings. *Energy Build.* **2014**, *82*, 250–262, doi:10.1016/j.enbuild.2014.07.004.

96. Cagno, E.; Micheli, G.J.L.; Di Foggia, G. Smart metering projects: an interpretive framework for successful implementation. *Int. J. Energy Sect. Manag.* **2018**, doi:10.1108/IJESM-08-2017-0009.
97. https://setis.ec.europa.eu/about-setis/set-plan-governance.
98. European Commission Energy Union Package - A Framework Strategy for a Resilient Energy Union with a Forward-Looking Climate Change Policy. *COM(2015) 80 Final* **2015**.
99. European Commission SET-Plan ACTION - Develop new materials and technologies for energy efficiency solutions for buildings. **2016**.
100. Van Cutsem, O.; Ho Dac, D.; Boudou, P.; Kayal, M. Cooperative energy management of a community of smart-buildings: A Blockchain approach. *Int. J. Electr. Power Energy Syst.* **2020**, *117*, 105643, doi:10.1016/j.ijepes.2019.105643.
101. Nikas, A.; Stavrakas, V.; Arsenopoulos, A.; Doukas, H.; Antosiewicz, M.; Witajewski-Baltvilks, J.; Flamos, A. Barriers to and consequences of a solar-based energy transition in Greece. *Environ. Innov. Soc. Transitions* **2020**, *35*, 383–399, doi:10.1016/j.eist.2018.12.004.
102. Shariatzadeh, F.; Mandal, P.; Srivastava, A.K. Demand response for sustainable energy systems: A review, application and implementation strategy. *Renew. Sustain. Energy Rev.* **2015**, *45*, 343–350, doi:10.1016/j.rser.2015.01.062.
103. Ma, W.; Xue, X.; Liu, G. Techno-economic evaluation for hybrid renewable energy system: Application and merits. *Energy* **2018**, *159*, 385–409, doi:10.1016/J.ENERGY.2018.06.101.
104. Eid, C.; Codani, P.; Perez, Y.; Reneses, J.; Hakvoort, R. Managing electric flexibility from Distributed Energy Resources: A review of incentives for market design. *Renew. Sustain. Energy Rev.* **2016**, *64*, 237–247, doi:10.1016/j.rser.2016.06.008.
105. Jiang, T.; Li, Z.; Jin, X.; Chen, H.; Li, X.; Mu, Y. Flexible operation of active distribution network using integrated smart buildings with heating, ventilation and air-conditioning systems. *Appl. Energy* **2018**, *226*, 181–196, doi:10.1016/j.apenergy.2018.05.091.
106. Bizon, N.; Lopez-Guede, J.M.; Kurt, E.; Thounthong, P.; Mazare, A.G.; Ionescu, L.M.; Iana, G. Hydrogen economy of the fuel cell hybrid power system optimized

by air flow control to mitigate the effect of the uncertainty about available renewable power and load dynamics. *Energy Convers. Manag.* **2019**, *179*, 152–165, doi:10.1016/j.enconman.2018.10.058.

107. Reynders, G.; Nuytten, T.; Saelens, D. Potential of structural thermal mass for demand-side management in dwellings. *Build. Environ.* **2013**, *64*, 187–199, doi:10.1016/j.buildenv.2013.03.010.
108. Patteeuw, D.; Reynders, G.; Bruninx, K.; Protopapadaki, C.; Delarue, E.; D'haeseleer, W.; Saelens, D.; Helsen, L. CO2-abatement cost of residential heat pumps with active demand response: demand- and supply-side effects. *Appl. Energy* **2015**, *156*, 490–501, doi:10.1016/J.APENERGY.2015.07.038.
109. Li, Y.; Wang, C.; Li, G.; Wang, J.; Zhao, D.; Chen, C. Improving operational flexibility of integrated energy system with uncertain renewable generations considering thermal inertia of buildings. *Energy Convers. Manag.* **2020**, *207*, 112526, doi:10.1016/j.enconman.2020.112526.
110. D'hulst, R.; Labeeuw, W.; Beusen, B.; Claessens, S.; Deconinck, G.; Vanthournout, K. Demand response flexibility and flexibility potential of residential smart appliances: Experiences from large pilot test in Belgium. *Appl. Energy* **2015**, *155*, 79–90, doi:10.1016/j.apenergy.2015.05.101.
111. Gandhi, P.; Brager, G.S. Commercial office plug load energy consumption trends and the role of occupant behavior. *Energy Build.* **2016**, doi:10.1016/j.enbuild.2016.04.057.
112. Mahdavi, A.; Tahmasebi, F.; Kayalar, M. Prediction of plug loads in office buildings: Simplified and probabilistic methods. *Energy Build.* **2016**, doi:10.1016/j.enbuild.2016.08.022.
113. Lund, H.; Werner, S.; Wiltshire, R.; Svendsen, S.; Thorsen, J.E.; Hvelplund, F.; Mathiesen, B.V.; Liu, T.; Bai, Z.; Zheng, Z.; et al. Lab-scale experiment of a closed thermochemical heat storage system including honeycomb heat exchanger. *Appl. Energy* **2019**, *188*, 1–8, doi:10.1016/j.apenergy.2016.12.041.
114. Lee, K. ho; Braun, J.E. Model-based demand-limiting control of building thermal mass. *Build. Environ.* **2008**, doi:10.1016/j.buildenv.2007.10.009.
115. Maasoumy, M.; Rosenberg, C.; Sangiovanni-Vincentelli, A.; Callaway, D.S. Model predictive control approach to online computation of demand-side flexibility of

commercial buildings HVAC systems for Supply Following. In Proceedings of the Proceedings of the American Control Conference; 2014; pp. 1082–1089.

116. Rotger-Griful, S.; Jacobsen, R.H.; Nguyen, D.; Sørensen, G. Demand response potential of ventilation systems in residential buildings. *Energy Build.* **2016**, doi:10.1016/j.enbuild.2016.03.061.

117. Beil, B.I.; Hiskens, I.; Backhaus, S. Commercial Building HVAC Demand Response. *Proc. IEEE* **2016**, doi:10.1109/JPROC.2016.2520640.

118. Tan, Z.; Yang, P.; Nehorai, A. An optimal and distributed demand response strategy with electric vehicles in the smart grid. *IEEE Trans. Smart Grid* **2014**, doi:10.1109/TSG.2013.2291330.

119. Schuller, A.; Flath, C.M.; Gottwalt, S. Quantifying load flexibility of electric vehicles for renewable energy integration. *Appl. Energy* **2015**, doi:10.1016/j.apenergy.2015.04.004.

120. Cusenza, M.A.; Guarino, F.; Longo, S.; Ferraro, M.; Cellura, M. Energy and environmental benefits of circular economy strategies: The case study of reusing used batteries from electric vehicles. *J. Energy Storage* **2019**, *25*, 100845, doi:10.1016/j.est.2019.100845.

121. Cusenza, M.A.; Bobba, S.; Ardente, F.; Cellura, M.; Di Persio, F. Energy and environmental assessment of a traction lithium-ion battery pack for plug-in hybrid electric vehicles. *J. Clean. Prod.* **2019**, doi:10.1016/j.jclepro.2019.01.056.

122. Jensen, S.Ø.; Marszal-Pomianowska, A.; Lollini, R.; Pasut, W.; Knotzer, A.; Engelmann, P.; Stafford, A.; Reynders, G. IEA EBC Annex 67 Energy Flexible Buildings. *Energy Build.* **2017**, *155*, 25–34, doi:10.1016/j.enbuild.2017.08.044.

123. Luc, K.M.; Heller, A.; Rode, C. Energy demand flexibility in buildings and district heating systems–a literature review. *Adv. Build. Energy Res.* **2019**, *13*, 241–263, doi:10.1080/17512549.2018.1488615.

124. Reynders, G.; Diriken, J.; Saelens, D. Generic characterization method for energy flexibility: Applied to structural thermal storage in residential buildings. *Appl. Energy* **2017**, *198*, 192–202, doi:10.1016/j.apenergy.2017.04.061.

125. Marszal-Pomianowska, A.; Heiselberg, P.; Kalyanova Larsen, O. Household electricity demand profiles - A high-resolution load model to facilitate modelling of energy flexible buildings. *Energy* **2016**, *103*, 487–501,

doi:10.1016/j.energy.2016.02.159.

126. Bertsch, J.; Growitsch, C.; Lorenczik, S.; Nagl, S. Flexibility in Europe's power sector-An additional requirement or an automatic complement? *Energy Econ.* **2016**, *53*, 118–131, doi:10.1016/j.eneco.2014.10.022.

127. Capuder, T.; Mancarella, P. Techno-economic and environmental modelling and optimization of flexible distributed multi-generation options. *Energy* **2014**, *71*, 516–533, doi:10.1016/j.energy.2014.04.097.

128. De Coninck, R.; Helsen, L. Quantification of flexibility in buildings by cost curves - Methodology and application. *Appl. Energy* **2016**, *162*, 653–665, doi:10.1016/j.apenergy.2015.10.114.

129. Finck, C.; Li, R.; Zeiler, W. Identification of a dynamic system model for a building and heating system including heat pump and thermal energy storage. *MethodsX* **2020**, *7*, 100866, doi:10.1016/j.mex.2020.100866.

130. Fischer, D.; Wolf, T.; Wapler, J.; Hollinger, R.; Madani, H. Model-based flexibility assessment of a residential heat pump pool. *Energy* **2017**, *118*, 853–864, doi:10.1016/j.energy.2016.10.111.

131. Hurtado, L.A.; Rhodes, J.D.; Nguyen, P.H.; Kamphuis, I.G.; Webber, M.E. Quantifying demand flexibility based on structural thermal storage and comfort management of non-residential buildings: A comparison between hot and cold climate zones. *Appl. Energy* **2017**, *195*, 1047–1054, doi:10.1016/j.apenergy.2017.03.004.

132. Junker, R.G.; Azar, A.G.; Lopes, R.A.; Lindberg, K.B.; Reynders, G.; Relan, R.; Madsen, H. Characterizing the energy flexibility of buildings and districts. *Appl. Energy* **2018**, *225*, 175–182, doi:10.1016/j.apenergy.2018.05.037.

133. Le Dréau, J.; Heiselberg, P. Energy flexibility of residential buildings using short term heat storage in the thermal mass. *Energy* **2016**, *111*, 991–1002, doi:10.1016/j.energy.2016.05.076.

134. Lopes, R.A.; Chambel, A.; Neves, J.; Aelenei, D.; Martins, J. A Literature Review of Methodologies Used to Assess the Energy Flexibility of Buildings. *Energy Procedia* **2016**, *91*, 1053–1058, doi:10.1016/j.egypro.2016.06.274.

135. Masy, G.; Georges, E.; Verhelst, C.; Lemort, V.; André, P. Smart grid energy flexible buildings through the use of heat pumps and building thermal mass as

energy storage in the belgian context. *Sci. Technol. Built Environ.* **2015**, *21*, 800–811, doi:10.1080/23744731.2015.1035590.

136. Reynders, G.; Amaral Lopes, R.; Marszal-Pomianowska, A.; Aelenei, D.; Martins, J.; Saelens, D. Energy flexible buildings: An evaluation of definitions and quantification methodologies applied to thermal storage. *Energy Build.* **2018**, *166*, 372–390, doi:10.1016/j.enbuild.2018.02.040.
137. Salom, J.; Widén, J.; Candanedo, J.; Sartori, I.; Voss, K.; Marszal, A. Understanding net zero energy buildings: Evaluation of load matching and grid interaction indicators. *Proc. Build. Simul. 2011 12th Conf. Int. Build. Perform. Simul. Assoc.* **2011**, *6*, 2514–2521.
138. Nuytten, T.; Claessens, B.; Paredis, K.; Van Bael, J.; Six, D. Flexibility of a combined heat and power system with thermal energy storage for district heating. *Appl. Energy* **2013**, *104*, 583–591, doi:10.1016/J.APENERGY.2012.11.029.
139. Vigna, I.; Pernetti, R.; Pasut, W.; Lollini, R. New domain for promoting energy efficiency: Energy Flexible Building Cluster. *Sustain. Cities Soc.* **2018**, *38*, 526–533, doi:10.1016/j.scs.2018.01.038.
140. Stinner, S.; Huchtemann, K.; Müller, D. Quantifying the operational flexibility of building energy systems with thermal energy storages. *Appl. Energy* **2016**, *181*, 140–154, doi:10.1016/j.apenergy.2016.08.055.
141. G. Reynders, R.A. Lopes, A. Marszal-Pomianowska, D. Aelenei, J. Martins, D.S. Energy flexible buildings: an evaluation of definitions and quantification methodologies applied to thermal storage, E. *Energy Build.* **2018**, *166*, 372–390.
142. Kathirgamanathan, A.; Péan, T.; Zhang, K.; De Rosa, M.; Salom, J.; Kummert, M.; Finn, D.P. Towards standardising market-independent indicators for quantifying energy flexibility in buildings. *Energy Build.* **2020**, *220*, 110027, doi:10.1016/j.enbuild.2020.110027.
143. MacDougall, P.; Roossien, B.; Warmer, C.; Kok, K. Quantifying flexibility for smart grid services. *IEEE Power Energy Soc. Gen. Meet.* **2013**, 1–5, doi:10.1109/PESMG.2013.6672817.
144. Li, J.; Fang, J.; Zeng, Q.; Chen, Z. Optimal operation of the integrated electrical and heating systems to accommodate the intermittent renewable sources. *Appl. Energy* **2016**, *167*, 244–254, doi:10.1016/j.apenergy.2015.10.054.

145. Zamani, A.G.; Zakariazadeh, A.; Jadid, S. Day-ahead resource scheduling of a renewable energy based virtual power plant. *Appl. Energy* **2016**, *169*, 324–340, doi:10.1016/j.apenergy.2016.02.011.
146. Liu, M.; Heiselberg, P. Energy flexibility of a nearly zero-energy building with weather predictive control on a convective building energy system and evaluated with different metrics. *Appl. Energy* **2019**, *233–234*, 764–775, doi:10.1016/j.apenergy.2018.10.070.
147. Kuboth, S.; Heberle, F.; König-Haagen, A.; Brüggemann, D. Economic model predictive control of combined thermal and electric residential building energy systems. *Appl. Energy* **2019**, *240*, 372–385, doi:10.1016/J.APENERGY.2019.01.097.
148. Niu, J.; Tian, Z.; Lu, Y.; Zhao, H. Flexible dispatch of a building energy system using building thermal storage and battery energy storage. *Appl. Energy* **2019**, *243*, 274–287, doi:10.1016/j.apenergy.2019.03.187.
149. Dominković, D.F.; Junker, R.G.; Lindberg, K.B.; Madsen, H. Implementing flexibility into energy planning models: Soft-linking of a high-level energy planning model and a short-term operational model. *Appl. Energy* **2020**, doi:10.1016/j.apenergy.2019.114292.
150. Pallonetto, F.; De Rosa, M.; Milano, F.; Finn, D.P. Demand response algorithms for smart-grid ready residential buildings using machine learning models. *Appl. Energy* **2019**, *239*, 1265–1282, doi:10.1016/j.apenergy.2019.02.020.
151. Zhou, Y.; Cao, S. Energy flexibility investigation of advanced grid-responsive energy control strategies with the static battery and electric vehicles: A case study of a high-rise office building in Hong Kong. *Energy Convers. Manag.* **2019**, *199*, 111888, doi:10.1016/j.enconman.2019.111888.
152. Finck, C.; Beagon, P.; Clauß, J.; Péan, T.; Vogler-Finck, P.J.; Zhang, K.; Montreal, P.; Kazmi, H. Review of applied and tested control possibilities for energy flexibility in buildings. **2018**, doi:10.13140/RG.2.2.28740.73609.
153. Cai, J.; Braun, J.E. A regulation capacity reset strategy for HVAC frequency regulation control. *Energy Build.* **2019**, *185*, 272–286, doi:10.1016/j.enbuild.2018.12.018.
154. Johra, H.; Heiselberg, P. Influence of internal thermal mass on the indoor thermal

dynamics and integration of phase change materials in furniture for building energy storage: A review. *Renew. Sustain. Energy Rev.* **2017**, *69*, 19–32, doi:10.1016/j.rser.2016.11.145.

155. Johra, H.; Heiselberg, P.; Dréau, J. Le Influence of envelope, structural thermal mass and indoor content on the building heating energy flexibility. *Energy Build.* **2019**, *183*, 325–339, doi:10.1016/J.ENBUILD.2018.11.012.
156. Six, D.; Desmedt, J.; Vanhoudt, D.; Van Bael, J. Exploring the flexibility potential of residential heat pumps combined with therm al energy storage for smart grids. *21st Int. Conf. Electr. Distrib.* **2011**.
157. Oldewurtel, F.; Sturzenegger, D.; Andersson, G.; Morari, M.; Smith, R.S. Towards a standardized building assessment for demand response. *Proc. IEEE Conf. Decis. Control* **2013**, 7083–7088, doi:10.1109/CDC.2013.6761012.
158. Arteconi, A.; Hewitt, N.J.; Polonara, F. Domestic demand-side management (DSM): Role of heat pumps and thermal energy storage (TES) systems. *Appl. Therm. Eng.* **2013**, *51*, 155–165, doi:10.1016/j.applthermaleng.2012.09.023.
159. Hedegaard, K.; Mathiesen, B.V.; Lund, H.; Heiselberg, P. Wind power integration using individual heat pumps – Analysis of different heat storage options. *Energy* **2012**, *47*, 284–293, doi:10.1016/J.ENERGY.2012.09.030.
160. Miezis, M.; Jaunzems, D.; Stancioff, N. Predictive Control of a Building Heating System. *Energy Procedia* **2017**, *113*, 501–508, doi:10.1016/j.egypro.2017.04.051.
161. Madsen, H.; Bacher, P.; Bauwens, G.; Deconinck, A.-H.; Reynders, G.; Roels, S.; Himpe, E.; Lethé, G. Thermal Performance Characterization using Time Series Data ; IEA EBC Annex 58 Guidelines. *DTU Comput. Report-2015* **2015**, *8*, 1–84.
162. Ottesen, S.Ø.; Tomasgard, A.; Fleten, S.E. Multi market bidding strategies for demand side flexibility aggregators in electricity markets. *Energy* **2018**, *149*, 120–134, doi:10.1016/j.energy.2018.01.187.
163. Yin, R.; Kara, E.C.; Li, Y.; DeForest, N.; Wang, K.; Yong, T.; Stadler, M. Quantifying flexibility of commercial and residential loads for demand response using setpoint changes. *Appl. Energy* **2016**, *177*, 149–164, doi:10.1016/j.apenergy.2016.05.090.
164. Eid, C.; Koliou, E.; Valles, M.; Reneses, J.; Hakvoort, R. Time-based pricing and electricity demand response: Existing barriers and next steps. *Util. Policy* **2016**, *40*,

15–25, doi:10.1016/j.jup.2016.04.001.

165. De Coninck, R.; Helsen, L. Bottom-up quantification of the flexibility potential of buildings. In Proceedings of the Proceedings of BS 2013: 13th Conference of the International Building Performance Simulation Association; 2013; pp. 3250–3258.
166. Ulbig, A.; Andersson, G. On operational flexibility in power systems. *IEEE Power Energy Soc. Gen. Meet.* **2012**, doi:10.1109/PESGM.2012.6344676.
167. Ulbig, A.; Andersson, G. Analyzing operational flexibility of electric power systems. *Int. J. Electr. Power Energy Syst.* **2015**, *72*, 155–164, doi:10.1016/j.ijepes.2015.02.028.
168. Wu, X.; Hu, X.; Moura, S.; Yin, X.; Pickert, V. Stochastic control of smart home energy management with plug-in electric vehicle battery energy storage and photovoltaic array. *J. Power Sources* **2016**, *333*, 203–212, doi:10.1016/j.jpowsour.2016.09.157.
169. Müller, D.; Monti, A.; Stinner, S.; Schlösser, T.; Schütz, T.; Matthes, P.; Wolisz, H.; Molitor, C.; Harb, H.; Streblow, R. Demand side management for city districts. *Build. Environ.* **2015**, *91*, 283–293, doi:10.1016/J.BUILDENV.2015.03.026.
170. Kazas, G.; Fabrizio, E.; Perino, M. Energy demand profile generation with detailed time resolution at an urban district scale: A reference building approach and case study. *Appl. Energy* **2017**, doi:10.1016/j.apenergy.2017.01.095.
171. Batić, M.; Tomašević, N.; Beccuti, G.; Demiray, T.; Vraneš, S. Combined energy hub optimisation and demand side management for buildings. *Energy Build.* **2016**, doi:10.1016/j.enbuild.2016.05.087.
172. Missaoui, R.; Joumaa, H.; Ploix, S.; Bacha, S. Managing energy Smart Homes according to energy prices: Analysis of a Building Energy Management System. *Energy Build.* **2014**, doi:10.1016/j.enbuild.2013.12.018.
173. Schibuola, L.; Scarpa, M.; Tambani, C. Demand response management by means of heat pumps controlled via real time pricing. *Energy Build.* **2015**, *90*, 15–28, doi:10.1016/J.ENBUILD.2014.12.047.
174. Setlhaolo, D.; Xia, X. Combined residential demand side management strategies with coordination and economic analysis. *Int. J. Electr. Power Energy Syst.* **2016**, doi:10.1016/j.ijepes.2016.01.016.
175. Ottesen, S.O.; Tomasgard, A. A stochastic model for scheduling energy flexibility

in buildings. *Energy* **2015**, *88*, 364–376, doi:10.1016/J.ENERGY.2015.05.049.

176. Kies, A.; Schyska, B.U.; Von Bremen, L. The demand side management potential to balance a highly renewable European power system. *Energies* **2016**, *9*, 1–15, doi:10.3390/en9110955.
177. Cheng, P.H.; Huang, T.H.; Chien, Y.W.; Wu, C.L.; Tai, C.S.; Fu, L.C. Demand-side management in residential community realizing sharing economy with bidirectional PEV while additionally considering commercial area. *Int. J. Electr. Power Energy Syst.* **2020**, *116*, 105512, doi:10.1016/j.ijepes.2019.105512.
178. Lampropoulos, I.; Kling, W.L.; Ribeiro, P.F.; Van Den Berg, J. History of demand side management and classification of demand response control schemes. *IEEE Power Energy Soc. Gen. Meet.* **2013**, 1–5, doi:10.1109/PESMG.2013.6672715.
179. Péan, T.Q.; Salom, J.; Costa-Castelló, R. Review of control strategies for improving the energy flexibility provided by heat pump systems in buildings. *J. Process Control* **2019**, 35–49, doi:10.1016/j.jprocont.2018.03.006.
180. Ortiz, J.; Guarino, F.; Salom, J.; Corchero, C.; Cellura, M. Stochastic model for electrical loads in Mediterranean residential buildings: Validation and applications. *Energy Build.* **2014**, doi:10.1016/j.enbuild.2014.04.053.
181. Johra, H.; Marszal-Pomianowska, A.; Ellingsgaard, J.R.; Liu, M. Building energy flexibility: A sensitivity analysis and key performance indicator comparison. *J. Phys. Conf. Ser.* **2019**, *1343*, doi:10.1088/1742-6596/1343/1/012064.
182. Alasseri, R.; Rao, T.J.; Sreekanth, K.J. Institution of incentive-based demand response programs and prospective policy assessments for a subsidized electricity market. *Renew. Sustain. Energy Rev.* **2020**, *117*, 109490, doi:10.1016/j.rser.2019.109490.
183. Karunanithi, K.; Saravanan, S.; Prabakar, B.R.; Kannan, S.; Thangaraj, C. Integration of Demand and Supply Side Management strategies in Generation Expansion Planning. *Renew. Sustain. Energy Rev.* **2017**, *73*, 966–982, doi:10.1016/J.RSER.2017.01.017.
184. Zheng, Y.; Jenkins, B.M.; Kornbluth, K.; Kendall, A.; Træholt, C. Optimization of a biomass-integrated renewable energy microgrid with demand side management under uncertainty. *Appl. Energy* **2018**, *230*, 836–844, doi:10.1016/j.apenergy.2018.09.015.

185. Mesarić, P.; Krajcar, S. Home demand side management integrated with electric vehicles and renewable energy sources. *Energy Build.* **2015**, *108*, 1–9, doi:10.1016/j.enbuild.2015.09.001.
186. Croce, D.; Giuliano, F.; Bonomolo, M.; Leone, G.; Musca, R.; Tinnirello, I. A decentralized load control architecture for smart energy consumption in small islands. *Sustain. Cities Soc.* **2020**, *53*, 101902, doi:10.1016/j.scs.2019.101902.
187. Kühnlenz, F.; Nardelli, P.H.J.; Karhinen, S.; Svento, R. Implementing flexible demand: Real-time price vs. market integration. *Energy* **2018**, *149*, 550–565, doi:10.1016/j.energy.2018.02.024.
188. Fell, M.J.; Shipworth, D.; Huebner, G.M.; Elwell, C.A. Public acceptability of domestic demand-side response in Great Britain: The role of automation and direct load control. *Energy Res. Soc. Sci.* **2015**, *9*, 72–84, doi:10.1016/j.erss.2015.08.023.
189. Albadi, M.H.; El-Saadany, E.F. A summary of demand response in electricity markets. *Electr. Power Syst. Res.* **2008**, *78*, 1989–1996, doi:10.1016/J.EPSR.2008.04.002.
190. Siano, P. Demand response and smart grids - A survey. *Renew. Sustain. Energy Rev.* **2014**, *30*, 461–478, doi:10.1016/j.rser.2013.10.022.
191. Bahmani, R.; Karimi, H.; Jadid, S. Stochastic electricity market model in networked microgrids considering demand response programs and renewable energy sources. *Int. J. Electr. Power Energy Syst.* **2020**, *117*, 105606, doi:10.1016/j.ijepes.2019.105606.
192. Ehnberg, J.; Ahlborg, H.; Hartvigsson, E. Approach for flexible and adaptive distribution and transformation design in rural electrification and its implications. *Energy Sustain. Dev.* **2020**, *54*, 101–110, doi:10.1016/j.esd.2019.10.002.
193. Georges, E.; Masy, G.; Verhelst, C.; Lemort, V.; André, P. Smart Grid Energy Flexible Buildings Through The Use Of Heat Pumps In The Belgian Context. *Sci. Technol. Built Environ.* **2015**, *21*, 800–811.
194. Stavrakas, V.; Flamos, A. A modular high-resolution demand-side management model to quantify benefits of demand-flexibility in the residential sector. *Energy Convers. Manag.* **2020**, *205*, 112339, doi:10.1016/j.enconman.2019.112339.
195. Cai, H.; Ziras, C.; You, S.; Li, R.; Honoré, K.; Bindner, H.W. Demand side management in urban district heating networks. *Appl. Energy* **2018**, *230*, 506–518,

doi:10.1016/j.apenergy.2018.08.105.

196. Aduda, K.O.; Labeodan, T.; Zeiler, W.; Boxem, G.; Zhao, Y. Demand side flexibility: Potentials and building performance implications. *Sustain. Cities Soc.* **2016**, *22*, 146–163, doi:10.1016/j.scs.2016.02.011.

197. Olsen, D.J.; Matson, N.; Sohn, M.D.; Rose, C.; Dudley, J.; Goli, S.; Kiliccote, S.; Hummon, M.; Palchak, D.; Jorgeson, J.; et al. Grid Integration of Aggregated Demand Response , Part 1 : Load Availability Profiles and Constraints for the Western Interconnection. *Lbnl - 6417E* **2013**.

198. Hummon, M.; Palchak, D.; Denholm, P.; Jorgenson, J.; Olsen, D.J.; Kiliccote, S.; Matson, N.; Sohn, M.; Rose, C.; Dudley, J.; et al. Grid Integration of Aggregated Demand Response, Part 2: Modeling Demand Response in a Production Cost Model. *Natl. Renew. Energy Lab.* **2013**.

199. Zheng, M.; Meinrenken, C.J.; Lackner, K.S. Smart households: Dispatch strategies and economic analysis of distributed energy storage for residential peak shaving. *Appl. Energy* **2015**, doi:10.1016/j.apenergy.2015.02.039.

200. Iwafune, Y.; Ikegami, T.; Fonseca, J.G.D.S.; Oozeki, T.; Ogimoto, K. Cooperative home energy management using batteries for a photovoltaic system considering the diversity of households. *Energy Convers. Manag.* **2015**, doi:10.1016/j.enconman.2015.02.083.

201. Nwulu, N.I.; Xia, X. Optimal dispatch for a microgrid incorporating renewables and demand response. *Renew. Energy* **2017**, *101*, 16–28, doi:10.1016/j.renene.2016.08.026.

202. Aalami, H.A.; Moghaddam, M.P.; Yousefi, G.R. Demand response modeling considering Interruptible/Curtailable loads and capacity market programs. *Appl. Energy* **2010**, *87*, 243–250, doi:10.1016/j.apenergy.2009.05.041.

203. Wang, Y.; Chen, Q.; Kang, C.; Zhang, M.; Wang, K.; Zhao, Y. Load profiling and its application to demand response: A review. *Tsinghua Sci. Technol.* **2015**, *20*, 117–129, doi:10.1109/tst.2015.7085625.

204. Torriti, J. A review of time use models of residential electricity demand. *Renew. Sustain. Energy Rev.* **2014**, *37*, 265–272, doi:10.1016/j.rser.2014.05.034.

205. De Rosa M, Carragher M, F.D. Flexibility assessment of a combined heat-power system (CHP) with energy storage under real-time energy price market framework.

Therm Sci Eng Prog 2018.

206. Clauß, J.; Stinner, S.; Sartori, I.; Georges, L. Predictive rule-based control to activate the energy flexibility of Norwegian residential buildings: Case of an air-source heat pump and direct electric heating. *Appl. Energy* **2019**, doi:10.1016/j.apenergy.2018.12.074.
207. Vogler-Finck, P.J.C.; Wisniewski, R.; Popovski, P. Reducing the carbon footprint of house heating through model predictive control – A simulation study in Danish conditions. *Sustain. Cities Soc.* **2018**, *42*, 558–573, doi:10.1016/j.scs.2018.07.027.
208. Dahl Knudsen, M.; Petersen, S. Demand response potential of model predictive control of space heating based on price and carbon dioxide intensity signals. *Energy Build.* **2016**, *125*, 196–204, doi:10.1016/j.enbuild.2016.04.053.
209. Liu, F.; Zhu, W.; Zhao, J. Model-based dynamic optimal control of a CO2 heat pump coupled with hot and cold thermal storages. *Appl. Therm. Eng.* **2018**, doi:10.1016/j.applthermaleng.2017.09.098.
210. Lizana, J.; Friedrich, D.; Renaldi, R.; Chacartegui, R. Energy flexible building through smart demand-side management and latent heat storage. *Appl. Energy* **2018**, *230*, 471–485, doi:10.1016/j.apenergy.2018.08.065.
211. Tronchin, L.; Manfren, M.; Nastasi, B. Energy efficiency, demand side management and energy storage technologies – A critical analysis of possible paths of integration in the built environment. *Renew. Sustain. Energy Rev.* **2018**, *95*, 341–353, doi:10.1016/J.RSER.2018.06.060.
212. Chenari, B.; Dias Carrilho, J.; Gameiro Da Silva, M. Towards sustainable, energy-efficient and healthy ventilation strategies in buildings: A review. *Renew. Sustain. Energy Rev.* **2016**, *59*, 1426–1447, doi:10.1016/j.rser.2016.01.074.
213. Li, X.; Wen, J. Review of building energy modeling for control and operation. *Renew. Sustain. Energy Rev.* **2014**, *37*, 517–537, doi:10.1016/j.rser.2014.05.056.
214. Caputo, P.; Costa, G.; Ferrari, S. A supporting method for defining energy strategies in the building sector at urban scale. *Energy Policy* **2013**, *55*, 261–270, doi:10.1016/j.enpol.2012.12.006.
215. Mason, K.; Grijalva, S. A review of reinforcement learning for autonomous building energy management. *Comput. Electr. Eng.* **2019**, *78*, 300–312, doi:10.1016/j.compeleceng.2019.07.019.

216. H. Madani, J. Claesson, P.L. A descriptive and comparative analysis of three common control techniques for an on/off controlled Ground Source Heat Pump (GSHP) system. *Energy Build.* **2013**, *65*, 1–9.
217. Miara, M.; Günther, D.; Leitner, Z.L.; Wapler, J. Simulation of an Air-to-Water Heat Pump System to Evaluate the Impact of Demand-Side-Management Measures on Efficiency and Load-Shifting Potential. *Energy Technol.* **2014**, doi:10.1002/ente.201300087.
218. Swan, L.G.; Ugursal, V.I. Modeling of end-use energy consumption in the residential sector: A review of modeling techniques. *Renew. Sustain. Energy Rev.* **2009**, *13*, 1819–1835, doi:10.1016/j.rser.2008.09.033.
219. Zanetti, E.; Aprile, M.; Kum, D.; Scoccia, R.; Motta, M. Energy saving potentials of a photovoltaic assisted heat pump for hybrid building heating system via optimal control. *J. Build. Eng.* **2020**, *27*, 100854, doi:10.1016/j.jobe.2019.100854.
220. Maddalena, E.T.; Lian, Y.; Jones, C.N. Data-driven methods for building control — A review and promising future directions. *Control Eng. Pract.* **2020**, *95*, 104211, doi:10.1016/j.conengprac.2019.104211.
221. Kumar, R.; Wenzel, M.J.; ElBsat, M.N.; Risbeck, M.J.; Drees, K.H.; Zavala, V.M. Stochastic model predictive control for central HVAC plants. *J. Process Control* **2020**, *90*, 1–17, doi:10.1016/j.jprocont.2020.03.015.
222. Woo, D.-O.; Junghans, L. Framework for model predictive control (MPC)-based surface condensation prevention for thermo-active building systems (TABS). *Energy Build.* **2020**, *215*, 109898, doi:10.1016/J.ENBUILD.2020.109898.
223. Knudsen, M.D.; Petersen, S. Economic model predictive control of space heating and dynamic solar shading. *Energy Build.* **2020**, *209*, doi:10.1016/j.enbuild.2019.109661.
224. Wolisz, H.; Kull, T.M.; Müller, D.; Kurnitski, J. Self-learning model predictive control for dynamic activation of structural thermal mass in residential buildings. *Energy Build.* **2020**, *207*, 109542, doi:10.1016/j.enbuild.2019.109542.
225. Salpakari, J.; Lund, P. Optimal and rule-based control strategies for energy flexibility in buildings with PV. *Appl. Energy* **2016**, *161*, 425–436, doi:10.1016/j.apenergy.2015.10.036.
226. Ahmad, A.; Khan, J.Y. Real-Time Load Scheduling, Energy Storage Control and

Comfort Management for Grid-Connected Solar Integrated Smart Buildings. *Appl. Energy* **2020**, doi:10.1016/j.apenergy.2019.114208.

227. Serale, G.; Fiorentini, M.; Capozzoli, A.; Bernardini, D.; Bemporad, A. Model Predictive Control (MPC) for enhancing building and HVAC system energy efficiency: Problem formulation, applications and opportunities. *Energies* **2018**, *11*, doi:10.3390/en11030631.
228. Afroz, Z.; Urmee, T.; Shafiullah, G.M.; Higgins, G. Real-time prediction model for indoor temperature in a commercial building. *Appl. Energy* **2018**, *231*, 29–53, doi:10.1016/j.apenergy.2018.09.052.
229. Afram, A.; Janabi-Sharifi, F. Theory and applications of HVAC control systems - A review of model predictive control (MPC). *Build. Environ.* **2014**, *72*, 343–355, doi:10.1016/j.buildenv.2013.11.016.
230. Fiorentini, M.; Wall, J.; Ma, Z.; Braslavsky, J.H.; Cooper, P. Hybrid model predictive control of a residential HVAC system with on-site thermal energy generation and storage. *Appl. Energy* **2017**, *187*, 465–479, doi:10.1016/j.apenergy.2016.11.041.
231. Cao, S.; Hou, S.; Yu, L.; Lu, J. Predictive control based on occupant behavior prediction for domestic hot water system using data mining algorithm. *Energy Sci. Eng.* **2019**, doi:10.1002/ese3.341.
232. Oldewurtel, F.; Parisio, A.; Jones, C.N.; Gyalistras, D.; Gwerder, M.; Stauch, V.; Lehmann, B.; Morari, M. Use of model predictive control and weather forecasts for energy efficient building climate control. *Energy Build.* **2012**, *45*, 15–27, doi:10.1016/j.enbuild.2011.09.022.
233. Zhang, Y.; Wang, R.; Zhang, T.; Liu, Y.; Guo, B. Model predictive control-based operation management for a residential microgrid with considering forecast uncertainties and demand response strategies. *IET Gener. Transm. Distrib.* **2016**, *10*, 2367–2378, doi:10.1049/iet-gtd.2015.1127.
234. Petrollese, M.; Valverde, L.; Cocco, D.; Cau, G.; Guerra, J. Real-time integration of optimal generation scheduling with MPC for the energy management of a renewable hydrogen-based microgrid. *Appl. Energy* **2016**, *166*, 96–106, doi:10.1016/j.apenergy.2016.01.014.
235. M. del M. Castilla, J.D. Álvarez, F. Rodríguez, M. Berenguel Comfort Control in

Buildings. *Springer London* **2014**.

236. Haghighi, M.M. Controlling Energy-Efficient Buildings in the Context of Smart Grid : A Cyber Physical System Approach. *Thesis Electr. Eng. Comput. Sci. Univ. Calif. Bekeley* **2013**.
237. Li, X.; Malkawi, A. Multi-objective optimization for thermal mass model predictive control in small and medium size commercial buildings under summer weather conditions. *Energy* **2016**, *112*, 1194–1206, doi:10.1016/j.energy.2016.07.021.
238. Tian, Z.; Si, B.; Wu, Y.; Zhou, X.; Shi, X. Multi-objective optimization model predictive dispatch precooling and ceiling fans in office buildings under different summer weather conditions. *Build. Simul.* **2019**, *12*, 999–1012, doi:10.1007/s12273-019-0543-3.
239. Prívara, S.; Široký, J.; Ferkl, L.; Cigler, J. Model predictive control of a building heating system: The first experience. *Energy Build.* **2011**, doi:10.1016/j.enbuild.2010.10.022.
240. Killian, M.; Kozek, M. Ten questions concerning model predictive control for energy efficient buildings. *Build. Environ.* **2016**, *105*, 403–412, doi:10.1016/j.buildenv.2016.05.034.
241. Prívara, S.; Cigler, J.; Váňa, Z.; Oldewurtel, F.; Sagerschnig, C.; Žáčeková, E. Building modeling as a crucial part for building predictive control. *Energy Build.* **2013**, *56*, 8–22, doi:10.1016/j.enbuild.2012.10.024.
242. Tahersima, F.; Madsen, P.P.; Andersen, P. An intuitive definition of demand flexibility in direct load control. *Proc. IEEE Int. Conf. Control Appl.* **2013**, 521–526, doi:10.1109/CCA.2013.6662802.
243. Fischer, D.; Madani, H. On heat pumps in smart grids: A review. *Renew. Sustain. Energy Rev.* **2017**, *70*, 342–357, doi:10.1016/J.RSER.2016.11.182.
244. Pallonetto, F.; Oxizidis, S.; Milano, F.; Finn, D. The effect of time-of-use tariffs on the demand response flexibility of an all-electric smart-grid-ready dwelling. *Energy Build.* **2016**, *128*, 56–67, doi:10.1016/j.enbuild.2016.06.041.
245. Lee, K.H.; Joo, M.C.; Baek, N.C. Experimental evaluation of simple thermal storage control strategies in low-energy solar houses to reduce electricity consumption during grid on-peak periods. *Energies* **2015**, *8*, 9344–9364, doi:10.3390/en8099344.
246. Ümitcan, H.; Keles, D.; Chiodi, A.; Hartel, R.; Mikuli, M. Analysis of the power-to-

heat potential in the European energy system. **2018**, *20*, 6–19, doi:10.1016/j.esr.2017.12.009.

247. Tarroja, B.; Mueller, F.; Eichman, J.D.; Samuelsen, S. Metrics for evaluating the impacts of intermittent renewable generation on utility load-balancing. *Energy* **2012**, *42*, 546–562, doi:10.1016/j.energy.2012.02.040.
248. Angenendt, G.; Zurmühlen, S.; Rücker, F.; Axelsen, H.; Sauer, D.U. Optimization and operation of integrated homes with photovoltaic battery energy storage systems and power-to-heat coupling. *Energy Convers. Manag. X* **2019**, *1*, 100005, doi:10.1016/j.ecmx.2019.100005.
249. Lamaison, N.; Collette, S.; Vallée, M.; Bavière, R. Storage influence in a combined biomass and power-to-heat district heating production plant. *Energy* **2019**, *186*, 115714, doi:10.1016/J.ENERGY.2019.07.044.
250. Federal Energy Regulatory Commission - FERC Benefits of Demand Response in Electricity Markets and Recommendations for Achieving Them. *U.S. Dep. Energy* **2006**, 122.
251. Sun, Y.; Wang, S.; Xiao, F.; Gao, D. Peak load shifting control using different cold thermal energy storage facilities in commercial buildings: A review. *Energy Convers. Manag.* **2013**, *71*, 101–114, doi:10.1016/j.enconman.2013.03.026.
252. Arteconi, A.; Polonara, F. Assessing the demand side management potential and the energy flexibility of heat pumps in buildings. *Energies* **2018**, *11*, 1–19, doi:10.3390/en11071846.
253. Le, K.X.; Huang, M.J.; Wilson, C.; Shah, N.N.; Hewitt, N.J. Tariff-based load shifting for domestic cascade heat pump with enhanced system energy efficiency and reduced wind power curtailment. *Appl. Energy* **2020**, *257*, 113976, doi:10.1016/j.apenergy.2019.113976.
254. Klein, K.; Kalz, D.; Herkel, S. Grid Impact of a Net-Zero Energy Building With BIPV Using Different Energy Management Strategies. *Cisbat 2015* **2015**, 579–584.
255. Koh, S.L.; Lim, Y.S. Methodology for assessing viability of energy storage system for buildings. *Energy* **2016**, *101*, 519–531, doi:10.1016/j.energy.2016.02.047.
256. Ioakimidis, C.S.; Thomas, D.; Rycerski, P.; Genikomsakis, K.N. Peak shaving and valley filling of power consumption profile in non-residential buildings using an electric vehicle parking lot. *Energy* **2018**, *148*, 148–158,

doi:10.1016/j.energy.2018.01.128.

257. Fischer, D.; Bernhardt, J.; Madani, H.; Wittwer, C. Comparison of control approaches for variable speed air source heat pumps considering time variable electricity prices and PV. *Appl. Energy* **2017**, *204*, 93–105, doi:10.1016/j.apenergy.2017.06.110.

258. Dar, U.I.; Sartori, I.; Georges, L.; Novakovic, V. Advanced control of heat pumps for improved flexibility of Net-ZEB towards the grid. *Energy Build.* **2014**, *69*, 74–84, doi:10.1016/j.enbuild.2013.10.019.

259. Luthander, R.; Widén, J.; Munkhammar, J.; Lingfors, D. Self-consumption enhancement and peak shaving of residential photovoltaics using storage and curtailment. *Energy* **2016**, *112*, 221–231, doi:10.1016/j.energy.2016.06.039.

260. Schram, W.L.; Lampropoulos, I.; van Sark, W.G.J.H.M. Photovoltaic systems coupled with batteries that are optimally sized for household self-consumption: Assessment of peak shaving potential. *Appl. Energy* **2018**, *223*, 69–81, doi:10.1016/j.apenergy.2018.04.023.

261. Pimm, A.J.; Cockerill, T.T.; Taylor, P.G. The potential for peak shaving on low voltage distribution networks using electricity storage. *J. Energy Storage* **2018**, *16*, 231–242, doi:10.1016/j.est.2018.02.002.

262. Emmi, G.; Zarrella, A.; De Carli, M. A heat pump coupled with photovoltaic thermal hybrid solar collectors: A case study of a multi-source energy system. *Energy Convers. Manag.* **2017**, *151*, 386–399, doi:10.1016/j.enconman.2017.08.077.

263. Newsham, G.R.; Bowker, B.G. The effect of utility time-varying pricing and load control strategies on residential summer peak electricity use: A review. *Energy Policy* **2010**, *38*, 3289–3296, doi:10.1016/j.enpol.2010.01.027.

264. Entrop, A.G.; Brouwers, H.J.H.; Reinders, A.H.M.E. Evaluation of energy performance indicators and financial aspects of energy saving techniques in residential real estate. *Energy Build.* **2010**, *42*, 618–629, doi:10.1016/j.enbuild.2009.10.032.

265. Péan T, Costa-Castelló R, S.J. Price and carbon-based energy flexibility of residential heating and cooling loads using model predictive control. *Sustain Cities Soc* **2019**.

266. Oprea, S.V.; Bara, A. Setting the Time-of-Use Tariff Rates with NoSQL and Machine Learning to a Sustainable Environment. *IEEE Access* **2020**, *8*, 25521–25530, doi:10.1109/ACCESS.2020.2969728.
267. Jain, S.; Jain, N.K. Cost of electricity banking under open-access arrangement: A case of solar electricity in India. *Renew. Energy* **2020**, *146*, 776–788, doi:10.1016/J.RENENE.2019.06.172.
268. Batlle, C.; Mastropietro, P.; Rodilla, P. Redesigning residual cost allocation in electricity tariffs: A proposal to balance efficiency, equity and cost recovery. *Renew. Energy* **2020**, *155*, 257–266, doi:10.1016/j.renene.2020.03.152.
269. Avdasheva, S.; Orlova, Y. Effects of long-term tariff regulation on investments under low credibility of rules: Rate-of-return and price cap in Russian electricity grids. *Energy Policy* **2020**, *138*, 111276, doi:10.1016/J.ENPOL.2020.111276.
270. D'Ettorre, F.; De Rosa, M.; Conti, P.; Schito, E.; Testi, D.; Finn, D.P. Economic assessment of flexibility offered by an optimally controlled hybrid heat pump generator: A case study for residential building. *Energy Procedia* **2018**, *148*, 1222–1229, doi:10.1016/j.egypro.2018.08.008.
271. Farulla, G.A.; Cellura, M.; Guarino, F.; Ferraro, M. A review of thermochemical energy storage systems for power grid support. *Appl. Sci.* **2020**, *10*, doi:10.3390/app10093142.
272. Ferraro, M.; Farulla, G.A.; Tumminia, G.; Guarino, F.; Aloisio, D.; Brunaccini, G.; Sergi, F.; Giusa, F.; Colino, A.E.; Cellura, M.; et al. Experimental and Computational Fluid Dynamic study of an active ventilated façade integrating battery and distributed MPPT. *Math. Model. Eng. Probl.* **2019**, *6*, 333–342, doi:10.18280/mmep.060303.
273. Casals, L.C.; Corchero, C.; Ortiz, J.; Salom, J.; Cardoner, D.; Igualada, L.; Carrillo, R.E.; Stauffer, Y. How building and district algorithms enhance renewable energy integration in energy markets. *Int. Conf. Eur. Energy Mark. EEM* **2019**, *2019-Septe*, doi:10.1109/EEM.2019.8916457.
274. Fischer, D.; Rautenberg, F.; Wirtz, T.; Wille-Haussmann, B.; Madani, H. Smart Meter Enabled Control for Variable Speed Heat Pumps to Increase PV Self-Consumption. In Proceedings of the 24th IIR International Congress of Refrigeration; 2015; p. ID:580.

275. Franco, A.; Fantozzi, F. Experimental analysis of a self consumption strategy for residential building: The integration of PV system and geothermal heat pump. *Renew. Energy* **2016**, *86*, 1075–1085, doi:10.1016/j.renene.2015.09.030.
276. De Coninck, R.; Baetens, R.; Saelens, D.; Woyte, A.; Helsen, L. Rule-based demand-side management of domestic hot water production with heat pumps in zero energy neighbourhoods. *J. Build. Perform. Simul.* **2014**, *7*, 271–288, doi:10.1080/19401493.2013.801518.
277. Razmara, M.; Bharati, G.R.; Hanover, D.; Shahbakhti, M.; Paudyal, S.; Robinett, R.D. Enabling Demand Response programs via Predictive Control of Building-to-Grid systems integrated with PV Panels and Energy Storage Systems. In Proceedings of the Proceedings of the American Control Conference; 2017.
278. Cao, S.; Hasan, A.; Sirén, K. Analysis and solution for renewable energy load matching for a single-family house. *Energy Build.* **2013**, *65*, 398–411, doi:10.1016/j.enbuild.2013.06.013.
279. Bruni, G.; Cordiner, S.; Mulone, V.; Rocco, V.; Spagnolo, F. A study on the energy management in domestic micro-grids based on model predictive control strategies q. *Energy Convers. Manag.* **2015**, *102*, 50–58, doi:10.1016/j.enconman.2015.01.067.
280. Zhao, Y.; Lu, Y.; Yan, C.; Wang, S. MPC-based optimal scheduling of grid-connected low energy buildings with thermal energy storages. *Energy Build.* **2015**, *86*, 415–426, doi:10.1016/j.enbuild.2014.10.019.
281. Brahman, F.; Honarmand, M.; Jadid, S. Optimal electrical and thermal energy management of a residential energy hub, integrating demand response and energy storage system. *Energy Build.* **2015**, *90*, 65–75, doi:10.1016/j.enbuild.2014.12.039.
282. Bandera, C.F.; Pachano, J.; Salom, J.; Peppas, A.; Ruiz, G.R. Photovoltaic plant optimization to leverage electric self consumption by harnessing building thermal mass. *Sustain.* **2020**, *12*, doi:10.3390/su12020553.
283. Molina, J.R.; Nuñez, M.M.; Aguiar, W.S.P.; Ortega, J.F.M. Business models in the Smart Grid: challenges, opportunities and proposals for prosumer profitability. *Energies* **2014**.
284. Finocchiaro, P.; Beccali, M.; Cellura, M.; Guarino, F.; Longo, S. Life Cycle Assessment of a compact Desiccant Evaporative Cooling system: The case study of the “Freescoo.” *Sol. Energy Mater. Sol. Cells* **2016**,

doi:10.1016/j.solmat.2016.03.026.

285. Leite, F.M.; Volse, R.A.; Roman, H.R.; Saffaro, F.A. Building condition assessment: adjustments of the Building Performance Indicator (BPI) for university buildings in Brazil. *Ambient. Construído* **2020**, *20*, 215–230, doi:10.1590/s1678-86212020000100370.

286. Li, H.; Hong, T.; Lee, S.H.; Sofos, M. System-level key performance indicators for building performance evaluation. *Energy Build.* **2020**, *209*, doi:10.1016/j.enbuild.2019.109703.

287. Clauß, J.; Finck, C.; Vogler-finck, P.; Beagon, P. Control strategies for building energy systems to unlock demand side flexibility – A review Norwegian University of Science and Technology , Trondheim , Norway Eindhoven University of Technology , Eindhoven , Netherlands Neogrid Technologies ApS / Aalborg. *15th Int. Conf. Int. Build. Perform.* **2017**, 611–620.

288. Finck, C.; Li, R.; Zeiler, W. Optimal control of demand flexibility under real-time pricing for heating systems in buildings: A real-life demonstration. *Appl. Energy* **2020**, *263*, 114671, doi:10.1016/j.apenergy.2020.114671.

289. Voss, K.; Sartori, I.; Napolitano, A.; Geier, S.; Gonçalves, H.; Hall, M.; Heiselberg, P.; Widén, J.; Candanedo, J.A.; Musall, E.; et al. Load Matching and Grid Interaction of Net Zero Energy Buildings. **2016**, 1–8, doi:10.18086/eurosun.2010.06.24.

290. Cellura, M.; Guarino, F.; Longo, S.; Tumminia, G.; Ferraro, M.; Sergi, F.; Aloisio, D.; Antonucci, V. Analysis of Load Match in Nearly Zero Energy Buildings: A parametric analysis of an Italian case study. *IEEE 4th Int. Forum Res. Technol. Soc. Ind. RTSI 2018 - Proc.* **2018**, 0–5, doi:10.1109/RTSI.2018.8548378.

291. Morstyn, T.; Hredzak, B.; Agelidis, V.G. Control Strategies for Microgrids with Distributed Energy Storage Systems: An Overview. *IEEE Trans. Smart Grid* **2018**, *9*, 3652–3666, doi:10.1109/TSG.2016.2637958.

292. Williams, J. Can low carbon city experiments transform the development regime? *Futures* **2016**, *77*, 80–96, doi:10.1016/j.futures.2016.02.003.

293. Managan, K.; Controls, J. Net Zero Communities : One Building at a Time The Opportunity at the Community Scale. **2012**, 180–192.

294. Li, X.; Wen, J.; Wu, T. Net-zero Energy Impact Building Clusters Emulator for

Operation Strategy Development. *ASHRAE Trans.* **2014**, 1–8.

295. Finck, C.; Li, R.; Kramer, R.; Zeiler, W. Quantifying demand flexibility of power-to-heat and thermal energy storage in the control of building heating systems. *Appl. Energy* **2018**, *209*, 409–425, doi:10.1016/j.apenergy.2017.11.036.
296. Taddeo, P.; Colet, A.; Carrillo, R.E.; Canals, L.C.; Schubnel, B.; Stauffer, Y.; Bellanco, I.; Garcia, C.C.; Salom, J. Management and activation of energy flexibility at building and market level: A residential case study. *Energies* **2020**, *13*, 1–18, doi:10.3390/en13051188.
297. Vigna, I.; Jaeger, I. De; Saelens, D.; Lovati, M.; Lollini, R.; Pernetti, R.; Milano, P.; Leuven, K.U. Evaluating energy and flexibility performance of building clusters Eurac Research , Bolzano , Italy Flemish Institute for Technological Research (VITO), Mol , Belgium Università degli studi di Trento , Trento , Italy. **2018**, 3326–3333.
298. Wang, J.; Liu, Y.; Ren, F.; Lu, S. Multi-objective optimization and selection of hybrid combined cooling, heating and power systems considering operational flexibility. *Energy* **2020**, *197*, 117313, doi:10.1016/j.energy.2020.117313.
299. Zhang, Y.; Campana, P.E.; Yang, Y.; Stridh, B.; Lundblad, A.; Yan, J. Energy flexibility from the consumer: Integrating local electricity and heat supplies in a building. *Appl. Energy* **2018**, *223*, 430–442, doi:10.1016/j.apenergy.2018.04.041.
300. Razmara, M.; Bharati, G.R.; Hanover, D.; Shahbakhti, M.; Paudyal, S.; Robinett, R.D. Building-to-grid predictive power flow control for demand response and demand flexibility programs. *Appl. Energy* **2017**, *203*, 128–141, doi:10.1016/j.apenergy.2017.06.040.
301. Xue, X.; Wang, S.; Sun, Y.; Xiao, F. An interactive building power demand management strategy for facilitating smart grid optimization. *Appl. Energy* **2014**, *116*, 297–310, doi:10.1016/j.apenergy.2013.11.064.
302. Staffell, I. Measuring the progress and impacts of decarbonising British electricity. *Energy Policy* **2017**, *102*, 463–475, doi:10.1016/j.enpol.2016.12.037.
303. Garg, A.; Maheshwari, J.; Mahapatra, D.; Kumar, S. Economic and environmental implications of demand-side management options. *Energy Policy* **2011**, doi:10.1016/j.enpol.2011.02.009.
304. Palizban, O.; Kauhaniemi, K. Energy storage systems in modern grids—Matrix of

technologies and applications. *J. Energy Storage* **2016**, *6*, 248–259, doi:10.1016/J.EST.2016.02.001.

305. Zidan, A.; El-Saadany, E.F. Distribution system reconfiguration for energy loss reduction considering the variability of load and local renewable generation. *Energy* **2013**, *59*, 698–707, doi:10.1016/j.energy.2013.06.061.
306. Locatelli, G.; Palerma, E.; Mancini, M. Assessing the economics of large Energy Storage Plants with an optimisation methodology. *Energy* **2015**, *83*, 15–28, doi:10.1016/j.energy.2015.01.050.
307. Byrne, R.H.; Nguyen, T.A.; Copp, D.A.; Chalamala, B.R.; Gyuk, I. Energy Management and Optimization Methods for Grid Energy Storage Systems. *IEEE Access* **2017**, *6*, 13231–13260, doi:10.1109/ACCESS.2017.2741578.
308. Lizana, J.; Chacartegui, R.; Barrios-Padura, A.; Valverde, J.M. Advances in thermal energy storage materials and their applications towards zero energy buildings: A critical review. *Appl. Energy* **2017**, *203*, 219–239, doi:10.1016/J.APENERGY.2017.06.008.
309. Arteconi, A.; Hewitt, N.J.; Polonara, F. State of the art of thermal storage for demand-side management. *Appl. Energy* **2012**, *93*, 371–389, doi:10.1016/J.APENERGY.2011.12.045.
310. Del Pero, C.; Aste, N.; Paksoy, H.; Haghighat, F.; Grillo, S.; Leonforte, F. Energy storage key performance indicators for building application. *Sustain. Cities Soc.* **2018**, *40*, 54–65, doi:10.1016/j.scs.2018.01.052.
311. Zhang, H.; Baeyens, J.; Cáceres, G.; Degrève, J.; Lv, Y. Thermal energy storage: Recent developments and practical aspects. *Prog. Energy Combust. Sci.* 2016, *53*, 1–40.
312. Parameshwaran, R.; Kalaiselvam, S.; Harikrishnan, S.; Elayaperumal, A. Sustainable thermal energy storage technologies for buildings: A review. *Renew. Sustain. Energy Rev.* 2012.
313. Carrillo, A.J.; González-Aguilar, J.; Romero, M.; Coronado, J.M. Solar Energy on Demand: A Review on High Temperature Thermochemical Heat Storage Systems and Materials. *Chem. Rev.* **2019**, *119*, 4777–4816, doi:10.1021/acs.chemrev.8b00315.
314. Mazman, M.; Cabeza, L.F.; Mehling, H.; Nogues, M.; Evliya, H.; Paksoy, H.Ö.

Utilization of phase change materials in solar domestic hot water systems. *Renew. Energy* **2009**, doi:10.1016/j.renene.2008.10.016.

315. Boait, P.J.; Dixon, D.; Fan, D.; Stafford, A. Production efficiency of hot water for domestic use. *Energy Build.* **2012**, doi:10.1016/j.enbuild.2012.07.011.
316. Armstrong, P.; Ager, D.; Thompson, I.; McCulloch, M. Improving the energy storage capability of hot water tanks through wall material specification. *Energy* **2014**, *78*, 128–140, doi:10.1016/j.energy.2014.09.061.
317. Cabeza, L.F.; Solé, A.; Barreneche, C. Review on sorption materials and technologies for heat pumps and thermal energy storage. *Renew. Energy* **2017**, *110*, 3–39, doi:10.1016/j.renene.2016.09.059.
318. Hinnells, M. Combined heat and power in industry and buildings. *Energy Policy* **2008**, *36*, 4522–4526, doi:10.1016/j.enpol.2008.09.018.
319. Scholz, D.; Müsgens, F. Increasing flexibility of combined heat and power plants with Power-to-Heat. *Int. Conf. Eur. Energy Mark. EEM* **2015**, *2015-Augus*, 5–9, doi:10.1109/EEM.2015.7216771.
320. Hirmiz, R.; Teamah, H.M.; Lightstone, M.F.; Cotton, J.S. Performance of heat pump integrated phase change material thermal storage for electric load shifting in building demand side management. *Energy Build.* **2019**, *190*, 103–118, doi:10.1016/J.ENBUILD.2019.02.026.
321. Paiho, S.; Saastamoinen, H.; Hakkarainen, E.; Similä, L.; Pasonen, R.; Ikäheimo, J.; Rämä, M.; Tuovinen, M.; Horsmanheimo, S. Increasing flexibility of Finnish energy systems—A review of potential technologies and means. *Sustain. Cities Soc.* 2018.
322. Yifan, Z.; Wei, H.; Le, Z.; Yong, M.; Lei, C.; Zongxiang, L.; Ling, D. Power and energy flexibility of district heating system and its application in wide-area power and heat dispatch. *Energy* **2020**, *190*, 116426, doi:10.1016/j.energy.2019.116426.
323. Good, N.; Mancarella, P. Flexibility in Multi-Energy Communities with Electrical and Thermal Storage: A Stochastic, Robust Approach for Multi-Service Demand Response. *IEEE Trans. Smart Grid* **2019**, *10*, 503–513, doi:10.1109/TSG.2017.2745559.
324. Pilpola, S.; Lund, P.D. Different flexibility options for better system integration of wind power. *Energy Strateg. Rev.* **2019**, *26*, 100368, doi:10.1016/J.ESR.2019.100368.

325. Patteeuw, D.; Henze, G.P.; Helsen, L. Comparison of load shifting incentives for low-energy buildings with heat pumps to attain grid flexibility benefits. *Appl. Energy* **2016**, *167*, 80–92, doi:10.1016/J.APENERGY.2016.01.036.
326. Zhao, X.; Fu, L.; Wang, X.; Sun, T.; Wang, J.; Zhang, S. Flue gas recovery system for natural gas combined heat and power plant with distributed peak-shaving heat pumps. *Appl. Therm. Eng.* **2017**, *111*, 599–607, doi:10.1016/J.APPLTHERMALENG.2016.09.130.
327. Y. V. Makarov, C. Loutan, and J.M. Operational impacts of wind generation on california power systems. *" IEEETrans. Power Syst.,* **2009**, *24*, 1039–1050.
328. Stinner, S.; Huchtemann, K.; Müller, D. Flexibility Quantification for Building Energy Systems with Heat Pumps. In Proceedings of the Proceedings of the 15th IBPSA Conference; 2017.
329. Stinner, S.; Streblow, R.; Müller, D. Operation flexibility of building energy systems with thermal storages. In Proceedings of the 14th International Conference of IBPSA - Building Simulation 2015, BS 2015, Conference Proceedings; 2015.
330. Bloess, A.; Schill, W.-P.; Zerrahn, A. Power-to-Heat for Renewable Energy Integration: Technologies, Modeling Approaches, and Flexibility Potentials. *SSRN Electron. J.* **2017**, doi:10.2139/ssrn.3028516.
331. Kensby, J.; Trüschel, A.; Dalenbäck, J.O. Potential of residential buildings as thermal energy storage in district heating systems - Results from a pilot test. *Appl. Energy* **2015**, *137*, 773–781, doi:10.1016/j.apenergy.2014.07.026.
332. Kuczyński, T.; Staszczuk, A. Experimental study of the influence of thermal mass on thermal comfort and cooling energy demand in residential buildings. *Energy* **2020**, *195*, doi:10.1016/j.energy.2020.116984.
333. Braun, J.E. Load control using building thermal mass. *J. Sol. Energy Eng. Trans. ASME* **2003**, *125*, 292–301, doi:10.1115/1.1592184.
334. Lauro, F.; Moretti, F.; Capozzoli, A.; Panzieri, S. Model predictive control for building active demand response systems. *Energy Procedia* **2015**, *83*, 494–503, doi:10.1016/j.egypro.2015.12.169.
335. Stötzer, M.; Hauer, I.; Richter, M.; Styczynski, Z.A. Potential of demand side integration to maximize use of renewable energy sources in Germany. *Appl. Energy* **2015**, *146*, 344–352, doi:10.1016/j.apenergy.2015.02.015.

336. Foteinaki, K.; Li, R.; Péan, T.; Rode, C.; Salom, J. Evaluation of energy flexibility of low-energy residential buildings connected to district heating. *Energy Build.* **2020**, *213*, 109804, doi:10.1016/j.enbuild.2020.109804.
337. Kazmi, H.; Suykens, J.; Balint, A.; Driesen, J. Multi-agent reinforcement learning for modeling and control of thermostatically controlled loads. *Appl. Energy* **2019**, *238*, 1022–1035, doi:10.1016/j.apenergy.2019.01.140.
338. Oldewurtel, F.; Borsche, T.; Bucher, M.; Fortenbacher, P.; Haring, M.G.V.T.; Mathieu, J.L.; Megel, O.; Vrettos, E.; Andersson, G. A framework for and assessment of demand response and energy storage in power systems. *Proc. IREP Symp. Bulk Power Syst. Dyn. Control - IX Optim. Secur. Control Emerg. Power Grid, IREP 2013* **2013**, 1–24, doi:10.1109/IREP.2013.6629419.
339. Romanchenko, D.; Kensby, J.; Odenberger, M.; Johnsson, F. Thermal energy storage in district heating: Centralised storage vs. storage in thermal inertia of buildings. *Energy Convers. Manag.* **2018**, doi:10.1016/j.enconman.2018.01.068.
340. Balint, A.; Kazmi, H. Determinants of energy flexibility in residential hot water systems. *Energy Build.* **2019**, *188–189*, 286–296, doi:10.1016/j.enbuild.2019.02.016.
341. Péan, T.; Torres, B.; Salom, J.; Ortiz, J. Representation of daily profiles of building energy flexibility. *eSim 2018, 10th Conf. IBPSA-Canada* **2018**, 153–162.
342. Kathirgamanathan, A.; Murphy, K.; Rosa, M. De; Mangina, E.; Finn, D.P. Aggregation of Energy Flexibility of Commercial Buildings. *Proc. eSim 2018, 10th Conf. IBPSA-Canada Montréal, QC, Canada, May 9-10, 2018* **2018**, 173–182.
343. Zhang, K.; Kummert, M. Potential of building thermal mass for energy flexibility in residential buildings: a sensitivity analysis. *Proc. eSim 2018, May 9-10, 2018* **2018**, 163–172.
344. Sunikka-Blank, M.; Galvin, R. Introducing the prebound effect: The gap between performance and actual energy consumption. *Build. Res. Inf.* **2012**, *40*, 260–273, doi:10.1080/09613218.2012.690952.
345. Holm, S.O.; Englund, G. Increased ecoefficiency and gross rebound effect: Evidence from USA and six European countries 1960-2002. *Ecol. Econ.* **2009**, *68*, 879–887, doi:10.1016/j.ecolecon.2008.07.006.
346. Gillingham, K.; Rapson, D.; Wagner, G. The rebound effect and energy efficiency

policy. *Rev. Environ. Econ. Policy* **2016**, *10*, 68–88, doi:10.1093/reep/rev017.

347. Figge, F.; Young, W.; Barkemeyer, R. Sufficiency or efficiency to achieve lower resource consumption and emissions? the role of the rebound effect. *J. Clean. Prod.* **2014**, *69*, 216–224, doi:10.1016/j.jclepro.2014.01.031.
348. O'Malley, M.; Kroposki, B.; Hannegan, B.; Madsen, H.; Andersson, M.; D'haeseleer, W.; McGranaghan, M.F.; Dent, C.; Strbac, G.; Baskaran, S.; et al. Energy Systems Integration. Defining and Describing the Value Proposition. *Nrel/Tp-5D00-66616* **2016**, 9.
349. Pepermans, G.; Driesen, J.; Haeseldonckx, D.; Belmans, R.; D'haeseleer, W. Distributed generation: Definition, benefits and issues. *Energy Policy* **2005**, doi:10.1016/j.enpol.2003.10.004.
350. Chicco, G.; Mancarella, P. Distributed multi-generation: A comprehensive view. *Renew. Sustain. Energy Rev.* **2009**, *13*, 535–551, doi:10.1016/j.rser.2007.11.014.
351. Kristiansen, A.B.; Ma, T.; Wang, R.Z. Perspectives on industrialized transportable solar powered zero energy buildings. *Renew. Sustain. Energy Rev.* **2019**, *108*, 112–124, doi:10.1016/j.rser.2019.03.032.
352. Ferraro, M.; Sergi, F.; Antonucci, V.; Guarino, F.; Tumminia, G.; Cellura, M. Load match and grid interaction optimization of a net zero energy building through electricity storage: An Italian case-study. *EEEIC 2016 - Int. Conf. Environ. Electr. Eng.* **2016**, doi:10.1109/EEEIC.2016.7555812.
353. Guarino, F.; Cassarà, P.; Longo, S.; Cellura, M.; Ferro, E. Load match optimisation of a residential building case study: A cross-entropy based electricity storage sizing algorithm. *Appl. Energy* **2015**, *154*, 380–391, doi:10.1016/j.apenergy.2015.04.116.
354. Pan, W.; Li, K. Clusters and exemplars of buildings towards zero carbon. *Build. Environ.* **2016**, *104*, 92–101, doi:10.1016/j.buildenv.2016.04.027.
355. Kim, J.H.; Kim, H.R.; Kim, J.T. Analysis of photovoltaic applications in zero energy building cases of IEA SHC/EBC Task 40/Annex 52. *Sustain.* **2015**, *7*, 8782–8800, doi:10.3390/su7078782.
356. Cellura, M.; Guarino, F.; Longo, S.; Mistretta, M. Energy life-cycle approach in Net zero energy buildings balance: Operation and embodied energy of an Italian case study. *Energy Build.* **2014**, *72*, 371–381, doi:10.1016/j.enbuild.2013.12.046.
357. Dávi, G.A.; Caamaño-Martín, E.; Rüther, R.; Solano, J. Energy performance

evaluation of a net plus-energy residential building with grid-connected photovoltaic system in Brazil. *Energy Build.* **2016**, *120*, 19–29, doi:10.1016/j.enbuild.2016.03.058.

358. Baetens, R.; de Coninck, R.; Helsen, L.; Saelens, D. The impact of load profile on the grid-interaction of building integrated photovoltaic (BIPV) systems in low-energy dwellings. *J. Green Build.* **2010**, *5*, 137–147, doi:10.3992/jgb.5.4.137.
359. Gjorgievski, V.Z.; Chatzigeorgiou, N.G.; Venizelou, V.; Christoforidis, G.C.; Georghiou, G.E.; Papagiannis, G.K. Evaluation of load matching indicators in residential PV systems-the case of Cyprus. *Energies* **2020**, *13*, 1–18, doi:10.3390/en13081934.
360. Kichou, S.; Skandalos, N.; Wolf, P. Evaluation of photovoltaic and battery storage effects on the load matching indicators based on real monitored data. *Energies* **2020**, *13*, doi:10.3390/en13112727.
361. Castillo-Cagigal, M.; Caamaño-Martín, E.; Matallanas, E.; Masa-Bote, D.; Gutiérrez, A.; Monasterio-Huelin, F.; Jiménez-Leube, J. PV self-consumption optimization with storage and Active DSM for the residential sector. *Sol. Energy* **2011**, *85*, 2338–2348, doi:10.1016/j.solener.2011.06.028.
362. Baetens, R.; De Coninck, R.; Van Roy, J.; Verbruggen, B.; Driesen, J.; Helsen, L.; Saelens, D. Assessing electrical bottlenecks at feeder level for residential net zero-energy buildings by integrated system simulation. *Appl. Energy* **2012**, *96*, 74–83, doi:10.1016/j.apenergy.2011.12.098.
363. Luthander, R.; Widén, J.; Nilsson, D.; Palm, J. Photovoltaic self-consumption in buildings: A review. *Appl. Energy* 2015.
364. Gautier, A.; Hoet, B.; Jacqmin, J.; Van Driessche, S. Self-consumption choice of residential PV owners under net-metering. *Energy Policy* **2019**, doi:10.1016/j.enpol.2019.01.055.
365. Bertsch, V.; Geldermann, J.; Lühn, T. What drives the profitability of household PV investments, self-consumption and self-sufficiency? *Appl. Energy* **2017**, doi:10.1016/j.apenergy.2017.06.055.
366. Mubarak, R.; Luiz, E.W.; Seckmeyer, G. Why PV modules should preferably no longer be oriented to the south in the near future. *Energies* **2019**, doi:10.3390/en12234528.

367. Yu, H.J.J. A prospective economic assessment of residential PV self-consumption with batteries and its systemic effects: The French case in 2030. *Energy Policy* **2018**, doi:10.1016/j.enpol.2017.11.005.
368. Li, Y.; Gao, W.; Zhang, X.; Ruan, Y.; Ushifusa, Y.; Hiroatsu, F. Techno-economic performance analysis of zero energy house applications with home energy management system in Japan. *Energy Build.* **2020**, *214*, doi:10.1016/j.enbuild.2020.109862.
369. Salom, J.; Marszal, A.J.; Candanedo, J.; Widén, J.; Byskov Lindberg, K.; Sartori, I. Analysis of Load Match and Grid Integration Indicators in Net Zero Energy Buildings with High-Resolution Data. A report of Subtask A IEA Task 40/Annex 52 Towards Net Zero Energy Solar Buildings. **2014**, 102.
370. Hadj Arab, A.; Chenlo, F.; Benghanem, M. Loss-of-load probability of photovoltaic water pumping systems. *Sol. Energy* **2004**, *76*, 713–723, doi:10.1016/j.solener.2004.01.006.
371. Sun, Y.; Ma, R.; Chen, J.; Xu, T. Heuristic optimization for grid-interactive net-zero energy building design through the glowworm swarm algorithm. *Energy Build.* **2020**, *208*, doi:10.1016/j.enbuild.2019.109644.
372. Yoon, Y.T.; Felder, F.A. Study of loss of load probability in designing installed capacity market. In Proceedings of the Proceedings of the IEEE Power Engineering Society Transmission and Distribution Conference; 2002.
373. Tumminia, G.; Guarino, F.; Longo, S.; Aloisio, D.; Cellura, S.; Sergi, F.; Brunaccini, G.; Antonucci, V.; Ferraro, M. Grid interaction and environmental impact of a net zero energy building. *Energy Convers. Manag.* **2020**, *203*, 112228, doi:10.1016/j.enconman.2019.112228.
374. Zhou, Y.; Cao, S. Quantification of energy flexibility of residential net-zero-energy buildings involved with dynamic operations of hybrid energy storages and diversified energy conversion strategies. *Sustain. Energy, Grids Networks* **2020**, *21*, 100304, doi:10.1016/j.segan.2020.100304.
375. Widén, J.; Wäckelgård, E.; Lund, P.D. Options for improving the load matching capability of distributed photovoltaics: Methodology and application to high-latitude data. *Sol. Energy* **2009**, *83*, 1953–1966, doi:10.1016/j.solener.2009.07.007.
376. Deng, S.; Wang, R.Z.; Dai, Y.J. How to evaluate performance of net zero energy

building - A literature research. *Energy* **2014**, *71*, 1–16, doi:10.1016/j.energy.2014.05.007.

377. Zhang, F.; de Dear, R.; Candido, C. Thermal comfort during temperature cycles induced by direct load control strategies of peak electricity demand management. *Build. Environ.* **2016**, *103*, 9–20, doi:10.1016/j.buildenv.2016.03.020.
378. Luthander, R.; Nilsson, A.M.; Widén, J.; Åberg, M. Graphical analysis of photovoltaic generation and load matching in buildings: A novel way of studying self-consumption and self-sufficiency. *Appl. Energy* **2019**, *250*, 748–759, doi:10.1016/j.apenergy.2019.05.058.
379. Cao, S.; Hasan, A.; Sirén, K. On-site energy matching indices for buildings with energy conversion, storage and hybrid grid connections. *Energy Build.* **2013**, *64*, 423–438, doi:10.1016/j.enbuild.2013.05.030.
380. Ala-Juusela, M.; Crosbie, T.; Hukkalainen, M. Defining and operationalising the concept of an energy positive neighbourhood. *Energy Convers. Manag.* **2016**, *125*, 133–140, doi:10.1016/j.enconman.2016.05.052.
381. Klein, K.; Herkel, S.; Henning, H.M.; Felsmann, C. Load shifting using the heating and cooling system of an office building: Quantitative potential evaluation for different flexibility and storage options. *Appl. Energy* **2017**, *203*, 917–937, doi:10.1016/j.apenergy.2017.06.073.
382. Ranaboldo, M.; Ferrer-Martí, L.; García-Villoria, A.; Pastor Moreno, R. Heuristic indicators for the design of community off-grid electrification systems based on multiple renewable energies. *Energy* **2013**, *50*, 501–512, doi:10.1016/j.energy.2012.11.025.
383. Holttinen, H.; Meibom, P.; Orths, A.; Lange, B.; O'Malley, M.; Tande, J.O.; Estanqueiro, A.; Gomez, E.; Söder, L.; Strbac, G.; et al. Impacts of large amounts of wind power on design and operation of power systems, results of IEA collaboration. *Wind Energy* **2011**, doi:10.1002/we.410.
384. Liu, C.; Xu, W.; Li, A.; Sun, D.; Huo, H. Analysis and optimization of load matching in photovoltaic systems for zero energy buildings in different climate zones of China. *J. Clean. Prod.* **2019**, *238*, 117914, doi:10.1016/j.jclepro.2019.117914.
385. Pean, T.; Costa-Castello, R.; Fuentes, E.; Salom, J. Experimental Testing of

Variable Speed Heat Pump Control Strategies for Enhancing Energy Flexibility in Buildings. *IEEE Access* **2019**, *7*, 37071–37087, doi:10.1109/ACCESS.2019.2903084.

386. Ahmadi, M.; Rosenberger, J.M.; Lee, W.J.; Kulvanitchaiyanunt, A. Optimizing Load Control in a Collaborative Residential Microgrid Environment. *IEEE Trans. Smart Grid* **2015**, *6*, 1196–1207, doi:10.1109/TSG.2014.2387202.
387. Milo, A.; Gaztañaga, H.; Etxeberria-Otadui, I.; Bacha, S.; Rodríguez, P. Optimal economic exploitation of hydrogen based grid-friendly zero energy buildings. *Renew. Energy* **2011**, *36*, 197–205, doi:10.1016/j.renene.2010.06.021.
388. Salom, J.; Widén, J.; Candanedo, J.; Sartori, I.; Voss, K.; Marszal, A. *Understanding net zero energy buildings: Evaluation of load matching and grid interaction indicators*; Vol. 6, pp. 2514–2521;.
389. De Coninck, R.; Baetens, R.; Verbruggen, B.; Driesen, J.; Saelens, D.; Helsen, L. Modelling and simulation of a grid connected photovoltaic heat pump system with thermal energy storage using Modelica. *8th Int. Conf. Syst. Simul. Build.* **2010**, P177.
390. Klein, K.; Langner, R.; Kalz, D.; Herkel, S.; Henning, H.M. Grid support coefficients for electricity-based heating and cooling and field data analysis of present-day installations in Germany. *Appl. Energy* **2016**, *162*, 853–867, doi:10.1016/j.apenergy.2015.10.107.
391. Fosas, D.; Nikolaidou, E.; Roberts, M.; Allen, S.; Walker, I.; Coley, D. Towards active buildings: Rating grid-servicing buildings. *Build. Serv. Eng. Res. Technol.* **2021**, *42*, 129–155.
392. Neukomm, M.; Nubbe, V.; Fares, R. Grid-interactive efficient buildings technical report series: Overview of research challenges and gaps. **2019**.
393. Schiller, S.R.; Schwartz, L.C.; Murphy, S. *Performance Assessments of Demand Flexibility from Grid-Interactive Efficient Buildings: Issues and Considerations*; Lawrence Berkeley National Lab.(LBNL), Berkeley, CA (United States), 2020;
394. Crosbie, T.; Short, M.; Dawood, M.; Charlesworth, R. Demand response in blocks of buildings: Opportunities and requirements. *Entrep. Sustain. Issues* **2017**, doi:10.9770/jesi.2017.4.3S(3).
395. Intergovernmental Panel on Climate Change *Climate Change 2014: Mitigation of*

Climate Change: Working Group III Contribution to the IPCC Fifth Assessment Report; 2014; ISBN 9781107415416.

396. Edenhofer, O.; Pichs-Madruga, R.; Sokona, Y.; Kadner, S.; Minx, J.; Brunner, S.; Agrawala, S.; Baiocchi, G.; Bashmakov, I.A.; Blanco, G.; et al. Climate Change 2014: Mitigation of climate change.Fifth Assessment Report of the Intergovernmental Panel on Climate Change. *Clim. Chang. 2014* **2014**, doi:10.1103/PhysRevD.70.106002.
397. Dagoumas, A.S.; Koltsaklis, N.E. Review of models for integrating renewable energy in the generation expansion planning. *Appl. Energy* **2019**, *242*, 1573–1587, doi:10.1016/J.APENERGY.2019.03.194.
398. Fang, J.; Liu, Q.; Guo, S.; Lei, J.; Jin, H. Spanning solar spectrum: A combined photochemical and thermochemical process for solar energy storage. *Appl. Energy* **2019**, *247*, 116–126, doi:10.1016/J.APENERGY.2019.04.043.
399. Hsieh, E.; Anderson, R. Grid flexibility: The quiet revolution. *Electr. J.* **2017**, *30*, 1–8, doi:10.1016/j.tej.2017.01.009.
400. Huber, M.; Dimkova, D.; Hamacher, T. Integration of wind and solar power in Europe: Assessment of flexibility requirements. *Energy* **2014**, *69*, 236–246, doi:10.1016/j.energy.2014.02.109.
401. Denholm, P.; Margolis, R.M. Evaluating the limits of solar photovoltaics (PV) in traditional electric power systems. *Energy Policy* **2007**, *35*, 2852–2861, doi:10.1016/j.enpol.2006.10.014.
402. DeCesaro, J.; Porter, K.; Milligan, M. Wind Energy and Power System Operations: A Review of Wind Integration Studies to Date. *Electr. J.* **2009**, *22*, 34–43, doi:10.1016/j.tej.2009.10.010.
403. Petersen, M.K.; Edlund, K.; Hansen, L.H.; Bendtsen, J.; Stoustrup, J. A taxonomy for modeling flexibility and a computationally efficient algorithm for dispatch in Smart Grids. In Proceedings of the Proceedings of the American Control Conference; 2013.
404. Graditi, G.; Di Silvestre, M.L.; Gallea, R.; Sanseverino, E.R. Heuristic-based shiftable loads optimal management in smart micro-grids. *IEEE Trans. Ind. Informatics* **2015**, *11*, 271–280, doi:10.1109/TII.2014.2331000.
405. Ferruzzi, G.; Cervone, G.; Delle Monache, L.; Graditi, G.; Jacobone, F. Optimal

bidding in a Day-Ahead energy market for Micro Grid under uncertainty in renewable energy production. *Energy* **2016**, *106*, 194–202, doi:10.1016/J.ENERGY.2016.02.166.

406. Enescu, D.; Chicco, G.; Porumb, R.; Seritan, G. Thermal energy storage for grid applications: Current status and emerging trends. *Energies* **2020**, *13*, doi:10.3390/en13020340.
407. van der Roest, E.; Snip, L.; Fens, T.; van Wijk, A. Introducing Power-to-H3: Combining renewable electricity with heat, water and hydrogen production and storage in a neighbourhood. *Appl. Energy* **2020**, *257*, 114024, doi:10.1016/J.APENERGY.2019.114024.
408. Kohlhepp, P.; Harb, H.; Wolisz, H.; Waczowicz, S.; Müller, D.; Hagenmeyer, V. Large-scale grid integration of residential thermal energy storages as demand-side flexibility resource: A review of international field studies. *Renew. Sustain. Energy Rev.* **2019**, *101*, 527–547, doi:10.1016/j.rser.2018.09.045.
409. Kiviluoma, J.; Meibom, P. Influence of wind power, plug-in electric vehicles, and heat storages on power system investments. *Energy* **2010**, *35*, 1244–1255, doi:10.1016/J.ENERGY.2009.11.004.
410. Stadler, I. Power grid balancing of energy systems with high renewable energy penetration by demand response. *Util. Policy* **2008**, *16*, 90–98, doi:10.1016/J.JUP.2007.11.006.
411. Bloess, A.; Schill, W.; Zerrahn, A. Power-to-heat for renewable energy integration : A review of technologies , modeling approaches , and fl exibility potentials. *Appl. Energy* **2018**, *212*, 1611–1626, doi:10.1016/j.apenergy.2017.12.073.
412. Hasan, K.N.; Preece, R.; Milanović, J. V. Existing approaches and trends in uncertainty modelling and probabilistic stability analysis of power systems with renewable generation. *Renew. Sustain. Energy Rev.* **2019**, *101*, 168–180, doi:10.1016/j.rser.2018.10.027.
413. Steffen, B.; Weber, C. Efficient storage capacity in power systems with thermal and renewable generation. *Energy Econ.* **2013**, *36*, 556–567, doi:10.1016/j.eneco.2012.11.007.
414. Beccali, M.; Cellura, M.; Mistretta, M. Environmental effects of energy policy in sicily: The role of renewable energy. *Renew. Sustain. Energy Rev.* **2007**, *11*, 282–

298, doi:10.1016/J.RSER.2005.02.001.

415. Navarro, L.; de Gracia, A.; Colclough, S.; Browne, M.; McCormack, S.J.; Griffiths, P.; Cabeza, L.F. Thermal energy storage in building integrated thermal systems: A review. Part 1. active storage systems. *Renew. Energy* **2016**, *88*, 526–547, doi:10.1016/j.renene.2015.11.040.

416. De Gracia, A.; Cabeza, L.F. Phase change materials and thermal energy storage for buildings. *Energy Build.* **2015**, *103*, 414–419, doi:10.1016/j.enbuild.2015.06.007.

417. Palomba, V.; Ferraro, M.; Frazzica, A.; Vasta, S.; Sergi, F.; Antonucci, V. Experimental and numerical analysis of a SOFC-CHP system with adsorption and hybrid chillers for telecommunication applications. *Appl. Energy* **2018**, *216*, 620–633, doi:10.1016/j.apenergy.2018.02.063.

418. Vasta, S.; Brancato, V.; La Rosa, D.; Palomba, V.; Restuccia, G.; Sapienza, A.; Frazzica, A. Adsorption heat storage: State-of-the-art and future perspectives. *Nanomaterials* **2018**, *8*, doi:10.3390/nano8070522.

419. Scapino, L.; Zondag, H.A.; Van Bael, J.; Diriken, J.; Rindt, C.C.M. Energy density and storage capacity cost comparison of conceptual solid and liquid sorption seasonal heat storage systems for low-temperature space heating. *Renew. Sustain. Energy Rev.* **2017**, *76*, 1314–1331, doi:10.1016/j.rser.2017.03.101.

420. Scapino, L.; Zondag, H.A.; Van Bael, J.; Diriken, J.; Rindt, C.C.M. Sorption heat storage for long-term low-temperature applications: A review on the advancements at material and prototype scale. *Appl. Energy* **2017**, *190*, 920–948, doi:10.1016/j.apenergy.2016.12.148.

421. Feng, D.; Feng, Y.; Qiu, L.; Li, P.; Zang, Y.; Zou, H.; Yu, Z.; Zhang, X. Review on nanoporous composite phase change materials: Fabrication, characterization, enhancement and molecular simulation. *Renew. Sustain. Energy Rev.* **2019**, *109*, 578–605, doi:10.1016/J.RSER.2019.04.041.

422. Badenhorst, H. A review of the application of carbon materials in solar thermal energy storage. *Sol. Energy* **2019**, *192*, 35–68, doi:10.1016/J.SOLENER.2018.01.062.

423. Bott, C.; Dressel, I.; Bayer, P. State-of-technology review of water-based closed seasonal thermal energy storage systems. *Renew. Sustain. Energy Rev.* **2019**, *113*, 109241, doi:10.1016/J.RSER.2019.06.048.

424. Palacios, A.; Cong, L.; Navarro, M.E.; Ding, Y.; Barreneche, C. Thermal conductivity measurement techniques for characterizing thermal energy storage materials – A review. *Renew. Sustain. Energy Rev.* **2019**, *108*, 32–52, doi:10.1016/J.RSER.2019.03.020.
425. Wu, S.; Yan, T.; Kuai, Z.; Pan, W. Thermal conductivity enhancement on phase change materials for thermal energy storage: A review. *Energy Storage Mater.* **2020**, *25*, 251–295, doi:10.1016/j.ensm.2019.10.010.
426. Olsthoorn, D.; Haghighat, F.; Mirzaei, P.A. Integration of storage and renewable energy into district heating systems: A review of modelling and optimization. *Sol. Energy* **2016**, *136*, 49–64, doi:10.1016/j.solener.2016.06.054.
427. Lund, H.; Werner, S.; Wiltshire, R.; Svendsen, S.; Thorsen, J.E.; Hvelplund, F.; Mathiesen, B.V. 4th Generation District Heating (4GDH). Integrating smart thermal grids into future sustainable energy systems. *Energy* **2014**, *68*, 1–11, doi:10.1016/j.energy.2014.02.089.
428. Münster, M.; Morthorst, P.E.; Larsen, H. V.; Bregnbæk, L.; Werling, J.; Lindboe, H.H.; Ravn, H. The role of district heating in the future Danish energy system. *Energy* **2012**, *48*, 47–55, doi:10.1016/J.ENERGY.2012.06.011.
429. Mikkola, J.; Lund, P.D. Modeling flexibility and optimal use of existing power plants with large-scale variable renewable power schemes. *Energy* **2016**, *112*, 364–375, doi:10.1016/J.ENERGY.2016.06.082.
430. Li, Z.; Wu, W.; Shahidehpour, M.; Wang, J.; Zhang, B. Combined heat and power dispatch considering pipeline energy storage of district heating network. *IEEE Trans. Sustain. Energy* **2016**, *7*, 12–22, doi:10.1109/TSTE.2015.2467383.
431. Werner, S. International review of district heating and cooling. *Energy* **2017**, *137*, 617–631, doi:10.1016/J.ENERGY.2017.04.045.
432. Schmidt, D. Low Temperature District Heating for Future Energy Systems. *Energy Procedia* **2018**, *149*, 595–604, doi:10.1016/j.egypro.2018.08.224.
433. del Hoyo Arce, I.; Herrero López, S.; López Perez, S.; Rämä, M.; Klobut, K.; Febres, J.A. Models for fast modelling of district heating and cooling networks. *Renew. Sustain. Energy Rev.* **2018**, *82*, 1863–1873, doi:10.1016/j.rser.2017.06.109.
434. Andersen, A.N.; Østergaard, P.A. Support schemes adapting district energy combined heat and power for the role as a flexibility provider in renewable energy

systems. *Energy* **2020**, *192*, 116639, doi:10.1016/j.energy.2019.116639.

435. Guney, M.S.; Tepe, Y. Classification and assessment of energy storage systems. *Renew. Sustain. Energy Rev.* **2017**, *75*, 1187–1197, doi:10.1016/j.rser.2016.11.102.
436. Singh Gaur, A.; Fitiwi, D.Z.; Curtis, J. Heat Pumps and Their Role in Decarbonising Heating Sector: A Comprehensive Review. **2019**.
437. Vanhoudt, D.; Geysen, D.; Claessens, B.; Leemans, F.; Jespers, L.; Van Bael, J. An actively controlled residential heat pump: Potential on peak shaving and maximization of self-consumption of renewable energy. *Renew. Energy* **2014**, *63*, 531–543, doi:10.1016/J.RENENE.2013.10.021.
438. Sweetnam, T.; Fell, M.; Oikonomou, E.; Oreszczyn, T. Domestic demand-side response with heat pumps: controls and tariffs. *Build. Res. Inf.* **2019**, *47*, 344–361, doi:10.1080/09613218.2018.1442775.
439. Fischer, D.; Toral, T.R.; Lindberg, K.B.; Wille-Haussmann, B.; Madani, H. Investigation of Thermal Storage Operation Strategies with Heat Pumps in German Multi Family Houses. *Energy Procedia* **2014**, *58*, 137–144, doi:10.1016/J.EGYPRO.2014.10.420.
440. Bach B, Werling J, Ommen T, Münster M, Morales JM, E.B. Integration of large-scale heat pumps in the district heating systems of Greater Copenhagen. *Energy* **2016**, *107*, 321–334.
441. Lund R, P.U. Mapping potential heat sources for heat pumps in district heating in Denmark. *Energy* **2016**, *110*, 129–138.
442. Arat H, A.O. Optimization of district heating system aided by geothermal heat pump: a novel multistage with multilevel ANN modelling. *Appl Therm Eng* **2017**, *111*, 608–23.
443. Chua, K.J.; Chou, S.K.; Yang, W.M. Advances in heat pump systems: A review. *Appl. Energy* **2010**, *87*, 3611–3624, doi:10.1016/j.apenergy.2010.06.014.
444. Wang, R.; Zhai, X. *Handbook of energy systems in green buildings*; 2018; ISBN 9783662491201.
445. Heinen, S.; Burke, D.; O'Malley, M. Electricity, gas, heat integration via residential hybrid heating technologies – An investment model assessment. *Energy* **2016**, *109*, 906–919, doi:10.1016/J.ENERGY.2016.04.126.
446. Bach, B.; Werling, J.; Ommen, T.; Münster, M.; Morales, J.M.; Elmegaard, B.

Integration of large-scale heat pumps in the district heating systems of Greater Copenhagen. *Energy* **2016**, *107*, 321–334, doi:10.1016/J.ENERGY.2016.04.029.

447. Levihn, F. CHP and heat pumps to balance renewable power production: Lessons from the district heating network in Stockholm. *Energy* **2017**, *137*, 670–678, doi:10.1016/J.ENERGY.2017.01.118.
448. Renaldi, R.; Kiprakis, A.; Friedrich, D. An optimisation framework for thermal energy storage integration in a residential heat pump heating system. *Appl. Energy* **2017**, *186*, 520–529, doi:10.1016/j.apenergy.2016.02.067.
449. Chwieduk, B.; Chwieduk, D. Performance analysis of a PV driven heat pump system during a heating season in high latitude countries. **2019**, 1–10.
450. Chwieduk, D. Analysis of utilisation of renewable energies as heat sources for heat pumps in building sector in Poland. *Renew. Energy* **1996**, *9*, 720–723, doi:10.1016/0960-1481(96)88385-6.
451. Kim, J.H.; Shcherbakova, A. Common failures of demand response. *Energy* **2011**, *36*, 873–880, doi:10.1016/j.energy.2010.12.027.
452. Hu, J.; Chen, W.; Yang, D.; Zhao, B.; Song, H.; Ge, B. Energy performance of ETFE cushion roof integrated photovoltaic/thermal system on hot and cold days. *Appl. Energy* **2016**, *173*, 40–51, doi:10.1016/j.apenergy.2016.03.111.
453. Bogdan, Ž.; Kopjar, D. Improvement of the cogeneration plant economy by using heat accumulator. *Energy* **2006**, *31*, 2285–2292, doi:10.1016/J.ENERGY.2006.01.012.
454. Beck, T.; Kondziella, H.; Huard, G.; Bruckner, T. Optimal operation, configuration and sizing of generation and storage technologies for residential heat pump systems in the spotlight of self-consumption of photovoltaic electricity. *Appl. Energy* **2017**, *188*, 604–619, doi:10.1016/j.apenergy.2016.12.041.
455. Jarre, M.; Noussan, M.; Simonetti, M. Primary energy consumption of heat pumps in high renewable share electricity mixes. *Energy Convers. Manag.* **2018**, *171*, 1339–1351, doi:10.1016/j.enconman.2018.06.067.
456. Tjaden, T.; Schnorr, F.; Weniger, J.; Bergner, J.; Quaschning, V. Einsatz von PV-Systemen mit Wärmepumpen und Batteriespeichern zur Erhöhung des Autarkiegrades in Einfamilienhaushalten. *30. Symp. Photovoltaische Solarenergie* **2015**, 20.

457. Binder, J.; Williams, C.O.O.; Kelm, T. Inreasing pv self-consumption, domestic energy autonomy and grid compatibility of pv systems using heat pumps, thermal storage and battery storage. In Proceedings of the 27 European Photovoltaic Solar Energy Conference and Exhibition; 2012; pp. 4030–4034.
458. Hong, J.; Kelly, N.J.; Richardson, I.; Thomson, M. Assessing heat pumps as flexible load. *Proc. Inst. Mech. Eng. Part A J. Power Energy* **2013**, doi:10.1177/0957650912454830.
459. Klaassen, E.A.M.; Asare-Bediako, B.; De Koning, C.P.; Frunt, J.; Slootweg, J.G. Assessment of an algorithm to utilize heat pump flexibility-theory and practice. In Proceedings of the 2015 IEEE Eindhoven PowerTech, PowerTech 2015; 2015.
460. Geyer, P.; Buchholz, M.; Buchholz, R.; Provost, M. Hybrid thermo-chemical district networks – Principles and technology. *Appl. Energy* **2017**, *186*, 480–491, doi:10.1016/J.APENERGY.2016.06.152.
461. Khudhair AM, F.M. A review on energy conservation in building applications with thermal storage by latent heat using phase change materials. *Energy Convers Manag.* **2004**, *45*, 263–275.
462. Tyagi VV, B.D. PCM thermal storage in buildings: a state of art. *Renew Sustain Energy Rev* **2007**, *11*, 1146–66.
463. Hauer, A.; Fischer, S.; Heinemann, U.; Schreiner M, S.W. Thermochemical energy storage and heat transformation of district heat for balancing of power in a district heat network (TCS II) Final report. In Proceedings of the Final report. Wuerzburg (Germany): Bayerisches Zentrum fuer Angewandte Energieforschung e.V.; 1999.
464. Hauer, A.; avemann, E.L. Open Absorption Systems for Air Conditioning and Thermal Energy Storage. In *Thermal Energy Storage for Sustainable Energy Consumption*; 2007; pp. 429–444.
465. Wang, W.; Hu, Y.; Yan, J.; Nyström, J.; Dahlquist, E. Combined heat and power plant integrated with mobilized thermal energy storage (M-TES) system. *Front. Energy Power Eng. China* **2010**, *4*, 469–474, doi:10.1007/s11708-010-0123-9.
466. Shkatulov, A.; Ryu, J.; Kato, Y.; Aristov, Y. Composite material " Mg(OH)2/vermiculite": A promising new candidate for storage of middle temperature heat. *Energy* **2012**, *44*, 1028–1034, doi:10.1016/j.energy.2012.04.045.
467. Aristov YI Challenging offers of material science for adsorption heat

transformation: a review. *Appl Therm Eng* **2013**, *50(2)*, 1610–1618.

468. Christidis, A.; Koch, C.; Pottel, L.; Tsatsaronis, G. The contribution of heat storage to the profitable operation of combined heat and power plants in liberalized electricity markets. *Energy* **2012**, *41*, 75–82, doi:10.1016/j.energy.2011.06.048.
469. Aghaei, J.; Alizadeh, M.I. Multi-objective self-scheduling of CHP (combined heat and power)-based microgrids considering demand response programs and ESSs (energy storage systems). *Energy* **2013**, *55*, 1044–1054, doi:10.1016/j.energy.2013.04.048.
470. Meroueh, L.; Chen, G. Thermal energy storage radiatively coupled to a supercritical Rankine cycle for electric grid support. *Renew. Energy* **2020**, *145*, 604–621, doi:10.1016/J.RENENE.2019.06.036.
471. Battaglia, M.; Haberl, R.; Bamberger, E.; Haller, M. Increased self-consumption and grid flexibility of PV and heat pump systems with thermal and electrical storage. *Energy Procedia* **2017**, *135*, 358–366, doi:10.1016/j.egypro.2017.09.527.
472. Oudalov, A.; Cherkaoui, R.; Beguin, A. Sizing and optimal operation of battery energy storage system for peak shaving application. *2007 IEEE Lausanne POWERTECH, Proc.* **2007**, 621–625, doi:10.1109/PCT.2007.4538388.
473. Levron, Y.; Shmilovitz, D. Power systems' optimal peak-shaving applying secondary storage. *Electr. Power Syst. Res.* **2012**, *89*, 80–84, doi:10.1016/J.EPSR.2012.02.007.
474. Tatsidjodoung, P.; Le Pierrès, N.; Luo, L. A review of potential materials for thermal energy storage in building applications. *Renew. Sustain. Energy Rev.* **2013**, *18*, 327–349, doi:10.1016/j.rser.2012.10.025.
475. Lizana, J.; Chacartegui, R.; Barrios-Padura, A.; Ortiz, C. Advanced low-carbon energy measures based on thermal energy storage in buildings: A review. *Renew. Sustain. Energy Rev.* **2018**, *82*, 3705–3749, doi:10.1016/j.rser.2017.10.093.
476. Tian, Y.; Zhao, C.Y. A review of solar collectors and thermal energy storage in solar thermal applications. *Appl. Energy* **2013**, *104*, 538–553, doi:10.1016/j.apenergy.2012.11.051.
477. Sarbu, I.; Sebarchievici, C. A comprehensive review of thermal energy storage. *Sustain.* **2018**, *10*, doi:10.3390/su10010191.
478. Gil, A.; Medrano, M.; Martorell, I.; Lázaro, A.; Dolado, P.; Zalba, B.; Cabeza, L.F.

State of the art on high temperature thermal energy storage for power generation. Part 1—Concepts, materials and modellization. *Renew. Sustain. Energy Rev.* **2010**, *14*, 31–55, doi:10.1016/J.RSER.2009.07.035.

479. Kerskes, H. Thermochemical Energy Storage. *Storing Energy* **2016**, 345–372, doi:10.1016/B978-0-12-803440-8.00017-8.
480. Ciulla, G.; Lo Brano, V.; Cellura, M.; Franzitta, V.; Milone, D. A finite difference model of a PV-PCM system. *Energy Procedia* **2012**, doi:10.1016/j.egypro.2012.11.024.
481. Bastien, D.; Athienitis, A.K. Passive thermal energy storage, part 2: Design methodology for solaria and greenhouses. *Renew. Energy* **2017**, *103*, 537–560, doi:10.1016/j.renene.2016.11.041.
482. NTNU_Master_Thesis.pdf.
483. Silva T, Vicente R, Soares N, F. V Experimental testing and numerical modelling of masonry wall solution with PCM incorporation: a passive construction solution. *Energy Build.* **2012**, *49*, 235–245.
484. Cabeza, L.F.; Castell, A.; Barreneche, C.; de Gracia, A.; Fernández, A.I. Materials used as PCM in thermal energy storage in buildings: A review. *Renew. Sustain. Energy Rev.* **2011**, *15*, 1675–1695, doi:10.1016/J.RSER.2010.11.018.
485. Zhou, D.; Zhao, C.Y.; Tian, Y. Review on thermal energy storage with phase change materials (PCMs) in building applications. *Appl. Energy* **2012**, *92*, 593–605, doi:10.1016/j.apenergy.2011.08.025.
486. Soares, N.; Costa, J.J.; Gaspar, A.R.; Santos, P. Review of passive PCM latent heat thermal energy storage systems towards buildings' energy efficiency. *Energy Build.* **2013**, *59*, 82–103, doi:10.1016/j.enbuild.2012.12.042.
487. Galazutdinova, Y.; Grágeda, M.; Cabeza, L.F.; Ushak, S. Novel inorganic binary mixture for low-temperature heat storage applications. *Int. J. Energy Res.* **2017**, *41*, 2356–2364, doi:10.1002/er.3805.
488. Sharma, R.K.; Ganesan, P.; Tyagi, V.V.; Metselaar, H.S.C.; Sandaran, S.C. Developments in organic solid–liquid phase change materials and their applications in thermal energy storage. *Energy Convers. Manag.* **2015**, *95*, 193–228, doi:10.1016/J.ENCONMAN.2015.01.084.
489. Su, W.; Darkwa, J.; Kokogiannakis, G. Review of solid–liquid phase change

materials and their encapsulation technologies. *Renew. Sustain. Energy Rev.* **2015**, *48*, 373–391, doi:10.1016/J.RSER.2015.04.044.

490. Noro, M.; Lazzarin, R.M.; Busato, F. Solar cooling and heating plants: An energy and economic analysis of liquid sensible vs phase change material (PCM) heat storage. *Int. J. Refrig.* **2014**, *39*, 104–116, doi:10.1016/j.ijrefrig.2013.07.022.
491. Tae Kim S, Ryu J, K.Y. Reactivity enhancement of chemical materials used in packed bed reactor of chemical heat pump. *Prog Nucl Energy* **2011**, *563*, 1027–1033.
492. Cot-Gores, J.; Castell, A.; Cabeza, L.F. Thermochemical energy storage and conversion: A-state-of-the-art review of the experimental research under practical conditions. *Renew. Sustain. Energy Rev.* **2012**, *16*, 5207–5224, doi:10.1016/j.rser.2012.04.007.
493. Abedin, A.H. A Critical Review of Thermochemical Energy Storage Systems. *Open Renew. Energy J.* **2011**, *4*, 42–46, doi:10.2174/1876387101004010042.
494. Pardo P, Deydier A, Anxionnaz-Minvielle Z, et al. A review on high temperature thermochemical heat energy storage. *Renew Sustain Energy Rev* **2014**, *32*, 591–610.
495. Aydin, D.; Casey, S.P.; Riffat, S. The latest advancements on thermochemical heat storage systems. *Renew. Sustain. Energy Rev.* **2015**, *41*, 356–367, doi:10.1016/j.rser.2014.08.054.
496. Alva, G.; Liu, L.; Huang, X.; Fang, G. Thermal energy storage materials and systems for solar energy applications. *Renew. Sustain. Energy Rev.* **2017**, *68*, 693–706, doi:10.1016/J.RSER.2016.10.021.
497. Abedin, A.H. *Thermochemical energy storage systems: Modelling, analysis and design*; Elsevier Inc., 2010; Vol. M. Sc; ISBN 9780128034408.
498. Kuznik, F.; Johannes, K. Thermodynamic efficiency of water vapor/solid chemical sorption heat storage for buildings: Theoretical limits and integration considerations. *Appl. Sci.* **2020**, *10*, doi:10.3390/app10020489.
499. Yu, N.; Wang, R.Z.; Wang, L.W. Sorption thermal storage for solar energy. *Prog. Energy Combust. Sci.* **2013**, *39*, 489–514, doi:10.1016/j.pecs.2013.05.004 Review.
500. Chen, X.; Wang, F.; Han, Y.; Yu, R.; Cheng, Z. Thermochemical storage analysis of the dry reforming of methane in foam solar reactor. *Energy Convers. Manag.* **2018**, *158*, 489–498, doi:10.1016/J.ENCONMAN.2017.12.066.

501. Frazzica, A.; Brancato, V.; Palomba, V.; Vasta, S. *Sorption thermal energy storage*; 2018; Vol. PartF13; ISBN 9783662491201.
502. Krönauer, A.; Lävemann, E.; Brückner, S.; Hauer, A. Mobile Sorption Heat Storage in Industrial Waste Heat Recovery. *Energy Procedia* **2015**, *73*, 272–280, doi:10.1016/J.EGYPRO.2015.07.688.
503. Reiser, A.; Bogdanović, B.; Schlichte, K. The application of Mg-based metal-hydrides as heat energy storage systems. *Int. J. Hydrogen Energy* **2000**, *25*, 425–430, doi:10.1016/S0360-3199(99)00057-9.
504. Stengler, J.; Linder, M. Thermal energy storage combined with a temperature boost: An underestimated feature of thermochemical systems. *Appl. Energy* **2020**, *262*, 114530, doi:10.1016/J.APENERGY.2020.114530.
505. Tesio, U.; Guelpa, E.; Verda, V. Integration of thermochemical energy storage in concentrated solar power. Part 2: Comprehensive optimization of supercritical CO2 power block. *Energy Convers. Manag. X* **2020**, *6*, 100038, doi:10.1016/J.ECMX.2020.100038.
506. Koohi-Fayegh, S.; Rosen, M.A. A review of energy storage types, applications and recent developments. *J. Energy Storage* **2020**, *27*, 101047, doi:10.1016/J.EST.2019.101047.
507. Wu, S.; Zhou, C.; Doroodchi, E.; Moghtaderi, B. Techno-economic analysis of an integrated liquid air and thermochemical energy storage system. *Energy Convers. Manag.* **2020**, *205*, 112341, doi:10.1016/J.ENCONMAN.2019.112341.
508. Lizana, J.; Bordin, C.; Rajabloo, T. Integration of solar latent heat storage towards optimal small-scale combined heat and power generation by Organic Rankine Cycle. *J. Energy Storage* **2020**, *29*, 101367, doi:10.1016/J.EST.2020.101367.
509. Poppi, S.; Sommerfeldt, N.; Bales, C.; Madani, H.; Lundqvist, P. Techno-economic review of solar heat pump systems for residential heating applications. *Renew. Sustain. Energy Rev.* 2018, *81*, 22–32.
510. Nic M, Jirat J, K.B. IUPAC compendium of chemical terminology. In *Oxford*; 2006.
511. Yu N, Wang RZ, W.L. Sorption thermal storage for solar energy. *Prog Energy Combust Sci* **2013**, *39*, 489–514.
512. Bai, Z.; Liu, Q.; Lei, J.; Jin, H. Investigation on the mid-temperature solar thermochemical power generation system with methanol decomposition. *Appl.*

Energy **2018**, *217*, 56–65, doi:10.1016/J.APENERGY.2018.02.101.

513. Stutz, B.; Le Pierres, N.; Kuznik, F.; Johannes, K.; Palomo Del Barrio, E.; Bédécarrats, J.P.; Gibout, S.; Marty, P.; Zalewski, L.; Soto, J.; et al. Stockage thermique de l'énergie solaire. *Comptes Rendus Phys.* **2017**, *18*, 401–414, doi:10.1016/j.crhy.2017.09.008.
514. Le Pierrès, N.; Huaylla, F.; Stutz, B.; Perraud, J. Long-term solar heat storage process by absorption with the KCOOH/H2O couple: Experimental investigation. *Energy* **2017**, *141*, 1313–1323, doi:10.1016/j.energy.2017.10.111.
515. Bush, H.E.; Loutzenhiser, P.G. Solar electricity via an Air Brayton cycle with an integrated two-step thermochemical cycle for heat storage based on Fe2O3/Fe3O4 redox reactions: Thermodynamic and kinetic analyses. *Sol. Energy* **2018**, *174*, 617–627, doi:10.1016/J.SOLENER.2018.09.043.
516. Hutchings, K.N.; Wilson, M.; Larsen, P.A.; Cutler, R.A. Kinetic and thermodynamic considerations for oxygen absorption/desorption using cobalt oxide. *Solid State Ionics* **2006**, *177*, 45–51, doi:10.1016/J.SSI.2005.10.005.
517. Singh, A.; Tescari, S.; Lantin, G.; Agrafiotis, C.; Roeb, M.; Sattler, C. Solar thermochemical heat storage via the Co3O4/CoO looping cycle: Storage reactor modelling and experimental validation. *Sol. Energy* **2017**, *144*, 453–465, doi:10.1016/J.SOLENER.2017.01.052.
518. Balasubramanian, G.; Ghommem, M.; Hajj, M.R.; Wong, W.P.; Tomlin, J.A.; Puri, I.K. Modeling of thermochemical energy storage by salt hydrates. *Int. J. Heat Mass Transf.* **2010**, *53*, 5700–5706, doi:10.1016/j.ijheatmasstransfer.2010.08.012.
519. Visscher, K.; Veldhuis, J.B.J. Comparison of candidate materials for seasonal storage of solar heat through dynamic simulation of building and renewable energy system. *Ninth Int. IBPSA Conf.* **2005**, 1285–1292.
520. Lucio, B.; Romero, M.; González-Aguilar, J. Analysis of solid-state reaction in the performance of doped calcium manganites for thermal storage. *Solid State Ionics* **2019**, *338*, 47–57, doi:10.1016/J.SSI.2019.05.007.
521. Imponenti, L.; Albrecht, K.J.; Wands, J.W.; Sanders, M.D.; Jackson, G.S. Thermochemical energy storage in strontium-doped calcium manganites for concentrating solar power applications. *Sol. Energy* **2017**, *151*, 1–13, doi:10.1016/J.SOLENER.2017.05.010.

522. Henninger, S.K.; Habib, H.A.; Janiak, C. MOFs as Adsorbents for Low Temperature Heating and Cooling Applications - Journal of the American Chemical Society (ACS Publications). *J AmChem Soc* **2009**, *131*, 2776–2777.
523. N'Tsoukpoe, K.E.; Perier-Muzet, M.; Le Pierrès, N.; Luo, L.; Mangin, D. Thermodynamic study of a LiBr–H2O absorption process for solar heat storage with crystallisation of the solution. *Sol. Energy* **2014**, *104*, 2–15, doi:10.1016/J.SOLENER.2013.07.024.
524. Leonzio, G. Solar systems integrated with absorption heat pumps and thermal energy storages: state of art. *Renew. Sustain. Energy Rev.* **2017**, *70*, 492–505, doi:10.1016/j.rser.2016.11.117.
525. Liu H, Edem N'Tsoukpoe K, Le Pierres N, et al. Evaluation of a seasonal storage system of solar energy for house heating using different absorption couples. *Energ Convers Manag.* **2011**, *52*, 2427–2436.
526. G. Li, Y. Hwang, R. Radermacher Review of cold storage materials for air condition application. *Int. J. Refrig* **2012**, *35*, 2053–2077.
527. Yu, N.; Wang, R.Z.; Wang, L.W. Theoretical and experimental investigation of a closed sorption thermal storage prototype using LiCl/water. *Energy* **2015**, *93*, 1523–1534, doi:10.1016/J.ENERGY.2015.10.001.
528. Zhang, Y.N.; Wang, R.Z.; Li, T.X. Experimental investigation on an open sorption thermal storage system for space heating. *Energy* **2017**, *141*, 2421–2433, doi:10.1016/J.ENERGY.2017.12.003.
529. Zhao, Y.J.; Wang, R.Z.; Li, T.X.; Nomura, Y. Investigation of a 10 kWh sorption heat storage device for effective utilization of low-grade thermal energy. *Energy* **2016**, *113*, 739–747, doi:10.1016/J.ENERGY.2016.07.100.
530. Bales, C. Final report of subtask B – chemical and sorption storage. **2008**.
531. Rammelberg, H.U.; Schmidt, T.; Ruck, W. Hydration and dehydration of salt hydrates and hydroxides for thermal energy storage - kinetics and energy release. *Energy Procedia* **2012**, *30*, 362–369, doi:10.1016/J.EGYPRO.2012.11.043.
532. Fumey, B.; Weber, R.; Gantenbein, P.; Daguenet-Frick, X.; Stoller, S.; Fricker, R.; Dorer, V. Operation Results of a Closed Sorption Heat Storage Prototype. *Energy Procedia* **2015**, *73*, 324–330, doi:10.1016/J.EGYPRO.2015.07.698.
533. Daguenet-Frick, X.; Dudita, M.; Omlin, L.; Paul, G. Seasonal Thermal Energy

Storage with Aqueous Sodium Hydroxide – Development and Measurements on the Heat and Mass Exchangers. *Energy Procedia* **2018**, *155*, 286–294, doi:10.1016/J.EGYPRO.2018.11.049.

534. Le´ pinasse E, S.B. Production de froid par couplage de re´ acteurs solide-gaz II: performance d'un pilote de 1 a? 2 kW. *Rev Int Froid* **1994**, *17*, 323–328.
535. Bao HS, Oliveira RG, Wang RZ, W.L. Choice of low temperature salt for a resorption refrigerator. *Ind. Eng. Chem. Res.* **2010**, *49*, 4897–903.
536. Bao HS, Wang RZ, W.L. A resorption refrigerator driven by low grade thermal energy. *Energy Convers. Manag.* **2011**, *52*, 2339–44.
537. Oliveira, R.G.; Wang, R.Z.; Kiplagat, J.K.; Wang, C.Y. Novel composite sorbent for resorption systems and for chemisorption air conditioners driven by low generation temperature. *Renew. Energy* **2009**, *34*, 2757–2764, doi:10.1016/j.renene.2009.05.016.
538. Wang C, Zhang P, W.R. Performance of solid–gas reaction heat transformer system with gas valve control. *Chem. Eng. Sci.* **2010**, *65*, 2910–2920.
539. Ma, Z.; Bao, H.; Roskilly, A.P. Seasonal solar thermal energy storage using thermochemical sorption in domestic dwellings in the UK. *Energy* **2019**, *166*, 213–222, doi:10.1016/j.energy.2018.10.066.
540. Wu, S.; Li, T.X.; Yan, T.; Wang, R.Z. Advanced thermochemical resorption heat transformer for high-efficiency energy storage and heat transformation. *Energy* **2019**, *175*, 1222–1233, doi:10.1016/j.energy.2019.03.159.
541. Nevau P, Castaing J, Mazet N, M.P. Performances expe´ rimentales de thermotransformateurs hautes tempe´ ratures et machines ?a froid ?a double effet ?a base d'ammoniacates. In Proceedings of the Proceedings of the Symposium Le froid ?a sorption solide Paris, France; 1992; pp. 173–178.
542. Ferrucci, F.; Stitou, D.; Ortega, P.; Lucas, F. Mechanical compressor-driven thermochemical storage for cooling applications in tropical insular regions. Concept and efficiency analysis. *Appl. Energy* **2018**, *219*, 240–255, doi:10.1016/J.APENERGY.2018.03.049.
543. Lehmann, C.; Beckert, S.; Gläser, R.; Kolditz, O.; Nagel, T. Assessment of adsorbate density models for numerical simulations of zeolite-based heat storage applications. *Appl. Energy* **2017**, *185*, 1965–1970,

doi:10.1016/J.APENERGY.2015.10.126.

544. Zettl, B.; Englmair, G.; Steinmaurer, G. Development of a revolving drum reactor for open-sorption heat storage processes. *Appl. Therm. Eng.* **2014**, *70*, 42–49, doi:10.1016/j.applthermaleng.2014.04.069.

545. Kerskes H, Mette B, Bertsch F, Asenbeck S, D.H. Development of a thermo-chemical energy storage for solar thermal applications. *ISES, sol world congr, Kassel, Ger.* **2011**.

546. de Boer R, Vanhoudt D, Claessens B, De Ridder F, Reynders G, Cuypers R, et al. Energy-hub for residential and commercial districts and transport.D3.2 report on a combination of thermal storage techniques and components; **2014**.

547. de Boer R, Smeding S, Zondag HA, K.G. Development of a prototype system for seasonal solar heat storage using an open sorption process. In Proceedings of the In: Eurotherm semin, #99 - adv therm energy storage; 2014; pp. 1–9.

548. Johannes, K.; Kuznik, F.; Hubert, J.-L.; Durier, F.; Obrecht, C. Design and characterisation of a high powered energy dense zeolite thermal energy storage system for buildings. *Appl. Energy* **2015**, *159*, 80–86, doi:10.1016/J.APENERGY.2015.08.109.

549. Tatsidjodoung, P.; Le Pierrès, N.; Heintz, J.; Lagre, D.; Luo, L.; Durier, F. Experimental and numerical investigations of a zeolite 13X/water reactor for solar heat storage in buildings. *Energy Convers. Manag.* **2016**, *108*, 488–500, doi:10.1016/J.ENCONMAN.2015.11.011.

550. Mehlhorn D, Valiullin R, Kärger J, Schumann K, Brandt A, U.B. Transport enhancement in binderless zeolite X- and A-type molecular sieves revealed by PFG NMR diffusometry. Micropor Mesopor Mat 2014;188:126–32. **2014**, *188*, 126–132.

551. Chan, K.C.; Chao, C.Y.H.; Sze-To, G.N.; Hui, K.S. Performance predictions for a new zeolite 13X/CaCl 2 composite adsorbent for adsorption cooling systems. *Int. J. Heat Mass Transf.* **2012**, *55*, 3214–3224, doi:10.1016/j.ijheatmasstransfer.2012.02.054.

552. Hongois, S.; Kuznik, F.; Stevens, P.; Roux, J.J. Development and characterisation of a new MgSO4-zeolite composite for long-term thermal energy storage. *Sol. Energy Mater. Sol. Cells* **2011**, *95*, 1831–1837, doi:10.1016/j.solmat.2011.01.050.

553. Whiting, G.T.; Grondin, D.; Stosic, D.; Bennici, S.; Auroux, A. Zeolite-MgCl 2

composites as potential long-term heat storage materials: Influence of zeolite properties on heats of water sorption. *Sol. Energy Mater. Sol. Cells* **2014**, *128*, 289–295, doi:10.1016/j.solmat.2014.05.016.

554. Dawoud B, A.Y. Experimental study on the kinetics of water vapour sorption on selective water sorbents, silica gel and alumina under typical operating conditions of sorption heat pumps. *Int J Heat Mass Transf* **2003**, *46*, 273–281.

555. Jänchen, J.; Schumann, K.; Thrun, E.; Brandt, A.; Unger, B.; Hellwig, U. Preparation, hydrothermal stability and thermal adsorption storage properties of binderless zeolite beads. *Int. J. Low-Carbon Technol.* **2012**, *7*, 275–279, doi:10.1093/ijlct/cts037.

556. Englmair, G.; Zettl, B.; Lager, D. Characterisation of a Rotating Adsorber Designed for Thermochemical Heat Storage Processes. In Proceedings of the Proc. EuroSun 2014 Conf, Aix-les-Bains; 2015; pp. 1–8.

557. Finck, C.; Henquet, E.; van Soest, C.; Oversloot, H.; de Jong, A.-J.; Cuypers, R.; Spijker, H. van't Experimental Results of a 3 kWh Thermochemical Heat Storage Module for Space Heating Application. *Energy Procedia* **2014**, *48*, 320–326, doi:10.1016/J.EGYPRO.2014.02.037.

558. Cuypers, R.; Maraz, N.; Eversdijk, J.; Finck, C.; Henquet, E.; Oversloot, H.; Spijker, H. van't; de Geus, A. Development of a Seasonal Thermochemical Storage System. *Energy Procedia* **2012**, *30*, 207–214, doi:10.1016/J.EGYPRO.2012.11.025.

559. Jänchen J, Ackermann D, Weiler E, Stach H, B.W. Calorimetric investigation on zeolites, AlPO4's and CaCl2 impregnated attapulgite for thermochemical storage of heat. *Thermochim Acta* **2005**, *434*, 37–41.

560. Engel, G. Sorption thermal energy storage: Hybrid coating/granules adsorber design and hybrid TCM/PCM operation. *Energy Convers. Manag.* **2019**, *184*, 466–474, doi:10.1016/J.ENCONMAN.2019.01.071.

561. Calabrese, L.; Brancato, V.; Palomba, V.; Frazzica, A.; Cabeza, L.F. Magnesium sulphate-silicone foam composites for thermochemical energy storage: Assessment of dehydration behaviour and mechanical stability. *Sol. Energy Mater. Sol. Cells* **2019**, *200*, 109992, doi:10.1016/J.SOLMAT.2019.109992.

562. Fasano, M.; Falciani, G.; Brancato, V.; Palomba, V.; Asinari, P.; Chiavazzo, E.; Frazzica, A. Atomistic modelling of water transport and adsorption mechanisms in

silicoaluminophosphate for thermal energy storage. *Appl. Therm. Eng.* **2019**, *160*, 114075, doi:10.1016/J.APPLTHERMALENG.2019.114075.

563. Oliveira RG, W.R. A consolidated calcium chloride-expanded graphite compound for use in sorption refrigeration systems. *Carbon N. Y.* **2007**, *45*, 390–396.

564. Oliveira RG, Wang RZ, W.C. Evaluation of the cooling performance of a consolidated expanded graphite-calcium chloride reactive bed for chemi- sorption icemaker. *Int. J. Refrig.* **2007**, *30*, 103–12.

565. Pal, M. Van Der; Smeding, S. THERMALLY DRIVEN AMMONIA-SALT TYPE II HEAT PUMP : DEVELOPMENT AND TEST OF A PROTOTYPE LiCl. *Energy* **2007**, 2–7.

566. Aidoun Z, T.M. Salt impregnated carbon fibres as the reactive medium in a chemical heat pump: the NH3–CoCl2 system. *Appl. Therm. Eng.* **2002**, *22*, 1163–74.

567. Ristic´ A, Logar NZ, Henninger SK, K.˘ V. The performance of small-pore-microporous aluminophosphates in low-temperature solar energy storage: the structure-property relationship. *Adv Funct Mater* **2012**, *22*, 1952–1957.

568. Kuznik, F.; Johannes, K.; Obrecht, C.; David, D. A review on recent developments in physisorption thermal energy storage for building applications. *Renew. Sustain. Energy Rev.* **2018**, *94*, 576–586, doi:10.1016/j.rser.2018.06.038.

569. Jänchen, J.; Ackermann, D.; Stach, H.; Brösicke, W. Studies of the water adsorption on Zeolites and modified mesoporous materials for seasonal storage of solar heat. *Sol. Energy* **2004**, *76*, 339–344, doi:10.1016/j.solener.2003.07.036.

570. Druske MM, Fopah-Lele A, Korhammer K, Rammelberg HU, Wegscheider N, Ruck WKL, et al. Developed Materials for Thermal Energy Storage: Synthesis and Characterization. In Proceedings of the Energy procedia.; 2014; pp. 196–199.

571. Ponomarenko IV, Glaznev IS, Gubar AV, Aristov YI, K.S. Synthesis and water sorption properties of a new composite ‘‘CaCl2 confined into SBA-15 pores”. *Microporous Mesoporous Mater 2010* **2010**, *129*, 243–250.

572. Tanashev YY, Krainov AV, A.Y. Thermal conductivity of composite sorbents ‘‘salt in porous matrix” for heat storage and transformation. *Appl Therm Eng* **2014**, *61*, 96–99.

573. Mahon, D.; Henshall, P.; Claudio, G.; Eames, P.C. Feasibility study of MgSO4 +

zeolite based composite thermochemical energy stores charged by vacuum flat plate solar thermal collectors for seasonal thermal energy storage. *Renew. Energy* **2020**, *145*, 1799–1807, doi:10.1016/J.RENENE.2019.05.135.

574. Wang, Q.; Xie, Y.; Ding, B.; Yu, G.; Ye, F.; Xu, C. Structure and hydration state characterizations of MgSO4-zeolite 13x composite materials for long-term thermochemical heat storage. *Sol. Energy Mater. Sol. Cells* **2019**, *200*, 110047, doi:10.1016/j.solmat.2019.110047.
575. Posern K, K.C. Calorimetric studies of thermochemical heat storage materials based on mixtures of MgSO4 and MgCl2. *Thermochim Acta2* **2010**, *129*, 243–250.
576. Casey SP, Elvins J, Riffat S, R.A. Salt impregnated desiccant matrices for ‘‘open” thermochemical energy storage—selection, synthesis and characterisation of candidate materials. *Energy Build* **2014**, *84*, 412–425.
577. Chen, C.; Lovegrove, K.M.; Sepulveda, A.; Lavine, A.S. Design and optimization of an ammonia synthesis system for ammonia-based solar thermochemical energy storage. *Sol. Energy* **2018**, *159*, 992–1002, doi:10.1016/J.SOLENER.2017.11.064.
578. Liu, T.; Bai, Z.; Zheng, Z.; Liu, Q.; Lei, J.; Sui, J.; Jin, H. 100 kWe power generation pilot plant with a solar thermochemical process: design, modeling, construction, and testing. *Appl. Energy* **2019**, *251*, 113217, doi:10.1016/J.APENERGY.2019.05.020.
579. H. Zondag, B. Kikkert, S. Smeding, R. de Boer, M.B. Prototype thermo- chemical heat storage with open reactor system. *Appl. Energy 109 360–365.* **2013**, *109*, 360–365.
580. Kato Y, Takahashi R, Sekiguchi T, et al. Study on medium-temperature chemical heat storage using mixed hydroxides. *Int J Refrig.* **2009**, *32*, 661–666.
581. Bayon, A.; Bader, R.; Jafarian, M.; Fedunik-Hofman, L.; Sun, Y.; Hinkley, J.; Miller, S.; Lipiński, W. Techno-economic assessment of solid–gas thermochemical energy storage systems for solar thermal power applications. *Energy* **2018**, *149*, 473–484, doi:10.1016/J.ENERGY.2017.11.084.
582. Mastronardo, E.; Bonaccorsi, L.; Kato, Y.; Piperopoulos, E.; Milone, C. Efficiency improvement of heat storage materials for MgO/H2O/Mg(OH)2 chemical heat pumps. *Appl. Energy* **2016**, *162*, 31–39, doi:10.1016/J.APENERGY.2015.10.066.
583. Shkatulov, A.; Krieger, T.; Zaikovskii, V.; Chesalov, Y.; Aristov, Y. Doping

magnesium hydroxide with sodium nitrate: A new approach to tune the dehydration reactivity of heat-storage materials. *ACS Appl. Mater. Interfaces* **2014**, *6*, 19966–19977, doi:10.1021/am505418z.

584. Sunku Prasad, J.; Muthukumar, P.; Desai, F.; Basu, D.N.; Rahman, M.M. A critical review of high-temperature reversible thermochemical energy storage systems. *Appl. Energy* **2019**, *254*, 113733, doi:10.1016/J.APENERGY.2019.113733.

585. Huang, C.; Xu, M.; Huai, X. Experimental investigation on thermodynamic and kinetic of calcium hydroxide dehydration with hexagonal boron nitride doping for thermochemical energy storage. *Chem. Eng. Sci.* **2019**, *206*, 518–526, doi:10.1016/J.CES.2019.06.002.

586. Sheppard, D.A.; Humphries, T.D.; Buckley, C.E. Sodium-based hydrides for thermal energy applications. *Appl. Phys. A Mater. Sci. Process.* **2016**, *122*, doi:10.1007/s00339-016-9830-3.

587. Shen, D.; Zhao, C.Y. Thermal analysis of exothermic process in a magnesium hydride reactor with porous metals. *Chem. Eng. Sci.* **2013**, *98*, 273–281, doi:10.1016/j.ces.2013.05.041.

588. Rönnebro, E.C.E.; Whyatt, G.; Powell, M.; Westman, M.; Zheng, F.; Fang, Z.Z. *Metal hydrides for high-temperature power generation*; 2015; Vol. 8;.

589. Pan, Z.; Zhao, C.Y. Dehydration/hydration of MgO/H2O chemical thermal storage system. *Energy* **2015**, *82*, 611–618, doi:10.1016/J.ENERGY.2015.01.070.

590. Shkatulov, A.I.; Kim, S.T.; Miura, H.; Kato, Y.; Aristov, Y.I. Adapting the MgO-CO2 working pair for thermochemical energy storage by doping with salts. *Energy Convers. Manag.* **2019**, *185*, 473–481, doi:10.1016/J.ENCONMAN.2019.01.056.

591. Gigantino, M.; Kiwic, D.; Steinfeld, A. Thermochemical energy storage via isothermal carbonation-calcination cycles of MgO-stabilized SrO in the range of 1000–1100 °C. *Sol. Energy* **2019**, *188*, 720–729, doi:10.1016/J.SOLENER.2019.06.046.

592. Donkers PAJ, Pel L, A.O. Experimental studies for the cyclability of salt hydrates for thermochemical heat storage. *J Energy Storage 2016;525–32.* **2016**, *5*, 25–32.

593. Sol, A.; e, I. Martorell, L.F.C. State of the art on gas-solid thermochemical energy storage systems and reactors for building applications, Renew. Sus- tain. Energy Rev. 47 (2015) 386e398. **2015**, *47*, 386–398.

594. Zondag HA, van Essen VM, Bleijendaal LPJ, Kikkert B, B.M. Application of MgCl2 6H2O for thermochemical seasonal solar heat storage. In Proceedings of the 5th Int renew energy storage conf. IRES 2010, Berlin, Germany.; 2010.
595. Mehrabadi, A.; Farid, M. New salt hydrate composite for low-grade thermal energy storage. *Energy* **2018**, *164*, 194–203, doi:10.1016/J.ENERGY.2018.08.192.
596. De Boer R, Haije WG, Veldhuis JBJ, S.S. Solid-sorption cooling with integrated thermal storage the SWEAT prototype. In Proceedings of the Int conf heat powered cycles, Larnaca, Cyprus.
597. Sakamoto, Y.; Yamamoto, H. Performance of Thermal Energy Storage Unit Using Solid Ammoniated Salt (CaCl₂-NH₃ System). *Nat. Resour.* **2014**, *05*, 337–342, doi:10.4236/nr.2014.58031.
598. Fadhel MI, Sopian K, Daud WRW, et al. Review on advanced of solar assisted chemical heat pump dryer for agriculture produce. *Renew Sustain Energy Rev.* **2011**, *15*, 1152–68.
599. Stitou D, Mazet N, M.S. Experimental investigation of a solid/gas thermochemical storage process for solar air conditioning. *Energy* **2011**.
600. Chen, X.; Zhang, D.; Wang, Y.; Ling, X.; Jin, X. The role of sensible heat in a concentrated solar power plant with thermochemical energy storage. *Energy Convers. Manag.* **2019**, *190*, 42–53, doi:10.1016/J.ENCONMAN.2019.04.007.
601. Khosa, A.A.; Zhao, C.Y. Heat storage and release performance analysis of CaCO3/CaO thermal energy storage system after doping nano silica. *Sol. Energy* **2019**, *188*, 619–630, doi:10.1016/J.SOLENER.2019.06.048.
602. Fernández, R.; Ortiz, C.; Chacartegui, R.; Valverde, J.M.; Becerra, J.A. Dispatchability of solar photovoltaics from thermochemical energy storage. *Energy Convers. Manag.* **2019**, *191*, 237–246, doi:10.1016/j.enconman.2019.03.074.
603. Ortiz, C.; Valverde, J.M.; Chacartegui, R.; Perez-Maqueda, L.A. Carbonation of Limestone Derived CaO for Thermochemical Energy Storage: From Kinetics to Process Integration in Concentrating Solar Plants. *ACS Sustain. Chem. Eng.* **2018**, *6*, 6404–6417, doi:10.1021/acssuschemeng.8b00199.
604. Meroueh, L.; Yenduru, K.; Dasgupta, A.; Jiang, D.; AuYeung, N. Energy storage based on SrCO3 and Sorbents—A probabilistic analysis towards realizing solar

thermochemical power plants. *Renew. Energy* **2019**, *133*, 770–786, doi:10.1016/J.RENENE.2018.10.071.

605. Takasu, H.; Hoshino, H.; Tamura, Y.; Kato, Y. Performance evaluation of thermochemical energy storage system based on lithium orthosilicate and zeolite. *Appl. Energy* **2019**, *240*, 1–5, doi:10.1016/j.apenergy.2019.02.054.
606. Kerskes, H.; Mette, B.; Bertsch, F.; Asenbeck, S.; Drück, H. Chemical energy storage using reversible solid/gas-reactions (CWS) - Results of the research project. In Proceedings of the Energy Procedia; 2012; Vol. 30, pp. 294–304.
607. Pebernet, L.; Ferrieres, X.; Pernet, S.; Michielsen, B.L.; Rogier, F.; Degond, P. Discontinuous Galerkin method applied to electromagnetic compatibility problems: Introduction of thin wire and thin resistive material models. In Proceedings of the IET Science, Measurement and Technology; 2008; Vol. 2, pp. 395–401.
608. Bales, C.; Gantenbein, P.; Jaenig, D.; Kerskes, H.; Summer, K.; Van Essen, M.; Weber, R. Laboratory Tests of Chemical Reactions and Prototype Sorption Storage Units, A Report of IEA Solar Heating and Cooling programme - Task 32. *Sol. Heat. Cool. Program.* **2008**, 55p.
609. Iammak K, Wongsuwan W, K.T. Investigation of modular chemical energy storage performance. In Proceedings of the In: Proc jt int conf energy environ, Hua Hin, Thailand; 2004.
610. Koepf E E; W, V.; A, M. PILOT - SCALE SOLAR REACTOR OPERATION AND CHARACTERIZATION FOR FUEL PRODUCTION VIA THE Zn / ZnO. *J. Appl. Energy* **2015**, *165*, 1004–1023.
611. Agrafiotis, C.; Thomey, D.; de Oliveira, L.; Happich, C.; Roeb, M.; Sattler, C.; Tsongidis, N.I.; Sakellariou, K.G.; Pagkoura, C.; Karagiannakis, G.; et al. Oxide particles as combined heat storage medium and sulphur trioxide decomposition catalysts for solar hydrogen production through sulphur cycles. *Int. J. Hydrogen Energy* **2019**, *44*, 9830–9840, doi:10.1016/j.ijhydene.2018.11.056.
612. Wu, S.; Zhou, C.; Doroodchi, E.; Moghtaderi, B. Thermodynamic analysis of a novel hybrid thermochemical-compressed air energy storage system powered by wind, solar and/or off-peak electricity. *Energy Convers. Manag.* **2019**, *180*, 1268–1280, doi:10.1016/j.enconman.2018.11.063.
613. Tescari, S.; Singh, A.; Agrafiotis, C.; de Oliveira, L.; Breuer, S.; Schlögl-Knothe,

B.; Roeb, M.; Sattler, C. Experimental evaluation of a pilot-scale thermochemical storage system for a concentrated solar power plant. *Appl. Energy* **2017**, *189*, 66–75, doi:10.1016/j.apenergy.2016.12.032.

614. Zhou, X.; Mahmood, M.; Chen, J.; Yang, T.; Xiao, G.; Ferrari, M.L. Validated model of thermochemical energy storage based on cobalt oxides. *Appl. Therm. Eng.* **2019**, *159*, 113965, doi:10.1016/j.applthermaleng.2019.113965.
615. Yilmaz, D.; Darwish, E.; Leion, H. Investigation of the combined Mn-Si oxide system for thermochemical energy storage applications. *J. Energy Storage* **2020**, *28*, 101180, doi:10.1016/j.est.2019.101180.
616. G.L. Smithson, N.N.B. The kinetics and mechanism of the hydation of magnesium oxide in a batch reactor. *Can. J. Chem. Eng. 47* **1969**, *47*, 508–513.
617. Feitknecht, W.; Braun, H. Der Mechanismus der Hydratation von Magnesiumoxid mit Wasserdampf. *Helv. Chim. Acta* **1967**, *50*, 2040–2053, doi:10.1002/hlca.19670500738.
618. Dai, L.; Long, X.F.; Lou, B.; Wu, J. Thermal cycling stability of thermochemical energy storage system Ca(OH)2/CaO. *Appl. Therm. Eng.* **2018**, *133*, 261–268, doi:10.1016/j.applthermaleng.2018.01.059.
619. F. Schaube, A. Kohzer, J. Schutz, A. Worner, H.M.-S. De- and rehy- dration of Ca(OH)2 in a reactor with direct heat transfer for thermochemical heat storage. Part A: experimental results. *Chem. Eng. Res. Des.* **2013**, *91*, 856–864.
620. Fujii, I.; Tsuchiya, K.; Higano, M.; Yamada, J. Studies of an energy storage system by use of the reversible chemical reaction: CaO + H2O ⇌ Ca(OH)2. *Sol. Energy* **1985**, *34*, 367–377, doi:10.1016/0038-092X(85)90049-0.
621. Yan, J.; Zhao, C.Y. Experimental study of CaO/Ca(OH)2 in a fixed-bed reactor for thermochemical heat storage. *Appl. Energy* **2016**, *175*, 277–284, doi:10.1016/J.APENERGY.2016.05.038.
622. Cosquillo Mejia, A.; Afflerbach, S.; Linder, M.; Schmidt, M. Experimental analysis of encapsulated CaO/Ca(OH)2 granules as thermochemical storage in a novel moving bed reactor. *Appl. Therm. Eng.* **2020**, *169*, 114961, doi:10.1016/J.APPLTHERMALENG.2020.114961.
623. X.F. Long, L. Dai, B. Lou, J.W. The kinetics research of thermochemical energy storage system Ca(OH)(2)/CaO. *Int. J. Energy Res.* **2017**, *41*, 1004–1013.

624. L. Andre, S. Abanades, G. Flamant Screening of thermochemical systems based on solid-gas reversible reactions for high temperature solar thermal energy storage,. *Renew. Sustain. Energy Rev.* **2016**, *64*, 707–715.

625. Yuan, Y.; Li, Y.; Zhao, J. Development on thermochemical energy storage based on CaO-based materials: A review. *Sustain.* **2018**, *10*, doi:10.3390/su10082660.

626. Funayama, S.; Takasu, H.; Zamengo, M.; Kariya, J.; Kim, S.T.; Kato, Y. Composite material for high-temperature thermochemical energy storage using calcium hydroxide and ceramic foam. *Energy Storage* **2019**, *1*, e53, doi:10.1002/est2.53.

627. H. Ogura, T. Yamamoto, H.K. Efficiencies of CaO/H2O/Ca(OH)2 chemical heat pump for heat storing and heating/cooling. *Energy* **2003**, *28*, 1479–1493.

628. M. Arjmand, L. Liu, I. Neretnieks Exergetic efficiency of high-temperature-lift chemical heat pump (CHP) based on CaO/CO2 and CaO/H2O working pairs,. *Int. J. Energy Res.* **2013**, *37(9)*, 1122–1131.

629. Mette, B.; Kerskes, H.; Drück, H.; Müller-Steinhagen, H. New highly efficient regeneration process for thermochemical energy storage. *Appl. Energy* **2013**, *109*, 352–359, doi:10.1016/j.apenergy.2013.01.087.

630. Libowitz, G.G. Metal hydrides for thermal energy storage. **1974**, 322–325.

631. Humphries, T.D.; Sheppard, D.A.; Li, G.; Rowles, M.R.; Paskevicius, M.; Matsuo, M.; Aguey-Zinsou, K.F.; Sofianos, M.V.; Orimo, S.I.; Buckley, C.E. Complex hydrides as thermal energy storage materials: Characterisation and thermal decomposition of Na2Mg2NiH6. *J. Mater. Chem. A* **2018**, *6*, 9099–9108, doi:10.1039/c8ta00822a.

632. Ward, P.A.; Corgnale, C.; Teprovich, J.A.; Motyka, T.; Hardy, B.; Sheppard, D.; Buckley, C.; Zidan, R. Technical challenges and future direction for high-efficiency metal hydride thermal energy storage systems. *Appl. Phys. A Mater. Sci. Process.* **2016**, *122*, doi:10.1007/s00339-016-9909-x.

633. Liu, Y.; He, J.; Teprovich, J.A.; Zidan, R.; Ward, P.A. High temperature thermal energy storage in the CaAl2 system. *J. Alloys Compd.* **2017**, *735*, 2611–2615, doi:10.1016/j.jallcom.2017.10.191.

634. Javadian, P.; Gharibdoust, S.H.P.; Li, H.W.; Sheppard, D.A.; Buckley, C.E.; Jensen, T.R. Reversibility of LiBH4 Facilitated by the LiBH4-Ca(BH4)2 Eutectic. *J. Phys. Chem. C* **2017**, *121*, 18439–18449, doi:10.1021/acs.jpcc.7b06228.

635. Nguyen, T.T.; Sheppard, D.A.; Buckley, C.E. Lithium imide systems for high temperature heat storage in concentrated solar thermal systems. *J. Alloys Compd.* **2017**, *716*, 291–298, doi:10.1016/j.jallcom.2017.04.208.

636. Ouyang, L.; Liu, F.; Wang, H.; Liu, J.; Yang, X.-S.; Sun, L.; Zhu, M. Magnesium-based hydrogen storage compounds: A review. *J. Alloys Compd.* **2020**, *832*, 154865, doi:10.1016/J.JALLCOM.2020.154865.

637. Sheppard, D.A.; Buckley, C.E. The potential of metal hydrides paired with compressed hydrogen as thermal energy storage for concentrating solar power plants. *Int. J. Hydrogen Energy* **2019**, *44*, 9143–9163, doi:10.1016/J.IJHYDENE.2019.01.271.

638. Manickam, K.; Mistry, P.; Walker, G.; Grant, D.; Buckley, C.E.; Humphries, T.D.; Paskevicius, M.; Jensen, T.; Albert, R.; Peinecke, K.; et al. Future perspectives of thermal energy storage with metal hydrides. *Int. J. Hydrogen Energy* **2019**, *44*, 7738–7745, doi:10.1016/J.IJHYDENE.2018.12.011.

639. CJ., F. Experimental study of salt hydrates for thermochemical seasonal heat storage. *Tech. Univ. Eindhoven* **2016**.

640. Mukherjee, A.; Majumdar, R.; Saha, S.K.; Kumar, L.; Subramaniam, C. Assessment of open thermochemical energy storage system performance for low temperature heating applications. *Appl. Therm. Eng.* **2019**, *156*, 453–470, doi:10.1016/j.applthermaleng.2019.04.096.

641. K.E. N'Tsoukpoe, T. Schmidt, H.U. Rammelberg, B.A. Watts, W.K.L.R. A systematic multi-step screening of numerous salt hydrates for low temperature thermochemical energy storage. *Appl. Energy* **2014**, *124*.

642. Tanguy G, Papillon P, P.C. Seasonal storage coupled to a solar combisystem:Dynamic simulations for process dimensioning. In Proceedings of the In: Proceedings of the EUROSUN-2nd international conference on solar heating, cooling and buildings; 2010.

643. Fopah-lele, A.; Gaston, J. Solar Energy Materials & Solar Cells A review on the use of SrBr 2 · 6H 2 O as a potential material for low temperature energy storage systems and building applications. *Sol. Energy Mater. Sol. Cells* **2017**, *164*, 175–187, doi:10.1016/j.solmat.2017.02.018.

644. Lahmidi H, Mauran S, G. V. Definition, test and simulation of a thermochemical

storage process adapted to solar thermal systems. *Sol Energy* **2006**, *80*, 883–93.

645. Mauran, S.; Lahmidi, H.; Goetz, V. Solar heating and cooling by a thermochemical process. First experiments of a prototype storing 60 kW h by a solid/gas reaction. *Sol. Energy* **2008**, *82*, 623–636, doi:10.1016/J.SOLENER.2008.01.002.
646. Clark, R.J.; Mehrabadi, A.; Farid, M. State of the art on salt hydrate thermochemical energy storage systems for use in building applications. *J. Energy Storage* **2020**, *27*, 101145, doi:10.1016/j.est.2019.101145.
647. Humphries, T.D.; Møller, K.T.; Rickard, W.D.A.; Sofianos, M.V.; Liu, S.; Buckley, C.E.; Paskevicius, M. Dolomite: A low cost thermochemical energy storage material. *J. Mater. Chem. A* **2019**, *7*, 1206–1215, doi:10.1039/c8ta07254j.
648. Serrano, D.; Horvat, A.; Sobrino, C.; Sánchez-Delgado, S. Thermochemical conversion of C. cardunculus L. in nitrate molten salts. *Appl. Therm. Eng.* **2019**, *148*, 136–146, doi:10.1016/J.APPLTHERMALENG.2018.11.047.
649. Benitez-Guerrero, M.; Sarrion, B.; Perejon, A.; Sanchez-Jimenez, P.E.; Perez-Maqueda, L.A.; Manuel Valverde, J. Large-scale high-temperature solar energy storage using natural minerals. *Sol. Energy Mater. Sol. Cells* **2017**, *168*, 14–21, doi:10.1016/J.SOLMAT.2017.04.013.
650. Barker R. The reversibility of the reaction CaCO3(s)⇌CaO(s)+CO2(g). *J Appl Chem Biotechnol* **1973**, *23*, 733–742.
651. Schmidt, M.; Linder, M. Power generation based on the Ca(OH)2/ CaO thermochemical storage system – Experimental investigation of discharge operation modes in lab scale and corresponding conceptual process design. *Appl. Energy* **2017**, *203*, 594–607, doi:10.1016/j.apenergy.2017.06.063.
652. A. Fopah-Lele, C. Rohde, K. Neumann, T. Tietjen, T. Rönnebeck, K.E. N'Tsoukpoe, T. Osterland, O. Opel, W.K.L. Ruck Lab-scale experiment of a closed thermo- chemical heat storage system including honeycomb heat exchanger,. *Energy* **2016**, *114*, 225–238.
653. Michel, B.; Neveu, P.; Mazet, N. Comparison of closed and open thermochemical processes, for long-term thermal energy storage applications. *Energy* **2014**, *72*, 702–716, doi:10.1016/j.energy.2014.05.097.
654. Eigenberger G, R.W. Catalytic fixed-bed reactors. *Ullmann's Encycl. Ind. Chem. Weinheim, Ger. Wiley–VCH Verlag;* 2000.

655. Zondag HA, Schuitema R, Bleijendaal LPJ, Gores JC, van Essen M, van Helden W, B.M. R&D of thermochemical reactor concepts to enable heat storage of solar energy in residential houses. In Proceedings of the Paper presented at the 3rd International Conference on Energy Sust.
656. Farcot, L.; Le Pierrès, N.; Michel, B.; Fourmigué, J.-F.; Papillon, P. Numerical investigations of a continuous thermochemical heat storage reactor. *J. Energy Storage* **2018**, *20*, 109–119, doi:10.1016/J.EST.2018.08.020.
657. Abedin AH, R.M. Assessment of a closed thermochemical energy storage using energy and exergy methods. *Appl. Energy* **2011**.
658. Belz, K.; Kuznik, F.; Werner, K.F.; Schmidt, T.; Ruck, W.K.L. *Thermal energy storage systems for heating and hot water in residential buildings*; Woodhead Publishing Limited, 2014; ISBN 9781782420965.
659. Welteroth, J.; Mittelbach, W. High Energy Density Sorption Heat Storage for Solar Space Heating (HYDES HEAT STORAGE), final report of EU project in the JOULE III program.
660. Ciconkov, R. Refrigerants: There is still no vision for sustainable solutions. *Int. J. Refrig.* 2018.
661. Li, T.X.; Wang, R.Z.; Yan, T.; Ishugah, T.F. Integrated energy storage and energy upgrade, combined cooling and heating supply, and waste heat recovery with solid-gas thermochemical sorption heat transformer. *Int. J. Heat Mass Transf.* **2014**, *76*, 237–246, doi:10.1016/j.ijheatmasstransfer.2014.04.046.
662. Yan, T.; Wang, C.Y.; Li, D. Performance analysis of a solid-gas thermochemical composite sorption system for thermal energy storage and energy upgrade. *Appl. Therm. Eng.* **2019**, *150*, 512–521, doi:10.1016/j.applthermaleng.2019.01.004.
663. Yang, S.; Deng, C.; Liu, Z. Optimal design and analysis of a cascade LiBr/H 2 O absorption refrigeration/transcritical CO 2 process for low-grade waste heat recovery. *Energy Convers. Manag.* **2019**, *192*, 232–242, doi:10.1016/j.enconman.2019.04.045.
664. Nasri, M.; Burger, I.; Michael, S.; Friedrich, H.E. Waste heat recovery for fuel cell electric vehicle with thermochemical energy storage. *2016 11th Int. Conf. Ecol. Veh. Renew. Energies, EVER 2016* **2016**, 1–6, doi:10.1109/EVER.2016.7476439.
665. Kuwata, K.; Masuda, S.; Kobayashi, N.; Fuse, T.; Okamura, T. *Thermochemical*

Heat Storage Performance in the Gas/Liquid-Solid Reactions of $SrCl_2$ with NH_3; 2016; Vol. 07;

666. Jarimi, H.; Aydin, D.; Yanan, Z.; Ozankaya, G.; Chen, X.; Riffat, S. Review on the recent progress of thermochemical materials and processes for solar thermal energy storage and industrial waste heat recovery. *Int. J. Low-Carbon Technol.* **2019**, *14*, 44–69, doi:10.1093/ijlct/cty052.

667. Kerkes, H.; Sommr, K.; Muller, H. *Monosorp – ein integrales konzept zur solarthermischen gebaudeheizung mit sorptionwarmespeicher. Technology report*; 2006; ISBN 978-3-934681-69-9.

668. Kerskes, H.; Asenbeck, S.; Bertsch, F.; Drück, H.; Mette, B. Development of a thermo-chemical energy storage for solar thermal applications. *30th ISES Bienn. Sol. World Congr. 2011, SWC 2011* **2011**, *6*, 4679–4685, doi:10.18086/swc.2011.29.14.

669. Stitou, D.; Mazet, N.; Mauran, S. Experimental investigation of a solid/gas thermochemical storage process for solar air-conditioning. *Energy* **2012**, *41*, 261–270, doi:10.1016/j.energy.2011.07.029.

670. Wagner, Waldemar; Jähnig, Dagmar; Hausner, Robert; Isaksson, C. Modularer Energiespeicher nach dem Sorptionsprinzip mit hoher Energiedichte (MODESTORE). In *final report of a project in the framework of the Austrian program 'Haus der Zukunft', contract number: 805768/7024 KA/TU*,; 2006.

671. Wagner, Waldemar; Jähnig, Dagmar; Hausner, Robert; Isaksson, C. Final reports EU project MODESTORE (Modular High Energy Density Sorption Storage), 5th framework program DG TREN, contract number: NNE5/2001/979, final reports, Deliverable D6: System prototype storage module (Austria), Deliverable D9: Installed system eq.

672. Lass-Seyoum, A.; Blicker, M.; Borozdenko, D.; Friedrich, T.; Langhof, T. Transfer of laboratory results on closed sorption thermo- chemical energy storage to a large-scale technical system. *Energy Procedia* **2012**, *30*, 310–320, doi:10.1016/J.EGYPRO.2012.11.037.

673. van Helden WGJ. Combined Development of Compact Thermal Energy Storage Technologies. **2015**.

674. Sanner, B.; Karytsas, C.; Mendrinos, D.; Rybach, L. Current status of ground source

heat pumps and underground thermal energy storage in Europe. *Geothermics* **2003**, doi:10.1016/S0375-6505(03)00060-9.

675. Zalba, B.; Marín, J.M.; Cabeza, L.F.; Mehling, H. Review on thermal energy storage with phase change: Materials, heat transfer analysis and applications. *Appl. Therm. Eng.* 2003.

676. Liu, M.; Steven Tay, N.H.; Bell, S.; Belusko, M.; Jacob, R.; Will, G.; Saman, W.; Bruno, F. Review on concentrating solar power plants and new developments in high temperature thermal energy storage technologies. *Renew. Sustain. Energy Rev.* 2016.

677. Hewitt, N.J. Heat pumps and energy storage - The challenges of implementation. *Appl. Energy* **2012**, doi:10.1016/j.apenergy.2010.12.028.

678. Wilson, G.; Soderholm, L. GROUND SOURCE HEAT PUMPS. In Proceedings of the Papers - Rural Electric Power Conference; 1984.

679. Datas, A.; Zeneli, M.; Del Cañizo, C.; Malgarinos, I.; Nikolopoulos, A.; Nikolopoulos, N.; Karellas, S.; Martí, A. Molten silicon storage of concentrated solar power with integrated thermophotovoltaic energy conversion. In Proceedings of the AIP Conference Proceedings; 2018.

680. Datas, A.; Ramos, A.; Martí, A.; del Cañizo, C.; Luque, A. Ultra high temperature latent heat energy storage and thermophotovoltaic energy conversion. *Energy* **2016**, doi:10.1016/j.energy.2016.04.048.

681. Cammarata, A.; Verda, V.; Sciacovelli, A.; Ding, Y. Hybrid strontium bromide-natural graphite composites for low to medium temperature thermochemical energy storage: Formulation, fabrication and performance investigation. *Energy Convers. Manag.* **2018**, *166*, 233–240, doi:10.1016/j.enconman.2018.04.031.

682. Fitó, J.; Coronas, A.; Mauran, S.; Mazet, N.; Perier-Muzet, M.; Stitou, D. Hybrid system combining mechanical compression and thermochemical storage of ammonia vapor for cold production. *Energy Convers. Manag.* **2019**, *180*, 709–723, doi:10.1016/J.ENCONMAN.2018.11.019.

683. Zhou, Q.; Du, D.; Lu, C.; He, Q.; Liu, W. A review of thermal energy storage in compressed air energy storage system. *Energy* **2019**, *188*, 115993, doi:10.1016/j.energy.2019.115993.

684. Wu, S.; Zhou, C.; Doroodchi, E.; Moghtaderi, B. A unique phase change redox

cycle using CuO/Cu 2 O for utility-scale energy storage. *Energy Convers. Manag.* **2019**, *188*, 366–380, doi:10.1016/j.enconman.2019.03.055.

685. Rodriguez-Hidalgo, M.C.; Rodriguez-Aumente, P.A.; Lecuona-Neumann, A.; Legrand, M. Thermo-chemical storage for renewable energies based on absorption: Getting a uniform injection into the grid. *Appl. Therm. Eng.* **2019**, *146*, 338–345, doi:10.1016/J.APPLTHERMALENG.2018.09.096.

686. Papadopoulos, A.M. "Forty years of regulations on the thermal performance of the building envelope in Europe: Achievements, perspectives and challenges." 942-952. *Energy Build.* **2016**, *127*.

687. Sozer, H. Improving energy efficiency through the design of the building envelope. *Build. Environ.* **2010**, *45*, 2581–2593, doi:10.1016/j.buildenv.2010.05.004.

688. Sanhudo, L.; Ramos, N.M.M.; Poças Martins, J.; Almeida, R.M.S.F.; Barreira, E.; Simões, M.L.; Cardoso, V. Building information modeling for energy retrofitting – A review. *Renew. Sustain. Energy Rev.* 2018.

689. Cascone, S.; Catania, F.; Gagliano, A.; Sciuto, G. A comprehensive study on green roof performance for retrofitting existing buildings. *Build. Environ.* **2018**, doi:10.1016/j.buildenv.2018.03.052.

690. Rabani, M.; Madessa, H.B.; Nord, N. A state-of-art review of retrofit interventions in buildings towards nearly zero energy level. In Proceedings of the Energy Procedia; 2017.

691. Colinart, T.; Bendouma, M.; Glouannec, P. Building renovation with prefabricated ventilated façade element: A case study. *Energy Build.* **2019**, *186*, 221–229, doi:10.1016/J.ENBUILD.2019.01.033.

692. Lai, C.-M.; Hokoi, S. Solar façades: A review. *Build. Environ.* **2015**, *91*, 152–165, doi:10.1016/J.BUILDENV.2015.01.007.

693. Zhang, T.; Tan, Y.; Yang, H.; Zhang, X. The application of air layers in building envelopes: A review. *Appl. Energy* **2016**, *165*, 707–734, doi:10.1016/J.APENERGY.2015.12.108.

694. Zhang, R.; Mirzaei, P.A.; Carmeliet, J. Prediction of the surface temperature of building-integrated photovoltaics: Development of a high accuracy correlation using computational fluid dynamics. *Sol. Energy* **2017**, *147*, 151–163, doi:10.1016/j.solener.2017.03.023.

695. Becker, G.; Krippner, R. *Gebäudeintegrierte Solartechnik Architektur gestalten mit Photovoltaik und Solarthermie*; 2016; ISBN 9783955533250.
696. S. Dubey, J.N. Sarvaiya, B. Seshadri Temperature Dependent Photovoltaic (PV) Efficiency and Its Effect on PV Production in the World. *Energy Procedia* **2013**, *33 (2013)*, 311–321.
697. Mingotti, N.; Chenvidyakarn, T.; Woods, A.W. The fluid mechanics of the natural ventilation of a narrow-cavity double-skin facade. *Build. Environ.* **2011**, *46*, 807–823, doi:10.1016/j.buildenv.2010.09.015.
698. Kaplani, E.; Kaplanis, S. Thermal modelling and experimental assessment of the dependence of PV module temperature on wind velocity and direction, module orientation and inclination. *Sol. Energy* **2014**, *107*, 443–460, doi:10.1016/j.solener.2014.05.037.
699. Agathokleous, R.A.; Kalogirou, S.A. Double skin facades (DSF) and building integrated photovoltaics (BIPV): A review of configurations and heat transfer characteristics. *Renew. Energy* **2016**, *89*, 743–756, doi:10.1016/j.renene.2015.12.043.
700. Lai, C.M.; Hokoi, S. Experimental and numerical studies on the thermal performance of ventilated BIPV curtain walls. *Indoor Built Environ.* **2017**, doi:10.1177/1420326X15611194.
701. Gan, G. Effect of air gap on the performance of building-integrated photovoltaics. *Energy* **2009**, doi:10.1016/j.energy.2009.04.003.
702. Getu, H.; Yang, T.; Athienitis, a K.; Fung, A. Computational Fluid Dynamics (CFD) Analysis of Air Based Building Integrated Photovoltaic Thermal (BIPV/T) Systems for Efficient Performance. *Int. Build. Perform. Simul. Assoc. - eSIM Conf.* **2014**.
703. Kant, K.; Anand, A.; Shukla, A.; Sharma, A. Heat transfer study of building integrated photovoltaic (BIPV) with nano-enhanced phase change materials. *J. Energy Storage* **2020**, *30*, 101563, doi:10.1016/j.est.2020.101563.
704. Lau, S.-K.; Zhao, Y.; Lau, S.S.Y.; Yuan, C.; Shabunko, V. An Investigation on Ventilation of Building-Integrated Photovoltaics System Using Numerical Modeling. *J. Sol. Energy Eng.* **2019**, *142*, doi:10.1115/1.4044623.
705. Mohammad, C.; Karava, P.; Savory, E. CFD simulations for evaluation of forced

convective heat transfer coefficients on Photovoltaic / Thermal systems integrated on the windward roof surface of a low-rise building. *Wind Eng.* **2010**.

706. Blocken, B.; Defraeye, T.; Derome, D.; Carmeliet, J. High-resolution CFD simulations for forced convective heat transfer coefficients at the facade of a low-rise building. *Build. Environ.* **2009**, doi:10.1016/j.buildenv.2009.04.004.
707. Roeleveld, D.; Kumar, R.; Naylor, D.; Fung, A.S. A CFD Study of Natural Convection Inside a BIPV/T System. *Proc. eSim 2016 Build. Perform. Simul. Conf.* **2016**, 319–326.
708. Sandberg, M.; Moshfegh, B. Buoyancy-induced air flow in photovoltaic facades: Effect of geometry of the air gap and location of solar cell modules. *Build. Environ.* **2002**, *37*, 211–218, doi:10.1016/S0360-1323(01)00025-7.
709. Zhang, R.; Gan, Y.; Mirzaei, P.A. A new regression model to predict BIPV cell temperature for various climates using a high-resolution CFD microclimate model. *Adv. Build. Energy Res.* **2020**, doi:10.1080/17512549.2019.1654917.
710. Thang, T. V.; Ahmed, A.; Kim, C.I.; Park, J.H. Flexible System Architecture of Stand-Alone PV Power Generation with Energy Storage Device. *IEEE Trans. Energy Convers.* **2015**, *30*, 1386–1396, doi:10.1109/TEC.2015.2429145.
711. Li, P.; Dargaville, R.; Cao, Y.; Li, D.Y.; Xia, J. Storage Aided System Property Enhancing and Hybrid Robust Smoothing for Large-Scale PV Systems. *IEEE Trans. Smart Grid* **2017**, *8*, 2871–2879, doi:10.1109/TSG.2016.2611595.
712. Ould Amrouche, S.; Rekioua, D.; Rekioua, T.; Bacha, S. Overview of energy storage in renewable energy systems. *Int. J. Hydrogen Energy* **2016**, *41*, 20914–20927, doi:10.1016/J.IJHYDENE.2016.06.243.
713. Aneke, M.; Wang, M. Energy storage technologies and real life applications – A state of the art review. *Appl. Energy* **2016**, *179*, 350–377, doi:10.1016/j.apenergy.2016.06.097.
714. Eurobat Battery energy storage in the EU. *Batter. Energy Storage EU* **2016**, 36.
715. Hammami, M.; Torretti, S.; Grimaccia, F.; Grandi, G. Thermal and Performance Analysis of a Photovoltaic Module with an Integrated Energy Storage System. *Appl. Sci.* **2017**, *7*, 1107, doi:10.3390/app7111107.
716. Wang, Q.; Ping, P.; Zhao, X.; Chu, G.; Sun, J.; Chen, C. Thermal runaway caused fire and explosion of lithium ion battery. *J. Power Sources* **2012**, *208*, 210–224,

doi:10.1016/j.jpowsour.2012.02.038.

717. Chen, D.; Jiang, J.; Kim, G.H.; Yang, C.; Pesaran, A. Comparison of different cooling methods for lithium ion battery cells. *Appl. Therm. Eng.* **2016**, doi:10.1016/j.applthermaleng.2015.10.015.

718. Zhao, R.; Zhang, S.; Liu, J.; Gu, J. A review of thermal performance improving methods of lithium ion battery: Electrode modification and thermal management system. *J. Power Sources* 2015.

719. Liu, H.; Wei, Z.; He, W.; Zhao, J. Thermal issues about Li-ion batteries and recent progress in battery thermal management systems: A review. *Energy Convers. Manag.* 2017.

720. Arora, S. Selection of thermal management system for modular battery packs of electric vehicles: A review of existing and emerging technologies. *J. Power Sources* 2018.

721. Bhattacharjee, A.; Mohanty, R.K.; Ghosh, A. Design of an Optimized Thermal Management System for Li-Ion Batteries under Different Discharging Conditions. *Energies* **2020**, *13*, 5695, doi:10.3390/en13215695.

722. Akbarzadeh, M.; Jaguemont, J.; Kalogiannis, T.; Karimi, D.; He, J.; Jin, L.; Xie, P.; Van Mierlo, J.; Berecibar, M. A novel liquid cooling plate concept for thermal management of lithium-ion batteries in electric vehicles. *Energy Convers. Manag.* **2021**, *231*, 113862, doi:10.1016/j.enconman.2021.113862.

723. Ma, S.; Jiang, M.; Tao, P.; Song, C.; Wu, J.; Wang, J.; Deng, T.; Shang, W. Temperature effect and thermal impact in lithium-ion batteries: A review. *Prog. Nat. Sci. Mater. Int.* 2018.

724. Gao, T.; Lu, W. Mechanism and effect of thermal degradation on electrolyte ionic diffusivity in Li-ion batteries: A molecular dynamics study. *Electrochim. Acta* **2019**, doi:10.1016/j.electacta.2019.134791.

725. Emre Gümüs su, Ö.E.⇑; Köksal, M. 3-D CFD modeling and experimental testing of thermal behavior of a Li-Ion battery. **2017**, *120*, 484–495, doi:10.1016/j.applthermaleng.2017.04.017.

726. Huang, Y.H.; Cheng, W.L.; Zhao, R. Thermal management of Li-ion battery pack with the application of flexible form-stable composite phase change materials. *Energy Convers. Manag.* **2019**, doi:10.1016/j.enconman.2018.12.064.

727. Jilte, R.D.; Kumar, R. Numerical investigation on cooling performance of Li-ion battery thermal management system at high galvanostatic discharge. *Eng. Sci. Technol. an Int. J.* **2018**, *21*, 957–969, doi:10.1016/j.jestch.2018.07.015.
728. Li, X.; He, F.; Ma, L. Thermal management of cylindrical batteries investigated using wind tunnel testing and computational fluid dynamics simulation. *J. Power Sources* **2013**, *238*, 395–402, doi:10.1016/j.jpowsour.2013.04.073.
729. Liu, X.; Ai, W.; Naylor Marlow, M.; Patel, Y.; Wu, B. The effect of cell-to-cell variations and thermal gradients on the performance and degradation of lithium-ion battery packs. *Appl. Energy* **2019**, doi:10.1016/j.apenergy.2019.04.108.
730. Lin, L.Y.; Ho, K.C. Dye-sensitized solar cells. In *Encyclopedia of Modern Optics*; 2018 ISBN 9780128149829.
731. Perez-Arriaga, I.J.; Batlle, C. Impacts of Intermittent Renewables on Electricity Generation System Operation. *Econ. Energy Environ. Policy* **2012**, *1*, doi:10.5547/2160-5890.1.2.1.
732. Agathokleous, R.A.; Kalogirou, S.A. Part I: Thermal analysis of naturally ventilated BIPV system: Experimental investigation and convective heat transfer coefficients estimation. *Sol. Energy* **2018**, doi:10.1016/j.solener.2018.02.048.
733. S. Nižetić, F. Grubišić-Čabo, I. Marinić-Kragić, A.M. Papadopoulos Experimental and numerical investigation of a backside convective cooling mechanism on photovoltaic panels. *Energy* **2016**, *111*, 211–225.
734. Ma, T.; Zhao, J.; Li, Z. Mathematical modelling and sensitivity analysis of solar photovoltaic panel integrated with phase change material. *Appl. Energy* **2018**, *228*, 1147–1158, doi:10.1016/j.apenergy.2018.06.145.
735. Kant, K.; Shukla, A.; Sharma, A.; Biwole, P.H. Heat transfer studies of photovoltaic panel coupled with phase change material. *Sol. Energy* **2016**, *140*, 151–161, doi:10.1016/J.SOLENER.2016.11.006.
736. Li, M.; Ma, T.; Liu, J.; Li, H.; Xu, Y.; Gu, W.; Shen, L. Numerical and experimental investigation of precast concrete facade integrated with solar photovoltaic panels. *Appl. Energy* **2019**, doi:10.1016/j.apenergy.2019.113509.
737. Evans, D.L. Simplified method for predicting photovoltaic array output. *Sol. Energy* **1981**, *27*, 555–560, doi:10.1016/0038-092X(81)90051-7.
738. Krimotat, A.; Sedarat, H. Structural modeling. *Bridg. Eng. Handb. Fundam. Second*

Ed. **2014**, 253–269, doi:10.1201/b15616.

739. Afonso, A.M.; Oliveira, M.S.N.; Oliveira, P.J.; Alves, M.A.; Pinho, F.T. *The Finite Volume Method in Computational Rheology*; 2012; Vol. M; ISBN 9783319168739.
740. Incropera, F.P.; DeWitt, D.P.; Bergman, T.L.; Lavine, A.S. heat and mass transfer - Incropera 6e. *Fundam. Heat Mass Transf.* 2007.
741. REYNOLDS TRANSPORT THEOREM. In *Multiphase Flow and Fluidization*; 1994.
742. Incropera, F.P. *Incropera - EN - Fundamentals of Heat and Mass Transfer*; 2015; ISBN 9781604138795.
743. Chhabra, R.P. Non-Newtonian fluids: An introduction. In *Rheology of Complex Fluids*; 2010 ISBN 9781441964939.
744. Notton, G.; Cristofari, C.; Mattei, M.; Poggi, P. Modelling of a double-glass photovoltaic module using finite differences. *Appl. Therm. Eng.* **2005**, *25*, 2854–2877, doi:10.1016/j.applthermaleng.2005.02.008.
745. Bazilian, M.D.; Kamalanathan, H.; Prasad, D.K. Thermographic analysis of a building integrated photovoltaic system. *Renew. Energy* **2002**, *26*, 449–461, doi:10.1016/S0960-1481(01)00142-2.
746. Nižetić, S.; Grubišić- Čabo, F.; Marinić-Kragić, I.; Papadopoulos, A.M. Experimental and numerical investigation of a backside convective cooling mechanism on photovoltaic panels. *Energy* **2016**, *111*, 211–225, doi:10.1016/j.energy.2016.05.103.
747. Churchill, S.W.; Chu, H.H.S. Correlating equations for laminar and turbulent free convection from a vertical plate. *Int. J. Heat Mass Transf.* **1975**, doi:10.1016/0017-9310(75)90243-4.
748. Jones, A.D.; Underwood, C.P. A thermal model for photovoltaic systems. *Fuel Energy Abstr.* **2002**, *43*, 199, doi:10.1016/s0140-6701(02)85831-3.
749. Michele, C. Termofluidodinamica di deflussi turbolenti. *Dip. dell'Innovazione Ind. e Digit. Univ. degli Stud. di Palermo*.
750. Di, F. Fondamenti di termofluidodinamica computazionale. **2014**.
751. Ma, T.; Yang, H.; Gu, W.; Li, Z.; Yan, S. Development of walkable photovoltaic floor tiles used for pavement. *Energy Convers. Manag.* **2019**, *183*, 764–771, doi:10.1016/J.ENCONMAN.2019.01.035.

752. Algazar, M.M.; AL-monier, H.; EL-halim, H.A.; Salem, M.E.E.K. Maximum power point tracking using fuzzy logic control. *Int. J. Electr. Power Energy Syst.* **2012**, *39*, 21–28, doi:10.1016/J.IJEPES.2011.12.006.

753. Lo Brano, V.; Ciulla, G. An efficient analytical approach for obtaining a five parameters model of photovoltaic modules using only reference data. *Appl. Energy* **2013**, doi:10.1016/j.apenergy.2013.06.046.